Silicon Phthalocyanines: Development of Structure-Property Relationships and Integration Into Organic Thin-Film Transistors and Sensors

By
Benjamin King

A THESIS
SUBMITTED TO THE UNIVERSITY OF OTTAWA
IN PARTIAL FULFILMENT OF THE REQUIREMENTS FOR THE DOCTOR OF PHILOSOPHY DEGRERE IN CHEMICAL ENGINEERING

DEPARTMENT OF CHEMICAL AND BIOLOGICAL ENGINEERING
UNIVERSITY OF OTTAWA

Abstract

Silicon phthalocyanines (R_2-SiPcs) are an emerging class of high-performance n-type or ambipolar organic semiconductors which have found application in organic electronic devices, including organic thin-film transistors (OTFTs), organic photovoltaics (OPVs) and organic light-emitting diodes (OLEDs). Owing to their tetravalent silicon metal centre, R_2-SiPcs can be substituted with a range of axial ligands including phenols, carboxylic acids, and silanes to tune their intermolecular interactions, optical properties, electronic properties and solubility. While early reports of R_2-SiPcs have demonstrated promising results, the relationship between their structure and performance in OTFTs is poorly understood. Additionally, many OTFTs with R_2-SiPcs as semiconductor only demonstrate n-type behaviour under inert atmospheres due to their shallow lowest unoccupied orbital level below -4.1 eV making them susceptible to electron trapping by moisture and oxygen. This thesis presents developments in both the understanding of how R_2-SiPc structure influences performance, device engineering and exploration of these materials in ammonia sensors. First, I develop of structure-property relationships for a catalogue of fifteen R_2-SiPcs integrated into OTFTs including eleven materials used in OTFTs for the first time. I then explore the influence of dielectric surface chemistry on the texture of R_2-SiPc films and their resulting performance in OTFTs using silane self-assembled monolayers and *para*-sexiphenyl to understand the weak epitaxial growth behaviour of this class of materials. Next, I report eight novel peripherally fluorinated and axially substituted silicon phthalocyanines (R_2-F_XSiPcs) to investigate the influence of peripheral and axial fluorination on air-stable electron transport and determine the threshold for achieving air-stable n-type OTFTs. Finally, I integrate R_2-F_XSiPcs into organic heterojunction ammonia gas sensors to understand the influence of peripheral fluorination on the majority charge carrier in this device architecture.

Résumé

Les phtalocyanines de silicium (R_2-SiPc) sont une classe de semiconducteur organique à hautes performances, de type n ou ambipolaire, qui ont trouvé application dans les transistors à couches minces organiques (OTFT pour *Organic Thin-Film Transistors*), les cellules photovoltaïques organiques (OPVs pour *Organic Photovoltaics*) et les diodes électroluminescentes organiques (OLEDs pour *Organic Light Emitting Diodes*). Grâce à leur centre métallique tétravalent de silicium, les R_2-SiPc peuvent être fonctionnalisées par plusieurs substituants axiaux tels que les phénols, les acides carboxyliques et les silanes afin de modifier les interactions intermoléculaires, les propriétés optiques et électroniques ainsi que la solubilité. Bien que les premiers travaux sur les R_2-SiPcs aient montrés des résultats prometteurs, la relation entre leur structure chimique et leurs performances dans des OTFTs n'est pas bien comprise. De plus, la plupart des transistors à base de R_2-SiPc ne montrent qu'un caractère de type n sous atmosphère inerte à cause de leur orbitale moléculaire non-occupée la plus haute (LUMO pour *Lowest Unccupied Molecular Orbital*) peu profonde, en dessous de -4.1 eV, qui les rend susceptibles au piégeage d'électrons par l'humidité et l'oxygène. Cette thèse présente les développements de notre compréhension de l'impact de la structure des R_2-SiPcs sur leurs propriétés et les performances des transistors à couches minces organiques, l'ingénierie des dispositifs et l'utilisation de ces matériaux dans des capteurs d'ammoniac. En premier, je développe les relations entre la structure et la performance pour une catalogue de quinze R_2-SiPc intégrées dans des transistors OTFT, dont onze pour qui cette application est une première. Ensuite, j'étudie l'influence de la chimie de surface de la couche diélectrique sur les couches de R_2-SiPc et leurs performances dans des transistors OTFT fonctionnalisés par des monocouches de silanes et le *para*-sexiphenyl pour comprendre la faible croissance épitaxiale de ces matériaux. Ensuite, j'étudie huit nouveaux dérivés de phtalocyanines de silicium fluorés en positions équatoriale et axiale (R_2-F_XSiPcs) pour étudier l'influence du degré de fluoration de la molécule sur la stabilité du transport des électrons à l'air et ainsi déterminer la limite permettant d'obtenir des OTFTs de type n stables à l'air. Enfin, j'intègre ces R_2-F_XSiPcs dans des capteurs de gaz en couches minces à hétérojonction organique pour la détection d'ammoniac afin d'étudier l'influence des fluors équatoriaux et axiaux sur le porteur de charge majoritaire dans cette architecture.

Acknowledgements

I would first like to thank my supervisor Prof. Benoît Lessard, who enabled me to achieve so much during my time at the University of Ottawa. The freedom I had to pursue my own research ideas provided me with incredibly valuable experiences that I will carry with me as I pursue a career as an independent researcher. Thank you for taking me on as an undergraduate student in 2015 and for continuing to believe in me and trusting me to do good work so many years later. I have grown so much thanks to your mentorship.

I would also like to thank all my collaborators and support staff for their knowledge and expertise. I would especially like to thank Prof. Marcel Bouvet and Sujithkumar Ganesh Moorthy hosting me and passing on their knowledge and expertise of gas sensors. I would also like to thank Prof. Guillaume Wantz and Prof. Damien Thuau for teaching me how to fabricate my first transistors. I would also like to thank all the beamline scientists who made our synchrotron experiments a success, including Dr. Adam Leontowich, Dr. Sufal Swaraj and Dr. Arnaud Hemmerle. Thank you as well to Dr. Chase Radford for sharing your knowledge on X-ray scattering and providing me with the tools to understand and interpret my synchrotron data.

I would also like to express my gratitude to members of the Lessard Research Group, past and present. Special thanks to Dr. Owen Melville, who mentored me from the start of my graduate studies, and Drs. Mario Vebber and Trevor Grant, who synthesized many of the materials that are a cornerstone of my work. I would also like to thank Dr. Nicole Rice and Dr. Joseph Manion for being incredible mentors and playing a significant role in keeping me grounded.

To Ryan, one of my best friends, thank you for everything; you are much more than “a solid B+”. To Chris, Curtis, Maddy, Kaitlin, Rose, Alizeh, Kris, Alex, and Tousy, your friendship is priceless. To my Leverage teammates, thank you for taking a chance on me and for imbuing me with a sense of community greater than any I have ever experienced. To Justin, thank you for being one of my best friends, a great roommate and forever one of my favourite Frisbee teammates.

Finally, I would like to express my thanks to my parents Joyce and Charles and my sisters Karyn and Stephanie, as well as my late grandmother Rita. I would not be who I am or where I am today without your unconditional love and support. You set me on the path to success.

Thank you to my thesis committee for your consideration of this report.

List of Peer-Reviewed Journal Article Contributions

Publications as Lead Author

Statement of contributions are found at the beginning of each chapter.

1. **King, B.**; Melville, O.; Rice, N.; Kashani, S.; Tonnelé, C.; Raboui, H.; Swaraj, S.; Grant, T. M.; McAfee, T.; Bender, T.; Ade, H.; Castet, F.; Muccioli, L.; Lessard, B. H.* Silicon phthalocyanines for n-type organic thin-film transistors: development of structure property relationships. *ACS Applied Electronic Materials*, **2021**, 3, 325-336.

2. **King, B.**; Daszczynski, A. J.; Rice, N.; Peltekoff, A. J.; Yutronkie, N. J.; Lessard, B. H.; Brusso, J. L.*, Cyanophenoxy-substituted silicon phthalocyanines for low threshold voltage n-type organic thin-film transistors, *ACS Applied Electronic Materials*, **2021**, 3, 2212-2223.

3. **King, B.**; Radford, C. L.; Ronnasi, B.; Lessard, B. H.*, Not Just Surface Energy: The Role of Bis(Pentafluorophenoxy) Silicon Phthalocyanine Axial Functionalization and Molecular Orientation on Organic Thin-Film Transistor Performance. *ACS Applied Mateials & Interfaces,* **2023**, *15*, 14937–14947.

4. **King, B.;** Vebber, M.; Ewenike, R.; Dupuy, M.; French, C.; Brusso, J.; Lessard, B. H.*, Peripherally fluorinated silicon phthalocyanines: how many fluorine groups are necessary for air-stable electron transport in organic thin-film transistors? *Chemistry of Materials*, **2023**, Accepted Manuscript.

5. **King, B.;** Ganesh Moorthy, S.; Lesniewska, E.; Meunier-Prest, R.; Bouvet, M.; Lessard, B. H.* Modulating the majority charge carrier type and performance of organic heterojunction ammonia sensors by increasing peripheral fluorination of the silicon phthalocyanine sublayer. *Sensors and Actuators B: Chemical*, Submitted Manuscript.

6. **King, B.;** Lessard, B. H.*, Review of recent advances and sensing mechanisms in solid-state organic thin-film transistor (OTFT) sensors. *Journal of Materials Chemistry C,* Submitted Manuscript.

Publications as Co-Author

The full abstract, links to the publications and statement of contributions are found in Chapter 7.

7. Brixi, S.; Lamontagne, H.; **King, B.**; Shuhendler, A. J.; Lessard, B. H.,* Exposure to Solvent Vapours for Enhanced N-type OTFT Stability. *RSC Materials Advances*, **2023**, Advance Article.

8. Vebber, M. C.; **King, B**.; French, C.; Toussignant, M.; Ronnasi, B.; Dindault, C.; Wantz, G.; Hirsch, L.; Brusso, J.; Lessard, B. H.,* From P-type to N-type: Peripheral Fluorination of Axially Substituted Silicon Phthalocyanines Enables Fine Tuning of Charge Transport. *Canadian Journal of Chemical Engineering,* **2023**, 101, 3019-3031

9. Ganesh Moorthy, S.; **King, B.**; Kumar, A.; Lesniewska, E.; Lessard, B. H.; Bouvet, M.*, (2023) Molecular Engineering of Silicon Phthalocyanine to Improve the Charge Transport and Ammonia Sensing Properties of Organic Heterojunction Gas Sensors. *Adv. Sensor Res.*, 2 (3), 2200030.

10. Mirka, B.; Rice, N. A.; Richard, C. M.; Lefebvre, D.; **King, B**.; Bodnaryk, W. J.; Fong, D.; Adronov, A.; Lessard, B. H.*; Contact Engineering in Single-Walled Carbon Nanotube Thin-Film Transistors: Implications for Silane-Treated SiO_2 Substrates. *ACS Applied Nano Materials*, **2022**, 5, 12487–12495.

11. Dindault, C.; **King, B.**; Williams, P.; Absi, J.; Faure, M.; Swaraj, S.; Lessard, B. H.*; Correlating morphology, molecular orientation and transistor performance of bis(penta fluorophenoxy) silicon phthalocyanine using Scanning Transmission X-ray Microscopy. *Chemistry of Materials*, **2022**, 34, 4496–4504.

12. Ganguly A.; **King, B.**; Lessard, B. H.*; Brusso, J.*; Employing aldol condensation to prepare benzodifurandione-based small molecules for application in thin-film transistors. *Synthetic Metals* **2022**, 287, 117090.

13. Cranston. R.; **King, B.**; Dindault, C.; Grant, T. M.; Rice, N. A.; Tonnelé, C.; Muccioli, L.; Castet, F.; Swaraj, S.; Lessard, B. H.*; Highlighting the processing versatility of a silicon phthalocyanine derivative for organic thin-film transistors. *Journal of Materials Chemistry C,* **2022**, 10, 485-495.

14. Cyr, M.; **King, B.**; Lessard, B. H.*; Brusso, J.*. Exploring ellagic acid as a building block in the design of organic semiconductors. *Dyes and Pigments*, **2022**, 199, 109998.

15. Yutronkie, N. J; **King, B.**; Melville, O. A.; Lessard, B. H.; Brusso, J. L., * Attaining air stability in high performing n-type phthalocyanine based organic semiconductors. *Journal of Materials Chemistry C,* **2021***, 9,* 10119-10126.

16. Melville, O.; Grant, T.; Lochhead, K.; **King, B.**; Ambrose, R.; Rice, N.; Boileau, N.; Peltekoff, A.; Tousignant, M.; Hill, I.; Lessard, B. H.* Contact Engineering using Manganese, Chromium and Bathocuproine in Group 14 Phthalocyanine Organic Thin-Film Transistors. *ACS Applied Electronic Materials,* **2020**, 2, 1313-1322.

Table of Contents

List of Figures

List of Tables

Nomenclature

AFM: atomic force microscopy

BGBC: bottom-gate bottom-contact

BGTC: bottom-gate top-contact

C: capacitance

C_i capacitance density

CV: cyclic voltammetry

DART-MS: direct analysis in real time mass spectrometry

DFT: density functional theory

E_G: Optical band gap

$E_{1/2}^{\mathrm{Red}}$: halfway potential

Δe: LUMO offset

F_{16}CuPc: hexadecylfluoro copper phthalocyanine

FPTS: trimethoxy(3,3,3-trifluoropropyl)silane

γ^{SD}: dispersive component of the surface energy

γ^{SP}: polar component of the surface energy

γ^{tot}: total surface energy

GIWAXS: grazing-incidence wide-angle X-ray scattering

g_m: transconductance

HOMO: highest occupied molecular orbital

I_{on}: on-state current

I_{off}: off-state current

$I_{on/off}$: ratio of on-state current to off-state current

I_{DS}: source-drain current

I_{GS}: source-gate current

k: dielectric constant (relative permittivity)

L: source-drain electrode channel length

LUMO: lowest-unoccupied molecular orbital

$LuPc_2$: lutetium phthalocyanine

NMR: nuclear magnetic resonance

OLED: organic light emitting diode

OPV: organic photovoltaic
OTFT: organic thin film transistor
ODTS: octadecyl(trichloro) silane
OTS: octyl(trichloro) silane
p-6P: para-sexiphenyl
Φ: work function
PhTS: Trichlorophenylsilane
PMMA: polymethyl methacrylate
PS: polystyrene
PSDF: power spectral density analysis
PVD: physical vapor deposition
PXRD: powder X-ray diffraction
R_2-SiPc: silicon phthalocyanine
R_2-F_XSiPc: peripherally fluorinated silicon phthalocyanine
RH: relative humidity
RMS: root mean square
SiO_2: silicon dioxide
t: thickness of the dielectric layer
TGA: thermogravimetric analysis
TGBC: top gate bottom contact
TGTC: top gate top contact
Tm: melting temperature
μ: mobility
μ_e: electron mobility
μ_h: hole mobility
UPS: ultraviolet photoelectron spectroscopy
UV-Vis: UV-visible spectroscopy
V_{GS}: gate-source voltage
V_{SD}: source-drain voltage
V_T: *threshold voltage*
W: width between the source drain electrodes

Z: impedance

Z': real portion of the impedance

Z'': imaginary portion of the impedance

Chapter 1. Introduction

A portion of section 1.2 in this chapter was published in the journal "Journal of Materials Chemistry C": King, B., Lessard, B. H., Review of recent advances and sensing mechanisms in solid-state organic thin-film transistor (OTFT) sensors, Journal of Materials Chemistry C., Submitted Manuscript.*

1.1 Organic Electronic Devices

Electronic devices using carbon-based (organic) semiconductors provide inherent benefits over inorganic semiconductors including being processable by low-cost, relatively low-energy-input manufacturing techniques,[1,2] and ease of integration into flexible substrates.[3,4] Additionally, organic semiconductors can be functionalized through a broad range of synthetic techniques to tune their solubility, physical properties, optical properties and electronic properties,[5–9] enabling the tailoring of these materials for different device applications including organic light-emitting diodes (OLEDs),[10] organic photovoltaic cells (OPVs),[11] organic thin-film transistors (OTFTs)[12] and chemical or biological sensors based on OTFTs and organic electrochemical transistors (OECTs).[13,14] Additionally, these materials can be integrated into printing technologies for large area and roll-to-roll electronics fabrication, which has the potential for low cost manufacturing.[15,16] These applications strongly depend on charge transport through the organic semiconductor materials,[17] or diffusion of analytes through the bulk of the semiconductor sensing element in the case of sensor applications.[18] Therefore, the design of molecular semiconductors and semiconducting polymers with favourable solid-state molecular stacking, as well as fabrication towards achieving highly crystalline films with precise control over their texture are paramount to developing the next generation of inexpensive and industrially-produced high-performance electronics.[19,20] Many different processing parameters can be controlled to tune the texture of organic semiconductor thin-films including deposition rate,[21] substrate temperature during deposition,[22] surface chemistry of the substrate,[23,24] post-deposition thermal annealing and solvent vapour annealing.[25–27] Continuing to develop molecular and polymer organic semiconductors and understanding of how processing influences device performance will enable the next generation of electronics that can supplement or surpass traditional silicon or metal oxide devices in a broad range of applications including as healthcare tools and for chemical and biological sensing.

1.2 Organic Thin-Film Transistors (OTFTs)

Organic thin-film transistors (OTFTs) are three-terminal devices consisting of a source and a drain electrode, a gate electrode, an organic semiconductor layer that enables the flow of electrons or holes from the source to drain electrodes, and a dielectric layer that modulates the charge transport in the semiconductor.[12,28,29] The current between the source and drain (I_{DS}) is therefore a function of the applied gate voltage (V_G) across the dielectric. Under a small, applied V_G, negligible I_{DS} flows across the semiconductor channel and the device is in the "off" state. However, at V_G beyond a threshold voltage (V_T), the dielectric becomes sufficiently polarized to populate the semiconductor/dielectric interface with charge carriers that I_{DS} increases and is further amplified with increasing V_G rendering the device "on". Key performance parameters of OTFTs including their ability to effectively switch between the off state and on state at a low magnitude of V_T, a high ratio of current between the off state and on state ($I_{on/off}$) and a high field-effect mobility (μ) which is the average charge carrier drift velocity per unit of electric field.[30] The architecture of an OTFT can be categorized under one of four designations based on the relative position of the organic semiconductor and the electrodes, including bottom-gate bottom-contact (BGBC), bottom-gate top-contact (BGTC), top-gate bottom-contact (TGBC) and top-gate top-contact (TGTC) structures (**Figure 1.1**).

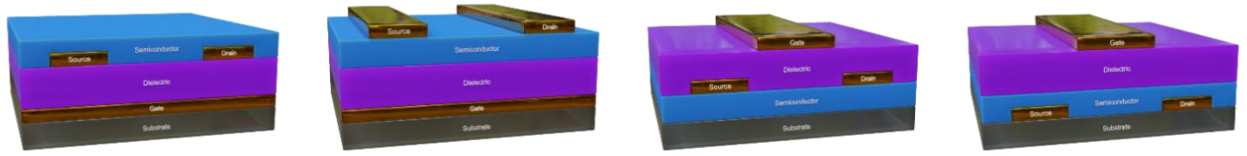

Bottom-Gate Bottom-Contact

Bottom-Gate Top-Contact

Top-Gate Top-Contact

Top-Gate Bottom-Contact

Figure 1.1 Schematic of four primary OTFT architectures.

1.2.1 OTFT operation and characterization

With respect to charge transport, transistors can be characterized as p-type (holes are majority charge carriers), n-type (electrons are majority charge carriers) or ambipolar (both hole and electron conduction are possible). OTFTs are typically modelled using equations similar to those for metal-oxide semiconductor field-effect transistors (MOSFETs).[12,31] Two types of plots used to characterize OTFTs are output curves and transfer curves. An output curve (**Figure 1.2A**) shows two distinct regions of transistor operation: the linear and saturation regions. In the linear region, $|V_{DS}| < |V_{GS} - V_T|$ and I_{DS} changes linearly with V_{DS}. In the saturation region, where $|V_{DS}| > |V_{GS} - V_T|$, the current begins to saturate and eventually becomes constant with increasing V_{DS}. A transfer curve (**Figure 1.2B**) is a plot of I_{DS} as a function of V_{GS} at a constant V_{DS}.

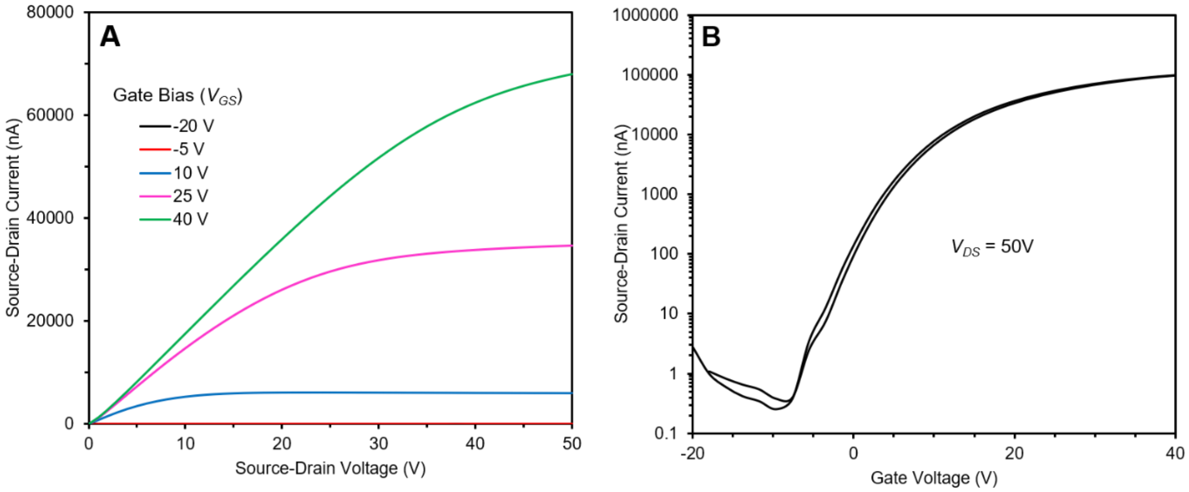

Figure 1.2 Sample A) output curve and B) transfer curve for an n-type OTFT. Reproduced with permission from data published in Reference 32. Copyright Royal Society of Chemistry 2023.

The field-effect mobility (μ) of an OTFT can be calculated in the linear region by rearranging **Equation 1.1** for the calculation of I_{DS} to yield **Equation 1.2**:

$$I_{DS} = \frac{\mu C_i W}{L}\left[(V_{GS} - V_T)V_{SD} - \frac{V_{SD}^2}{2}\right] \tag{1.1}$$

$$\mu_{lin} = \frac{L}{W C_i V_{SD}}\left[\frac{\partial I_{DS}}{\partial V_{GS}}\right] \tag{1.2}$$

where L and W represent the channel length and width, respectively. The capacitance of the gate dielectric (C_i) is calculated using $C_i = \frac{\varepsilon_0 \varepsilon_r}{d}$, where d is the dielectric thickness, ε_0 is the permittivity of free space and ε_r is the dielectric constant of the dielectric material. The field-effect mobility (μ) of an OTFT can be calculated in the saturation region by rearranging equation **1.3** for the calculation of I_{DS} to yield **Equation 1.4A** or **1.4B**:

$$I_{DS} = \frac{\mu C_i W}{2L}(V_{GS} - V_T)^2 \tag{1.3}$$

$$\mu_{sat} = \frac{L}{WC_i}\left[\frac{\partial^2 I_{DS}}{\partial V_{GS}^2}\right] \tag{1.4A}$$

$$\mu_{sat} = \frac{2L}{WC_i}\left[\frac{\partial\sqrt{I_{DS}}}{\partial V_G}\right]^2 \tag{1.4B}$$

Critical device parameters such as μ and V_T can also be extracted from transfer curve data. In the saturation region, the slope of adjacent data points for $\sqrt{I_{DS}}$ vs V_{GS} can be taken to generate a plot of μ vs V_{GS}. V_T can be calculated from the average x-intercept of linearized data for $\sqrt{I_{DS}}$ vs V_{GS} in the same measurement range. A sample parameter extraction from saturation regime transfer curve data is shown in **Figure 1.3**.

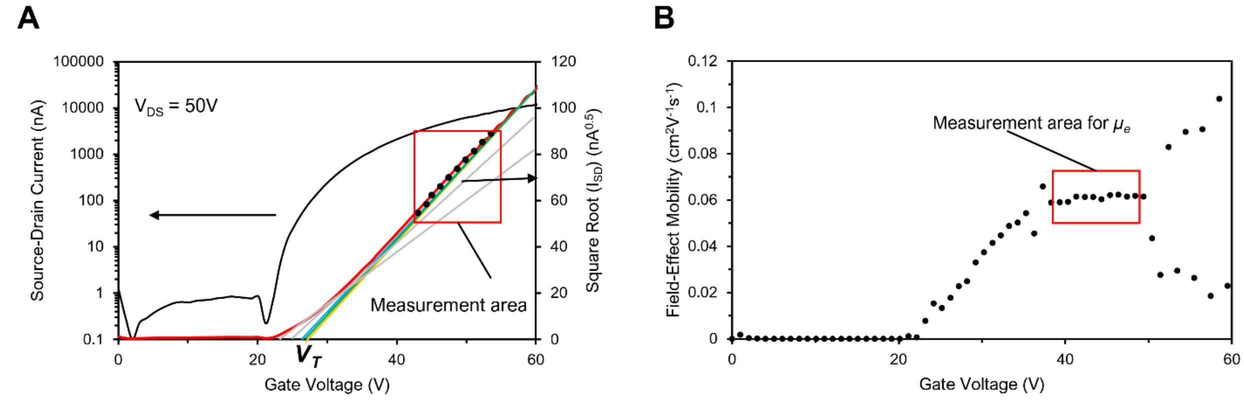

Figure 1.3 A) Characteristic forward saturation region transfer curve and B) μ_e vs V_{GS} for a forward sweep of I_{DS} vs V_{GS} with μ_e extracted from the average of values in the measurement area (red box). Figure reproduced with permission from Reference 33. Copyright American Chemical Society 2021.

1.2.2 Engineering the Semiconductor-Dielectric Interface in OTFTs

The interfaces of organic electronic devices play an important role in their performance, including in film nucleation and growth, charge injection and charge transport across the semiconductor-dielectric interface of OTFTs. A significant amount of work has been undertaken to explore the use of self-assembled monolayers (SAMs)[34,35] and molecular templates[23] for the growth of organic semiconductor films to achieve high-performance OTFTs and organic photovoltaics. Surface templating techniques are useful for improving the performance of evaporated or solution-processed OTFTs and has been found to have an influence on the crystallinity of meniscus coated semiconductor films.[36] Since the effective conductive channel in OTFTs is the first several molecular layers (nanometers) of the organic semiconductor in contact with the dielectric, and since charge carrier migration is primarily realized by hopping between molecules,[17,37] tuning this interface is critical for tuning the performance of OTFTs.

SAMs are highly oriented two-dimensional molecular arrangements which can be formed on the surface of a variety of OTFT components primarily utilized for tuning the surface chemistry of the substrate[38] or the work function of metal electrodes.[39,40] SAM formation requires the chemisorption on a surface followed by spontaneous organization into 2D-crystalline long-range molecularly ordered domains.[41] Molecules typically used to form SAMs are composed of three parts: the head group that is reactive with the substrate or electrode surface, the backbone made of an aliphatic chain or oligomer and the terminal group which dictates semiconductor-substrate interactions, surface energy and OTFT performance (**Figure 1.4A**).[42] Common head groups for SAMs include organosilanes,[42] carboxylic acids,[43] and phosphonic acids,[44] which require a hydroxylated surface group to form SAMs on oxide surfaces (**Figure 1.4B, left**), or thiols (HS-R-X, where R is the aliphatic chain and X is the terminal group) which form covalent bonds with gold electrodes due to an oxidative addition reaction (**Figure 1.4B, right**).[45] SAM molecules can also be further functionalized by nucleophilic substitution, click chemistry, photochemical reactions and other chemical reactions summarized in a recent review by Hoeppener et al.[46] The properties of organosilane and phosphonic acid SAM terminal groups have been shown to directly influence the V_T of OTFTs. The mechanism of V_T shift in OTFTs incorporating a range of SAMs is the permanent dipoles of the molecules resulting in the formation of an electrostatic potential that can generate or withdraw mobile charge carriers in the semiconductor channel.[47,48] For example, Halik and coworkers reported BGTC OTFTs with seven phosphonic acids and found an inverse linear relationship between the dipole moment of the SAM-forming molecule and the resulting device V_Ts across a range of semiconductors including fullerene (C_{60}), pentacene and α,α′-dihexylsexithiophene (DH6T).[49] Vuillaume et al. demonstrated a similar inverse relationship between SAM charge density and V_T for a catalogue of ten organosilane molecules in BGBC OTFTs based on amorphous polytriarylamine and polycrystalline pentacene.[50]

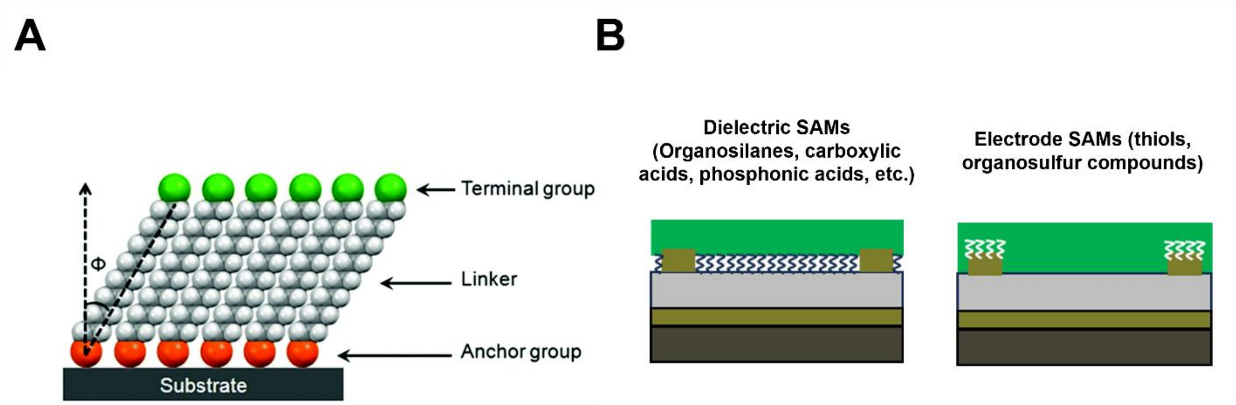

Figure 1.4 A) Generic structure of SAM molecules and B) BGBC device structure showing the integration of dielectric SAMs (left) and electrode SAMs (right) into the device architecture. Figure A reproduced with permission from Reference 51. Copyright Royal Society of Chemistry 2018.

The terminal group of SAMs can also have a direct effect on charge carrier μ in OTFTs by tuning the surface energy (γ) of the dielectric.[52] Typically, the total surface energy of the dielectric (γ^{tot}) is defined as the sum of its polar (γ^{p}) component and dispersive component (γ^{d}) which are related to the polarity of the surface and can be determined by contact angle measurements with different solvents.[53] Many different calculation approaches exist to calculate the surface energy of substrates which have been summarized by Kwok and Neumann.[54] One strategy for achieving high μ in OTFTs is to minimize γ. This strategy was previously reported in work by Tokito and coworkers who found an inverse relationship between the surface energy calculated on increasingly hydrophilic SAMs and μ in poly(2,5-bis(3-hexadecylthiophene-2-yl)thieno[3,2-b]thiophene) (PB16TTT).[55] Additionally, Diao et al. demonstrated that minimizing the surface energy in solution-coated polymer semiconductor-based OTFTs resulted in the formation of larger crystalline domains, a greater degree of crystalline polymer domains oriented “edge-on” and an increase in nearly one order of magnitude in μ.[36] However, the relationship between γ and μ has been demonstrated to be more complex and a more promising strategy of matching the surface energy of the dielectric to that of the organic semiconductor has been shown to induce large grains with low grain boundary density and more favourable conditions for charge transport.[56,57] Liu et al. demonstrated a direct effect of surface energy on carrier transport in OTFTs where matching the γ^{tot} of SAM-modified or molecular-template-modified dielectrics while minimizing γ^{p} could be directly correlated with an increase in μ for both Ph5T2 single-crystal OTFTs and polycrystalline pentacene and ZnPc OTFTs.[58] Finally, SAMs can influence the majority charge carrier type of organic semiconductors as demonstrated by Takimiya et al. who achieved unipolar hole and electron transport from the ambipolar polymer semiconductor poly{[N,N′-bis(2-decyltetradecyl)- naphtho[2,3-b:6,7-b′]dithiophene-4,5,9,10-tetracarboxidiimide- 2,7-diyl]-alt-5,5′-(2,2′-bithiophene)} (PNDTI-BT-DT) through functionalization with a fluorinated SAM and dimethylamino SAM, respectively.[59]

Polymer brushes are another class of SAM utilized in OTFTs primarily to enhance their bias stress stability.[60] Bias stress stability, or minimizing the shift in V_T after repeated use under gate bias stress can be significantly improved by engineering the interface between the gate dielectric and the semiconductor.[61] The two primary polymer grafting techniques to attach polymers to dielectric surfaces are grafting-to and grafting-from. In the “grafting-to” approach, polymer brushes are attached to the substrate through chemical coupling or a condensation reaction, while the “grafting-from” approach usually involves some form of surface-initiated polymerization.[62] Many polymers for a grafting-to approach are commercially available and synthesized by coupling a polymer chain to a silane, which provides a pathway for grafting that is similar to SAMs such as octodecyltrichlorosilane (OTS).[15,63] Grafting-from by surface-initiated polymerization has been reported by employing three techniques: Nitroxide-Mediated Polymerization (NMP),[64,65] Atom-Transfer Radical Polymerization (ATRP)[66–68] and Reversible addition-fragmentation chain transfer polymerization (RAFT).[69] NMP in particular is a simple, robust and scalable technique which can be used to synthesize well-defined polymers which is compatible with both grafting-to and grafting-from approaches.[65] NMP is generally desirable over ATRP where transition metal catalysts can still be present in the final polymers[70] and RAFT where sulfer-based chain transfer agents have to be removed.[71] NMP has also been used to synthesize a broad range of vinylic homopolymers, including styrenics,[72] methacrylates,[73] acrylamides[71] and carbazole-based pendant polymers. A wide variety of grafted polymers and pathways for their synthesis are available, so a robust and scalable technique should be chosen that best compliments fabrication.[74] A schematic of grafting-to and grafting-from approaches are demonstrated in **Figure 1.5**.

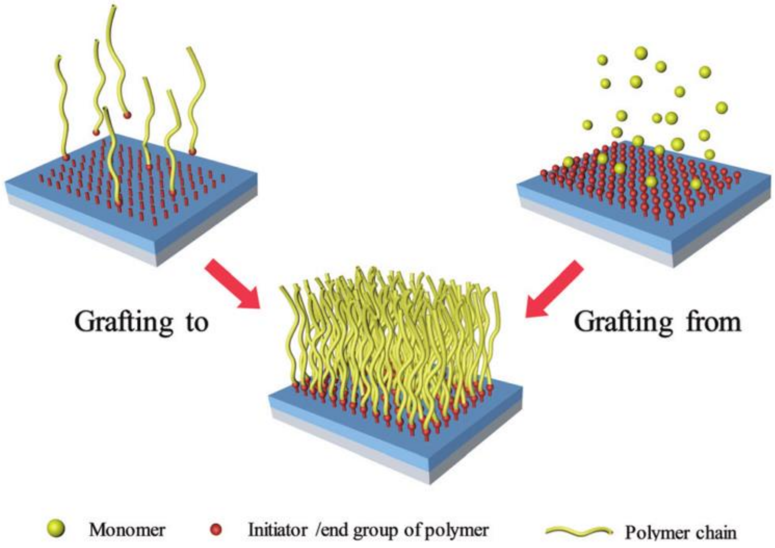

Figure 1.5 Schematic diagram of "Grafting-to" and "Grafting-from" surface modification techniques. Figure reproduced with permission from Reference 62. Copyright Royal Society of Chemistry 2020.

Kim et al. demonstrated that fluorinated polymer brushes based on poly(pentafluorostyrene) improved bias stress stability of pentacene and perylene diimide-based OTFTs by a factor of three to six compared to SiO_2 and a fluorinated alkyl SAM as demonstrated by a reduced threshold voltage shift (ΔV_T) in device transfer characteristics as a result of stress testing.[75] Ha et al. inkjet-printed silane-capped polystyrene as a dielectric interlayer in flexible all-inkjet-printed transistors incorporating 6,13-Bis(triisopropylsilylethynyl)pentacene (TIPS-Pentacene) as the semiconductor and observed a bias stress shift of under 0.5V before and after applying a mechanical bending force to the device, while observing a bias shift of 1.5 to 2.5 V for untreated devices.[15] Finally, work by Lee et al. determined that for grafted poly(styrene) brushes, a molecular weight of 8 $kg \cdot mol^{-1}$ resulted in the maximum grafting density of 0.38 $chains \cdot nm^{-2}$ compared to brushes with molecular weights of 25, 108 and 135 $kg \cdot mol^{-1}$.[76] High molecular weight polymers were found to block active sites for polymer grafting which could result in an increase of charge traps, which has an impact on the performance of resulting OTFTs.

Molecular templates, which differ from SAMs in that they are not covalently bound to the surface, are another popular class of materials which have been leveraged to fabricate high-performance OTFTs through a phenomenon known as weak epitaxial growth (WEG).[77] WEG can be achieved by evaporating rod-like molecules as a templating layer at the semiconductor-dielectric interface and is often paired with molecular semiconductors such as metal phthalocyanines (MPcs).[35,78,79] This template typically yields a highly-ordered surface where molecules have an "edge-on" orientation in which charges hop between molecules across the surface of the substrate.[19] A typical WEG template layer is *para*-sexiphenyl (*p*-6P)[22,80,81] which was used to increase the hole μ in ZnPc OTFTs by an order of magnitude from 10^{-2} to 10^{-1} $cm^2 \cdot V^{-1} \cdot s^{-1}$.[82] High-performance OTFTs achieved by leveraging WEG for highly crystalline organic semiconductors has motivated the design of a plethora of other templating layers for OTFTs and OPVs summarized in a review by Jones et al.[79]

1.2.3 OTFTs as Transducers for Oxidative and Reductive Gas Sensors

OTFTs are an effective platform for chemical and biological sensing with the primary mechanism of operation being the interactions between an analyte and the semiconductor resulting in a rapid, concentration-dependant response.[13,83,84] Typical OTFT-based gas sensors will experience reversible or permanent changes/shifts in V_T, μ, I_{DS} or $I_{on/off}$ when exposed to different concentrations of analyte. To quantify these changes in sensor performance, key parameters of merit can be extracted including relative response (*RR*), sensitivity (*S*), response/recovery time (typically demoted as t_{90}) and the limit of detection (*LOD*). Relative response can be calculated from Equation 1.1:

$$RR\ (\%) = \frac{Y_f - Y_0}{Y_0} \times 100\% \tag{1.1}$$

Where Y_f and Y_0 are an electrical parameter at final conditions (after exposure) and initial conditions, respectively. Relative response is typically calculated using sensor I_{DS} at constant applied V_{DS} and V_G,[83,85] or from measuring changes in V_T from transfer curves.[86,87] The *S* is typically defined as the slope of the linear relationship between *RR* and analyte concentration reported in $\% \cdot ppm^{-1}$ or $\% \cdot ppb^{-1}$ and calculated from Equation 1.2:

$$S = \frac{\partial(RR)}{\partial C} \tag{1.2}$$

Where *C* denotes analyte concentration, and the line is effectively a calibration curve for the sensor. The *LOD* of a sensor during dynamic measurements (current as a function of time and concentration) can be calculated from Equation 1.3:

$$LOD = \frac{3N}{S \times I_0} \tag{1.3}$$

Where N is the noise of the sensor signal estimated by determining the standard deviation of the sensor signal during the recovery period, S is the sensitivity of the sensor in ppm^{-1} or ppb^{-1}, and I_0 is the estimated baseline current of the sensor. Response time (t_{90}) is typically defined as the time of current change from the baseline current (I_0) to 90% of the current maximum, i.e., $I_0 + 0.9\Delta I$, where ΔI is the difference between I and I_0 while recovery time (t_{10}) is defined as the time required to return from ΔI to $I_0 + 0.1\ \Delta I$ or 10% of the current maximum. Finally, the selectivity is a quantitative measure of whether the sensor can differentiate between a mix of components that may interfere with the detection of a desired analyte.

Organic semiconductors are assembled from a series of aromatic and conjugated functional groups with a large number of delocalized π-electrons making them susceptible to oxidative and reductive processes which is responsible for the charge transport from one molecule to another. The bonding and local environment of the delocalized π-electrons make the corresponding organic semiconductors either more susceptible to oxidative gases such as O_2, NO_2, etc. or reductive gases such as NH_3, H_2S, etc.[88,89] Oxidative gases are typically recognized as p-dopants in organic semiconductors and diffusion to the semiconductor-dielectric interface typically results in an accumulation of holes, enhancement of the device's current, when operating in p-type, by trapping free electrons[90] while exposure to reductive gases often causes a drop in current when operating in p-type. Conversely, exposure to oxidative gases leads to additional holes at the interface which reduces the current of a device being operated in n-type operation, due to recombination with the free electron carriers, and exposure to reductive gases increases device current,.[91] Therefore, redox mechanisms can be leveraged for the development of high-performance OTFT gas sensors. Among strong redox gases, the quantification of NH_3, H_2S, NO/NO_2 and SO_2 are is particularly useful since they are industrially produced chemicals or pollutants generated as a result of manufacturing processes or emitted in automobile combustion engines.[92,93] A number of organic semiconductors incorporated into OTFTs have been reported to be sensitive to NH_3[94–100], H_2S,[101–104] NO_2,[105–111] and SO_2[112]. Often OTFT sensors offer advantages over metal-oxide-based sensors owing to their less strict operational requirements such as the ability to sense NH_3 at room temperature rather than at > 100 °C for metal oxide-based field-effect transistor-based sensors.[94,113] Some work has been undertaken towards understanding how to further enhance the sensitivity of OTFT sensors towards oxidative and reductive gases. For example, K.N. Narayanan Unni and coworkers. demonstrated that as NH_3 concentration increases, the density of interfacial charge traps also increases resulting in a reduction of μ and I_{on}/I_{off} ratio in dinaphtho [2,3-b:2′,3′-f]thieno [3,2-b]thiophene (DNTT)-based OTFT sensors. The effect of increasing NH_3 concentration on the I_{on}/I_{off} ratio is stronger in devices where the semiconductor layer was less thick, enabling easier diffusion of the analyte to the dielectric-semiconductor interface.[98] The rate of diffusion through the bulk of the film, as well as the rate of absorption and desorption of gases to the semiconductor-dielectric interface have an effect on sensor response as demonstrated by Chi and coworkers who fabricated OTFT sensors with a spirobifluorene-based polymer as the semiconductor with thicknesses from 5 to 25 nm.[104] The magnitude of the sensor response increased as the active layer thickness decreased from 25 nm to 20 nm, followed by a decrease in the magnitude of the response as thickness further decreased to 15 nm and 5 nm, respectively. This was attributed to the rate of desorption of gas molecules exceeding the rate of adsorption of gas molecules to the semiconductor-dielectric interface. Optimized devices with an active layer thickness of 20 nm demonstrated a sensitivity of 95% at 1 ppm and a LOD of 1 ppb with a 15 second response time.

1.3 Metal Phthalocyanines as Organic Semiconductors

1.3.1 Metal Phthalocyanines

Phthalocyanines (Pcs) are aromatic compounds composed of four nitrogen-linked isoindole units forming a conjugated macrocycle. Pcs can chelate a metal or metalloid atom through two covalent bonds and two coordination bonds to form thermally stable metal phthalocyanines (MPcs, **Figure 1.6**) which are useful as dyes and pigments and as active materials in organic electronic devices.[114–117] MPcs can be chemically modified by changing the metal/metalloid core,[118,119] adding peripheral substituents,[120,121] or with axial substitutions covalently bonded to the metal/metalloid core,[122,123] enabling the synthesis of a wide library of functional materials with tunable physical and optoelectronic properties. The functionalization of MPcs has enabled them to be solution processable, making these materials attractive candidates for printable electronics.[124,125]

The central atom of the MPc contributes to its geometry and electronic properties. For example, MPcs incorporating Zn, Cu, Co, Mn, and Fe have planar strctures,[126] while TiOPc possesses a cone-shaped structure and can form both concave and convex pairs in the solid-state.[127] A wide variety of MPcs containing different metal cores have been incorporated into organic electronic devices (**Figure 1.6**), such as divalent MPcs (with no axial groups) including CuPc[128] and ZnPc,[121] trivalent MPcs (with one axial group) including AlPc-Cl,[126] and tetravalent MPcs (with two axial groups) including SiPc-Cl$_2$ and SnPc-Cl$_2$.[22] Peripheral functionalization of of MPcs also influences their electronic properties. For example, peripheral fluorination of MPcs such as copper phthalocyanine (CuPc), results in a reduction in its lowest unoccupied molecular orbital (LUMO), enabling air-stable electron conduction.[120,129] MPcs are generally hole conducting, or p-type,[126] however there are a few derivatives that are primarily electron conducting, or n-type, including SiPcs,[63] SnPcs[125] and F$_{16}$-CuPc.[126] The ability of these planar MPcs to form highly-ordered thin-films makes them ideal candidates for organic thin-film transistors (OTFTs).[119]

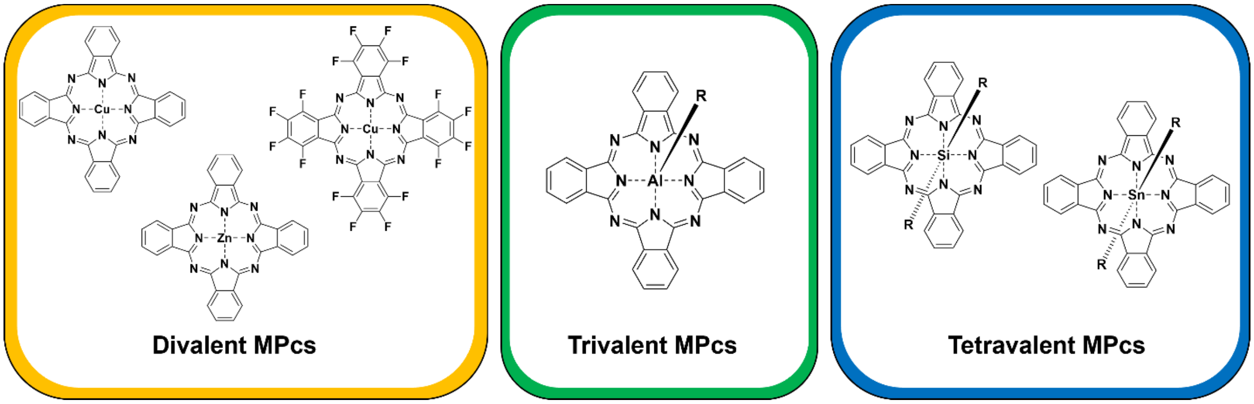
Divalent MPcs
Trivalent MPcs
Tetravalent MPcs

Figure 1.6 Examples of MPcs incorporated into organic electronic devices.

1.3.2 Silicon Phthalocyanines

Silicon phthalocyanines (R$_2$-SiPcs) with a tetravalent Si atom and two axial substituents are advantageous since axial functionalization with phenoxy (PhO) substituents,[33] benzoate substituents (BnO)[63] and silanes[130] can be utilized to modify molecular packing and increase the amount of π-orbital overlap between neighboring molecules or impact solubility.[131] There are multiple solid state packing motifs observed in adjacent the R$_2$-SiPc macrocycles (**Figure 1.7**) including combinations of benzene-benzene and benzene-isoindole stacking.[132] A greater degree of π-orbital overlap and π- π interactions enables greater charge transport in SiPc materials, which is advantageous for their application in organic electronic devices.[116] For example, the functionalization of unsubstituted dichloro-SiPc (Cl$_2$-SiPc) with pentafluorophenoxy (-OC$_6$F$_5$) moieties resulted in improved solid-state packing and a reduction in minimum π-π stacking distance from 3.977 Å for the unsubstituted Cl_2-SiPc to 3.654 Å for the bis(pentafluorophenoxy)-SiPc (($F_5PhO)_2$-SiPc). This improved solid-state arrangement resulted in an eight-fold increase in power conversion efficiency of ($F_5PhO)_2$-SiPc incorporated as an active layer in organic photovoltaic (OPV) devices.[116] This enhanced stacking observed by single crystal X-ray diffraction (XRD) measurements and resulting improvement of device performance compared to Cl_2-SiPc was also observed for other fluorophenoxy-substituted R_2-SiPcs.[133]

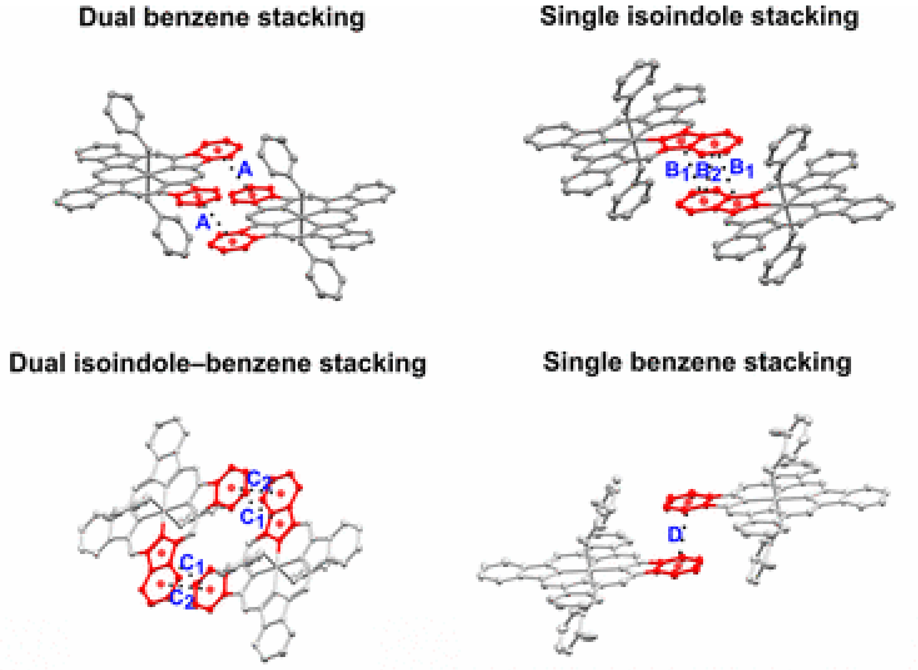

Figure 1.7 π- π interaction modes of R_2-SiPcs. Reproduced with permission from Reference 132. Copyright American Chemical Society 2018.

1.3.3 Peripheral Fluorination of Metal Phthalocyanines

The introduction of electron-withdrawing groups to the periphery of organic semiconductors often results in a downward shift in their frontier molecular orbitals, which can result in a change in the majority charge carrier type from holes to electrons[134,135] or enable air-stable electron transport in n-type semiconductors.[5,136] Similar functionality has been imparted on the periphery of MPcs to switch their behaviour from p-type to n-type in OTFTs with the earliest report of peripherally fluorinated MPcs reported by Bao and coworkers who synthesized F_{16}CuPc, F_{16}ZnPc, F_{16}CoPc and F_{16}FePc which yielded electron mobilities (μ_e) from 10^{-6} up to 10^{-2} $cm^2 \cdot V^-$

$^{1}\cdot s^{-1}$.[129] Single crystals of $F_{16}CuPc$, $F_{16}CoPc$ and $F_{16}ZnPc$ were grown and incorporated into OTFTs by Kloc and coworkers who determined that the central metal atom dictates the transport properties of fluorinated metal phthalocyanines with a higher estimated electron transfer integral.[120] Intermediate degrees of peripheral fluorination of MPcs can also enable ambipolar OTFTs. For example, Kloc and coworkers reported $F_{X}MPcs$ with Cu and Zn metal centers and where X = 0, 4, 8 or 16 peripheral fluorine atoms to tune the electronic properties of the organic semiconductor from p-type to n-type.[128] $F_{X}ZnPc$ transitioned from p-type to n-type behaviour when the number of peripheral fluorine atoms increased from 4 to 8, while four peripheral fluorine atoms was sufficient to induce ambipolar behaviour in $F_{X}CuPc$ derivatives, with $F_{4}CuPc$ and $F_{8}CuPc$ demonstrating ambipolar behaviour. In both cases, $F_{0}MPc$ derivatives were unipolar p-type and $F_{16}MPc$ derivatives were ambipolar n-type. Axially and peripherally fluorinated silicon phthalocyanine (F_{2}-$F_{16}SiPc$), the first peripherally fluorinated R_{2}-$F_{X}SiPc$ derivative ever reported, was synthesized by Yutronkie et al and incorporated into OTFTs, achieving μ_e of up to 0.3 $cm^{2}\cdot V^{-1}\cdot s^{-1}$ in N_2 and 0.072 $cm^{2}\cdot V^{-1}\cdot s^{-1}$ in air, exceeding the performance of $F_{16}CuPc$ which is widely used as an n-type MPc organic semiconductor.[32] Due to the significant batch-to-batch variation of this molecule, a new synthetic pathway was developed by Vebber et al. to synthesize the first R_{2}-$F_{X}SiPc$ derivatives substituted with phenol axial ligands and where X = 0, 4, 8 or 16 peripheral fluorine atoms (**Figure 1.8**).[137] When characterized in N_2, the derivative with zero peripheral fluorine atoms demonstrated uniquely p-type behaviour while derivatives with four peripheral fluorine atoms demonstrated ambipolar behaviour. Derivatives with eight and sixteen peripheral fluorine atoms yielded unipolar n-type OTFTs with the fully peripherally fluorinated derivative being the only one to have air stable electron transport.

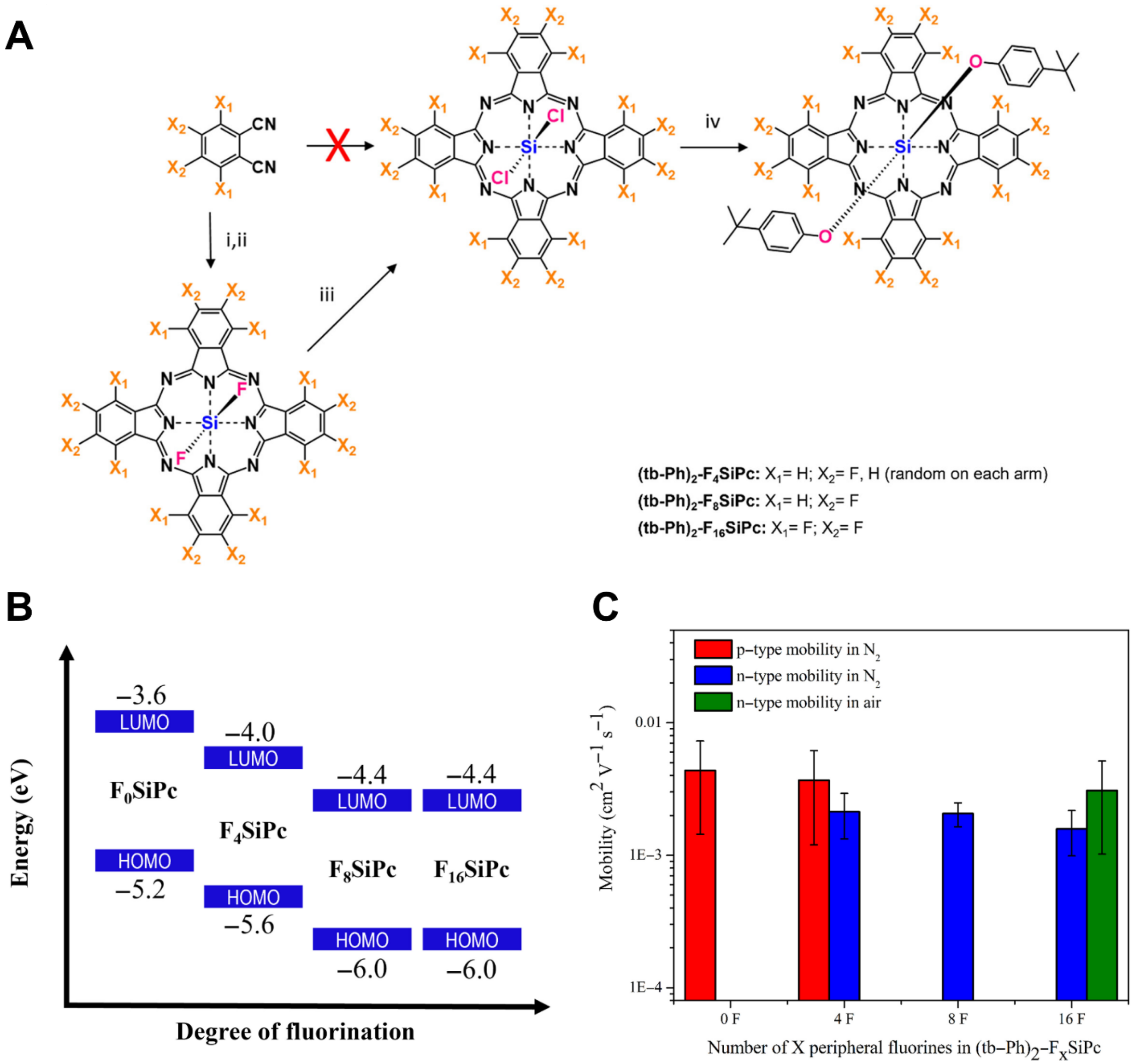

Figure 1.8 A) Synthetic pathway used in the production of functionalized F_XSiPcs, B) highest occupied molecular orbital (HOMO) and lowest unoccupied molecular orbital (LUMO) energy levels of (tb-Ph)$_2$-F_XSiPc estimated from ultraviolet photoelectron spectroscopy (UPS) and C) N-type and p-type mobilities of (tb-Ph)2-F_XSiPc as a function of peripheral fluorination. Figures reproduced from Reference 137. Copyright Wiley 2023.

1.4 Organic Heterojunction Devices as Transducers for Gas Sensors

Organic heterojunction devices for ammonia (NH_3) and ozone (O_3) gas sensing were initially reported by Bouvet and coworkers as an alternative to chemiresistors and organic thin-film transistor sensors based on MPcs.[138] These heterojunction devices are based on two organic semiconductors with different work functions and conductivities, enabling the accumulation of opposite charge carriers (electrons and holes) at the organic-organic interface due to accumulation/depletion heterojunction effects.[139] The top layer of the organic heterojunction device is typically lutetium bisphthalocyanine ($LuPc_2$) which is one of the first reported intrinsic molecular semiconductors with a high conductivity of 10^{-5} $\Omega^{-1}\cdot cm^{-1}$ at room temperature[140] compared to divalent metal phthalocyanines and other organic semiconductors (10^{-13} $\Omega^{-1}\cdot cm^{-1}$), which are typically used as sublayers.[141,142] Due to its radical nature, it can easily lose and gain an electron yielding an activation energy of 0.5 eV for the creation of charge carriers.[143] OTFTs based on $LuPc_2$ have demonstrated n-type behaviour under vacuum and p-type behaviour in air.[144] Robert et al. demonstrated the first thin-film gas sensors based on $LuPc_2$ as the sensing element for the detection of HCl, Cl_2, H_2S, SO_2 and NO_2 based on a planar conductometric sensor architecture with reproducible conductivity changes in the device shown for concentrations of NO_2 at 2 ppm.[145] The semiconducting nature of $LuPc_2$ has also motivated its incorporation into electronic tongues reported by Rodriguez-Méndez et al. for wine discrimination.[146]

1.4.1 Organic Heterojunction Gas Sensor Operation

To operate an organic heterojunction device (**Figure 1.9**), a bias is first applied between the two sets of interdigitated electrodes, resulting in the injection of electrons or holes into the device depending on the nature of the sublayer.[147] Due to the relatively low conductivity of the sublayer compared to the organic-organic interface and the interelectrode distance being substantially larger than the electrode-$LuPc_2$ distance, charge carriers travel vertically through the bulk of the sublayer to the organic-organic interface and across the device due to the high mobility of free charge carriers accumulated at the interface. Reductive or oxidative gases can either donate or withdraw electrons from the bilayer depending on the nature of the analyte, and changing the concentration of mobile charge carriers in the $LuPc_2$ top layer and the organic-organic interface,[147] resulting in a change in the current measured across the device. In the case of NH_3, which is an electron donating gas, a p-type heterojunction device will undergo a "turn-off" response which manifests as a concentration-dependent decrease in current, while an n-type heterojunction device will undergo a "turn-on" response which manifests as a concentration-dependent increase in current.[138] Conversely, for oxidizing or electron accepting gases such as NO_2 or O_3, p-type devices will undergo a "turn-on" response while n-type devices will undergo a "turn-off" response. Similar parameters of merit to OTFT sensors can be extracted from the dynamic response of heterojunction gas sensors including *RR*, *S*, t_{90} and *LOD*.

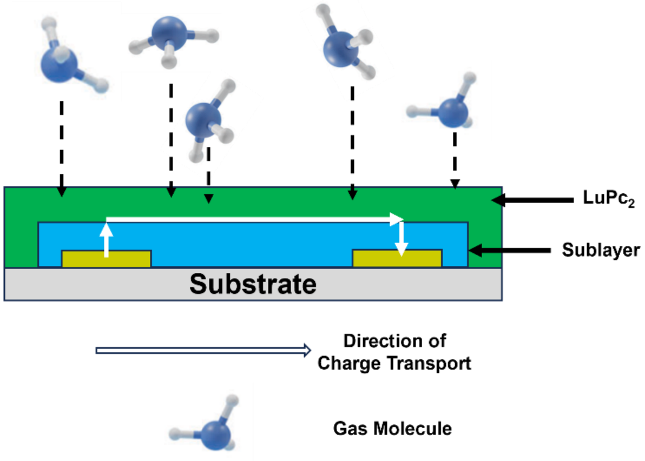

Figure 1.9 Cross-sectional schematic of an organic heterojunction gas sensor

1.4.2 Tuning the Majority Charge Carrier in Organic Heterojunction Gas Sensors

The direction of charge carrier transport is primarily dictated by the frontier molecular orbitals of the sublayer and the work function difference ($\Delta\Phi$) between the organic materials in the bilayer (**Figure 1.10**).[148] If the work function of the sublayer is greater than that of $LuPc_2$, electrons hop from the semi-occupied molecular orbital (SOMO) of $LuPc_2$ to the LUMO of the sublayer, resulting in n-type conduction. Conversely, if the work function of the sublayer is lesser than that of $LuPc_2$, electrons will hop from the HOMO of the sublayer to the SOMO of $LuPc_2$ resulting in p-type conduction.[149]

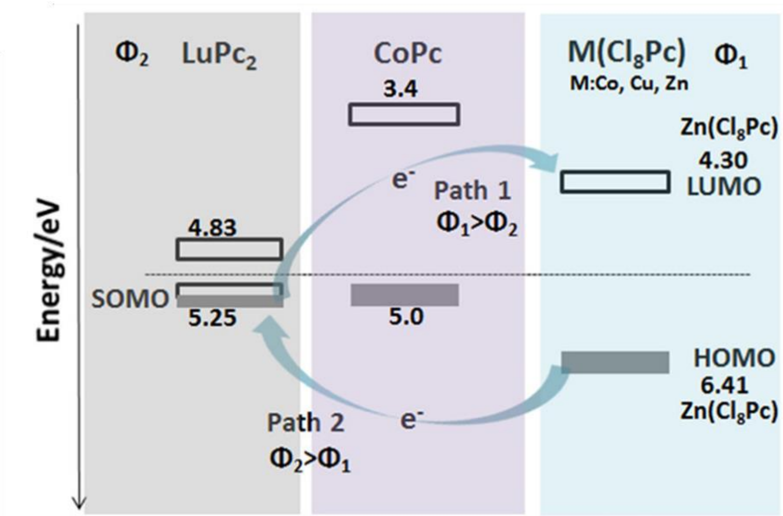

Figure 1.10 Charge hopping at bilayer interface depending on the work function (Φ) of each semiconductor in the heterojunction. Reproduced with permission from Reference 149. Copyright American Chemical Society 2020.

There are three reported methods to change the majority charge carrier type in the organic heterojunction device. The first method is changing the central metal atom of the sublayer MPc structure which has an impact on its electronic properties[115] and can result in either hole transporting or electron transporting organic semiconductors.[126] The effect of the central metal atom on the behaviour of organic heterojunctions was demonstrated by Bouvet and coworkers who incorporated CoPc, Zn(Cl_8Pc), Co(Cl_8Pc), Cu(Cl_8Pc) into devices as the sublayer with $LuPc_2$ as the top layer (**Figure 1.11**).[149] Octochlorinated MPc sublayers with Zn (**Figure 1.11A**) and Cu (**Figure 1.11C**) central metal atoms demonstrated a “turn-off” response, while the octochlorinated MPc sublayer with a Co central metal atom (**Figure 1.11B**) demonstrated a “turn-on” response.

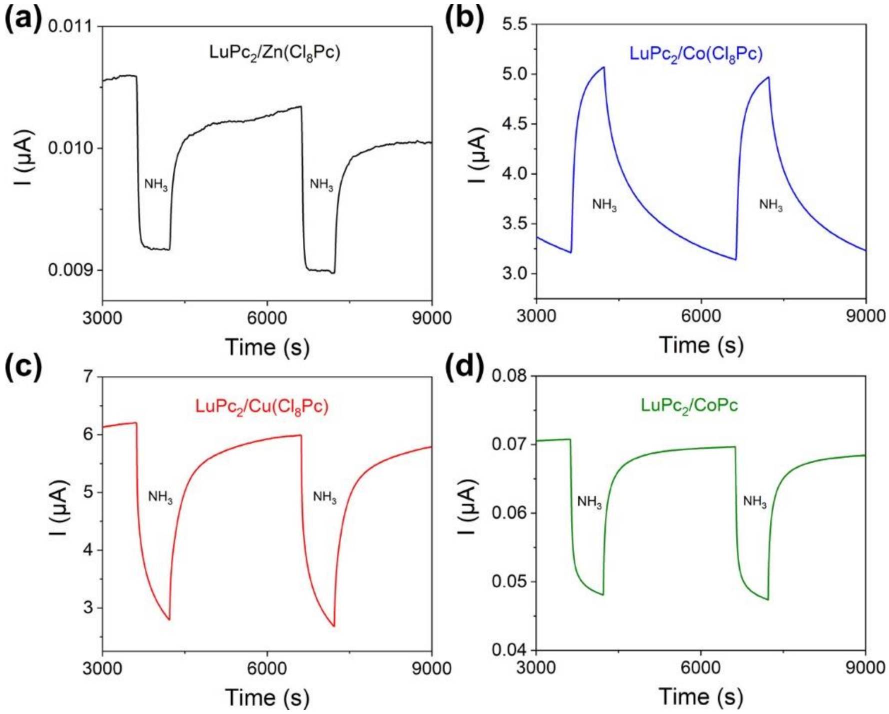

Figure 1.11 Current variation as a function of time of $LuPc_2/Cl_XMPc$ heterojunctions, exposed to 90 ppm NH_3 for 10 min-long periods separated by 40 min-long rest periods in synthetic air with 30% RH at a bias of 1 V. Reproduced with permission from Reference 149. Copyright American Chemical Society 2020.

The second method to change the majority charge carrier in organic heterojunction devices is including peripheral substituents in the MPc structure, which as previously discussed results in a shift in the frontier molecular orbitals of organic semiconductors and can result in a change from hole transporting to ambipolar or electron transporting semiconductors which has been demonstrated when progressively fluorinating F_XCuPc[128] or R_2-F_XSiPcs.[137] In organic heterojunction devices, the peripheral chlorination of CoPc is sufficient to change the majority charge carrier in the device from a "turn-off" response (**Figure 1.11D**) to a "turn-on" response (**Figure 1.11B**).[149] The original report of organic heterojunction gas sensors based on a MPc / $LuPc_2$ heterostructure also demonstrated the effect of peripheral substituents through the opposite response of CuPc and $F_{16}CuPc$ to NH_3 and O_3.[138] Solubilizing functional alkyl chains can also be incorporated into the MPc structure to tune the majority charge carrier, which was demonstrated with three NiPc derivatives containing hexal-sulfanyl, hexyl-sulfonyl and a combination of hexyl-sulfanyl and p-carboxyphenoxy moieties, respectively, in organic heterojunction devices with $LuPc_2$ as the top layer.[150] Electron-donating hexyl-sulfanyl groups in the periphery of two of the derivatives resulted in a "turn-off" response which is consistent with the p-type behaviour of NiPc OTFTs[126] while the weakly electron-accepting hexyl-sulfonyl groups resulted in a "turn-on" response of the devices. This work demonstrates that organic heterojunction devices can be fabricated with solution processable MPc sublayers and that weak electron-accepting peripheral substituents are sufficient to tune the majority charge carrier of the devices. The final method to change the majority charge carrier in organic heterojunction devices is through stimulus by a light source, which was demonstrated by Bouvet and coworkers who used visible light to switch the response of an $F_8CuPc/LuPc_2$ heterojunction from p-type to n-type.[151] The ambipolarity of $F_8CuPc/LuPc_2$ heterojunctions was independent of applied voltage and was attributed to the visible light desorbing molecular oxygen from the sublayer and suppressing the concentration of hole carriers while promoting the concentration of electrons. While light stimulus resulted in a change in device behaviour for $F_8CuPc/LuPc_2$ heterojunctions, exposing $CuPc/LuPc_2$ and $F_{16}CuPc/LuPc_2$ to light did not result in a polarity change.

1.5 Scope of the Thesis

This thesis will focus on the fabrication and characterization of OTFTs and heterojunction gas sensors with thermally evaporated R_2-F_XSiPcs as the active semiconducting layer with the purpose of developing relationships between the chemical structure of the phthalocyanine derivatives, their optical and electronic properties, and their resulting device performance. **Chapter 2** develops initial structure-property relationships between the axial substituents, thin-film texture, and device performance for eleven previously reported R_2-SiPc derivatives, with six of these derivatives being reported in OTFTs for the first time. In addition to electronic characterization of the devices, thin-films of R_2-SiPcs were characterized by atomic force microscopy (AFM) to extract textural information and by grazing-incidence wide-angle X-Ray scattering (GIWAXS) to determine the molecular orientation of R_2-SiPcs relative to the substrate. Single crystal data of R_2-SiPcs was used to develop charge-transfer models by density functional theory computational modelling by collaborators to further understand the impact of the axial group on intermolecular interactions and electronic performance. **Chapter 3** reports four additional R_2-SiPc derivatives, with three novel materials containing cyanophenoxy and fluoro-cyano-phenoxy axial groups developed based on the relationships developed in **Chapter 2** to further push the V_T of R_2-SiPc-based OTFTs towards 0V. In this work, the optical properties of these derivatives were characterized by UV-Vis, and electrochemical properties were characterized by cyclic voltammetry. We observed a dewetting of one of the R_2-SiPcs from the substrate surface, which necessitated the use of polymer brushes as a SAM fabricated through a "grafting-to" approach to stabilize the semiconductor film.

In **Chapter 4**, I report our champion R_2-SiPc material, bis(pentafluorophenoxy) silicon phthalocyanine (F_{10}-SiPc) on a range of functional surfaces to understand the influence of surface chemistry on R_2-SiPc films and OTFT performance. The functional surfaces we use in this work include a range of alkyl-SAM lengths (C_8, C_{18}), terminal groups (F_3, CH_3, C_6H_5) as well as *p*-6P as a template layer to determine whether F_{10}-SiPc demonstrates similar WEG behaviour to divalent and trivalent MPcs which yield highly crystalline films and edge-on molecular orientation.

In **Chapter 5**, I incorporate twelve R_2-F_XSiPcs with increasing axial and peripheral fluorination (X = 0, 4 or 16 F) into BGTC OTFTs to investigate how the degree of axial and peripheral fluorination influences thin-film texture, device performance and n-type air stability. This work builds on an initial report by Vebber et al. who reported the first phenol-substituted peripherally fluorinated R_2-F_XSiPcs and demonstrated air-stable electron transport for bis(tertbutylphenoxy) hexadecylfluoro silicon phthalocyanine ((tb)$_2$-F_{16}SiPc)[137] I characterized the optical and electronic properties of these materials by UV-Visible spectroscopy and ultraviolet photoelectron spectroscopy to determine their frontier molecular orbitals and completed long-term air stability studies of R_2-F_{16}SiPc derivatives supplement initial electrical characterization of all twelve reported derivatives. This work demonstrated the threshold for air-stable electron transport in R_2-F_XSiPc-based OTFTs did not simply depend on peripheral substitution and that axial fluorination has a role in stabilizing the device.

In **Chapter 6** we incorporate all three bis(pentafluorophenoxy) silicon phthalocyanines with zero, four and sixteen peripheral fluorine atoms into organic heterojunction devices with $LuPc_2$ as the sublayer to investigate their NH_3 gas sensing properties. These three materials were selected to determine the threshold for organic heterojunction devices to change from a turn-off response to a turn-on response under NH_3 exposure based on initial reports of Cl_2-SiPc and $(345FPhO)_2$-SiPc both yielding a turn-off response. I characterized powders, crystals and films of peripherally fluorinated derivatives of R_2-F_XSiPcs by Raman spectroscopy for the first time and measured the dynamic sensor response in the range of 1 ppm to 90 ppm. I also characterized all three heterojunction devices with impedance spectroscopy to determine their bulk and interfacial charge transport properties. To further optimize the devices, I thermally annealed $(F_5PhO)_2$-SiPc/$LuPc_2$ heterojunctions under vacuum to tune the interfaces of the device and characterized these changes by impedance spectroscopy. After thermal annealing, I report a two-fold enhancement in the sensitivity of devices likely related to a reduction in the resistance to interfacial charge transport, demonstrating the potential of postdeposition processing on bulk heterojunction gas sensors for the first time.

In **Chapter 7** of my thesis, I present the overall conclusions from my work and make recommendations about future research directions related to the incorporation of R_2-F_XSiPcs into thin film electronic devices. Finally, in **Chapter 8**, I provide abstracts and context to papers I have contributed to during my Ph.D.

References

(1) Azzopardi, B.; Emmott, C. J. M.; Urbina, A.; Krebs, F. C.; Mutale, J.; Nelson, J. Economic Assessment of Solar Electricity Production from Organic-Based Photovoltaic Modules in a Domestic Environment. *Energy Environ. Sci.* **2011**, *4* (10), 3741–3753. https://doi.org/10.1039/c1ee01766g.

(2) Mulligan, C. J.; Wilson, M.; Bryant, G.; Vaughan, B.; Zhou, X.; Belcher, W. J.; Dastoor, P. C. A Projection of Commercial-Scale Organic Photovoltaic Module Costs. *Sol. Energy Mater. Sol. Cells* **2014**, *120* (PART A), 9–17. https://doi.org/10.1016/j.solmat.2013.07.041.

(3) Yao, Y.; Huang, W.; Chen, J.; Liu, X.; Bai, L.; Chen, W.; Cheng, Y.; Ping, J.; Marks, T. J.; Facchetti, A. Flexible and Stretchable Organic Electrochemical Transistors for Physiological Sensing Devices. *Adv. Mater.* **2023**, *35* (35), 2209906. https://doi.org/10.1002/adma.202209906.

(4) Yang, Y.; Gao, W. Wearable and Flexible Electronics for Continuous Molecular Monitoring. *Chem. Soc. Rev.* **2019**, *48* (6), 1465–1491. https://doi.org/10.1039/c7cs00730b.

(5) Jones, B. A.; Facchetti, A.; Wasielewski, M. R.; Marks, T. J. Tuning Orbital Energetics in Arylene Diimide Semiconductors. Materials Design for Ambient Stability of n-Type Charge Transport. *J. Am. Chem. Soc.* **2007**, *129* (49), 15259–15278. https://doi.org/10.1021/ja075242e.

(6) Wöbkenberg, P. H.; Ball, J.; Kooistra, F. B.; Hummelen, J. C.; De Leeuw, D. M.; Bradley, D. D. C.; Anthopoulos, T. D. Low-Voltage Organic Transistors Based on Solution Processed Semiconductors and Self-Assembled Monolayer Gate Dielectrics. *Appl. Phys. Lett.* **2008**, *93* (1). https://doi.org/10.1063/1.2954015.

(7) Virkar, A. A.; Mannsfeld, S.; Bao, Z.; Stingelin, N. Organic Semiconductor Growth and Morphology Considerations for Organic Thin-Film Transistors. *Adv. Mater.* **2010**, *22* (34), 3857–3875. https://doi.org/10.1002/adma.200903193.

(8) Cranston, R.; King, B.; Dindault, C.; Grant, T. M.; Rice, N.; Tonnelé, C.; Muccioli, L.; Castet, F.; Swaraj, S.; Lessard, B. H. Highlighting the Processing Versatility of a Silicon Phthalocyanine Derivative for Organic Thin-Film Transistors. *J. Mater. Chem. C* **2022**, *10* (2). https://doi.org/10.1039/d1tc05238a.

(9) Zhan, X.; Facchetti, A.; Barlow, S.; Marks, T. J.; Ratner, M. A.; Wasielewski, M. R.; Marder, S. R. Rylene and Related Diimides for Organic Electronics. *Adv. Mater.* **2011**, *23* (2), 268–284. https://doi.org/10.1002/adma.201001402.

(10) Suresh, S. M.; Zhang, L.; Matulaitis, T.; Hall, D.; Si, C.; Ricci, G.; Slawin, A. M. Z.; Warriner, S.; Beljonne, D.; Olivier, Y.; Samuel, I. D.; Zysman-Colman, E. Judicious Heteroatom Doping Produces High Performance Deep Blue/Near UV Multiresonant Thermally Activated Delayed Fluorescence OLEDs. *Adv. Mater.* **2023**, *35* (33), 2300997. https://doi.org/10.1002/adma.202300997.

(11) Sampson, K. L.; Nyikos, S. R.; Morse, G. E.; Bender, T. P. Sequentially Solution-Deposited Active Layer: Ideal Organic Photovoltaic Device Architecture for Boron Subphthalocyanine as a Nonfullerene Acceptor. *ACS Appl. Energy Mater.* **2021**, *4* (2), 1237–1249. https://doi.org/10.1021/acsaem.0c02528.

(12) Quinn, J. T. E.; Zhu, J.; Li, X.; Wang, J.; Li, Y. Recent Progress in the Development of N-Type Organic Semiconductors for Organic Field Effect Transistors. *J. Mater. Chem. C* **2017**, *5* (34), 8654–8681. https://doi.org/10.1039/c7tc01680h.

(13) Lin, P.; Yan, F. Organic Thin-Film Transistors for Chemical and Biological Sensing. *Adv. Mater.* **2012**, *24* (1), 34–51. https://doi.org/10.1002/adma.201103334.

(14) Marks, A.; Griggs, S.; Gasparini, N.; Moser, M. Organic Electrochemical Transistors: An Emerging Technology for Biosensing. *Adv. Mater. Interfaces* **2022**, *9* (6), 1–23. https://doi.org/10.1002/admi.202102039.

(15) Ha, J.; Chung, S.; Pei, M.; Cho, K.; Yang, H.; Hong, Y. One-Step Interface Engineering for All-Inkjet-Printed, All-Organic Components in Transparent, Flexible Transistors and Inverters: Polymer Binding. *ACS Appl. Mater. Interfaces* **2017**, *9* (10), 8819–8829. https://doi.org/10.1021/acsami.6b14702.

(16) Klauk, H. Organic Transistors on Paper : A Brief Review. *J. Mater. Chem. C* **2019**, *7* (19), 5522--5533. https://doi.org/10.1039/c9tc00793h.

(17) Shuai, Z.; Geng, H.; Xu, W.; Liao, Y.; André, J. M. From Charge Transport Parameters to Charge Mobility in Organic Semiconductors through Multiscale Simulation. *Chem. Soc. Rev.* **2014**, *43* (8), 2662–2679. https://doi.org/10.1039/c3cs60319a.

(18) Tran, V. Van; Jeong, G.; Kim, K. S.; Kim, J.; Jung, H. R.; Park, B.; Park, J. J.; Chang, M. Facile Strategy for Modulating the Nanoporous Structure of Ultrathin π-Conjugated Polymer Films for High-Performance Gas Sensors. *ACS Sensors* **2022**, *7* (1), 175–185. https://doi.org/10.1021/acssensors.1c01942.

(19) Ward, J. W.; Li, R.; Obaid, A.; Payne, M. M.; Smilgies, D. M.; Anthony, J. E.; Amassian, A.; Jurchescu, O. D. Rational Design of Organic Semiconductors for Texture Control and Self-Patterning on Halogenated Surfaces. *Adv. Funct. Mater.* **2014**, *24* (32), 5052–5058. https://doi.org/10.1002/adfm.201400219.

(20) Cheon, H. J.; Li, X.; Jeong, Y. J.; Sung, M. J.; Li, Z.; Jeon, I.; Tang, X.; Girma, H. G.; Kong, H.; Kwon, S. K.; An, T. K.; Kim, S. H.; Kim, Y. H. A Novel Design of Donor-Acceptor Polymer Semiconductors for Printed Electronics: Application to Transistors and Gas Sensors. *J. Mater. Chem. C* **2020**, *8* (25), 8410–8419. https://doi.org/10.1039/d0tc01341b.

(21) Comeau, Z. J.; Cranston, R. R.; Lamontagne, H. R.; Harris, C. S.; Shuhendler, A. J.; Lessard, B. H. Surface Engineering of Zinc Phthalocyanine Organic Thin-Film Transistors Results in Part-per-Billion Sensitivity towards Cannabinoid Vapor. *Commun. Chem.* **2022**, *5* (1), 1–8. https://doi.org/10.1038/s42004-022-00797-y.

(22) Song, D.; Wang, H.; Zhu, F.; Yang, J.; Tian, H.; Geng, Y.; Yan, D. Phthalocyanato Tin(IV) Dichloride: An Air-Stable, High-Performance, n-Type Organic Semiconductor with a High Field-Effect Electron Mobility. *Adv. Mater.* **2008**, *20* (11), 2142–2144. https://doi.org/10.1002/adma.200702439.

(23) Guo, J.; Liu, D.; Li, W.; Yu, B.; Tian, H.; Zhu, F.; Yan, D. High-Performance 2,9-DPh-DNTT Organic Thin-Film Transistor by Weak Epitaxy Growth Method. *Org. Electron.* **2021**, *93* (December 2020), 2–7. https://doi.org/10.1016/j.orgel.2021.106170.

(24) Bräuer, B.; Kukreja, R.; Virkar, A.; Akkerman, H. B.; Fognini, A.; Tyliszczak, T.; Bao, Z.

Carrier Mobility in Pentacene as a Function of Grain Size and Orientation Derived from Scanning Transmission X-Ray Microscopy. *Org. Electron.* **2011**, *12* (11), 1936–1942. https://doi.org/10.1016/j.orgel.2011.08.007.

(25) Park, D.; Tarsoly, G.; Kwon, D.; Shin, T. J.; Pyo, S. Photo-Response Modulation of Organic Transistors for Multi-Level Light Sensing Using Active Layer Microstructure Control. *J. Mater. Chem. C* **2023**, *11* (13). https://doi.org/10.1039/d3tc00454f.

(26) Sun, K.; Xiao, Z.; Hanssen, E.; Klein, M. F. G.; Dam, H. H.; Pfaff, M.; Gerthsen, D.; Wong, W. W. H.; Jones, D. J. The Role of Solvent Vapor Annealing in Highly Efficient Air-Processed Small Molecule Solar Cells. *J. Mater. Chem. A* **2014**, *2* (24), 9048–9054. https://doi.org/10.1039/c4ta01125b.

(27) Mascaro, D. J.; Thompson, M. E.; Smith, H. I.; Bulović, V. Forming Oriented Organic Crystals from Amorphous Thin Films on Patterned Substrates via Solvent-Vapor Annealing. *Org. Electron.* **2005**, *6* (5–6), 211–220. https://doi.org/10.1016/j.orgel.2005.07.001.

(28) Wang, C.; Dong, H.; Hu, W.; Liu, Y.; Zhu, D. Semiconducting π-Conjugated Systems in Field-Effect Transistors: A Material Odyssey of Organic Electronics. *Chem. Rev.* **2012**, *112* (4), 2208–2267. https://doi.org/10.1021/cr100380z.

(29) Waldrip, M.; Jurchescu, O. D.; Gundlach, D. J.; Bittle, E. G. Contact Resistance in Organic Field-Effect Transistors: Conquering the Barrier. *Adv. Funct. Mater.* **2020**, *30* (20), 1904576. https://doi.org/10.1002/adfm.201904576.

(30) Locklin, J.; Roberts, M. E.; Mannsfeld, S. C. B.; Bao, Z. Optimizing the Thin Film Morphology of Organic Field-Effect Transistors: The Influence of Molecular Structure and Vacuum Deposition Parameters on Device Performance. *J. Macromol. Sci. Part C Polym. Rev.* **2006**, *46* (1), 79–101. https://doi.org/10.1080/15321790500471244.

(31) Nunes, G.; Zane, S. G.; Meth, J. S. Styrenic Polymers as Gate Dielectrics for Pentacene Field-Effect Transistors. *J. Appl. Phys.* **2005**, *98* (10), 1–6. https://doi.org/10.1063/1.2134884.

(32) Yutronkie, N. J.; King, B.; Melville, O. A.; Lessard, H. Attaining Air Stability in High Performing N-Type Phthalocyanine Based Organic Semiconductors. *J. Mater. Chem.* **2021**, *9* (31), 10119–10126. https://doi.org/10.1039/d1tc02275j.

(33) King, B.; Melville, O. A.; Rice, N. A.; Kashani, S.; Tonnelé, C.; Raboui, H.; Swaraj, S.; Grant, T. M.; McAfee, T.; Bender, T. P.; Ade, H.; Castet, F.; Muccioli, L.; Lessard, B. H. Silicon Phthalocyanines for N-Type Organic Thin-Film Transistors: Development of Structure Property Relationships. *ACS Appl. Electron. Mater.* **2021**, *3* (1), 325–336. https://doi.org/https://dx.doi.org/10.1021/acsaelm.0c00871.

(34) Kim, S.; Yoo, H. Self-Assembled Monolayers: Versatile Uses in Electronic Devices from Gate Dielectrics, Dopants, and Biosensing Linkers. *Micromachines* **2021**, *12* (5). https://doi.org/10.3390/mi12050565.

(35) King, B.; Radford, C. L.; Ronnasi, B. Not Just Surface Energy: The Role of Bis(Pentafluorophenoxy) Silicon Phthalocyanine Axial Functionalization and Molecular Orientation on Organic Thin-Film Transistor Performance. *ACS Appl. Mater. Interfaces Interfaces* **2023**, *15* (11), 14937–14947. https://doi.org/10.1021/acsami.2c22789.

(36) Zhang, F.; Mohammadi, E.; Luo, X.; Strzalka, J.; Mei, J.; Diao, Y. Critical Role of Surface Energy in Guiding Crystallization of Solution-Coated Conjugated Polymer Thin Films. *Langmuir* **2018**, *34* (3), 1109–1122. https://doi.org/10.1021/acs.langmuir.7b02807.

(37) Deng, Y.; Quinn, J.; Sun, B.; He, Y.; Ellard, J.; Li, Y. Thiophene-S,S-Dioxidized Indophenine (IDTO) Based Donor-Acceptor Polymers for n-Channel Organic Thin Film Transistors. *RSC Adv.* **2016**, *6* (41), 34849–34854. https://doi.org/10.1039/c6ra03221d.

(38) Nicosia, C.; Huskens, J. Reactive Self-Assembled Monolayers: From Surface Functionalization to Gradient Formation. *Mater. Horizons* **2014**, *1* (1), 32–45. https://doi.org/10.1039/c3mh00046j.

(39) Zhou, Y.; Fuentes-hernandez, C.; Shim, J.; Meyer, J.; Giordano, A. J.; Li, H.; Winget, P.; Papadopoulos, T.; Cheun, H.; Kim, J.; Fenoll, M.; Dindar, A.; Haske, W.; Najafabadi, E.; Khan, T. M.; Sojoudi, H.; Barlow, S.; Graham, S.; Brédas, J.; Marder, S. R.; Kahn, A.; Kippelen, B. A Universal Method to Produce Low–Work Function Electrodes for Organic Electronics. *Science (80-.).* **2012**, *336*, 327–333.

(40) Li, S.; Guérin, D.; Lmimouni, K. Improving Performance of OFET by Tuning Occurrence of Charge Transport Based on Pentacene Interaction with SAM Functionalized Contacts. *Microelectron. Eng.* **2018**, *195* (February), 62–67. https://doi.org/10.1016/j.mee.2018.04.002.

(41) Robin, M.; Harnois, M.; Molard, Y.; Jacques, E. Improvement of N-Type OTFT Electrical Stability by Gold Electrode Modification. *Org. Electron.* **2016**, *39*, 214–221. https://doi.org/10.1016/j.orgel.2016.10.004.

(42) Ito, Y.; Virkar, A. A.; Mannsfeld, S.; Joon, H. O.; Toney, M.; Locklin, J.; Bao, Z. Crystalline Ultrasmooth Self-Assembled Monolayers of Alkylsilanes for Organic Field-Effect Transistors. *J. Am. Chem. Soc.* **2009**, *131* (26), 9396–9404. https://doi.org/10.1021/ja9029957.

(43) Fleischli, F. D.; Suàrez, S.; Schaer, M.; Zuppiroli, L. Organic Thin-Film Transistors : The Passivation of the Dielectric-Pentacene Interface by Dipolar Self-Assembled Monolayers. *Langmuir* **2010**, *26* (18), 15044–15049. https://doi.org/10.1021/la102060u.

(44) Acharya, R.; Peng, B.; Chan, P. K. L.; Schmitz, G.; Klauk, H. Achieving Ultralow Turn-On Voltages in Organic Thin-Film Transistors: Investigating Fluoroalkylphosphonic Acid Self-Assembled Monolayer Hybrid Dielectrics. *ACS Appl. Mater. Interfaces* **2019**, *11* (30), 27104–27111. https://doi.org/10.1021/acsami.9b04361.

(45) Ulman, A. Formation and Structure of Self-Assembled Monolayers. *Chem. Rev.* **1996**, *96* (4), 1533–1554. https://doi.org/10.1021/cr9502357.

(46) Wang, L.; Schubert, U. S.; Hoeppener, S. Surface Chemical Reactions on Self-Assembled Silane Based Monolayers. *Chem. Soc. Rev.* **2021**, *50* (11), 6507–6540. https://doi.org/10.1039/d0cs01220c.

(47) Chung, Y.; Verploegen, E.; Vailionis, A.; Sun, Y.; Nishi, Y.; Murmann, B.; Bao, Z. Controlling Electric Dipoles in Nanodielectrics and Its Applications for Enabling Air-Stable n-Channel Organic Transistors. *Nano Lett.* **2011**, *11* (3), 1161–1165. https://doi.org/10.1021/nl104087u.

(48) Gholamrezaie, F.; Andringa, A. M.; Roelofs, W. S. C.; Neuhold, A.; Kemerink, M.; Blom, P. W. M.; De Leeuw, D. M. Charge Trapping by Self-Assembled Monolayers as the Origin of the Threshold Voltage Shift in Organic Field-Effect Transistors. *Small* **2012**, *8* (2), 241–245. https://doi.org/10.1002/smll.201101467.

(49) Salinas, M.; Jäger, C. M.; Amin, A. Y.; Dral, P. O.; Meyer-Friedrichsen, T.; Hirsch, A.; Clark, T.; Halik, M. The Relationship between Threshold Voltage and Dipolar Character of Self-Assembled Monolayers in Organic Thin-Film Transistors. *J. Am. Chem. Soc.* **2012**, *134* (30), 12648–12652. https://doi.org/10.1021/ja303807u.

(50) Celle, C.; Suspène, C.; Ternisien, M.; Lenfant, S.; Guérin, D.; Smaali, K.; Lmimouni, K.; Simonato, J. P.; Vuillaume, D. Interface Dipole : Effects on Threshold Voltage and Mobility for Both Amorphous and Poly-Crystalline Organic Field Effect Transistors. *Org. Electron.* **2014**, *15* (3), 729–737. https://doi.org/10.1016/j.orgel.2014.01.003.

(51) Liu, D.; Miao, Q. Recent Progress in Interface Engineering of Organic Thin Film Transistors with Self-Assembled Monolayers. *Mater. Chem. Front.* **2018**, *2* (1), 11–21. https://doi.org/10.1039/c7qm00279c.

(52) Yang, S. Y.; Shin, K.; Park, C. E. The Effect of Gate-Dielectric Surface Energy on Pentacene Morphology and Organic Field-Effect Transistor Characteristics. *Adv. Funct. Mater.* **2005**, *15* (11), 1806–1814. https://doi.org/10.1002/adfm.200400486.

(53) Owens, D. K.; Wendt, R. C. Estimation of Surface Free Energy of Polymers. *J. Appl. Polym. Sci.* **1969**, *13*, 1741–1747. https://doi.org/https://doi.org/10.1002/app.1969.070130815.

(54) Kwok, D. Y.; Neumann, A. W. *Contact Angle Measurement and Contact Angle Interpretation*; 1999; Vol. 81. https://doi.org/10.1016/S0001-8686(98)00087-6.

(55) Umeda, T.; Kumaki, D.; Tokito, S. Surface-Energy-Dependent Field-Effect Mobilities up to 1 Cm2 /V s for Polymer Thin-Film Transistor. *J. Appl. Phys.* **2009**, *105* (2), 024516. https://doi.org/10.1063/1.3072669.

(56) Di, C.; Liu, Y.; Yu, G.; Zhu, D. Interface Engineering: An Effective Approach toward High-Performance Organic Field-Effect Transistors. *Acc. Chem. Res.* **2009**, *42* (10), 1573–1583. https://doi.org/10.1021/ar9000873.

(57) Zhao, C.; Li, A.; Chen, X.; Ali, M. U.; Meng, H. Hysteresis Effect in Organic Thin Film Transistors Based on Naphthalene Tetracarboxylic Diimide Derivatives. *Appl. Phys. Lett.* **2021**, *118* (19). https://doi.org/10.1063/5.0045183.

(58) Zhou, S.; Tang, Q.; Tian, H.; Zhao, X.; Tong, Y.; Barlow, S.; Marder, S. R.; Liu, Y. Direct Effect of Dielectric Surface Energy on Carrier Transport in Organic Field-Effect Transistors. *ACS Appl. Mater. Interfaces* **2018**, *10* (18), 15943–15951. https://doi.org/10.1021/acsami.8b02304.

(59) Nakano, M.; Osaka, I.; Takimiya, K. Control of Major Carriers in an Ambipolar Polymer Semiconductor by Self-Assembled Monolayers. *Adv. Mater.* **2017**, *29* (1), 1602893. https://doi.org/10.1002/adma.201602893.

(60) Lee, W. H.; Choi, H. H.; Kim, D. H.; Cho, K. 25th Anniversary Article: Microstructure Dependent Bias Stability of Organic Transistors. *Adv. Mater.* **2014**, *26* (11), 1660–1680. https://doi.org/10.1002/adma.201304665.

(61) Kalb, W. L.; Mathis, T.; Haas, S.; Stassen, A. F.; Batlogg, B. Organic Small Molecule Field-Effect Transistors with Cytop^{TM} Gate Dielectric: Eliminating Gate Bias Stress Effects. *Appl. Phys. Lett.* **2007**, *90* (9), 1–4. https://doi.org/10.1063/1.2709894.

(62) Wang, S.; Wang, Z.; Li, J.; Li, L.; Hu, W. Surface-Grafting Polymers: From Chemistry to Organic Electronics. *Mater. Chem. Front.* **2020**, *4* (3), 692–714. https://doi.org/10.1039/c9qm00450e.

(63) Melville, O. A.; Grant, T. M.; Lessard, H. Silicon Phthalocyanines as N-Type Semiconductors in Organic Thin Film Transistors. *J. Mater. Chem. C* **2018**, *6*, 5482–5488. https://doi.org/10.1039/c8tc01116h.

(64) Melville, O. A.; King, B.; Imperiale, C.; Lessard, B. H. Orthogonally Processable Carbazole-Based Polymer Thin Films by Nitroxide-Mediated Polymerization. *Langmuir* **2016**, *32*, 13640–13648.

(65) Cunningham, M.; Billon, L.; Save, M. *Surface-Initiated Nitroxide- Mediated Polymerization*; 2015.

(66) Page, Z. A.; Narupai, B.; Pester, C. W.; Bou Zerdan, R.; Sokolov, A.; Laitar, D. S.; Mukhopadhyay, S.; Sprague, S.; McGrath, A. J.; Kramer, J. W.; Trefonas, P.; Hawker, C. J. Novel Strategy for Photopatterning Emissive Polymer Brushes for Organic Light Emitting Diode Applications. *ACS Cent. Sci.* **2017**, *3* (6), 654–661. https://doi.org/10.1021/acscentsci.7b00165.

(67) Li, L.; Hu, W.; Chi, L.; Fuchs, H. Polymer Brush and Inorganic Oxide Hybrid Nanodielectrics for High Performance Organic Transistors. *J. Phys. Chem. B* **2010**, *114* (16), 5315–5319. https://doi.org/10.1021/jp100928d.

(68) Ge, F.; Wang, X.; Zhang, Y.; Song, E.; Zhang, G.; Lu, H.; Cho, K.; Qiu, L. Modulating the Surface via Polymer Brush for High-Performance Inkjet-Printed Organic Thin-Film Transistors. *Adv. Electron. Mater.* **2017**, *3* (1). https://doi.org/10.1002/aelm.201600402.

(69) Tria, M. C.; Liao, K. S.; Alley, N.; Curran, S.; Advincula, R. Electrochemically Crosslinked Surface-Grafted PVK Polymer Brushes as a Hole Transport Layer for Organic Photovoltaics. *J. Mater. Chem.* **2011**, *21* (28), 10261–10264. https://doi.org/10.1039/c1jm11068c.

(70) Lessard, B. H. *Novel Materials : From Nanoporous Materials to Micro-Electronics*; 2016.

(71) Savelyeva, X.; Li, L.; Maric, M. Using Controlled Radical Polymerization to Confirm the Lower Critical Solution Temperature of an N-(Alkoxyalkyl) Acrylamide Polymer in Aqueous Solution. *J. Polym. Sci. Part A Polym. Chem.* **2015**, *53* (1), 59–67. https://doi.org/10.1002/pola.27437.

(72) Vinas, J.; Chagneux, N.; Gigmes, D.; Trimaille, T.; Favier, A.; Bertin, D. SG1-Based Alkoxyamine Bearing a N-Succinimidyl Ester: A Versatile Tool for Advanced Polymer Synthesis. *Polymer (Guildf).* **2008**, *49* (17), 3639–3647. https://doi.org/10.1016/j.polymer.2008.06.017.

(73) Lessard, B. H.; Marić, M. Incorporating Glycidyl Methacrylate into Block Copolymers Using Poly(Methacrylate-Ran-Styrene) Macroinitiators Synthesised by Nitroxide Mediated Polymerization. *J. Polym. Sci. Part A Polym. Chem.* **2009**, *47* (10), 2574–2588.

https://doi.org/10.1002/pola.

(74) Lessard, B. H.; Savelyeva, X.; Marić, M. Smart Morpholine-Functional Statistical Copolymers Synthesized by Nitroxide Mediated Polymerization. *Polym. (United Kingdom)* **2012**, *53* (25), 5649–5656. https://doi.org/10.1016/j.polymer.2012.10.020.

(75) Kim, K.; An, T. K.; Kim, J.; Jeong, Y. J.; Jang, J.; Kim, H.; Baek, J. Y.; Kim, Y. H.; Kim, S. H.; Park, C. E. Grafting Fluorinated Polymer Nanolayer for Advancing the Electrical Stability of Organic Field-Effect Transistors. *Chem. Mater.* **2014**, *26* (22), 6467–6476. https://doi.org/10.1021/cm5030266.

(76) Lee, S.; Jang, M.; Yang, H. Optimized Grafting Density of End-Functionalized Polymers to Polar Dielectric Surfaces for Solution-Processed Organic Field-Effect Transistors. *ACS Appl. Mater. Interfaces* **2014**, *6* (22), 20444–20451. https://doi.org/10.1021/am506024s.

(77) Yang, J.; Yan, D. Weak Epitaxy Growth of Organic Semiconductor Thin Films. *Chem. Soc. Rev.* **2009**, *38* (9), 2634–2645. https://doi.org/10.1039/b815723p.

(78) Ewenike, R.; King, B.; Battaglia, A.; Quezada Borja, J.; Lin, Z.; Manion, J.; Brusso, J.; Kelly, T.; Seferos, D.; Lessard, B. H. Towards Weak Epitaxial Growth of Silicon Phthalocyanines, How the Choice of Optimal Templating Layer Differs from Traditional Phthalocyanines. *ACS Appl. Electron. Mater.* **2023**, *Submitted*.

(79) Yang, J.; Yan, D.; Jones, T. S. Molecular Template Growth and Its Applications in Organic Electronics and Optoelectronics. *Chem. Rev.* **2015**, *115* (11), 5570–5603. https://doi.org/10.1021/acs.chemrev.5b00142.

(80) Zhang, Y.; Wei, X.; Zhang, H.; Chen, X.; Wang, J. Ambipolar Organic Transistors with High on/off Ratio by Introducing a Modified Layer of Gate Insulator. *Appl. Surf. Sci.* **2018**, *427*, 452–457. https://doi.org/10.1016/j.apsusc.2017.08.116.

(81) Yang, J.; Wang, T.; Wang, H.; Zhu, F.; Li, G.; Yan, D. Ultrathin-Film Growth of Para-Sexiphenyl (I): Submonolayer Thin-Film Growth as a Function of the Substrate Temperature. *J. Phys. Chem. B* **2008**, *112* (26), 7816–7820. https://doi.org/10.1021/jp711455u.

(82) Wang, H.; Zhu, F.; Yang, J.; Geng, Y.; Yan, D. Weak Epitaxy Growth Affording High-Mobility Thin Films of Disk-like Organic Semiconductors. *Adv. Mater.* **2007**, *19* (16), 2168–2171. https://doi.org/10.1002/adma.200602566.

(83) Mabeck, J. T.; Malliaras, G. G. Chemical and Biological Sensors Based on Organic Thin-Film Transistors. *Anal. Bioanal. Chem.* **2005**, *384* (2), 343–353. https://doi.org/10.1007/s00216-005-3390-2.

(84) Wu, M.; Hou, S.; Yu, X.; Yu, J. Recent Progress in Chemical Gas Sensors Based on Organic Thin Film Transistors. *J. Mater. Chem. C* **2020**, *8* (39), 13482–13500. https://doi.org/10.1039/d0tc03132a.

(85) Shin, S. Y.; Jang, M.; Cheon, H. J.; Go, S.; Yoon, H.; Chang, M. Nanostructure-Assisted Solvent Vapor Annealing of Conjugated Polymer Thin Films for Enhanced Performance in Volatile Organic Compound Sensing. *Sensors Actuators B Chem.* **2022**, *351* (July 2021), 1–11. https://doi.org/10.1016/j.snb.2021.130951.

(86) Roberts, M. E.; Mannsfeld, S. C. B.; Tang, M. L.; Bao, Z. Influence of Molecular Structure

and Film Properties on the Water-Stability and Sensor Characteristics of Organic Transistors. *Chem. Mater.* **2008**, *20* (23), 7332–7338. https://doi.org/10.1021/cm802530x.

(87) Zhao, S.; Hou, S.; Fan, H.; Wang, Z.; Yu, J. High Performance Nitrogen Dioxide Sensor Based on Organic Thin-Film Transistor Utilizing P3HT/OH-MWCNTs Blend Film. *Synth. Met.* **2020**, *269* (September), 116569. https://doi.org/10.1016/j.synthmet.2020.116569.

(88) Zhang, C.; Chen, P.; Hu, W. Organic Field-Effect Transistor-Based Gas Sensors. *Chem. Soc. Rev.* **2015**, *44* (8), 2087–2107. https://doi.org/10.1039/C4CS00326H.

(89) Ganesh Moorthy, S.; King, B.; Kumar, A.; Lesniewska, E.; Lessard, B. H.; Bouvet, M. Molecular Engineering of Silicon Phthalocyanine to Improve the Charge Transport and Ammonia Sensing Properties of Organic Heterojunction Gas Sensors. *Advaned Sens. Res.* **2023**, *2200030*, 1–13. https://doi.org/10.1002/adsr.202200030.

(90) Meijer, E. J.; Detcheverry, C.; Baesjou, P. J.; Van Veenendaal, E.; De Leeuw, D. M.; Klapwijk, T. M. Dopant Density Determination in Disordered Organic Field-Effect Transistors. *J. Appl. Phys.* **2003**, *93* (8), 4831–4835. https://doi.org/10.1063/1.1559933.

(91) Bengasi, G.; Meunier-Prest, R.; Baba, K.; Kumar, A.; Pellegrino, A. L.; Boscher, N. D.; Bouvet, M. Molecular Engineering of Porphyrin-Tapes/Phthalocyanine Heterojunctions for a Highly Sensitive Ammonia Sensor. *Adv. Electron. Mater.* **2020**, *6* (12), 1–12. https://doi.org/10.1002/aelm.202000812.

(92) Chehade, G.; Dincer, I. Progress in Green Ammonia Production as Potential Carbon-Free Fuel. *Fuel* **2021**, *299* (February), 120845. https://doi.org/10.1016/j.fuel.2021.120845.

(93) Timmer, B.; Olthuis, W.; Van Den Berg, A. Ammonia Sensors and Their Applications - A Review. *Sensors Actuators, B Chem.* **2005**, *107* (2), 666–677. https://doi.org/10.1016/j.snb.2004.11.054.

(94) Xie, T.; Xie, G.; Su, Y.; Hongfei, D.; Ye, Z.; Jiang, Y. Ammonia Gas Sensors Based on Poly (3-Hexylthiophene)-Molybdenum Disulfide Film Transistors. *Nanotechnology* **2016**, *27* (6). https://doi.org/10.1088/0957-4484/27/6/065502.

(95) Yu, J.; Yu, X.; Zhang, L.; Zeng, H. Ammonia Gas Sensor Based on Pentacene Organic Field-Effect Transistor. *Sensors Actuators, B Chem.* **2012**, *173*, 133–138. https://doi.org/10.1016/j.snb.2012.06.060.

(96) Zhou, X.; Niu, K.; Wang, Z.; Huang, L.; Chi, L. An Ammonia Detecting Mechanism for Organic Transistors as Revealed by Their Recovery Processes. *Nanoscale* **2018**, *10* (18), 8832–8839. https://doi.org/10.1039/c8nr01275j.

(97) Lu, J.; Liu, D.; Zhou, J.; Chu, Y.; Chen, Y.; Wu, X.; Huang, J. Porous Organic Field-Effect Transistors for Enhanced Chemical Sensing Performances. *Adv. Funct. Mater.* **2017**, *27* (20). https://doi.org/10.1002/adfm.201700018.

(98) Darshan, V.; Rajeev, V. R.; Unni, K. N. N. Enhanced Performance of Room Temperature Ammonia Sensors Using Morphology-Controlled Organic Field-Effect Transistors. *Org. Electron.* **2021**, *98* (November 2021), 106280. https://doi.org/10.1016/j.orgel.2021.106280.

(99) Yang, Y.; Zhang, G.; Luo, H.; Yao, J.; Liu, Z.; Zhang, D. Highly Sensitive Thin-Film Field-Effect Transistor Sensor for Ammonia with the DPP-Bithiophene Conjugated Polymer Entailing Thermally Cleavable Tert-Butoxy Groups in the Side Chains. *ACS Appl. Mater.*

Interfaces **2016**, *8* (6), 3635–3643. https://doi.org/10.1021/acsami.5b08078.

(100) Wang, Z.; Liu, Z.; Chen, L.; Yang, Y.; Ma, J.; Zhang, X. Highly Sensitive Field-Effect Ammonia / Amine Sensors with Low Driving Voltage Based on Low Bandgap Polymers. *Adv. Electron. Mater.* **2018**, *4* (5), 1800025. https://doi.org/10.1002/aelm.201800025.

(101) Cao, Z.; Huo, X.; Ma, Q.; Song, J.; Pan, Q.; Chen, L.; Lai, J.; Shan, X.; Gao, J. TFT-CN / P3HT Blending Active Layer Based Two-Component Organic Field-Effect Transistor for Improved H2S Gas Detection. *Sensors Actuators B. Chem.* **2023**, *385*, 133685. https://doi.org/10.1016/j.snb.2023.133685.

(102) Li, X.; Jiang, Y.; Xie, G.; Tai, H.; Sun, P.; Zhang, B. Copper Phthalocyanine Thin Film Transistors for Hydrogen Sulfide Detection. *Sensors Actuators, B Chem.* **2013**, *176*, 1191–1196. https://doi.org/10.1016/j.snb.2012.09.084.

(103) Luo, H.; Chen, S.; Liu, Z.; Zhang, C.; Cai, Z.; Chen, X. A Cruciform Electron Donor – Acceptor Semiconductor with Solid-State Red Emission : 1D / 2D Optical Waveguides and Highly Sensitive / Selective Detection of H 2 S Gas. *Adv. Funct. Mater.* **2014**, *24* (27), 4250–4258. https://doi.org/10.1002/adfm.201304027.

(104) Lv, A.; Wang, M.; Wang, Y.; Bo, Z.; Chi, L. Investigation into the Sensing Process of High-Performance H2S Sensors Based on Polymer Transistors. *Chem. – A Eur. J.* **2016**, *22* (11), 3521–3890. https://doi.org/10.1002/chem.201504196.

(105) Wang, Z.; Hu, J.; Lu, J.; Zhu, X.; Zhou, X.; Huang, L.; Chi, L. Charge Transport Manipulation via Interface Doping : Achieving Ultrasensitive Organic Semiconductor Gas Sensors. *ACS Appl. Mater. Interfaces* **2023**, *15* (6), 8355–8366. https://doi.org/10.1021/acsami.2c20391.

(106) Zhuang, X.; Han, S.; Huai, B.; Shi, W.; Junsheng, Y. Sub-Ppm and High Response Organic Thin-Film Transistor NO2 Sensor Based on Nanofibrillar Structured TIPS-Pentacene. *Sensors Actuators, B Chem.* **2019**, *279* (2), 238–244. https://doi.org/10.1016/j.snb.2018.10.002.

(107) Zhang, X.; Wang, B.; Huang, L.; Huang, W.; Wang, Z.; Zhu, W.; Chen, Y.; Mao, Y. L.; Facchetti, A.; Marks, T. J. Breath Figure–Derived Porous Semiconducting Films for Organic Electronics. *Sci. Adv.* **2020**, *6* (13), 1–10. https://doi.org/10.1126/sciadv.aaz1042.

(108) Wang, Z.; Huang, L.; Zhu, X.; Zhou, X.; Chi, L. An Ultrasensitive Organic Semiconductor NO2 Sensor Based on Crystalline TIPS-Pentacene Films. *Adv. Mater.* **2017**, *29* (38), 1–8. https://doi.org/10.1002/adma.201703192.

(109) Wang, L.; Wang, L.; Li, G.; Zhu, Y.; Liu, C.; Zeng, L.; Zhong, S.; Wang, L. J. Three-Dimensional CuPc Films Decorated with Well-Ordered PVA Parallel Nanofiber Arrays for Low Concentration Detecting NO2 Sensor. *Sensors Actuators, B Chem.* **2021**, *337* (2), 129781. https://doi.org/10.1016/j.snb.2021.129781.

(110) Jeong, G.; Cheon, H. J.; Shin, S. Y.; Wi, E.; Kyokunzire, P.; Cheon, H.; Van Tran, V.; Vu, T. T.; Chang, M. Improved NO2 Gas Sensing Performance of Nanoporous Conjugated Polymer (CP) Thin Films by Incorporating Preformed CP Nanowires. *Dye. Pigment.* **2023**, *214* (2), 111235. https://doi.org/10.1016/j.dyepig.2023.111235.

(111) Zhu, Y.; Zhang, Y.; Yu, J.; Zhou, C.; Yang, C.; Wang, L.; Wang, L.; Ma, L.; Wang, L. J.

Highly-Sensitive Organic Field Effect Transistor Sensors for Dual Detection of Humidity and NO2. *Sensors Actuators B Chem.* **2023**, *374* (October 2022), 132815. https://doi.org/10.1016/j.snb.2022.132815.

(112) Shaymurat, T.; Tang, Q.; Tong, Y.; Dong, L.; Liu, Y. Gas Dielectric Transistor of CuPc Single Crystalline Nanowire for SO2 Detection down to Sub-Ppm Levels at Room Temperature. *Adv. Mater.* **2013**, *25* (16), 2269–2273. https://doi.org/10.1002/adma.201204509.

(113) Kwak, D.; Lei, Y.; Maric, R. Ammonia Gas Sensors: A Comprehensive Review. *Talanta* **2019**, *204* (June), 713–730. https://doi.org/10.1016/j.talanta.2019.06.034.

(114) Song, D.; Zhu, F.; Yu, B.; Huang, L.; Geng, Y.; Yan, D. Tin (IV) Phthalocyanine Oxide: An Air-Stable Semiconductor with High Electron Mobility. *Appl. Phys. Lett.* **2008**, *92* (14), 143303. https://doi.org/10.1063/1.2903486.

(115) Boileau, N. T.; Cranston, R.; Mirka, B.; Melville, O. A.; Lessard, B. H. Metal Phthalocyanine Organic Thin-Film Transistors: Changes in Electrical Performance and Stability in Response to Temperature and Environment. *RSC Adv.* **2019**, *9* (37), 21478–21485. https://doi.org/10.1039/c9ra03648b.

(116) Lessard, B. H.; White, R. T.; Al-Amar, M.; Plint, T.; Castrucci, J. S.; Josey, D. S.; Lu, Z. H.; Bender, T. P. Assessing the Potential Roles of Silicon and Germanium Phthalocyanines in Planar Heterojunction Organic Photovoltaic Devices and How Pentafluoro Phenoxylation Can Enhance π-π Interactions and Device Performance. *ACS Appl. Mater. Interfaces* **2015**, *7* (9), 5076–5088. https://doi.org/10.1021/am508491v.

(117) McAfee, T.; Hoffman, B. C.; You, X.; Atkin, J. M.; Ade, H.; Dougherty, D. B. Morphological, Optical, and Electronic Consequences of Coexisting Crystal Orientations in β-Copper Phthalocyanine Thin Films. *J. Phys. Chem. C* **2016**, *120* (33), 18616–18621. https://doi.org/10.1021/acs.jpcc.6b05043.

(118) Beaumont, N.; Castrucci, S.; Sullivan, P.; Morse, G. E.; Paton, A. S.; Lu, Z.; Bender, T. P.; Jones, T. S. Acceptor Properties of Boron Subphthalocyanines in Fullerene Free Photovoltaics. *J. Phys. Chem. C* **2014**, *118*, 14814–14823. https://doi.org/10.1021/jp503578g.

(119) Li, Q.; Tang, Q.; Li, H.; Hu, W.; Yang, X.; Shuai, Z.; Liu, Y.; Zhu, D. Organic Thin-Film Transistors of Phthalocyanines. *Pure Appl. Chem.* **2008**, *80* (11), 2231–2240. https://doi.org/10.1351/pac200880112231.

(120) Jiang, H.; Ye, J.; Hu, P.; Wei, F.; Du, K.; Wang, N.; Ba, T.; Feng, S.; Kloc, C. Fluorination of Metal Phthalocyanines: Single-Crystal Growth, Efficient N-Channel Organic Field-Effect Transistors, and Structure-Property Relationships. *Sci. Rep.* **2014**, *4*, 7573. https://doi.org/10.1038/srep07573.

(121) Chaure, N. B.; Basova, T.; Zahedi, M.; Ray, A. K.; Sharma, A. K.; Durmuş, M.; Ahsen, V. Solution Processed Tetrasubstituted Zinc Phthalocyanine as an Active Layer in Organic Field Effect Transistors. *J. Appl. Phys.* **2010**, *107* (11), 2–7. https://doi.org/10.1063/1.3428386.

(122) Pearson, A. J.; Plint, T.; Jones, S. T. E.; Lessard, B. H.; Credgington, D.; Bender, T. P.; Greenham, N. C. Silicon Phthalocyanines as Dopant Red Emitters for Efficient Solution

Processed OLEDs. *J. Mater. Chem. C* **2017**, *5* (48), 12688–12698. https://doi.org/10.1039/c7tc03946h.

(123) Melville, O. A.; Grant, T. M.; Lochhead, K.; King, B.; Ambrose, R.; Rice, N. A.; Boileau, N. T.; Peltekoff, A. J.; Tousignant, M.; Hill, I. G.; Lessard, B. H. Contact Engineering Using Manganese, Chromium, and Bathocuproine in Group 14 Phthalocyanine Organic Thin-Film Transistors. *ACS Appl. Electron. Mater.* **2020**, *2* (5), 1313–1322. https://doi.org/10.1021/acsaelm.0c00104.

(124) Zysman-Colman, E.; Ghosh, S. S.; Xie, G.; Varghese, S.; Chowdhury, M.; Sharma, N.; Cordes, D. B.; Slawin, A. M. Z.; Samuel, I. D. W. Solution-Processable Silicon Phthalocyanines in Electroluminescent and Photovoltaic Devices. *ACS Appl. Mater. Interfaces* **2016**, *8* (14), 9247–9253. https://doi.org/10.1021/acsami.5b12408.

(125) Grant, T. M.; Rice, N. A.; Muccioli, L.; Castet, F.; Lessard, B. H. Solution-Processable n-Type Tin Phthalocyanines in Organic Thin Film Transistors and as Ternary Additives in Organic Photovoltaics. *ACS Appl. Electron. Mater.* **2019**, *1* (4), 494–504. https://doi.org/10.1021/acsaelm.8b00113.

(126) Melville, O. A.; Lessard, B. H.; Bender, T. P. Phthalocyanine-Based Organic Thin-Film Transistors: A Review of Recent Advances. *ACS Applied Materials & Interfaces*. 2015, pp 13105–13118. https://doi.org/10.1021/acsami.5b01718.

(127) Li, L.; Tang, Q.; Li, H.; Yang, X.; Hu, W.; Song, Y.; Shuai, Z.; Xu, W.; Liu, Y.; Zhu, D. An Ultra Closely π-Stacked Organic Semiconductor for High Performance Field-Effect Transistors. *Adv. Mater.* **2007**, *19* (18), 2613–2617. https://doi.org/10.1002/adma.200700682.

(128) Jiang, H.; Hu, P.; Ye, J.; Li, Y.; Li, H.; Zhang, X.; Li, R.; Dong, H.; Hu, W.; Kloc, C. Molecular Crystal Engineering: Tuning Organic Semiconductor from p-Type to n-Type by Adjusting Their Substitutional Symmetry. *Adv. Mater.* **2017**, *29* (10). https://doi.org/10.1002/adma.201605053.

(129) Bao, Z.; Lovinger, A. J.; Brown, J. New Air-Stable n-Channel Organic Thin Film Transistors. *J. Am. Chem. Soc.* **1998**, *7863* (24), 207–208. https://doi.org/10.1021/ja9727629.

(130) Cranston, R. R.; Vebber, M. C.; Berbigier, J. F.; Rice, N. A.; Tonnelé, C.; Comeau, Z. J.; Boileau, N. T.; Brusso, J. L.; Shuhendler, A. J.; Castet, F.; Muccioli, L.; Kelly, T. L.; Lessard, B. H. Thin-Film Engineering of Solution-Processable n-Type Silicon Phthalocyanines for Organic Thin-Film Transistors. *ACS Appl. Mater. Interfaces* **2021**, *13* (1), 1008–1020. https://doi.org/10.1021/acsami.0c17657.

(131) Lessard, B. H.; Lough, A. J.; Bender, T. P. Crystal Structures of Bis(Phenoxy)Silicon Phthalocyanines: Increasing π-π Interactions, Solubility and Disorder and No Halogen Bonding Observed. *Acta Crystallogr. Sect. E Crystallogr. Commun.* **2016**, *72*, 988–994. https://doi.org/10.1107/S205698901600935X.

(132) Raboui, H.; Lough, A. J.; Plint, T.; Bender, T. P. Position of Methyl and Nitrogen on Axial Aryloxy Substituents Determines the Crystal Structure of Silicon Phthalocyanines. *Cryst. Growth Des.* **2018**, *18* (5), 3193–3201. https://doi.org/10.1021/acs.cgd.8b00298.

(133) Lessard, B. H.; Grant, T. M.; White, R.; Thibau, E.; Lu, Z. H.; Bender, T. P. The Position

and Frequency of Fluorine Atoms Changes the Electron Donor/Acceptor Properties of Fluorophenoxy Silicon Phthalocyanines within Organic Photovoltaic Devices. *J. Mater. Chem. A* **2015**, *3* (48), 24512–24524. https://doi.org/10.1039/c5ta07173a.

(134) Liu, Q.; Wang, Y.; Kohara, A.; Matsumoto, H.; Manzhos, S.; Feron, K.; Bottle, S. E.; Bell, J.; Michinobu, T.; Sonar, P. Tuning the Charge Carrier Polarity of Organic Transistors by Varying the Electron Affinity of the Flanked Units in Diketopyrrolopyrrole-Based Copolymers. *Adv. Funct. Mater.* **2020**, *30* (7), 1–9. https://doi.org/10.1002/adfm.201907452.

(135) Li, P.; Shi, J.; Lei, Y.; Huang, Z.; Lei, T. Switching P-Type to High-Performance n-Type Organic Electrochemical Transistors via Doped State Engineering. *Nat. Commun.* **2022**, *13* (1). https://doi.org/10.1038/s41467-022-33553-w.

(136) Anthopoulos, T. D.; Anyfantis, G. C.; Papavassiliou, G. C.; De Leeuw, D. M. Air-Stable Ambipolar Organic Transistors. *Appl. Phys. Lett.* **2007**, *90* (12). https://doi.org/10.1063/1.2715028.

(137) Vebber, M. C.; King, B.; French, C.; Toussignant, M.; Ronnasi, B.; Dindault, C.; Wantz, G.; Hirsch, L.; Brusso, J.; Lessard, B. H. From P-type to N-type: Peripheral Fluorination of Axially Substituted Silicon Phthalocyanines Enables Fine Tuning of Charge Transport. *Can. J. Chem. Eng.* **2023**, No. January, 1–13. https://doi.org/10.1002/cjce.24843.

(138) Parra, V.; Brunet, J.; Pauly, A.; Bouvet, M. Molecular Semiconductor-Doped Insulator (MSDI) Heterojunctions: An Alternative Transducer for Gas Chemosensing. *Analyst* **2009**, *134* (9), 1776–1778. https://doi.org/10.1039/b906786h.

(139) Wang, H.; Yan, D. Organic Heterostructures in Organic Field-Effect Transistors. *NPG Asia Mater.* **2010**, *2* (2), 69–78. https://doi.org/10.1038/asiamat.2010.44.

(140) Belarbi, Z.; Sirlin, C.; Simon, J.; Andre, J. J. Electrical and Magnetic Properties of Liquid Crystalline Molecular Materials: Lithium and Lutetium Phthalocyanine Derivatives. *J. Phys. Chem.* **1989**, *93* (24), 8105–8110. https://doi.org/10.1021/j100361a026.

(141) Bouvet, M.; Xiong, H.; Parra, V. Molecular Semiconductor-Doped Insulator (MSDI) Heterojunctions: Oligothiophene/Bisphtalocyanine (LuPc2) and Perylene/Bisphthalocyanine as New Structures for Gas Sensing. *Sensors Actuators, B Chem.* **2010**, *145* (1), 501–506. https://doi.org/10.1016/j.snb.2009.12.064.

(142) Wannebroucq, A.; Gruntz, G.; Suisse, J.-M.; Nicolas, Y.; Meunier-Prest, R.; Mateos, M.; Toupance, T.; Bouvet, M. New N-Type Molecular Semiconductor – Doped Insulator (MSDI) Heterojunctions Combining a Triphenodioxazine (TPDO) and the Lutetium Bisphthalocyanine (LuPc 2) for Ammonia Sensing. *Sensors Actuators B. Chem.* **2018**, *255* (2), 1694–1700. https://doi.org/10.1016/j.snb.2017.08.184.

(143) Bouvet, M.; Parra, V.; Locatelli, C.; Xiong, H. Electrical Transduction in Phthalocyanine-Based Gas Sensors: From Classical Chemiresistors to New Functional Structures. *Journal of Porphyrins and Phthalocyanines*. 2009, pp 84–91. https://doi.org/10.1142/S108842460900019X.

(144) Guillaud, G.; Al Sadoun, M.; Maitrot, M.; Simon, J.; Bouvet, M. Field-Effect Transistors Based on Intrinsic Molecular Semiconductors. *Chem. Phys. Lett.* **1990**, *167* (6), 503–506.

(145) Trometer, M.; Even, R.; Simon, J.; Dubon, A.; Laval, J. Y.; Germain, J. P.; Maleysson, C.; Pauly, A.; Robert, H. Lutetium Bisphthalocyanine Thin Films for Gas Detection. *Sensors Actuators B. Chem.* **1992**, *8* (2), 129–135. https://doi.org/10.1016/0925-4005(92)80169-X.

(146) Parra, V.; Arrieta, Á. A.; Fernández-Escudero, J. A.; Íñiguez, M.; Saja, J. A. De; Rodríguez-Méndez, M. L. Monitoring of the Ageing of Red Wines in Oak Barrels by Means of an Hybrid Electronic Tongue. *Anal. Chim. Acta* **2006**, *563* (1-2 SPEC. ISS.), 229–237. https://doi.org/10.1016/j.aca.2005.09.044.

(147) Kumar, A.; Meunier-Prest, R.; Bouvet, M. Organic Heterojunction Devices Based on Phthalocyanines: A New Approach to Gas Chemosensing. *Sensors (Switzerland)* **2020**, *20* (17), 1–25. https://doi.org/10.3390/s20174700.

(148) Bouvet, M.; Gaudillat, P.; Kumar, A.; Sauerwald, T.; Schüler, M.; Schütze, A.; Suisse, J. M. Revisiting the Electronic Properties of Molecular Semiconductor - Doped Insulator (MSDI) Heterojunctions through Impedance and Chemosensing Studies. *Org. Electron.* **2015**, *26*, 345–354. https://doi.org/10.1016/j.orgel.2015.07.052.

(149) Ouedraogo, S.; Meunier-Prest, R.; Kumar, A.; Bayo-Bangoura, M.; Bouvet, M. Modulating the Electrical Properties of Organic Heterojunction Devices Based on Phthalocyanines for Ambipolar Sensors. *ACS Sensors* **2020**, *5* (6), 1849–1857. https://doi.org/10.1021/acssensors.0c00877.

(150) Şahin, Z.; Meunier-Prest, R.; Dumoulin, F.; Kumar, A.; Isci, Ü.; Bouvet, M. Tuning of Organic Heterojunction Conductivity by the Substituents' Electronic Effects in Phthalocyanines for Ambipolar Gas Sensors. *Sensors Actuators, B Chem.* **2021**, *332*, 129505. https://doi.org/10.1016/j.snb.2021.129505.

(151) Kikobo, G. L.; Kumar, A.; Vibhu, V.; Ouedraogo, S.; Deshotel, A.; Mateos, M.; Meunier-Prest, R.; Bouvet, M. Photon Assisted-Inversion of Majority Charge Carriers in Molecular Semiconductor-Based Organic Heterojunctions. *J. Mater. Chem. C* **2021**, *9* (14), 5008–5020. https://doi.org/10.1039/d0tc05828a.

Chapter 2. Silicon phthalocyanines for n-type organic thin-film transistors: development of structure property relationships

This chapter was published in the journal "ACS Applied Electronic Materials": King, B.; Melville, O.; Rice, N.; Kashani, S.; Tonnelé, C.; Raboui, H.; Swaraj, S.; Grant, T. M.; McAfee, T.; Bender, T.; Ade, H.; Castet, F.; Muccioli, L.; Lessard, B. H. Silicon phthalocyanines for n-type organic thin-film transistors: development of structure property relationships. ACS Applied Electronic Materials,* ***2021****, 3, 325-336.*

Context

In this work, I led a multi-institution collaboration to build the first survey of silicon phthalocyanine (R_2-SiPc) derivatives in organic thin-film transistors (OTFTs). I incorporated 11 SiPcs derivatives with different axial ligands which were synthesized at the University of Ottawa or by collaborators at the University of Toronto into OTFTs. As discussed in Chapter 1, the selection of axial substituent for R_2-SiPcs have a significant influence on their optical properties, intermolecular packing in the solid state, and electronic properties. We correlated these device data with density functional theory calculations based on single crystal data which provided estimations of relative mobilities and electronic transfer integrals which are both related to charge transport. We were primarily interested in the influence of the axial group on thin-film texture and device performance since to this point many derivatives had been reported but no systematic screening had been completed.

Contributions

I prepared and characterized OTFTs from 11 R_2-SiPc derivatives by physical vapour deposition and processed analyzed device data. I performed UV-Vis spectroscopy and X-ray diffraction measurements. Dr. Nicole Rice performed AFM measurements and I interpreted the data. I wrote the manuscript with input from Prof. Lessard, Dr. Melville, Dr. Rice, and Dr. McAfee. All co-authors reviewed the manuscript prior to submission for peer-review. Written sections on DFT calculations were performed and interpreted by Prof. Castet, Prof. Muccioli, and Dr. Tonnelé. GIWAXS data was collected by Dr. Swaraj and processed and interpreted by Dr. Kashani and Dr. McAfee. Phthalocyanine derivatives were synthesized by Dr. Grant and Dr. Raboui.

Abstract

Silicon phthalocyanines (SiPcs) have shown great potential as n-type or ambipolar organic semiconductors in organic thin-film transistors (OTFTs) and organic photovoltaics (OPVs). Although properly designed SiPcs rival current state-of-the-art n-type organic semiconducting materials, relatively few structure-property relationships have been established to determine the impact of axial substituents on OTFT performance, hindering the intelligent design of the next generation of SiPcs. To address this omission we have developed structure-property relationships for vapor-deposited SiPcs with phenoxy axial substituents. In addition to thorough electrical characterization of bottom-gate top-contact OTFTs, we extensively investigated SiPc thin-films using X-ray diffraction (XRD), atomic force microscopy (AFM), grazing-incidence wide-angle X-ray scattering (GIWAXS) and density functional theory (DFT) modelling. OTFT performance, including relative electron mobility (μ_e) of materials, was in general agreement with values obtained through DFT modelling including reorganization energy. Another significant trend observed from device performance was that increasing the electron-withdrawing character of the axial pendant groups led to a reduction in threshold voltage (V_T) from 47.9 V to 21.1 V. This was corroborated by DFT modelling, which predicted that V_T decreases with the square of the dipole induced at the interface between the SiPc pendant and substrate. Discrepancies between modelling predictions and experimental results can be explained through analysis of thin-film morphology and orientation by AFM and GIWAXS. Our results demonstrate that a combination of DFT modeling to select prospective candidate materials, combined with appropriate processing conditions to deposit molecules with a favourable thin-film morphology in an "edge-on" orientation relative to the substrate, yields high-performance n-type SiPc-based OTFTs.

2.1 Introduction

The development of electron-conducting (n-type) organic semiconductors for organic thin-film transistors (OTFTs) is essential to the advancement of low-cost, mechanically robust printable electronic components for applications such as inverters or sensors.[1] However, the majority of high-performance organic semiconducting materials reported in the literature behave as hole-conducting (p-type).[2] One of the key factors that determines whether a molecule behaves as a n- or p-type semiconductor is how its frontier molecular orbitals interact with other device components, such as the electrodes or buffer layers.[3] Shifting the relative energy levels of the highest occupied molecular orbital (HOMO) and the lowest unoccupied molecular orbital (LUMO) of the organic semiconductor with respect to the Fermi level of the metallic source and drain electrodes through the synthesis of novel materials may result in changes in transport type, apparent mobility and ambient stability in OTFTs.[4] Altering the molecular structure of the semiconductor may also influence intermolecular interactions and orientations, and consequently thin-film morphology and charge transport.[5] Understanding how tailoring the organic semiconductor molecular structure affects intermolecular interactions is essential for developing specific structure-property relationships for the realization of stable high-performance n-type organic electronic devices.[6]

Design rules relating molecular structure to intermolecular interactions, solid state packing, and charge transport in OTFTs have been developed for some classes of p- and n-type materials. The addition of conjugated substituents to an organic semiconductor can improve π-orbital overlap and therefore charge transport mobility in single crystal or thin-film transistors.[7] For example, incorporating two phenyl substituents on anthracene (2,6-DPA) results in stronger π-π interactions, yielding hole mobilities (μ_h) of up to 14.8 $cm^2V^{-1}s^{-1}$ in OTFTs.[8] Similar performance improvements as a result of chemical modification have been reported for derivatives of perylene diimide,[2] naphthalene diimide[5,9] and benzothienoisoindigo.[10] Altering molecular structure can also impact molecular alignment with an "edge-on" configuration, where the conjugated molecular core is perpendicular to the substrate surface and charge transport occurs parallel to the channel through overlapping π-orbitals, resulting in improved field-effect mobility.[11–13] Molecular overlap and edge-on orientation can be further promoted through modifications in surface chemistry and thermal annealing.[14]

Metal and metalloid phthalocyanines (MPcs) are a large class of stable organic semiconductors that are relatively easy to synthesize from inexpensive reagents.[15] A wide variety of MPcs containing different metal cores have been incorporated into OTFTs, such as divalent MPcs (with no axial groups) including CuPc[4] and ZnPc,[16] trivalent MPcs (with one axial group) including AlPc-Cl,[17] and tetravalent MPcs (with two axial groups) including SiPc-Cl_2 and SnPc-Cl_2.[18] MPcs are generally p-type,[17] however there are a few derivatives that are primarily n-type, including SiPcs,[19] SnPcs[20] and F_{16}-CuPc.[17] The ability of these planar MPcs to form highly-ordered thin-films makes them ideal candidates for OTFTs.[21] The highest reported mobility of MPcs in OTFTs is for TiOPc thin-films with average hole mobilities on the order of 10 $cm^2V^{-1}s^{-1}$.[22] This superior performance was attributed to significant molecular overlap, low intermolecular stacking distances of 3.145 to 3.211 Å, and their tendency to arrange in an "edge-on" orientation when deposited on an octyl(trichloro)silane (OTS)-modified substrate.[22]

SiPcs with a tetravalent Si atom and two axial substituents (**Figure 1**) have recently shown promise as n-type or ambipolar organic semiconductors, with various derivatives incorporated into organic light-emitting diodes,[23,24] organic solar cells[25] and OTFTs.[19,26] Vapour-deposited SiPcs with phenoxy (PhO) and carboxyl (R-COO) axial substituents are of particular interest due to their relatively good performance as n-type materials in OTFTs[19,27] and as non-fullerene electron acceptors in solar cells.[28] The highest reported electron mobility (μ_e) for n-type SiPcs is ~ 0.5 $cm^2V^{-1}s^{-1}$ from F_{10}-SiPc (**3**, **Figure 1**), which is comparable or exceeds other MPcs in n-type OTFTs,[28] and implying the potential of this class of MPcs to rival other state-of-the-art n-type organic semiconductors.[26,29] Despite this excellent potential, only a few structure-property relationships have been established to determine the impact of the axial substituents on SiPc-based OTFT performance. Several studies indicate that the choice of axial group affects SiPc packing in the single crystal, often changing the π-π stacking distance, herringbone angle, and degree of molecular overlap.[30,31] To this end, Gali et al. demonstrated that density functional theory (DFT) calculations in combination with kinetic Monte Carlo simulations could be used to screen the potential of several compounds by estimating mobility and its directionality, and identified compound **9** (3I-SiPc) which has never been previously incorporated into OTFTs as possessing better 1D single crystal charge transport, and compound **3** (F_{10}-SiPc) as the best for 2D single crystal charge transport.[32] Melville et al. found that increasing the size of the molecular pendant decreased mobility for carboxyl-functionalized SiPcs **10** (PhCOO-SiPc) and **11** (NpCOO-SiPc) and their anthracene-substituted analogue in OTFTs.[19] Despite their bulkier axial groups, SiPcs **2** (345F-SiPc) and **3** (F_{10}-SiPc) outperformed dichloro-substituted $SiCl_2Pc$ in terms of threshold voltage (V_T) and μ_e, indicating a complex interplay between the substituent and device performance.[30] Understanding these structure-property relationships will aid in the design of novel axially-substituted SiPcs for high-performance n-type OTFTs.

In this study we report the electrical characteristics and comprehensive discussion of structure-property relationships of axially substituted SiPcs **1 – 11** (**Figure 2.1**) incorporated into bottom-gate top-contact (BGTC) OTFTs and relate these results to predictions from DFT calculations. Materials **1, 2** and **4 – 11** were incorporated into BGTC OTFTs for the first time; material **3** was previously reported in BGTC OTFTs,[27] and compounds **2** (345F-SiPc), **3** (F_{10}-SiPc), **10** (PhCOO-SiPc) and **11** (NpCOO-SiPc) have been reported in bottom-gate bottom-contact (BGBC) OTFTs.[19,23,30] The films were characterized using powder X-Ray diffraction (PXRD), atomic force microscopy (AFM) and grazing-incidence wide-angle X-ray scattering (GIWAXS) to correlate thin-film formation with single crystal structure, molecular orientation on the substrate, and electrical performance parameters such as μ_e and V_T. DFT calculations were performed to investigate intrinsic material properties and to provide a basis of comparison to electrical characterization of devices.

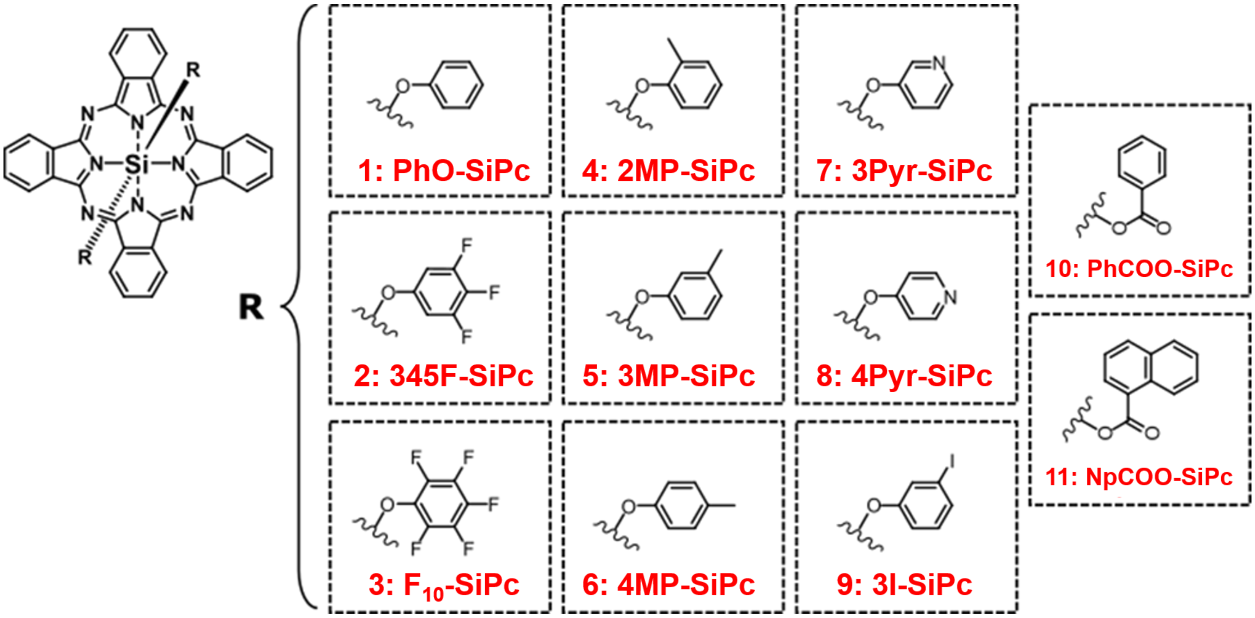

Figure 2.1 Chemical structures of SiPc derivatives incorporated into BGTC OTFTs.

2.2 Experimental Section

Experimental

Synthesis of SiPc derivatives

SiPcs **1** (PhO-SiPc),[31] **2** (345F-SiPc),[30] **3** (F_{10}-SiPc),[28] **4 – 8** (2MP-SiPc, 3MP-SiPc, 4MP-SiPc, 3Pyr-SiPc, 4Pyr-SiPc)[31], **9** (3I-SiPc),[33] and **10** (PhCOO-SiPc) and **11** (NpCOO-SiPc)[19] were synthesized according to previously reported procedures.

Computational Modelling

Molecular structures were optimized in the gas phase using Density Functional Theory (DFT) at the B3LYP/6-31G(d) level. Franck-Condon vertical excitation energies and oscillator strengths were computed using time-dependent (TD) DFT with the same exchange-correlation functional and basis set. The electronic parameters driving the electron transport in the framework of the Marcus theory, namely the reorganization energies and transfer integrals, were also calculated at the B3LYP/6-31G(d) level using the approximations detailed in our previous works.[20,31,34] Internal reorganization energies (λ), which describe the intramolecular geometric relaxation effects occurring between two molecular sites M_1 and M_2 upon the electron transfer reaction $M_1^- + M_2 \rightarrow M_1 + M_2^-$, were calculated using the four-point expression based on adiabatic potential energy surfaces.[35] Transfer integrals (J_k) characterizing the electronic coupling between molecular neighbours were calculated using molecular pairs k extracted from the crystallographic structures, assuming a strict degeneracy of the lowest-unoccupied molecular orbitals. The hopping rates ν_k between two neighbouring sites are given by the Marcus equation, and depend on the square of the electronic couplings J_k:

$$\nu_k = \frac{2\pi^{3/2}}{h\sqrt{\lambda k_B T}} J_k^2 \exp\left(-\frac{\lambda}{4k_B T}\right) \tag{2.1}$$

where h is the Planck constant. The relative electron mobilities along the crystal axes $i = a, b, c$, were evaluated at zero field in the ideal case of no energetic disorder, using the Einstein's expression relating the mobility μ_i with the diffusion coefficient D_i:[36]

$$\mu_i = \frac{e}{k_B T} D_i = \frac{e}{k_B T}\frac{1}{2}\sum_k \nu_k \left(\vec{r}_k \cdot \vec{e}_i\right)^2 \tag{2.2}$$

where T = 300 K, and e and k_B are the elementary charge and Boltzmann constant, respectively. In **Equation 2.2**, the sum runs over all pairs of molecular neighbours separated by the distance vector $\vec{r}_k$ and $\vec{e}_i$ is a cell axis unit vector. **Equation 2.1** and **Equation 2.2** provide mobility values that correspond to the maximum achievable for a defect-free single crystal, and might be considered as an upper limit of experimentally measured mobilities.[37,38] The dimensionality of the electron transport was qualitatively assigned using the following definitions, considering mobilities along the i, j, and k crystallographic directions with $\mu_i > \mu_j > \mu_k$:

$$\begin{aligned}&1\text{D}: \mu_i/\mu_j \geq 3; \mu_i/\mu_k \geq 3\\&2\text{D}: \mu_i/\mu_j < 3; \mu_i/\mu_k \geq 3\\&3\text{D}: \mu_i/\mu_j < 3; \mu_i/\mu_k < 3\end{aligned} \tag{2.3}$$

Molecular properties and electronic couplings were calculated using the Gaussian 16[39] and ORCA[40] programs, respectively.

Preparation of devices

N-doped silicon substrates with a 300 nm thermally-grown SiO_2 dielectric layer (Ossila) were washed with acetone and isopropanol to remove a protective photoresist and dried with nitrogen. Substrates were then sonicated sequentially for 5 minutes in acetone and methanol, dried under a nitrogen stream, and treated with oxygen plasma for 15 minutes. The cleaned substrates were rinsed with water followed by isopropanol, dried under nitrogen, and then reacted for 72 h in 1% v/v octyl(trichloro)silane (OTS) toluene solution. OTS-treated substrates were washed with toluene and dried under vacuum at 70 °C for 1 h. Bottom-gate top-contact (BGTC) OTFTs were fabricated from each of the 11 SiPc derivatives. First, a 300 Å SiPc film was thermally deposited as the active semiconducting layer on a substrate held at room temperature by physical vapour deposition (PVD) through a square shadow mask at a rate of 0.2 Å/s ($P < 2 \times 10^{-6}$ Torr). Source and drain electrodes (channel length L = 30 μm, width W = 1000 μm) were obtained by depositing 100 Å of Mn at a rate of 0.5 Å/s, followed by 500 Å of Ag at a rate of 1 Å/s through shadow masks (Ossila) to yield 20 individual transistors per substrate. Additional devices fabricated with Ag-only electrodes (500 Å) were also prepared using the same deposition rate and shadow masks; electrical characterization of these devices can be found in **Table 2.6** of the Supporting Information.

OTFT testing & electrical characterization

All devices were measured at room temperature in a nitrogen glovebox. Electrical characterization of OTFTs was performed using a custom-built auto-tester with brass alloy contact tips plated with 20 μm gold on 100 μm nickel. The tester was connected to a Keithley 2614B source meter to set the gate-source voltage (V_{GS}) and source-drain voltage (V_{SD}) and measure the source-drain current (I_{DS}). Output curves were obtained by fixing the V_{GS} at discrete values between 0 and 60 V and sweeping the V_{SD}. Transfer curves were obtained by fixing V_{SD} in the saturation region at +50 V. V_{GS} was applied with a duty cycle of 20 % and a frequency of 10 Hz to reduce gate bias stress. For a duty cycle of 20%, gate bias stress is only applied for a 20 ms (2 Hz) interval between 80 ms (8 Hz) intervals of zero applied gate bias stress which has been found to improve device stability during operation and make the extraction of V_T more reliable.[26,41] The electron field-effect mobilities (μ_e) were calculated using the following equation for the saturation region:

$$I_{DS} = \frac{\mu_e C_i W}{2L}(V_{GS} - V_T)^2 \tag{4}$$

Where L and W represent the channel length (30 µm) and width (1000 µm), respectively. The capacitance of the gate dielectric (C_i) is calculated using $C_i = \frac{\varepsilon_0 \varepsilon_r}{d}$, where d is the thickness of the SiO_2 dielectric (300 nm) and ε_r is the dielectric constant of SiO_2. The slope of adjacent data points for $\sqrt{I_{DS}}$ vs V_{GS} is taken at every point in the measurement range to generate a plot of μ_e vs V_{GS}. The average of all μ_e values in a 10V measurement range where the curve is constant is taken as μ_e for each working device. An example of this parameter extraction is shown for material **2** (345F-SiPc) in the Supporting Information (**Figure 2.7**). The threshold voltage (V_T) was calculated from the average x-intercept of linearized data for $\sqrt{I_{DS}}$ vs V_{GS} in the same measurement range.

Thin film characterization

Solid-state UV-Vis absorption spectroscopy was performed with a Cary 5000 spectrophotometer on 30 nm films deposited on glass slides. Powder X-ray diffraction (PXRD) measurements on 30 nm SiPc films deposited on OTS-functionalized Si/SiO_2 substrates (no electrodes) were performed using a Rigaku Ultima IV powder diffractometer with an X-ray source of Cu Kα (λ = 1.5418 Å) at a scan range of $5° < 2\theta < 20°$ and a scan rate of 0.5 °/min. Peak integrals were determined by manually defining the peak position and baseline. Atomic force microscopy (AFM) images were obtained with a Bruker Dimension Icon using ScanAsyst-Air probes, in ScanAsyst mode with a scan rate of 0.6 Hz. Grazing-incidence wide-angle X-ray scattering (GIWAXS) measurements were performed at the SIRIUS beamline at SOLEIL Synchrotron in Saint-Aubin, France.[42] The sample-to-detector distance was 312 mm, and the X-ray energy was 11 keV. Grazing incidence patterns used in this work were taken at α = 0.2° to 0.22° with 10 images at an exposure time of 10 s each. The final spectra are the sum of the ten images. The detector was placed at an angle of 16.1° from the sample plane. Films for GIWAXS were vapor-deposited on SiO_2 during the same deposition as films eventually used as OTFTs. The X-ray data was processed with a modified NIKA package in Igor 6.32A software environment.[43] Material **1** (PhO-SiPc) lattice parameters used for simulation of reciprocal space maps from GIWAXS experiments: a = 9.672 Å, b = 19.237 Å, c = 9.950 Å, α = γ =90°, and β = 118.677°.[31] Material **3** (F_{10}-SiPc) lattice parameters used for simulation of reciprocal space maps: a = 8.342 Å, b = 10.320 Å, c = 11.529 Å, α = 72.509° γ = 70.101°, and β = 83.223°.[28] Material **5** (3MP-SiPc) lattice parameters used for simulation of reciprocal space maps: a = 10.268 Å, b = 16.604 Å, c = 11.487 Å, α = γ = 90°, and β = 115.824°.[31] Material **8** (4Pyr-SiPc) lattice parameters used for simulation of reciprocal space maps: a = 9.734 Å, b = 19.134 Å, c = 9.898 Å, α = γ = 90°, and β = 118.694°.[31] Material **11** (NpCOO-SiPc) lattice parameters used for simulation of reciprocal space maps: a = 8.693 Å, b = 10.890 Å, c = 11.602 Å, α = 104.591 γ = 92.148°, and β = 109.742°.[19]

2.3 Results and Discussion

Computational Results

Charge transport properties measured or calculated on perfectly ordered single crystals cannot be directly compared to device performances obtained for polycrystalline or amorphous thin-films.[1] However, these data may shed light upon intrinsic material properties and help identify candidate materials suitable for applications in organic electronic devices.[32] A summary of single crystal packing motifs, stacking types and π-π stacking distances are provided in **Table 2.4** of the Supporting Information. Here, DFT calculations were first carried out to determine key molecular electronic properties such as the frontier energy levels, electron affinity, and reorganization energy (**Table 2.1**). The energy and strength of the transition toward the two nearly-degenerate singlet excited states were also calculated for each material. Considering **1** (PhO-SiPc) as the reference compound, reinforcing the electron-withdrawing character of the phenoxy group by either grafting halogen substituents (2 [345F-SiPc], 3 [F_{10}-SiPc], **9** [3I-SiPc]) or replacing the phenyl by a pyridine ring (**7** [3Pyr-SiPc] and **8** [4Pyr-SiPc]) lowers HOMO and LUMO levels without a significant impact on the DFT HOMO-LUMO gap, although electron affinity is also considerably lowered. Conversely, adding a methyl group to any position of the phenoxy ring (**4** – **6** [2MP-SiPc, 3MP-SiPc and 4MP-SiPc]) or using axial substituents of larger size (**10** [PhCOO-SiPc], **11** [NpCOO-SiPc]) has a negligible impact on frontier energy levels and electron affinity. Since the nature of the axial substituent hardly affects the HOMO-LUMO gap, all compounds display similar

$S_0 \rightarrow S_1$ absorption properties ($\Delta E_{ge} \sim 2$ eV and oscillator strength $f_{ge} \sim 0.35$), similarly to SiPcs bearing silyl-oxide axial groups.[34]

Table 2.1 DFT energy values of the HOMO, LUMO, LUMO+1, electron affinity (EA, obtained from differences in the total energies of the charged and neutral molecules in their optimized geometries), internal reorganization energies for electrons (λ), and TD-DFT vertical transition energies (ΔE_{ge} and $\Delta E_{ge'}$) and corresponding oscillator strengths (f_{ge} and $f_{ge'}$) from the ground state ($g = S_0$) towards the nearly-degenerate excited singlet states (e and e′), calculated at the B3LYP/6-31G(d) level. All energies are given in eV units.

Material	E_{HOMO}	E_{LUMO}	E_{LUMO+1}	**EA**	**λ**	ΔE_{ge} (f_{ge})	$\Delta E_{ge'}$ ($f_{ge'}$)
1 (PhO-SiPc)	-5.11	-2.97	-2.92	2.01	0.199	2.02 (0.339)	2.06 (0.333)
2 (345F-SiPc)	-5.37	-3.26	-3.21	2.30	0.207	2.00 (0.335)	2.05 (0.358)
3 (F_{10}-SiPc)	-5.27	-3.17	-3.13	2.21	0.191	1.99 (0.331)	2.01 (0.349)
4 (2MP-SiPc)	-5.15	-3.02	-2.96	2.08	0.232	2.02 (0.341)	2.06 (0.345)
5 (3MP-SiPc)	-5.10	-2.93	-2.93	2.00	0.247	2.04 (0.340)	2.04 (0.345)
6 (4MP-SiPc)	-5.09	-2.92	-2.92	1.99	0.244	2.04 (0.350)	2.05 (0.350)
7 (3Pyr-SiPc)	-5.23	-3.11	-3.06	2.15	0.213	2.00 (0.338)	2.06 (0.363)
8 (4Pyr-SiPc)	-5.31	-3.19	-3.14	2.23	0.208	2.01 (0.339)	2.05 (0.363)
9 (3I-SiPc)	-5.24	-3.10	-3.09	2.18	0.241	2.03 (0.344)	2.03 (0.345)
10 (PhCOO-SiPc)	-5.06	-2.95	-2.91	1.99	0.209	2.01 (0.359)	2.03 (0.337)
11 (NpCOO-SiPc)	-5.08	-2.98	-2.94	2.06	0.226	1.99 (0.315)	2.02 (0.324)

Consistent with previous reports,[20,31,34] all phthalocyanine derivatives studied here display rather low internal reorganization energy, a molecular property that must be minimized to favor electron delocalization and transport (**Equation 2.2**). Since these energies do not show large variations (λ values are within a 50 meV range) in these structurally-similar systems, electronic couplings J_k, which result from the intimate supramolecular organization within the crystal are the main parameters determining specific charge transport characteristics. As reported in **Table 2.5** and **Figure 2.6** the nature of peripheral substituents has a strong impact on the molecular arrangement and spatial overlap, translating into large variations of the transfer integrals. For instance, compound **9** (3I) exhibits the largest couplings along the π-stacking direction (86 meV), while they are one order of magnitude lower along the other directions, which prefigures 1D electron transport. Although transfer integrals are two times smaller in the other crystals, secondary couplings with significant magnitude are also present, like in **4** (2MP-SiPc), that offer multiple charge transport pathways and favors multi-dimensional conductivity. Reorganization energies and transfer integrals were subsequently employed to evaluate the relative electron mobilities along the three crystalline axes, together with the expected dimensionality of the transport properties as defined in **Equation 2.3** (**Table 2.2**).

Table 2.2 Computed electron mobilities along *a, b, c* crystallographic directions (with maximum values in bold), average mobility ($\mu_{avg} = (\mu_a + \mu_b + \mu_c) / 3$), and dimensionality (D) of the electron transport, as defined in **Equation 2.3**.

Material	μ_a ($cm^2\ V^{-1}\ s^{-1}$)	μ_b ($cm^2\ V^{-1}\ s^{-1}$)	μ_c ($cm^2\ V^{-1}\ s^{-1}$)	μ_{avg} ($cm^2\ V^{-1}\ s^{-1}$)	**D**
1 (PhO-SiPc)	1.287	0.202	**2.075**	1.188	2D
2 (345F-SiPc)	**2.864**	0.301	0.761	1.309	1D
3 (F_{10}-SiPc)	**3.072**	0.084	0.642	1.266	1D
4 (2MP-SiPc)	0.265	0.443	**0.946**	0.551	2D
5 (3MP-SiPc)	**0.824**	0.181	0.219	0.408	1D
6 (4MP-SiPc)	0.614	**2.731**	0.083	1.143	1D
7 (3Pyr-SiPc)	**1.092**	0.096	0.067	0.418	1D
8 (4Pyr-SiPc)	1.117	0.180	**1.857**	1.051	2D
9 (3I-SiPc)	0.314	0.000	**5.393**	1.902	1D
10 (PhCOO-SiPc)	1.052	0.321	**2.545**	1.306	2D
11 (NpCOO-SiPc)	**0.869**	0.110	0.447	0.475	2D

Electrical Characterization and Device Performance

OTFTs fabricated from **1 – 11** were prepared on octyl(trichloro)silane (OTS)-modified SiO_2 substrates with silver-manganese (AgMn) electrodes (see Experimental for full details). We recently demonstrated that Ag electrodes with Mn interlayers could be used as a cost-effective and high-performance alternative to gold (Au) electrodes, with the lower work function of Mn with respect to Au (~ 4 eV vs 5 eV) facilitating better electron injection into SiPcs LUMO orbitals, which according to IPES measurements possess energies (electron affinities) roughly around 4 eV.[27] Previous experiments demonstrated that devices employing material **3** (F_{10}-SiPc) as a semiconductor with AgMn electrodes demonstrated reduced V_T, improved linear region μ_e and reduced contact resistance when compared with devices employing bare Ag electrodes. We observed similar trends with the SiPcs investigated in this report, with most devices fabricated using AgMn electrodes (**Table 2.3**) outperforming those with bare Ag electrodes (Supporting Information, **Table 2.6**). A summary of device saturation region data including μ_e, V_T, I_{on} and the ratio of on to off current ($I_{on/off}$) is presented in **Table 2.3**. Representative output and transfer curves for an OTFT prepared from **3** (F_{10}-SiPc), which had the superlative μ_e and lowest V_T with Ag/Mn electrodes, are shown in **Figure 2.2** (representative output and transfer curves for all other materials can be found in **Figures 2.8 – 2.18**). It should be noted that for some materials, a degradation in I_{SD} at high V_G in output curves occurs. This phenomenon is likely a result of bias stress causing electron trapping at the semiconductor-dielectric interface or in the semiconductor itself, resulting in a shift of V_T during measurement.[41] Similar degradation of I_{DS} at high V_G in output curves has been observed in other n-type devices incorporating TiOPc,[44] peripherally fluorinated CuPc[45] and perylene diimide.[46] This effect can be suppressed by modifying the surface chemistry at the semiconductor-dielectric interface[7,47,48] or applying a pulsed gate.[41] The exploration of alternative surface chemistries on device performance is outside the scope of this work. However, to reduce the impact of gate bias stress on extracted parameters, a pulsed gate was applied for transfer curve measurements as outlined in the Experimental section.

Table 2.3 Electrical performance of SiPcs 1 – 11 with AgMn electrodes.

Material	μ_e [cm^2 V^{-1} s^{-1}][a]	V_T [V] [a]	I_{on} [a]	$I_{on/off}$[a]
1 (PhO-SiPc)	8.3 ± 7.5 x10^{-3}	37.1 ± 3.4	1.20 x10^{-6}	10^4-10^5
2 (345F-SiPc)	6.4 ± 2.1 x10^{-2}	29.5 ± 3.3	1.10 x10^{-5}	10^6
3 (F_{10}-SiPc)	1.1 ± 0.61 x10^{-1}	21.1 ± 8.4	3.79 x10^{-5}	10$^{5-6}$
4 (2MP-SiPc)	1.2 ± 0.24 x10^{-3}	46.8 ± 2.9	4.97 x10^{-8}	10^3
5 (3MP-SiPc)	1.8 ± 0.82 x10^{-2}	34.8 ± 5.3	2.66 x10^{-6}	10^4-10^5
6 (4MP-SiPc)	1.9 ± 0.62 x10^{-3}	47.9 ± 1.3	6.31 x10^{-8}	10^3
7 (3Pyr-SiPc)	8.5 ± 10 x10^{-3}	*	1.60 x10^{-7}	10^1
8 (4Pyr-SiPc)	1.5 ± 1.1 x10^{-2}	*	5.30 x10^{-6}	10^1
9 (3I-SiPc)	3.1 ± 2.3 x10^{-3}	29.2 ± 2.6	5.30 x10^{-7}	10^4
10 (PhCOO-SiPc)	6.3 ± 2.3 x10^{-3}	35.0 ± 1.1	2.66 x10^{-6}	10^4-10^5
11 (NpCOO-SiPc)	2.1 ± 0.88 x10^{-3}	41.8 ± 2.3	1.57 x10^{-7}	10^3-10^4

[a] μ_e and V_T were calculated based on mean values, while I_{on} and $I_{on/off}$ were calculated based on median values

* Values could not be calculated accurately due to high off current causing deviation from Equation 1

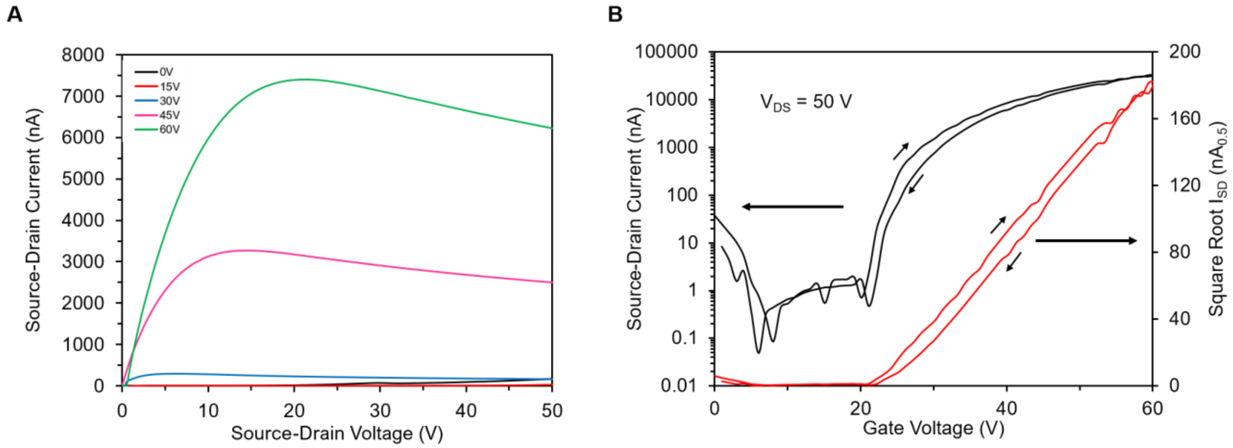

Figure 2.2 Representative A) output curves and B) transfer curve (V_{DS} = 50 V) for BGTC OTFTs fabricated from material 3 (F_{10}-SiPc).

Fluorinated compounds **2** (345F-SiPc) and **3** (F_{10}-SiPc) were the best performing materials in OTFTs, with the highest μ_e and lowest V_T among all the SiPc derivatives investigated, and device performance of material **3** (F_{10}-SiPc) was comparable to previously published values for top-contact devices.[27] The decrease in current at high V_{DS} shown in **Figure 2.2A** for **3 (F_{10}-SiPc)** and several other SiPc materials (Supporting Information) can be attributed to their slightly ambipolar nature, resulting in weak hole conduction capabilities.[26,27] However, this ambipolar behaviour can be suppressed by device engineering at the semiconductor/dielectric interface[49] and semiconductor/electrode interface.[3,27] Ambipolar nature was predicted from DFT modelling for materials **5** and **9** (3MP-SiPc and 3I-SiPc, respectively).[32] Materials **7** (3Pyr-SiPc) and **8** (4Pyr-SiPc), which both contain pyridine axial groups, exhibited a high I_{off} on the order of 100 nA that is unique to pyridoxy derivatives in this study.

We found that the strongest DFT-based predictors of high experimental mobility in SiPc OTFTs were a low internal reorganization energy (λ) and large μ_a. Overall trends in experimental mobility measured in this study (**Table 2.3**) correlate well with these metrics in ranked analyses. Fluorinated SiPcs **2** (345F-SiPc) and **3** (F_{10}-SiPc) that displayed the highest two mobility values (10^{-2} cm^{2}V^{-1}s^{-1} < μ_e < 10^{-1} cm^{2}V^{-1}s^{-1}) also had the two largest predicted μ_a and the first and third lowest reorganization energies predicted for materials **1** – **11**. Materials **4** (2MP-SiPc) and **6** (4MP-SiPc), with the lowest two OTFT mobilities ($\mu_e \approx 1\text{-}2$x10^{-3} cm^{2}V^{-1}s^{-1}), had the lowest and third lowest predicted μ_a and the second and fourth highest predicted λ. Material **5** (3MP-SiPc) was a consistent outlier, displaying the third largest experimental μ_e (1.8 x10^{-2} cm^{2}V^{-1}s^{-1}) despite having the highest predicted λ and the fourth-lowest predicted μ_a. The discrepancy between the relative experimental and theoretical mobility for material **5** can likely be attributed to its ability to form superior thin-films with a favourable grain structure, as discussed in a later section of this work. There are some reasonable explanations for these trends. As previously discussed, it has been observed in that higher charge carrier mobilities can be achieved by lower reorganization energies and larger intermolecular transfer integrals[8,22] Thus, the small differences in predicted λ could manifest as larger changes in thin-film devices. For theoretical mobility, it is possible that the much stronger correlation of experimental mobility with μ_a rather than with μ_b, μ_c and μ_{ave} could indicate information about how nucleation and film growth occur for SiPcs, although this merits further investigation. Overall, the theoretical values calculated using DFT show promise as a useful tool for screening candidate materials for high-mobility OTFTs, despite the fact that thin-film morphology is an obvious confounding factor that should also be considered when establishing structure-property relationships.

We correlated the V_T of devices as a function of the Hammett parameter,[50] which estimates the electron donating or withdrawing character of substituents on the phenolic pendant groups on the SiPc, with results depicted in **Figure 2.3A** for materials **1** – **6**, **9** and **10**. Materials **7** (3Pyr-SiPc) and **8** (4Pyr-SiPc) were excluded from this analysis because Hammett parameters cannot be calculated for pyridine substituents, and compound **11** was also excluded as it is a naphthalene derivative. We show for that first time that in general, V_T decreases as the electron withdrawing character of axial group increases, resulting in SiPc materials with fluorinated pendant groups having lower V_T values compared to weakly electron-donating methyl-substituted pendant groups (4 – 6 [2MP-SiPc, 3MP-SiPc and 4MP-SiPc]). Additionally, the relationship between DFT calculated dipoles of the axial substituents and experimental V_T of the SiPcs was investigated (**Figure 2.3B**), as the self-assembled monolayer (SAM) formed by OTS and resulting electric dipoles induced by the interfacial contact of the SAM and semiconductor can profoundly impact OFET electrical characteristics.[51,52] However, this effect strongly depends on the dipole sign and orientation, dictated here by the interaction between the OTS-modified substrate, the axial groups and the phthalocyanine core. For a strong correlation with the V_T to hold, one would need to have identical orientations for all the compounds. Within this assumption, it can be seen in **Figure 2.3B** that V_T decreases slightly with the square of the dipole (which is in turn proportional to the square of the energetic disorder),[53] and that the correlation fails for compound **3** (F_{10}-SiPc) as it possesses a unique anisotropic morphology which will be elaborated upon in a subsequent section. Overall, the correlations highlighted in **Figure 2.3** suggest that SiPcs with stronger electron-withdrawing axial groups could yield OTFTs with lower operating voltages on OTS-treated surfaces, which is desirable if these materials are eventually incorporated into commercial applications.[54]

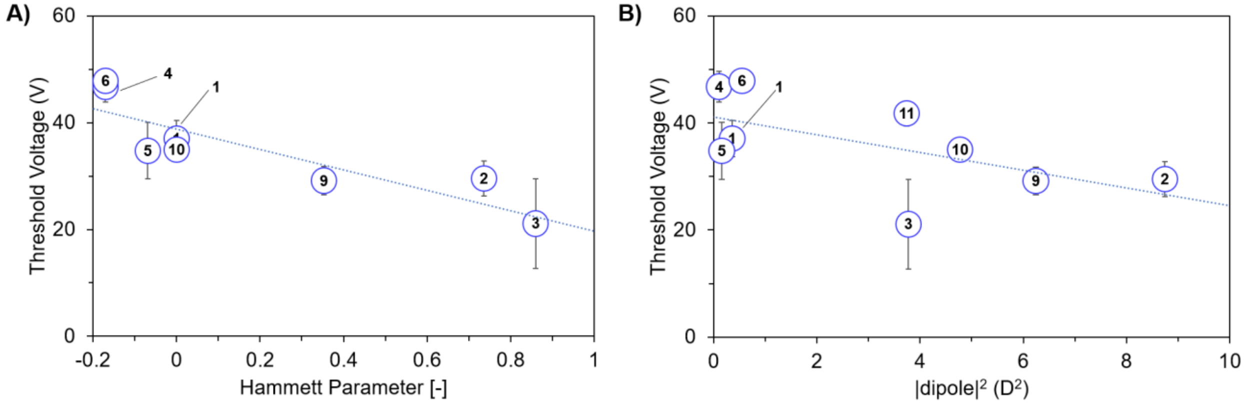

Figure 2.3 V_T of SiPc OTFTs as a function of A) the Hammett parameter of the SiPc pendant group for materials 1 – 6, 9 – 10 and B) the strength of the DFT-calculated SiH_3-R dipole for materials 1 – 6 and 9 – 11.

Thin-Film Properties

The molecular packing, texture, and morphology of organic semiconductors in thin films is critical to device performance,[5,7] and it is essential to characterize thin-film morphologies through multiple techniques to develop structure-property relationships. Powder X-Ray diffraction (PXRD) results from thin films (**Figure 2.19A**) displayed greater diffraction intensity for films of SiPcs with smaller molecular weight axial groups (**Figure 2.194B**), indicating higher structural order or degree of crystallinity. This could be due to the ease of rotation of the smaller pendant axial groups, leading to more organized crystals. Materials **1** (PhO-SiPc)**, 7** (3Pyr-SiPc) and **8** (4Pyr-SiPc) have the lowest molecular weight axial groups and therefore the highest degree of crystalline order, while materials **10** (PhCOO-SiPc) and **11** (NpCOO-SiPc) have high molecular weight axial groups and a low degree of crystalline order. Unfortunately, no direct correlation between PXRD intensity and μ_e or V_T was found, suggesting PXRD results alone are not enough to derive structure-property relationships for OTFT performance.

Atomic force microscopy (AFM) was performed on films of SiPc materials **1 – 11** to further investigate their morphology (**Figure 2.4**). Several prototypical morphologies were observed in our SiPc films. Materials **1** (PhO), **5** (3MP-SiPc) and **7** (3Pyr-SiPc) all yielded regular rounded anisotropic grains across the substrate in the thin-film phase. The second observed motif was for material **2** (345F-SiPc), which formed anisotropic plate-like sheets across the substrate with a broad dispersity of crystallite sizes. These plate-like sheets resemble AlPc-Cl and TiOPc films, which also form large overlapping grains in thin films deposited by PVD.[55] The third unique motif was observed for material **3** (F_{10}-SiPc), which was comprised of rectangular anisotropic crystallites in the thin-film, consistent with results observed in previous studies where it was deposited on an OTS-modified substrate at room temperature.[26]. The fourth and most frequent motif was small, randomly oriented isotropic grains, observed for materials **4** (2MP-SiPc), **6** (4MP-SiPc), **8** (4Pyr-SiPc), and **10** (PhCOO-SiPc), which closely resemble film morphologies we reported for MgPc.[55]. Finally, material **9** (3I) exhibited a unique and highly disordered morphology where crystallites grew in multiple directions and orientations relative to the substrate, while material **11** (NpCOO-SiPc) formed an amorphous film with no discernible structural features. Materials with anisotropic crystallite morphologies (like **1**, **3** and **5**) generally performed better in the OTFTs, which can be attributed to fewer grain boundaries in the thin-film between the source and drain electrodes, reducing the resistance to charge transport across the channel.[7] Additionally, anisotropic features appeared to grow horizontally across the channel, which could also lead to improved charge transport.

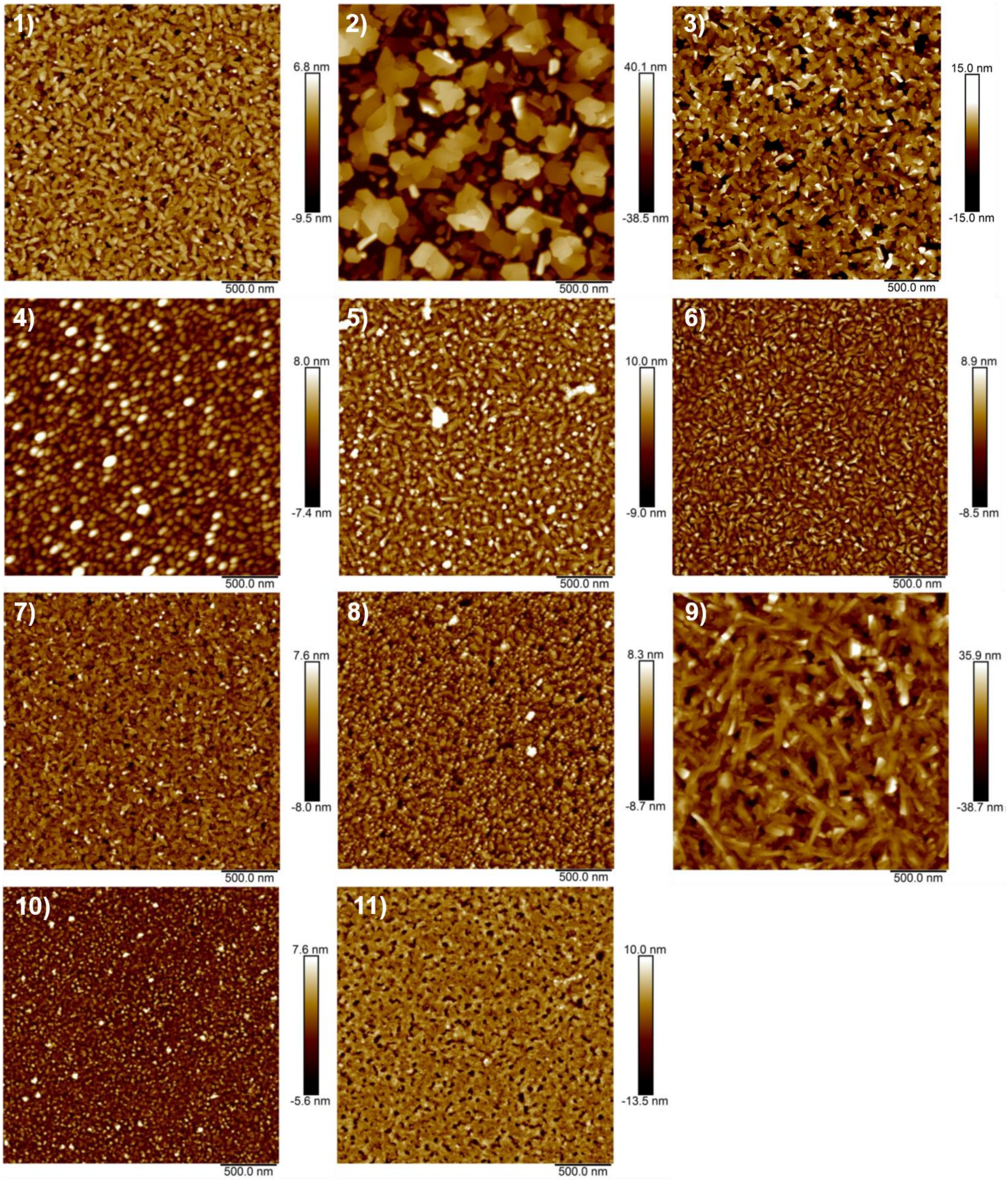

Figure 2.4 Atomic force microscopy (AFM) images of materials 1 – 11.

Thin-film morphologies of materials **1 – 11** can offer some explanations for deviations in relative mobility estimations by DFT compared to relative experimental performance when incorporated into devices. Grain structure[56] and RMS roughness[57] are both important film morphology features that can dramatically impact charge transport. For example, material **5** was predicted by DFT to have among the lowest μ_e of all 11 materials surveyed in this study. However, it performed relatively well with the third-highest average mobility, with a μ_e greater than $1\text{x}10^{-2}$ $cm^2V^{-1}s^{-1}$. Thin-films of material **5** (3MP-SiPc) form regular rounded anisotropic grains across the substrate with a low RMS roughness of 3.33 nm (**Table 2.7**), which could be conducive to favourable charge transport properties in a device, especially if these grains transport charge along the favoured crystallographic axis (μ_a). Materials **1** (PhO-SiPc) and **7** (3Pyr-SiPc), which exhibit similar μ_e on the order of $8\text{x}10^{-3}$ $cm^2V^{-1}s^{-1}$, have the same grain structure and RMS roughness values below 2.5 nm. Conversely, compounds **9** (3I-SiPc) and **11** (NpCOO-SiPc) both displayed relatively poor performance in devices, with μ_e on the order of $2\text{-}3\text{x}10^{-3}$ $cm^2V^{-1}s^{-1}$. Material **9** formed uneven feather-like grains with a large RMS roughness of 9.1 nm and three-dimensional growth on the substrate, all of which could have resulted in its smaller μ_e. Thin-films of material **11** did possess low RMS roughness of 1.56 nm, however the film is amorphous and has small structural features.

In addition to AFM imaging, GIWAXS measurements were performed to evaluate the polycrystalline structure and texture of SiPc thin films to further correlate their structural properties with experimental device μ_e. Materials **1** (PhO-SiPc), **3** (F10-SiPc), **5** (3MP-SiPc), **8** (4Pyr-SiPc) and **11** (NpCOO-SiPc) were selected to survey SiPcs with a broad range of functionalities and mobility values in BGTC devices. The thin-film crystal structure and molecular orientation was determined using GIWAXS data coupled with reciprocal space maps (RSMs). This method has previously been employed to identify the crystallite structure and orientation of β-phase CuPc in thin films.[58] To identify the structure and orientation of SiPc molecules responsible for GIWAXS peaks, RSMs of materials **1, 3**, **5**, **8** and **11** with (*HKL*) orientations between ± 3 were simulated. 2D GIWAXS plots and RSMs for materials analyzed by GIWAXS can be found in the Supporting Information (**Figures S20** – **S24**). While materials **3** (F_{10}-SiPc) and **11** (NpCOO-SiPc) had easily identifiable scattering peaks that corresponded to single crystal data, materials **1** (PhO-SiPc), **5** (3MP-SiPc), and **8** (4Pyr-SiPc) formed polymorphs that differed from the crystal structure of their single crystal counterparts, making it not possible to identify their crystal structure or orientation. For material **3** (F_{10}-SiPc), the (010) and (001) orientations were found to be in agreement with observed scattering peak locations (**Figure 2.5A**), with (010) considered to be the dominant orientation. Due to overlap in scattering data between the (010) and (001) peaks, a quantitative estimate of the ratio of the (010) orientation to the (001) orientation is not possible. For material **11** (NpCOO-SiPc) only the (001) orientation was identified in the GIWAXS data (**Figure 2.5B**). An illustration of the orientations identified in 2D GIWAXS data can be found below for materials **3** (F_{10}-SiPc, **Figure 2.5E**) and **11** (NpCOO-SiPc, **Figure 2.5F**).

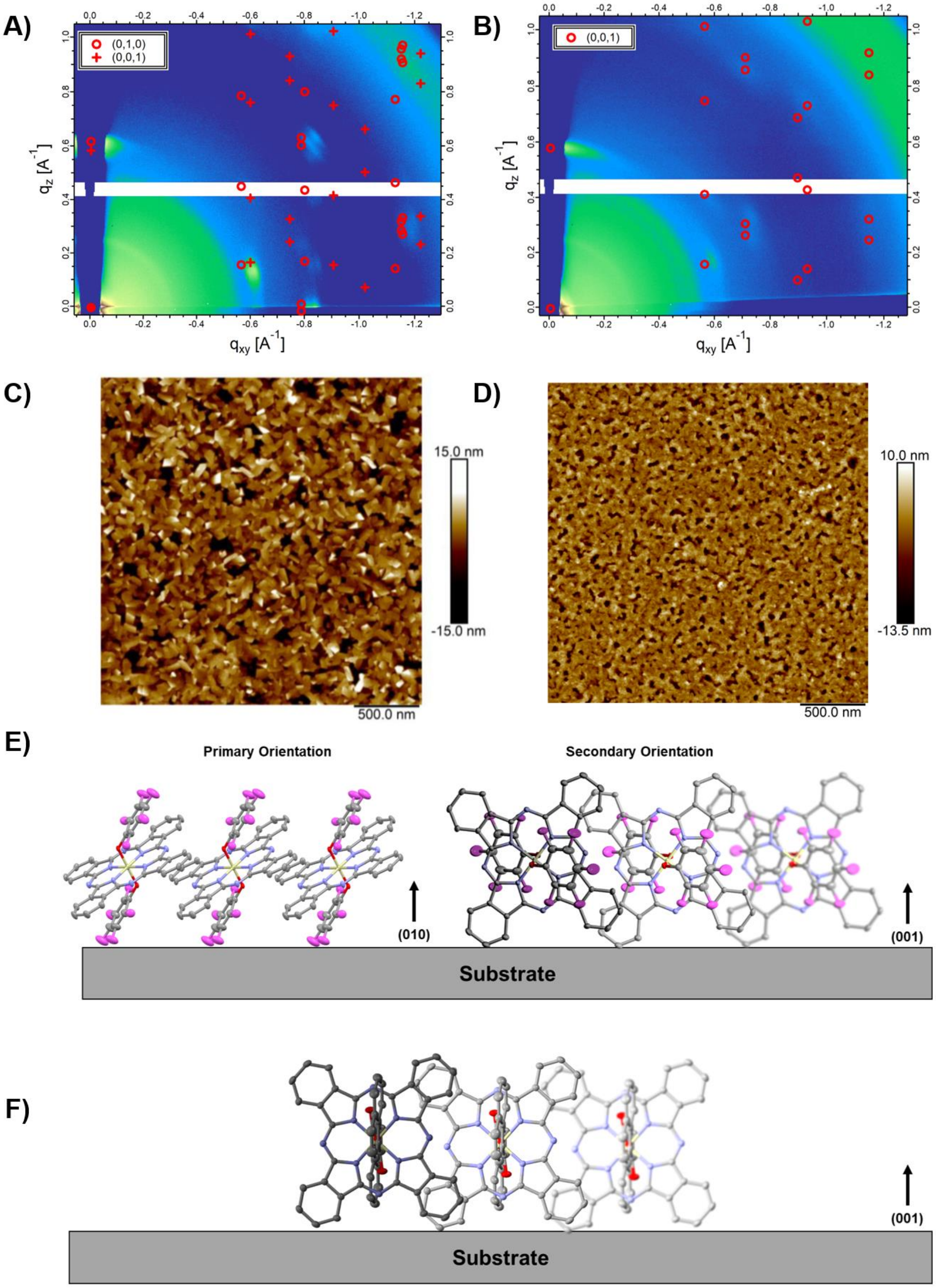

Figure 2.5 2D scattering patterns for films of materials A) 3 (F_{10}-SiPc) and B) 11 (NpCOO-SiPc) at $\alpha = 0.22°$ determined by GIWAXS. AFM height images of C) 3 and D) 11, and schematic of orientations relative to the substrate of molecular (SiPc) plane identified by GIWAXS for materials E) 3 and F) 11.

According to 2D GIWAXS scattering patterns, material **11** has a dominant orientation with the phthalocyanine macrocycle plane being preferentially aligned perpendicular to the substrate surface (pseudo edge-on) at an angle of 80.4° from the surface. Material **3** assumes mixed orientations, with the phthalocyanine plane either preferentially oriented parallel to the substrate (pseudo face-on) at an angle of 35.6° from the surface, or pseudo edge-on at an angle of 79.7° from the surface. Additionally, while both materials possess a lamellar solid state packing motif with dual phenyl-phenyl stacking, material **11** has a shorter π-π stacking distance of 3.650 Å[19] compared to material **3** which has a *π*- *π* stacking distance of 3.769 Å.[28]

Considering only the GIWAXS data, material **11** (1-napthoate) would be predicted to have a (relatively) higher μ_e based on its pseudo edge-on orientation compared to material **3** ; however, this was not observed experimentally. This discrepancy can be explained using our DFT results, as material **11** had one of the lowest predicted conductivities of all the SiPc materials owing to its low degree of electronic coupling along the directions parallel to the substrate (26 meV, **Table 2.4**). Conversely, material **3** exhibits relatively high electronic couplings along the (100) direction according to DFT (43 meV), and is therefore expected to have a greater single crystal μ_e. This direction of strong electronic coupling for material **3** also corresponds to the direction of dual benzene stacking in the pseudo edge-on configuration identified by GIWAXS, which likely contributes to the resultant μ_e of material 3 in devices. Furthermore, thin-film morphology and microstructure have an impact of charge carrier mobility. Material **3** has regular anisotropic grains across the substrate that could be a more favourable morphology for charge transport than small isotropic features or amorphous films, which likely also contributes to material **3** having a greater μ_e than material **11**. These results clearly demonstrate that while DFT is a powerful tool for helping to predict possible organic semiconductor candidates for device applications, thorough analysis of thin films through multiple techniques must also be performed to elucidate why certain candidate materials perform better than others. Deposition rate,[17] substrate temperature[59,60] and surface chemistry[22,61] also influence the crystallinity of thin-films and molecular orientation on the substrate and device performance. This has also been reported for SiPcs, with the thin-film crystallinity and mobilities of materials 3 (F_{10}-SiPc) 10 (PhCOO-SiPc) in bottom-contact devices found to be dependant on substrate temperature and selection of silane as a surface treatment.[19,26] Based on previous results, further optimization of the best candidate materials identified in this study is warranted in future work.

2.4 Conclusion

Structure-property relationships for a series of substituted phenoxy silicon phthalocyanines were developed by performing DFT calculations, electrical characterization of these materials in BGTC OTFTs, and thorough characterization of their thin-film morphologies. Materials **1** and **4 – 9** were incorporated into OTFTs for the first time. DFT calculations were performed on all SiPc derivatives to estimate μ_e in single crystals and used as a basis for estimating relative performances of OTFTs. Experimental OTFT performances (including μ_e) demonstrated the strongest relative correlation with parameters λ and μ_a as predicted by DFT calculations. We also demonstrate for the first time through electrical characterization of devices that increasing the electron-withdrawing character of pendant groups, measured in terms of Hammett parameter, or reducing the interfacial electric dipole between the insulating and semiconducting layers, could be correlated to a decrease in average V_T from 47.9 V to 21.1 V. AFM measurements showed that our 11 SiPc derivatives resulted in the formation of six different prototypical morphologies from the same deposition conditions, including: regular rounded anisotropic grains, anisotropic plate-like sheets, rectangular anisotropic grains, small isotropic grains, highly disordered crystallites and amorphous films. GIWAXS measurements indicated that although the orientation of SiPc molecules relative to substrate surface is important for charge transport, supramolecular interactions in the form of π-orbital overlap and the ability of these materials to form well-ordered films with anisotropic grain structures also drive device performance. Overall, predictive techniques including DFT and functional group analysis will enable the intelligent design of the next iteration of SiPcs. These computations, combined with characterization techniques including AFM and GIWAXS, can lead to the identification of optimal thin-film processing conditions and yield high-performance n-type SiPc-based OTFTs.

Acknowledgments

The Natural Sciences and Engineering Research Council of Canada (2015-509 03987 and STPGP 506661-17 to B.H.L). B.K and K.L also thanks NSERC for the CGS-M and USRA, respectively. Computer time was provided by the Mésocentre de Calcul Intensif Aquitain (MCIA) of the University of Bordeaux and financed by the Conseil Régional d'Aquitaine and the French Ministry of Research and Technology. We also thank Centre for Research in Photonics at the University of Ottawa (CRPuO) for access to the AFM. We acknowledge Synchrotron SOLEIL for providing beamtime. We would also like to sincerely thank Dr. P. Fontaine for helpful discussions and Dr. A.

Hemmerle and N. Aubert for assistance during GIWAXS measurements. Work by S.K and H. A. supported by Goodnight Innovation Distinguished Professorship. Help with GIWAXS data acquisition and analysis by Z. Peng and Z. Wang (NCSU) is greatly acknowledged.

Supporting Information

Table 2.4 Summary of single-crystal packing motifs, stacking types and π – π stacking distances for materials 1 – 11. The shortest stacking distance is highlighted in bold.

Material	Bridge	Packing Motif	Stacking Types[a)]	A (Å)	B1 [b)] (Å)	B2 [b)] (Å)	C1 [c)] (Å)	C2 [c)] (Å)	D (Å)	Source
1 (PhO-SiPc)	PhO	Herringbone	2 (AB)	3.771	3.673	**3.564**				[31]
2 (345F-SiPc)	PhO	Herringone	1 (B)		3.716	**3.580**				[30]
3 (F_{10}-SiPc)	PhO	Lamellar	1 (A)	**3.769**						[28]
4 (2MP-SiPc)	PhO	Lamellar	3 (BCD)		**3.567**	3.826	3.862	3.828	3.826	[31]
5 (3MP-SiPc)	PhO	68°	1 (B)		3.797	**3.671**				[31]
6 (4MP-SiPc)	PhO	Lamellar	1 (B)		**3.599**	3.648				[31]
7 (3Pyr-SiPc)	PhO	22°	1 (C)				3.932	**3.709**		[31]
8 (4Pyr-SiPc)	PhO	Herringbone	2 (AB)	3.762	**3.580**	3.601				[31]
9 (3I-SiPc)	PhO	Herringbone	1 (C)				**3.716**	3.810		[33]
10 (PhCOO-SiPc)	R-COO	Lamellar	2 (AB)	3.738	3.882	**3.554**				[19]
11 (NpCOO-SiPc)	R-COO	Lamellar	1 (A)	**3.650**						[19]

a) A = dual benzene-benzene stacking, B = single benzene-benzene and single benzene-isoindole stacking, C = dual benzene-isoindole stacking, D = single benzene-benzene stacking

b) B1 = benzene-isoindole stacking distance, B2 = benzene-benzene stacking distance

c) C1 = benzene-isoindole 1 stacking distance, C2 = benzene-isoindole 2 stacking distance

Table 2.5 Non-negligible transfer integrals ($J_k \geq 1$, in units of meV), calculated between a reference molecule and its first neighbours. The crystallographic directions corresponding to intermolecular vectors joining the reference molecule with its neighbours are given in the basis of direct lattice vectors.

Material	Direction: J_k
1 (PhO)	±(1, 0, 1): **47**; ±(0, 0, 1): **19**; (0, ±1/2, ±1/2): **7**; ±(1, 0, 0): **1**
2 (345F)	±(1, 0 0): **37**; ±(1/2, ±1/2, 1/2): **10**; ±(1, 0, 1): **14**
3 (F10)	±(1, 0, 0): **43**; ±(1, 0, -1): **12**; ±(0, 1, -1): **5**
4 (2MP)	(0, 1/2, ±1/2): **25**; (-1, 1/2, 1/2): **17**; (0, -1/2, -1/2): **16**; (-1, -1/2, 1/2): **10**; (1, 1/2, -1/2): **10**; (-1, -1/2, -1/2): **2**; ±(1, 0, 0): **1**; ±(0, 1, 0): **1**
5 (3MP)	±(1, 0, 0): **25**; (1/2, ±1/2, 1/2): **11**; (−1/2, ±1/2, −1/2): **10**; ±(1, 0, 1): **8**
6 (4MP)	±(0, 1, 1): **47**; ±(1, -1, 0): **10**; (1, 0, -1): **9**; ±(1, 0, 0): **1**
7 (3Pyr)	±(1, 0, 0): **28**; ±(1, 1/2, 1/2): **6**; ±(1, -1/2, 1/2): **6**; ±(0, 1, 0): **4**
8 (4Pyr)	±(1, 0, 1): **44**; ±(0, 0, 1): **21**; (0, ±1/2, ±1/2): **7**; ±(1, 0, 0): **1**
9 (3I)	±(0, 0, 1): **86**; ±(1, 0, 0): **4**
10 (BnO)	±(0, 0, 1): **34**; ±(1, 0, 0): **20**; ±(1, 1, 1): **10**
11 (NpO)	±(1, 0, 0): **26**; ±(0, 0, 1): **12**; ±(1, 1, 1): **10**; ±(0, 1, 0): **1**

* Compound **10** is not reported since it was not possible to obtain a single crystal

Figure 2.6 Top views of the molecular dimers giving rise to the largest electronic couplings, as extracted from periodic replicas of experimental crystal structures.

1 (PhO-SiPc)

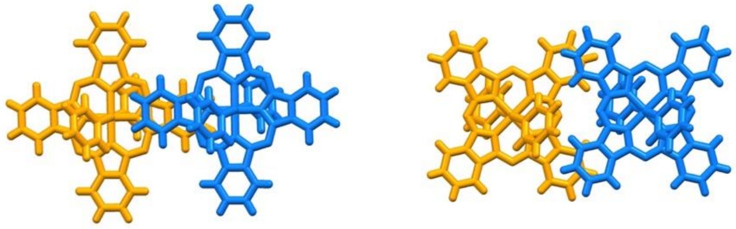

±(1, 0, 1): **47 meV**

±(0, 0, 1): **19 meV**

Figure 2.6: *continued*.

2 (345F-SiPc)

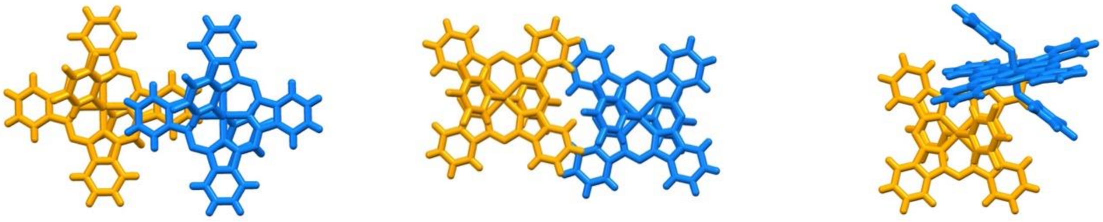

±(1, 0 0): **37 meV**

±(1, 0, 1): **14 meV**

±(1/2, ±1/2, 1/2): **10 meV**

3 (F_{10}-SiPc)

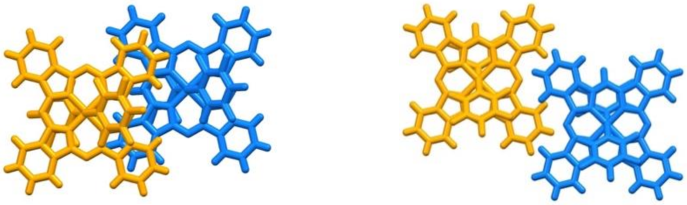

±(1, 0, 0): **43 meV**

±(1, 0, -1): **12 meV**

4 (2MP-SiPc)

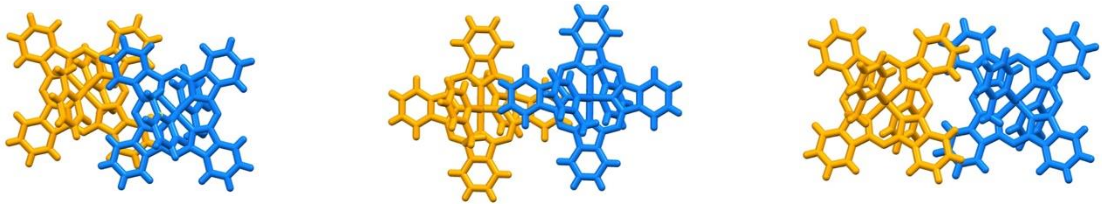

(0, 1/2, -1/2): **25 meV**

(0, 1/2, 1/2): **25 meV**

(-1, 1/2, 1/2): **17 meV**

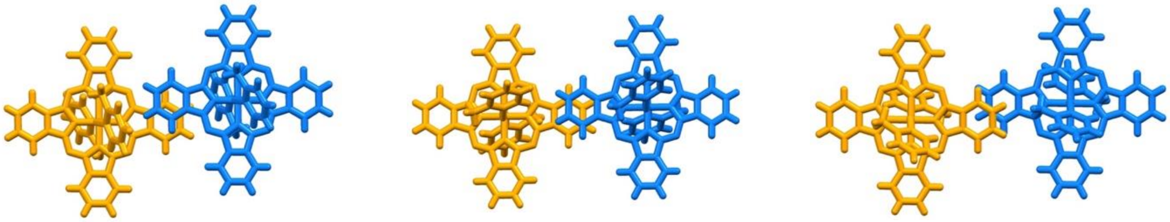

(0, -1/2, -1/2): **16 meV**

(-1, -1/2, 1/2): **10 meV**

(1, 1/2, -1/2): **12 meV**

Figure 2.6: *continued*.

5 (3MP-SiPc)

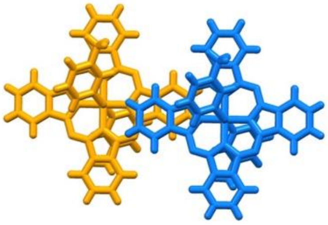
±(1, 0, 0): **25 meV**

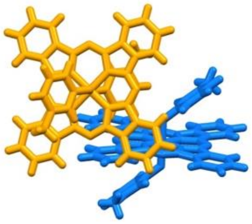
(1/2, ±1/2, 1/2): **11 meV**

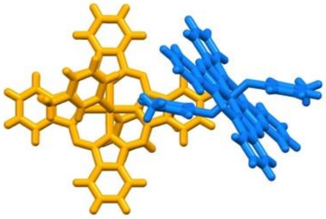
(−1/2, ±1/2, −1/2): **10 meV**

6 (4MP-SiPc)

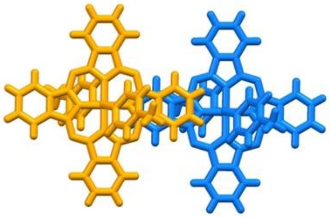
±(0, 1, 1): **47 meV**

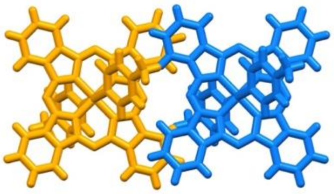
±(1, -1, 0): **10 meV**

7 (3Pyr-SiPc)

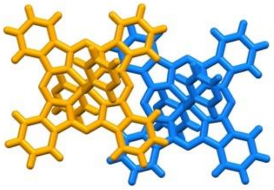
±(1, 0, 0): **28 meV**

8 (4Pyr-SiPc)

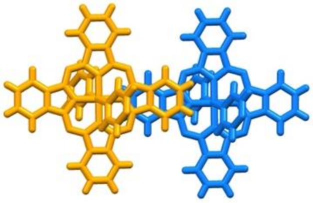
±(1, 0, 1): **44 meV**

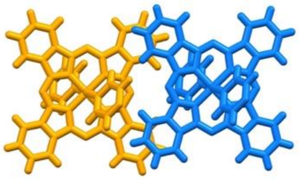
±(0, 0, 1): **21 meV**

Figure 2.6: *continued*.

9 (3I-SiPc)

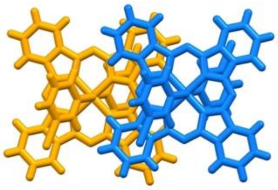

±(0, 0, 1): **86 meV**

10 (PhCOO-SiPc)

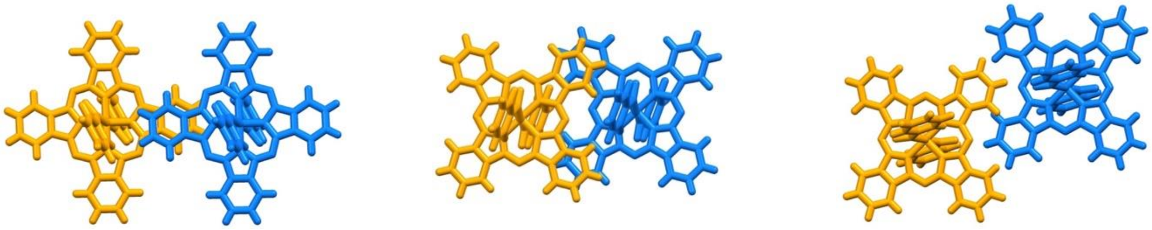

±(0, 0, 1): **34 meV** ±(1, 0, 0): **20 meV** ±(1, 1, 1): **10 meV**

11 (NpCOO-SiPc)

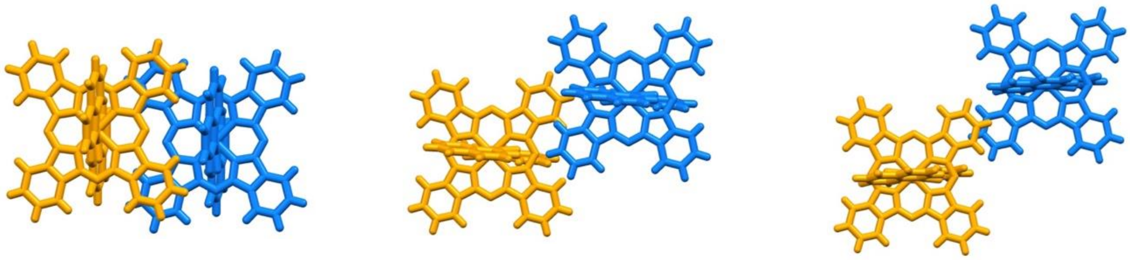

±(1, 0, 0): **26 meV** ±(0, 0, 1): **12 meV** ±(1, 1, 1): **10 meV**

Table 2.6 Electrical performance of SiPcs 1 – 11 with Ag electrodes.

Material	μ_e [cm^2 V^{-1} s^{-1}][a]	V_T [V] [a]	I_{on} [a]	$I_{on/off}$ [a]
1 (PhO-SiPc)	7.7 ±7.4 x10^{-3}	40.5 ± 1.8	2.47 x10^{-7}	10^4
2 (345F-SiPc)	4.7±1.1 x10^{-2}	28.9 ± 2.1	6.23 x10^{-6}	10^5
3 (F10-SiPc)	7.1 ± 3.0 x10^{-2}	39.7 ± 1.4	5.68 x10^{-6}	10^5
4 (2MP-SiPc)	1.0 ± 0.30 x10^{-3}	48.7 ± 0.7	3.86 x10^{-8}	10^3
5 (3MP-SiPc)	8.0 ± 1.7 x10^{-3}	34.1 ± 0.4	1.04 x10^{-6}	10^4-10^5
6 (4MP-SiPc)	1.6 ± 0.29 x10^{-2}	41.9 ± 2.1	1.12 x10^{-6}	10^4-10^5
7 (3Pyr-SiPc)	2.0 ± 1.2 x10^{-4}	*	5.90 x10^{-6}	10^0
8 (4Pyr-SiPc)	7.0 ± 2.0 x10^{-3}	*	3.70 x10^{-6}	10^1
9 (3I-SiPc)	4.6 ± 0.74 x10^{-4}	44.5 ± 2.7	2.20 x10^{-8}	10^3
10 (PhCOO-SiPc)	2.3 ± 0.69 x10^{-4}	36.2 ± 7.3	1.90 x10^{-8}	10^2-10^3
11 (NpCOO-SiPc)	3.9 ± 1.5 x10^{-3}	40.7 ± 0.8	2.31 x10^{-7}	10^3-10^4

[a] μ_e and V_T were calculated based on mean values, while I_{on} and $I_{on/off}$ were calculated based on median values

* Values could not be calculated accurately due to high off current causing deviation from Equation 1

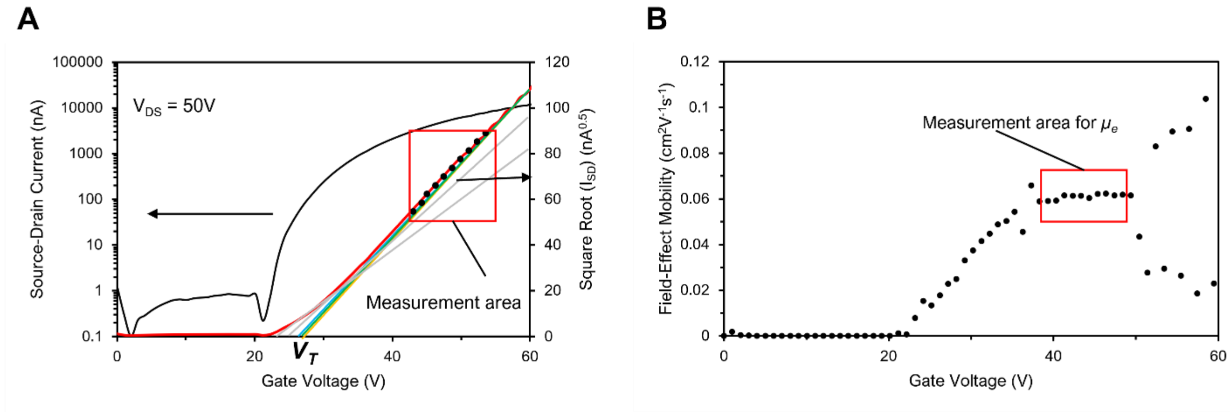

Figure 2.7. A) Characteristic forward transfer curve and B) μ_e vs V_{GS} for a forward sweep of I_{DS} vs V_{GS} for 345F-SiPc (2) with μ_e extracted from the average of values in the measurement area (red box)

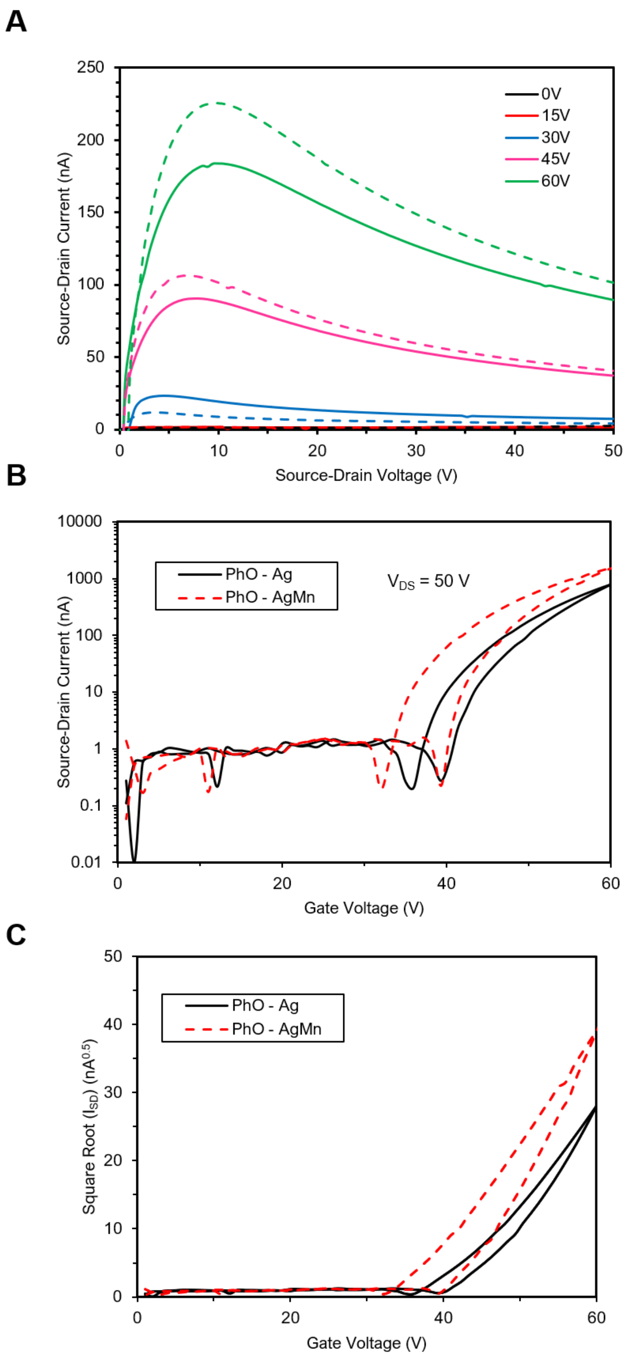

Figure 2.8 A) Output, B) transfer and C) $\sqrt{\boldsymbol{I_{DS}}}$ vs V_{GS} curves for PhO-SiPc (1) with Ag (solid lines) and Ag/Mn (dotted lines) electrode configurations.

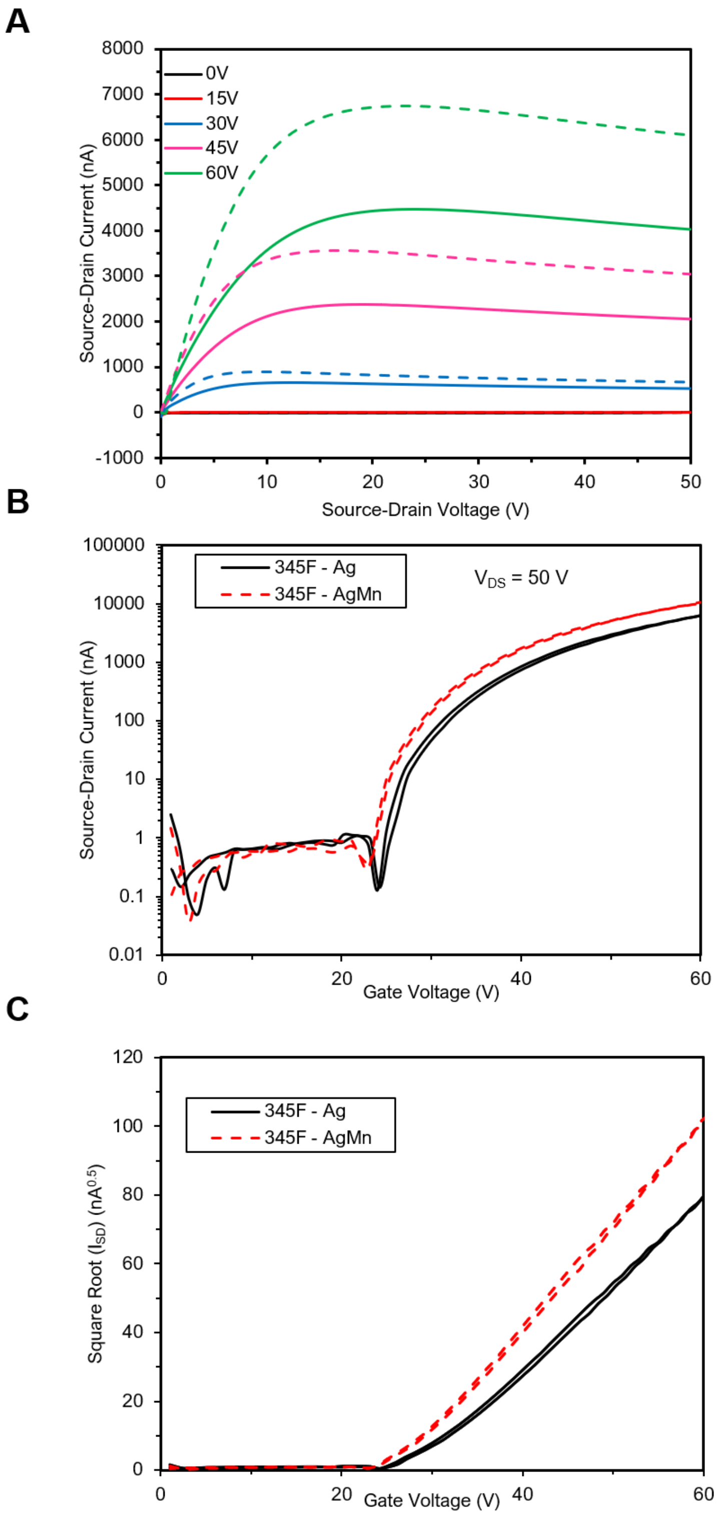

Figure 2.9: A A) Output, B) transfer and C) $\sqrt{I_{DS}}$ vs V_{GS} curves for 345F-SiPc (2) with Ag (solid lines) and Ag/Mn (dotted lines) electrode configurations.

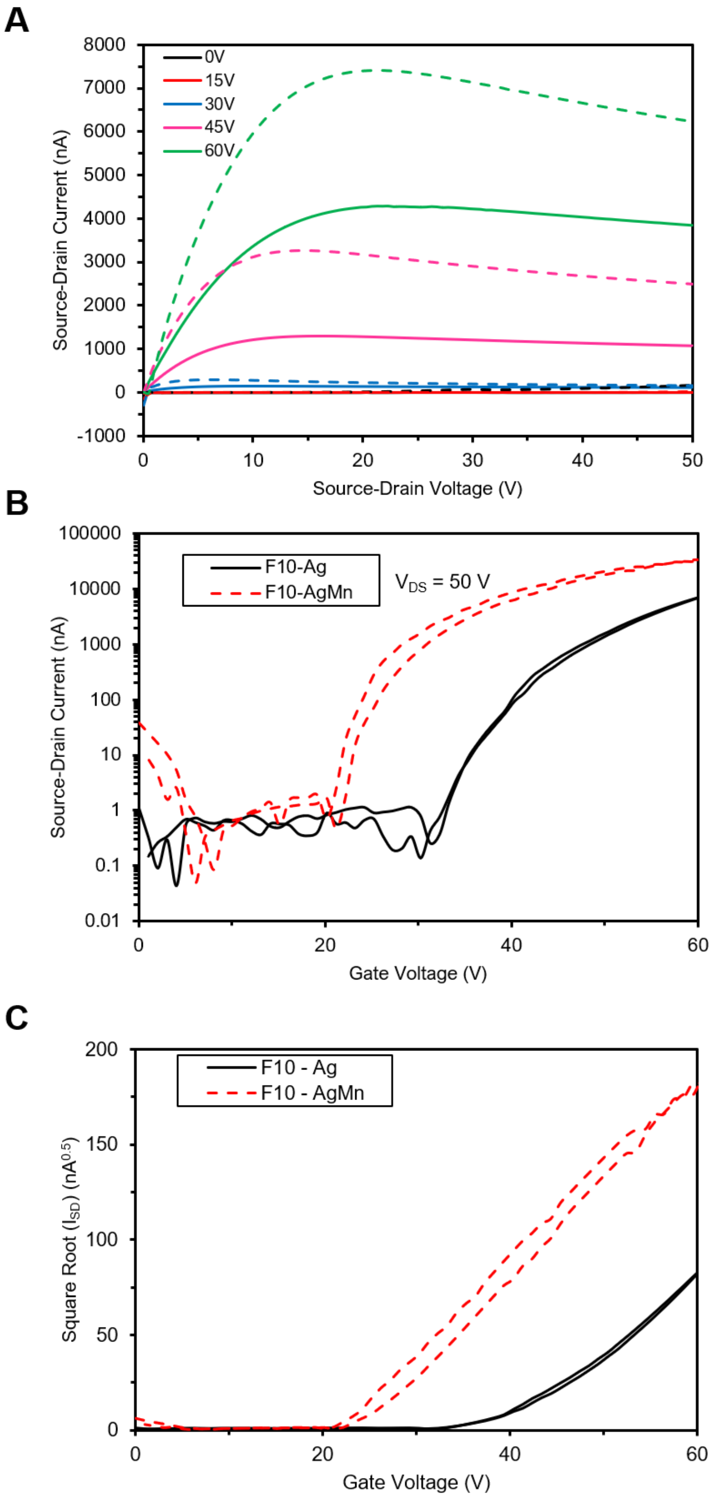

Figure 2.10 A) Output, B) transfer and C) $\sqrt{I_{DS}}$ vs V_{GS} curves for F$_{10}$-SiPc (3) with Ag (solid lines) and Ag/Mn (dotted lines) electrode configurations.

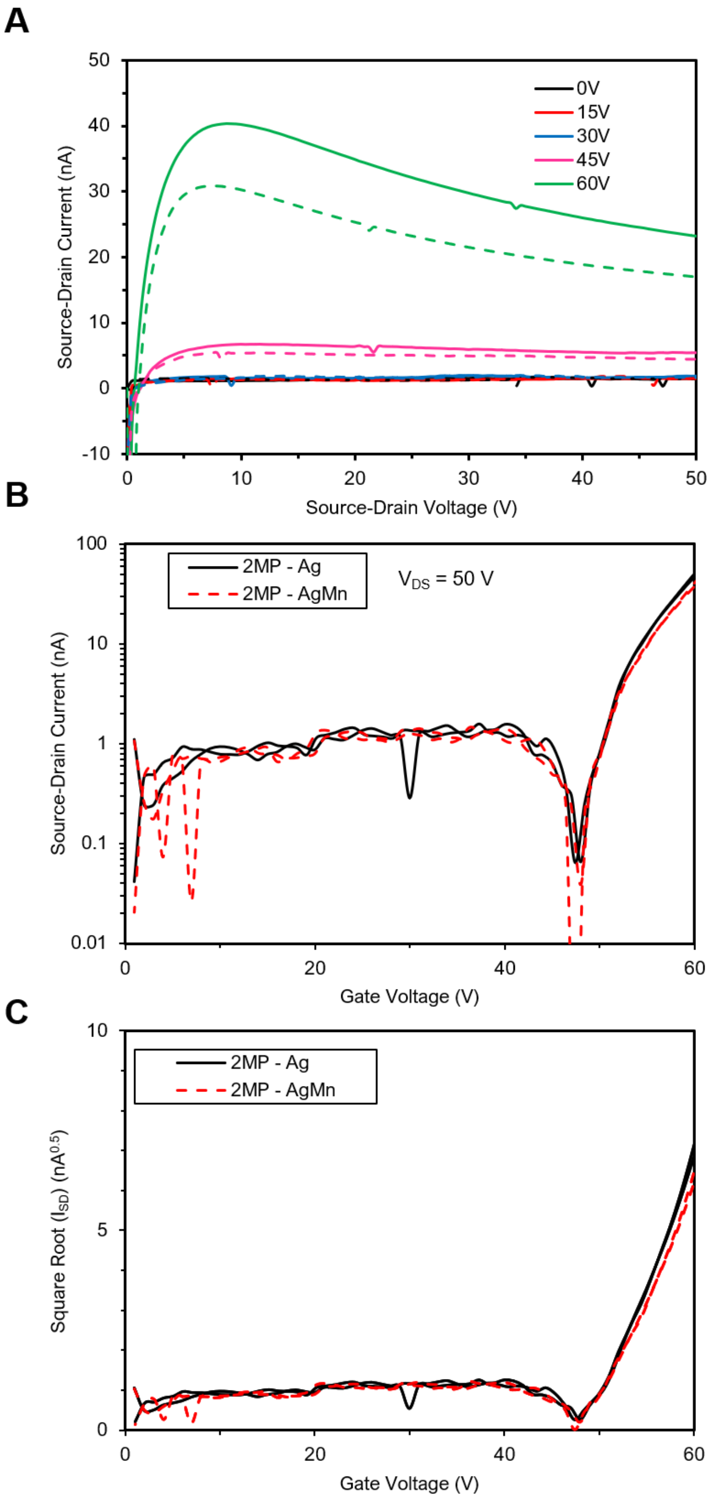

Figure 2.11 A) Output, B) transfer and C) $\sqrt{\boldsymbol{I_{DS}}}$ vs V_{GS} curves for 2MP-SiPc (4) with Ag (solid lines) and Ag/Mn (dotted lines) electrode configurations.

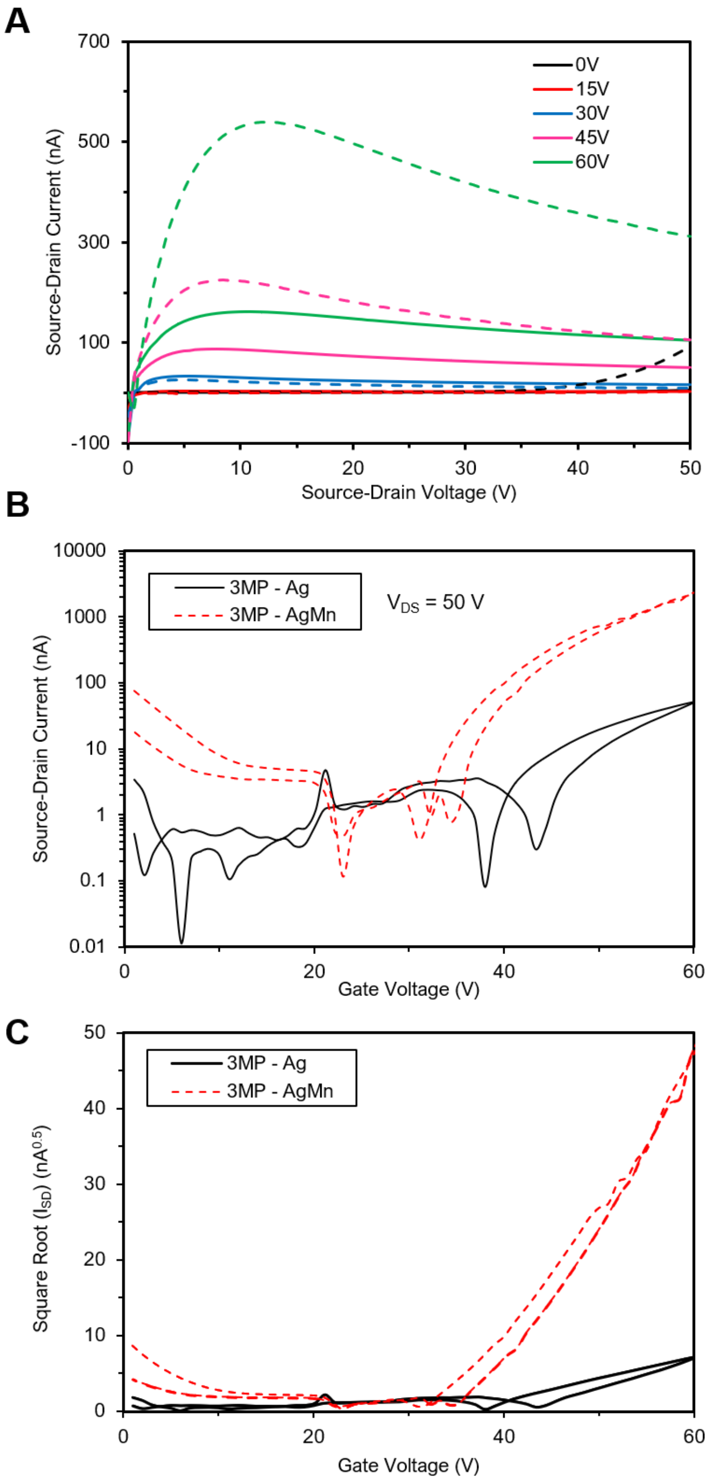

Figure 2.12 A) Output, B) transfer and C) $\sqrt{I_{DS}}$ vs V_{GS} curves for 3MP-SiPc (5) with Ag (solid lines) and Ag/Mn (dotted lines) electrode configurations.

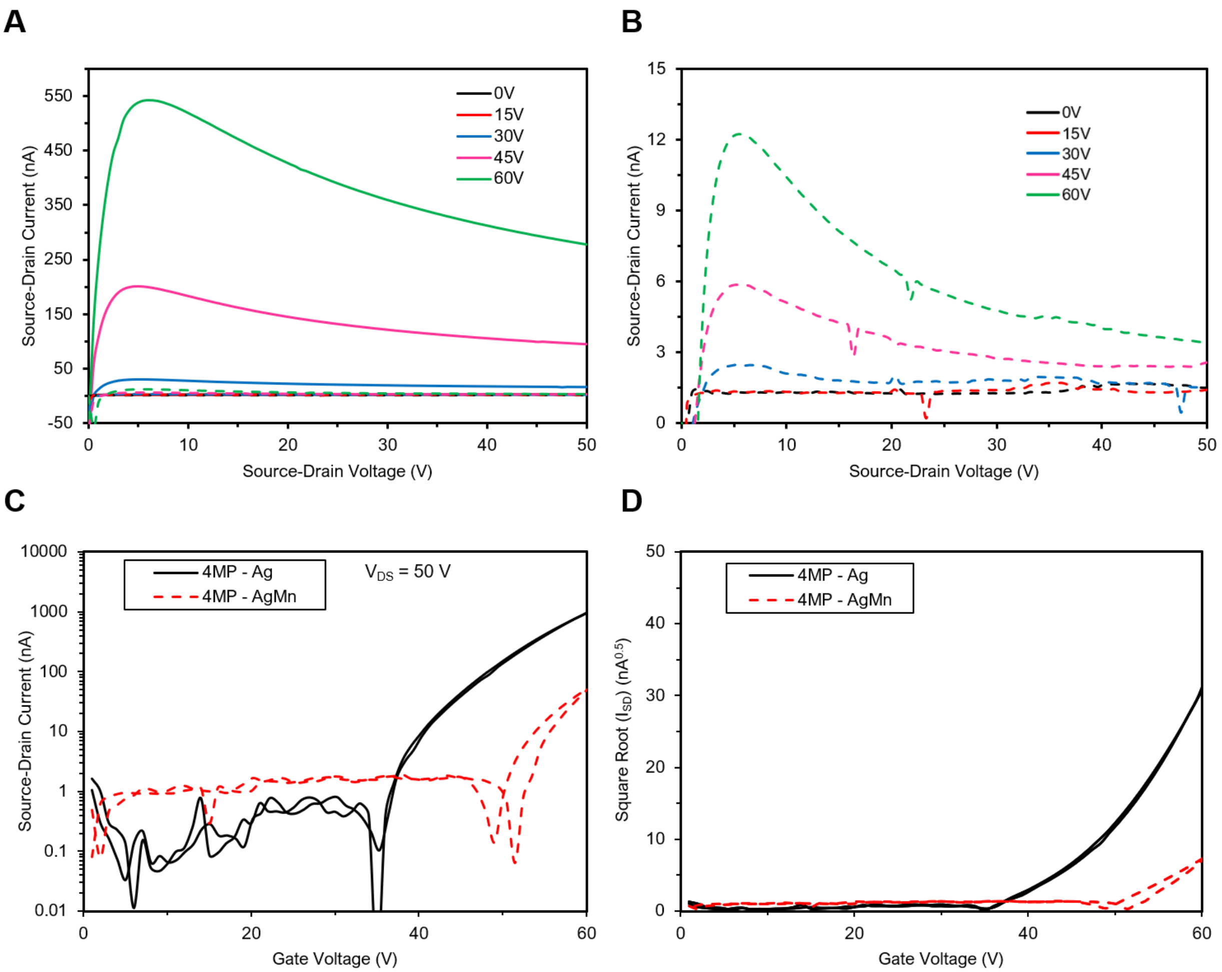

Figure 2.13 A and B) Output, C) transfer and D) $\sqrt{\boldsymbol{I_{DS}}}$ vs V_{GS} curves for 4MP-SiPc (6) with Ag (solid lines) and Ag/Mn (dotted lines) electrode configurations.

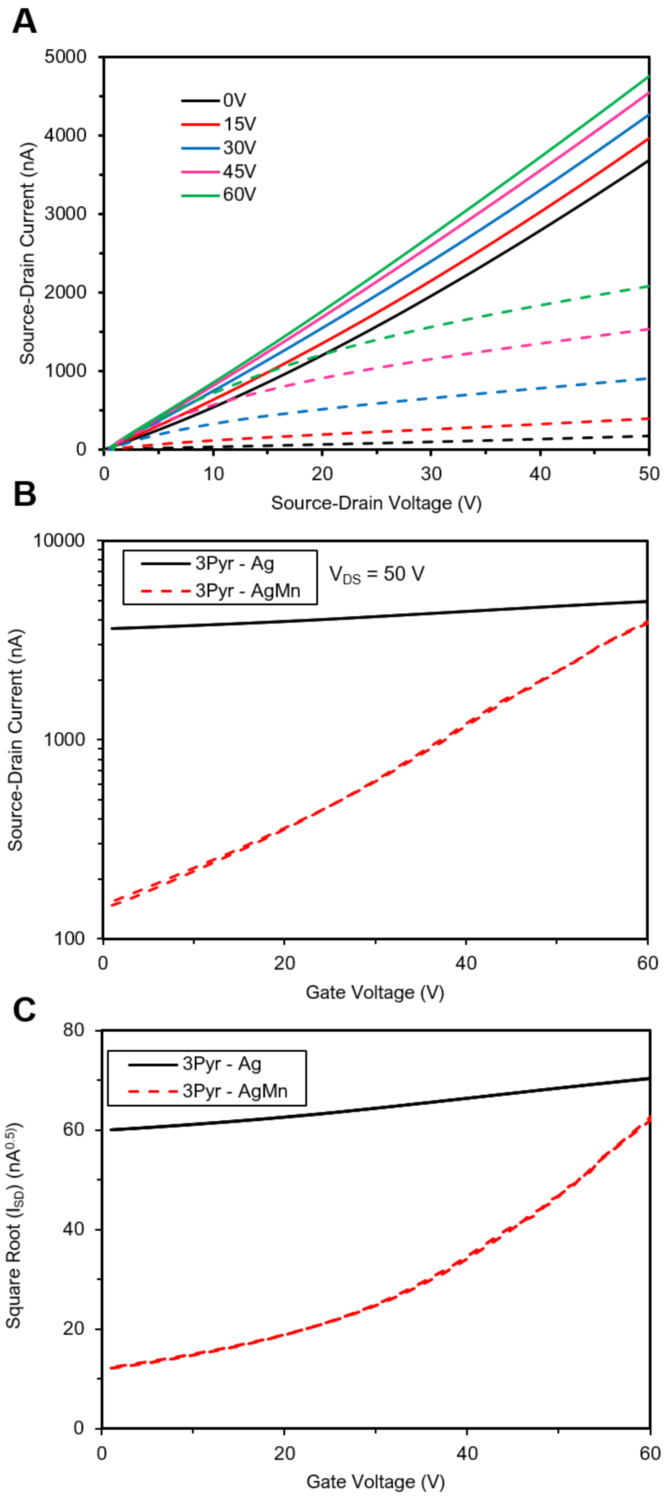

Figure 2.14 A) Output, B) transfer and C) $\sqrt{I_{DS}}$ vs V_{GS} curves for 3Pyr-SiPc (7) with Ag (solid lines) and Ag/Mn (dotted lines) electrode configurations.

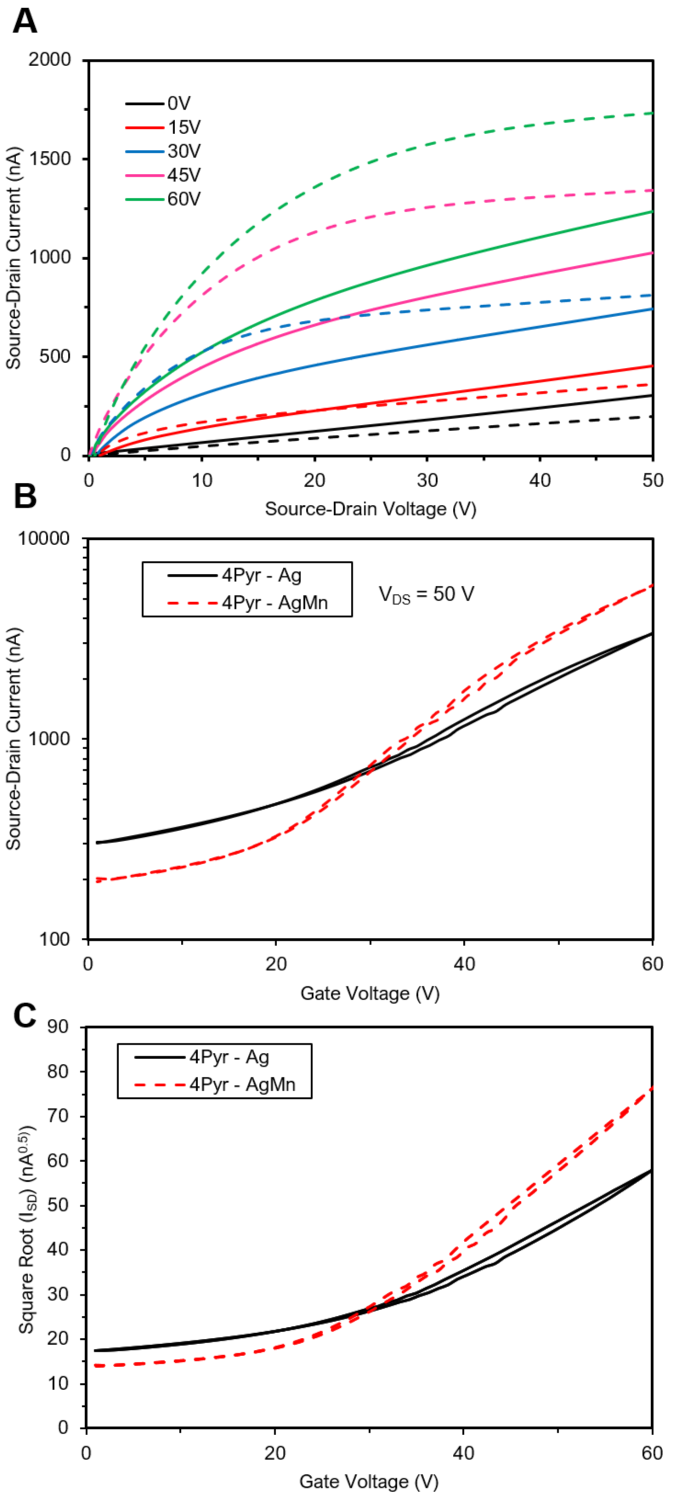

Figure 2.15 A) Output, B) transfer and C) $\sqrt{\boldsymbol{I_{DS}}}$ vs V_{GS} curves for 4Pyr-SiPc (8) with Ag (solid lines) and Ag/Mn (dotted lines) electrode configurations.

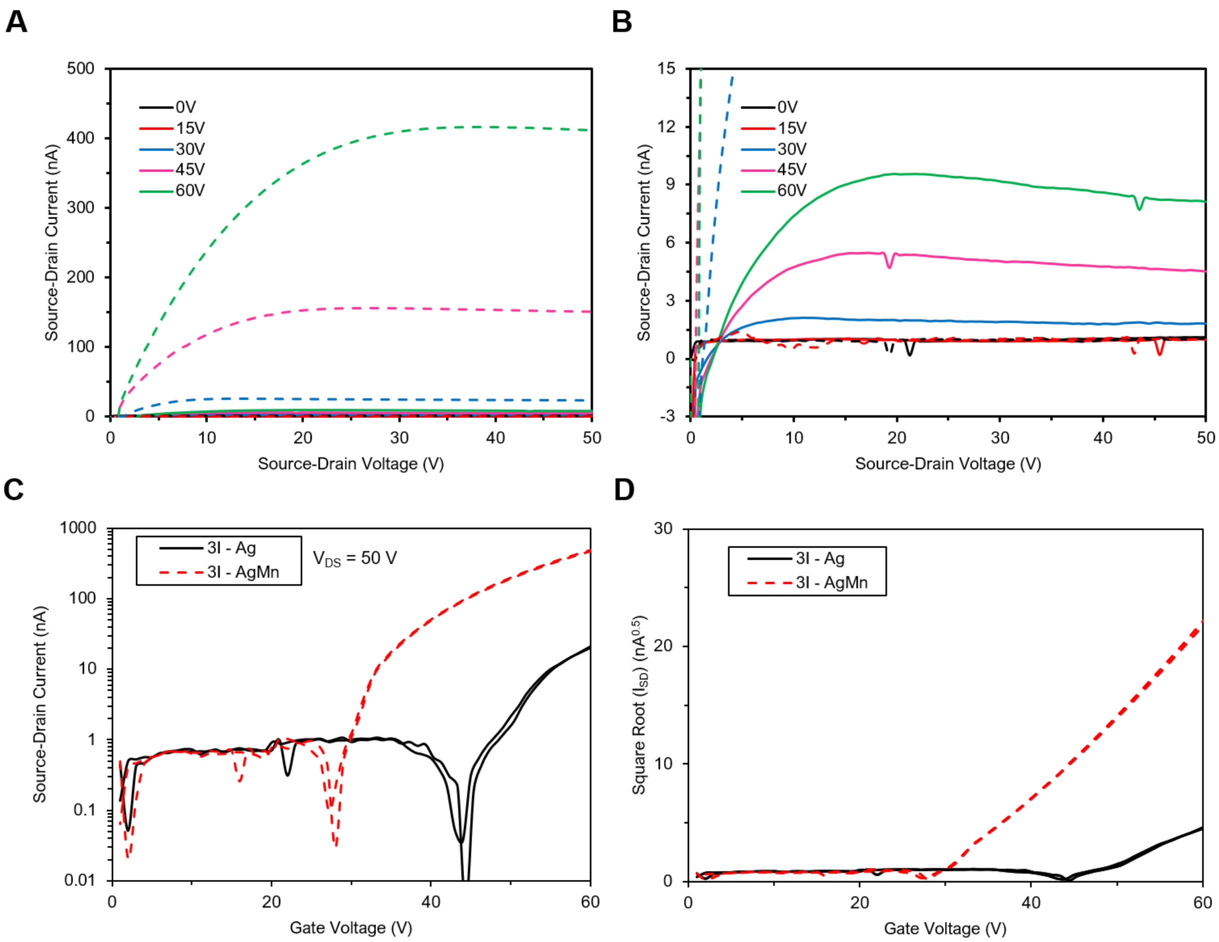

Figure 2.16 A and B) Output, C) transfer and D) $\sqrt{I_{DS}}$ vs V_{GS} curves for 3I-SiPc (9) with Ag (solid lines) and Ag/Mn (dotted lines) electrode configurations.

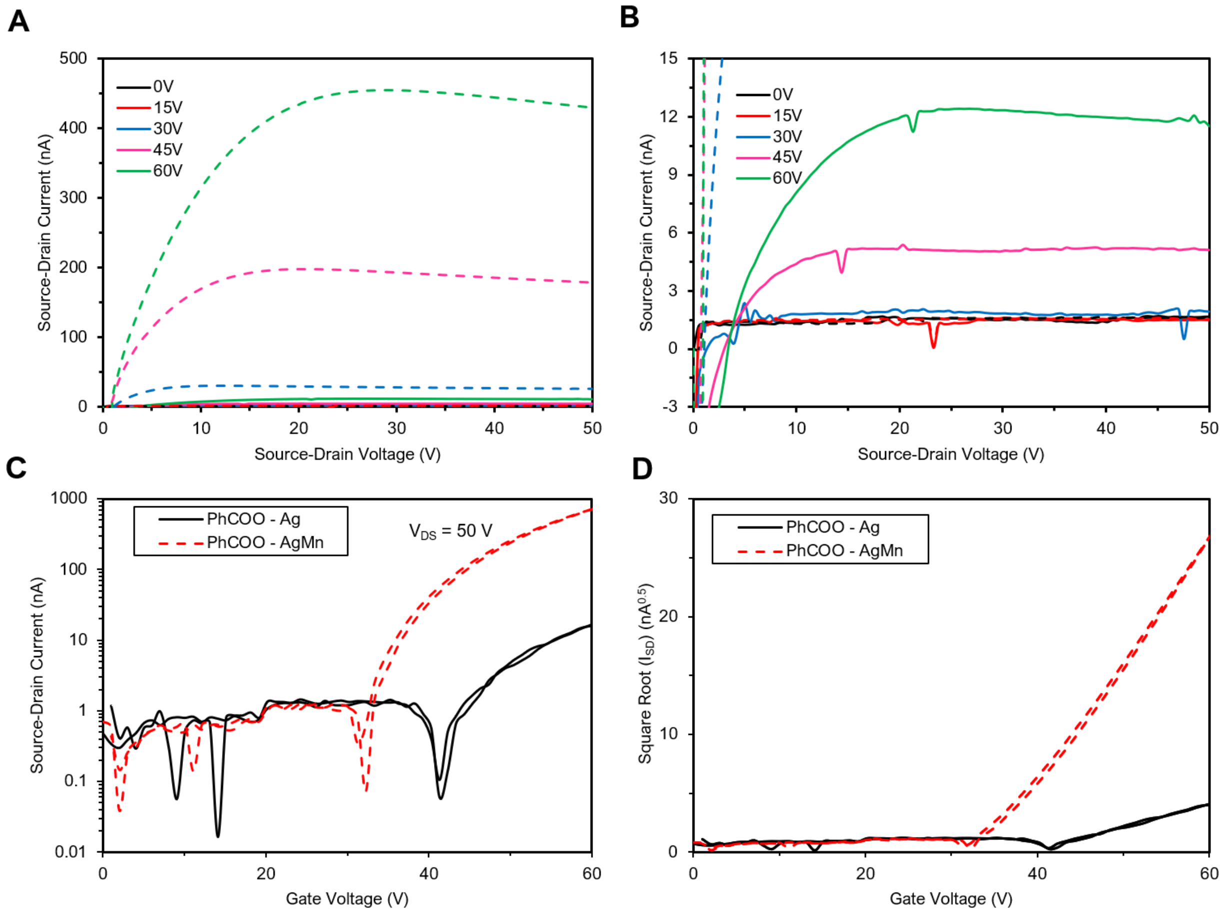

Figure 2.17 A and B) Output, C) transfer and D) $\sqrt{I_{DS}}$ vs V_{GS} curves for PhCOO-SiPc (10) with Ag (solid lines) and Ag/Mn (dotted lines) electrode configurations.

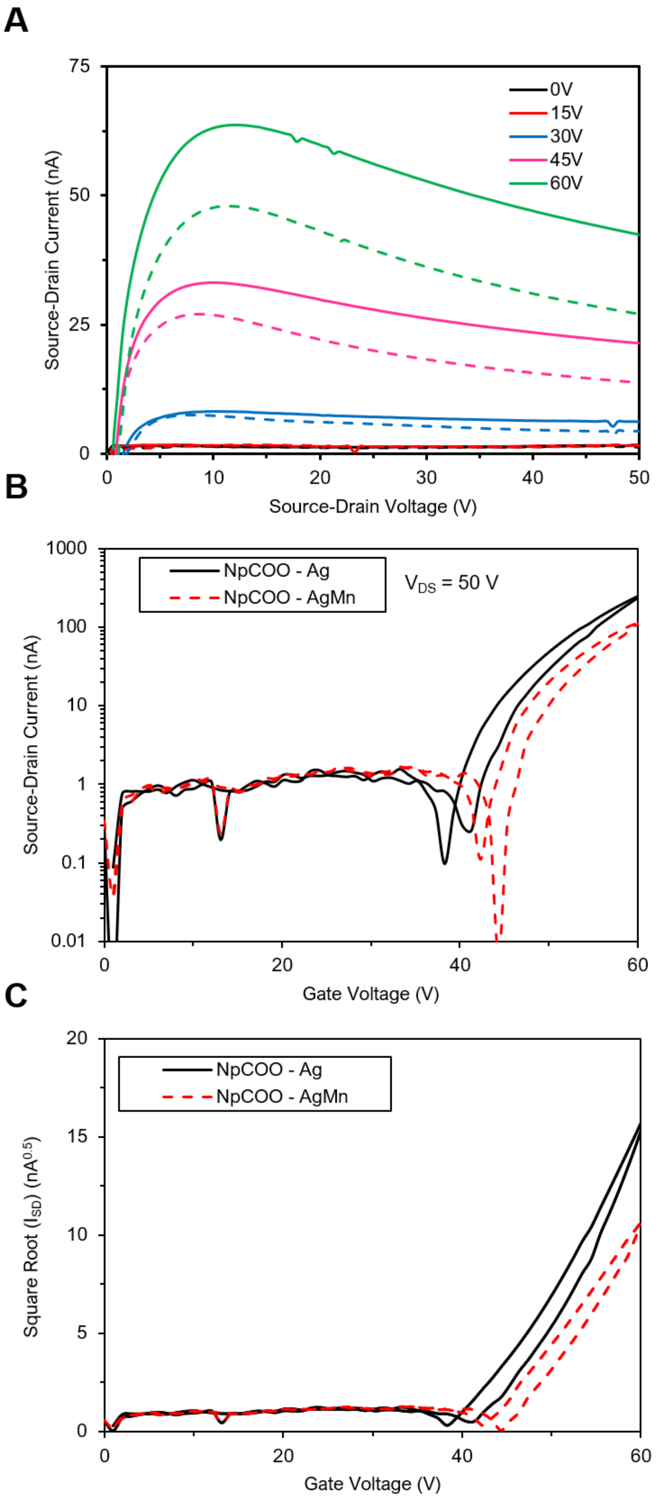

Figure 2.18 A) Output, B) transfer and C) $\sqrt{I_{DS}}$ vs V_{GS} curves for NpCOO-SiPc (11) with Ag (solid lines) and Ag/Mn (dotted lines) electrode configurations.

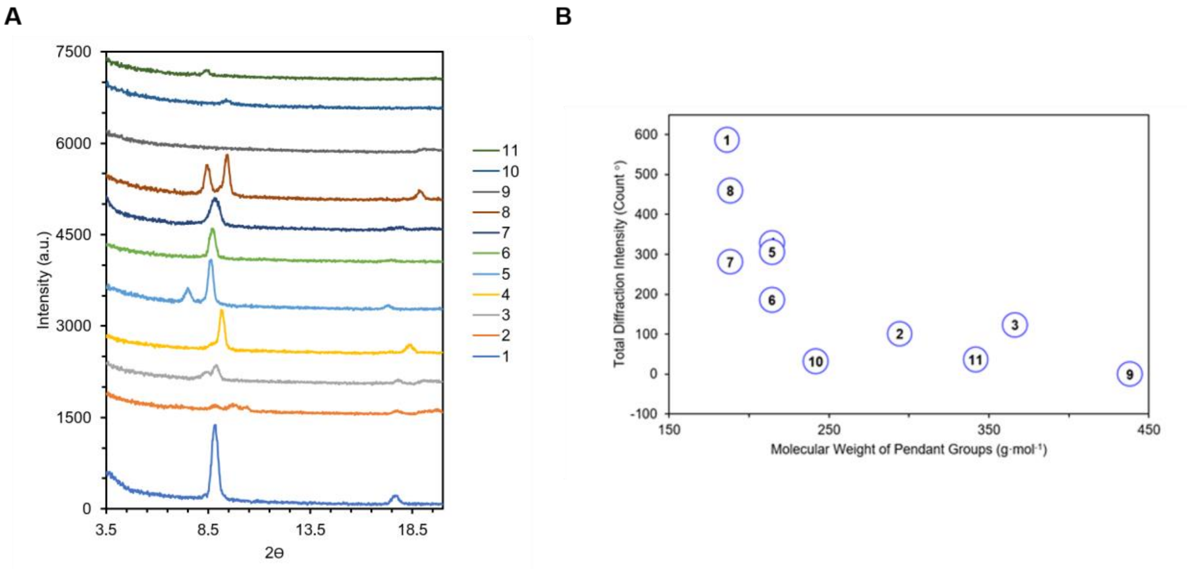

Figure 2.19 A) PXRD data for materials 1 – 11, scanned from 3.5° < 2$\boldsymbol{\theta}$ < 20°, and B) total PXRD diffraction intensity for materials 1 – 11 as a function of pendant group molecular weight.

Table 2.7 Average RMS surface roughness of materials 1 – 11, calculated from AFM images.

Material	Average RMS Roughness (nm)
1 (PhO-SiPc)	2.07
2 (345F-SiPc)	14.50
3 (F10-SiPc)	3.94
4 (2MP-SiPc)	2.70
5 (3MP-SiPc)	3.34
6 (4MP-SiPc)	2.33
7 (3Pyr-SiPc)	2.87
8 (4Pyr-SiPc)	2.05
9 (3I-SiPc)	9.11
10 (PhCOO-SiPc)	1.56
11 (NpCOO-SiPc)	2.58

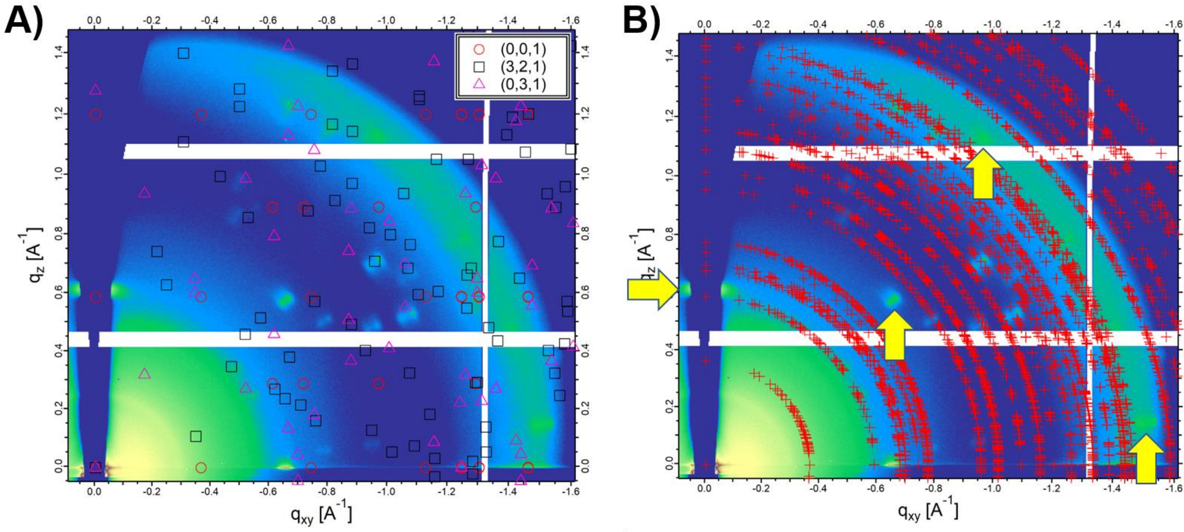

Figure 2.20 A) 2D scattering pattern with likely orientations based on simulated HKL orientations from -3 to +3 of the single crystal and B) reciprocal space map (RSM) model for all HKL orientations from -3 to +3 simulated, plotted over 2D scattering pattern and compared with magnitude of (q_{xy}, q_z) for material 1 (PhO-SiPc) at α = 0.2° determined by GIWAXS. Arrows indicate scattering data that does not correspond to single-crystal data.

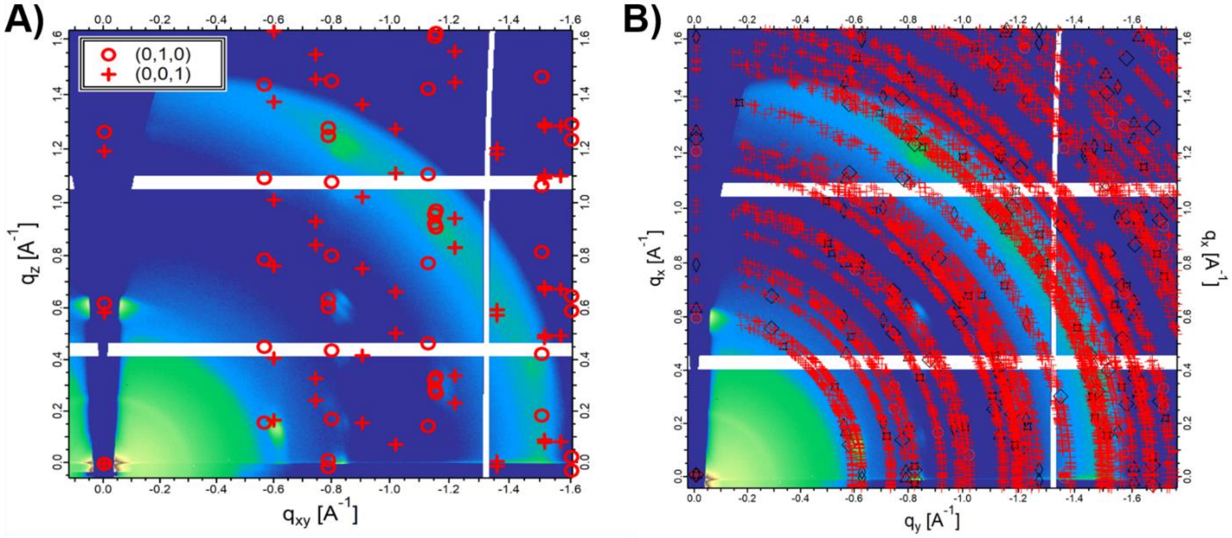

Figure 2.21 A) 2D scattering pattern with identified molecular orientations based on single crystal data and B) reciprocal space map (RSM) model for all HKL orientations from -3 to +3 simulated, plotted over 2D scattering pattern and compared with magnitude of (q_{xy}, q_z) for material 3 (F_{10}-SiPc) at α = 0.22° determined by GIWAXS.

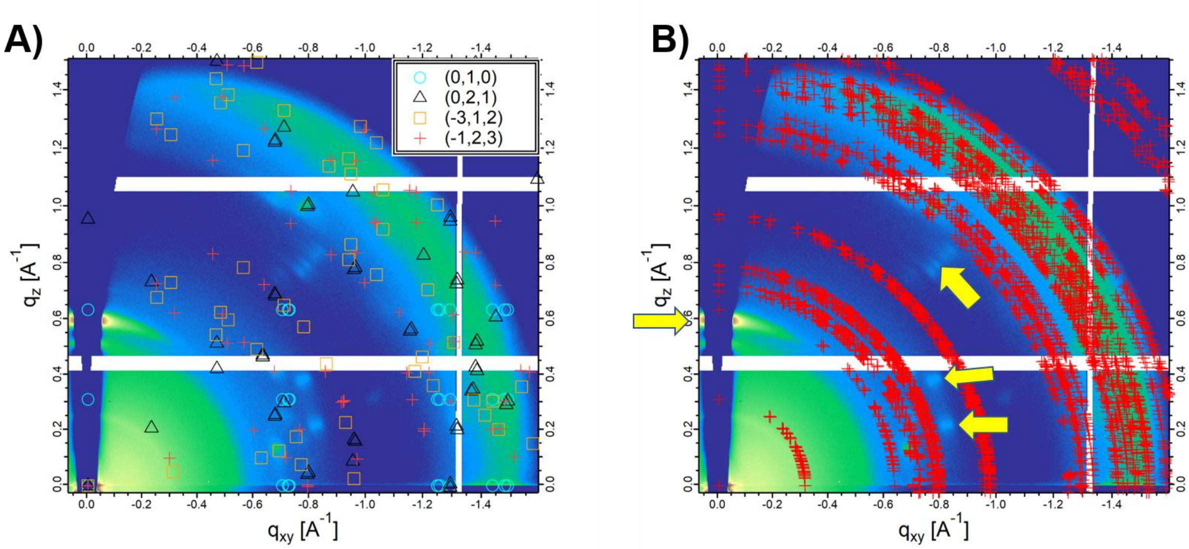

Figure 2.22 A) 2D scattering pattern with likely orientations based on simulated HKL orientations from -3 to +3 of the single crystal and B) reciprocal space map (RSM) model for all HKL orientations from -3 to +3 simulated, plotted over 2D scattering pattern and compared with magnitude of (q_{xy}, q_z) for material 5 (3MP-SiPc) at α = 0.2° determined by GIWAXS. Arrows indicate scattering data that does not correspond to single-crystal data.

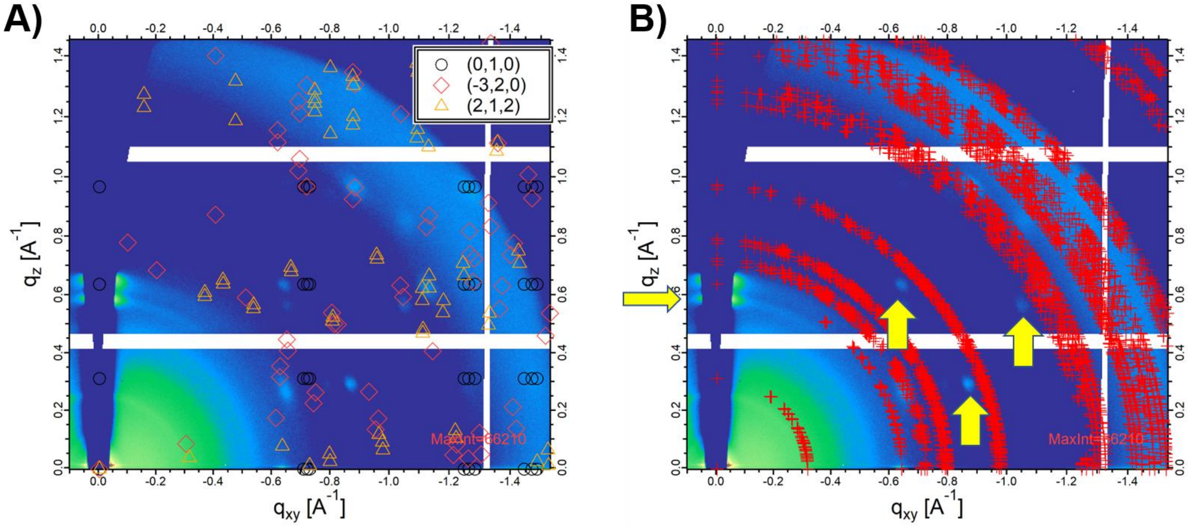

Figure 2.23 A) 2D scattering pattern with likely orientations based on simulated HKL orientations from -3 to +3 of the single crystal and B) reciprocal space map (RSM) model for all HKL orientations from -3 to +3 simulated, plotted over 2D scattering pattern and compared with magnitude of (q_{xy}, q_z) for material 8 (4Pyr-SiPc) at α = 0.22° determined by GIWAXS. Arrows indicate scattering data that does not correspond to single-crystal data.

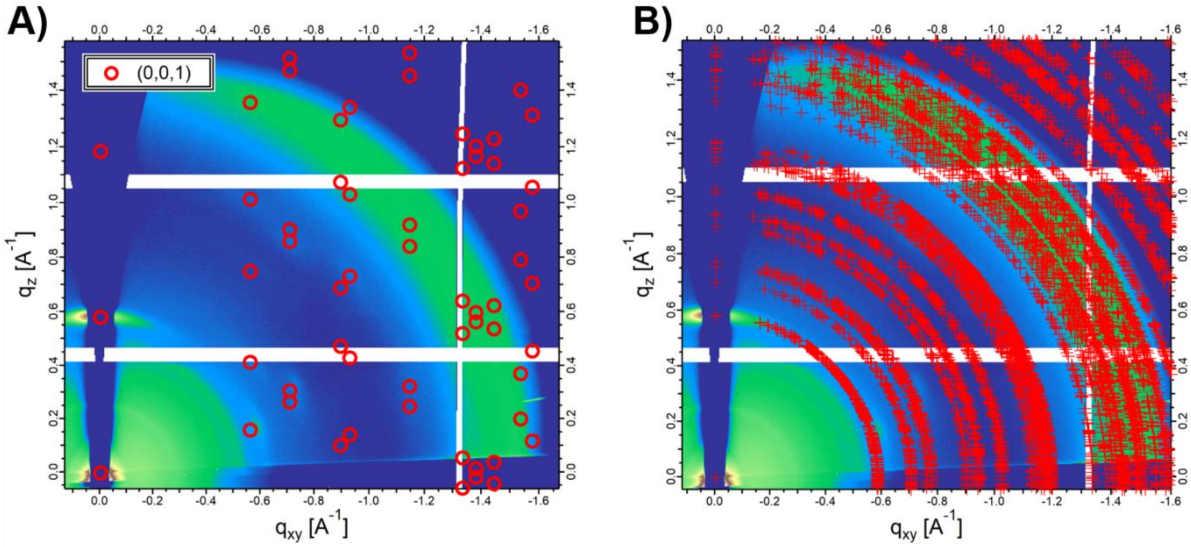

Figure 2.24 A) 2D scattering pattern with identified molecular orientations based on single crystal data and B) reciprocal space map (RSM) model for all HKL orientations from -3 to +3 simulated, plotted over 2D scattering pattern and compared with magnitude of (q_{xy}, q_z) for material 11 (NpCOO-SiPc) at $\alpha = 0.22°$ determined by GIWAXS.

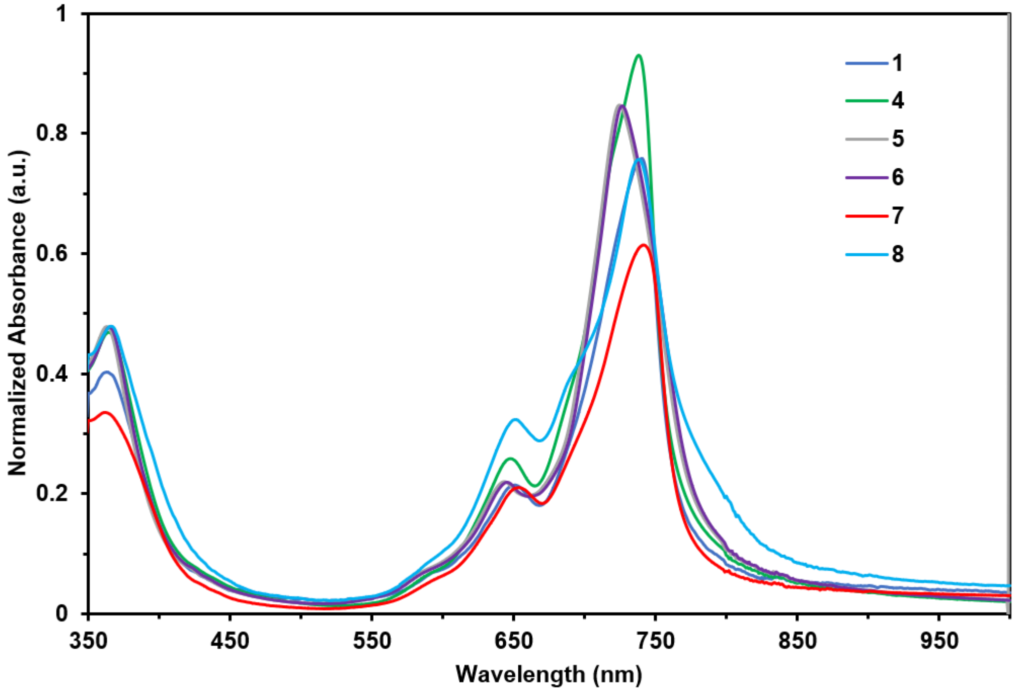

Figure 2.25 Solid state UV-Vis spectra for previously unreported SiPcs in OTFTs.

References

(1) Wen, Y.; Liu, Y. Recent Progress in N-Channel Organic Thin-Film Transistors. *Adv. Mater.* **2010**, *22* (12), 1331–1345. https://doi.org/10.1002/adma.200901454.

(2) Zhan, X.; Facchetti, A.; Barlow, S.; Marks, T. J.; Ratner, M. A.; Wasielewski, M. R.; Marder, S. R. Rylene and Related Diimides for Organic Electronics. *Adv. Mater*. **2011**, 268–284. https://doi.org/10.1002/adma.201001402.

(3) Quinn, J. T. E.; Zhu, J.; Li, X.; Wang, J.; Li, Y. Recent Progress in the Development of N-Type Organic Semiconductors for Organic Field Effect Transistors. *J. Mater. Chem. C* **2017**, *5* (34), 8654–8681. https://doi.org/10.1039/c7tc01680h.

(4) Jiang, H.; Hu, P.; Ye, J.; Li, Y.; Li, H.; Zhang, X.; Li, R.; Dong, H.; Hu, W.; Kloc, C. Molecular Crystal Engineering: Tuning Organic Semiconductor from P-Type to N-Type by Adjusting Their Substitutional Symmetry. *Adv. Mater.* **2017**, *29* (10), 1605053. https://doi.org/10.1002/adma.201605053.

(5) Shukla, D.; Nelson, S. F.; Freeman, D. C.; Rajeswaran, M.; Ahearn, W. G.; Meyer, D. M.; Carey, J. T. Thin-Film Morphology Control in Naphthalene-Diimide-Based Semiconductors: High Mobility N-Type Semiconductor for Organic Thin-Film Transistors. *Chem. Mater.* **2008**, *20* (24), 7486–7491. https://doi.org/10.1021/cm802071w.

(6) Curtis, M. D.; Cao, J.; Kampf, J. W. Solid-State Packing of Conjugated Oligomers: From π-Stacks to the Herringbone Structure. *J. Am. Chem. Soc.* **2004**, *126* (13), 4318–4328. https://doi.org/10.1021/ja0397916.

(7) Chen, M.; Yan, L.; Zhao, Y.; Murtaza, I.; Meng, H.; Huang, W. Anthracene-Based Semiconductors for Organic Field-Effect Transistors. *J. Mater. Chem. C* **2018**, *6* (28), 7416–7444. https://doi.org/10.1039/c8tc01865k.

(8) Liu, J.; Dong, H.; Wang, Z.; Ji, D.; Cheng, C.; Geng, H.; Zhang, H.; Zhen, Y.; Jiang, L.; Fu, H.; Bo, Z.; Chen, W.; Shuai, Z.; Hu, W. Thin Film Field-Effect Transistors of 2,6-Diphenyl Anthracene (DPA). *Chem. Commun.* **2015**, *51*, 11777--11779. https://doi.org/10.1039/x0xx00000x.

(9) Takimiya, K.; Nakano, M. Thiophene-Fused Naphthalene Diimides: New Building Blocks for Electron Deficient P-Functional Materials. *Bull. Chem. Soc. Jpn.* **2018**, *91* (1), 121–140. https://doi.org/10.1246/bcsj.20170298.

(10) Hasegawa, T.; Ashizawa, M.; Matsumoto, H. Design and Structure-Property Relationship of Benzothienoisoindigo in Organic Field Effect Transistors. *RSC Adv.* **2015**, *5* (75), 61035–61043. https://doi.org/10.1039/c5ra07660a.

(11) Kline, R. J.; Hudson, S. D.; Zhang, X.; Gundlach, D. J.; Moad, A. J.; Jurchescu, O. D.; Jackson, T. N.; Subramanian, S.; Anthony, J. E.; Toney, M. F.; Richter, L. J. Controlling the Microstructure of Solution-Processable Small Molecules in Thin-Film Transistors through Substrate Chemistry. *Chem. Mater.* **2011**, *23* (5), 1194–1203. https://doi.org/10.1021/cm102834m.

(12) Ward, J. W.; Li, R.; Obaid, A.; Payne, M. M.; Smilgies, D. M.; Anthony, J. E.; Amassian, A.; Jurchescu, O. D. Rational Design of Organic Semiconductors for Texture Control and Self-Patterning on Halogenated Surfaces. *Adv. Funct. Mater.* **2014**, *24* (32), 5052–5058.

https://doi.org/10.1002/adfm.201400219.

(13) Waldrip, M.; Jurchescu, O. D.; Gundlach, D. J.; Bittle, E. G. Contact Resistance in Organic Field-Effect Transistors: Conquering the Barrier. *Adv. Funct. Mater.* **2019**, 1–31. https://doi.org/10.1002/adfm.201904576.

(14) Piliego, C.; Jarzab, D.; Gigli, G.; Chen, Z.; Facchetti, A.; Loi, M. A. High Electron Mobility and Ambient Stability in Solution-Processed Perylene-Based Organic Field-Effect Transistors. *Adv. Mater.* **2009**, *21* (16), 1573–1576. https://doi.org/10.1002/adma.200803207.

(15) Jiang, H.; Ye, J.; Hu, P.; Wei, F.; Du, K.; Wang, N.; Ba, T.; Feng, S.; Kloc, C. Fluorination of Metal Phthalocyanines: Single-Crystal Growth, Efficient N-Channel Organic Field-Effect Transistors, and Structure-Property Relationships. *Sci. Rep.* **2014**, *4*, 1–6. https://doi.org/10.1038/srep07573.

(16) Chaure, N. B.; Basova, T.; Zahedi, M.; Ray, A. K.; Sharma, A. K.; Durmuş, M.; Ahsen, V. Solution Processed Tetrasubstituted Zinc Phthalocyanine as an Active Layer in Organic Field Effect Transistors. *J. Appl. Phys.* **2010**, *107* (11), 2–7. https://doi.org/10.1063/1.3428386.

(17) Melville, O. A.; Lessard, B. H.; Bender, T. P. Phthalocyanine-Based Organic Thin-Film Transistors: A Review of Recent Advances. *ACS Applied Materials & Interfaces*. 2015, pp 13105–13118. https://doi.org/10.1021/acsami.5b01718.

(18) Song, D.; Wang, H.; Zhu, F.; Yang, J.; Tian, H.; Geng, Y.; Yan, D. Phthalocyanato tin(IV) Dichloride: An Air-Stable, High-Performance, N-Type Organic Semiconductor with a High Field-Effect Electron Mobility. *Adv. Mater.* **2008**, *20* (11), 2142–2144. https://doi.org/10.1002/adma.200702439.

(19) Melville, O. A.; Grant, T. M.; Lessard, H. Silicon Phthalocyanines as N-Type Semiconductors in Organic Thin Film Transistors. *J. Mater. Chem. C* **2018**, *6*, 5482–5488. https://doi.org/10.1039/c8tc01116h.

(20) Grant, T. M.; Rice, N. A.; Muccioli, L.; Castet, F.; Lessard, B. H. Solution-Processable N-Type Tin Phthalocyanines in Organic Thin Film Transistors and as Ternary Additives in Organic Photovoltaics. *ACS Appl. Electron. Mater.* **2019**, *1* (4), 494–504. https://doi.org/10.1021/acsaelm.8b00113.

(21) Li, Q.; Tang, Q.; Li, H.; Hu, W.; Yang, X.; Shuai, Z.; Liu, Y.; Zhu, D. Organic Thin-Film Transistors of Phthalocyanines. *Pure Appl. Chem.* **2008**, *80* (11), 2231–2240. https://doi.org/10.1351/pac200880112231.

(22) Li, L.; Tang, Q.; Li, H.; Yang, X.; Hu, W.; Song, Y.; Shuai, Z.; Xu, W.; Liu, Y.; Zhu, D. An Ultra Closely π-Stacked Organic Semiconductor for High Performance Field-Effect Transistors. *Adv. Mater.* **2007**, *19* (18), 2613–2617. https://doi.org/10.1002/adma.200700682.

(23) Pearson, A. J.; Plint, T.; Jones, S. T. E.; Lessard, B. H.; Credgington, D.; Bender, T. P.; Greenham, N. C. Silicon Phthalocyanines as Dopant Red Emitters for Efficient Solution Processed OLEDs. *J. Mater. Chem. C* **2017**, *5* (48), 12688–12698. https://doi.org/10.1039/c7tc03946h.

(24) Plint, T.; Lessard, B. H.; Bender, T. P. Assessing the Potential of Group 13 and 14 Metal/metalloid Phthalocyanines as Hole Transport Layers in Organic Light Emitting Diodes. *J. Appl. Phys.* **2016**, *119* (14), 145502. https://doi.org/https://doi.org/10.1063/1.4945377.

(25) Grant, T. M.; Gorisse, T.; Dautel, O.; Wantz, G.; Lessard, B. H. Multifunctional Ternary Additive in Bulk Heterojunction OPV: Increased Device Performance and Stability. *J. Mater. Chem. A* **2017**, 1581–1587. https://doi.org/10.1039/C6TA08593H.

(26) Melville, O. A.; Grant, T. M.; Mirka, B.; Boileau, N. T.; Park, J.; Lessard, B. H. Ambipolarity and Air Stability of Silicon Phthalocyanine Organic Thin-Film Transistors. *Adv. Electron. Mater.* **2019**, *1900087*, 1–7. https://doi.org/10.1002/aelm.201900087.

(27) Melville, O. A.; Grant, T. M.; Lochhead, K.; King, B.; Ambrose, R.; Rice, N. A.; Boileau, N. T.; Peltekoff, A. J.; Tousignant, M.; Hill, I. G.; Lessard, B. H. Contact Engineering Using Manganese, Chromium, and Bathocuproine in Group 14 Phthalocyanine Organic Thin-Film Transistors. *ACS Appl. Electron. Mater.* **2020, 2** (5), 1313–1322. https://doi.org/10.1021/acsaelm.0c00104.

(28) Lessard, B. H.; White, R. T.; Al-Amar, M.; Plint, T.; Castrucci, J. S.; Josey, D. S.; Lu, Z. H.; Bender, T. P. Assessing the Potential Roles of Silicon and Germanium Phthalocyanines in Planar Heterojunction Organic Photovoltaic Devices and How Pentafluoro Phenoxylation Can Enhance π-π Interactions and Device Performance. *ACS Appl. Mater. Interfaces* **2015**, *7* (9), 5076–5088. https://doi.org/10.1021/am508491v.

(29) Paterson, A. F.; Singh, S.; Fallon, K. J.; Hodsden, T.; Han, Y.; Schroeder, B. C.; Bronstein, H.; Heeney, M.; McCulloch, I.; Anthopoulos, T. D. Recent Progress in High-Mobility Organic Transistors: A Reality Check. *Adv. Mater.* **2018**, *30* (36), 1–33. https://doi.org/10.1002/adma.201801079.

(30) Lessard, B. H.; Grant, T. M.; White, R.; Thibau, E.; Lu, Z. H.; Bender, T. P. The Position and Frequency of Fluorine Atoms Changes the Electron Donor/acceptor Properties of Fluorophenoxy Silicon Phthalocyanines within Organic Photovoltaic Devices. *J. Mater. Chem. A* **2015**, *3* (48), 24512–24524. https://doi.org/10.1039/c5ta07173a.

(31) Raboui, H.; Lough, A. J.; Plint, T.; Bender, T. P. Position of Methyl and Nitrogen on Axial Aryloxy Substituents Determines the Crystal Structure of Silicon Phthalocyanines. *Cryst. Growth Des.* **2018**, *18* (5), 3193–3201. https://doi.org/10.1021/acs.cgd.8b00298.

(32) Gali, S. M.; Matta, M.; Lessard, B. H.; Castet, F.; Muccioli, L. Ambipolarity and Dimensionality of Charge Transport in Crystalline Group 14 Phthalocyanines: A Computational Study. *J. Phys. Chem. C* **2018**, *122* (5), 2554–2563. https://doi.org/10.1021/acs.jpcc.7b11588.

(33) Lessard, B. H.; Lough, A. J.; Bender, T. P. Crystal Structures of Bis(phenoxy)silicon Phthalocyanines: Increasing π-π Interactions, Solubility and Disorder and No Halogen Bonding Observed. *Acta Crystallogr. Sect. E Crystallogr. Commun.* **2016**, *72*, 988–994. https://doi.org/10.1107/S205698901600935X.

(34) Cranston, R.; Vebber, M. C.; Berbigier, J. F.; Rice, N. A.; Tonnelé, C.; Comeau, Z.; Boileau, N. T.; Shuhendler, A. J.; Castet, F.; Muccioli, L.; Kelly, T L.; Lessard, B. H. Thin-Film Engineering of Solution Processable N-Type Silicon Phthalocyanines for Organic Thin-

Film Transistors. *ACS Appl. Mater. Interfaces,* **2020**, *Submitted.*

(35) Coropceanu, V.; Malagoli, M.; da Silva Filho, D. A.; Gruhn, N. E.; Bill, T. G.; Brédas, J. L. Hole- and Electron-Vibrational Couplings in Oligoacene Crystals: Intramolecular Contributions. *Phys. Rev. Lett.* **2002**, *89* (27), 1–4. https://doi.org/10.1103/PhysRevLett.89.275503.

(36) Coropceanu, V.; Cornil, J.; da Silva Filho, D. A.; Olivier, Y.; Silbey, R.; Brédas, J. L. Charge Transport in Organic Semiconductors. *Chem. Rev.* **2007**, *107* (4), 926–952. https://doi.org/10.1021/cr050140x.

(37) Reese, C.; Bao, Z. High-Resolution Measurement of the Anisotropy of Charge Transport in Single Crystals. *Adv. Mater.* **2007**, *19* (24), 4535–4538. https://doi.org/10.1002/adma.200701139.

(38) Molinari, A. S.; Alves, H.; Chen, Z.; Facchetti, A.; Morpurgo, A. F. High Electron Mobility in Vacuum and Ambient for PDIF-CN2 Single-Crystal Transistors. *J. Am. Chem. Soc.* **2009**, *131* (7), 2462–2463. https://doi.org/10.1021/ja809848y.

(39) Frisch, M. J.; Trucks, G. W.; Schlegel, H. B.; Scuseria, G. E.; Robb, M. A.; Cheeseman, J. R.; Scalmani, G.; Barone, V.; Petersson, G. A.; Nakatsuji, H.; Li, X.; Caricato, M.; Marenich, A. V.; Bloino, J.; Janesko, B. G.; Gomperts, R.; Mennucci, B.; Hratchian, H. P.; Ortiz, J. V.; Izmaylov, A. F.; Sonnenberg, J. L.; Williams-Young, D.; Ding, F.; Lipparini, F.; Egidi, F.; Goings, J.; Peng, B.; Petrone, A.; Henderson, T.; Ranasinghe, D.; Zakrzewski, V. G.; Gao, J.; Rega, N.; Zheng, G.; Liang, W.; Hada, M.; Ehara, M.; Toyota, K.; Fukuda, R.; Hasegawa, J.; Ishida, M.; Nakajima, T.; Honda, Y.; Kitao, O.; Nakai, H.; Vreven, T.; Throssell, K.; Montgomery, J. A., Jr.; Peralta, J. E.; Ogliaro, F.; Bearpark, M. J.; Heyd, J. J.; Brothers, E. N.; Kudin, K. N.; Staroverov, V. N.; Keith, T. A.; Kobayashi, R.; Normand, J.; Raghavachari, K.; Rendell, A. P.; Burant, J. C.; Iyengar, S. S.; Tomasi, J.; Cossi, M.; Millam, J. M.; Klene, M.; Adamo, C.; Cammi, R.; Ochterski, J. W.; Martin, R. L.; Morokuma, K.; Farkas, O.; Foresman, J. B.; Fox, D. J. Gaussian 16, Revision A.03; Gaussian, Inc.: Wallingford, CT, 2016.

(40) Neese, F. The ORCA Program System. *Wiley Interdiscip. Rev. Comput. Mol. Sci.* **2012**, *2* (1), 73–78. https://doi.org/10.1002/wcms.81.

(41) Sirringhaus, H. Reliability of Organic Field-Effect Transistors. *Adv. Mater.* **2009**, *21* (38–39), 3859–3873. https://doi.org/10.1002/adma.200901136.

(42) Fontaine, P.; Ciatto, G.; Aubert, N.; Goldmann, M. Soft Interfaces and Resonant Investigation on Undulator Source: A Surface X-Ray Scattering Beamline to Study Organic Molecular Films at the SOLEIL Synchrotron. *Sci. Adv. Mater.* **2014**, *6* (11), 2312–2316. https://doi.org/https://doi.org/10.1166/sam.2014.2189.

(43) Ilavsky, J. Nika : Software for Two-Dimensional Data Reduction. *J. Appl. Crystallogr.* **2012**, *45*, 324–328. https://doi.org/10.1107/S0021889812004037.

(44) Zhang, Y.; Wei, X.; Zhang, H.; Chen, X.; Wang, J. Ambipolar Organic Transistors with High On/off Ratio by Introducing a Modified Layer of Gate Insulator. *Appl. Surf. Sci.* **2018**, *427*, 452–457. https://doi.org/10.1016/j.apsusc.2017.08.116.

(45) Shao, X.; Wang, S.; Li, X.; Su, Z.; Chen, Y.; Xiao, Y. Single Component P-, Ambipolar and N-Type OTFTs Based on Fluorinated Copper Phthalocyanines. *Dye. Pigment.* **2016**,

132, 378–386. https://doi.org/10.1016/j.dyepig.2016.05.020.

(46) Ma, L.; Qin, D.; Liu, Y.; Zhan, X. N-Type Organic Light-Emitting Transistors with High Mobility and Improved Air Stability. *J. Mater. Chem. C* **2018**, *6* (3), 535–540. https://doi.org/10.1039/c7tc04556e.

(47) Wang, S.; Wang, Z.; Li, J.; Li, L.; Hu, W. Surface-Grafting Polymers: From Chemistry to Organic Electronics. *Mater. Chem. Front.* **2020**, *4* (3), 692–714. https://doi.org/10.1039/c9qm00450e.

(48) Kim, K.; An, T. K.; Kim, J.; Jeong, Y. J.; Jang, J.; Kim, H.; Baek, J. Y.; Kim, Y. H.; Kim, S. H.; Park, C. E. Grafting Fluorinated Polymer Nanolayer for Advancing the Electrical Stability of Organic Field-Effect Transistors. *Chem. Mater.* **2014**, *26* (22), 6467–6476. https://doi.org/10.1021/cm5030266.

(49) Nakano, M.; Osaka, I.; Takimiya, K. Control of Major Carriers in an Ambipolar Polymer Semiconductor by Self-Assembled Monolayers. *Adv. Mater.* **2017**, *29* (1). 1602893. https://doi.org/10.1002/adma.201602893.

(50) Star, A.; Han, T. R.; Gabriel, J. C. P.; Bradley, K.; Grüner, G. Interaction of Aromatic Compounds with Carbon Nanotubes: Correlation to the Hammett Parameter of the Substituent and Measured Carbon Nanotube FET Response. *Nano Lett.* **2003**, *3* (10), 1421–1423. https://doi.org/10.1021/nl0346833.

(51) Chung, Y.; Verploegen, E.; Vailionis, A.; Sun, Y.; Nishi, Y.; Murmann, B.; Bao, Z. Controlling Electric Dipoles in Nanodielectrics and Its Applications for Enabling Air-Stable N-Channel Organic Transistors. *Nano Lett.* **2011**, *11* (3), 1161–1165. https://doi.org/10.1021/nl104087u.

(52) Mityashin, A.; Roscioni, O. M.; Muccioli, L.; Zannoni, C.; Geskin, V.; Cornil, J.; Janssen, D.; Steudel, S.; Genoe, J.; Heremans, P. Multiscale Modeling of the Electrostatic Impact of Self-Assembled Monolayers Used as Gate Dielectric Treatment in Organic Thin-Film Transistors. *ACS Appl. Mater. Interfaces* **2014**, *6* (17), 15372–15378. https://doi.org/10.1021/am503873f.

(53) Novikov, S. V.; Dunlap, D. H.; Kenkre, V. M.; Parris, P. E.; Vannikov, A. V. Essential Role of Correlations in Governing Charge Transport in Disordered Organic Materials. *Phys. Rev. Lett.* **1998**, *81* (20), 4472–4475. https://doi.org/10.1103/PhysRevLett.81.4472.

(54) Wang, Q.; Jiang, S.; Qian, J.; Song, L.; Zhang, L.; Zhang, Y.; Zhang, Y.; Wang, Y. Low-Voltage, High-Performance Organic Field-Effect Transistors Based on 2D Crystalline Molecular Semiconductors. *Sci. Rep.* **2017**, *7*, 1–8. https://doi.org/10.1038/s41598-017-08280-8.

(55) Boileau, N. T.; Cranston, R.; Mirka, B.; Melville, O. A.; Lessard, B. H. Metal Phthalocyanine Organic Thin-Film Transistors: Changes in Electrical Performance and Stability in Response to Temperature and Environment. *RSC Adv.* **2019**, *9* (37), 21478–21485. https://doi.org/10.1039/c9ra03648b.

(56) Lin, H.; Zhao, W.; Kong, X.; Li, L.; Li, Y.; Kuang, P.; Zhang, Y.; Zhang, L.; Sun, M.; Tao, S. Critical Impact of Gate Dielectric Interfaces on the Trap States and Cumulative Charge of High-Performance Organic Thin Field Transistors. *Mater. Sci. Semicond. Process.* **2019**, *91*, 275–280. https://doi.org/10.1016/j.mssp.2018.11.019.

(57) Jung, Y.; Kline, R. J.; Fischer, D. A.; Lin, E. K.; Heeney, M.; Mcculloch, I.; DeLongchamp, D. M. The Effect of Interfacial Roughness on the Thin Film Morphology and Charge Transport of High-Performance Polythiophenes. *Adv. Funct. Mater*. **2008**, *18* (5), 742–750. https://doi.org/10.1002/adfm.200701089.

(58) McAfee, T.; Hoffman, B. C.; You, X.; Atkin, J. M.; Ade, H.; Dougherty, D. B. Morphological, Optical, and Electronic Consequences of Coexisting Crystal Orientations in β-Copper Phthalocyanine Thin Films. *J. Phys. Chem. C* **2016**, *120* (33), 18616–18621. https://doi.org/10.1021/acs.jpcc.6b05043.

(59) Schmidt, R.; Ling, M. M.; Oh, J. H.; Winkler, M.; Könemann, M.; Bao, Z.; Würthner, F. Core-Fluorinated Perylene Bisimide Dyes: Air Stable N-Channel Organic Semiconductors for Thin Film Transistors with Exceptionally High on-to-off Current Ratios. *Adv. Mater*. **2007**, *19* (21), 3692–3695. https://doi.org/10.1002/adma.200701478.

(60) Yun, S. W.; Kim, J. H.; Shin, S.; Yang, H.; An, B. K.; Yang, L.; Park, S. Y. High-Performance N-Type Organic Semiconductors: Incorporating Specific Electron-Withdrawing Motifs to Achieve Tight Molecular Stacking and Optimized Energy Levels. *Adv. Mater.* **2012**, *24* (7), 911–915. https://doi.org/10.1002/adma.201103978.

(61) Salinas, M.; Jäger, C. M.; Amin, A. Y.; Dral, P. O.; Meyer-Friedrichsen, T.; Hirsch, A.; Clark, T.; Halik, M. The Relationship between Threshold Voltage and Dipolar Character of Self-Assembled Monolayers in Organic Thin-Film Transistors. *J. Am. Chem. Soc.* **2012**, *134* (30), 12648–12652. https://doi.org/10.1021/ja303807u.

Chapter 3. Cyanophenoxy-Substituted Silicon Phthalocyanines for Low Threshold Voltage n-Type Organic Thin-Film Transistors

This chapter was published in the journal "ACS Applied Electronic Materials": King, B.; Daszczynski, A. J.; Rice, N.; Peltekoff, A. J.; Yutronkie, N. J.; Lessard, B. H.; Brusso, J. L.*, Cyanophenoxy-substituted silicon phthalocyanines for low threshold voltage n-type organic thin-film transistors, *ACS Applied Electronic Materials*, **2021**, 3, 2212-2223.

Context

In this work, I continued to build on one of the key structure-property relationships we developed in Chapter 2 by integrating three novel R_2-SiPc derivatives and one previously reported R_2-SiPc derivative into OTFTs for the first time. These derivatives were designed to have axial groups with stronger electron withdrawing character than F_{10}-SiPc with the goal of further reducing their threshold voltage towards 0V. The relationship between electron-withdrawing character of the axial groups and device threshold voltage developed in Chapter 2 held for these additional materials at two different dielectric thicknesses and we achieved a further reduction in threshold voltage for the derivative with 3-fluoro, 4-cyanophenoxy axial substituents ((3F,4CN)$_2$-SiPc) with a record low value of 4.8 V. We also observed some dewetting of (3F,4CN)$_2$-SiPc from the OTS surface, which we addressed by fabricating devices on polystyrene brush-functionalized surfaces, resulting in stable films beyond seven days.

Contributions

I prepared and characterized OTFTs from four silicon phthalocyanine derivatives by physical vapour deposition and processed and analyzed device data. I performed solid state UV-Vis spectroscopy, and X-ray diffraction measurements. Dr. Nicole Rice performed AFM measurements and I interpreted the data. Polymer brush materials were synthesized by myself or Dr. Peltekoff. I wrote the manuscript with input from Prof. Lessard, Prof. Brusso, Dr. Rice and Dr. Yutronkie. Phthalocyanines were synthesized by Mr. Daszczynski and DFT calculations were completed by Dr. Yutronkie. Solution-state UV-Vis spectroscopy, cyclic voltammetry, thermogravimetric analysis, nuclear magnetic resonance spectroscopy and elemental analysis were performed and interpreted by Mr. Daszczynski and by Dr. Yutronkie.

Abstract

Silicon phthalocyanines (SiPcs) are a class of n-type or ambipolar organic semiconductors that have been incorporated in organic thin-film transistors (OTFTs), organic light-emitting diodes (OLEDs) and organic photovoltaics (OPVs). Despite a relatively large catalogue of previously reported SiPc materials, fabricated OTFTs with these materials typically have threshold voltages above 10 V, limiting their usage in commercial devices due to exceedingly high power consumption. Recent studies have suggested that threshold voltage can be reduced in OTFTs prepared from phenoxy-substituted SiPcs by introducing electron-withdrawing groups onto the phenoxy moieties. Herein, we report the synthesis and characterization of three SiPcs with phenoxy axial substituents containing nitrile and fluorine functional groups. These SiPcs, along with 3,5-difluorophenoxy SiPc were evaluated as candidate materials for n-type OTFTs. We found that further increasing the electron-withdrawing character of the pendant phenoxy groups of the SiPc resulted in a significant decrease in average threshold V_T with the lowest reported value being 4.8 V, the lowest V_T reported for a phenoxy-SiPc-based OTFT exceeding the previous record low of 7.8 V attributed to F_{10}-SiPc. This decrease in threshold voltage could be directly correlated to the Hammett parameter of the axial functional groups. Furthermore, it was noted that dewetting occurred when the SiPcs pendant phenoxy was substituted at the para position with a nitrile group combined with ortho- or meta-substituted fluorines, which was attributed to interactions at the semiconductor/dielectric interface. Depositing these SiPcs on silane-terminated poly(styrene) brush modified substrates improved long-term stability, demonstrated by a minimal change in surface morphology according to atomic force microscopy (AFM) images.

3.1 Introduction

Metal and metalloid phthalocyanines (MPcs) are a large class of thermally stable organic semiconductors, with an abundance of structures possible through easily accessible synthetic routes using relatively inexpensive starting materials.[1,2] MPcs can be chemically modified by changing the metal/metalloid core,[3,4] adding peripheral substituents,[5,6] or with axial substitutions covalently bonded to the metal/metalloid core,[7,8] enabling the synthesis of a wide library of functional materials with tunable optoelectronic properties. Many MPcs have been incorporated into organic electronic devices, including organic light-emitting diodes (OLEDs),[7] organic photovoltaics (OPVs)[9] and organic thin-film transistors (OTFTs).[4] Low manufacturing costs, synthetic simplicity and preferential solid-state molecular packing make MPcs ideal candidates for OTFTs in paricular.[4] To date, the greatest reported mobility for MPc-based OTFTs is for devices incorporating titanium dioxide phthalocyanine (TiOPc) as a semiconductor, which exhibits a hole mobility (μ_h) on the order of 10 $cm^2V^{-1}s^{-1}$.[4] While MPcs like TiOPc are generally p-type,[4] examples of n-type derivatives do exist, including silicon phthalocyanines (SiPcs),[8,10] tin phthalocyanines (SnPcs)[2] and peripherally-fluorinated copper phthalocyanine (F_{16}-CuPc).[11]

SiPcs have recently shown great potential for applications as n-type or ambipolar (both n- and p-type) organic semiconductors, with various derivatives incorporated into OLEDs,[7] OPVs[9] and OTFTs.[12] Previous studies have demonstrated that the choice of axial substituent can significantly impact the solid-state arrangement of the SiPc macrocycle, including through variations in the π-π stacking distances, herringbone angle, and degree of molecular overlap, yielding dramatically different device performance.[13–15] Vapor-deposited SiPcs with a phenoxy (PhO) axial substituent are of particular interest due to their relatively good performance in OTFTs[10] and as donor and acceptor materials on solar cells.[15] The highest reported electron mobility (μ_e) of ≈ 0.5 $cm^2V^{-1}s^{-1}$ was achieved for pentafluoro-phenoxy silicon phthalocyanine (F_{10}-SiPc),[8] suggesting that properly designed SiPcs are capable of exceeding other MPcs in n-type OTFTs and can possibly rival current state-of-the-art n-type organic semiconductors. However, the lowest reported average threshold voltage (V_T) for n-type SiPcs in OTFTs is 7.8 V fabricated on 230 nm-thick octyl(trichloro)silane (OTS)-modified SiO_2,[8] with the majority of vapor-deposited SiPcs yielding V_T values above 15 V on both 230 nm and 300 nm-thick OTS-modified SiO_2.[8,16] In order to achieve commercialization of n-type OTFT devices with a SiPc semiconductor, operating voltages must be further reduced to minimize power consumption.[17,18] In our recent work, we identified that increasing the electron-withdrawing character, or Hammett parameter,[19,20] of the axial phenoxy groups led to a reduction in average V_T from 46.8 V to 21.1 V in SiPc materials.[16] Additionally, density functional theory (DFT) modelling identified a similar trend between V_T and the square of the dipole induced at the interface between the organic semiconductor and the head group on the OTS-modified substrate. This combination of experimental results and DFT modelling suggests that SiPcs with stronger electron-withdrawing axial groups could lead to OTFTs with lower V_Ts, which are desirable for the commercialization of SiPc based OTFTs.[21,22]

The addition of electron-withdrawing substituents to tune the electronic characteristics and V_T of other organic semiconductors in OTFTs has been observed previously in the literature. For example, going from dicyano to tetracyano peripherally substituted TIPS pentacene reduced V_T from 25 V to 3 V for electron transport.[23] Similarly, the synthesis of a 5,7,12,14-tetracyano pentacene resulted in a slight reduction in V_T and suppression of ambipolar character when compared with its 6,13-dicyanopentacene analogue.[24] The addition of trifluoromethyl groups at the 3,5-phenyl positions a trifluoromethylphenyl(thiophen-2-yl)acrylonitrile π-conjugated system resulted in a slight reduction in V_T when compared to an identical molecule functionalized with a trifluoromethyl group in the 4-phenyl positon.[25] Tuning of the induced dipole at the semiconductor-dielectric interface through the selection of self-assembled monolayer (SAM) headgroups has also been previously reported. SAM selection can influence the p- and n-type characteristics of ambipolar OTFTs by tuning the electric dipole at the interface.[26] A study incorporating pentacene, α,α′-dihexylsexithiophene, and fullerene on six alkyl-SAMs resulted in a linear correlation between device V_T and SAM dipole moment.[27]

Motivated by the aforementioned results, we herein report the electrical characteristics of axially substituted SiPcs (R_2-SiPcs) **1 – 4** (**Figure 3.1A**) with Hammett parameters between +0.660 and +0.997 in bottom-gate top-contact (BGTC) OTFTs. The Hammett parameter of material **4** (3F,4CN-SiPc, +0.997) is larger than the previously reported greatest Hammett parameter for a phenoxy-SiPc derivative incorporated into OTFTs (F_{10}-SiPc, with a value of +0.860).[16] The complete synthesis, as well as thermal and electrochemical characterization of materials **1**, **3** and **4** are presented here for the first time, while material **2** has previously been reported in planar heterojunction OPV devices as both an electron-donating and an electron-accepting material.[15] All four materials were integrated into OTFTs for the first time and the resulting thin films were analyzed by Ultraviolet-visible (UV-Vis) spectroscopy, powder X-Ray diffraction (PXRD), and atomic force microscopy (AFM). An additional study was completed where polymer brush SAMs were incorporated into the device architecture to enhance the stability of material **4** on the dielectric. Polymer brushes have previously been reported to reduce interfacial charge traps and enhance the stability of OTFTs.[28–30] This study confirms the hypothesis in our previous report that Hammett parameters, or the electron withdrawing character of R_2-SiPc pendant groups, are a reliable predictor of OTFT V_T performance, providing an invaluable tool for the intelligent design of the next generation of R_2-SiPc materials.

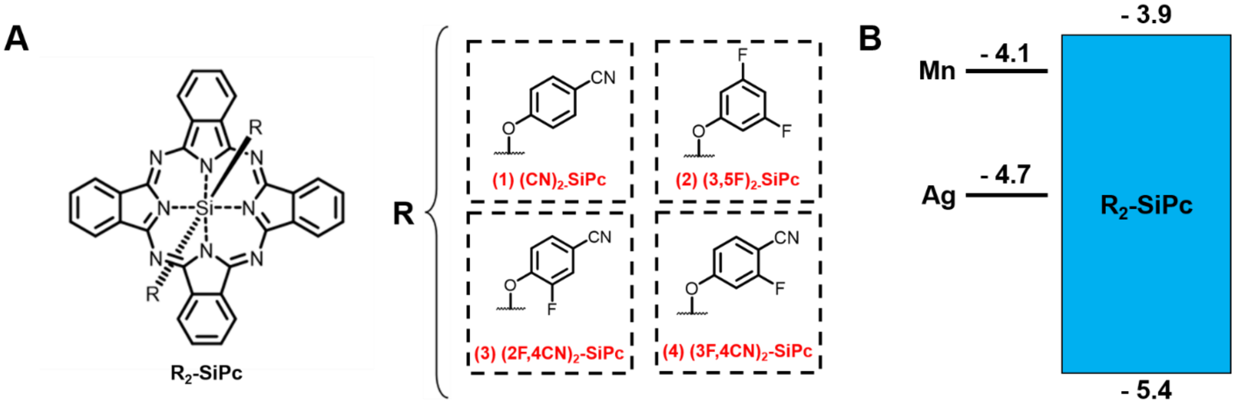

Figure 3.1 A) R$_2$-SiPc derivatives incorporated into BGTC OTFTs in this study and B) the band structure of the SiPcs used in this study and the metal electrode work function values.

3.2 Experimental Section

Synthetic Procedure for R$_2$-SiPc Derivatives 1–4

Silicon phthalocyanine dichloride (Cl_2^{-}SiPc) was synthesized according to literature procedures.[31] Material **2** (bis(3,5-difluorophenoxy) silicon phthalocyanine, (3,5F)$_2$-SiPc) was synthesized according to the literature.[15] Materials **1** (bis(4-cyanophenoxy) silicon phthalocyanine, (4CN)$_2$-SiPc), **3** (bis(2-fluoro-4-cyanophenoxy) silicon phthalocyanine, (2F,4CN)$_2$-SiPc) and **4** (bis(3-fluoro-4-cyanophenoxy) silicon phthalocyanine, (3F,4CN)$_2$-SiPc) were all synthesized using the following procedure: Cl_2-SiPc (1.00 g, 1.64 mmol) was added to a three-neck round-bottom flask outfitted with a reflux condenser and nitrogen inlet, followed by 6 times molar excess of 4-cyanophenol (98%**,** Oakwood Chemical; 1.17g, 9.84 mmol), 3,5-difluorophenol (98%**,** Oakwood Chemical; 1.28g, 9.84 mmol), 2-fluoro-4-hydroxybenzonitrile (99%**,** Oakwood Chemical; 1.35g, 9.84 mmol) or 3-fluoro-4-hydroxybenzonitrile (98%**,** Oakwood Chemical; 1.35g, 9.84 mmol). The contents of the reactor were dissolved in 60 mL chlorobenzene (99.5%, Caledon Laboratories) and stirred at 120 °C for 34 h under a nitrogen atmosphere. The reaction mixture was then cooled to room temperature and concentrated under reduced pressure. The product was precipitated out of solution by adding the concentrated reaction mixture to 300 – 500 mL of methanol, followed by vacuum filtration and successive washes with water, methanol, and acetone to yield a dark blue powder. Prior to incorporation into devices, materials were purified by train sublimation at 354 °C (27 mTorr) using CO_2 as a carrier gas. Post-sublimation yields for compounds **1** – **4** were between 70 – 80 %. All proton NMR (^{1}H NMR) spectra are found in the Supporting Information (SI) **Figures 3.9 – 3.12**.

Synthesis of bis(4-cyanophenoxy) silicon phthalocyanine ((4CN)$_2$-SiPc, 1). Yield before sublimation: 0.93 g (73%, 1.20 mmol). UV-Vis (CHCl$_3$) λ_{max} = 684 nm. ^{1}H NMR (**Figure 3.9**) (400 MHz, CDCl$_3$): δ 9.66 (m, 8H), 8.43 (m, 8H), 5.91 (m, 4H), 2.46 (m, 4H). EA: expected wt%: C (71.12%), H (3.11%) and N (18.03%) – analysis wt% C (71.26%), H (3.09%) and N (18.26%). Given the low solubility of this compound, ^{13}C NMR spectroscopic analysis was not possible. Nonetheless, the identity of this compound was confirmed by ^{1}H NMR spectroscopy and elemental analysis.

Synthesis of bis(3,5-difluorophenoxy) silicon phthalocyanine ((3,5F)$_2$-SiPc, 2). Yield before sublimation: 1.14 g (87%, 1.42 mmol). UV-Vis (CHCl$_3$) λ_{max} = 684 nm. ^{1}H NMR (**Figure 3.10**) (400 MHz, CDCl$_3$): δ 9.67 (m, 8H), 8.41 (m, 8H), 5.19 (m, 2H), 2.01 (m, 4H). EA: expected wt%: C (66.16%), H (2.78%) and N (14.03%) – analysis wt% C (66.39%), H (2.76%) and N (14.28%). Given the low solubility of this compound, ^{13}C NMR spectroscopic analysis was not possible. Nonetheless, the identity of this compound was confirmed by ^{1}H NMR spectroscopy and elemental analysis.

Synthesis of bis(2-fluoro-4-cyanophenoxy) silicon phthalocyanine ((2F,4CN)$_2$-SiPc, 3). Yield before sublimation: 1.16 g (87%, 1.43 mmol). UV-Vis (CHCl$_3$) λ_{max} = 685 nm ^{1}H NMR (**Figure 3.11**) (400 MHz, CDCl$_3$): δ 9.68 (m, 8H), 8.46 (m, 8H), 5.84 (m, 2H), 2.29 (m, 4H). EA: expected wt%: C (67.97%), H (2.73%) and N (17.23%) – analysis wt% C (67.81%), H (2.64%) and N (17.09%). Given the low solubility of this compound, ^{13}C NMR spectroscopic analysis was not possible. Nonetheless, the identity of this compound was confirmed by ^{1}H NMR spectroscopy and elemental analysis.

Synthesis of bis(3-fluoro-4-cyanophenoxy) silicon phthalocyanine ((3F,4CN)$_2$-SiPc, 4). Yield before sublimation: 1.00 g (75%, 1.23 mmol). UV-Vis (CHCl$_3$) λ_{max} = 686 nm ^{1}H NMR (**Figure 3.12**) (400 MHz, CDCl$_3$): δ 9.67 (m, 8H), 8.43 (m, 8H), 5.72 (m, 4H), 2.43 (m, 2H). EA: expected wt%: C (67.97%), H (2.73%) and N (17.23%) – analysis wt% C (68.23%), H (2.66%) and N (17.43%). Given the low solubility of this compound, ^{13}C NMR spectroscopic analysis was not possible. Nonetheless, the identity of this compound was confirmed by ^{1}H NMR spectroscopy and elemental analysis.

Characterization

UV-visible absorption (UV-Vis) spectra were obtained using a Varian Cary Series 6000 UV-Vis-NIR spectrophotometer. Solution spectra were measured in chloroform (HPLC-grade) in a 1 cm quartz cuvette, while solid state spectra were obtained from the transmittance of 30 nm thick films deposited by thermal evaporation onto glass microscope slides. ^{1}H NMR were obtained on a Bruker Avance 400 MHz spectrometer, with all spectra referenced to the deuterated solvent peak at 7.26 ppm. Due to the poor solubility of materials **1 – 4**, ^{13}C NMR could not be obtained. Cyclic voltammetry (CV) was performed using a Bioanalytical Systems Inc. (BASi) Epsilon potentiostat with C3 cell stand, BASi Epsilon EC software (V 2.13.77 (c) 2013BASi) and employing a glass cell and platinum wires for working and counter and pseudo-reference electrodes, respectively. The measurements were carried out in dichloromethane (dried over 4Å sieves in an argon environment) containing 0.1 M tetrabutylammonium hexafluorophosphate (Aldrich) as a supporting electrolyte, with a scan rate of 100 mV s^{-1}. The experiments were referenced to the Fc/Fc^+ redox couple of ferrocene at +0.475 V vs. SCE.[32] All thermogravimetric analysis (TGA) measurements were performed in using a Discovery 5500 from TA Instruments under nitrogen atmosphere at a heating rate of 5.0 °C per minute from room temperature to 700 °C. Elemental analysis (EA) measurements on materials **1 - 4** were performed by Atlantic Microlab (Norcross, GA 30071).

Single crystals of all compounds for X-ray diffraction were achieved through train sublimation. Data collection for single crystals of **1**, **2**, **3**, and **4** (**Table 3.4**) were obtained on a Bruker KAPPA APEX-II CCD diffractometer (graphite monochromated Mo K_α radiation, λ = 0.71073 Å, ω-scans with a 0.5° step in ω) at 200 K, except for the single crystal of **2** which was collected at 298 K. Absorption corrections were applied by using the semi-empirical method of the SADABS program[33] for all samples. The structures were solved using SHELXT[34] and refined by full-matrix least-squares methods on F^2 with SHELXL-2015[35] in anisotropic approximation for all non-hydrogen atoms. The hydrogen atoms were constrained to ride on their parent atoms with C-H = 0.95 Å and $U_{\text{iso}} = 1.2U_{\text{eq}}(\text{C})$. PXRD measurements were performed using a Rigaku Ultima IV powder diffractometer with an X-ray source of Cu Kα (λ = 1.5418 Å) at a scan range of $5° < 2\theta < 20°$ at a scan rate of 0.5 ° min^{-1}. Measurements were performed on a 30 nm R_2-SiPc film deposited upon an OTS-functionalized Si/SiO_2 substrate with no electrodes. Peak integrals were determined by manually defining the peak and baseline. AFM images were obtained with a Bruker

Dimension Icon Atomic Force Microscope System, using ScanAsyst-Air probes, in ScanAsyst mode with a scan rate of 0.6 Hz.

Device Preparation

Heavily N-doped silicon substrates with a 300 nm silicon dioxide (SiO_2) dielectric layer (purchased from Ossila) and a 230 nm SiO_2 dielectric layer (purchased from Wafer Pro) were washed with acetone and isopropyl alcohol to remove a protective photoresist. Substrates were then sonicated sequentially in acetone and methanol for 5 minutes each, followed by drying with a stream of nitrogen, prior to being cleaned by a 15-minute plasma treatment.

Alkyl-Silane Surface Treatment

Cleaned substrates were rinsed with water and isopropanol, then dried with nitrogen before a 24 h surface treatment in 1% v/v octyl(trichloro)silane (OTS). OTS-treated substrates were washed with toluene and isopropanol then dried under vacuum at 70 °C for 1 h.

Polymer Brush Surface Treatment

(Aminopropyl)trimethoxysilane (APTMS)-terminated polymer brushes comprised of poly(styrene) (PS) or poly(methyl methacrylate-*ran*-styrene) (PMMA/S) ($M_w = 25000\ g{\cdot}mol^{-1}$, Đ < 1.2) were synthesized based on previously reported procedures.[36] Polymer brush surfaces were fabricated by first spin-casting 0.6 mL of 5 mg/mL solution of polymer dissolved in toluene at 3000 rpm for 30 s on the Si/SiO_2 substrate. The substrate was then annealed in air at 100 °C for 1 h to ensure the coupling reaction was complete before being sonicated in toluene for 10 minutes (to remove excess polymer), dried with a stream of nitrogen, and finally dried under vacuum at 70 °C for 1 hour. A schematic of OTS and polymer-brush modified substrates and polymers used in this study are provided in the Supporting Information (**Figure 3.8**).

Top-Contact Device Fabrication

Bottom-gate top-contact (BGTC) OTFTs were fabricated by thermally depositing a 300 Å film of **1** – **4** under vacuum by physical vapour deposition (PVD) at a rate of 0.2 Å s^{-1} ($P < 2 \times 10^{-6}$ Torr) through a square shadow mask on OTS-modified, bare SiO_2 or polymer brush-modified substrates held at room temperature. The oxide layer of the Si/SiO_2 substrate was scratched with a diamond-tipped pen to ensure contact with the gate before source and drain electrodes (channel length L = 30 μm, channel width W = 1000 μm) were fabricated by depositing 100 Å of manganese

(Mn) at a rate of 0.5 Å s^{-1} immediately followed by 500 Å of silver (Ag) at a rate of 1 Å s^{-1} through shadow masks obtained from Ossila. This process yielded 20 individual transistors per substrate. Additional devices fabricated with Ag-only electrodes (500 Å) were also prepared using the same deposition rate and shadow masks; the electrical characterization of these devices can be found in **Table 3.6** of the Supporting Information.

OTFT Testing & Electrical Characterization

Electrical characterization of OTFTs was performed using a custom-build auto-tester with brass alloy contact tips plated with 20 µm gold on 100 µm nickel. The tester was connected to a Keithley 2614B where the gate-source voltage (V_{GS}) and source-drain voltage (V_{DS}) could be set at constant values and the source-drain current (I_{DS}) was measured. Output curves were obtained by increasing V_{GS} by increments of +15 V per step from 0 to 60 V and sweeping the V_{DS} from 0 to 50 V. Transfer curves were obtained by fixing V_{DS} in the saturation region at +50 V. V_{GS} was applied by pulsing with a duty cycle of 20% and a frequency of 10 Hz, to reduce gate bias stress. The application of a pulsed gate has been found to improve device stability during operation and make the extraction of V_T more reliable.[12,37] A duty cycle of 20% at a frequency of 10 Hz results in the application of V_{GS} for a 20 ms (2 Hz) interval between 80 ms (8 Hz) intervals of zero applied gate bias stress. The electron field-effect mobilities (μ_e) were calculated using **Equation 3.1** for the saturation region:

$$I_{DS} = \frac{\mu_e C_i W}{2L}(V_{GS} - V_T)^2 \tag{3.1}$$

where L and W represent the channel length and width, respectively. The capacitance of the gate dielectric (C_i) is calculated using $C_i = \frac{\varepsilon_0 \varepsilon_r}{d}$, where d is the thickness of the SiO_2 dielectric (230 nm), ε_r is the dielectric constant of SiO_2 and ε_0 is the permittivity of free space. The change in capacitance and dielectric constant as a result of modifying the SiO_2 surface with OTS and polymer brushes is negligible.[28,29] μ_e was determined by calculating the slope of best fit of $\sqrt{I_{DS}}$ as a function of V_{GS} once this function became linear. The threshold voltage (V_T) was calculated from the average x-intercept of linearized data for $\sqrt{I_{DS}}$ vs V_{GS} in an identical measurement range as for the calculation of μ_e.

Computational Modelling

All calculations were performed at the DFT level using the B3LYP functional, as contained in the Gaussian 09W suite of programs.[38] Molecular dipoles of H_3SiR were taken from geometry optimization calculations using the 6-311+G(2d,p) basis set without symmetry constraints.

3.3 Results and Discussion

Optical, Electrochemical and Thermal Characterization of R_2-SiPc Derivatives

R_2-SiPc derivatives **1** – **4** (**Figure 3.1**) were synthesized through the reactions of Cl_2-SiPc with their corresponding phenolic precursors, with all products obtained in excellent yields and high purity (^1H NMRs in the ESI, Figures S1 – S4). UV-Vis absorption spectroscopy was performed on chloroform solutions of **1** – **4**, as well as thin films deposited on glass by thermal evaporation (**Figure 3.2**). The max peak absorbance (λ_{max}) and the optical band gap (E_g^{opt}), which was estimated from the onset of the corresponding absorbance spectra, can be found in **Table 3.1**. R_2-SiPcs containing cyano-phenoxy groups (**1,** $(4CN)_2$-SiPc)], **3** $(2F,4CN)_2$-SiPc) and **4** $(3F,4CN)_2$-SiPc)) yielded similar λ_{max} values in solutionto other previously reported SiPc materials, including material **2** ($(3,5F)_2$-SiPc)).[10,15] However, in the solid state the λ_{max} for **2** ($(3,5F)_2$-SiPc) had a significant bathochromic shift compared to the other three materials, suggesting a slightly higher degree of intermolecular interactions in the solid state as well as potentially better packing in thin films.[39] This observation is further corroborated through analyzing films of materials **1 – 4** through PXRD and AFM which will be discussed further in the Thin-Film Characterization section. CV was performed on solutions of **1** – **4** dissolved in dichloromethane; tabulated measurements can also be found in **Table 3.1** and corresponding voltammograms are provided in the Supporting Information (**Figure 3.14**). A quasi-reversible oxidation process is observed for all derivatives with similar half oxidation ($E_{1/2}^{0/+}$) and reduction ($E_{1/2}^{-/0}$) potentials. The HOMO energy levels (E_{HOMO}) were estimated using the onset of the oxidation potentials, while the LUMO energy levels were estimated from both the onset of the reduction potentials and from the sum of E_{HOMO} and E_g^{opt} of the films determined by UV-Vis.[40–43] Unsurprisingly, the potential at which the oxidation and reduction events occur are similar within this family of R_2-SiPcs. Furthermore, UV-Vis and CV data indicate that the addition of fluorine in the axial phenoxy substituent has a minimal impact on the band gap of the materials used in this study, as evidenced by the negligible shift in λ_{max}.

Thermal characterization of **1** – **4** was performed using TGA, with decomposition temperature (T_d) determined at 5% weight loss (**Table 3.1**). TGA curves for materials **1** – **4** and additional thermal characterization values can be found in **Figure 3.15** and **Table 3.5** of the ESI, respectively.

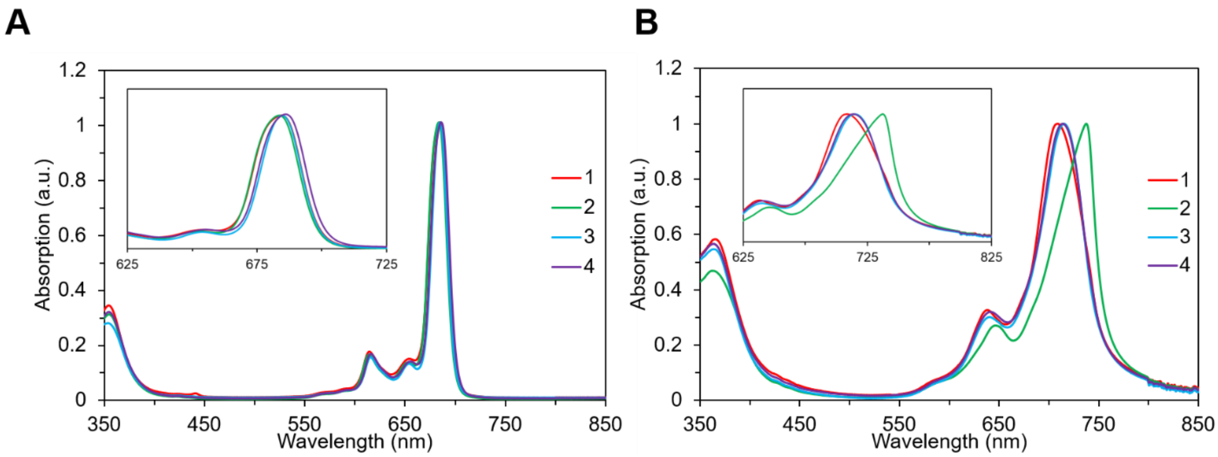

Figure 3.2 UV-Vis absorption spectra of materials **1** – **4** in A) solution and B) solid state.

Table 3.1 Optical, electrochemical and thermal properties for materials **1** – **4**.

Material	**λ_{max} (nm) CHCl₃ / Film**	**E_g^{opt} (eV)$^{a)}$ CHCl₃ / Film**	**$E_{1/2}^{0/+}$ (V)**	**$E_{1/2}^{-/0}$ (V)**	**E_{HOMO} (V)$^{b)}$**	**E_{LUMO} (V)$^{b)}$**	**T_d (°C)$^{c)}$**
1 (4CN)$_2$-SiPc	684 / 741	1.77 / 1.67	1.01	-0.70	-5.4	-3.9 (-3.8)	462
2 (3,5F)$_2$-SiPc	684 / 752	1.77 / 1.65	0.92	-0.79	-5.4	-3.9 (-3.7)	394
3 (2F,4CN)$_2$-SiPc	685/ 741	1.77 / 1.67	0.90	-0.80	-5.4	-3.9 (-3.7)	415
4 (3F,4CN)$_2$-SiPc	686/ 741	1.76 / 1.67	0.95	-0.78	-5.5	-3.9 (-3.8)	396

a) E_g^{opt} values were calculated from the onset of the absorption. Thin films were deposited by physical vapour deposition.

b) E_{HOMO} and E_{LUMO} values were calculated using equations $E_{HOMO}(\text{eV}) = -e((E_{ox} - E_{Fc/Fc^+}) + 4.8)$ and $E_{LUMO}(\text{eV}) = -e((E_{red} - E_{Fc/Fc^+}) + 4.8)$.[44] Values of E_{LUMO} calculated by $E_{HOMO} + E_g^{opt}{}_{Film}$ are shown in brackets.

c) T_d is determined by thermogravimetric analysis when 95 wt% is reached.

Electronic Characterization

OTFTs were fabricated on OTS-modified Si/SiO$_2$ substrates using **1** – **4** as the organic semiconductor. The semiconductor layer was fabricated by PVD, with devices completed by depositing silver-manganese (AgMn) electrodes on top of the R$_2$-SiPc layers. This electrode combination was chosen as previous work demonstrated that Ag electrodes modified with Mn interlayers were a cost-effective and high-performing alternative to gold electrodes in R_2-SiPc OTFTs.[8] A summary of device performance, including μ_e, V_T, I_{on} and the ratio of on current to off current ($I_{on/off}$), and Hammett parameters of each of the four materials, is presented in **Table 3.2**. In this analysis, the Hammett parameter for the ortho-substituted fluorine in material **3** (2F,4CN) was assumed to have an equivalent value to a para-substituted fluorine. Since a distinct linear region was not observed in the output data for these devices, transfer curves were obtained and evaluated in the saturation regime only. Representative transfer curves for materials **1** – **4** are shown in **Figure 3**Error! Reference source not found.**.3**, and characteristic output curves can be in t he Supporting Information (**Figures 3.16 – 3.19**). Motivated by the idea of comparing large-Hammett parameter materials **3** ($(2F,4CN)_2$-SiPc) and **4** ($(3F,4CN)_2$-SiPc) to F_{10}-SiPc deposited on 230 nm-thick OTS-modified SiO_2,[8] which has the lowest-reported V_T of any vapor-deposited phenoxy-SiPc in the literature, materials **3** and **4** were deposited on identical 230 nm-thick OTS-modified SiO_2 substrates. It has been previously reported in the literature that reducing oxide thickness in transistors results in a decrease in V_T[45,46] which is corroborated by comparing previously reported average V_T values for F_{10}-SiPc OTFTs on 230 nm-thick (7.8 V)[8] and 300 nm-thick (21.1 V)[16] OTS-modified SiO_2 substrates.

Table 3.2 Electrical performance of OTFTs prepared from materials **1** – **4**.

Material	**SiO_2 Oxide Thickness (nm)**	**μ_e [$cm^2V^{-1}s^{-1}$]** a) (x 10^{-3})	**V_T [V]** a)	**Hammett parameter [-]**[20]	**I_{on} [A]** a) (x 10^{-7})	**$I_{on/off}$** a)	**n** b)
1 $(4CN)_2$-SiPc	300	1.3 ± 0.70	24 ± 1.7	+ 0.660	2.55	10^3-10^4	20
2 $(3,5F)_2$-SiPc	300	8.8 ± 3.8	24 ± 4.2	+ 0.674	16.3	10^5	24
3 $(2F,4CN)_2$-SiPc	230	0.90 ± 0.69	8.1 ± 5.0	+ 0.722	3.72	10^3-10^4	44
4 $(3F,4CN)_2$-SiPc	230	0.52 ± 0.43	4.8 ± 3.1	+ 0.997	2.34	10^2-10^3	23

a) electron mobility (μ_e) and the threshold voltage (V_T) were calculated based on mean values while the on current (I_{on}) and the ratio of on current/off current ($I_{on/off}$) were calculated based on the median values of obtained devices.

b) n indicates number of OTFT devices included in averages

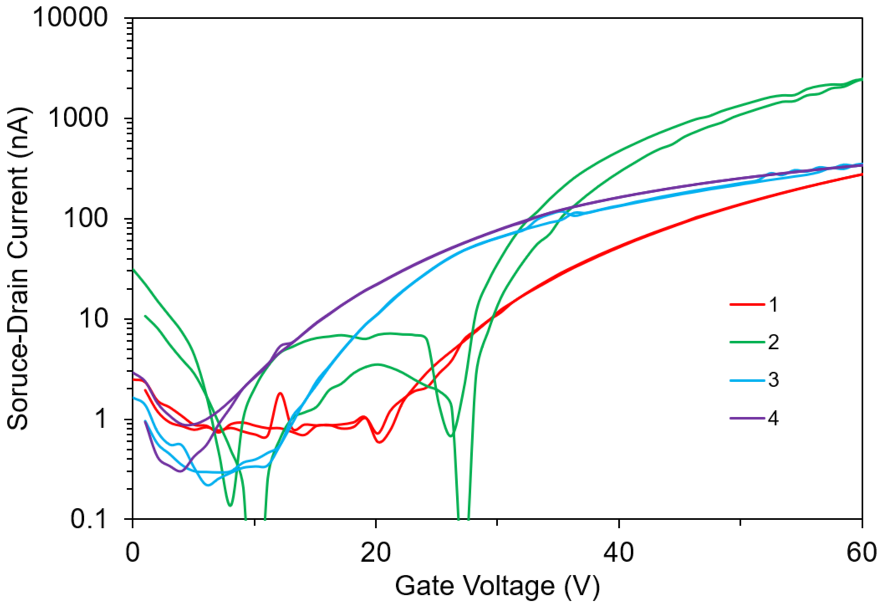

Figure 3.3 Representative transfer curves from BGTC OTFTs of materials **1** – **4** fabricated by PVD. Materials **1** and **2** were deposited on 300 nm-thick OTS-modified SiO_2 while materials **3** and **4** were deposited on 230 nm-thick OTS-modified SiO_2.

Within this series of R_2-SiPcs, BGTC OTFTs fabricated using **4** ((3F,4CN)$_2$-SiPc) resulted in the lowest V_T of 4.8 ± 3.1 V (**Table 3.2**), which represents the lowest average value ever recorded for vapor-deposited phenoxy-SiPc materials in OTFTs, surpassing the lowest reported value of 7.8 ± 1.4V for F_{10}-SiPc on an identical dielectric.[8] The addition of nitrile substituents to drop the V_T of n-type OTFTs has been exploited previously in peripherally-substituted TIPS pentacene, where going from a dicyano to tetracyano derivative reduced the V_T from 25 to 3 V for n-type charge transport.[23] The trend in experimental V_T values for the four R_2-SiPcs in this study match perfectly with our expectations as material **4** has the highest Hammett parameter of all R_2-SiPcs, and consequently the lowest V_T. To further illustrate this relationship, for comparative purposes the V_T of R_2-SiPc devices as a function of Hammett parameter is presented in **Figure 3.4** for materials **1** – **4** as well as nine previously reported OTFTs incorporating R_2-SiPcs with AgMn electrodes in an identical BGTC device architecture on either 230 nm-thick or 300 nm-thick OTS-modified SiO_2 .[8,16] Material **3** ((2F,4CN)$_2$-SiPc) in this study, which like **4** ((3F4,CN)$_2$-SiPc) contains a nitrile functionality, has the third-greatest Hammett parameter value of the 13 R_2-SiPcs shown in **Figure 4** and resulted in a similarly low V_T when integrated into OTFTs. However, the inclusion of nitrile functionality alone is not enough as material **1** ((4CN$_2$-SiPc) had a relatively higher V_T value in

OTFTs when compared with material **2** ($(3,5F)_2$-SiPc) and previously reported F_{10}-SiPc on 300 nm-thick OTS-modified SiO_2 dielectrics.[16] This suggests that while the electron-withdrawing characteristics of cyano-phenoxy axial substituents contribute to the observed reduction in V_T, this effect can be dramatically enhanced by additional fluorine substituents at the ortho or meta positions of the phenoxy ring. Experimental μ_e and $I_{on/off}$ of materials **1 – 4** are consistent with previously reported phenoxy-substituted SiPcs in BGTC OTFTs.[8,16] Materials **1** ($(4CN)_2$-SiPc), **3** ($(2F,4CN)_2$-SiPc) and **4** ($(3F,4CN)_2$-SiPc) which all contain a cyanophenoxy axial substituent resulted in slightly lower μ_e than material **2** ($(3,5F)_2$-SiPc), which can be attributed to the poor thin-film morphologies of these materials and will be discussed further in the Thin-Film Characterization section. The structure-property relationship of stronger electron withdrawing character of R_2-SiPc axial pendant groups to V_T does not hold for μ_e for thin-films. This is primarily related to confounding factors that impact mobility including resistance to charge injection which can be resolved by introducing charge injection interlatyers[8,47] and thin-film morphology, which was discussed in our previous work covering an initial catalogue of previously-reported R_2-SiPc materials.[16] In this previous work, we observed a range of isotropic and anisotropic thin-film morphologies and found that anisotropic grain structures across the substrate enabled by favourable film growth was a greater driver of μ_e than axial group selection. Additionally, DFT calculations have demonstrated that intermolecular electronic coupling has a strong impact on theoretical field-effect mobilities, making it a good predictor for high-mobility R_2-SiPc materials as polycrystalline thin-films in devices.[16,48] Intermolecular interactions can be further enhanced to improve charge transport mobility, however these interactions are not necessarily related to electron donating or withdrawing character of functional groups.[10,13,15] While μ_e of materials **3** and **4** are relatively low compared to state-of-the-art MPc and R_2-SiPc materials, these observations confirm that designing R_2-SiPc materials with stronger electron-withdrawing groups result in OTFTs with lower V_T. Confirming that this trend continues to hold with stronger electron-withdrawing pendants will enable the design of next-generation R_2-SiPcs with a combination of high μ_e and low V_T by further tuning pendant groups to optimize intermolecular interactions and electronic coupling[16,49] while incorporating electron-withdrawing moieties to reduce V_T.

One potential mechanism which could explain that stronger electron-donating or electron-withdrawing pendants impact device V_T could be related to interfacial dipoles induced by contact between the dielectric surface and the pendant group of the organic semiconductor. This relationship was highlighted in our previous study where experimentally determined V_T were plotted against DFT-calculated dipoles, resulting in a similar linear relationship to Hammett parameter as a function of V_T. This mechanism is corroborated in other studies, however it is the SAM group rather than the organic semiconductor that is modified to tune V_T.[27,50] As previously discussed, it has been demonstrated that electric dipoles of SAM head groups can impact OTFT electrical characteristics depending on dipole sign and orientation.[51,52] The relationship between the calculated SiH_3-R dipoles of the axial substituent and the experimental V_T of 16 R_2-SiPcs was also investigated and is shown in **Figure 3.20** of the Supporting Information. The additional SiPcs included in this survey were previously reported pyridoxy-SiPcs and napthoate-SiPc where estimation of the Hammett parameter was not possible and 246F-SiPc reported in a previous study fabricated on 230 nm-thick OTS-modified SiO_2 dielectric. The trend observed in materials **1** – **4** is consistent with our previous work, where we identified that V_T decreases slightly with the square of the induced interfacial dipole (D^2).[16]

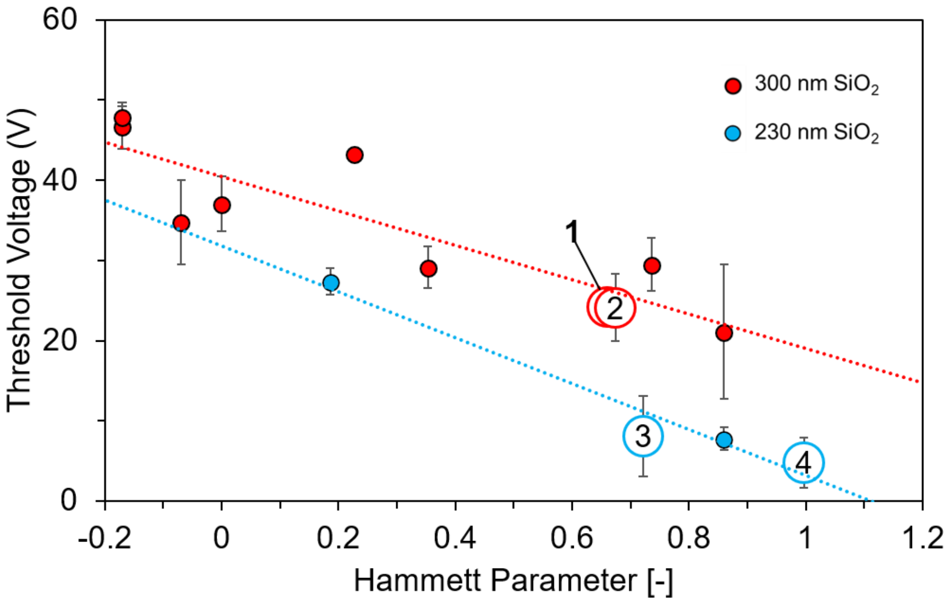

Figure 3.4 V_T of SiPc OTFTs as a function of Hammett parameter of axial pendant groups for R_2-SiPcs **1** – **4** and R_2-SiPcs reported in our previous studies on 230 nm-thick (blue circles)[8] and 300 nm-thick (red circles) OTS-modified SiO_2.[16]

Thin-Film Characterization

The morphology, texture and molecular packing of thin-film organic semiconductors is critical to device performance.[53,54] Thin-film morphologies for materials **1** – **4** were therefore thoroughly investigated to provide insight into the performance of OTFTs in this study. PXRD traces of films are presented in **Figure 3.5**. Diffraction intensity was negligible for cyano-phenoxy substituted SiPc materials, indicating poor structural order in the thin-film. Material **2** had an intense diffraction peak in the range of 6 – 9° common to previously reported R_2-SiPc materials.[12,16] The significant diffraction peak for material **2** corresponding to the (011) plane identified from the single-crystal data also suggests that some features of the single crystal are maintained in the solid-state film as well as improved intermolecular interactions, which were hypothesized based on the observed peak broadening and red shifting of λ_{max} in solid-state UV-Vis compared to solution measurements. Conversely, materials **1, 3** and **4** have negligible diffraction intensity and no observable shift in λ_{max} in the solid-state UV-Vis measurements compared to solution measurements, indicating that films are amorphous. These results partially explain the experimental μ_e values measured in this study, with OTFTs prepared from **2** resulting in good μ_e and OTFTs prepared from **1**, **3** and **4** resulting in relatively poor μ_e.

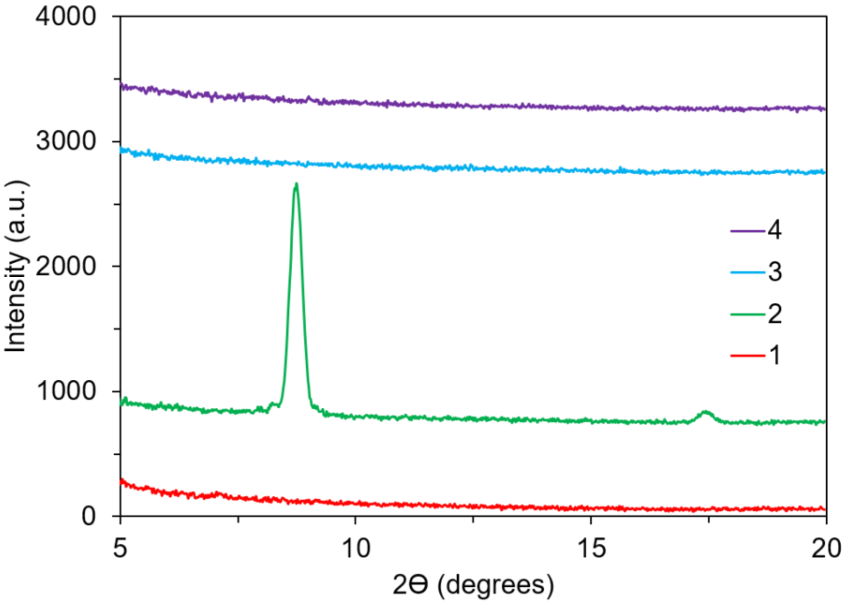

Figure 3.5 PXRD data for materials **1** – **4**.

AFM images of thin-films of materials **1** – **4** fabricated through PVD revealed three distinct morphologies (**Figure 3.6**). Material **1** ((4CN)$_2$-SiPc) produced highly disordered, relatively large feather-like grains with no preferential direction across the substrate, a morphology that was previously observed in an R$_2$-SiPc substituted with *m*-iodophenol.[16] Material **2** ((3,5F)$_2$-SiPc) provided regular rounded anisotropic grains across the substrate, which is similar to other fluorophenoxy-SiPc thin-films.[16] And finally, the morphology of materials **3** and **4** can be described as possessing small, isotropic grains, similar to film morphologies reported for magnesium phthalocyanines (MgPc).[55] Materials with anisotropic crystallite morphologies have been shown to perform better in OTFTs, which can be attributed to fewer grain boundaries in the thin-film between the source and drain electrodes, thus reducing resistance to charge transport across the channel.[56] This was the case for material **2**, which had the greatest μ_e of the four materials in this study. Additionally, the direction of growth of anisotropic features appeared to be parallel to the substrate. This morphology could also lead to favourable charge transport if the long axis of the grains, typically associated with the π-stacking direction, are oriented across the channel.[57–59] The large, amorphous features of thin-films of material **1**, and the small isotropic grains of **3** and **4**, are likely the reasons for negligible PXRD diffraction and poor μ_e relative to material **2**. Additionally, these findings corroborate the slight red shift observed in solid state UV-Vis for material **2**, which was attributed to better molecular packing in thin-films.

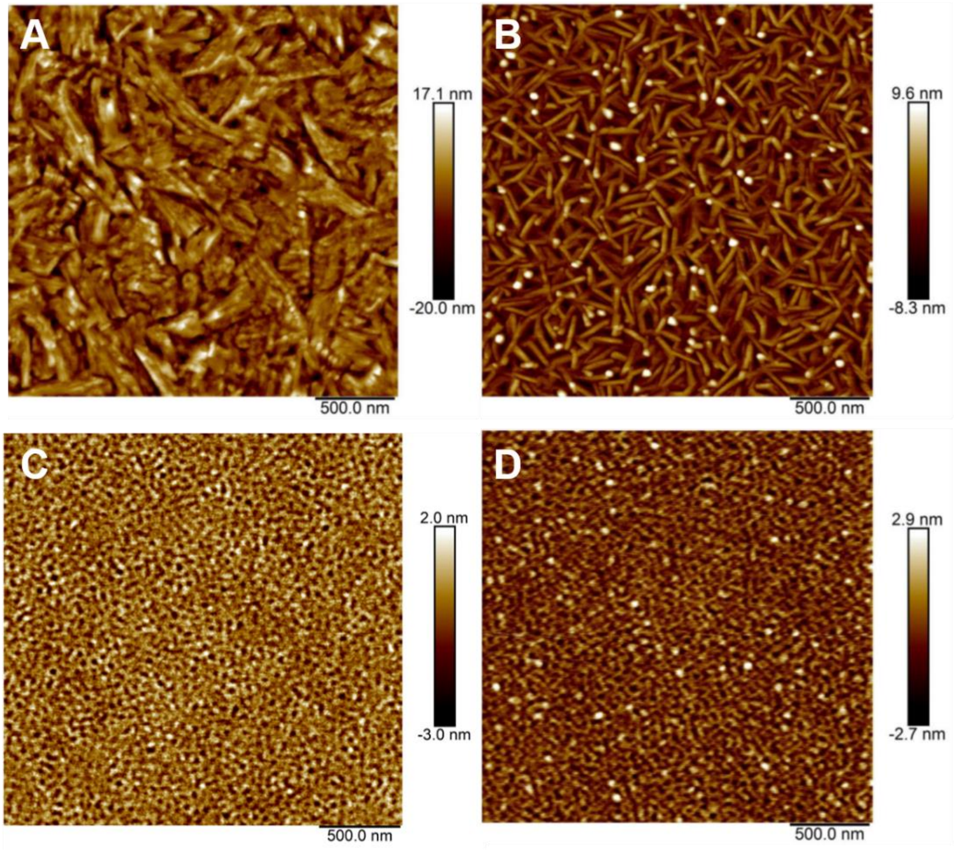

Figure 3.6 AFM height images of thin films of A) **1** (4CN) B) **2** (3,5F) C) **3** (2F,4CN) and D) **4** (3F,4CN) on OTS-modified SiO_2. Images were obtained immediately after deposition of the thin films.

Throughout the AFM measurements we observed some unusual changes in film morphology and decided to investigate the stability of the films over a few days. AFM images were obtained for thin-films of materials **1** – **4** on OTS-modified SiO_2 surfaces immediately after deposition and again after seven days of exposure to air. While the morphologies of materials **1** and **2** remained unchanged, materials **3** and **4** underwent dewetting on the OTS-modified dielectric surface, resulting in the formation of large crystalline aggregates and exposed sections of the substrate, as evidenced by the increase in RMS roughness by a factor of 5-10 (**Table 3.7**) and larger visible features. An example of the resulting crystallites formed in films of **4** after several days in air is shown in **Figure 3.7B**, with images for material **3** in the Supporting Information (**Figure 3.21**). To the best of our knowledge, there are no other reports of surface dewetting for phthalocyanine materials in the literature.

Surface dewetting is a type of interfacial degradation that can be related to the crystal structure of a thin-film or the surface energy at the semiconductor/substrate interface.[60] Dewetting has been observed on a time scale of as little as tens of minutes for some organic semiconductors.[61] In thermally evaporated thin-films, dewetting arises when a film is deposited during a non-equilibrium growth phase and is therefore not the favoured morphology which would occur in films deposited at ambient conditions.[62] Examples of organic semiconductor dewetting has been reported for films of dinaphthothienothiophene[63] (DNTT) and diindenoperylene,[60] where monolayer migration was observed and resulted in the formation of islands or column-like structures. This phenomenon was observed for films deposited on SiO_2, as well as on alkyl SAMs including OTS.[61,63] It is possible to select an interfacial material that decelerates the rate of dewetting, as reported for DNTT deposited on dodecylphosphonic acid.[63]

Selecting an alternative surface to small molecule alkyl silanes like OTS could therefore mitigate dewetting of materials **3** and **4** at the organic semiconductor/dielectric interface. Grafted polymer brushes have previously been employed as interfacial layers to improve the electrical stability of OTFTs. For example, polymer brush-modified SiO_2 resulted in a reduction of V_T shift as a result of stress testing in pentacene and perylene diimide devices by a factor of three to six.[29] Additionally, polymer brush surfaces provide greater surface coverage compared to alkyl-SAMs, yielding more uniform surfaces for deposition and fewer charge traps.[28,64] As with the OTS SAM layer discussed previously, the use of polymer brushes has also been reported to have a negligible impact on the capacitance of the dielectric surface.[28,29] We therefore fabricated BGTC OTFT devices with **4** deposited on SiO_2 with four different surface treatments in an attempt to minimize surface dewetting and enhance the long-term stability of the resulting films. Material **4** was selected as a case study and films were deposited on bare SiO_2, (**Figure 3.7C – D**), grafted poly(styrene) (gPS) brushes (**Figure 3.7E – F**) and grafted poly(methyl methacrylate-*ran*-styrene) (gPMMA/S) brushes (**Figure 3.7G – H**). AFM images of films of material **4** on each of the dielectric surfaces were taken immediately after deposition and again after seven days of exposure to air to evaluate their stability. Initial images on all four films showed a similar amorphous morphology with low RMS roughness between 0.31 and 0.76 nm. For measurements taken seven days after deposition, thin-films on bare SiO_2, the OTS control and gPMMA/S brushes all showed similar dewetting and recrystallization, with an increase in film RMS roughness above 3.5 nm.

However, on the gPS brush-treated surface, the film remains largely unchanged after seven days in air, indicating that material **4** has a greater affinity for this interfacial layer.

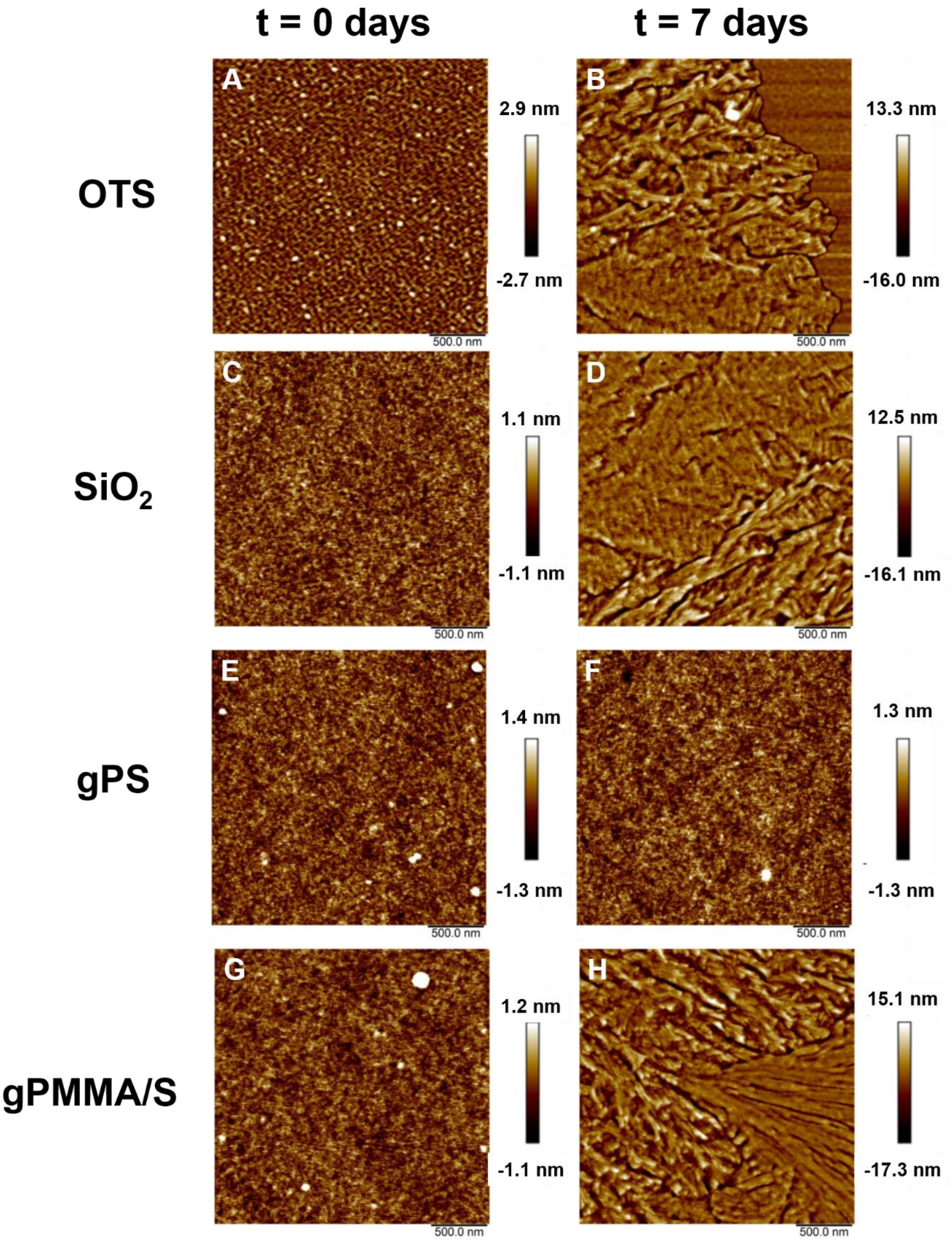

Figure 3.7 AFM height images of thin films of material **4** (3F,4CN) deposited on OTS (A and B), native SiO_2 (C and D), grafted poly(styrene) (E and F) and grafted poly(methyl methacrylate-*ran*-styrene) (G and H) at t = 0 days and t = 7 days.

OTFTs were also fabricated using material **4** on the various dielectric surfaces, with device performance summarized in **Table 3.3**. Characteristic transfer curves for devices fabricated using material **4** deposited on different dielectric surfaces are found in **Figure 3.8**, with representative output curves in **Figures 3.22 – 3.24** in the Supporting Information. These studies reveal that while the nature of the dielectric/semiconductor interfacial layer has a negligible impact on the resulting OTFT μ_e and $I_{on/off}$, the use of polymer brushes did result in a slight decrease in $I_{on/off}$ and an appreciable shift in V_T. Similar to changing the SiPc phenoxy pendant group, these results could be attributed to a change in the magnitude of the dipole induced by the interfacial contact between the semiconductor and dielectric surface.[65] As previously discussed, it has been reported that SAM and polymer brush headgroups and electric dipoles can profoundly impact OTFT electrical characteristics and reduce charge trap sites at the organic semiconductor/dielectric interface.[29,51,52] However, a DFT model of the polymer brush surfaces is needed to validate this observation which is not within the scope of this work.

Table 3.3 Summary of OTFT device performance on various 230-nm thick SiO_2 and SAM-modified SiO_2 surfaces for material **4** (3F,4CN).

Material	**Surface Treatment**	μ_e **[cm^{2}V^{-1}s^{-1}]**$^{a)}$ **(x 10^{-4})**	V_T **[V]** $^{a)}$	I_{on} **[A]** $^{a)}$ (x 10^{-7})	$I_{on/off}$ $^{a)}$	n $^{b)}$
4 $(3F,4CN)_2$-SiPc	OTS	5.2 ± 4.3	4.8 ± 3.1	2.34	10^2-10^3	23
4 $(3F,4CN)_2$-SiPc	None	5.1 ± 3.7	4.8 ± 4.7	3.07	10^1-10^2	26
4 $(3F,4CN)_2$-SiPc	gPS	1.9 ± 0.86	-6.1 ± 4.4	1.77	10^1-10^2	27
4 $(3F,4CN)_2$-SiPc	gPMMA/S	3.2 ± 2.2	-5.5 ± 6.4	2.59	10^1-10^2	33

a) electron mobility (μ_e) and the threshold voltage (V_T) were calculated based on mean values while the on current (I_{on}) and the ratio of on current to off current ($I_{on/off}$) were calculated based on median values.

b) *n* indicates the number of OTFT devices included in averages

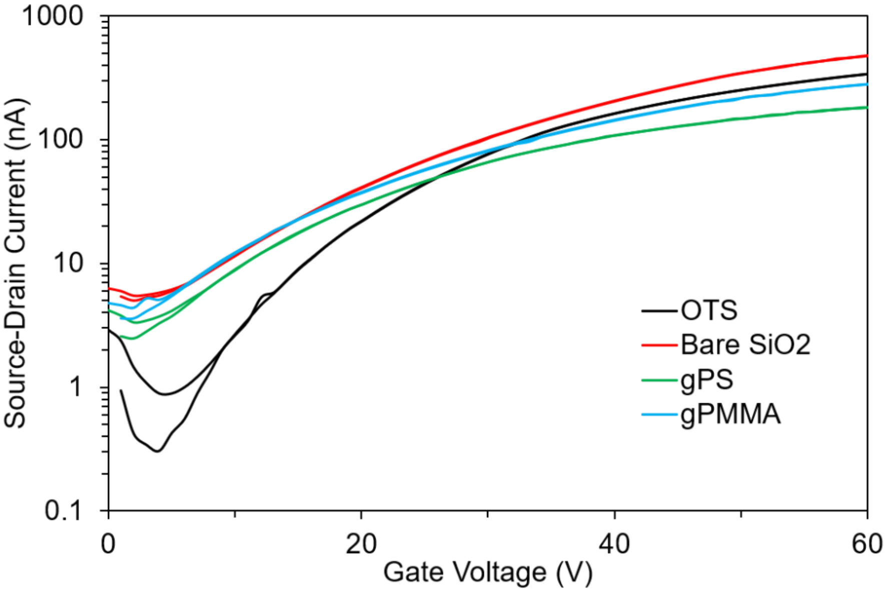

Figure 3.8 Representative transfer curves for BGTC OTFTs of material **4** (3F,4CN) on different dielectric surfaces with AgMn electrodes.

3.4 Conclusion

A series of R_2-SiPcs with phenoxy pendant groups having strong electron withdrawing moieties, as characterized by Hammett parameters from +0.660 to +0.997, were incorporated into bottom-gate top-contact OTFTs. Materials **1** ((4CN)$_2$-SiPc), **3** **(**(2F,4CN)$_2$-SiPc), and **4** ((3F,4CN)$_2$-SiPc) were synthesized and reported for the first time, while all three materials in addition to the previously reported (3,5F)$_2$-SiPc (**2**) were incorporated into OTFTs for the first time. Increasing the Hammett parameter of the pendant group resulted in a subsequent decrease in average V_T, which corroborates results from a previous survey of electron conducting R_2-SiPcs where a decrease in V_T was directly correlated to increasing the electron-withdrawing character of axial phenoxy pendant groups. An average V_T of 4.8 V was reported for for material **4** deposited on 230 nm-thick OTS-modified SiO_2, which represents the lowest absolute reported value for vapour-deposited phenoxy-SiPc derivatives, exceeding the record of 7.8 ± 1.4 V measured for BGTC OTFTs based on F_{10}-SiPc fabricated on an identical dielectric surface. AFM measurements demonstrated that films of materials **3** ((2F,4CN)$_2$-SiPc) and **4** ((3F,4CN)$_2$-SiPc) underwent surface dewetting on the substrate over time, resulting in the formation of large crystalline domains. The stability of thin-films of material **4** was found to increase when deposited on poly(styrene) polymer brush-modified substrates. Dewetting after seven days still occurred for material **4** when deposited on bare SiO_2, OTS or grafted poly(methyl methacrylate-*ran*-styrene) polymer brushes. Additionally, the use of poly(styrene) polymer brushes resulted in a further reduction in in V_T of material **4**, indicating that further engineering of the semiconductor/dielectric interface can be used to increase film stability and crystallization while tuning the V_T of devices.

Acknowledgements

The Natural Sciences and Engineering Research Council of Canada (NSERC) (2016-05591 to J.L.B; 2015-509 03987 and STPGP 506661-17 to B.H.L), the Canada Research Chairs Program 950-230724 (B.H.L.). B.K thanks NSERC for the CGS-M. We also thank the Centre for Research in Photonics at the University of Ottawa (CRPuO) for access to the AFM.

Supporting Information

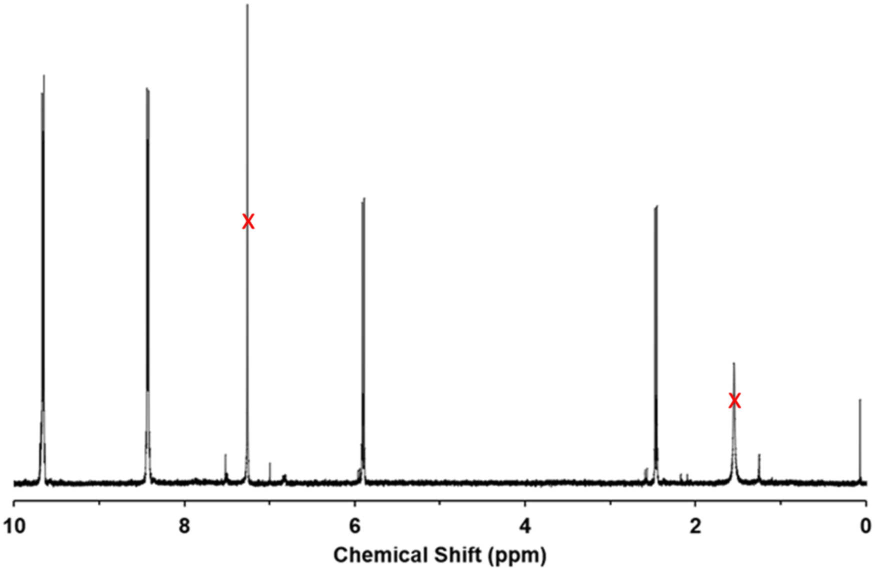

Figure 3.9 ^{1}H NMR of material **1** (4-cyano) in $CDCl_3$.

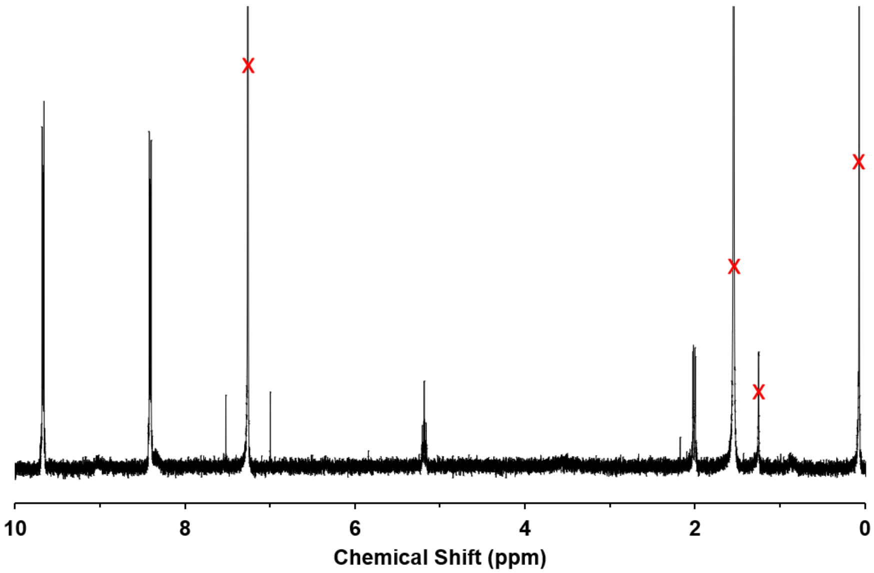

Figure 3.10 ^{1}H NMR of material **2** (3,5-difluoro) in $CDCl_3$.

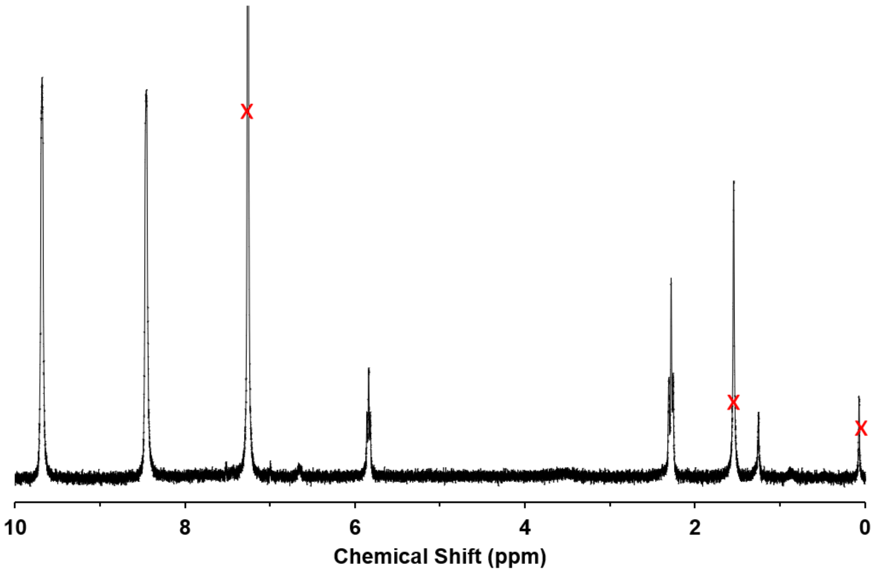

Figure 3.11 ^{1}H NMR of material **3** (2-fluoro, 4-cyano) in $CDCl_3$.

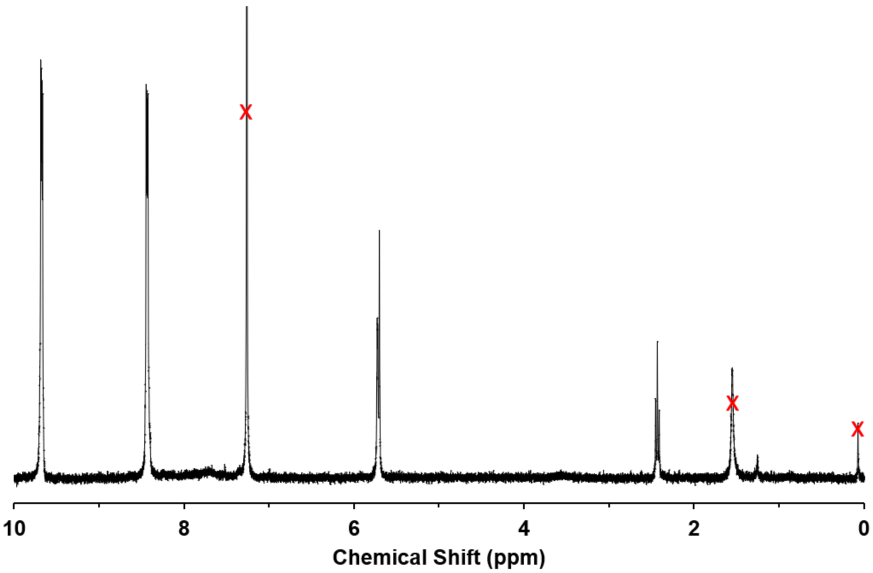

Figure 3.12 ^{1}H NMR of material **4** (3-fluoro, 4-cyano) in $CDCl_3$.

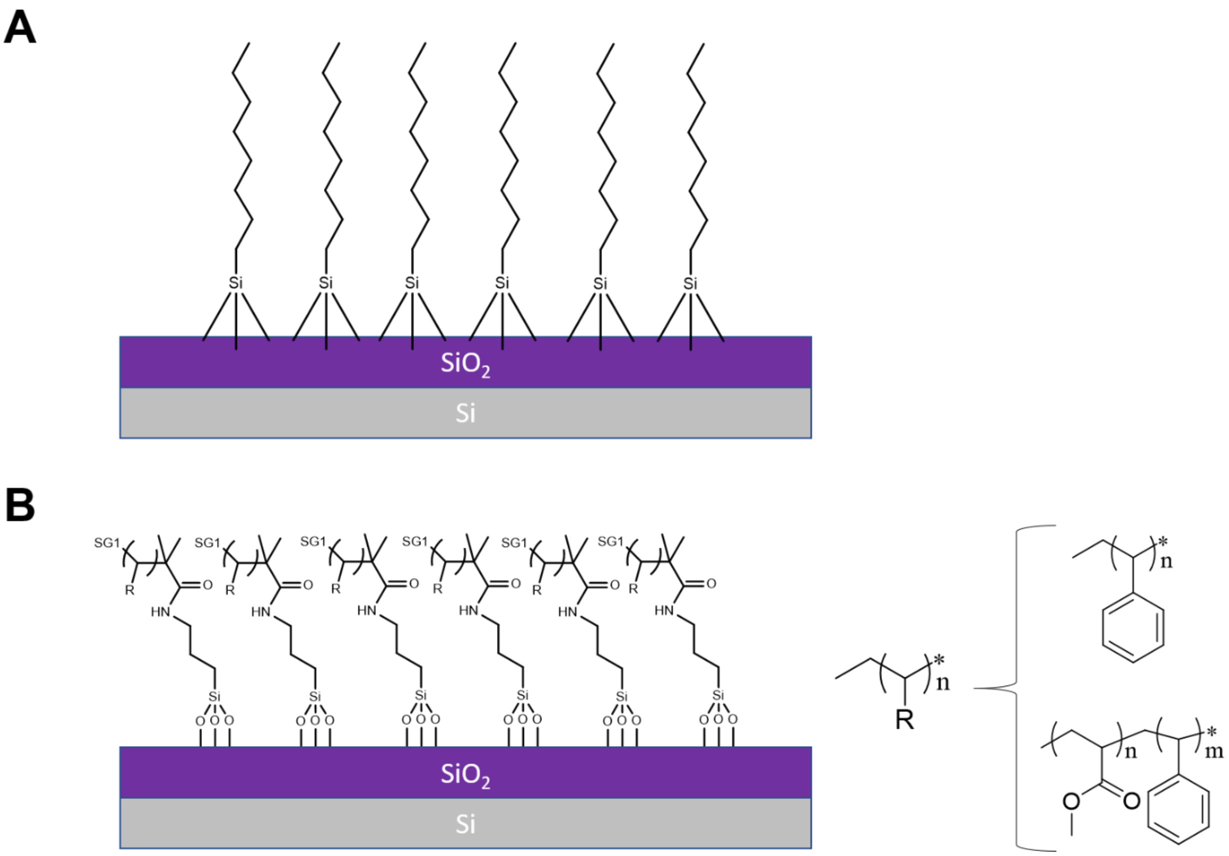

Figure 3.13 Schematic of an SiO_2 dielectric functionalized with A) OTS and B) polymer brushes and chemical structures of polymer brushes used in this study.

Table 3.4 Crystallographic data and selected data collection parameters for materials **1**, **2**, **3** and **4**.

	1 (4CN)$_2$-SiPc	**2 (3,5F)$_2$-SiPc**	**3 (2F,4CN)$_2$-SiPc**	**4 (3F,4CN)$_2$-SiPc**
Formula	$C_{46}H_{24}N_{10}O_2Si$	$C_{44}H_{22}F_4N_8O_2Si$	$C_{46}H_{22}F_2N_{10}O_2Si$	$C_{46}H_{22}F_2N_{10}O_2Si$
Formula Weight	776.84	798.78	812.82	812.82
Crystal System	Monoclinic	Monoclinic	Monoclinic	Monoclinic
Space Group	$P2_1/a$	$P2_1/c$	$P2_1/n$	$P2_1/a$
a (Å)	8.2762(3)	8.4672(6)	9.9565(7)	8.299(2)
b (Å)	17.8197(6)	13.5981(10)	20.1034(13)	17,792(5)
c (Å)	12.9674(5)	15.3177(11)	10.1637(7)	13.276(4)
α (°)	90	90	90	90
β (°)	106.8773(10)	97.400(2)	116.5530(10)	106.471(6)
γ (°)	90	90	90	90
V (Å^3)	1830.05(12)	1749.0(2)	1819.8(2)	1879.7(10)
Z	2	2	2	2
ρ_{calc} (g·cm^3)	1.410	1.517	1.483	1.436
T (K)	200.05	298(2)	200.05	200.05
μ (mm^{-1})	0.122	0.144	0.134	0.129
$2\Theta_{max}$ (°)	33.407	26.461	28.503	20.273
Total Reflections	86237	18904	39448	17896
Unique Reflections	6904	3590	4618	2895
R_1, wR_2 (on F^2)	0.0537, 0.1190	0.0676, 0.0996	0.0480, 0.1008	0.0879, 0.1133

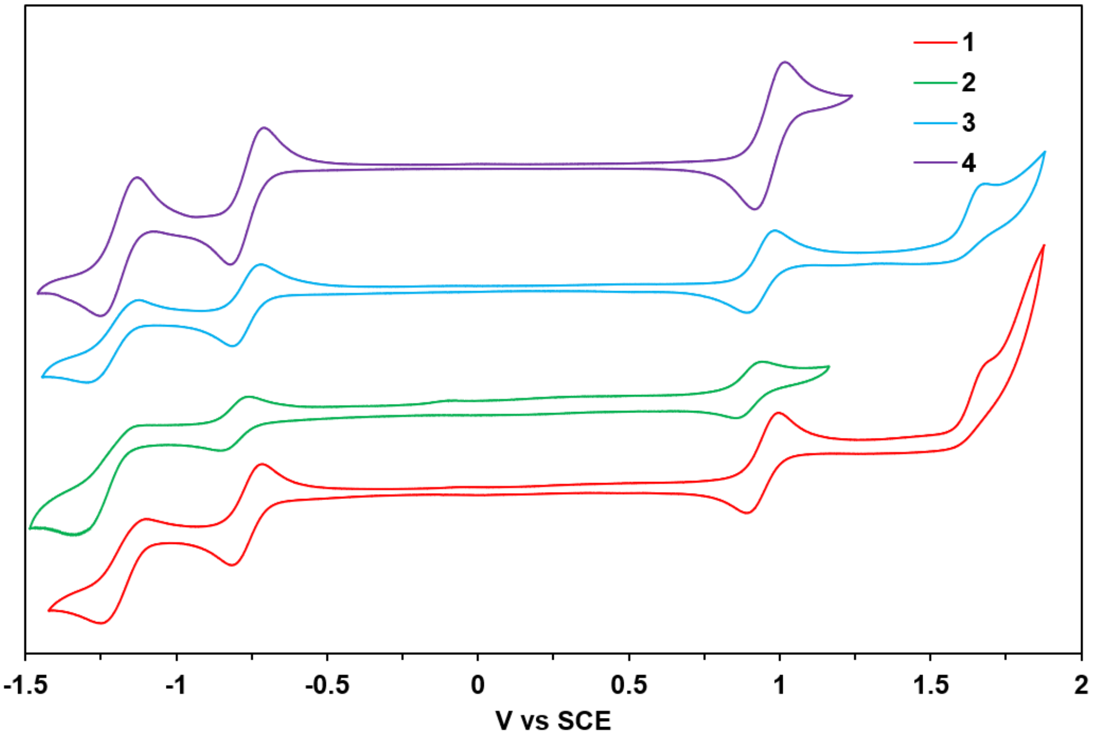

Figure 3.14 Cyclic voltammograms (CVs) of materials **1** – **4**. CVs were performed in dichloromethane at 100 mV s^{-1} with 0.1 M n-Bu_4NPF_6 as supporting electrolyte.

Table 3.5 Thermal stability results of materials **1** – **4**.

Derivative	***T*_onset_ (°C)**	***T*_d_ (°C)**
1 $(4CN)_2$-SiPc	423	462
2 $(3,5F)_2$-SiPc	365	394
3 $(2F,4CN)_2$-SiPc	372	415
4 $(3F,4CN)_2$-SiPc	374	396

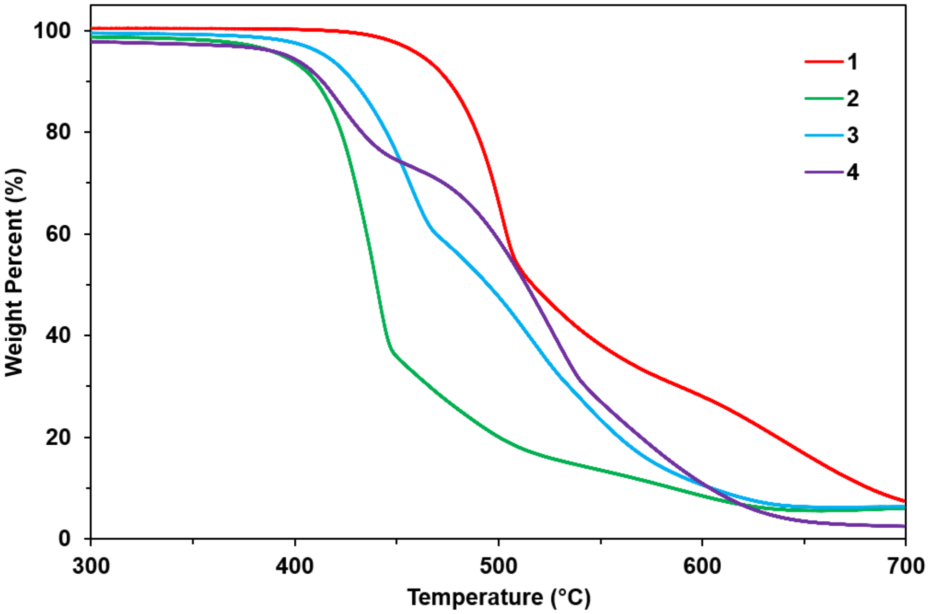

Figure 3.15 TGA traces of materials **1** – **4**.

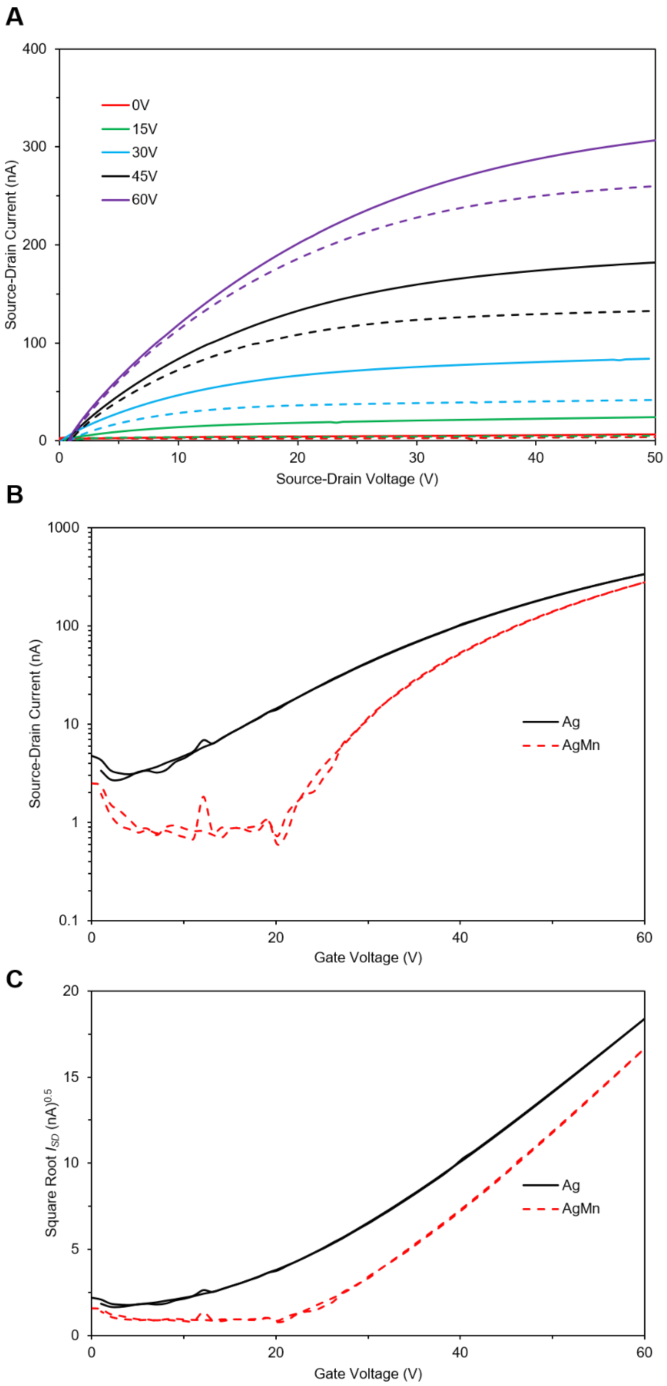

Figure 3.16 A) Output, B) transfer and C) $\sqrt{I_{SD}}$ vs V_G curves for material **1** (4CN) with Ag (solid lines) and Ag/Mn (dotted lines) electrode configurations deposited on 300 nm-thick OTS-modified SiO_2.

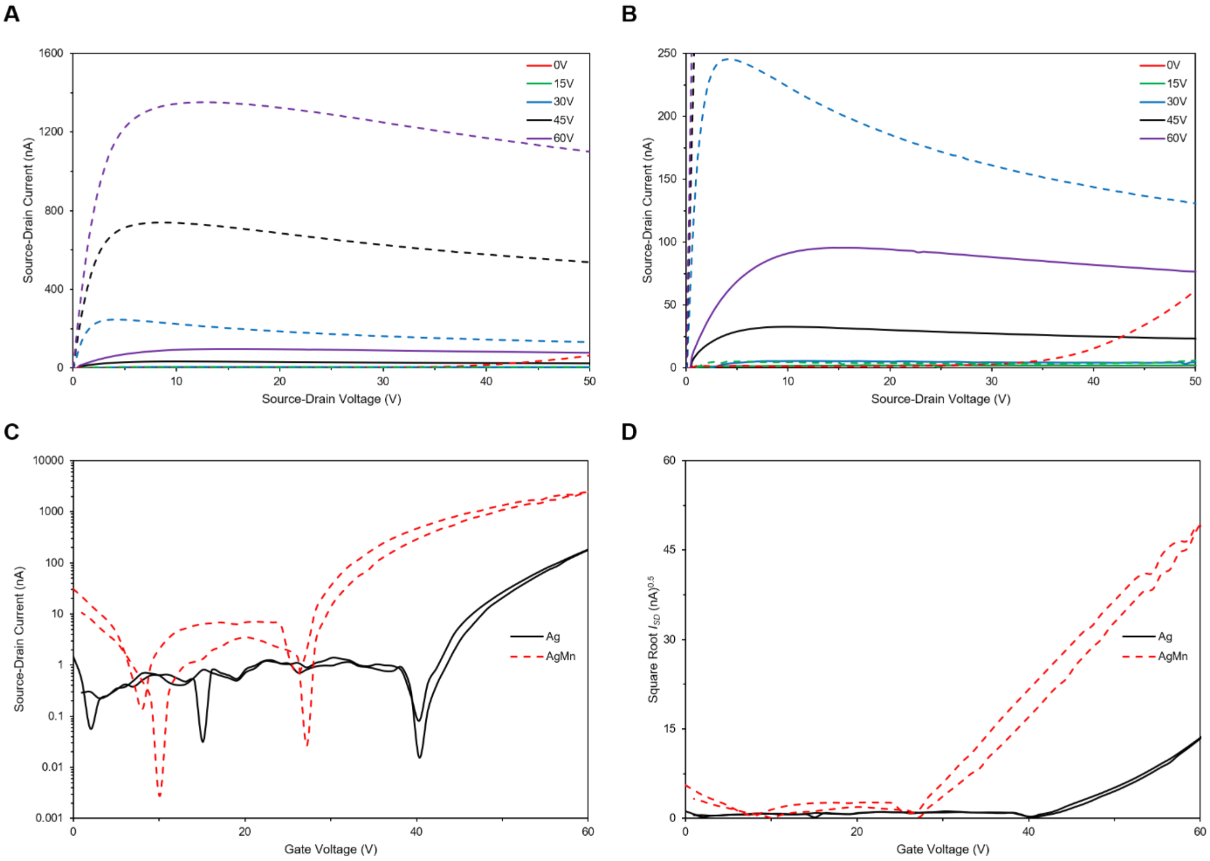

Figure 3.17 A and B) Output curves, C) transfer curves and D) $\sqrt{I_{SD}}$ vs V_G curves for material **2** (3,5F) with Ag (solid lines) and Ag/Mn (dotted lines) electrode configurations deposited on 300 nm-thick OTS-modified SiO$_2$.

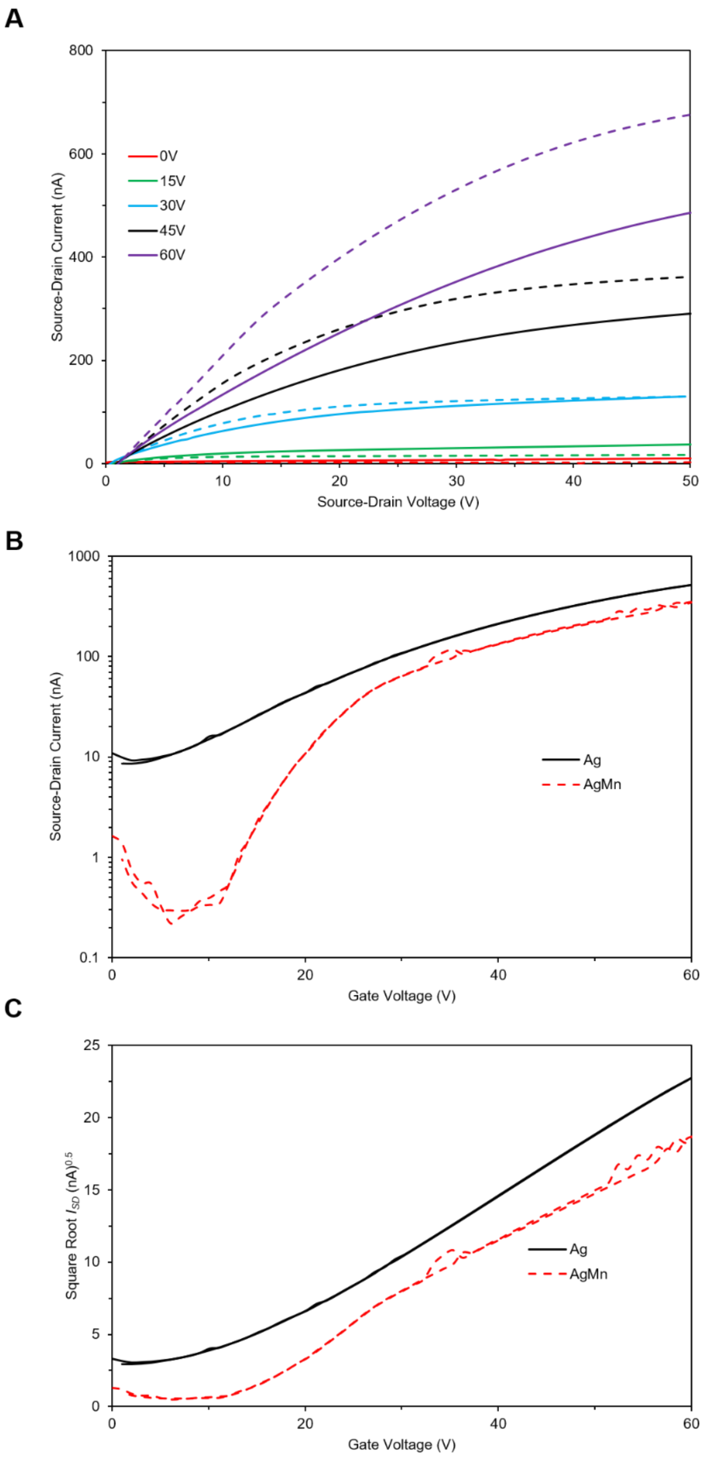

Figure 3.18 A) Output, B) transfer and C) $\sqrt{I_{SD}}$ vs V_G curves for material **3** (2F,4CN) with Ag (solid lines) and Ag/Mn (dotted lines) electrode configurations deposited on 230 nm-thick OTS-modified SiO_2.

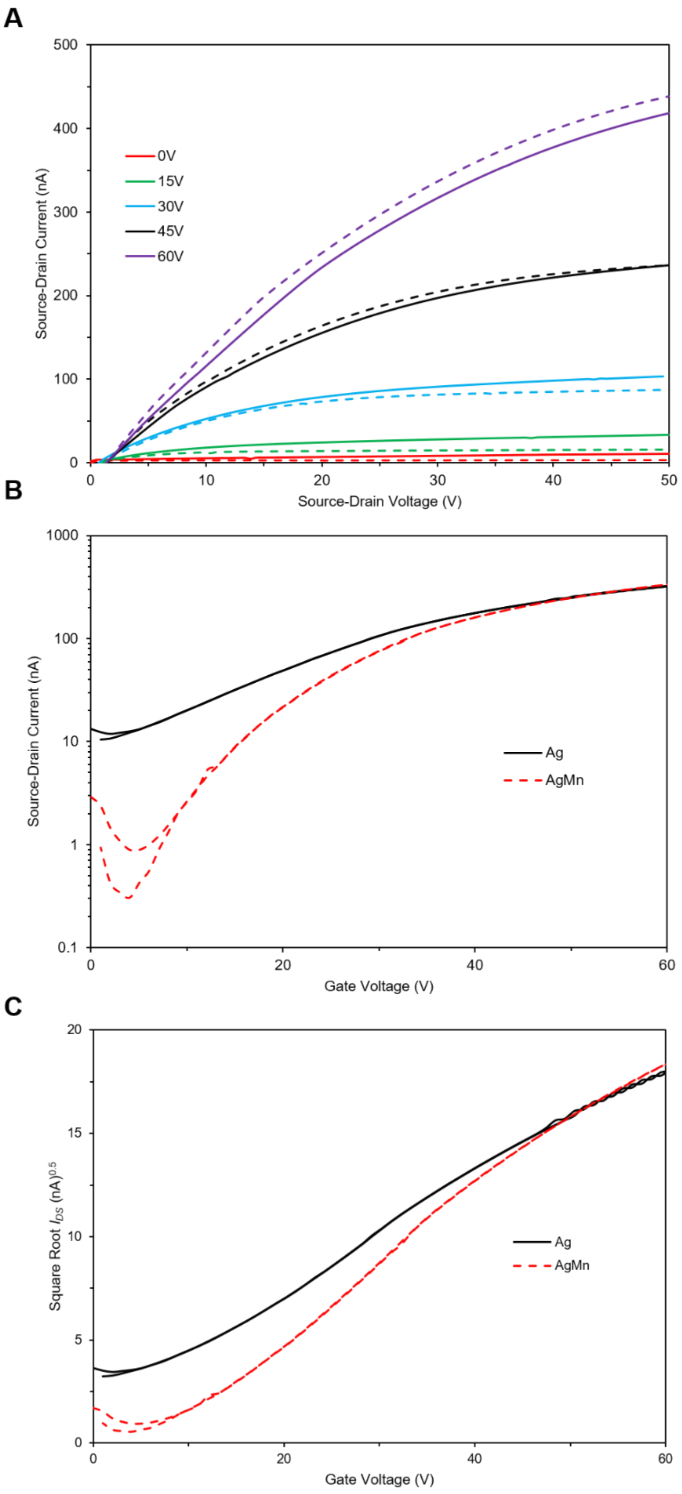

Figure 3.19 A) Output, B) transfer and C) $\sqrt{I_{SD}}$ vs V_G curves for material **4** (3F,4CN) with Ag (solid lines) and Ag/Mn (dotted lines) electrode configurations deposited on 230 nm-thick OTS-modified SiO_2.

Table 3.6 Electrical performance of OTFTs prepared from materials **1** – **4** with Ag electrodes.

Material	SiO_2 Oxide Thickness (nm)	Electrode	μ_{ave} [cm^2/V·s] (x 10^{-3})	$V_{T, ave}$ [V]	Hammett Parameter [-]	I_{on} [A] (x 10^{-7})	$I_{on/off}$	n[a)]
1 $(4CN)_2$-SiPc	300	Ag	0.91 ± 0.62	15.5 ± 1.3	+ 0.660	2.33	10^2	25
2 $(3,5F)_2$-SiPc	300	Ag	3.9 ± 1.1	44.4 ± 1.0	+ 0.674	1.88	10^4	33
3 $(2F,4CN)_2$-SiPc	230	Ag	0.82 ± 0.64	4.6 ± 4.2	+ 0.722	4.40	10^2	42
4 $(3F,4CN)_2$-SiPc	230	Ag	0.30 ± 0.43	-11.2 ± 6.1	+ 0.997	2.13	10^1	32

a) *n* indicates number of devices.

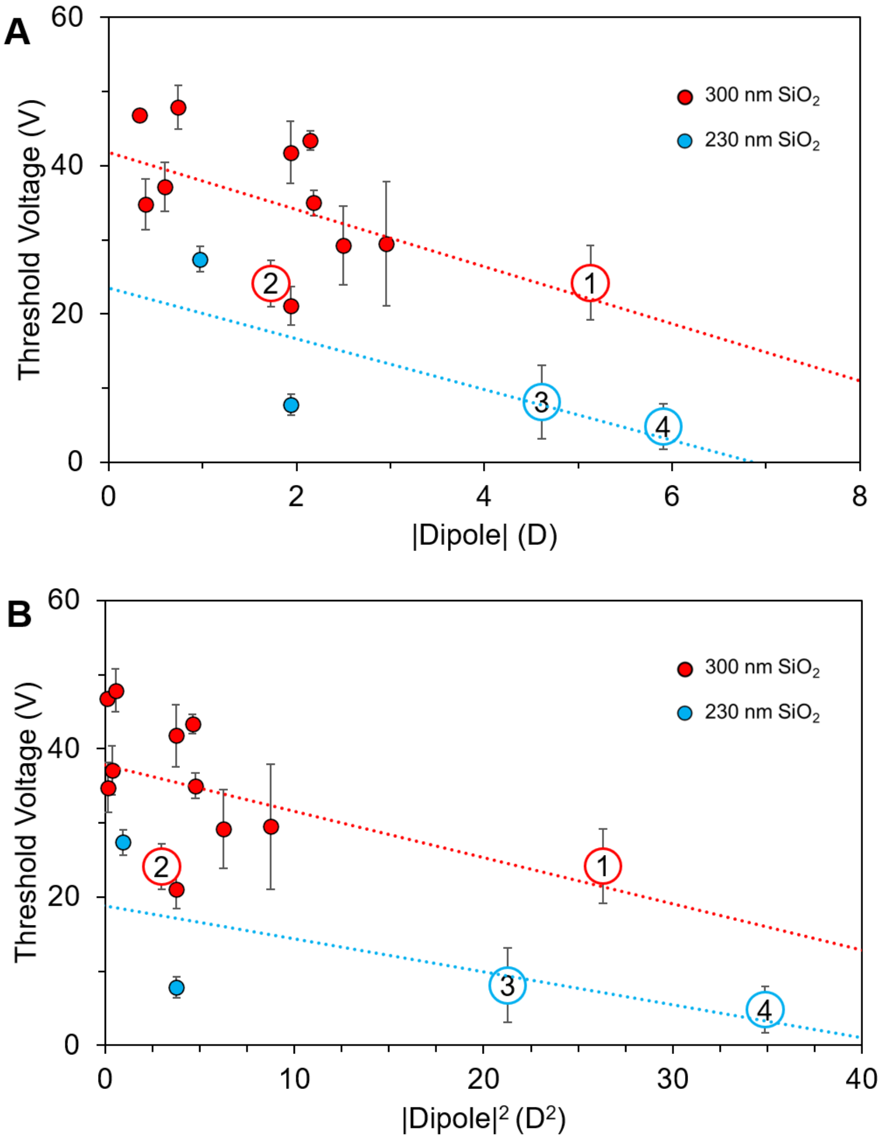

Figure 3.20 V_T of SiPc OTFTs as a function of A) DFT-calculated SiH_3-R dipole and B) the square of the SiH_3-R dipole for R_2-SiPcs **1** – **4** and R_2-SiPcs reported in our previous studies on 230 nm-thick (blue circles)[8] and 300 nm-thick (red circles) OTS-modified SiO_2.[16]

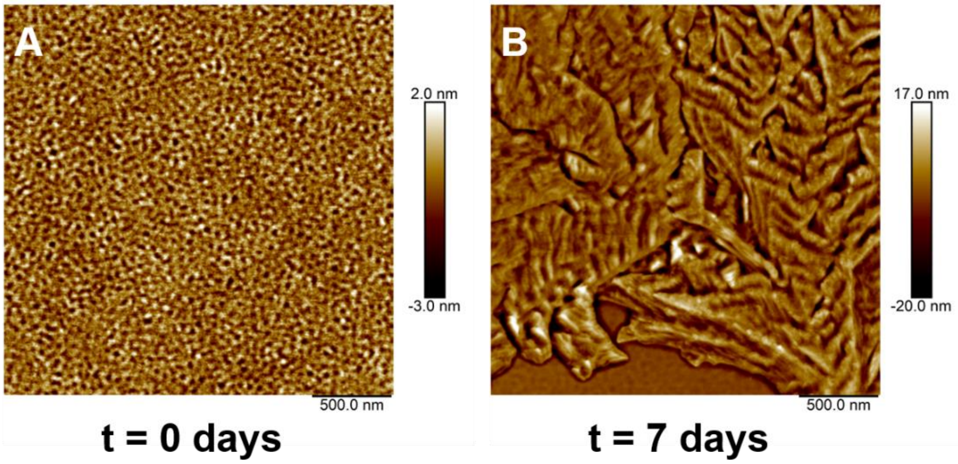

Figure 3.21 AFM height images of thin films of material **3** (2F,4CN) deposited on OTS at A) t = 0 days and B) t = 7 days.

Table 3.7 Average RMS surface roughness of material **4** on different dielectric surfaces calculated from AFM images

Material	**Surface Treatment**	**RMS Roughness t = 0 days (nm)**	**RMS Roughness t = 7 days (nm)**
1 $(4CN)_2$-SiPc	OTS	0.76	3.74
2 $(3,5F)_2$-SiPc	None	0.31	3.55
3 $(2F,4CN)_2$-SiPc	gPS	0.43	0.43
4 $(3F,4CN)_2$-SiPc	gPMMA/S	0.51	4.27

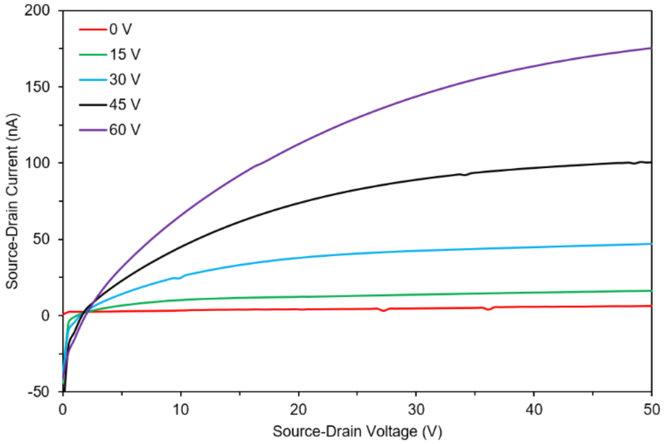

Figure 3.22 Output curves for material **4** (3F,4CN) with Ag/Mn electrodes deposited on bare 230 nm-thick SiO_2.

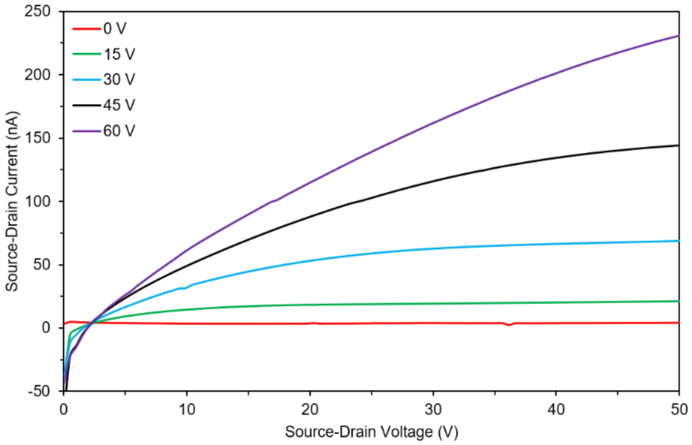

Figure 3.23 Output curves for material **4** (3F,4CN) with Ag/Mn electrodes deposited on a styrene polymer brush surface.

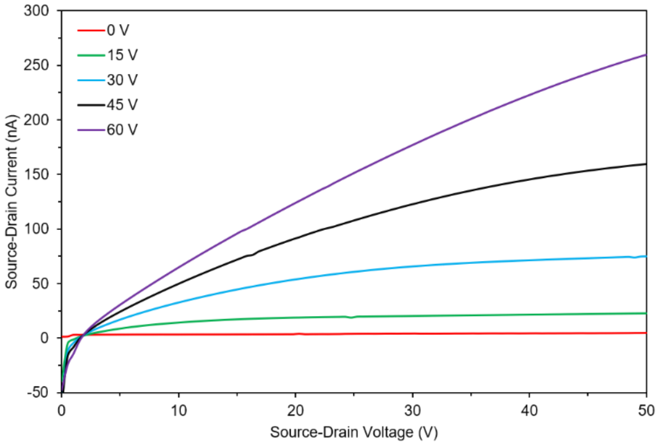

Figure 3.24 Output curves for material **4** (3F,4CN) with Ag/Mn electrodes deposited on a poly(methyl methacrylate) polymer brush surface.

References

(1) Yutronkie, N. J.; Grant, T. M.; Melville, O. A.; Lessard, B. H.; Brusso, J. L. Old Molecule , New Chemistry : Exploring Silicon Phthalocyanines as Emerging N-Type Materials in Organic Electronics. *Materials (Basel).* **2019**, *12*, 1334-1-1334–1338. https://doi.org/doi:10.3390/ma12081334.

(2) Song, D.; Wang, H.; Zhu, F.; Yang, J.; Tian, H.; Geng, Y.; Yan, D. Phthalocyanato Tin(IV) Dichloride: An Air-Stable, High-Performance, n-Type Organic Semiconductor with a High Field-Effect Electron Mobility. *Adv. Mater.* **2008**, *20* (11), 2142–2144. https://doi.org/10.1002/adma.200702439.

(3) Beaumont, N.; Castrucci, S.; Sullivan, P.; Morse, G. E.; Paton, A. S.; Lu, Z.; Bender, T. P.; Jones, T. S. Acceptor Properties of Boron Subphthalocyanines in Fullerene Free Photovoltaics. *J. Phys. Chem. C* **2014**, *118*, 14814–14823. https://doi.org/10.1021/jp503578g.

(4) Li, Q.; Tang, Q.; Li, H.; Hu, W.; Yang, X.; Shuai, Z.; Liu, Y.; Zhu, D. Organic Thin-Film Transistors of Phthalocyanines. *Pure Appl. Chem.* **2008**, *80* (11), 2231–2240. https://doi.org/10.1351/pac200880112231.

(5) Jiang, H.; Ye, J.; Hu, P.; Wei, F.; Du, K.; Wang, N.; Ba, T.; Feng, S.; Kloc, C. Fluorination of Metal Phthalocyanines: Single-Crystal Growth, Efficient N-Channel Organic Field-Effect Transistors, and Structure-Property Relationships. *Sci. Rep.* **2014**, *4*, 1–6. https://doi.org/10.1038/srep07573.

(6) Chaure, N. B.; Basova, T.; Zahedi, M.; Ray, A. K.; Sharma, A. K.; Durmuş, M.; Ahsen, V. Solution Processed Tetrasubstituted Zinc Phthalocyanine as an Active Layer in Organic Field Effect Transistors. *J. Appl. Phys.* **2010**, *107* (11), 2–7. https://doi.org/10.1063/1.3428386.

(7) Pearson, A. J.; Plint, T.; Jones, S. T. E.; Lessard, B. H.; Credgington, D.; Bender, T. P.; Greenham, N. C. Silicon Phthalocyanines as Dopant Red Emitters for Efficient Solution Processed OLEDs. *J. Mater. Chem. C* **2017**, *5* (48), 12688–12698. https://doi.org/10.1039/c7tc03946h.

(8) Melville, O. A.; Grant, T. M.; Lochhead, K.; King, B.; Ambrose, R.; Rice, N. A.; Boileau, N. T.; Peltekoff, A. J.; Tousignant, M.; Hill, I. G.; Lessard, B. H. Contact Engineering Using Manganese, Chromium, and Bathocuproine in Group 14 Phthalocyanine Organic Thin-Film Transistors. *ACS Appl. Electron. Mater.* **2020,** *2* (5), 1313–1322. https://doi.org/10.1021/acsaelm.0c00104.

(9) Grant, T. M.; Gorisse, T.; Dautel, O.; Wantz, G.; Lessard, B. H. Multifunctional Ternary Additive in Bulk Heterojunction OPV: Increased Device Performance and Stability. *J. Mater. Chem. A* **2017**, 1581–1587. https://doi.org/10.1039/C6TA08593H.

(10) Melville, O. A.; Grant, T. M.; Lessard, H. Silicon Phthalocyanines as N-Type Semiconductors in Organic Thin Film Transistors †. *J. Mater. Chem. C* **2018**, *6*, 5482–5488. https://doi.org/10.1039/c8tc01116h.

(11) Boileau, N. T.; Melville, O. A.; Mirka, B.; Cranston, R.; Lessard, B. H. P and N Type Copper Phthalocyanines as Effective Semiconductors in Organic Thin-Film Transistor Based DNA Biosensors at Elevated Temperatures. *RSC Adv.* **2019**, *9* (4), 2133–2142.

https://doi.org/10.1039/c8ra08829b.

(12) Melville, O. A.; Grant, T. M.; Mirka, B.; Boileau, N. T.; Park, J.; Lessard, B. H. Ambipolarity and Air Stability of Silicon Phthalocyanine Organic Thin-Film Transistors. *Adv. Electron. Mater.* **2019**, *1900087*, 1–7. https://doi.org/10.1002/aelm.201900087.

(13) Raboui, H.; Lough, A. J.; Plint, T.; Bender, T. P. Position of Methyl and Nitrogen on Axial Aryloxy Substituents Determines the Crystal Structure of Silicon Phthalocyanines. *Cryst. Growth Des.* **2018**, *18* (5), 3193–3201. https://doi.org/10.1021/acs.cgd.8b00298.

(14) Lessard, B. H.; White, R. T.; Al-Amar, M.; Plint, T.; Castrucci, J. S.; Josey, D. S.; Lu, Z. H.; Bender, T. P. Assessing the Potential Roles of Silicon and Germanium Phthalocyanines in Planar Heterojunction Organic Photovoltaic Devices and How Pentafluoro Phenoxylation Can Enhance π-π Interactions and Device Performance. *ACS Appl. Mater. Interfaces* **2015**, *7* (9), 5076–5088. https://doi.org/10.1021/am508491v.

(15) Lessard, B. H.; Grant, T. M.; White, R.; Thibau, E.; Lu, Z. H.; Bender, T. P. The Position and Frequency of Fluorine Atoms Changes the Electron Donor/Acceptor Properties of Fluorophenoxy Silicon Phthalocyanines within Organic Photovoltaic Devices. *J. Mater. Chem. A* **2015**, *3* (48), 24512–24524. https://doi.org/10.1039/c5ta07173a.

(16) King, B.; Melville, O. A.; Rice, N. A.; Kashani, S.; Tonnelé, C.; Raboui, H.; Swaraj, S.; Grant, T. M.; McAfee, T.; Bender, T. P.; Ade, H.; Castet, F.; Muccioli, L.; Lessard, B. H. Silicon Phthalocyanines for N-Type Organic Thin-Film Transistors: Development of Structure Property Relationships. *ACS Appl. Electron. Mater.* **2021**, *3* (1), 325-336. https://doi.org/https://dx.doi.org/10.1021/acsaelm.0c00871.

(17) Kano, M.; Minari, T.; Tsukagoshi, K. Improvement of Subthreshold Current Transport by Contact Interface Modification in P-Type Organic Field-Effect Transistors. *Appl. Phys. Lett.* **2009**, *94*, 143304-1-143304–3. https://doi.org/10.1063/1.3115826.

(18) Li, Q.; Zhang, Y.; Li, H.; Tang, Q.; Jiang, L.; Chi, L.; Fuchs, H.; Hu, W. Battery Drivable Organic Single-Crystalline Transistors Based on Surface Grafting Ultrathin Polymer Dielectric. *Adv. Funct. Mater.* **2009**, *19* (18), 2987–2991. https://doi.org/10.1002/adfm.200900443.

(19) Star, A.; Han, T. R.; Gabriel, J. C. P.; Bradley, K.; Grüner, G. Interaction of Aromatic Compounds with Carbon Nanotubes: Correlation to the Hammett Parameter of the Substituent and Measured Carbon Nanotube FET Response. *Nano Lett.* **2003**, *3* (10), 1421–1423. https://doi.org/10.1021/nl0346833.

(20) Hansch, C.; Leo, A.; Taft, R. W. A Survey of Hammett Substituent Constants and Resonance and Field Parameters. *Chem. Rev.* **1991**, *91* (2), 165–195. https://doi.org/10.1021/cr00002a004.

(21) Wang, Q.; Jiang, S.; Qian, J.; Song, L.; Zhang, L.; Zhang, Y.; Zhang, Y.; Wang, Y. Low-Voltage, High-Performance Organic Field-Effect Transistors Based on 2D Crystalline Molecular Semiconductors. *Sci. Rep.* **2017**, *7*, 1–8. https://doi.org/10.1038/s41598-017-08280-8.

(22) Paterson, A. F.; Singh, S.; Fallon, K. J.; Hodsden, T.; Han, Y.; Schroeder, B. C.; Bronstein, H.; Heeney, M.; McCulloch, I.; Anthopoulos, T. D. Recent Progress in High-Mobility Organic Transistors: A Reality Check. *Adv. Mater.* **2018**, *30* (36), 1–33.

https://doi.org/10.1002/adma.201801079.

(23) Gruntz, G.; Lee, H.; Hirsch, L.; Castet, F.; Toupance, T.; Briseno, A. L.; Nicolas, Y. Nitrile Substitution Effect on Triphenodioxazine-Based Materials for Liquid-Processed Air-Stable n-Type Organic Field Effect Transistors. *Adv. Electron. Mater.* **2015**, *1* (6), 1500072. https://doi.org/10.1002/aelm.201500072.

(24) Glöcklhofer, F.; Petritz, A.; Karner, E.; Bojdys, M. J.; Stadlober, B.; Fröhlich, J.; Unterlass, M. M. Dicyano- and Tetracyanopentacene: Foundation of an Intriguing New Class of Easy-to-Synthesize Organic Semiconductors. *J. Mater. Chem. C* **2017**, *5* (10), 2603–2610. https://doi.org/10.1039/c7tc00143f.

(25) Yun, S. W.; Kim, J. H.; Shin, S.; Yang, H.; An, B. K.; Yang, L.; Park, S. Y. High-Performance n-Type Organic Semiconductors: Incorporating Specific Electron-Withdrawing Motifs to Achieve Tight Molecular Stacking and Optimized Energy Levels. *Adv. Mater.* **2012**, *24* (7), 911–915. https://doi.org/10.1002/adma.201103978.

(26) Nakano, M.; Osaka, I.; Takimiya, K. Control of Major Carriers in an Ambipolar Polymer Semiconductor by Self-Assembled Monolayers. *Adv. Mater.* **2017**, *29* (1), 1602893. https://doi.org/10.1002/adma.201602893.

(27) Salinas, M.; Jäger, C. M.; Amin, A. Y.; Dral, P. O.; Meyer-Friedrichsen, T.; Hirsch, A.; Clark, T.; Halik, M. The Relationship between Threshold Voltage and Dipolar Character of Self-Assembled Monolayers in Organic Thin-Film Transistors. *J. Am. Chem. Soc.* **2012**, *134* (30), 12648–12652. https://doi.org/10.1021/ja303807u.

(28) Lee, S.; Jang, M.; Yang, H. Optimized Grafting Density of End-Functionalized Polymers to Polar Dielectric Surfaces for Solution-Processed Organic Field-Effect Transistors. *ACS Appl. Mater. Interfaces* **2014**, *6* (22), 20444–20451. https://doi.org/10.1021/am506024s.

(29) Kim, K.; An, T. K.; Kim, J.; Jeong, Y. J.; Jang, J.; Kim, H.; Baek, J. Y.; Kim, Y. H.; Kim, S. H.; Park, C. E. Grafting Fluorinated Polymer Nanolayer for Advancing the Electrical Stability of Organic Field-Effect Transistors. *Chem. Mater.* **2014**, *26* (22), 6467–6476. https://doi.org/10.1021/cm5030266.

(30) Ha, J.; Chung, S.; Pei, M.; Cho, K.; Yang, H.; Hong, Y. One-Step Interface Engineering for All-Inkjet-Printed, All-Organic Components in Transparent, Flexible Transistors and Inverters: Polymer Binding. *ACS Appl. Mater. Interfaces* **2017**, *9* (10), 8819–8829. https://doi.org/10.1021/acsami.6b14702.

(31) Lowbry, M. K.; Starshak, A. J.; John, S. J.; Esposito, N.; Krueger, P. C.; Kenney, M. E. Dichloro(Phthalocyanino)Silicon. *Inorg. Chem.* **1965**, *4* (1), 128. https://doi.org/10.1021/ic50023a036.

(32) Aranzaes, J. R.; Daniel, M. C.; Astruc, D. Metallocenes as References for the Determination of Redox Potentials by Cyclic Voltammetry - Permethylated Iron and Cobalt Sandwich Complexes, Inhibition by Polyamine Dendrimers, and the Role of Hydroxy-Containing Ferrocenes. *Can. J. Chem.* **2006**, *84* (2), 288–299. https://doi.org/10.1139/V05-262.

(33) Bruker in APEX3, SAINT, SADABS and TWINABS, Vol. Bruker Analytical X-Ray Instruments Inc. Bruker: Madison, WI 2016.

(34) Sheldrick, G. M. SHELXT – Integrated Space-Group and Crystal- Structure Determination.

Acta Crystallogr. Sect. A **2015**, *71*, 3–8. https://doi.org/10.1107/S2053273314026370.

(35) Sheldrick, G. M. Crystal Structure Refinement with SHELXL. *Acta Crystallogr. Sect. C* **2015**, *71*, 3–8. https://doi.org/10.1107/S2053229614024218.

(36) Melville, O. A.; King, B.; Imperiale, C.; Lessard, B. H. Orthogonally Processable Carbazole-Based Polymer Thin Films by Nitroxide-Mediated Polymerization. *Langmuir* **2016**, *32* (51), 13640–13648. https://doi.org/10.1021/acs.langmuir.6b03920.

(37) Sirringhaus, H. Reliability of Organic Field-Effect Transistors. *Adv. Mater.* **2009**, *21* (38–39), 3859–3873. https://doi.org/10.1002/adma.200901136.

(38) Frisch, M. J.; G. W. Trucks, G. W.; Schlegel, H. B.; Scuseria, G. E.; Robb, M. A.; Cheeseman, J. R.; Scalmani, G.; Barone, V.; Mennucci, B.; Petersson, G. A.; Nakatsuji, H.; Caricato, M.; Li, X.; Hratchian, H. P.; Izmaylov, A. F.; Bloino, J.; Zheng, G.; Sonnenberg, J. L.; Hada, M.; Ehara, M.; Toyota, K.; Fukuda, R.; Hasegawa, J.; Ishida, M.; Nakajima, T.; Honda, Y.; Kitao, O.; Nakai, H.; Vreven, T.; Montgomery, J.; Peralta, J.A., J. E.; Ogliaro, F.; Bearpark, M.; Heyd, J. J.; Brothers, E.; Kudin, K. N.; Staroverov, V. N.; Kobayashi, R.; Normand, J.; Raghavachari, K.; Rendell, A.; Burant, J. C.; Iyengar, S. S.; Tomasi, J.; Cossi, M.; Rega, N.; Millam, N. J.; Klene, M.; Knox, J. E.; Cross, J. B.; Bakken, V.; Adamo, C.; Jaramillo, J.; Gomperts, R.; Stratmann, R. E.; Yazyev, O.; Austin, A. J.; Cammi, R.; Pomelli, C.; Ochterski, J. W.; Martin, R. W.; Morokuma, K.; Zakrzewski, V. G.; Voth, G. A.; Salvador, P.; Dannenberg, J. J.; Dapprich, S.; Daniels, A. D.; Farkas, O.; Foresman, J. B.; Ortiz, J. V.; Cioslowski, J.; Fox, D. J. Gaussian 09, Revis. D.01, Gaussian, Inc.: Wallingford, CT. *Gaussian 09, Revis. D.01,* **2009**.

(39) Costa, J. C. S.; Taveira, R. J. S.; Lima, C. F. R. A. C.; Mendes, A.; Santos, L. M. N. B. . Optical Band Gaps of Organic Semiconductor Materials. *Opt. Mater. (Amst).* **2016**, *58*, 51–60. https://doi.org/10.1016/j.optmat.2016.03.041.

(40) Noviandri, I.; Brown, K. N.; Fleming, D. S.; Gulyas, P. T.; Lay, P. A.; Masters, A. F.; Phillips, L. The Decamethylferrocenium/Decamethylferrocene Redox Couple: A Superior Redox Standard to the Ferrocenium/Ferrocene Redox Couple for Studying Solvent Effects on the Thermodynamics of Electron Transfer. *J. Phys. Chem. B* **1999**, *103* (32), 6713–6722. https://doi.org/10.1021/jp991381+.

(41) Li, S.; Yuan, Z.; Yuan, J.; Deng, P.; Zhang, Q.; Sun, B. An Expanded Isoindigo Unit as a New Building Block for a Conjugated Polymer Leading to High-Performance Solar Cells. *J. Mater. Chem. A* **2014**, *2* (15), 5427–5433. https://doi.org/10.1039/c3ta15291j.

(42) Li, Y.; Cao, Y.; Gao, J.; Wang, D.; Yu, G.; Heeger, A. J. Electrochemical Properties of Luminescent Polymers and Polymer Light-Emitting Electrochemical Cells. *Synth. Met.* **1999**, *99* (3), 243–248. https://doi.org/10.1016/s0379-6779(99)00007-7.

(43) Sasa, N.; Okada, K.; Nakamuar, K.; Okada, S. Synthesis, Structural and Conformational Analysis and Chemical Properties of Phthalocyaninatometal Complexes. *J. Mol. Sci.* **1998**, *446*, 163–178.

(44) Dadvand, A.; Sun, W. H.; Moiseev, A. G.; Bélanger-Gariépy, F.; Rosei, F.; Meng, H.; Perepichka, D. F. 1,5-, 2,6- and 9,10-Distyrylanthracenes As Luminescent Organic Semiconductors. *J. Mater. Chem. C* **2013**, *1* (16), 2817–2825. https://doi.org/10.1039/c3tc30247d.

(45) Zhang, Y.; Sun, M.; Joglekar, S. J.; Fujishima, T.; Palacios, T. Threshold Voltage Control by Gate Oxide Thickness in Fluorinated GaN Metal-Oxide-Semiconductor High-Electron-Mobility Transistors. *Appl. Phys. Lett.* **2013**, *103* (3), 033524. https://doi.org/10.1063/1.4815923.

(46) Aghamohammadi, M.; Rödel, R.; Zschieschang, U.; Ocal, C.; Boschker, H.; Weitz, R. T.; Barrena, E.; Klauk, H. Threshold-Voltage Shifts in Organic Transistors Due to Self-Assembled Monolayers at the Dielectric: Evidence for Electronic Coupling and Dipolar Effects. *ACS Appl. Mater. Interfaces* **2015**, *7* (41), 22775–22785. https://doi.org/10.1021/acsami.5b02747.

(47) Waldrip, M.; Jurchescu, O. D.; Gundlach, D. J.; Bittle, E. G. Contact Resistance in Organic Field-Effect Transistors: Conquering the Barrier. *Adv. Funct. Mater.* **2019**, 1–31. https://doi.org/10.1002/adfm.201904576.

(48) Gali, S. M.; Matta, M.; Lessard, B. H.; Castet, F.; Muccioli, L. Ambipolarity and Dimensionality of Charge Transport in Crystalline Group 14 Phthalocyanines: A Computational Study. *J. Phys. Chem. C* **2018**, *122* (5), 2554–2563. https://doi.org/10.1021/acs.jpcc.7b11588.

(49) Cranston, R.; Vebber, M. C.; Berbigier, J. F.; Rice, N. A.; Tonnelé, C.; Comeau, Z.; Boileau, N. T.; Shuhendler, A. J.; Castet, F.; Muccioli, L.; Kelly, T. L.; Lessard, B. H. Thin-Film Engineering of Solution Processable n-Type Silicon Phthalocyanines for Organic Thin-Film Transistors. *ACS Appl. Mater. Interfaces,* **2021**, 13 (1), 1008–1020. doi:10.1021/acsami.0c17657.

(50) Opatkiewicz, J. P.; Lemieux, M. C.; Liu, D.; Vosgueritchian, M.; Barman, S. N.; Elkins, C. M.; Hedrick, J.; Bao, Z. Using Nitrile Functional Groups to Replace Amines for Solution-Deposited Single-Walled Carbon Nanotube Network Films. *ACS Nano* **2012**, *6* (6), 4845–4853. https://doi.org/10.1021/nn300124y.

(51) Chung, Y.; Verploegen, E.; Vailionis, A.; Sun, Y.; Nishi, Y.; Murmann, B.; Bao, Z. Controlling Electric Dipoles in Nanodielectrics and Its Applications for Enabling Air-Stable n-Channel Organic Transistors. *Nano Lett.* **2011**, *11* (3), 1161–1165. https://doi.org/10.1021/nl104087u.

(52) Mityashin, A.; Roscioni, O. M.; Muccioli, L.; Zannoni, C.; Geskin, V.; Cornil, J.; Janssen, D.; Steudel, S.; Genoe, J.; Heremans, P. Multiscale Modeling of the Electrostatic Impact of Self-Assembled Monolayers Used as Gate Dielectric Treatment in Organic Thin-Film Transistors. *ACS Appl. Mater. Interfaces* **2014**, *6* (17), 15372–15378. https://doi.org/10.1021/am503873f.

(53) Chen, M.; Yan, L.; Zhao, Y.; Murtaza, I.; Meng, H.; Huang, W. Anthracene-Based Semiconductors for Organic Field-Effect Transistors. *J. Mater. Chem. C* **2018**, *6* (28), 7416–7444. https://doi.org/10.1039/c8tc01865k.

(54) Shukla, D.; Nelson, S. F.; Freeman, D. C.; Rajeswaran, M.; Ahearn, W. G.; Meyer, D. M.; Carey, J. T. Thin-Film Morphology Control in Naphthalene-Diimide-Based Semiconductors: High Mobility n-Type Semiconductor for Organic Thin-Film Transistors. *Chem. Mater.* **2008**, *20* (24), 7486–7491. https://doi.org/10.1021/cm802071w.

(55) Boileau, N. T.; Cranston, R.; Mirka, B.; Melville, O. A.; Lessard, B. H. Metal

Phthalocyanine Organic Thin-Film Transistors: Changes in Electrical Performance and Stability in Response to Temperature and Environment. *RSC Adv.* **2019**, *9* (37), 21478–21485. https://doi.org/10.1039/c9ra03648b.

(56) Yadav, S.; Kumar, P.; Ghosh, S. Optimization of Surface Morphology to Reduce the Effect of Grain Boundaries and Contact Resistance in Small Molecule Based Thin Film Transistors. *Appl. Phys. Lett.* **2012**, *101* (19), 193307. https://doi.org/10.1063/1.4766913.

(57) Reese, C.; Bao, Z. High-Resolution Measurement of the Anisotropy of Charge Transport in Single Crystals. *Adv. Mater.* **2007**, *19* (24), 4535–4538. https://doi.org/10.1002/adma.200701139.

(58) Li, R.; Hu, W.; Liu, Y.; Zhu, D. Micro- and Nanocrystals of Organic Semiconductors. *Acc. Chem. Res.* **2010**, *43* (4), 529–540. https://doi.org/10.1021/ar900228v.

(59) Lee, W. H.; Lim, J. A.; Kim, D. H.; Cho, J. H.; Jang, Y.; Kim, Y. H.; Han, J. I.; Cho, K. Room-Temperature Self-Organizing Characteristics of Soluble Acene Field-Effect Transistors. *Adv. Funct. Mater.* **2008**, *18* (4), 560–565. https://doi.org/10.1002/adfm.200701087.

(60) Turak, A. Interfacial Degradation in Organic Optoelectronics. *RSC Adv.* **2013**, *3* (18), 6188–6225. https://doi.org/10.1039/c2ra22770c.

(61) Kowarik, S.; Gerlach, A.; Sellner, S.; Cavalcanti, L.; Schreiber, F. Dewetting of an Organic Semiconductor Thin Film Observed in Real-Time. *Adv. Eng. Mater.* **2009**, *11* (4), 291–294. https://doi.org/10.1002/adem.200800289.

(62) Burke, S. A.; Topple, J. M.; Grütter, P. Molecular Dewetting on Insulators. *J. Phys. Condens. Matter* **2009**, *21* (42), 423101. https://doi.org/10.1088/0953-8984/21/42/423101.

(63) Breuer, T.; Karthäuser, A.; Klemm, H.; Genuzio, F.; Peschel, G.; Fuhrich, A.; Schmidt, T.; Witte, G. Exceptional Dewetting of Organic Semiconductor Films: The Case of Dinaphthothienothiophene (DNTT) at Dielectric Interfaces. *ACS Appl. Mater. Interfaces* **2017**, *9* (9), 8384–8392. https://doi.org/10.1021/acsami.6b15902.

(64) Ge, F.; Wang, X.; Zhang, Y.; Song, E.; Zhang, G.; Lu, H.; Cho, K.; Qiu, L. Modulating the Surface via Polymer Brush for High-Performance Inkjet-Printed Organic Thin-Film Transistors. *Adv. Electron. Mater.* **2017**, *3* (1), 1600402. https://doi.org/10.1002/aelm.201600402.

(65) Celle, C.; Suspène, C.; Ternisien, M.; Lenfant, S.; Guérin, D.; Smaali, K.; Lmimouni, K.; Simonato, J. P.; Vuillaume, D. Interface Dipole : Effects on Threshold Voltage and Mobility for Both Amorphous and Poly-Crystalline Organic Field Effect Transistors. *Org. Electron.* **2014**, *15* (3), 729–737. https://doi.org/10.1016/j.orgel.2014.01.003.

Chapter 4: Not just surface energy: The role of bis(pentafluorophenoxy) silicon phthalocyanine axial functionalization and molecular orientation on organic thin film transistor performance.

This chapter was published in the journal "ACS Applied Materials & Interfaces": King, B.; Radford, C. L.; Vebber, M. C.; Ronnasi, B.; Lessard, B. H., Not Just Surface Energy: The Role of Bis(Pentafluorophenoxy) Silicon Phthalocyanine Axial Functionalization and Molecular Orientation on Organic Thin-Film Transistor Performance. ACS Applied Mateials & Interfaces, 2023, 15, 14937–14947.*

Context

In this work, I reported an in-depth analysis of functional surfaces of varying surface energies and terminal groups to probe the influence on their structure on thin-film forming properties of the organic semiconductor F_{10}-SiPc and its performance in OTFTs. This work was motivated by the fact that unlike divalent metal phthalocyanines, F_{10}-SiPc possesses axial synthetic groups that may affect interactions between the molecule and the surface, necessitating different surface chemistry to optimize OTFT performance. Among these surfaces, films deposited on *para-sexiphenyl* (*p-6P*) yielded unique results for a metal phthalocyanine (MPc)-based semiconductor. Typically, MPcs have been observed to form highly crystalline films with molecules "standing up" on *p-6P*. However, the pentafluorophenoxy axial groups on F_{10}-SiPc make the molecule non-planar like other MPcs and resulting films probed by GIWAXS demonstrated that a mixture of orientations is obtained. This work therefore demonstrated that axial groups on the silicon phthalocyanine core play a role in semiconductor-surface interactions and that the development of new interlayers for the optimization of these semiconductors is required.

Contributions

I prepared and characterized functional surfaces and OTFTs prepared by physical vapour deposition, as well as processed and analyzed device data. I also synthesized, purified, and characterized F_{10}-SiPc. I completed atomic force microscopy measurements, contact angle measurements and grazing-incidence wide-angle X-ray scattering (GIWAXS) measurements. I calculated surface energies and developed power spectral density functions. I processed and interpreted GIWAXS data with guidance and input from Dr. Radford. Nuclear magnetic resonance spectroscopy was completed, processed, and interpreted by Dr. Vebber and Ms. Ronnasi. I wrote the manuscript with input from Prof. Lessard and Dr. Radford.

Abstract

Understanding the effect of surface chemistry on the dielectric-semiconductor interface, thin-film morphology and molecular alignment enables the optimization of organic thin-film transistors (OTFTs). We explored the properties of thin films of bis(pentafluorophenoxy) silicon phthalocyanine (F_{10}-SiPc) evaporated onto silicon dioxide (SiO_2) surfaces modified by self-assembled monolayers (SAMs) of varying surface energies and by weak epitaxial growth (WEG). The total surface energy (γ^{tot}), dispersive component of the total surface energy (γ^{d}) and the polar component of the total surface energy (γ^{p}) were calculated using the Owens-Wendt method and related to electron field-effect mobility of devices (μ_e) and it was determined that minimizing γ^{p} and matching γ^{tot} yielded films with the largest relative domain sizes and highest resulting μ_e. Subsequent analyses were completed using atomic force microscopy (AFM) and grazing-incidence wide-angle X-ray scattering (GIWAXS) to relate surface chemistry to thin-film morphology and molecular order at the surface and semiconductor-dielectric interface, respectively. Films evaporated on n-octyltrichlorosilane (OTS) yielded devices with the highest average μ_e, of 7.2×10^{-2} $cm^2 \cdot V^{-1} \cdot s^{-1}$ which we attributed to it having both the largest domain length which were extracted from power spectral density function (PSDF) analysis and a subset of molecules with a pseudo edge-on orientation relative to the substrate. Films of F_{10}-SiPc with the mean molecular orientation of the π-stacking direction being more edge-on relative the substrate also generally resulted in OTFTs with a lower average V_T. Unlike conventional MPcs, F_{10}-SiPc films fabricated by WEG experienced no macrocycle in an edge-on configuration. These results demonstrate the critical role of the axial group in F_{10}-SiPc on WEG, molecular orientation and morphology as a function of surface chemistry the choice of SAMs.

4.1 Introduction

Engineering the interfaces of thin-film electronics including organic thin-film transistors (OTFTs) are critical to optimizing their performance.[1,2] Modifying the semiconductor-dielectric interface is particularly useful for improving device performance by minimizing interfacial charge traps,[3] and can enable the manipulation and control of nucleation,[4] crystallization and subsequent growth of organic semiconducting thin-films.[5] Understanding and controlling the dielectric-semiconductor interface in OTFTs is primarily critical to maximizing the field-effect mobility (μ) and minimizing the threshold voltage (V_T).[6–8] The observed μ in OTFTs depends on both intermolecular factors such as electronic coupling between molecules,[9] as well as characteristics of the device including thin-film texture,[10] dielectric capacitance and thickness.[11] The most common modification to the semiconductor-dielectric interface is by self-assembled monolayers (SAMs), which are ultra-thin molecular layers in the form of silane- or phosphonic acid-terminated alkyl chains[5] or polymers[12,13] covalently bound to a dielectric surface. Beyond influencing the long range crystalline order of organic semiconducting thin-films, SAMs can be functionalized to influence electrical characteristics of OTFTs.[8,14] For example, a linear correlation has been identified between the induced interfacial dipole at the semiconductor-dielectric interface and V_T for pentacene, α,α′-dihexylsexithiophene and fullerene deposited on six self-assembled monolayers (SAMs) in bottom-gate top-contact OTFTs.[7] This work provided a general approach to tuning the V_T of OTFTs with SAMs. In some cases, functional SAMs can also be used to tune semiconductor polarity from p- to n-type in ambipolar semiconductors.[15] Beyond SAMs, weak epitaxy growth (WEG) has also been employed as a method to improve the performance of organic semiconductors in OTFTs.[16] WEG can be achieved by evaporating rod-like molecules as a templating layer at the semiconductor-dielectric interface in devices using disk-shaped molecular semiconductors such as metal phthalocyanines (MPcs).[17] This template typically yields a highly-ordered surface where molecules have an "edge-on" orientation in which the π-stacking direction of molecules is oriented perpendicular to the substrate. The semiconductor deposited on top of this highly-ordered surface is typically epitaxially oriented relative to the template layer and yields high-quality films with similar edge-on π- π stacking relative to the substrate. An early example of WEG for high μ OTFTs was reported for ZnPc, evaporated on *para*-sexiphenyl (*p*-6P) which resulted in an order of magnitude increase in hole μ from 10^{-2} $cm^2 \cdot V^{-1} \cdot s^{-1}$ to 10^{-1} $cm^2 \cdot V^{-1} \cdot s^{-1}$.[18] The WEG method with a thin interlayer of *p*-6P has also been used to improve the crystalline order and performance of other MPcs and semiconducting small molecules including TiOPc[19] and 2,9-DPh-DNTT.[20]

Silicon phthalocyanines (R_2-SiPcs) are an emerging class of MPc which have functional groups at varying angles relative to the π-stacking Pc plane,[21] with disparate surface interactions to classically disk-shaped MPcs. R_2-SiPcs have shown promise as n-type or ambipolar semiconductors with derivatives incorporated into OTFTs.[22–24] Our group has previously reported structure-property relationships of a catalogue of 11 axially substituted R_2-SiPcs in bottom-gate top-contact (BGTC) OTFTs where increasing the electron withdrawing character of the axial substituent resulted in lower device V_T.[25] This observation was further corroborated through the design of three additional R_2-SiPcs with cyanophenoxy axial groups where a record-low V_T of 4.8 V was achieved for bis(3-fluoro-4-cyano phenoxy) silicon phthalocyanine.[26] Beyond changes to V_T, axial functionalization enabled the tuning of electronic coupling and intermolecular interactions.[25] It was found that better electronic coupling between molecules also yielded devices with higher μ. Electron mobilities (μ_e) of up to 10^{-1} $cm^2 \cdot V^{-1} \cdot s^{-1}$ have been reported for the best performing and most promising R_2-SiPc, bis(pentafluorophenoxy) silicon phthalocyanine (**F_{10}-SiPc**) in OTFTs,[23] which is comparable to or exceeds that of state of the art MPcs, tin phthalocyanine (R_2-SnPc) derivatives and F_{16}CuPc, in n-type OTFTs.[27,28] The first report of R_2-SiPcs as active n-type materials in OTFTs demonstrated that substrate temperature during deposition and the SAM selected for modifying the SiO_2 dielectric both resulted in changes in μ_e and V_T, indicating that processing conditions play a significant role in device performance.[22,23,29] In one case, evaporating bis(benzoate)silicon phthalocyanine onto an octyl(trichlorosilane) (OTS)-modified substrate maintained at 200 °C resulted in an order of magnitude increase in μ_e compared to devices fabricated on substrates held at room temperature. Post-deposition thermal annealing of solution processed R_2-SiPc and R_2-SnPc films up to 100 °C also influenced the μ_e and V_T of resulting OTFTs.[30] Additionally, engineering of the semiconductor-electrode interface identified manganese as a useful charge injection interlayer when paired with conductive silver electrodes to increase μ_e and reduce V_T for F_{10}-SiPc in BGTC OTFTs.[27] In the same study, manganese, chromium and bathocuproine were all found to reduce contact resistance in BGTC OTFTs when paired with gold or silver electrodes, indicating that contact engineering was a valuable tool for optimizing SiPc-based OTFTs.

In this work, we further develop relationships between surface chemistry, thin-film microstructure, and device performance for OTFTs employing **F_{10}-SiPc** as the active semiconducting layer by deposition on various self-assembled monolayers or fabricated by WEG using *p*-6P as an interlayer (**Figure 4.1**). SAMs selected in this study employ different terminal end groups and lengths to yield a broad range of surfaces for the investigation of various templating layers on μ and V_T. In addition to electronic characterization, films were characterized by atomic force microscopy (AFM), and grazing incidence wide-angle X-ray scattering (GIWAXS) to correlate device performance with thin film morphology, crystallinity, and molecular orientation relative to the substrate. Contact angle measurements were also employed to determine how surface energy influences thin-film microstructure. We demonstrate that films fabricated on OTS-modified substrates provided the best μ_e and V_T, partially due to the larger crystallite size and more favourable molecular orientation. We additionally demonstrate that there are factors beyond surface energy that play a role in molecular orientation, crystallite size and device performance.

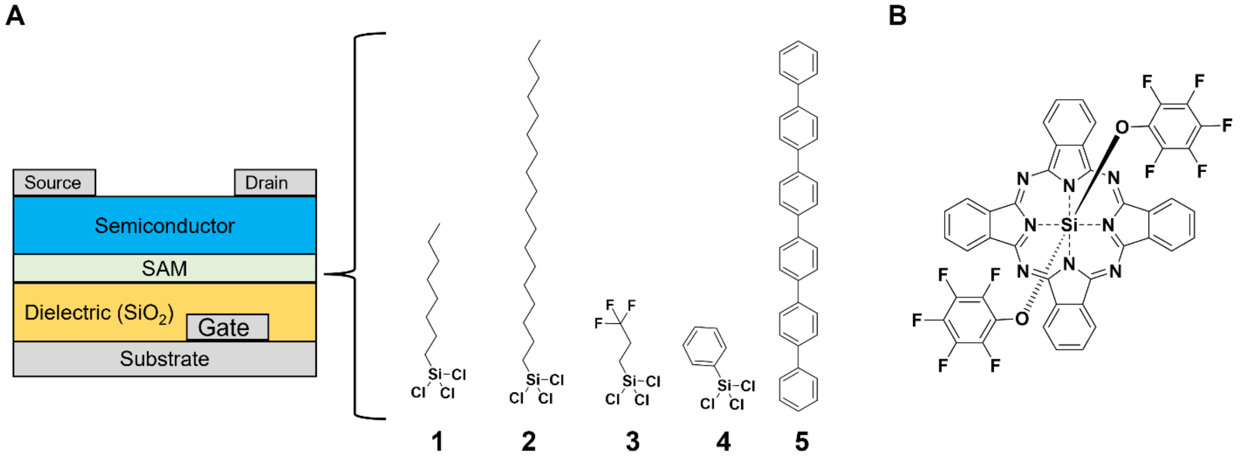

Figure 4.1 A) Schematic of a bottom-gate top-contact OTFT and chemical structures of self assembled monolayers (1) octyl(trichlorosilane) (OTS), (2) octadecyl(trichlorosilane) (ODTS), (3) trichloro(3,3,3-trifluoropropyl)silane (FPTS), (4) phenyltrichlorosilane (PhTS) and (5) *p*-sexiphenyl (*p*-6P) and B) chemical structure of the organic semiconductor silicon bis(pentafluorophenoxy) phthalocyanine (F$_{10}$-SiPc)

4.2 Experimental Section

Materials

n-Octyltrichlorosilane (OTS, >98%) and *para*-sexiphenyl (*p*-6P) were purchased from TCI America. Trichloro(octadecyl)silane (ODTS, >90%) and Trichloro(3,3,3-trifluoropropyl)silane (FPTS, 97%) were purchased from Sigma Aldrich. Phenyltrichlorosilane (PhTS, 97%) was purchased from Oakwood Chemical.

Synthesis and Characterization of F$_{10}$-SiPc

Bis(pentafluorophenoxy) silicon phthalocyanine (**F$_{10}$-SiPc**) was synthesized according to a previously reported literature procedure.[27] NMR was collected on a Bruker AVANCE III HD 500 MHz spectrometer with 80 scans taken for ^1H NMR and 600 scans taken for ^{19}F NMR in deuterated benzene (C_6D_6). NMR spectra are found in the Supporting Information (**Figure 4.20 – 4.21**). ^1H

NMR: 9.61 ppm (m, 8H); 7.83 ppm (m, 8H). ^{19}F NMR: -162.2 ppm (m, 2H); -166.4 ppm (m, 2H), -167.8 (m, 1H).

Device Fabrication

N-doped silicon substrates with a 230 nm thermally grown SiO_2 layer from WaferPro were washed with acetone and isopropanol to remove a protective photoresist and subsequently dried with a nitrogen stream. Substrates were then sonicated sequentially for 5 min in both acetone and methanol, followed by drying with a nitrogen stream and treatment with oxygen plasma for 15 min. Cleaned substrates which underwent silane treatment were then rinsed with water and isopropanol, dried with a nitrogen stream, and reacted for 1 h in one of a 1% v/v OTS-toluene solution, 1% v/v ODTS solution, 0.1% v/v FPTS solution or 1% v/v PTS solution. Treated substrates were washed with toluene to remove unreacted silane and dried under a nitrogen stream followed by being baked under vacuum at 70 °C for 1 h before being transferred to a nitrogen glovebox. 6P surfaces were fabricated by thermally evaporating a 2 nm layer of 6P by physical vapor deposition (PVD) at 0.05 Å/s ($P < 2 \times 10^{-6}$ Torr) through a square shadow mask on a substrate held at 180 °C. OTFTs were then fabricated by thermally depositing a 500 Å-thick film of **F_{10}-SiPc** as the active semiconducting layer by PVD through a square shadow mask on substrates held at 100 °C at a rate of 0.2 Å/s ($P < 2 \times 10^{-6}$ Torr). Two corners of each substrate were then scratched with a diamond-tipped pen to expose bare silicon. Source-drain electrodes (L = 30 µm, W = 1000 µm) obtained by depositing 100 Å of manganese at a rate of 0.5 Å/s followed by 500 Å of silver at a rate of 1 Å/s through shadow masks obtained by Ossila to yield 20 individual transistors per substrate.

Electrical Characterization

Bottom-gate top-contact (BGTC) OTFTs were measured at room temperature in a nitrogen glovebox. Electrical characterization of BGTC OTFTs was performed using a custom-built autotester with brass alloy contact tips plated with 20 µm of gold on 100 µm of nickel. The autotester was connected to a Keithley 2614B source meter to set the gate-source voltage (V_{GS}) and source-drain voltage (V_{SD}) to measure the source-drain current (I_{SD}). Output curves were obtained by fixing V_{GS} at discrete values between 0 V and +60 V and sweeping V_{SD} between 0 and +50 V. Transfer characteristics were obtained by fixing V_{SD} in the saturation region at +50V and sweeping V_{GS} between 0 and +60V. During the measurement of transfer characteristics, V_{GS} was applied at a duty cycle of 20% and a frequency of 10 Hz to reduce gate bias stress. A duty cycle of 20% at a frequency of 10 Hz corresponds to gate vias stress being applied for a 20 ms (2 Hz) interval between 80 ms (8 Hz) intervals of zero applied gate bias stress. Applying a pulsed gate can improve device stability during operation and make the extraction of threshold voltage V_T more reliable.[23,31] The electron field-effect mobility (μ_e) was calculated using **Equation 4.1**:

$$I_{DS} = \frac{\mu_e C_i W}{2L}(V_{GS} - V_T)^2 \tag{4.1}$$

Where L and W represent the channel length and width, respectively. The capacitance of the gate dielectric (C_i) is calculated using $C_i = \frac{\varepsilon_0 \varepsilon_r}{d}$, where d is the thickness of the SiO_2 dielectric (230 nm), ε_r is the dielectric constant of SiO_2 and ε_0 is the permittivity of free space. μ_e was determined by calculating the slope of best fit of a 10V region of $\sqrt{I_{DS}}$ as a function of V_{GS} when the curve became linear. The threshold voltage (V_T) was calculated from the *x*-intercept of linearized data for $\sqrt{I_{DS}}$ vs V_{GS} in the same measurement range.

Atomic Force Microscopy (AFM)

AFM images were obtained with a Bruker Dimension Icon Atomic Force Microscope System, using ScanAsyst-Air probes, in ScanAsyst mode with a scan rate of 0.85 Hz.

Contact Angle Measurements

Contact angle measurements were obtained using a VCA Optima goniometer from AST Products Inc. 1.0 µm droplets of deionized water and diiodomethane (Merck) were deposited statically from a needle and imaged directly after using a five-point curve fitting. The dispersive component (γ^d) and a polar component (γ^p) of surface energy were calculated by solving a system of two equations of the same form with values for deionized water and diiodomethane.[32]

$$1 + cos\theta = \frac{2(\gamma_s^d)^{\frac{1}{2}}(\gamma_{lv}^d)^{\frac{1}{2}}}{\gamma_{lv}} + \frac{2(\gamma_s^p)^{\frac{1}{2}}(\gamma_{lv}^p)^{\frac{1}{2}}}{\gamma_{lv}} \tag{4.2}$$

Where $cos\theta$ is the contact angle of deionized water or diiodomethane on the substrate, γ_s^d and γ_s^p are the dispersive and polar components of the surface energy of the substrate, γ_{lv}^d and γ_{lv}^p are the dispersive and polar components of the surface energy of the reference liquid and γ_{lv} is the total surface energy of the reference liquid. The total surface energy (γ_{tot}) is the sum of the polar and dispersive components. The surface energy parameters for the reference liquids were γ_{lv}^{d} = 21.8 mJ/m^2, γ_{lv}^{p} = 51.0 mJ/m^2 and γ_{lv} = 72.8 mJ/m^2 for water and γ_{lv}^{d} = 49.5 mJ/m^2, γ_{lv}^{p} = 1.3 mJ/m^2 and γ_{lv} = 50.8 mJ/m^2 for diiodomethane.[32–34]

Grazing Incidence Wide-Angle X-Ray Scattering (GIWAXS)

GIWAXS measurements were performed at the SIRIUS beamline at the SOLEIL synchrotron in Saint-Aubin, France.[35] The sample to detector distance was 339 mm and the X-ray energy was 10 keV. The detector was placed at an angle of 8.9°. Grazing incidence patterns were taken at $\alpha = 0.1°$ with 10 images taken at an exposure time of 10 s each. The final spectra are the sum of 10 images. The GIWAXS data were calibrated against a silver behenate standard and analyzed using the GIXSGUI software package.[36]

4.3 Results and Discussion

OTFTs fabricated on monolayers **1 – 5** were prepared on Si/SiO$_2$ substrates with silver-manganese (AgMn) electrodes, using the fluorinated **F$_{10}$-SiPc** semiconductor (see Experimental section for fabrication procedure). Our group has demonstrated that Ag electrodes with an Mn interlayer are a cost-effective and high-performance alternative to Au electrodes owed to the lower work function of Mn, enabling better electron injection into the LUMO of **F$_{10}$-SiPc**, which according to inverse photoemission spectroscopy (IPES) is around 4 eV.[27] Substrates were held at 100 °C during the deposition of **F$_{10}$-SiPc** since this temperature has been demonstrated to yield improved thin-film texture and OTFTs with a higher average μ_e than those fabricated on substrates held at room temperature.[37] The results are highlighted in **Table 4.1**, where the OTS surface yields the highest μ_e and the lowest V_T, whereas the fluorinated FPTS has the lowest μ_e and the second highest V_T. Interestingly, the trend for relative μ_e differs from our previous results for the non-fluorinated bis(benzoate)silicon phthalocyanine (PhCOO-SiPc) where evaporation on ODTS yielded a slightly higher average μ_e and reduced V_T compared to OTS.[22] Additionally, unlike asymmetric solution-processed SiPcs with an axial fluorine group,[38] performance on FPTS was substantially worse for **F$_{10}$-SiPc**; the hypothesized F-F interactions of the asymmetrical system seem to be different from those observed with **F$_{10}$-SiPc**. Comparing these three data sets demonstrate that axial groups play a crucial role in interactions with the dielectric, and different considerations related to surface chemistry are required to optimize individual R$_2$-SiPcs in OTFTs.

Table 4.1 Electrical performance of F_{10}-SiPc evaporated on monolayers 1 – 5 with AgMn electrodes

Monolayer	**μ_e [$cm^2 \cdot V^{-1} \cdot s^{-1}$]^a (x 10^{-2})**	**V_T [V]^a**	**I_{on} [A]^b**	**I_{on}/I_{off}**	***n***
1 (OTS)	7.2 ± 4.5	8.0 ± 2.1	2.96×10^{-5}	10^5 - 10^6	38
2 (ODTS)	2.9 ± 0.9	17.0 ± 1.8	9.34×10^{-6}	10^5 - 10^6	36
3 (FPTS)	0.13 ± 0.07	12.6 ± 3.9	6.56×10^{-7}	10^3	35
4 (PhTS)	5.3 ± 1.2	11.3 ± 1.5	1.68×10^{-5}	10^5 - 10^6	37
5 (*p*-6P)	4.6 ± 1.4	8.0 ± 2.0	2.71×10^{-5}	10^5	34

a) μ_e and V_T were calculated based on mean values
b) I_{on} calculated based on median values

The surface energy (γ) of the dielectric surface used as a template for semiconductor film growth is a parameter that impacts the performance of materials in OTFTs.[34] The total surface energy (γ^{tot}) can be expressed as the sum of the dispersive component (γ^d) and a polar component (γ^p) which are related to the polarity of SAMs and can be determined by contact angle measurements using different solvents (see Experimental section).[32] Typically, low surface energies yield OTFTs with higher μs.[34] However, one recent study demonstrated that matching γ_{tot} to the surface energy of the semiconductor while maximizing γ^d and minimizing γ^p led to the highest μ for molecular single-crystal devices.[39] These results demonstrated that a complex interplay exists between the surface energy of the dielectric and resulting device performance. Similar studies have been applied to polycrystalline OTFTs,[33] including relationships between surface energy and OTFT performance for solution-processed R_2-SiPcs where increasing the water contact angle of silane-modified surfaces resulted in increasing device performance R_2-SiPcs. However, beyond a contact angle of 109° devices were no longer functional, indicating that there is a threshold beyond which R_2-SiPcs begin to have worse performance as dielectric surface energy decreases.[38] To this end, we measured the surface energy components of SAMs **1 – 5** using the Owens-Wendt method with deionized water and diiodomethane as reference liquids (**Figure 4.2**, **Table 4.2**) to investigate potential relationships between γ and device performance for **F_{10}-SiPc**-based OTFTs.

Table 4.2 Surface energy of SAM-modified dielectrics 1 – 5 on 230 nm-thick SiO_2 [a)]

Surface	**Contact Angle (degrees)**		γ_s^d **(mJ·m^{-2})**	γ_s^p **(mJ·m^{-2})**	γ^{tot} **(mJ·m^{-2})**
	DI Water	**Diiodomethane**			
1 (OTS)	80.27 ± 0.91	58.62 ± 2.77	25.61 ± 2.40	7.02 ± 1.16	32.63 ± 1.28
2 (ODTS)	102.88 ± 1.72	69.57 ± 1.37	22.37 ± 0.95	0.76 ± 0.23	23.13 ± 0.72
3 (FPTS)	89.78 ± 1.01	74.40 ± 0.35	17.61 ± 0.19	5.63 ± 0.14	23.24 ± 0.18
4 (PhTS)	80.27 ± 0.91	43.10 ± 1.47	34.89 ± 0.96	4.40 ± 0.52	39.28 ± 0.52
5 (*p*-6P)	79.32 ± 5.15	44.93 ± 2.10	33.66 ± 2.52	5.06 ± 3.32	38.71 ± 0.82
F_{10}-SiPc	94.91 ± 4.32	38.84 ± 3.11	40.18 ± 1.12	0.27 ± 0.06	40.45 ± 1.16

a) The total surface energy γ^{tot} is broken up into its dispersive component (γ^d) and a polar component (γ^p).

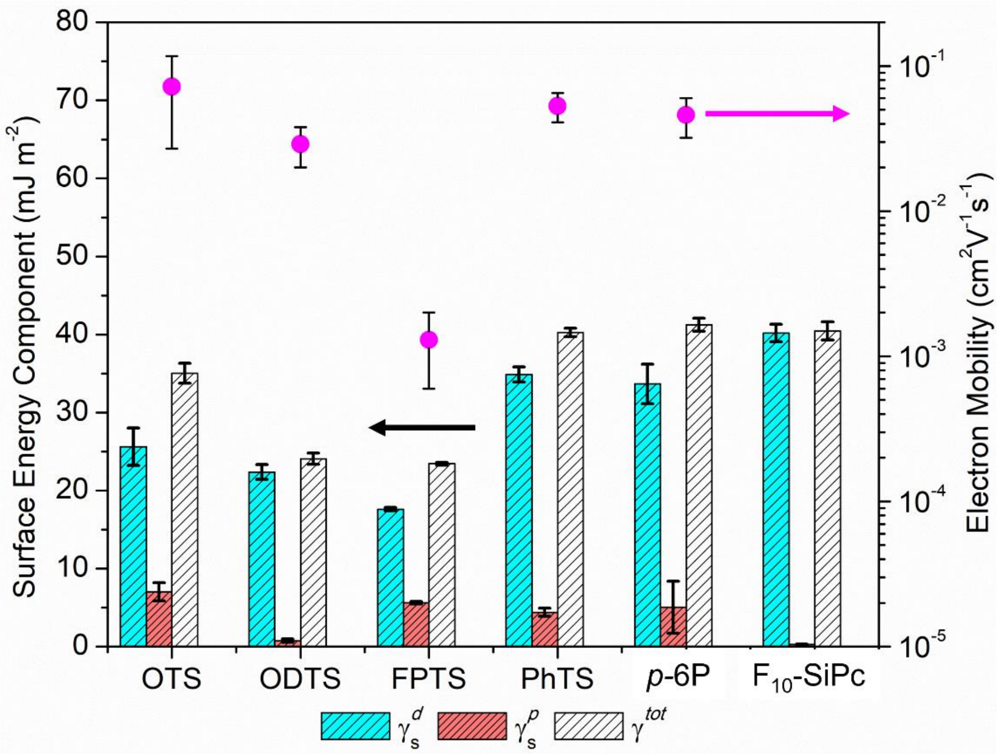

Figure 4.2 Comparison of surface energy (bars) of modified dielectrics and average μ_e (mangenta dots) of F_{10}-SiPc OTFTs. The total surface energy γ^{tot} is broken up into its dispersive component (γ^d) and a polar component (γ^p). The black line represents the total surface energy of an F_{10}-SiPc thin-film.

From our measurements, we expect OTS to have a higher overall surface energy than ODTS since in a similar study of phosphonic acids, increasing the length of the terminal alkyl group of an otherwise identical molecule resulted in reduced γ^d, γ^p and γ^{tot}.[40] FPTS and ODTS had the lowest γ^{tot} of all five surfaces and largest difference in γ^{tot} from **F_{10}-SiPc** and resulted in the worst-performing devices in this study. Furthermore, FPTS had a relatively large γ^p component as a percentage of its γ_{tot} and yielded devices with at least an order of magnitude lower μ_e than devices fabricated on ODTS. Devices with similar surface energies but worse performance as a result of a larger relative γ^p component is consistent with literature observations using other semiconductors.[39] Devices fabricated on PhTS and *p*-6P yielded similar results, with *p*-6P having a relatively larger γ^p component for similar surface energies and a worse average μ_e. Both SAMs were a better match for the surface energy of **F_{10}-SiPc** and resulted in higher average μ_e than devices fabricated on ODTS and FPTS, a trend which is consistent with literature observations for similar materials. Devices fabricated on OTS-modified SiO_2 resulted in the highest average μ_e despite the γ^{tot} of OTS being a relatively poor match for **F_{10}-SiPc** and OTS possessing a relatively large γ^p indicating that there may be more complex interactions that require consideration beyond surface energy matching. Based on these results, measuring γ^d, γ^p and γ^{tot} is useful for predicting how surface chemistry influences charge transport in **F_{10}-SiPc**-based OTFTs. Although the performance for organic single crystals[39] and highly ordered polymers[34] tend to align with the measured surface energy, evaporated polycrystalline pentacene thin-films display little correlation between charge transport and SAM surface energy for a range of novel SAMs.[41] Therefore, for polycrystalline thin-films it appears that other factors beyond the surface energy of the SAM, such as terminal group functionality, influence the resulting film morphologies, molecular orientation and resulting device performance.

Thin-Film Characterization

The microstructure and morphology of organic semiconducting films are critical to their performance in OTFTs.[42] Understanding the relationship between dielectric surface modification and the microstructure of these films will also further enable the development of relationships between the surface chemistry of the dielectric and performance of **F_{10}-SiPc** in OTFTs. Atomic force microscopy was performed on **F_{10}-SiPc** films evaporated on top of treated surfaces (**Figure 4.3**). **F_{10}-SiPc** evaporated on OTS yielded large, anisotropic features consistent with observations from our previous work.[25,37] **F_{10}-SiPc** evaporated on ODTS yielded a topography with large, anisotropic grains similar to OTS, but with different packing, yielding larger oriented features and larger grain boundaries. Films evaporated on FPTS and PhTS both yielded small, similarly sized isotropic features while films evaporated on *p*-6P yielded small, slightly anisotropic grains across the substrate. It is important to note that *p*-6P is a templating layer which is dissimilar to others in this study since it forms on the surface as aggregates with a second monolayer beginning to nucleate once the coverage of the initial monolayer reaches approximately 85%.[43] Therefore, there is potential for an uneven surface which is unfavourable for film growth that must be considered. An AFM image of a *p*-6P templating layer evaporated at an elevated substrate temperature of 180 °C is provided in the Supporting Information (**Figure 4.13**). This image demonstrates that while there is good surface coverage by the monolayer there is some exposed SiO_2 which may interrupt domain growth or result in different in-plane orientation similar to metal free phthalocyanine on *p*-6P-modified substrates.[44] To better quantify the differences in thin film microstructure and domain size from AFM images, radial power spectral density functions (PSDFs) of images were used (**Figure 4.3F**, **Table 4.3** of Supporting Information). PSDFs of AFM images provides comparable information to resonant soft X-ray scattering measurements and can provide information about domain size and size distribution.[45–47] The mode domain size of films evaporated on OTS and ODTS are nearly indistinguishable from each other (14.6 nm). Films evaporated on FPTS and *p*-6P yielded the smallest mode domain size (12.5 nm and 11.7 nm, respectively), while films evaporated on PhTS have an intermediate mode domain size (13.4 nm). The relatively small domain size of films evaporated on top of *p*-6P could be attributed to the interruption of nucleation and crystallization owing to the incomplete coverage of the SiO_2 substrate by the templating layer. Interestingly, while films evaporated on top of *p*-6P yield smaller domains than films evaporated on top of FPTS, the performance of resulting transistors is better by over one order of magnitude. This could potentially be attributed to better surface energy matching with the organic semiconductor F_{10}-SiPc or more favourable molecular orientation of some domains with respect to the substrate, which is a useful feature of WEG and *p*-6P.[16] The surfaces yielding the largest distribution of **F_{10}-SiPc** feature sizes are ODTS and PhTS (full-width half-maximum of 0.40 nm^{-1} and 0.46 nm^{-1}, respectively) with ODTS having a larger population of disproportionately small features (q = 0.8 nm^{-1} and q = 1.0 nm^{-1}). This population of disproportionately small features may result from large grain boundaries observed visually in the

AFM. While ODTS yields relatively large mode feature sizes, the broad distribution size (FWHM = 0.40 nm^{-1}) and large grain boundaries could corroborate the poor overall OTFTs performance of **F_{10}-SiPc** films on ODTS compared to films on surfaces that yield a smaller dispersion of better-connected crystallites.

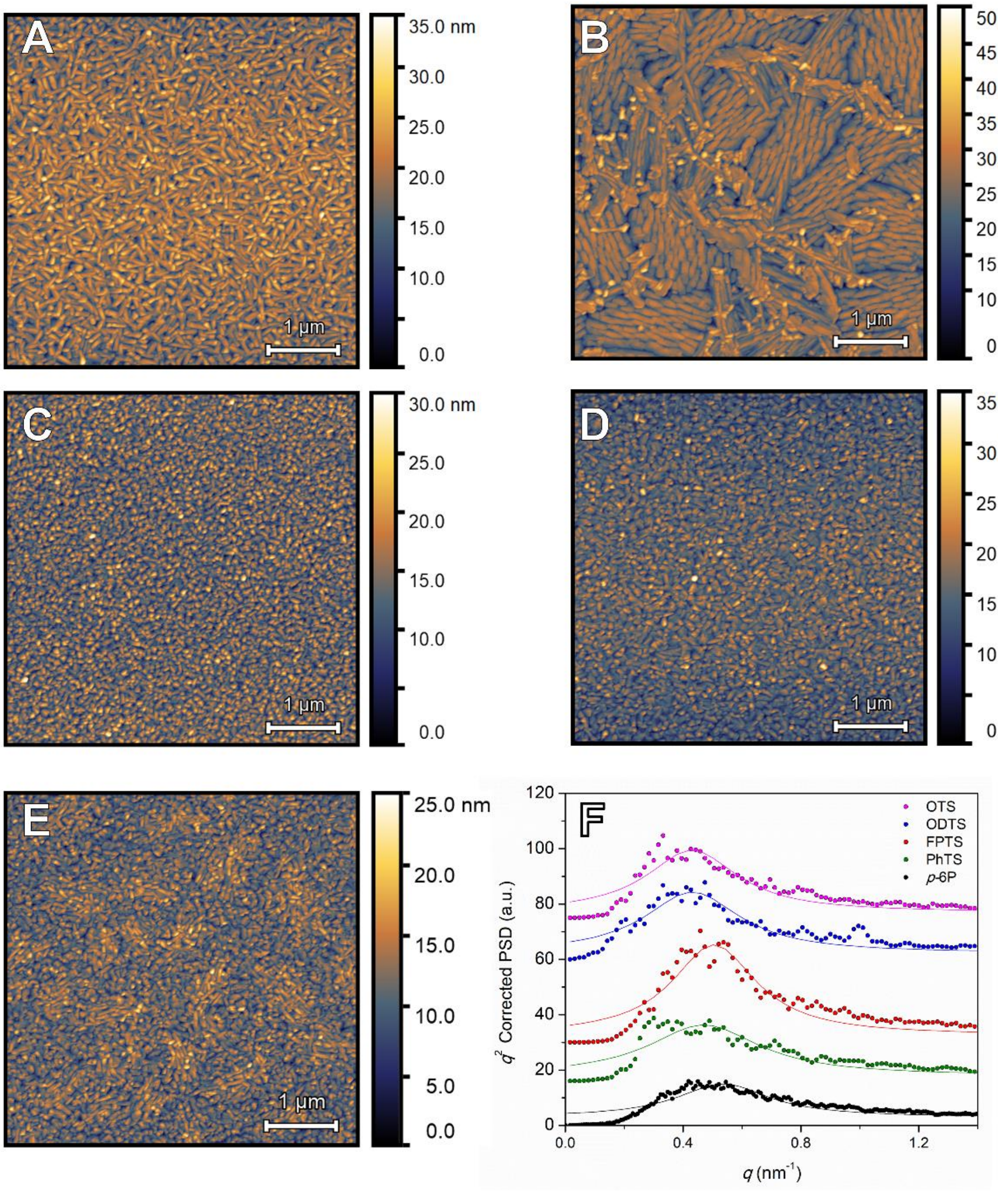

Figure 4.3 Atomic force microscopy images (5μm x 5μm) of 80 nm-thick films of F_{10}-SiPc films evaporated on top of monolayers A) OTS, B) ODTS, C) FPTS, D) PhTS, E) *p*-6P and F) radial power spectral density functions calculated from AFM height images and corrected by q^2. The raw data (symbols) are shown alongside Lorentzian fits as a guide to the eye.

Synchrotron radiation experiments are a valuable tool to further characterize semiconducting thin-films and develop relationships between structure, device architecture, processing conditions and OTFT performance.[48,49] For example having a greater degree of π-orbital overlap perpendicular to the channel (edge-on morphologies) often results in higher OTFT μs.[50,51] GIWAXS measurements were performed on films in this work with 2D scattering maps shown in **Figure 4.4**. Scattering data collected from GIWAXS provides insight into relative crystalline order and the amount of diffracting crystalline mass in films.[48] The beam flux was stable during measurements and all films were evaporated during the same deposition. Therefore, all films have comparable thicknesses, where relative intensities differ only in the amount of *crystalline* material in the film. Owing to the polycrystalline nature of films, quantitative analysis of crystalline mass could not be completed due to convolution of multiple diffraction planes in scattering peaks in the azimuth linecut (**Figure 4.14**). However, except for films evaporated on FPTS, where the electron density of fluorine at the surface could amplify scattering intensity,[52] relative crystallinity could be approximated by GIWAXS. A summary of the primary scattering feature corresponding to the (010) and (001) planes is found in **Table 4.4.** The relative crystalline mass of **F_{10}-SiPc** samples evaporated on top of monolayers **1 – 5** based on the integrated scattering feature from q = 0.55 to 0.70 Å^{-1} from largest quantity to smallest quantity is *p*-6P, OTS, PhTS, then ODTS.

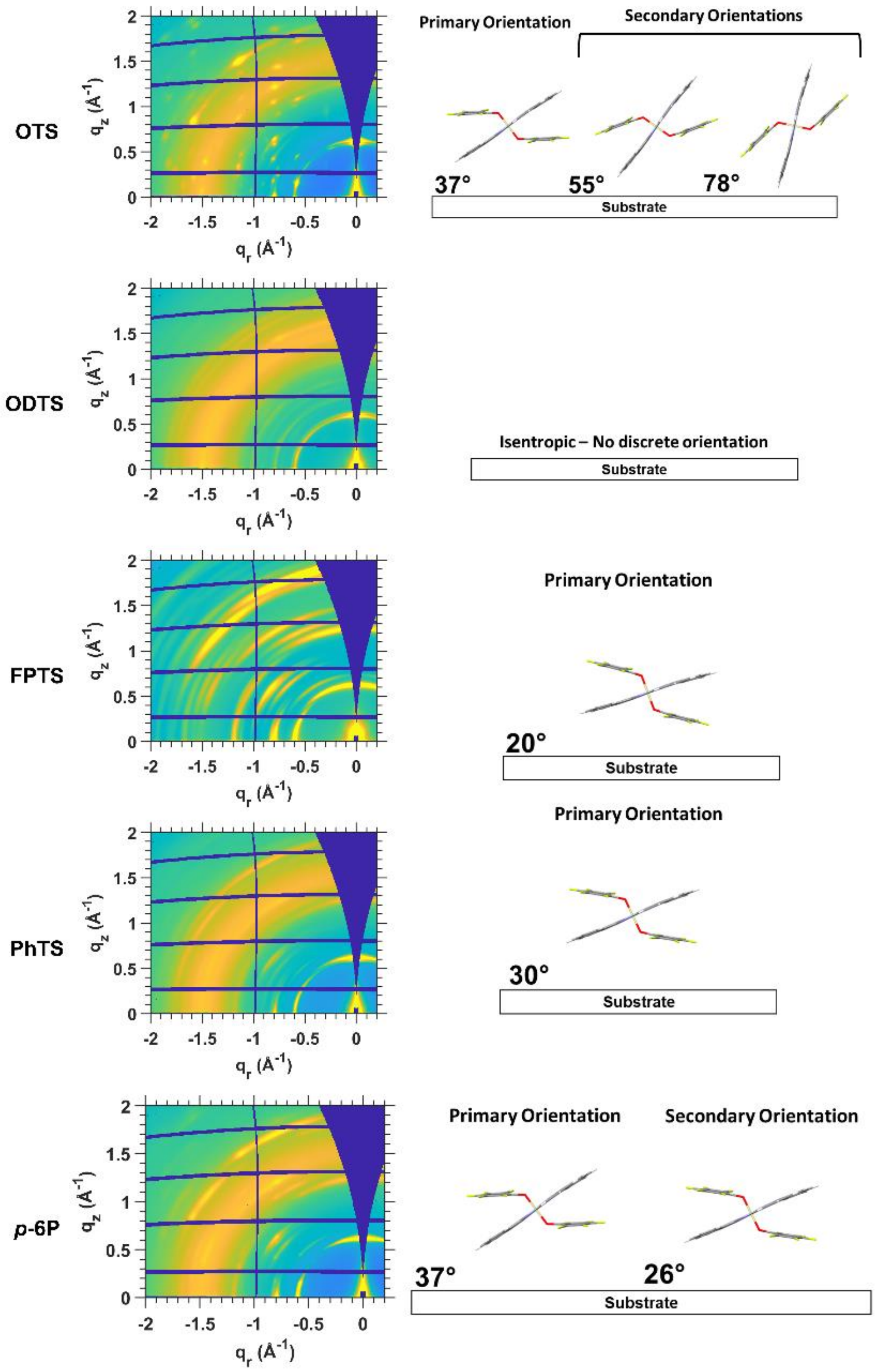

Figure 4.4 2D GIWAXS patterns for F_{10}-SiPc films deposited on treated SiO_2 surfaces with monolayers 1 – 5 and mode molecular orientation of F_{10}-SiPc relative to the substrate at the peak centre of scattering intensity features extracted from χ linecuts of the (132) plane (q = 1.9 Å^{-1})

Interestingly, while films evaporated on *p*-6P yielded relatively small domain features compared to other semiconductor films in this study, the relative amount of crystalline mass is among the largest, demonstrating that WEG is a useful technique for yielding crystalline films of R_2-SiPcs. However, unlike planar MPc molecules which typically stack standing up relative to the substrate, control over molecular orientation of tetravalent F_{10}-SiPc is not as straightforward. Additional information related to the orientations and packing modes can be extracted from χ linecuts (**Figure 4.15-4.19**), where χ is the angle of diffraction from the specular reflection to the horizontal axis (q_{xy}). From investigating linecuts in the χ direction (where χ is the angle between the q_r and the q_z axes) distributions of orientations of molecules relative to the substrate can be determined.[53] χ-direction linecuts in this work were analyzed at $q = 0.60$ Å^{-1} (001 phase), $q = 0.62$ Å^{-1} (010 phase), $q = 1.02$ Å^{-1} (1 -1 0 phase) $q = 1.80$ Å^{-1} (123 phase) and $q = 1.90$ Å^{-1} (132 phase). These regions were of interest because they enabled us to extract some molecular orientation distribution data without missing data because of space between detectors. While χ-direction linecuts were taken at multiple q values to corroborate mode molecular orientation angles, the $q = 1.90$ Å^{-1} (132 phase) is of particular interest because it is approximately parallel to the phthalocyanine ring and perpendicular to the π- π stacking direction. Therefore, electron transport likely occurs through this plane.[54] **F_{10}-SiPc** films evaporated on top of OTS (1) provided films with the narrowest distribution of orientations as shown by intense spot-like scattering features. This is further demonstrated by linecuts in the χ direction of scattering data corresponding to diffracting planes (**Figure 4.15 – 4.19**) where films evaporated on OTS yielded narrower features. Conversely, films evaporated on ODTS and FPTS yielded the broadest and second broadest (ring-like) scattering features, respectively, and therefore a broad distribution of molecular orientations relative to the substrate with ODTS having the lowest crystalline order relative to the substrate. Additionally, we observe the weakest relative signal strength of all samples for films evaporated on top of ODTS (**Figure 4.14**) indicative of a lower amount of crystalline material within the film. Films evaporated on PhTS and *p*-6P yielded sharper scattering features than those from films evaporated on ODTS and FPTS, which indicates a narrower distribution of orientations but were still not as well-ordered as films evaporated on OTS.

The major orientation of the (132) plane of **F_{10}-SiPc** evaporated on OTS is a narrow distribution with a mode angle of 37° from the substrate, with two minor modes at 55° and 78° (**Figure 4.4**); this is similar to what was observed in our previous work for **F_{10}-SiPc** films evaporated on top of OTS at room temperature.[25] Films evaporated on OTS are the only ones that demonstrated significant pseudo edge-on (greater than 45° Pc-stacking angle) orientation (**Figure 4**). The absence of edge-on packing modes is expected to severely limit the horizontal charge-transfer and reduce the μ_e.[53] Films evaporated on ODTS show minimal preferential orientation shown by arcs that span significant portions of the q range in the χ direction and no significant orientational scattering features in χ linecuts. **F_{10}-SiPc** films evaporated on top of FPTS and PhTS displayed one dominant crystallite orientation from χ linecuts, but with broader distributions around the mode value. Films evaporated on FPTS showed a large distribution of orientations, likely resulting in less conformity in the film; additionally, films on FPTS demonstrated a mode orientation with the MPc macrocycle (132)-plane only 20° from the substrate, the closest of all the films to a face-on orientation which should yield the poorest horizontal charge-carrier transport.[50] Films evaporated on PhTS and p-6P result in **F_{10}-SiPc** molecules that are similarly pseudo face-on, but the mode orientation is less parallel with the substrate (30° and 26-37°, respectively) and with a narrower relative distribution of orientations than films evaporated on FPTS. From the χ-linecut at $q = 1.02$ Å^{-1}, the scattering feature of films evaporated on FPTS have a FWHM of 18.4° compared to 14.0° and 10.2° for PhTS and p-6P, respectively, meaning that the packing mode has a broader overall distribution of orientations. It should be noted that p-6P has two overlapping distributions of orientations, as evidenced by a peak corresponding to the mode orientation having a shoulder (**Figure 4.17-4.19**), indicating that there may be some additional disorder at the semiconductor-dielectric interface present compared to films evaporated on PhTS owing to the observed incomplete coverage of the p-6P templating layer.

F_{10}-SiPc in films evaporated on top of p-6P templating layers are also relatively unique when compared with other MPcs. Typically, MPcs on p-6P demonstrate primarily edge-on or standing up orientations relative to the substrate.[17–19,55,56] While these literature observations demonstrate the benefits of p-6P for fabrication of highly crystalline films and well-oriented films of both planar MPcs and MPcs substituted with small axial groups, additional considerations are required for R_2-SiPcs including **F_{10}-SiPc**, which does not demonstrate primarily edge-on orientation or an improvement on μ_e when compared to benchmark devices fabricated on OTS. Compared to vanadyl phthalocyanine (VOPc) and dichlorotin phthalocyanine (Cl_2-SnPc), larger axial group of **F_{10}-SiPc** appears to dominate the interactions with the p-6P surface, resulting in mixed orientation of molecules at the surface of the substrate. Comparing the primary and secondary orientations of VOPc[56] and Cl_2-SnPc[55] on *p*-6P to **F_{10}-SiPc** on *p*-6P (**Figure 4.5**) shows the stark difference between the angle of the Pc ring, presumably due to the influence of the axial substitutions of **F_{10}-SiPc**. Overall, the axial groups of **F_{10}-SiPc** appear to result in films where molecules are oriented in a more face-on orientation than typical MPcs, and that OTS provides the strongest templating layer to yield films with a more pseudo face-on orientation.

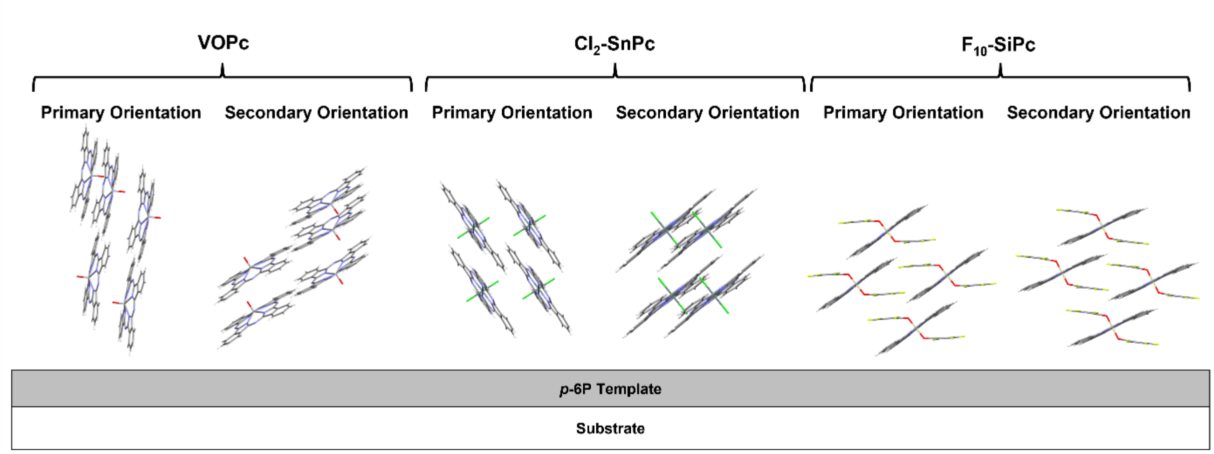

Figure 4.5 Primary and secondary mode molecular orientations for films of VOPc (ref. 53, CCDC 1017243), Cl_2-SnPc (ref. 52, CCDC 214377) and F_{10}-SiPc (this work) evaporated on top of *p*-6P.

Further insight of the relative performance of **F_{10}-SiPc** on different modified dielectrics can be extracted by analyzing AFM and GIWAXS data in tandem. Films evaporated on OTS have a relatively large mode aggregate size as extracted by AFM and most preferential orientation of π-π stacking relative to the substrate as demonstrated by χ linecuts. This preferential orientation where some molecules are oriented in a pseudo edge-on fashion combined with large aggregates are all favourable for charge transport.[49,57] While films evaporated on ODTS had similarly large aggregates, the lack of preferential ordering of molecules, relatively low amount of crystalline mass and large grain boundaries in the film yielded poor performance compared to OTS manifesting itself as a lower μ_e and higher V_T. Devices fabricated on FPTS-modified SiO_2 yielded **F_{10}-SiPc** films with the second-smallest mean and mode aggregate size and among the broadest distribution of ordered molecules relative to the substrate other than ODTS, with preferentially ordered molecules being primarily face-on. The combination of these factors in addition so the large surface energy mismatch likely resulted in OTFTs with poor μ_e. Finally, devices fabricated on PhTS and *p*-6P resulted in **F_{10}-SiPc** films with similar orientations and similar surface energy, however, *p*-6P surface layers yielded films with crystallites oriented relatively more face on than in films of PhTS and the resultant OTFTs had a lower average V_T. Molecular orientation can have an influence on the ionization potential of a semiconducting film[58] and on injection barrier between the source electrode and the semiconductor.[9] The V_T of OTFTs can be impacted by changes to the injection barrier.[59] For example, OTFTs fabricated with OTS and *p*-6P both have films with molecules having the most pseudo edge-on characteristics and have a similarly low average V_T of 8.0 V. OTFTs utilizing PhTS as the templating layer have films with the Pc-plane oriented at an average angle of 30° from the substrate compared to only 20° for FPTS and has a lower average V_T by 1.3V. OTFTs utilizing ODTS as a templating layer have an isotropic distribution with no preferential orientation and the highest average V_T. These results suggest that control of molecular orientation of **F_{10}-SiPc** could be important to reducing the operating voltage of devices, and demonstrate that interlayer functionality, surface energy and thin-film microstructure are closely related and are an important factor in determining appropriate device architectures for different materials.

4.4 Conclusion

In this work, we developed an understanding of the behaviour of **F_{10}-SiPc** as an organic semiconductor in OTFTs by exploring the influence of surface chemistry at the dielectric-semiconductor interface on grain structure and molecular orientation. **F_{10}-SiPc** evaporated on OTS-modified dielectrics yielded devices with the highest μ_e of all five conditions, which we attributed to films with the largest domain size as determined by PSDF analysis and crystalline domains of molecules with a pseudo edge-on orientation relative to the substrate. Conversely, films evaporated on FPTS yielded devices with the lowest μ_e of all five conditions, which we attributed to a relatively small average domain size and a broad distribution of primarily pseudo face-on molecular orientations. Surface energy measurements on all five templating layers and **F_{10}-SiPc** demonstrated that while matching the total surface energy of the **F_{10}-SiPc** layer does yield relatively good μ_e, however there are additional confounding factors to the optimization of polycrystalline thin-films that influence the morphology and solid-state structure, and ultimately the final device performance such as selection of templating layers that induce favourable molecular orientation for optimal charge transport parallel to the substrate. Films of **F_{10}-SiPc** with the mean molecular orientation of the π-stacking direction being more edge-on relative the substrate were also found to yield OTFTs with a lower average V_T, which could be related to the dependence of the injection barrier between the source electrode and semiconductor on molecular orientation. We also demonstrated that the phenoxy axial group of **R_2-SiPcs** result in different behaviour than other planar MPcs and planar molecules in the context of fabricating films by weak epitaxy growth (WEG), demonstrated by a mix of pseudo face-on orientations extracted from GIWAXS measurements, rather than adopting some degree of edge-on orientation for divalent CuPc and ZnPc or Cl_2-SnPc. While the WEG method still yielded relatively well-ordered films with a relatively large amount of crystalline mass, pentafluorophenoxy axial groups evidently interact with the monolayer, therefore complicating interactions that occur at the semiconductor-dielectric interface compared to divalent and unsubstituted tetravalent analogues. This work therefore demonstrates that axial groups of **R_2-SiPc**s and potentially other MPcs play a significant role in the molecular orientation at the interface as a result of changes in interaction with the surface chemistry and that this chemical handle may be a useful tool in tuning semiconductor-substrate interactions, and ultimately improving the device performance.

Acknowledgements

This work was supported by NSERC Discovery grant RGPIN 2020-04079 (B.H.L.), the Canada Research Chairs Program 950-230724 (B.H.L.) and NSERC CGS-D (B.K. and C.L.R.). Infrastructure used to complete this work was acquired using CFI-JELF #30488 (B.H.L.) and NSERC RTI 472921-2015 (B.H.L.). We recognize the Centre for Research in Photonics at the University of Ottawa (CRPuO) for allowing access to the AFM. The authors express gratitude to SOLEIL Synchrotron facility in Saint-Aubin, France for providing beamtime for GIWAXS measurements and to beamline scientist Arnaud Hemmerle.

Supporting Information

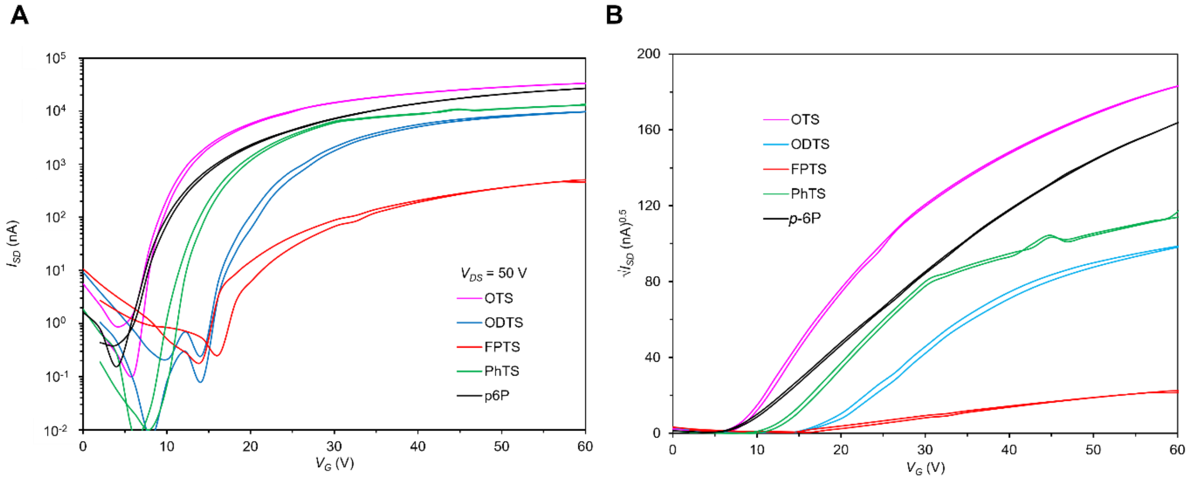

Figure 4.6 A) Transfer curves and B) $\sqrt{I_{SD}}$ vs V_G curves for F$_{10}$-SiPc OTFTs where V_{DS} = 50 V.

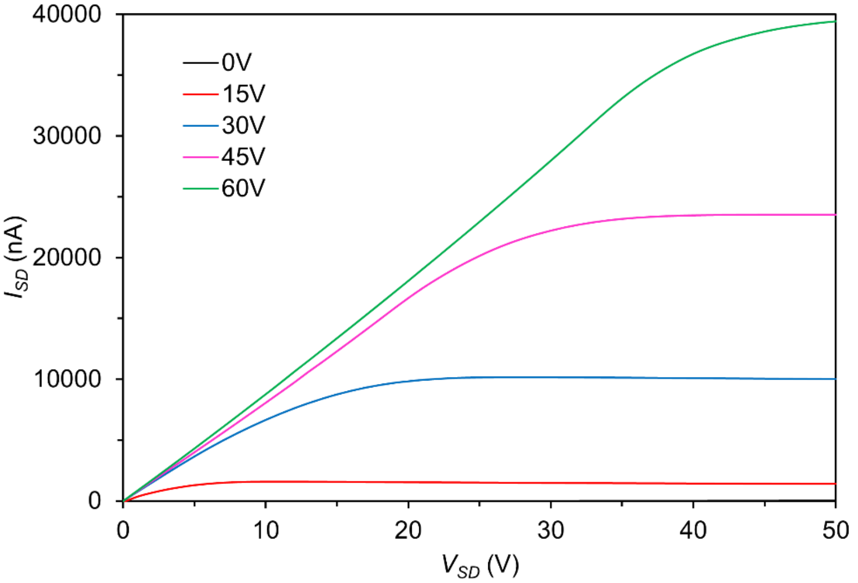

Figure 4.7 Output curves for F$_{10}$-SiPc OTFTs fabricated on OTS (1)

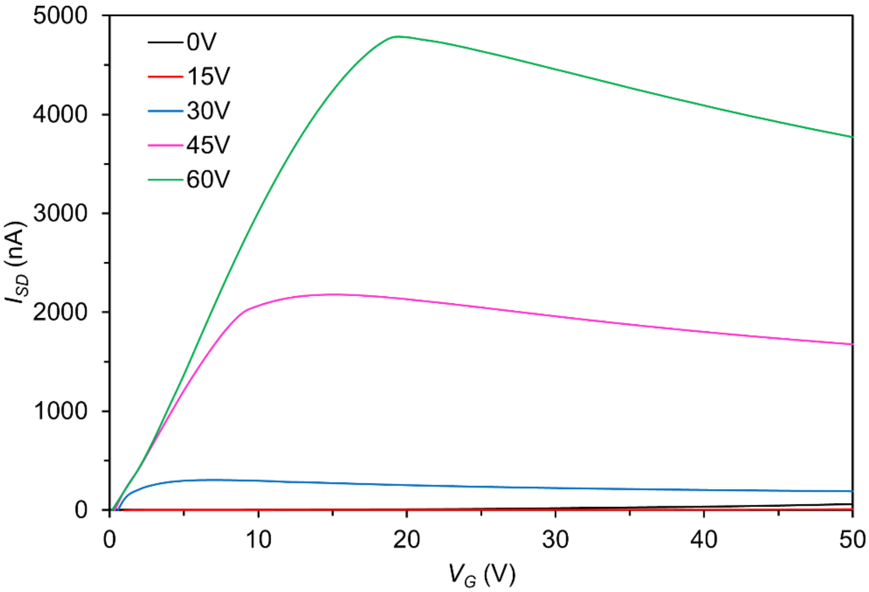

Figure 4.8 Output curves for F_{10}-SiPc OTFTs fabricated on ODTS (2)

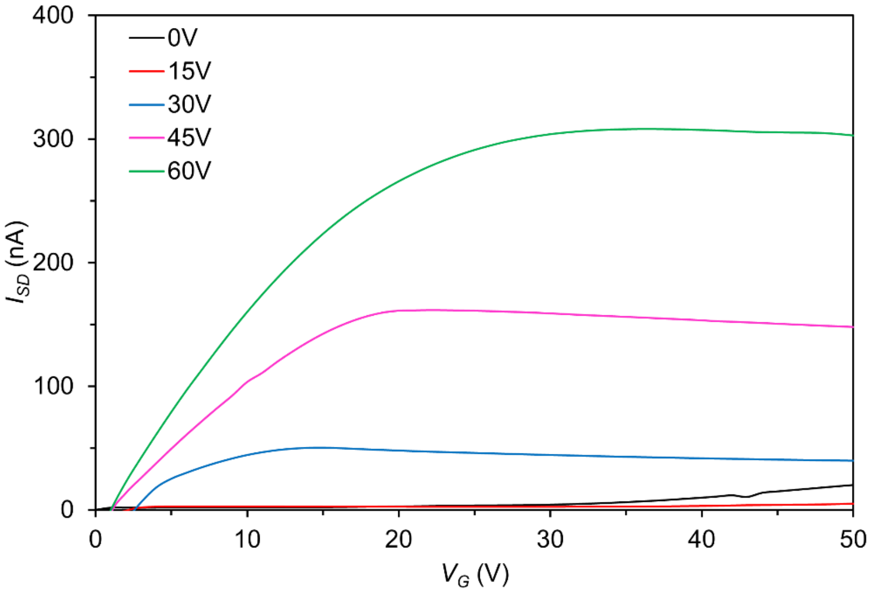

Figure 4.9 Output curves for F_{10}-SiPc OTFTs fabricated on FPTS (3)

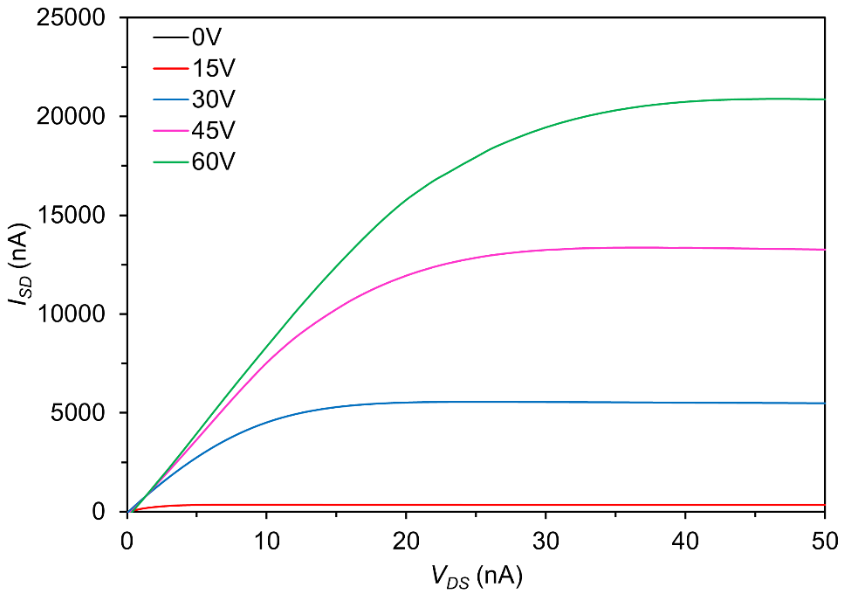

Figure 4.10 Output curves for F_{10}-SiPc OTFTs fabricated on PhTS (4)

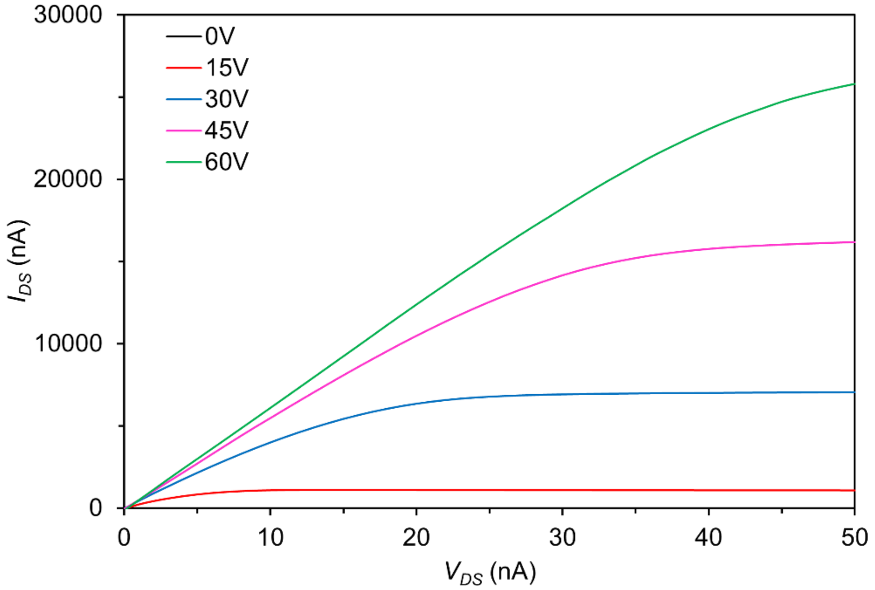

Figure 4.11 Output curves for F_{10}-SiPc OTFTs fabricated on *p*-6P (5)

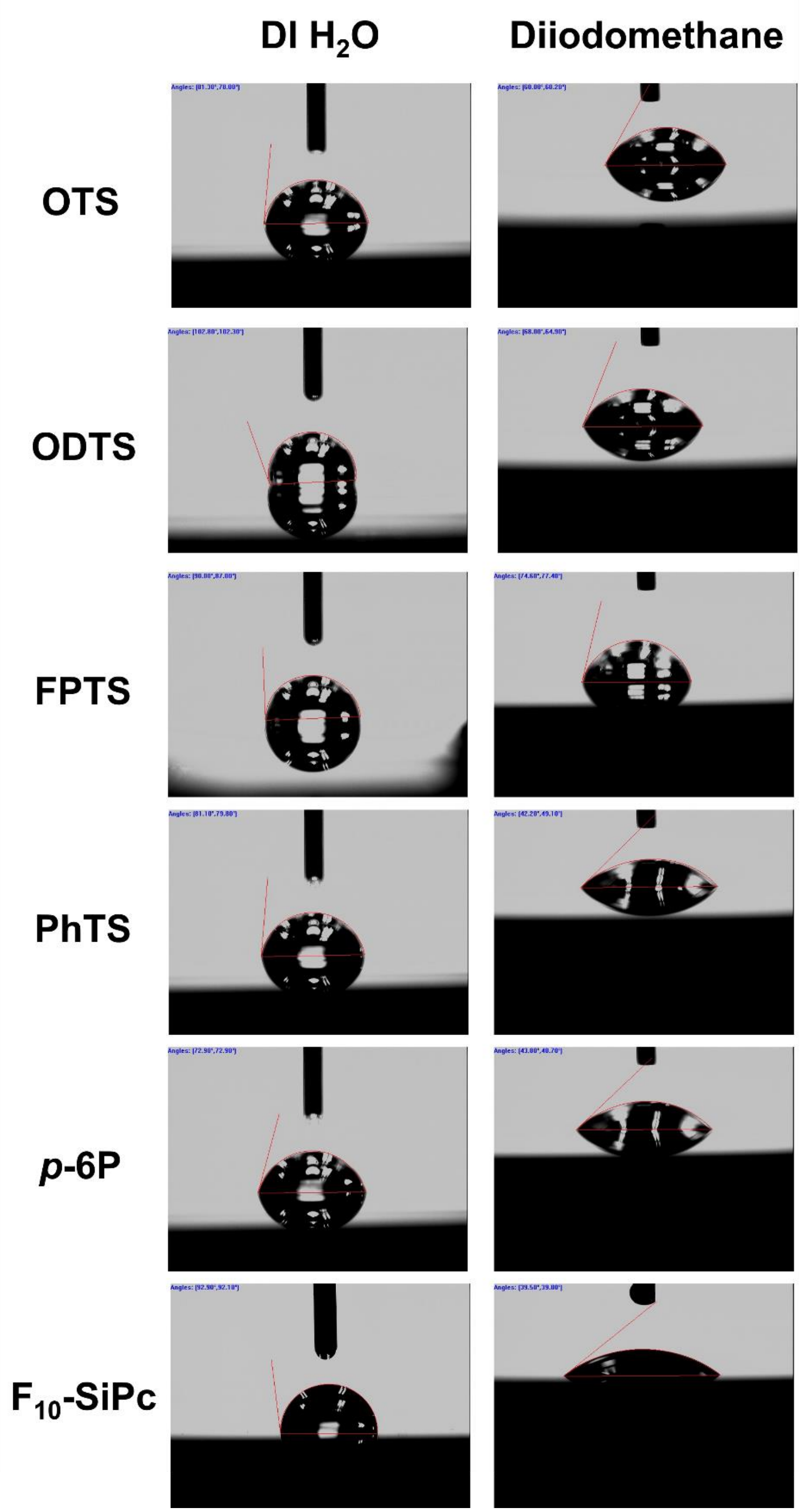

Figure 4.12 Contact angle images using solvents A-E) deionized water and F-J) diiodomethane on films of F_{10}-SiPc evaporated on top of OTS, ODTS, FPTS, PhTS and *p*-6P

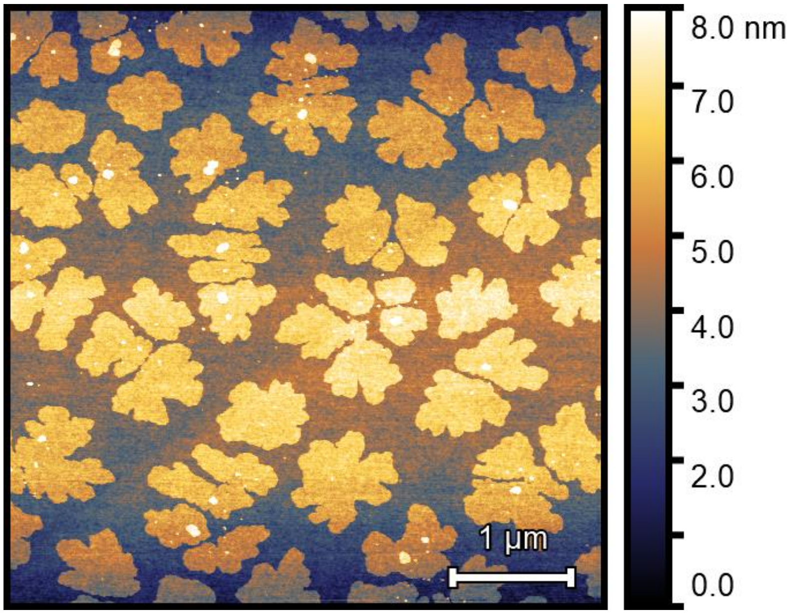

Figure 4.13 AFM image of *p*-6P thermally evaporated on 230 nm-thick SiO_2 at a substrate temperature of 180 °C.

Table 4.3 Radial power spectral density values calculated from AFM height images and corrected by q^2.

Surface	Iq^2_{max}	Mode Domain Size (nm)	FWHM
1 (OTS)	0.332	14.6	0.375
2 (ODTS)	0.332	14.6	0.395
3 (FPTS)	0.537	12.6	0.349
4 (PhTS)	0.300	13.4	0.458
5 (*p*-6P)	0.450	11.7	0.384

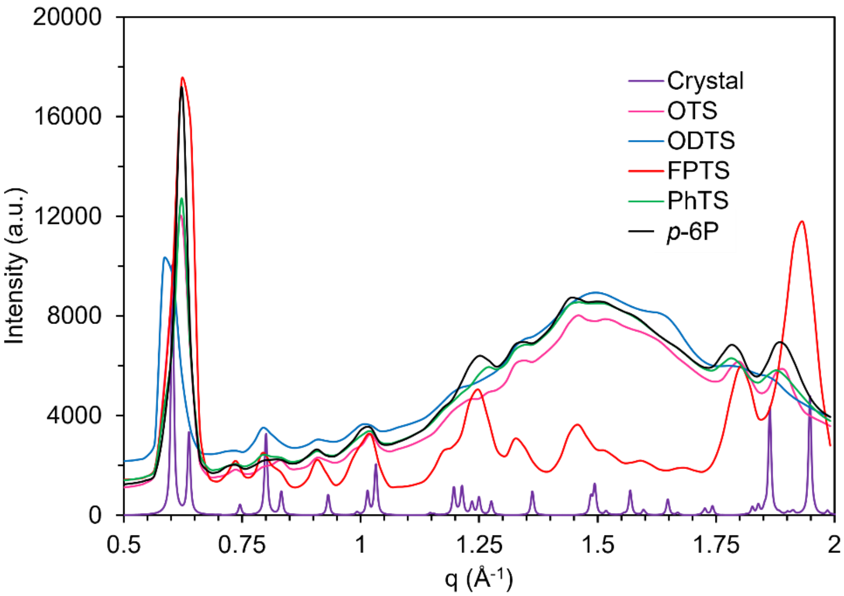

Figure 4.14 Azimuth linecuts of F_{10}-SiPc evaporated on modified dielectrics 1 – 5 and single crystal X-ray diffraction pattern of F_{10}-SiPc (CCDC deposit #1034275)

Table 4.4 Position, peak integration and peak height of azimuth linecut scattering feature of F_{10}-SiPc films evaporated on modified dielectrics 1 – 5, encompassing the (010) and (001) planes, taken from q = 0.55 Å^{-1} to q = 0.70 Å^{-1}.

Surface	Peak Centre	Area	Height
1 (OTS)	0.616	605.52	10984
2 (ODTS)	0.597	540.27	9785
3 (FPTS)[a]	0.625	915.09	17554
4 (PhTS)	0.621	586.55	11234
5 (*p*-6P)	0.621	676.87	16051

a) Electron density of fluorine at the semiconductor-dielectric interface may enhance X-ray scattering of films deposited on FPTS.

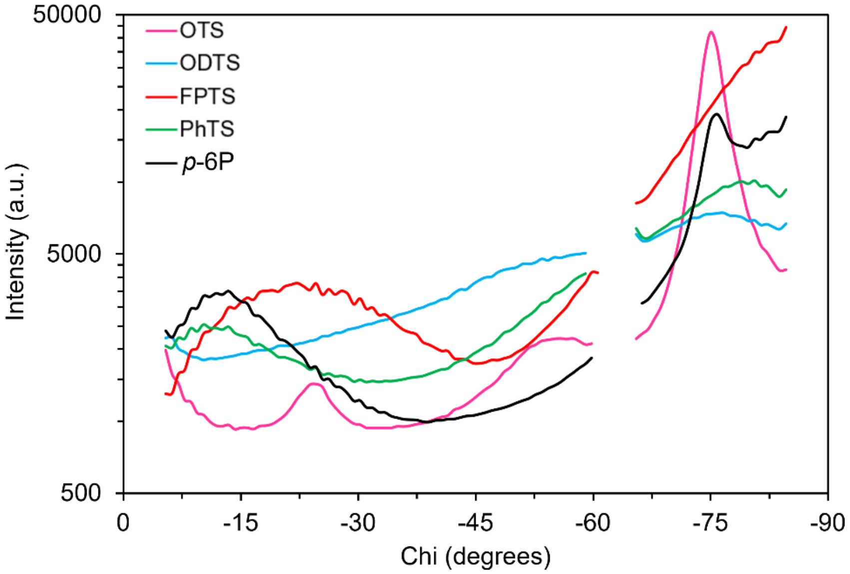

Figure 4.15. Linecut in the χ-direction at q = 0.60 Å^{-1} for films of F_{10}-SiPc evaporated on modified dielectrics 1 – 5, corresponding to the (001) phase.

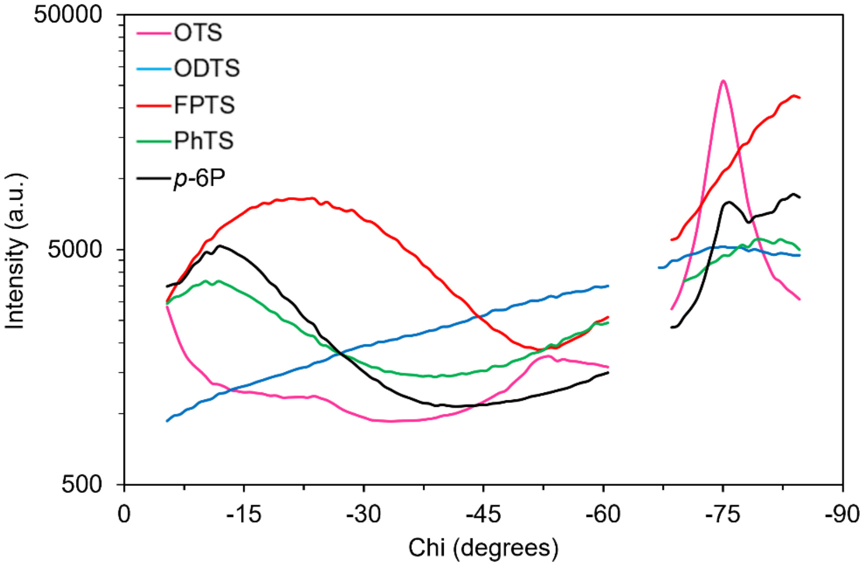

Figure 4.16 Linecut in the χ-direction at q = 0.62 Å^{-1} for films of F_{10}-SiPc evaporated on modified dielectrics 1 – 5, corresponding to the (010) plane.

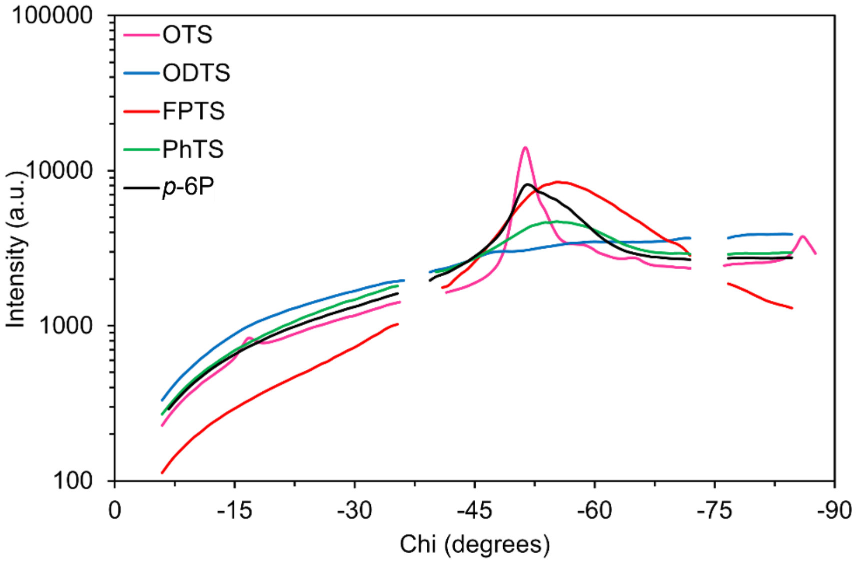

Figure 4.17 Linecut in the χ-direction at q = 1.02 Å^{-1} for films of F_{10}-SiPc evaporated on modified dielectrics 1 – 5, corresponding to the (1-10) plane.

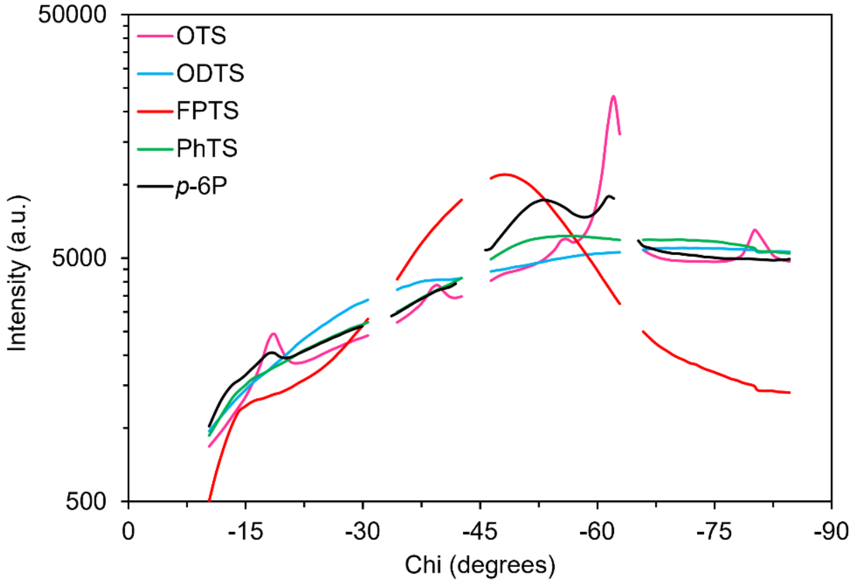

Figure 4.18 Linecut in the χ-direction at q = 1.80 Å^{-1} for films of F_{10}-SiPc evaporated on modified dielectrics 1 – 5, corresponding to the (123) phase

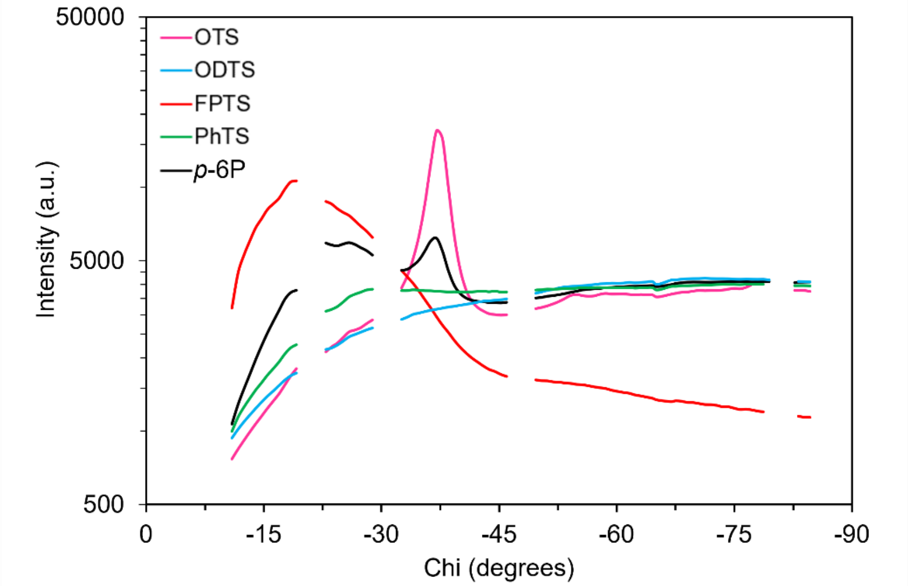

Figure 4.19 Linecut in the χ-direction at q = 1.90 Å^{-1} for films of F_{10}-SiPc evaporated on modified dielectrics 1 – 5, corresponding to the (132) plane.

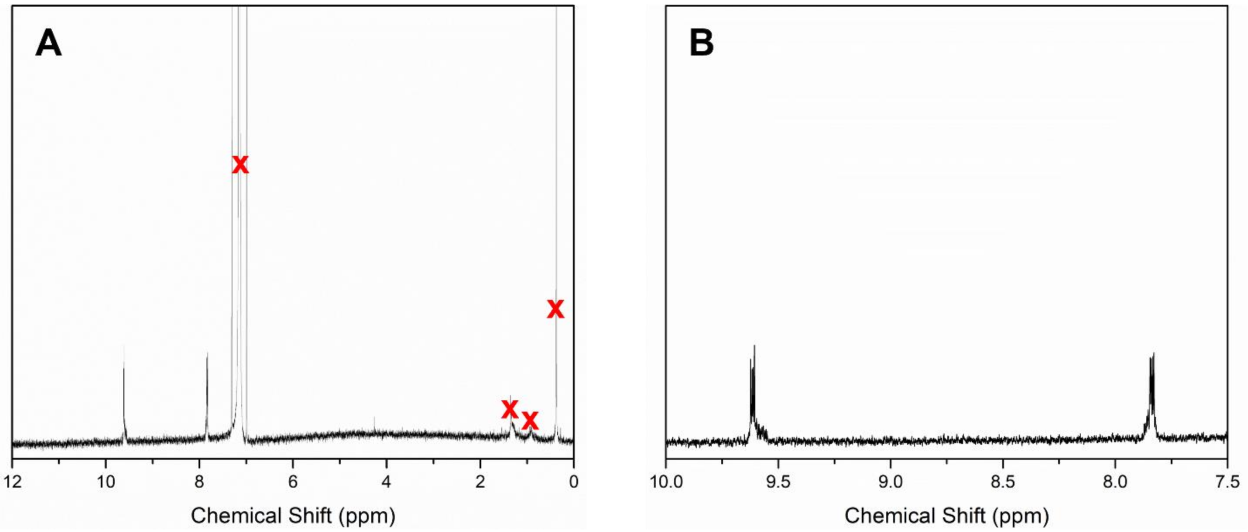

Figure 4.20 A) Complete and B) inset ^{1}H NMR spectra of F_{10}-SiPc in C_6D_6. Solvent peaks are marked by a red X.

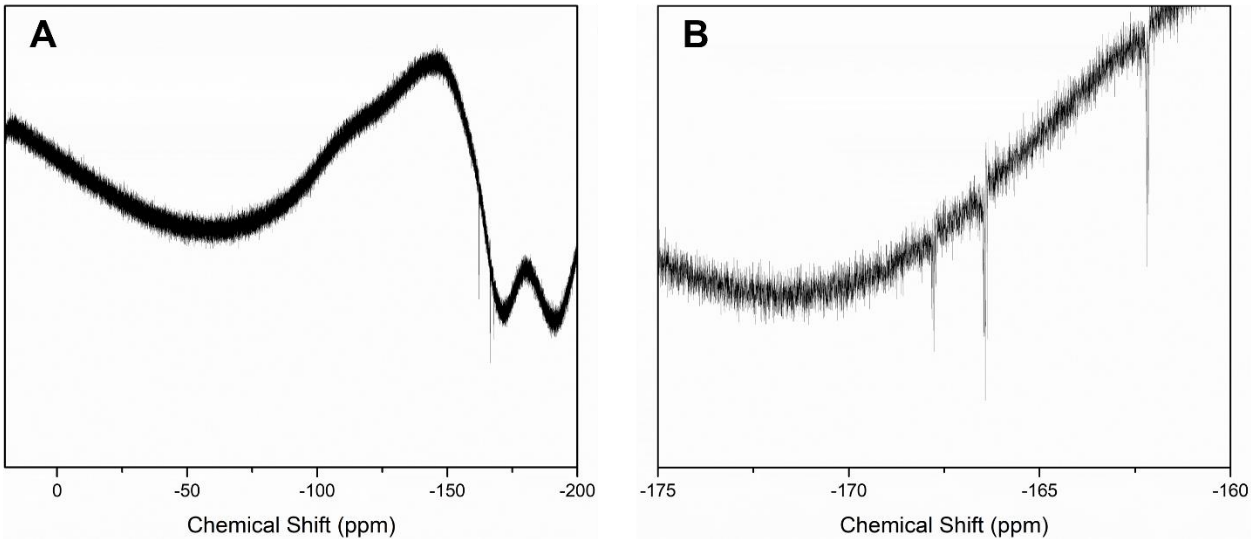

Figure 4.21. A) Complete and B) inset ^{19}F NMR spectra of F_{10}-SiPc in C_6D_6.

References

(1) Yadav, S.; Kumar, P.; Ghosh, S. Optimization of Surface Morphology to Reduce the Effect of Grain Boundaries and Contact Resistance in Small Molecule Based Thin Film Transistors. *Appl. Phys. Lett.* **2012**, *101* (19). https://doi.org/10.1063/1.4766913.

(2) Virkar, A. A.; Mannsfeld, S.; Bao, Z.; Stingelin, N. Organic Semiconductor Growth and Morphology Considerations for Organic Thin-Film Transistors. *Adv. Mater.* **2010**, *22* (34), 3857–3875. https://doi.org/10.1002/adma.200903193.

(3) Haneef, H. F.; Zeidell, A. M.; Jurchescu, O. D. Charge Carrier Traps in Organic Semiconductors: A Review on the Underlying Physics and Impact on Electronic Devices. *J. Mater. Chem. C* **2020**, *8* (3), 759–787. https://doi.org/10.1039/c9tc05695e.

(4) Kim, K.; An, T. K.; Kim, J.; Jeong, Y. J.; Jang, J.; Kim, H.; Baek, J. Y.; Kim, Y. H.; Kim, S. H.; Park, C. E. Grafting Fluorinated Polymer Nanolayer for Advancing the Electrical Stability of Organic Field-Effect Transistors. *Chem. Mater.* **2014**, *26* (22), 6467–6476. https://doi.org/10.1021/cm5030266.

(5) Ito, Y.; Virkar, A. A.; Mannsfeld, S.; Joon, H. O.; Toney, M.; Locklin, J.; Bao, Z. Crystalline Ultrasmooth Self-Assembled Monolayers of Alkylsilanes for Organic Field-Effect Transistors. *J. Am. Chem. Soc.* **2009**, *131* (26), 9396–9404. https://doi.org/10.1021/ja9029957.

(6) Aghamohammadi, M.; Rödel, R.; Zschieschang, U.; Ocal, C.; Boschker, H.; Weitz, R. T.; Barrena, E.; Klauk, H. Threshold-Voltage Shifts in Organic Transistors Due to Self-Assembled Monolayers at the Dielectric: Evidence for Electronic Coupling and Dipolar Effects. *ACS Appl. Mater. Interfaces* **2015**, *7* (41), 22775–22785. https://doi.org/10.1021/acsami.5b02747.

(7) Salinas, M.; Jäger, C. M.; Amin, A. Y.; Dral, P. O.; Meyer-Friedrichsen, T.; Hirsch, A.; Clark, T.; Halik, M. The Relationship between Threshold Voltage and Dipolar Character of Self-Assembled Monolayers in Organic Thin-Film Transistors. *J. Am. Chem. Soc.* **2012**, *134* (30), 12648–12652. https://doi.org/10.1021/ja303807u.

(8) Shin, N.; Schellhammer, K. S.; Lee, M. H.; Zessin, J.; Hambsch, M.; Salleo, A.; Ortmann, F.; Mannsfeld, S. C. B. Electronic Doping and Enhancement of N-Channel Polycrystalline OFET Performance through Gate Oxide Modifications with Aminosilanes. *Adv. Mater. Interfaces* **2021**, *8* (16), 1–12. https://doi.org/10.1002/admi.202100320.

(9) Li, P.; Lu, Z. Interface Engineering in Organic Electronics : Energy-Level Alignment and Charge Transport. *Small Sci.* **2021**, *1* (1), 2000015 (1-20). https://doi.org/10.1002/smsc.202000015.

(10) Virkar, A. A.; Mannsfeld, S. C. B.; Bao, Z. Energetics and Stability of Pentacene Thin Films on Amorphous and Crystalline Octadecylsilane Modified Surfaces. *J. Mater. Chem.* **2010**, *20* (13), 2664–2671. https://doi.org/10.1039/b921767c.

(11) Yang, S. Y.; Shin, K.; Park, C. E. The Effect of Gate-Dielectric Surface Energy on Pentacene Morphology and Organic Field-Effect Transistor Characteristics. *Adv. Funct. Mater.* **2005**, *15* (11), 1806–1814. https://doi.org/10.1002/adfm.200400486.

(12) Wang, S.; Wang, Z.; Li, J.; Li, L.; Hu, W. Surface-Grafting Polymers: From Chemistry to Organic Electronics. *Mater. Chem. Front.* **2020**, *4* (3), 692–714. https://doi.org/10.1039/c9qm00450e.

(13) Lee, S.; Jang, M.; Yang, H. Optimized Grafting Density of End-Functionalized Polymers to Polar Dielectric Surfaces for Solution-Processed Organic Field-Effect Transistors. *ACS Appl. Mater. Interfaces* **2014**, *6* (22), 20444–20451. https://doi.org/10.1021/am506024s.

(14) Celle, C.; Suspène, C.; Ternisien, M.; Lenfant, S.; Guérin, D.; Smaali, K.; Lmimouni, K.; Simonato, J. P.; Vuillaume, D. Interface Dipole : Effects on Threshold Voltage and Mobility for Both

Amorphous and Poly-Crystalline Organic Field Effect Transistors. *Org. Electron.* **2014**, *15* (3), 729–737. https://doi.org/10.1016/j.orgel.2014.01.003.

(15) Nakano, M.; Osaka, I.; Takimiya, K. Control of Major Carriers in an Ambipolar Polymer Semiconductor by Self-Assembled Monolayers. *Adv. Mater.* **2017**, *29* (1). https://doi.org/10.1002/adma.201602893.

(16) Yang, J.; Yan, D. Weak Epitaxy Growth of Organic Semiconductor Thin Films. *Chem. Soc. Rev.* **2009**, *38* (9), 2634–2645. https://doi.org/10.1039/b815723p.

(17) Yang, J.; Yan, D.; Jones, T. S. Molecular Template Growth and Its Applications in Organic Electronics and Optoelectronics. *Chem. Rev.* **2015**, *115* (11), 5570–5603. https://doi.org/10.1021/acs.chemrev.5b00142.

(18) Wang, H.; Zhu, F.; Yang, J.; Geng, Y.; Yan, D. Weak Epitaxy Growth Affording High-Mobility Thin Films of Disk-like Organic Semiconductors. *Adv. Mater.* **2007**, *19* (16), 2168–2171. https://doi.org/10.1002/adma.200602566.

(19) Zhang, Y.; Wei, X.; Zhang, H.; Chen, X.; Wang, J. Ambipolar Organic Transistors with High on/off Ratio by Introducing a Modified Layer of Gate Insulator. *Appl. Surf. Sci.* **2018**, *427*, 452–457. https://doi.org/10.1016/j.apsusc.2017.08.116.

(20) Guo, J.; Liu, D.; Li, W.; Yu, B.; Tian, H.; Zhu, F.; Yan, D. High-Performance 2,9-DPh-DNTT Organic Thin-Film Transistor by Weak Epitaxy Growth Method. *Org. Electron.* **2021**, *93* (December 2020), 2–7. https://doi.org/10.1016/j.orgel.2021.106170.

(21) Raboui, H.; Lough, A. J.; Plint, T.; Bender, T. P. Position of Methyl and Nitrogen on Axial Aryloxy Substituents Determines the Crystal Structure of Silicon Phthalocyanines. *Cryst. Growth Des.* **2018**, *18* (5), 3193–3201. https://doi.org/10.1021/acs.cgd.8b00298.

(22) Melville, O. A.; Grant, T. M.; Lessard, H. Silicon Phthalocyanines as N-Type Semiconductors in Organic Thin Film Transistors. *J. Mater. Chem. C* **2018**, *6*, 5482–5488. https://doi.org/10.1039/c8tc01116h.

(23) Melville, O. A.; Grant, T. M.; Mirka, B.; Boileau, N. T.; Park, J.; Lessard, B. H. Ambipolarity and Air Stability of Silicon Phthalocyanine Organic Thin-Film Transistors. *Adv. Electron. Mater.* **2019**, *1900087*, 1–7. https://doi.org/10.1002/aelm.201900087.

(24) Lessard, B. H. The Rise of Silicon Phthalocyanine : From Organic Photovoltaics to Organic Thin Film Transistors. *ACS Appl. Mater. Interfaces* **2021**, *13* (27), 31321–31330. https://doi.org/10.1021/acsami.1c06060.

(25) King, B.; Melville, O. A.; Rice, N. A.; Kashani, S.; Tonnelé, C.; Raboui, H.; Swaraj, S.; Grant, T. M.; McAfee, T.; Bender, T. P.; Ade, H.; Castet, F.; Muccioli, L.; Lessard, B. H. Silicon Phthalocyanines for N-Type Organic Thin-Film Transistors: Development of Structure–Property Relationships. *ACS Appl. Electron. Mater.* **2021**, *3* (1), 325–336. https://doi.org/10.1021/acsaelm.0c00871.

(26) King, B.; Daszcynski, A. J.; Rice, N. A.; Peltekoff, A. J.; Yutronkie, N. J.; Lessard, B. H.; Brusso, J. L. Cyanophenoxy-Substituted Silicon Phthalocyanines for Low Threshold Voltage n-Type Organic Thin-Film Transistors. *ACS Appl. Electron. Mater.* **2021**, *3* (5), 2212–2223. https://doi.org/10.1021/acsaelm.1c00175.

(27) Melville, O. A.; Grant, T. M.; Lochhead, K.; King, B.; Ambrose, R.; Rice, N. A.; Boileau, N. T.; Peltekoff, A. J.; Tousignant, M.; Hill, I. G.; Lessard, B. H. Contact Engineering Using Manganese, Chromium, and Bathocuproine in Group 14 Phthalocyanine Organic Thin-Film Transistors. *ACS Appl. Electron. Mater.* **2020**, *2* (5), 1313–1322. https://doi.org/10.1021/acsaelm.0c00104.

(28) Shao, X.; Wang, S.; Li, X.; Su, Z.; Chen, Y.; Xiao, Y. Single Component P-, Ambipolar and n-Type OTFTs Based on Fluorinated Copper Phthalocyanines. *Dye. Pigment.* **2016**, *132*, 378–386. https://doi.org/10.1016/j.dyepig.2016.05.020.

(29) Cranston, R. R.; Lessard, B. H. Metal Phthalocyanines: Thin-Film Formation, Microstructure, and Physical Properties. *RSC Adv.* **2021**, *11* (35), 21716–21737. https://doi.org/10.1039/d1ra03853b.

(30) Cranston, R. R.; Vebber, M. C.; Rice, N. A.; Tonnelé, C.; Castet, F.; Muccioli, L.; Brusso, J. L.; Lessard, B. H. N-Type Solution-Processed Tin versus Silicon Phthalocyanines: A Comparison of Performance in Organic Thin-Film Transistors and in Organic Photovoltaics. *ACS Appl. Electron. Mater.* **2021**, *3* (4), 1873–1885. https://doi.org/10.1021/acsaelm.1c00114.

(31) Sirringhaus, H. Reliability of Organic Field-Effect Transistors. *Adv. Mater.* **2009**, *21* (38–39), 3859–3873. https://doi.org/10.1002/adma.200901136.

(32) Owens, D. K.; Wendt, R. C. Estimation of Surface Free Energy of Polymers. *J. Appl. Polym. Sci.* **1969**, *13*, 1741–1747. https://doi.org/https://doi.org/10.1002/app.1969.070130815.

(33) Zhao, C.; Li, A.; Chen, X.; Ali, M. U.; Meng, H. Hysteresis Effect in Organic Thin Film Transistors Based on Naphthalene Tetracarboxylic Diimide Derivatives. *Appl. Phys. Lett.* **2021**, *118* (19). https://doi.org/10.1063/5.0045183.

(34) Umeda, T.; Kumaki, D.; Tokito, S. Surface-Energy-Dependent Field-Effect Mobilities up to 1 Cm2 /V s for Polymer Thin-Film Transistor. *J. Appl. Phys.* **2009**, *105* (2). https://doi.org/10.1063/1.3072669.

(35) Fontaine, P.; Ciatto, G.; Aubert, N.; Goldmann, M. Soft Interfaces and Resonant Investigation on Undulator Source: A Surface X-Ray Scattering Beamline to Study Organic Molecular Films at the SOLEIL Synchrotron. *Sci. Adv. Mater.* **2014**, *6* (11), 2312–2316. https://doi.org/https://doi.org/10.1166/sam.2014.2189.

(36) Jiang, Z. GIXSGUI: A MATLAB Toolbox for Grazing-Incidence X-Ray Scattering Data Visualization and Reduction, and Indexing of Buried Three-Dimensional Periodic Nanostructured Films. *J. Appl. Crystallogr.* **2015**, *48*, 917–926. https://doi.org/10.1107/S1600576715004434.

(37) Dindault, C.; King, B.; Williams, P.; Absi, J. H.; Faure, M. D. M.; Swaraj, S.; Lessard, H. Correlating Morphology, Molecular Orientation, and Transistor Performance of Bis(Penta Fl Uorophenoxy)Silicon Phthalocyanine Using Scanning Transmission X - Ray Microscopy. *Chem. Mater.* **2022**, *34* (10), 4496–4504. https://doi.org/10.1021/acs.chemmater.2c00277.

(38) Cranston, R. R.; Vebber, M. C.; Berbigier, J. F.; Brusso, J. L.; Kelly, T. L.; Lessard, B. H. High Performance Solution Processed N-Type OTFTs through Surface Engineered F-F Interactions Using Asymmetric Silicon Phthalocyanines. *Adv. Electron. Mater.* **2022**, 2200696. https://doi.org/10.1002/aelm.202200696.

(39) Zhou, S.; Tang, Q.; Tian, H.; Zhao, X.; Tong, Y.; Barlow, S.; Marder, S. R.; Liu, Y. Direct Effect of Dielectric Surface Energy on Carrier Transport in Organic Field-Effect Transistors. *ACS Appl. Mater. Interfaces* **2018**, *10* (18), 15943–15951. https://doi.org/10.1021/acsami.8b02304.

(40) Liu, D.; Xu, X.; Su, Y.; He, Z.; Xu, J.; Miao, Q. Self-Assembled Monolayers of Phosphonic Acids with Enhanced Surface Energy for High-Performance Solution-Processed N-Channel Organic Thin-Film Transistors. *Angew. Chemie - Int. Ed.* **2013**, *52* (24), 6222–6227. https://doi.org/10.1002/anie.201300353.

(41) Hutchins, D. O.; Weidner, T.; Baio, J.; Polishak, B.; Acton, O.; Cernetic, N.; Ma, H.; Jen, A. K. Y. Effects of Self-Assembled Monolayer Structural Order, Surface Homogeneity and Surface Energy on Pentacene Morphology and Thin Film Transistor Device Performance. *J. Mater. Chem. C* **2013**, *1* (1), 101–113. https://doi.org/10.1039/c2tc00378c.

(42) Shukla, D.; Nelson, S. F.; Freeman, D. C.; Rajeswaran, M.; Ahearn, W. G.; Meyer, D. M.; Carey, J. T. Thin-Film Morphology Control in Naphthalene-Diimide-Based Semiconductors: High Mobility n-Type Semiconductor for Organic Thin-Film Transistors. *Chem. Mater.* **2008**, *20* (24), 7486–7491. https://doi.org/10.1021/cm802071w.

(43) Yang, J.; Wang, T.; Wang, H.; Zhu, F.; Li, G.; Yan, D. Ultrathin-Film Growth of Para-Sexiphenyl (I): Submonolayer Thin-Film Growth as a Function of the Substrate Temperature. *J. Phys. Chem. B* **2008**, *112* (26), 7816–7820. https://doi.org/10.1021/jp711455u.

(44) Yang, J.; Wang, T.; Wang, H.; Zhu, F.; Li, G.; Yan, D. Weak Epitaxy Growth of Metal-Free Phthalocyanine on p-Sexiphenyl Monolayer and Double-Layer Films. *J. Phys. Chem. B* **2008**, *112* (10), 3132–3137. https://doi.org/10.1021/jp711161f.

(45) Ye, L.; Stuard, S. J.; Ade, H. Soft X-Ray Scattering Characterization of Polymer Semiconductors. In *Conjugated Polymers: Properties, Processing and Applications*; 2019; pp 427–458. https://doi.org/10.1201/9780429190520-13.

(46) Radford, C. L.; Pettipas, R. D.; Kelly, T. L. Watching Paint Dry: Operando Solvent Vapor Annealing of Organic Solar Cells. *J. Phys. Chem. Lett.* **2020**, *11* (15), 6450–6455. https://doi.org/10.1021/acs.jpclett.0c01934.

(47) Mukherjee, S.; Herzing, A. A.; Zhao, D.; Wu, Q.; Yu, L.; Ade, H.; Delongchamp, D. M.; Richter, L. J. Morphological Characterization of Fullerene and Fullerene-Free Organic Photovoltaics by Combined Real and Reciprocal Space Techniques. *J. Mater. Res.* **2017**, *32* (10), 1921–1934. https://doi.org/10.1557/jmr.2017.131.

(48) Rivnay, J.; Mannsfeld, S. C. B.; Miller, C. E.; Salleo, A.; Toney, M. F. Quantitative Determination of Organic Semiconductor Microstructure from the Molecular to Device Scale. *Chem. Rev.* **2012**, *112* (10), 5488–5519. https://doi.org/10.1021/cr3001109.

(49) Peng, Z.; Ye, L.; Ade, H. Understanding, Quantifying, and Controlling the Molecular Ordering of Semiconducting Polymers: From Novices to Experts and Amorphous to Perfect Crystals. *Mater. Horizons* **2022**, *9* (2), 577–606. https://doi.org/10.1039/d0mh00837k.

(50) Ward, J. W.; Li, R.; Obaid, A.; Payne, M. M.; Smilgies, D. M.; Anthony, J. E.; Amassian, A.; Jurchescu, O. D. Rational Design of Organic Semiconductors for Texture Control and Self-Patterning on Halogenated Surfaces. *Adv. Funct. Mater.* **2014**, *24* (32), 5052–5058. https://doi.org/10.1002/adfm.201400219.

(51) Zhang, X.; Bronstein, H.; Kronemeijer, A. J.; Smith, J.; Kim, Y.; Kline, R. J.; Richter, L. J.; Anthopoulos, T. D.; Sirringhaus, H.; Song, K.; Heeney, M.; Zhang, W.; McCulloch, I.; Delongchamp, D. M. Molecular Origin of High Field-Effect Mobility in an Indacenodithiophene-Benzothiadiazole Copolymer. *Nat. Commun.* **2013**, *4*, 1–9. https://doi.org/10.1038/ncomms3238.

(52) Mrkyvkova, N.; Nadazdy, P.; Hodas, M.; Chai, J.; Wang, S.; Chi, D.; Sojkova, M.; Hulman, M.; Chumakov, A.; Konovalov, O. V; Hinderhofer, A.; Jergel, M.; Majkova, E.; Si, P.; Schreiber, F. Simultaneous Monitoring of Molecular Thin Film Morphology and Crystal Structure by X - Ray Scattering. *Cryst. Growth Des.* **2020**, *20* (8), 5269–5276. https://doi.org/10.1021/acs.cgd.0c00448.

(53) Cranston, R. R.; Vebber, M. C.; Berbigier, J. F.; Rice, N. A.; Tonnelé, C.; Comeau, Z. J.; Boileau, N. T.; Brusso, J. L.; Shuhendler, A. J.; Castet, F.; Muccioli, L.; Kelly, T. L.; Lessard, B. H. Thin-Film Engineering of Solution-Processable n-Type Silicon Phthalocyanines for Organic Thin-Film Transistors. *ACS Appl. Mater. Interfaces* **2021**, *13* (1), 1008–1020. https://doi.org/10.1021/acsami.0c17657.

(54) Gali, S. M.; Matta, M.; Lessard, B. H.; Castet, F.; Muccioli, L. Ambipolarity and Dimensionality of Charge Transport in Crystalline Group 14 Phthalocyanines: A Computational Study. *J. Phys. Chem.*

C **2018**, *122* (5), 2554–2563. https://doi.org/10.1021/acs.jpcc.7b11588.

(55) Song, D.; Wang, H.; Zhu, F.; Yang, J.; Tian, H.; Geng, Y.; Yan, D. Phthalocyanato Tin(IV) Dichloride: An Air-Stable, High-Performance, n-Type Organic Semiconductor with a High Field-Effect Electron Mobility. *Adv. Mater.* **2008**, *20* (11), 2142–2144. https://doi.org/10.1002/adma.200702439.

(56) Wang, H.; Song, D.; Yang, J.; Yu, B.; Geng, Y.; Yan, D. High Mobility Vanadyl-Phthalocyanine Polycrystalline Films for Organic Field-Effect Transistors. *Appl. Phys. Lett.* **2007**, *90*, 253510. https://doi.org/10.1063/1.2751103.

(57) Li, L.; Tang, Q.; Li, H.; Yang, X.; Hu, W.; Song, Y.; Shuai, Z.; Xu, W.; Liu, Y.; Zhu, D. An Ultra Closely π-Stacked Organic Semiconductor for High Performance Field-Effect Transistors. *Adv. Mater.* **2007**, *19* (18), 2613–2617. https://doi.org/10.1002/adma.200700682.

(58) Duhm, S.; Heimel, G.; Salzmann, I.; Glowatzki, H.; Johnson, R. L.; Rabe, P.; Koch, N. Orientation-Dependent Ionization Energies and Interface Dipoles in Ordered Molecular Assemblies. *Nat. Mater.* **2008**, *7*, 326–332. https://doi.org/10.1038/nmat2119.

(59) Giraudet, L.; Simonetti, O. Threshold Voltage and Turn-on Voltage in Organic Transistors : Sensitivity to Contact Parasitics. *Org. Electron.* **2011**, *12* (1), 219–225. https://doi.org/10.1016/j.orgel.2010.11.002.

Chapter 5. Peripherally fluorinated silicon phthalocyanines: how many fluorine groups are necessary for air-stable electron transport in organic thin-film transistors?

This chapter was published in the journal "ACS Chemistry of Materials": King, B., Vebber, M.; Ewenike, R.; Dupuy, M.; French, C.; Brusso, J.; Lessard, B. H., Peripherally fluorinated silicon phthalocyanines: how many fluorine groups are necessary for air-stable electron transport in organic thin-film transistors? Chemistry of Materials, 2023, Accepted Manuscript.*

Context

In this work, I report eight novel axially substituted and peripherally fluorinated silicon phthalocyanine derivatives (R_2-F_XSiPcs) in addition to four previously reported non-peripherally fluorinated silicon phthalocyanine derivatives (R_2-SiPcs) and investigated the threshold at which these derivatives would demonstrate air-stable electron transport. Additionally, the first reported R_2-F_XSiPc (F_2-F_{16}SiPc) suffered from batch-to-batch variation during synthesis and the first reported phenol-substituted R_2-F_XSiPcs had relatively poor performance in OTFTs, motivating the development of additional novel derivatives. Of the twelve reported derivatives, I found that all four R_2-F_{16}SiPcs and one R_2-F_4SiPc ($(F_5PhO)_2$-F_4SiPc) demonstrated air stable electron transport, which is the first report of a non-F_{16}SiPc derivative to show n-type operation in air. This work was significant because we established concrete structure property relationships between structure of fluorinated R_2-F_XSiPcs, lowest unoccupied molecular orbital and the corresponding threshold for air-stable electron transport in OTFTs based on these materials.

Contributions

I prepared and characterized OTFTs of twelve R_2-F_XSiPcs with assistance from Mr. Ewenike and Mr. French, who I mentored and trained to acquire the data, as well as processed and analyzed device data. I completed AFM measurements, UV-Vis spectroscopy measurements and XRD measurements and interpreted the data. I also developed power spectral density functions based on AFM images. I interpreted UPS data with input from Dr. Vebber. R_2-F_XSiPcs were synthesized and purified by Dr. Vebber and Ms. Dupuy. NMR spectroscopy and CV measurements were completed and interpreted by Dr. Vebber and Ms. Dupuy, while DART-MS were interpreted by Dr. Vebber. I wrote the manuscript with input from Prof. Lessard, Prof. Brusso, and Dr. Vebber. All co-authors reviewed the manuscript prior to submission. The device stack in Figure 1 was developed by Dr. Joseph Manion.

Abstract

Silicon phthalocyanines (R_2-SiPcs) are an emerging class of high-performance n-type semiconductors used in organic electronics which historically have suffered from operational instability in air. We report the synthesis of R_2-SiPcs with ranging degrees of peripheral fluorination, R_2-F_xSiPcs (X = 0, 4, or 16) and different axial phenoxy groups leading to 12 derivatives with 0 to 26 fluorine atoms in the molecular structure and going from non-operational devices in ambient conditions to fully air stable operation in organic thin-film transistors (OTFTs). Ultraviolet photoelectron spectroscopy (UPS) revealed that the peripheral fluorination of R_2-F_xSiPcs caused a decrease of up to 0.9 eV in the energy level of the lowest unoccupied molecular orbital (LUMO). This reduction in LUMO energy level coincides with a decrease in the threshold voltage (V_T) of the resulting OTFT. All compounds containing 16 peripheral fluorine atoms and one of four compounds containing four peripheral fluorine atoms in OTFTs yielded air stable electron transport in ambient conditions at a humidity of 40%. Power spectral density functions (PSDF) from atomic force microscopy (AFM) imaging also demonstrated that for similar morphologies across a series of compounds with the same axial group, larger domain size and a smaller density of grain boundaries in the film led to a higher overall electron mobility (μ_e).

5.1 Introduction

To develop electronic components, including CMOS-like integrated circuits, it is crucial to actively expand the available catalogue of n-type or electron transporting organic semiconductors for organic thin-film transistors (OTFTs).[1] While hole-transporting or p-type materials typically reach high charge carrier mobilities (μ) in ambient conditions, the development of air stable electron transporting materials is more challenging.[2,3] To achieve electron transport in ambient conditions and prevent electron trapping due to moisture and oxygen, researchers have shown that a lowest unoccupied molecular orbital (LUMO) of -4.0 eV or deeper is typically required.[4,5] One method widely used to synthesize organic semiconductors capable of air-stable electron transport is the introduction of electron-withdrawing groups such as fluorine molecules or cyano (CN) moieties into the π-conjugated building blocks.[6–8] Similar incorporation of electron-withdrawing groups into organic semiconducting molecules and small polymers have also been employed as a strategy to convert the majority charge carrier type from holes to electrons.[9,10]

Metal and metalloid-containing phthalocyanines (MPcs) are a popular class of organic semiconductors that have been incorporated into p-type OTFTs,[11] primarily owing to their chemical versatility, good thermal stability and low-cost synthesis.[12] Similar to other organic semiconductors, a broad range of synthetic options are available to tune the physical, chemical and optical properties of MPcs through substitution of different metal cores and the inclusion of peripheral, bay or axial substituents.[13] The use of electron withdrawing groups on the periphery of MPc, such as hexadecafluorinated MPcs, is a classic approach to induce n-type behaviour in an MPc-based OTFT.[14–16] The functionalization of MPcs has enabled their use in a broad range of applications including gas sensors for the detection of ammonia and[17,18] cannabinoids,[19,20] or for measuring ionizing radiation.[21]

Silicon phthalocyanines (R_2-SiPcs) are among the rare examples of MPcs that can effectively transport electrons without peripheral fluorination and have been incorporated into OTFTs which could operate as both n-type and ambipolar devices.[22–24] R_2-SiPcs possess a tetravalent metal centre, which provides opportunity for a axial functionalization with carboxylic acids,[22] phenols[25] and silanes.[26] Axial functionalization of R_2-SiPcs results in changes to intermolecular stacking, optical properties, and solubility with only small changes to the frontier molecular orbitals,[27,28] which makes molecular engineering of these materials a useful tool to enhance interfacial interactions in devices and improve their performance. We reported a drop in OTFT device threshold voltage (V_T) as we increased the electron withdrawing character of the axial substituent of the R_2-SiPc.[29,30] While high performing under nitrogen atmosphere and under vacuum, silicon bis(pentafluorophenoxy) phthalocyanine (F_{10}-SiPc) experiences a significant drop in performance with exposure to air and often stops functioning after several minutes of operation.[25,31] The desire for long-term air-stable electron transport motivated the synthesis of silicon bis(fluoro) hexadecafluorinated phthalocyanine, F_2-F_{16}SiPc, with a LUMO of -4.8 eV, which is 0.7 eV deeper than F_{10}-SiPc and provided improved air stability with an electron mobilities of up to 10^{-1} $cm^2 \cdot V^{-1} \cdot s^{-1}$.[32] While promising, the purification of F_2-F_{16}SiPc is challenging leading to problematic batch to batch variation. Furthermore, the strength of the Si-F bonds (~580 kJ/mol) compared to Si-O bonds (~450 kJ/mol) made the fluoride ion difficult to displace with typical oxygen-containing axial groups such as phenols and carboxylic acids, which readily react with Cl_2-SiPc at moderate temperatures.[24,33] Recently we developed a new synthetic approach to achieve axial chlorination by reacting the axial fluorine-containing derivative with boron trichloride (BCl_3) as an effective strategy to obtain peripherally fluorinated derivatives with axial chlorines which could then be further functionalization with phenols and carboxylic acids.[34]

In this work, we compare and report eight novel and four previously reported silicon phthalocyanine derivatives with 0, 4 or 16 peripheral fluorine groups and axial phenoxy groups with 0, 3 or 5 fluorine atoms (R_2-F_xSiPcs) which were all integrated into BGTC OTFTs (**Figure 5.1**). The optical, electronic and morphological properties of these compounds were characterized by UV-Vis spectroscopy and ultraviolet photoelectric spectroscopy (UPS), powder X-ray diffraction (PXRD) and atomic force microscopy (AFM). OTFTs using Ag and Ag/Mn electrodes in both inert conditions as well as in air led to a correlation between LUMO and V_T where all devices with a LUMO of -4.4 eV or deeper led to air stable n-type performance.

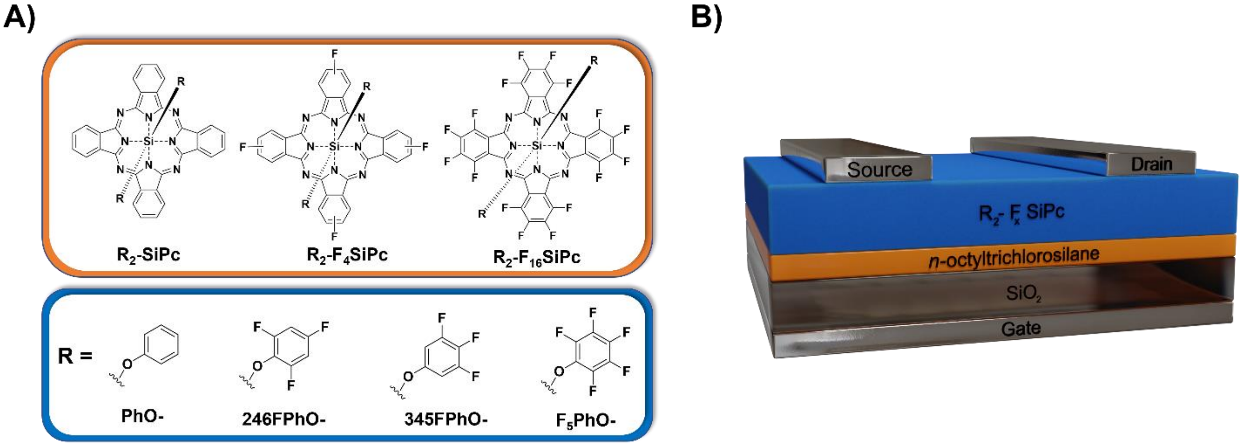

Figure 5.1 A) Chemical structures of R_2-F_xSiPcs and axial phenoxy groups in this work and B) schematic of a bottom-gate top-contact (BGTC) OTFT.

5.2 Experimental Section

Materials

Tetrafluorophthalonitrile (98%), and 4-fluorophthalonitrile (98%), phenol (98%), pentafluorophenol (97%), 3,4,5-trifluorophenol (95%) and 2,4,6-trifluorophenol were purchased from TCI America. Lithium bis(trimethylsilyl)amide (LiHMDS, 97%), silicon tetrachloride (99%), tetraline (anhydrous, 99%) and chlorobenzene (anhydrous, 99%) were purchased from Sigma–Aldrich.

Synthesis

Dichloro silicon phthalocyanine (Cl_2-SiPc),[35] silicon tetrafluorophthalocyanine (Cl_2-F_4SiPc) and silicon hexadexafluorophthalocyanine (Cl_2-F_{16}SiPc),[34] and their axial functionalization[31] were obtained following procedures previously reported in the literature with generic synthetic pathways shown in **Figure 5.2**. All twelve structures reported in this work are shown in **Figure 5.8** of the Supporting Information. Axially functionalized R_2-F_xSiPcs have been purified by train sublimation at 130 mtorr and temperatures ranging from 275°C to 315°C, using CO_2 as carrier gas. Confirmation of the novel functionalized F_4SiPcs and F_{16}SiPcs was acquired by proton nuclear magnetic resonance (^{1}HNMR), fluorine-19 nuclear magnetic resonance (^{19}FNMR) and high-resolution mass spectroscopy (HR-MS), employing a direct analysis in real time (DART) probe. Data for the four non-peripherally fluorinated R_2-SiPcs have been published elsewhere.[27,31,36]

Bis(phenoxy)silicon tetrafluorophthalocyanine ((PhO)$_2$-F_4SiPc): ^{1}HNMR (**Figure 5.17A**): 9.56 ppm (m, 4H); 9.20 ppm (m, 4H); 8.05 ppm (m, 4H), 5.71 ppm (m, 2H), 5.55 ppm (m, 4H), 2.35 ppm (d, 4H); ^{19}FNMR (**Figure 5.17B**): −105.9 ppm (m). HR-MS (**Figure 5.9**): expected mass 798.2 and obtained mass 799.2. Yield = 36% after sublimation.

Bis(2,4,6-trifluorophenoxy)silicon tetrafluorophthalocyanine ((246FPhO)$_2$-F_4SiPc): Too insoluble for NMR characterization (**Figure 5.19**). HR-MS **(Figure 5.11**): expected mass 906.1 and obtained mass 907.1. Connectivity confirmed by SC-XRD. Yield = 23% after sublimation.

Bis(3,4,5-trifluorophenoxy)silicon tetrafluorophthalocyanine ((345FphO)$_2$-F_4SiPc): ^{1}HNMR (**Figure 5.21A**): 9.62 ppm (m, 4H); 9.25 ppm (m, 4H), 8.11 (m, 4H), 2.02 ppm (dd, 4H); ^{19}FNMR (**Figure 5.21B**): -104.3 ppm (m), -135.8 ppm (d), -170.8 ppm (t). HR-MS (**Figure 5.13**): expected mass 906.1 and obtained mass 907.1. Yield = 43% after sublimation.

Bis(pentafluorophenoxy)silicon tetrafluorophthalocyanine ((F_5PhO)$_2$-F_4SiPc): ^{1}HNMR (**Figure 5.23A**): 9.62 ppm (m, 4H); 9.25 ppm (m, 4H), 8.11 (m, 4H); ^{19}FNMR (**Figure 5.23**): -104.6 ppm (m), -165.5 ppm (d), -162.0 ppm (t) -167.2 ppm (t). HR-MS (**Figure 5.15**): expected mass 978.1 and obtained mass 979.1. Yield = 57% after sublimation.

Bis(phenoxy)silicon hexadecafluorofluorophthalocyanine ((PhO)$_2$-F_{16}SiPc): ^{1}HNMR (**Figure 5.18A**): 5.87 ppm (t, 2H), 5.75 ppm (t, 4H), 2.46 ppm (d, 4H); ^{19}FNMR (**Figure 5.18B**):

−136.7 ppm (m), -145.4 ppm (m). HR-MS (**Figure 5.10**): expected mass 1014.0 and obtained mass 1015.1. Yield = 15% after sublimation.

Bis(2,4,6-trifluorophenoxy)silicon hexadecafluorofluorophthalocyanine ((246FphO)$_2$-F$_{16}$SiPc): ^{1}HNMR (**Figure 5.20A**): 2.16 ppm (dd, 4H); ^{19}FNMR (**Figure 5.20B**):-116.5 (t), -130.1 (d), -136.7 ppm (m), -145.4 ppm (m). HR-MS (**Figure 5.12**): expected mass 1122.0 and obtained mass 1123.0. Yield = 12% after sublimation.

Bis(3,4,5-trifluorophenoxy)silicon hexadecafluorofluorophthalocyanine ((345FphO)$_2$-F$_{16}$SiPc): ^{1}HNMR (**Figure 5.22A**): 5.23 ppm (m, 4H); ^{19}FNMR (**Figure 5.22B**): -135.2 (dd), -136.7 ppm (m), -145.4 ppm (m), -168.2 (t). HR-MS (**Figure 5.14**): expected mass 1122.0 and obtained mass 1123.0. Yield = 15% after sublimation.

Bis(pentafluorophenoxy)silicon hexadecafluorofluorophthalocyanine ((F$_5$PhO)$_2$-F$_{16}$SiPc): ^{1}HNMR (**Figure 5.24A**): no peaks; ^{19}FNMR (**Figure 5.24B**): −135.7 ppm (m), -144.2 ppm (m), -162.2 ppm (d), -163.1 ppm (t) -164.4 ppm (t). HR-MS (**Figure 5.16**): expected mass 1193.9 and obtained mass 1195.0. Yield = 22% after sublimation.

Material Characterization

NMR data were collected using a Bruker Avance II 400 MHz instrument. Direct analysis in real time mass spectrometry (DART-MS) was collected at the AIMS Mass Spectrometry Laboratory at the University of Toronto (Toronto, Canada). The UV-Vis spectra of R$_2$-F$_x$SiPc solutions in THF were recorded in a Cary 5000 spectrometer, using a 1cm quartz cuvette, and in the range of 300 to 800 nm. UV-Vis of R$_2$-F$_x$SiPcs films were recorded in the same spectrometer from 300 to 1000 nm due to peak broadening. Cyclic voltammetry experiments were recorded with the aid of a potentiostat, with three platinum wires serving as the working, auxiliary and reference electrodes. Saturated solutions of SiPcs in dry THF were employed (due to low solubility) with 0.05M tetrabutylammonium perchlorate as the auxiliary electrolyte. The characterizations were performed between -1.5 and +1.0 V, and Ferrocene's oxidation was used as a reference potential. Ultraviolet photoelectric spectroscopy (UPS) data collected at Surface Science Western (Western University, London, Ontario, Canada). The UPS analyses were carried out with a Kratos AXIS Supra X-ray photoelectron spectrometer using a He(I) source (21.22 eV, 30 mA). Analyses were carried out with an analysis area of 55 microns and a pass energy of 10 eV. A 9 Volt offset is applied during sample analysis (corrected out in the spectra). Samples were electrically well connected to the spectrometer sample stage using copper tape. Energy levels were independently calculated from UPS spectra, using gold as a reference.

Organic Thin-Film Transistor Fabrication

N-doped silicon substrates with a 230 nm thermally grown SiO_2 layer were obtained from WaferPro and sequentially washed with acetone and isopropanol, followed by drying with a stream of compressed nitrogen. Substrates were then sonicated sequentially in both acetone and methanol for 5 min, followed by drying with a nitrogen stream and treatment with oxygen plasma for 15 minutes in a Harrick Plasma Cleaner (model no. PDC-32G). Plasma-treated substrates were then washed with water and isopropanol, dried with a nitrogen stream and then placed face-up in a 20 mL scintillation vial, where they were reacted in a 3 mL solution of 1% v/v OTS in anhydrous toluene at 70 °C for 1 h. Silane-treated substrates were then washed with toluene to remove unreacted silane and dried under a nitrogen stream, followed by annealing under vacuum at 70 °C for 1h to remove excess toluene. Dried substrates were finally transferred to a nitrogen glovebox. OTFTs with **R_2-F_xSiPcs** as the active semiconducting layer were fabricated by first thermally depositing a 500 Å-thick film of **R_2-F_xSiPc** as the active semiconducting layer by PVD through a square shadow mask on substrates held at room temperature at a rate of 0.2 Å s^{-1} ($P < 2 \times 10^{-6}$ Torr). After breaking vacuum, two corners of each substrate were scratched with a diamond-tipped pen to expose bare silicon. Source-drain electrodes (L = 30 μm, W = 1000 μm) were then obtained by depositing 100 Å of manganese at a rate of 0.5 Å s^{-1} followed by 500 Å of silver at a rate of 1 Å s^{-1} ($P < 2 \times 10^{-6}$ Torr) through shadow masks obtained by Ossila to yield 20 individual transistors per substrate. Additional OTFTs were also fabricated using silver electrodes evaporated under identical conditions without the use of a manganese interlayer.

Organic Thin-Film Transistor Characterization

Bottom-gate top-contact (BGTC) OTFTs were measured at room temperature in a nitrogen glovebox ($[O_2] < 0.1$ ppm and $[H_2O] < 0.1$ ppm) and in air at a humidity of 40%. Electrical characterization of BGTC OTFTs were performed in identical custom-built autotesters with brass alloy contact tips plated with 20 μm of gold on 100 μm of nickel. The autotesters were connected to a Keithley 2614B source meters to set the gate-source voltage (V_{GS}) and source-drain voltage (V_{SD}) to measure the source-drain current (I_{SD}). Output curves were obtained by fixing V_{GS} at discrete values between -10 V and +50 V and sweeping V_{SD} between 0 and +50 V. Transfer characteristics were obtained by fixing V_{SD} in the saturation region at +50V and sweeping V_{GS} between -20 V or -10 V and +50V. During the measurement of transfer characteristics, V_{GS} was applied at a duty cycle of 20% and a frequency of 10 Hz to reduce gate bias stress. A duty cycle of 20% at a frequency of 10 Hz corresponds to gate bias stress being applied for a 20 ms (2 Hz) interval between 80 ms (8 Hz) intervals of zero applied gate bias stress. Applying a pulsed gate during device operation can improve the device stability by reducing the reduction in current due to gate bias stress and make the extraction of threshold voltage V_T more reliable.[23,37] Devices were first measured in nitrogen, then after being exposed to air for 5 minutes and finally after being stored at room temperature at humidity of 40% for 24 hours, 7 days and 14 days.

The electron field-effect mobility (μ_e) in the saturation region was calculated using **Equation 6.1**:

$$I_{DS} = \frac{\mu_e C_i W}{2L}(V_{GS} - V_T)^2 \tag{6.1}$$

Where L and W represent the length and width of the channel, respectively. The capacitance of the gate dielectric (C_i) is calculated using $C_i = \frac{\varepsilon_0 \varepsilon_r}{d}$, where d is the thickness of the SiO_2 dielectric (230 nm), ε_r is the relative dielectric constant of SiO_2 ($\varepsilon_r = 3.9$) and ε_0 is the permittivity of free space. μ_e was determined by calculating the slope of best fit of a 10V region of $\sqrt{I_{DS}}$ as a function of V_{GS} when the curve became linear. The threshold voltage (V_T) was calculated from the x-intercept of linearized data for $\sqrt{I_{DS}}$ vs V_{GS} in the same measurement range.

The saturation region transconductance ($g_{m,\,sat}$) was calculated using **Equation 6.2**, which defines the change in drain current with respect to the corresponding change in gate voltage:

$$g_{m,sat} = \frac{\partial I_{DS}}{\partial V_{GS}} \tag{6.2}$$

The transconductance was calculated by taking the difference in I_{DS} with respect to V_{GS} in an identical region to that which was used to calculate μ_e.

Atomic Force Microscopy (AFM)

AFM images were obtained with a Bruker Dimension Icon Atomic Force Microscope System, using ScanAsyst-Air probes, in ScanAsyst mode with a scan rate of 0.85 Hz.

Powder X-Ray Diffraction (PXRD)

PXRD measurements on 50 nm R_2-F_xSiPc films deposited on OTS-treated SiO_2 substrates without electrodes were performed using a Rigaku Ultima IV powder diffractometer with an X-ray source of Cu Kα ($\lambda = 1.5418$ Å) at a scan range of $5° < 2\theta < 20°$ and a scan rate of $0.5°\cdot min^{-1}$.

5.3 Results and Discussion

We synthesized twelve R_2-F_xSiPcs (**Figure 5.2, Figure 5.8**) with increasing axial and peripheral fluorination from 0 to 26 fluorine atoms containing phenol (PhO), 2,4,6-trifluorophenol (246FPhO), 3,4,5-trifluorophenol (345FPhO) and pentafluorophenol (F_5PhO). Synthesis was adapted from an original reaction by Yutronkie et al. which was the first reported peripherally-fluorinated SiPc (F_2-F_{16}SiPc),[32] where R_2-F_4SiPc and R_2-F_{16}SiPc derivatives had to be achieved by first synthesizing core molecules with axial fluorine groups (F_2-F_xSiPc) and then substituting axial fluorine groups with boron trichloride (BCl_3) to obtain Cl_2-F_4SiPc and Cl_2-F_{16}SiPc.[34] Once derivatives were functionalized with axial chlorine moieties, substitution with phenols was carried out under similar conditions to non-fluorinated analogues in chlorobenzene. All twelve derivatives were purified by train sublimation and the corresponding characterization can be found in the Supporting Information.

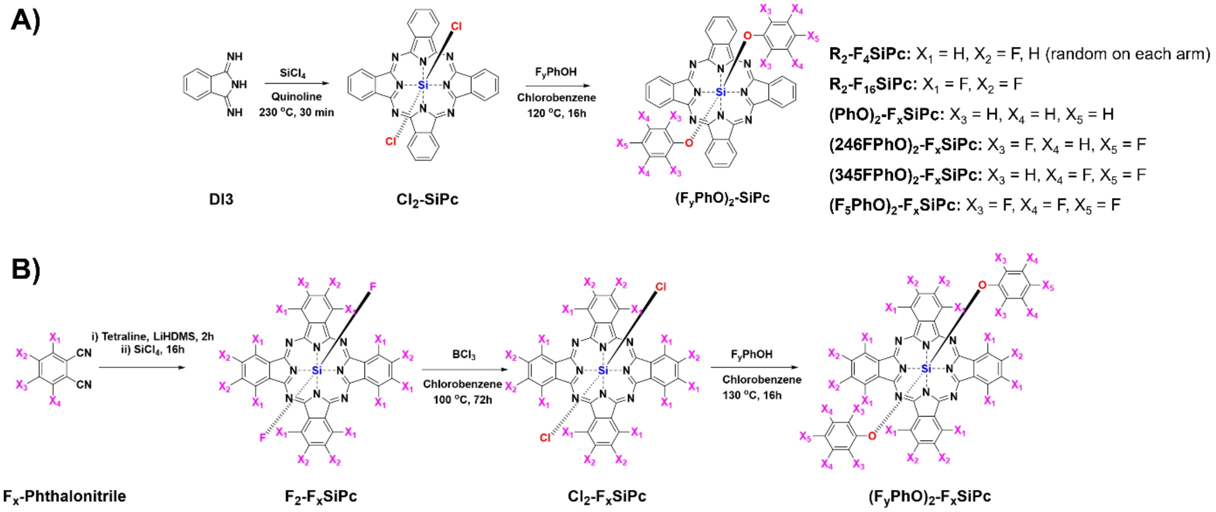

Figure 5.2 Synthetic pathways used in the production of functionalized A) R_2-SiPcs and B) R_2-F_xSiPcs

Material Characterization (Optical, Electrochemical, UPS)

The optical and electrochemical properties of R_2-F_xSiPcs in this work have been evaluated by ultraviolet photoelectron spectroscopy (UPS, **Figure 5.3**), UV-Vis spectroscopy in both solution and for solid thin films (**Figure 5.3**), and by cyclic voltammetry in solution (**Figure 5.25**). A summary of key values extracted by these techniques can be found in **Table 5.1**. The optical band gap (E_G) measured in solution has small variations across the synthetic compounds with the narrowest E_G arising from R_2-F_{16}SiPc derivatives. In solid films, there is a red shift of λ_{max} and resultant narrowing of E_G by 0.3 – 0.5 eV relative to solution measurements. Both a shift in λ_{max} and broadening have been observed in R_2-SiPc and CuPc films, and are a result of intermolecular solid-state interactions in the film.[16,38,39] Cyclic voltammetry was performed using three electrode system in DCM. The cyclic voltammograms are found in the supporting information and display typical structures as expected for R_2-SiPc**.**[34,36,38] HOMO and LUMO levels were estimated using UPS (**Table 5.1**). HOMO energy level values were confirmed for the derivatives by obtaining the work function (Φ) and LUMO offset (Δe) determined by UPS, while the LUMO energy levels were estimated from the HOMO levels and the solid state E_G (**Table 5.1**). UPS for (246FPhO)$_2$-SiPc and (F_5PhO)$_2$-SiPc were consistent with measurements previously reported by Bender and coworkers validating these materials and the UPS system.[31] Peripheral fluorination of R_2-F_xSiPcs results in a decrease in HOMO of 0.6 eV to 1.0 eV and therefore a deeper LUMO which is consistent with our previous reports[32,34] as well as for reports of F_xCuPc[16] and F_xZnPc.[40] A deeper LUMO should enable air-stable electron transport by reducing oxidation of electrons induced by atmospheric gases including oxygen and moisture.[4,41]

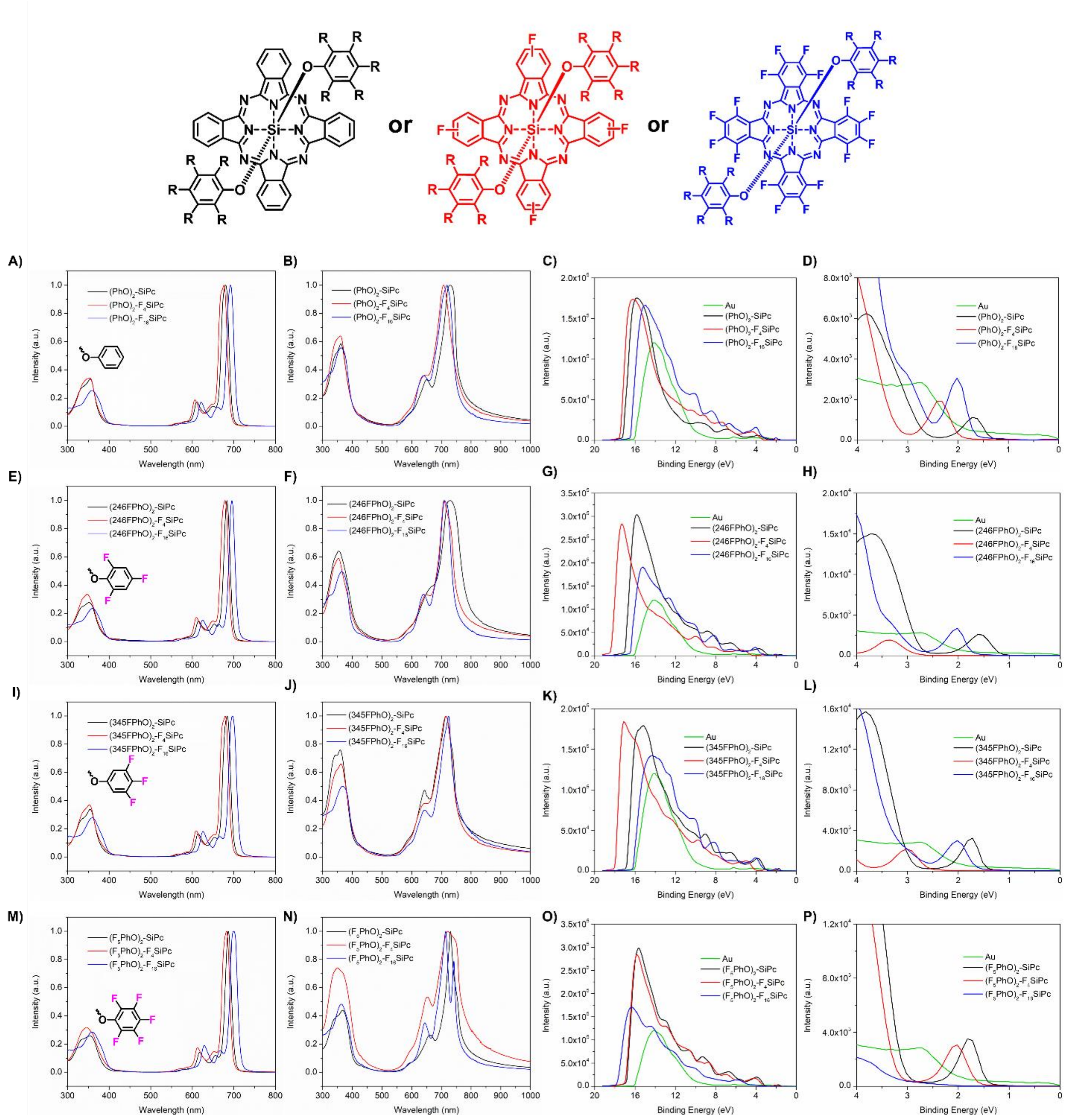

Figure 5.3 Solution UV-Vis (A, E, I, M), solid-state UV-Vis (B, F, J, N), UPS spectra (C, G, K, O) and inset of trailing edge of UPS spectra (D, H, L, P) for R_2-F_xSiPcs in this work for axial groups **A**-D) PhO, C and E-H) 246FPhO, I - L) 345FPhO and M - P) F_5PhO.

Table 5.1 Optical, electrochemical and UPS characterization of (F$_x$PhO)$_2$-F$_y$SiPcs

Material	λ_{max}^{a} DCM / Film (nm)	E_G^{a} DCM / Film (eV)	$E_{1/2}^{Red}$ (V)	Φ^{b} (eV)	Δe^{b} (eV)	$LUMO$ / $HOMO_{UPS}$^{b} (eV)
(PhO)$_2$-SiPc	680 / 730	1.8 / 1.5	-0.82	4.0	1.3	-3.8 / -5.3
(PhO)$_2$-F$_4$SiPc	676 / 707	1.8 / 1.5	-0.77	3.6	1.9	-4.0 / -5.5
(PhO)$_2$-F$_{16}$SiPc	692 / 718	1.7 / 1.6	-0.79/-0.26	4.7	1.6	-4.7 / -6.3
(246FPhO)$_2$-SiPc	683 / 730	1.8 / 1.4	-0.75	4.2	1.2	-3.9 / -5.4
(246FPhO)$_2$-F$_4$SiPc	679 / 710	1.8 / 1.5	-0.79	2.8	2.7	-4.1 / -5.5
(246FPhO)$_2$-F$_{16}$SiPc	695 / 710	1.7 / 1.6	-0.87/-0.22	4.7	1.7	-4.8 / -6.4
(345FPhO)$_2$-SiPc	684 / 715	1.8 / 1.4	-1.14/-0.62	4.3	1.4	- 4.1 / -5.7
(345FPhO)$_2$-F$_4$SiPc	679 / 715	1.8 / 1.5	-0.79/-0.22	3.2	2.6	- 4.2 / -5.8
(345FPhO)$_2$-F$_{16}$SiPc	696 / 724	1.7 / 1.4	-0.82/-0.20	5.0	1.6	-4.9 / -6.6
(F$_5$PhO)$_2$-SiPc	686 / 730	1.8 / 1.5	-0.73	4.4	1.4	-4.2 / -5.8
(F$_5$PhO)$_2$-F$_4$SiPc	682 / 721	1.8 / 1.3	-0.52/-1.10	4.3	1.6	- 4.4 / -5.9
(F$_5$PhO)$_2$-F$_{16}$SiPc	692 / 714	1.7 / 1.6	-0.70 / -0.08	3.4	3.0	- 4.9 / -6.4

a. Peak absorbance from a THF solution and Optical band gap characterized using the onset of the absorption in both solution and thin film.

b. Energy levels and work function estimated from UPS spectra, with a + 9 V bias, 21.22 eV emission source and calibrated using an Au reference. We estimated the ionization energy (IE) to be equal to the HOMO energy level and LUMO = HOMO + E$_{G,Film}$.

Electronic Characterization of Materials in Organic Thin-Film Transistors

R$_2$-F$_x$SiPcs were incorporated into BGTC OTFTs as the semiconducting layer with n-octyltrichlorosilane (OTS)-functionalized SiO$_2$ as the dielectric and either Ag or Ag/Mn electrodes (see Experimental for fabrication procedure). We have demonstrated that manganese (Mn) is a useful contact interlayer for enhancing the electronic performance of OTFTs incorporating R$_2$-SiPcs due to a better energetic alignment of the work function (-4.1) contact with the LUMO of the semiconductor, reducing contact resistance to charge injection.[31] However, the work function of Ag (-4.7 eV) is a better match to the LUMO of R$_2$-F$_{16}$SiPcs (**Table 5.1**), and therefore device performance with both electrode configurations were reported. Devices incorporating Ag/Mn electrodes are reported in **Table 5.2** while devices incorporating Ag electrodes are reported in **Table 5.6** in the supporting information. Transfer curves for all BGTC OTFTs are shown in **Figure 5.4** (transfer curves, Ag/Mn electrodes), **Figure 5.26** (transfer curves, Ag electrodes) and **Figure**

5.29 (output curves, both Ag and Ag/Mn contacts) of the supporting information. Average μ_e across the series of R_2-F_xSiPcs in OTFTs was similar to previously reported phenoxy-SiPc derivatives by our group.[30,31,42] The best performing derivatives in the series were the three materials having the pentafluorophenoxy (F_5PhO) moieties, including the two materials with the highest μ_e ((F_5PhO)$_2$-SiPc, $\mu_e = 9.6 \pm 3.0 \times 10^{-2}$ cm^2·V^{-1}·s^{-1} and (F_5PhO)$_2$-F_{16}SiPc, $\mu_e = 2.2 \pm 0.3 \times 10^{-2}$ cm^2·V^{-1}·s^{-1}) and the two materials with a V_T closest to 0 V ((F_5PhO)$_2$-F_4SiPc, $V_T = 0.8 \pm 1.5$ V and (F_5PhO)$_2$-F_{16}SiPc, $V_T = 0.1 \pm 1$ V). In fact, for devices fabricated in an identical architecture and under identical conditions, ((F_5PhO)$_2$-F_4SiPc and (F_5PhO)$_2$-F_{16}SiPc both have a V_T closer to 0V than the previous record of 4.8 ± 3.1 V reported for bis(3-fluoro-4-cyanophenoxy) silicon phthalocyanine.[30] V_T for devices of (F_5PhO)$_2$-F_{16}SiPc with Ag electrodes are also similar to those our group reported for F_{16}CuPc on OTS.[32] These results are promising because unlike F_{16}CuPc and other hexadecafluorophthalocyanines we can modify the functionality of the axial position to improve solid state interactions and molecular arrangement between the semiconductor and the dielectric surface to further improve μ_e.[43]

Table 5.2 Electrical performance of OTFTs incorporating evaporated R$_2$-F$_x$SiPcs with AgMn electrodes.

Material	**μ_e [cm^2·V^{-1}·s^{-1}]^a**	***V_T* [V]^a**	***I_{on}* [A]^b**	***I_{on}/I_{off}***	***n***
(PhO)$_2$-SiPc	7.1 ± 6.5 x10^{-4}	24.1 ± 4.1	1.29 x10^{-7}	10^3 - 10^4	37
(PhO)$_2$-F$_4$SiPc	3.0 ± 1.6 x10^{-3}	11.7 ± 1.8	1.16 x10^{-6}	10^4 – 10^5	37
(PhO)$_2$-F$_{16}$SiPc	1.7 ± 1.2 x10^{-3}	7.6 ± 1.6	1.08 x10^{-6}	10^4	39
(246FPhO)$_2$-SiPc	2.0 ± 1.2 x10^{-3}	16.4 ± 6.2	9.03 x10^{-7}	10^4	33
(246FPhO)$_2$-F$_4$SiPc	1.9 ± 1.1 x10^{-2}	9.2 ± 1.4	9.47 x10^{-6}	10^4 - 10^5	38
(246FPhO)$_2$-F$_{16}$SiPc	4.8 ± 1.6 x10^{-3}	9.0 ± 0.3	2.95 x10^{-6}	10^3	39
(345FPhO)$_2$-SiPc	1.6 ± 0.7 x10^{-2}	4.4 ± 4.7	1.22 x10^{-5}	10^4 - 10^5	38
(345FPhO)$_2$-F$_4$SiPc	2.2 ± 1.7 x10^{-4}	9.8 ± 2.6	5.44 x10^{-7}	10^3	35
(345FPhO)$_2$-F$_{16}$SiPc	2.4 ± 1.1 x10^{-3}	-11.0 ± 5.4	2.90 x10^{-6}	10^3	35
(F$_5$PhO)$_2$-SiPc	9.6 ± 3.0 x10^{-2}	5.4 ± 2.5	4.82 x10^{-5}	10^4 - 10^5	38
(F$_5$PhO)$_2$-F$_4$SiPc	1.6 ± 0.3 x10^{-2}	0.8 ± 1.5	1.17 x10^{-5}	10^4 - 10^5	37
(F$_5$PhO)$_2$-F$_{16}$SiPc	2.2 ± 0.3 x10^{-2}	0.1 ± 1	2.48 x10^{-5}	10^3 - 10^4	40

a) μ_e and *VT* were calculated based on average values

b) *Ion calculated based on median value*

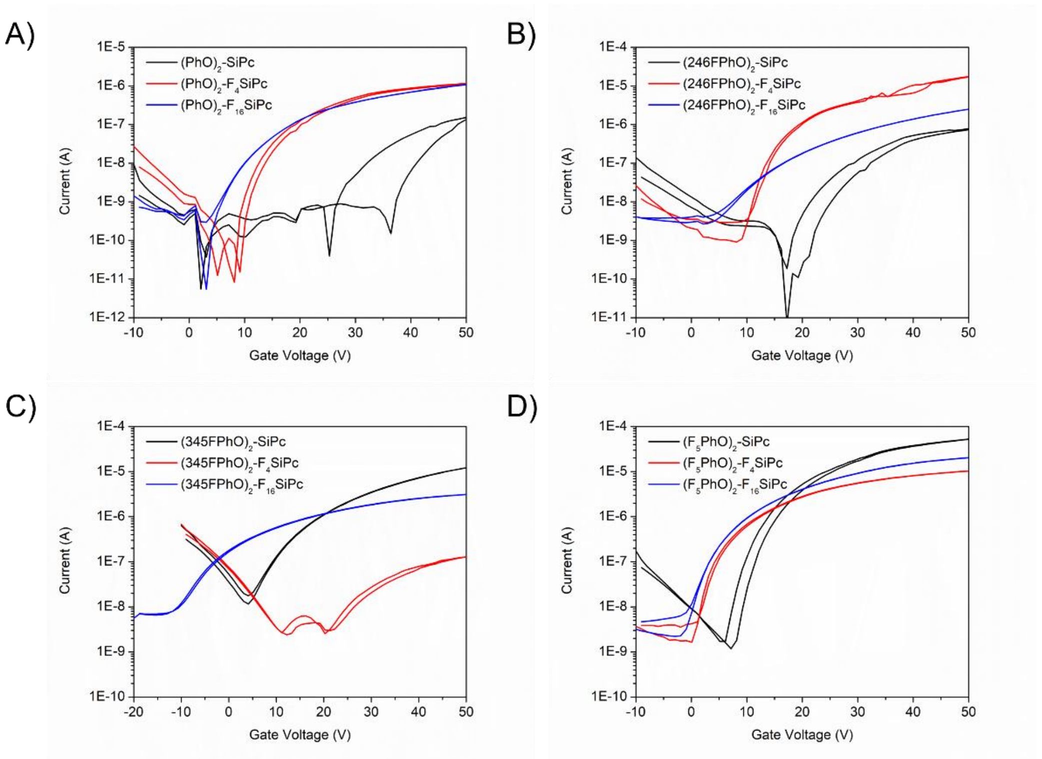

Figure 5.4 Transfer curves (V_{DS} = 50V) R$_2$-F$_x$SiPc derivatives in OTFTs employing Ag/Mn electrodes measured in a nitrogen glovebox: A) (PhO)$_2$-F$_x$SiPc, B) (246FPhO)$_2$-F$_x$SiPc, C) (345FPhO)$_2$-F$_x$SiPc and D) (F$_5$PhO)$_2$-F$_x$SiPc.

To develop a relationship between device performance and material properties we generated plots of V_T in N$_2$ as a function of LUMO (**Figure 5.5**). There is a clear decrease in V_T as the LUMO level of the derivative deepens when using both Ag and Ag/Mn electrodes, suggesting easier electron injection for both architectures.[44] At a relative humidity of 40%, R$_2$-F$_x$SiPcs characterized by a LUMO between -3.6 eV and -4.2eV were not air stable while those with a value between -4.4 eV to -4.9 eV exhibited air-stable electron transport. Of the 12 R$_2$-F$_x$SiPcs incorporated into OTFTs in this work, all four R$_2$-F$_{16}$SiPc derivatives yielded OTFTs with air stable electron transport, but only one of the four R$_2$-F$_4$SiPc derivatives, (F$_5$PhO)$_2$-F$_4$SiPc, had functional devices in air. The rest did not exhibit air-stable behaviour. A comparison of devices incorporating the three (F$_5$PhO)$_2$-F$_x$SiPc derivatives in BGTC OTFTs with Ag electrodes in air is presented in **Table 5.3**. Transfer and output curves for characteristic (F$_5$PhO)$_2$-F$_4$SiPc in air are presented in **Figure 5.27** of the supporting information. We surmise that the air stability of electron transport of (F$_5$PhO)$_2$-F$_4$SiPc in OTFTs can be partially attributed to its low-lying LUMO level, which is identical to that of (tb-PhO)$_2$-F$_{16}$SiPc reported in our previous work at -4.4 eV.[34] However, in comparing the ambient stability of $(F_5PhO)_2$-F_4SiPc to $(F_5PhO)_2$-F_4SiPc and (tb-PhO)$_2$-F_{16}SiPc upon initial exposure to air, it is clear that the R_2-F_{16}SiPc derivatives suffer from less degradation in μ_e and V_T. For example, the R_2-F_{16}SiPc derivatives experience a decrease in μ_e of under 50% while $(F_5PhO)_2$-F_4SiPc experiences a decrease in average μ_e of up to two orders of magnitude. Degradation of μ_e during exposure to oxygen has been tied to the formation of localized electronic states below the LUMO of semiconducting polymers in the literature which can act as shallow electron traps.[45] (F_5PhO)2-F_4SiPc also has fewer peripheral fluorine atoms in the molecular structure which could otherwise participate in stabilizing electron transport in the material.[46] While axial fluorination can enable a deeper LUMO and electron transport in ambient conditions, a complex interplay exists between the role of fluorination, LUMO and air-stability of these compounds.[47] In reporting OTFTs with air-stable electron transport using $(F_5PhO)_2$-F_4SiPc, we demonstrate for the first time that the axial substituent in R_2-F_xSiPcs can enable ambient stability of the n-type operation of this class of semiconductor. These results are consistent with those obtained for other organic semiconductors with electron-deficient functional groups that are not part of the π-conjugated molecular core, where n-type operation in air could be further stabilized in devices based on diimide semiconductors.[48,49]

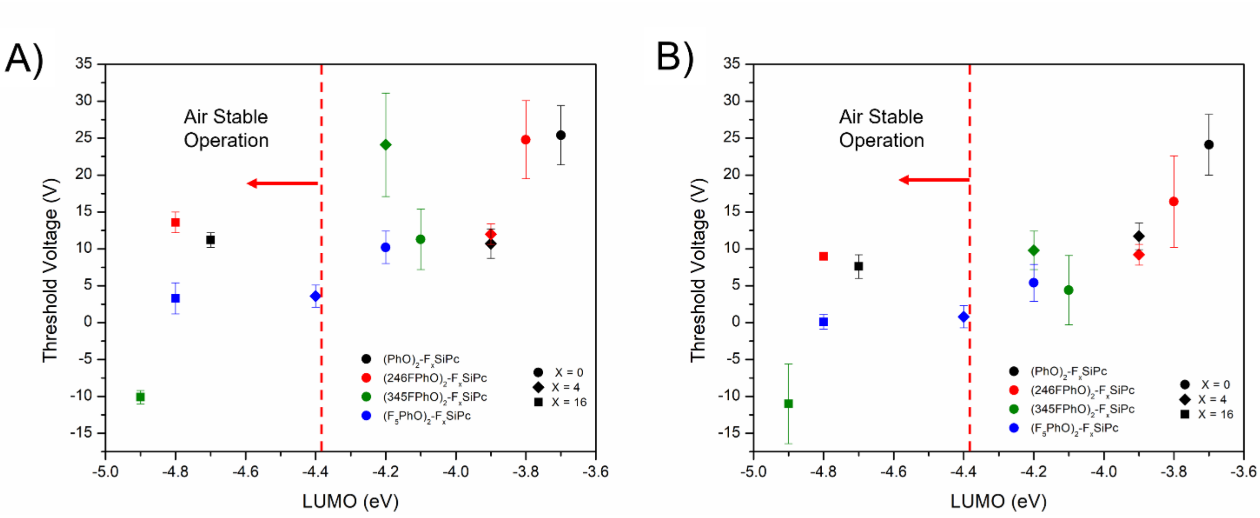

Figure 5.5 Device V_T versus absolute value of LUMO for R_2-F_xSiPcs in this work employing A) Ag and B) AgMn electrodes. Axial groups are represented by black (PhO), red (246FPhO), green (345FPhO) and blue (F_5PhO) symbols, while the number of peripheral fluorines are represented by circles (F = 0), diamonds (F = 4) and squares (F = 16).

Table 5.3 Summary of device parameters in N_2 and after initial exposure to air for (F_5PhO)-F_XSiPcs in BGTC OTFTs using Ag electrodes

Material	N_2				Air (t = 5 min)			
	μ_e $[cm^2 \cdot V^{-1} \cdot s^{-1}]^a$	V_T [V]^a	I_{on} [A]^b	I_{on}/I_{off}	μ_e $[cm^2 \cdot V^{-1} \cdot s^{-1}]^a$	V_T [V]^a	I_{on} [A]^b	I_{on}/I_{off}
$(F_5PhO)_2$-$F_{16}SiPc$	1.1 ± 0.3 x10^{-2}	10.2 ± 2.2	8.15 x10^{-6}	10^5	[-]	[-]	[-]	[-]
$(F_5PhO)_2$-F_4SiPc	5.1 ± 4.8 x10^{-3}	6.3 ± 1.5	2.81 x10^{-6}	10^4 - 10^5	4.5 ± 10.4 x10^{-5}	32.2 ± 12.7	5.46 x10^{-7}	10^3
$(F_5PhO)_2$-$F_{16}SiPc$	1.3 ± 0.4 x10^{-2}	3.3 ± 2.1	1.33 x10^{-5}	10^3 - 10^4	8.1 ± 0.3 x10^{-3}	10.1 ± 4.1	4.91 x10^{-6}	10^3 – 10^4

Long term Air Stability of R_2-$F_{16}SiPc$ Derivatives

We characterized all 12 R_2-F_xSiPcs in BGTC OTFTs in ambient conditions to evaluate how increasing peripheral and axial fluorination influences air stability. We previously performed preliminary characterization of air-stability and found that hexadecafluorinated SiPcs showed promise while operating under ambient conditions. [32,34] Of the 12 R_2-F_xSiPcs measured in ambient conditions in this work, only those with a LUMO deeper than -4.4 eV could transport electrons (**Figure 5.5**). To effectively compare the stability of the R_2-$F_{16}SiPc$ derivatives in ambient conditions, these materials were further characterized over fourteen days to observe the long-term performance change over time in a humid environment, with transfer curves shown in **Figure 5.28** and output curves shown in **Figure 5.30**. To evaluate the longer-term stability of R_2-$F_{16}SiPcs$ μ_e, V_T and saturation transconductance were extracted from OTFTs and plotted after being stored in ambient conditions for 5 minutes, 24 hours, 7 days (168 hours) and 14 days (336 hours) in **Figure 5.6**. μ_e and V_T values for initial exposure to air and after 14 days are summarized for each material in **Table 5.4** with the full series of data including transconductance in **Tables 5.7-5.9** of the Supporting Information. The trend for transconductance and μ_e are similar, with an initial decrease after 24 hours and beyond 168 hours for $(345FPhO)_2$-$F_{16}SiPc$ and $(F_5PhO)_2$-$F_{16}SiPc$. The μ_e, V_T and saturation transconductance remained relatively stable for $(246FPhO)_2$-$F_{16}SiPc$ and $(PhO)_2$-$F_{16}SiPc$ while V_T remained relatively constant after initial exposure for $(F_5PhO)_2$-$F_{16}SiPc$. Additionally, the average V_T of $(F_5PhO)_2$-$F_{16}SiPc$ after initial exposure to air showed a smaller overall change compared to F_2-$F_{16}SiPc$, with a ΔV_T of 6.8 V for $(F_5PhO)_2$-$F_{16}SiPc$ versus 9.8 V for

F_2-F_{16}SiPc.[32] The V_T of (345FPhO)-F_{16}SiPc demonstrated the largest increase from first exposure to the end of the measurement period with an additional ΔV_T of 14.7 V. These results demonstrate that the choice of axial substituents impact the operational stability of OTFTs and their electronic properties over time. Molecular structure having an influence on operational stability of OTFTs is consistent with other small molecule semiconductors such as diimide-based molecules.[48,50]

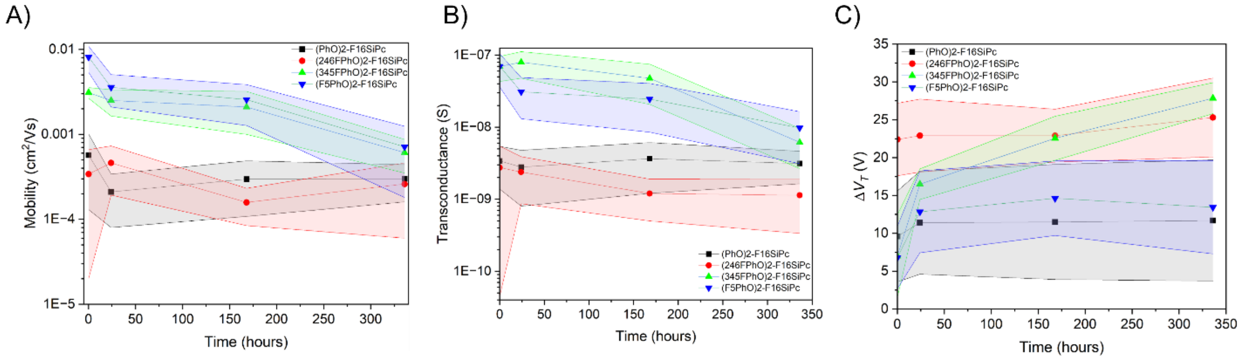

Figure 5.6 Plots of A) electron mobility, B) transconductance and C) change in V_T over time of (F_XPhO)-F_{16}SiPcs in BGTC OTFTs using Ag electrodes. Clear bands represent the standard deviation of data.

Table 5.4 Summary of device parameters in N$_2$ and up to 14 days for (F$_X$PhO)-F$_{16}$SiPcs in BGTC OTFTs using Ag electrodes.

Condition	**Material**	**μ_e [cm^2·V^{-1}·s^{-1}]^a**	**V_T [V]^a**	**I_{on} [A]^b**	**I_{on}/I_{off}**
N$_2$	(PhO)$_2$-F$_{16}$SiPc	1.1 ± 0.6 x10^{-3}	11.2 ± 1.0	8.06 x10^{-7}	10^4
	(246FPhO)$_2$-F$_{16}$SiPc	2.3 ± 0.6 x10^{-3}	13.6 ± 1.4	1.17 x10^{-6}	10^3
	(345FPhO)$_2$-F$_{16}$SiPc	3.4 ± 1.9 x10^{-3}	-10.1 ± 0.9	5.99 x10^{-6}	10^3
	(F$_5$PhO)$_2$-F$_{16}$SiPc	1.3 ± 0.4 x10^{-2}	3.3 ± 2.1	1.33 x10^{-5}	10^3 – 10^4
Air, t = 5 min	(PhO)$_2$-F$_{16}$SiPc	5.7 ± 4.4 x10^{-4}	20.8 ± 6.0	2.62 x 10^{-7}	10^3 - 10^4
	(246FPhO)$_2$-F$_{16}$SiPc	3.4 ± 3.2 x10^{-4}	36.0 ± 4.8	4.20 x10^{-8}	10^3
	(345FPhO)$_2$-F$_{16}$SiPc	3.1 ± 0.4 x10^{-3}	3.1 ± 5.5	4.34 x10^{-6}	10^3
	(F$_5$PhO)$_2$-F$_{16}$SiPc	8.1 ± 0.3 x10^{-3}	10.1 ± 4.1	4.91 x10^{-6}	10^3 – 10^4
Air, t = 14 days	(PhO)$_2$-F$_{16}$SiPc	3.0 ± 1.4 x10^{-4}	22.9 ± 8.0	7.16 x10^{-8}	10^3
	(246FPhO)$_2$-F$_{16}$SiPc	2.6 ± 2.0 x10^{-4}	38.9 ± 5.2	8.22 x10^{-9}	10^2 - 10^3
	(345FPhO)$_2$-F$_{16}$SiPc	6.1 ± 2.6 x10^{-4}	17.8 ± 2.1	5.01 x10^{-7}	10^3
	(F$_5$PhO)$_2$-F$_{16}$SiPc	7.1 ± 5.3 x10^{-4}	16.8 ± 6.2	1.82 x10^{-7}	10^3 – 10^4

a) μ_e and VT were calculated based on average values

b) Ion calculated based on median value

In addition to low lying LUMO energy levels, there are two other related factors that influence the oxygen and moisture sensitivity of OTFT device: the molecular functional groups and the resulting semiconductor film structure.[4,51] The addition of fluorinated substituents such as perfluorobenzene as side chains in diimide molecules demonstrated improved resistance to bias stress and performance degradation in molecular semiconductor-based OTFTs, which the authors partially attributed to the hydrophobicity of the side chain protecting the π-conjugated core.[48] This effect of fluorine-containing substituents or compounds on reducing the diffusion of moisture to the dieletric-semiconductor interface has also been shown for blends of TIPS ternary blends with poly(pentafluorostyrene) and polystyrene.[52] Among the four R$_2$-F$_{16}$SiPc derivatives reported in this work, we observed different degrees of performance degradation over time after exposure to air. To further probe factors influencing air-stable electron transport, thin-film semiconductors were characterized by atomic force microscopy (AFM, **Figure 5.7**) and X-ray diffraction (XRD, **Figure 5.31**).

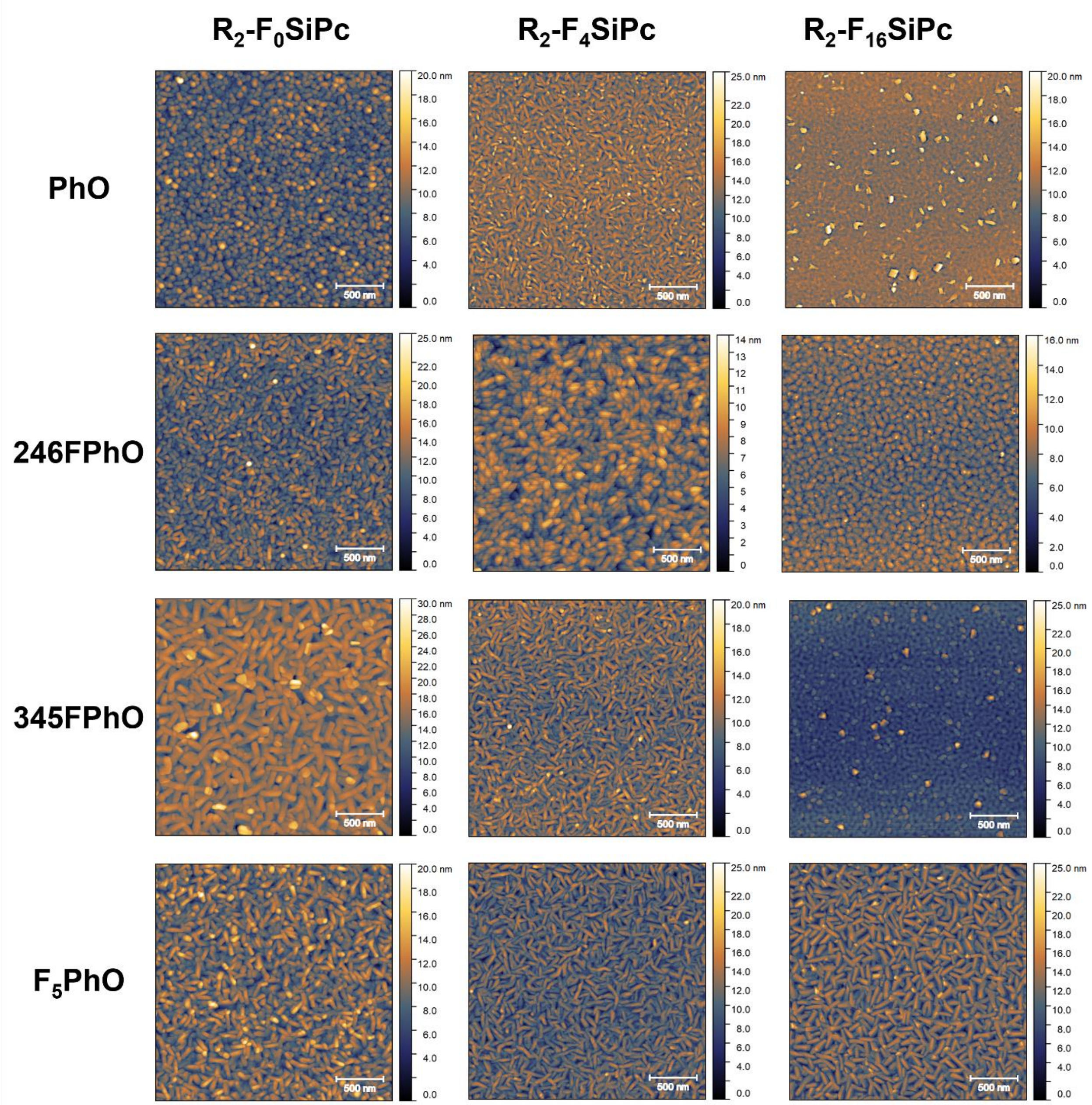

Figure 5.7 Atomic force microscopy images of R_2-F_xSiPcs in this work. Rows represent identical axial groups and columns represent number of peripheral fluorine atoms for a given functionalized R_2-F_xSiPc.

Films of R_2-F_xSiPcs were characterized with a range of morphologies including amorphous films with small crystalline grains ((PhO)$_2$-F_{16}SiPc and (345FPhO)$_2$-F_{16}SiPc), densely packed isotropic grains and randomly oriented needle-like anisotropic grains ((345FPhO)$_2$-SiPc and all (F_5PhO)$_2$-F_xSiPc derivatives). These morphologies are consistent with our previous reports which demonstrate that the choice of axial groups can induce significant differences in morphology for phenoxy-substituted R_2-SiPcs.[30,34,42] The texture of films fabricated from $(F_5PhO)_2$-F_xSiPc have similar features, with various sizes of needle-like anisotropic grains (**Figure 5.7**). Additionally, OTFTs made from this subset of materials led to the best μ_e (**Table 5.2**) suggesting this morphology is favoured for charge transport. This is consistent with our previous reports of non-peripherally fluorinated R_2-SiPcs where films with anisotropic features across the substrate yielded better-performing OTFTs.[4253,54] In addition to AFM, PXRD can provide insight into the crystallinity of the films which is often correlated to performance. While PXRD patterns of R_2-F_xSiPcs generally demonstrated good crystalline diffraction for R_2-SiPcs and R_2-F_4SiPcs compounds, diffraction of R_2-F_{16}SiPcs was less significant suggesting a more amorphous film. The additional fluorine groups in the periphery of R_2-F_{16}SiPcs could provide additional substrate interactions disrupting intermolecular interactions and film growth.[55] The radial power spectral density functions (PSDFs) of the AFM data, was used to characterize the domain size, distribution of grain sizes and other differences in thin-film microstructure.[56,57] PSDF generated from AFM images provides similar data to resonant soft X-ray scattering.[56,58] A summary of PSDF data and roughness extracted from AFM images is presented in **Table 5.5** and is visualized in **Figure 5.32** of the Supporting Information. $\boldsymbol{Iq^2_{\max}}$ is the maximum corrected intensity and the q-value where it occurs typically refers to the domain size with the largest population in the film, and where a smaller q means a greater domain size. Greater domain size typically means a lower density of grain boundaries which is often correlated to μ_e in small molecule semiconductors[59,60] including SiPcs. The Full width half max (FWHM) of the PSDF (**Table 5.5**) can also provide insight into the size distribution of domains in the film.

Table 5.5 Summary of radial power spectral density values calculated from AFM height images and corrected by q^2, mode domain sizes by PSDF analysis, RMS roughness calculated from AFM images and electron mobility of devices using AgMn electrodes.

Material	Iq^2_{max}	**Mode Domain Size (nm)**	**FWHM**	**RMS Roughness (nm)**	μ_e **[cm^2·V^{-1}·s^{-1}]**[a]
$(PhO)_2$-SiPc	0.53	11.9	0.34	2.21	7.1 ± 6.5 x10^{-4}
$(PhO)_2$-F_4SiPc	0.72	8.7	0.49	2.21	3.0 ± 1.6 x10^{-3}
$(PhO)_2$-F_{16}SiPc	0.66	9.5	0.54	1.31	1.7 ± 1.2 x10^{-3}
$(246FPhO)_2$-SiPc	0.62	10.1	0.44	2.47	2.0 ± 1.2 x10^{-3}
$(246FPhO)_2$-F_4SiPc	0.45	14.0	0.48	1.50	1.9 ± 1.1 x10^{-2}
$(246FPhO)_2$-F_{16}SiPc	0.47	13.4	0.18	1.44	4.8 ± 1.6 x10^{-3}
$(345FPhO)_2$-SiPc	0.35	18.0	0.40	2.51	1.6 ± 0.7 x10^{-2}
$(345FPhO)_2$-F_4SiPc	0.61	10.3	0.49	1.98	2.2 ± 1.7 x10^{-4}
$(345FPhO)_2$-F_{16}SiPc	0.64	9.8	0.36	1.69	2.4 ± 1.1 x10^{-3}
$(F_5PhO)_2$-SiPc	0.44	14.3	0.34	2.24	9.6 ± 3.0 x10^{-2}
$(F_5PhO)_2$-F_4SiPc	0.72	8.7	0.52	2.35	1.6 ± 0.3 x10^{-2}
$(F_5PhO)_2$-F_{16}SiPc	0.52	12.1	0.36	2.57	2.2 ± 0.3 x10^{-2}

a) **μe** and *VT* were calculated based on average values

PSDF data demonstrates that there is no correlation between the degree of peripheral fluorination and average domain size or distribution of domain sizes. However, in comparing the series of $(F_5PhO)_2$-F_xSiPc which have a similar texture of needle-like anisotropic grains and a range of domain sizes between 8.7 nm and 14.3 nm, μ_e increases with increasing domain size and decreasing dispersity of domain sizes. The same effect of domain size and dispersity is observed for $(345FPhO)_2$-SiPc and $(345FPhO)_2$-F_4SiPc where OTFTs fabricated with the $(345FPhO)_2$-SiPc demonstrate an increase in μ_e of almost two orders of magnitude for an increase in average domain size of 7.7 nm. The degradation in performance of $(345FPhO)_2$-F_{16}SiPc shown by the largest shift in V_T after first exposure can be attributed to film morphology. $(345FPhO)_2$-F_{16}SiPc has among the smallest average domain sizes extracted from PSDF analysis meaning that there is a higher density of grains for adsorption of moisture and subsequent diffusion to the dielectric interface. While we expect a similar increase in V_T over time for $(PhO)_2$-F_{16}SiPc, the AFM shows a film that has a more densely packed texture which could slow diffusion of moisture through the bulk of the film. These results suggest that while LUMO level is important to provide air-stable performance, choice of phenoxy group is equally important as it will dictate the resulting film structure which will lead to improved device performance in N_2 and air.

5.4 Conclusion

We report the synthesis and characterization of twelve R_2-F_xSiPcs with varying degrees of peripheral and axial fluorination and incorporate them as the semiconductor into BGTC OTFTs. HOMO and LUMO values were calculated with experimental values extracted by UPS and solid-state UV-Vis, showing a drop in LUMO of up to 0.9 eV for fully peripherally fluorinated materials. We demonstrate a clear relationship between OTFT V_T and semiconductor LUMO levels for both Ag and Ag/Mn electrodes. While a deeper LUMO of the four R_2-F_{16}SiPc compounds resulted in a better alignment with the work function of Ag electrodes, devices incorporated into OTFTs with Ag electrodes and a Mn contact interlayer yielded higher μ_e and V_T closer to 0 V. Of the R_2-F_xSiPcs in this work, the four R_2-F_{16}SiPc and $(F_5PhO)_2$-F_4SiPc demonstrated air-stable electron transport at room temperature and a humidity of 40%. The four R_2-F_{16}SiPc derivatives demonstrated only a small change in V_T over 14 days stored in ambient conditions after their first measurement. $(F_5PhO)_2$-F_{16}SiPc displayed the least change in V_T over 14 days compared to all other reported derivatives including previously reported F_2-F_{16}SiPc. $(F_5PhO)_2$-F_4SiPc, which has a similar LUMO level to previously reported air-stable (tb-PhO)$_2$-F_{16}SiPc, could also transport electrons after exposure to air which demonstrates for the first time that the axial substituent of R_2-F_XSiPcs can influence the ambient stability of electron transport in this class of semiconductors. This work provides a clear structure property relationship between the role of axial and peripheral fluorination on the optical and electrical properties of R_2-F_xSiPcs and provides clear guidelines for designing air stable, n-type semiconductors expands the catalogue of available air-stable n-type semiconductors with few simple synthetic steps. Finally, this study demonstrates that peripheral fluorination can be tuned to provide air-stable operation while phenoxy groups can be used to control solid state arrangement and film formation which is critical for charge transport and device application.

Acknowledgements

This work was supported by NSERC Discovery grant RGPIN 2020-04079 (B.H.L.), the Canada Research Chairs Program 950-230724 (B.H.L.) and NSERC CGS-D (B.K.). Infrastructure used to complete this work was acquired using CFI-JELF #30488 (B.H.L.) and NSERC RTI

472921-2015 (B.H.L.). We recognize the Centre for Research in Photonics at the University of Ottawa (CRPuO) for allowing access to the AFM.

Supporting Information

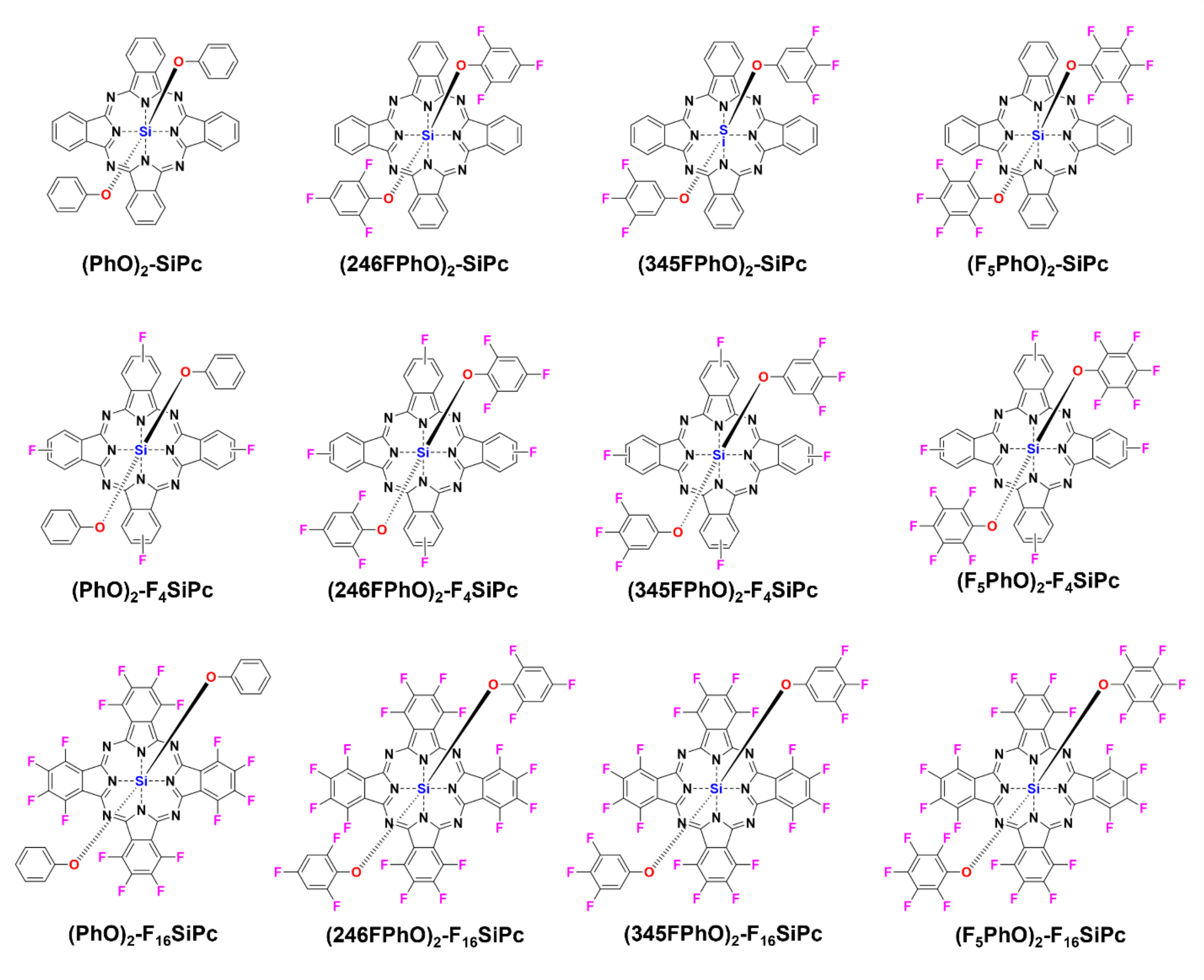

Figure 5.8 Structures of R_2-F_xSiPcs reported in this work.

Mass Spec

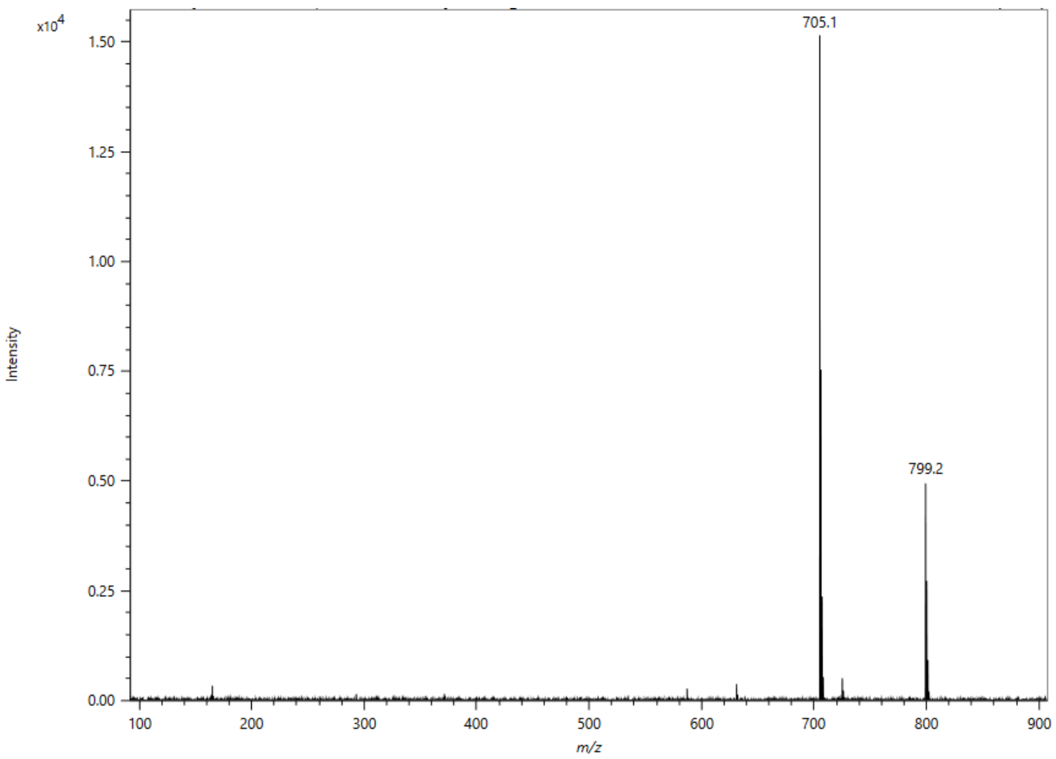

Figure 5.9 DART HR-MS spectrum of $(PhO)_2$-F_4SiPc.

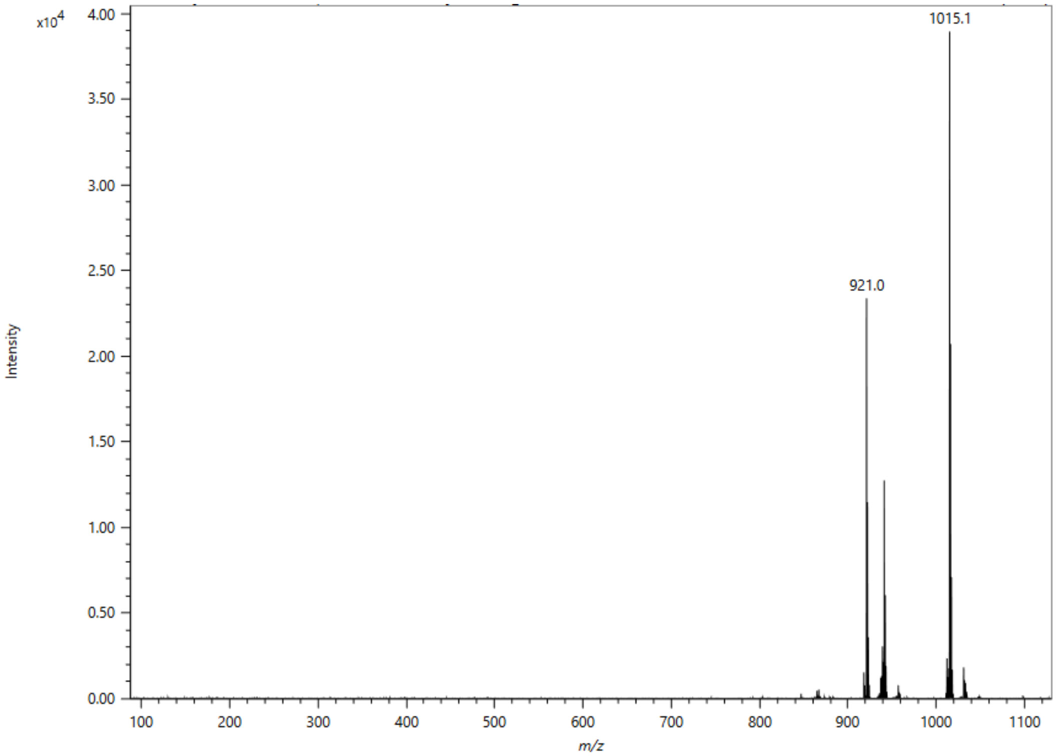

Figure 5.10 DART HR-MS spectrum of $(PhO)_2$-F_{16}SiPc.

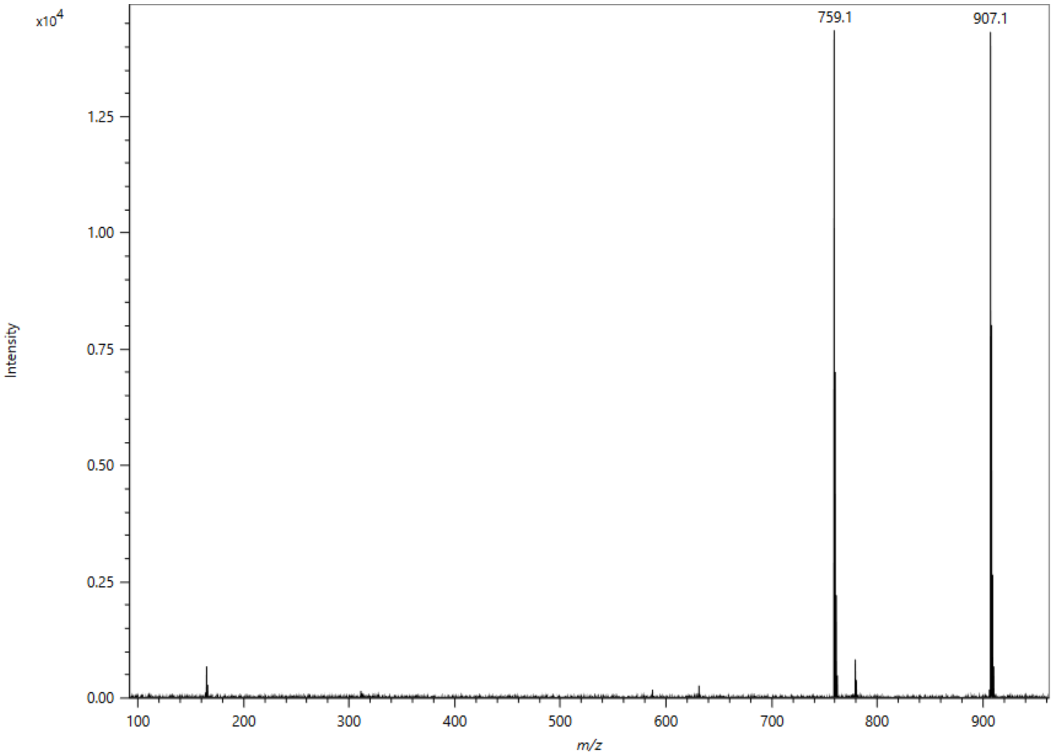

Figure 5.11 DART HR-MS spectrum of (246F-PhO)$_2$-F_4SiPc.

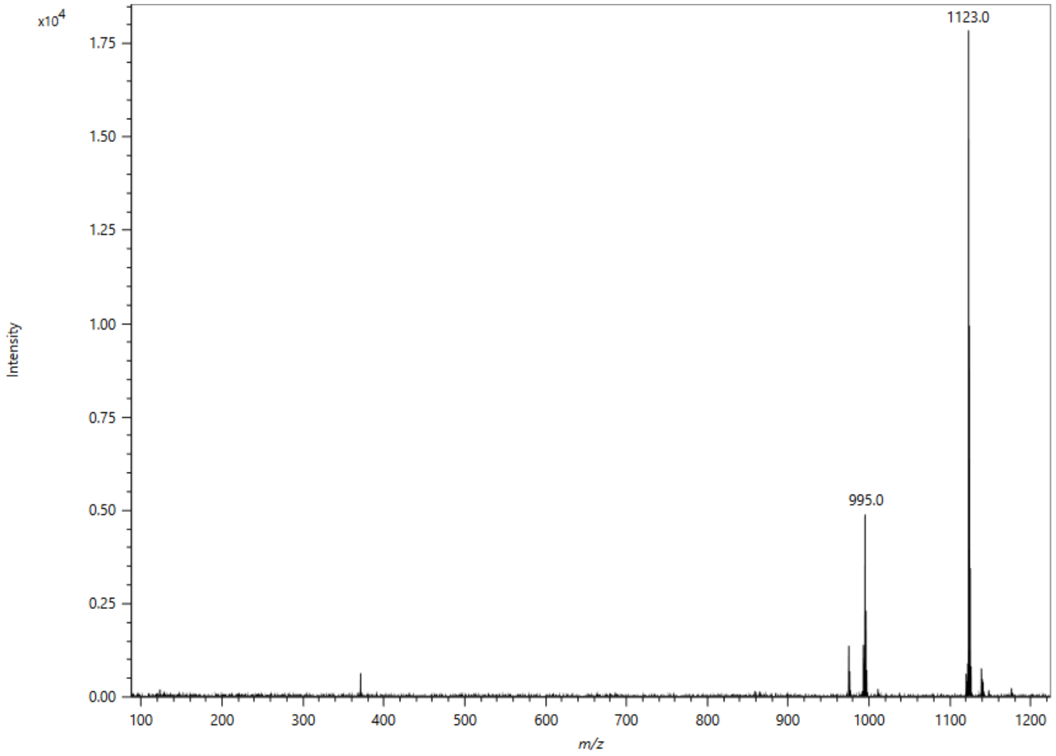

Figure 5.12 DART HR-MS spectrum of $(246FPhO)_2$-F_{16}SiPc.

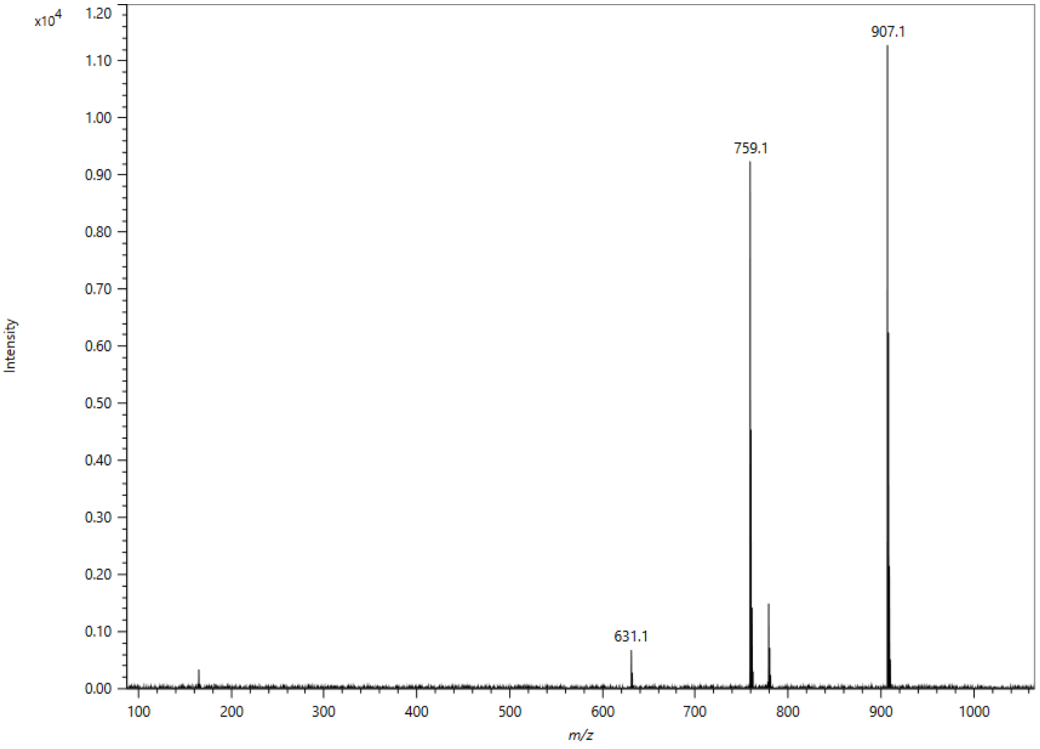

Figure 5.13 DART HR-MS spectrum of $(345FPhO)_2$-F_4SiPc.

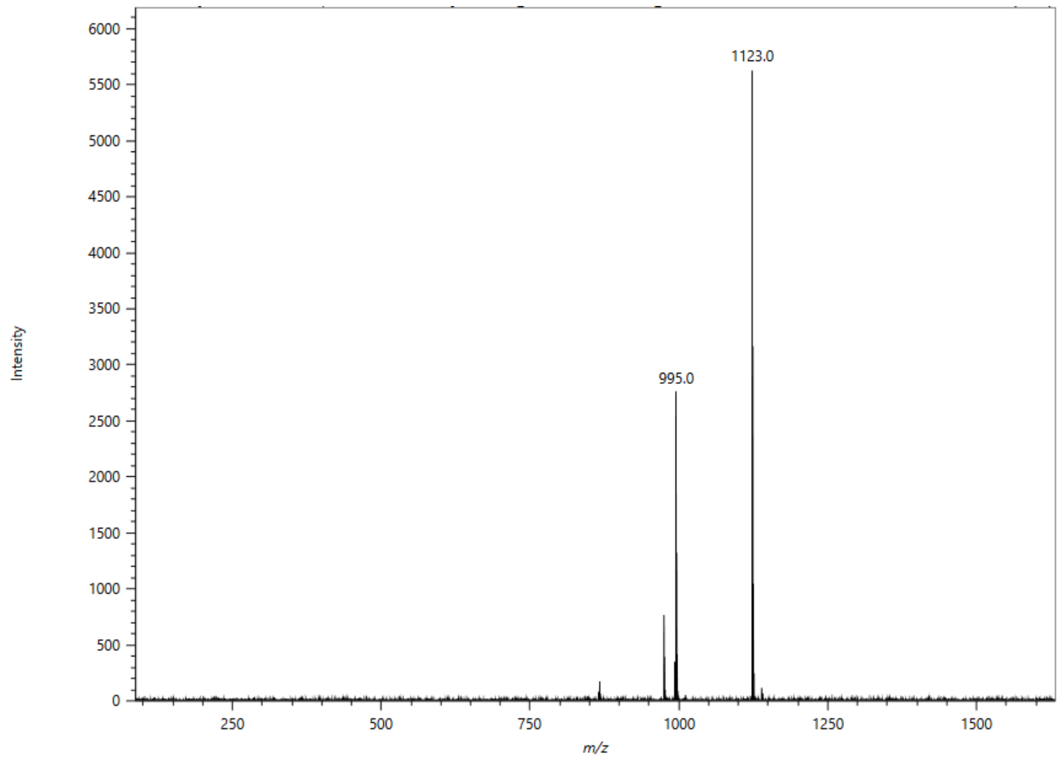

Figure 5.14 DART HR-MS spectrum of $(345FPhO)_2$-$F_{16}SiPc$.

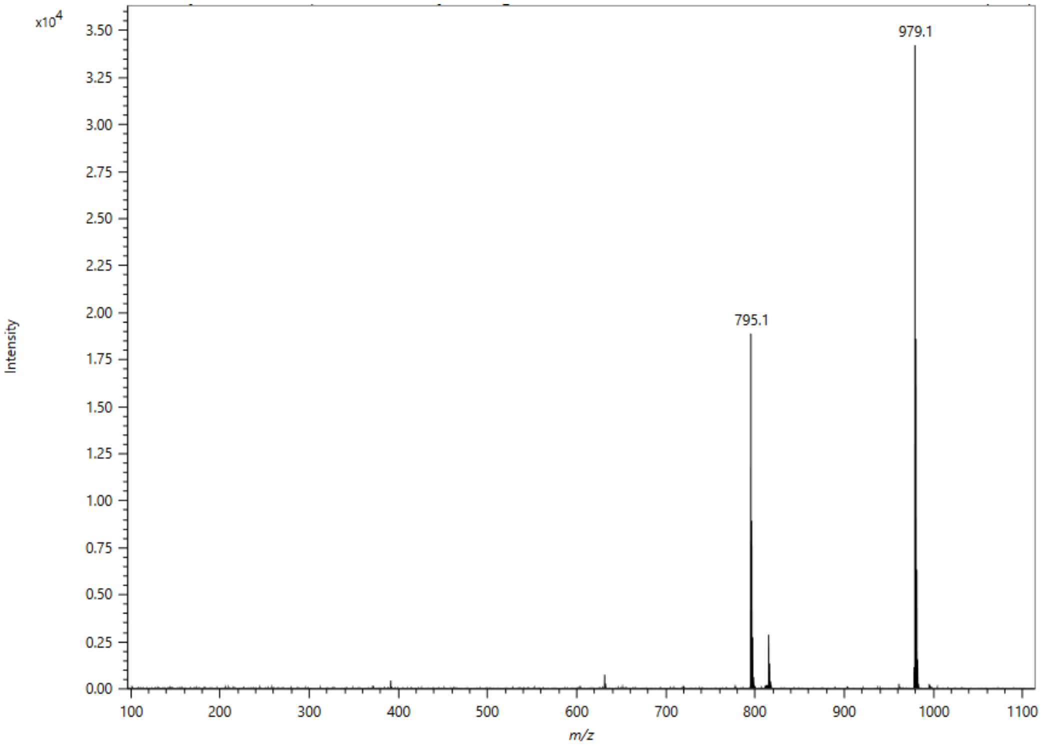

Figure 5.15 DART HR-MS spectrum of $(F_5PhO)_2$-F_4SiPc.

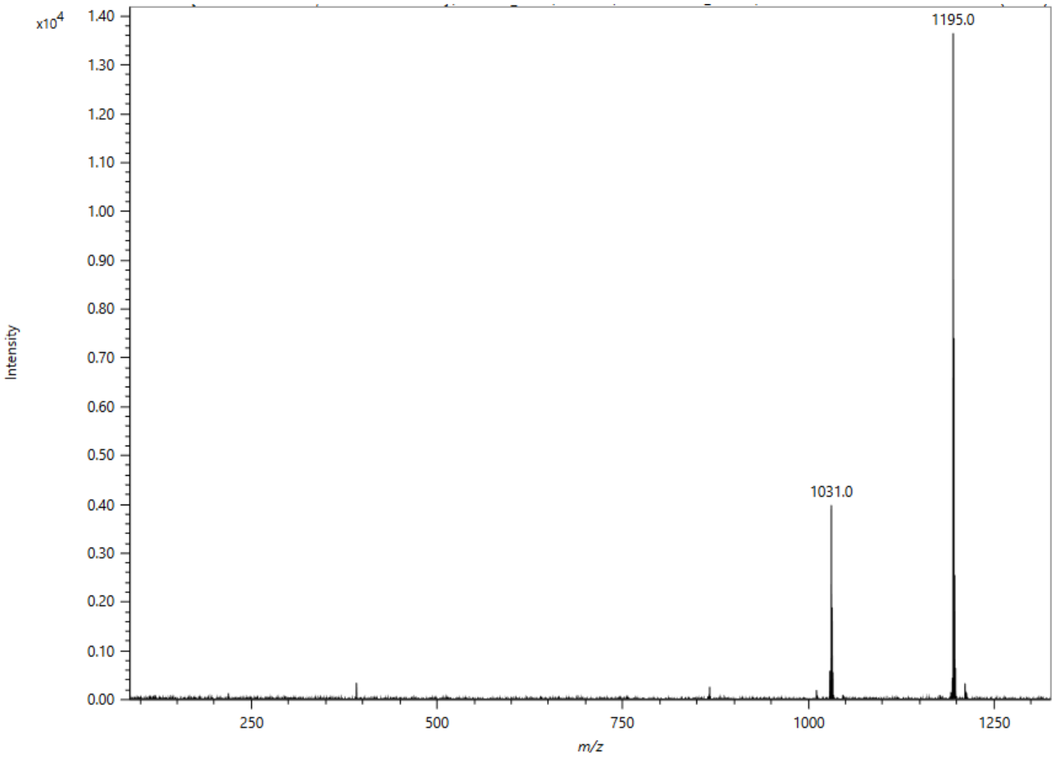

Figure 5.16 DART HR-MS spectrum of $(F_5PhO)_2$-F_{16}SiPc.

NMR

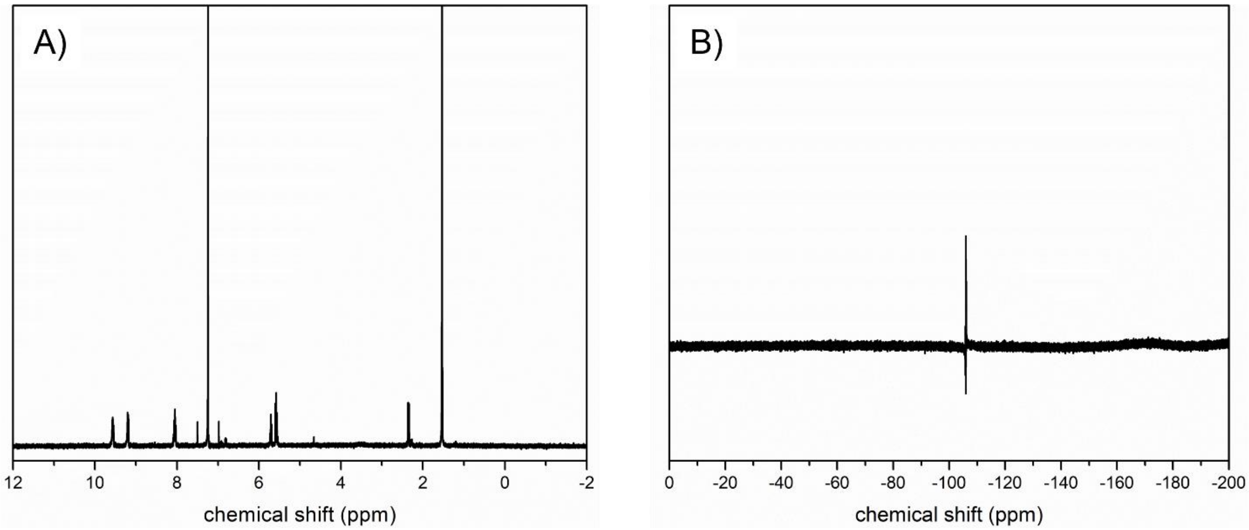

Figure 5.17 A) ^{1}H NMR and B) ^{19}F NMR spectra of $(PhO)_2$-F_4SiPc in deuterated chloroform

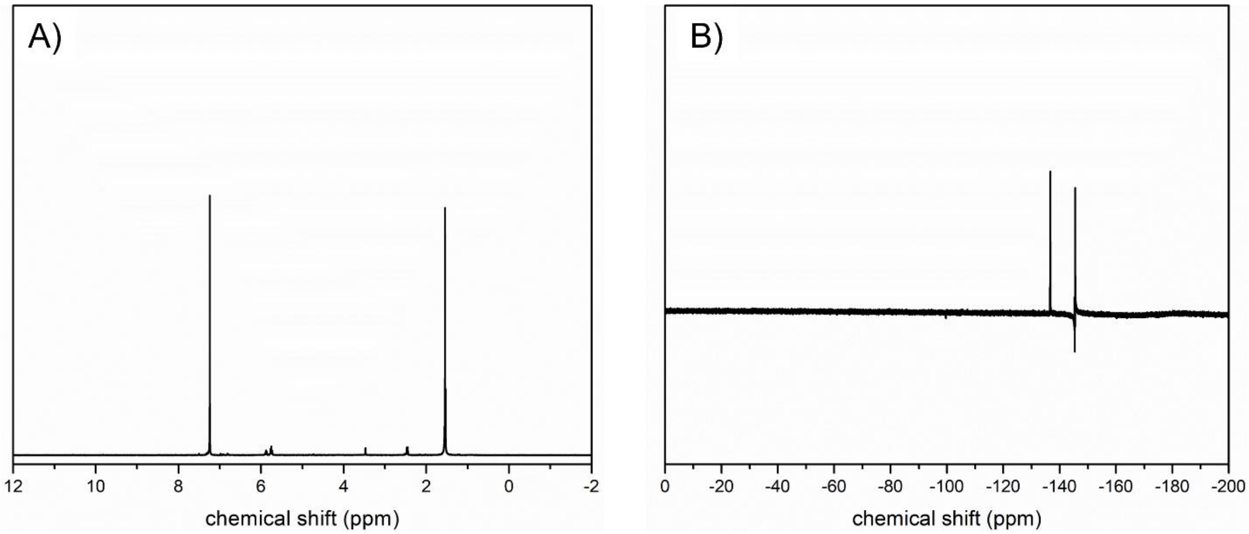

Figure 5.18 A) ^{1}H NMR and B) ^{19}F NMR spectra of $(PhO)_2$-F_{16}SiPc in deuterated chloroform

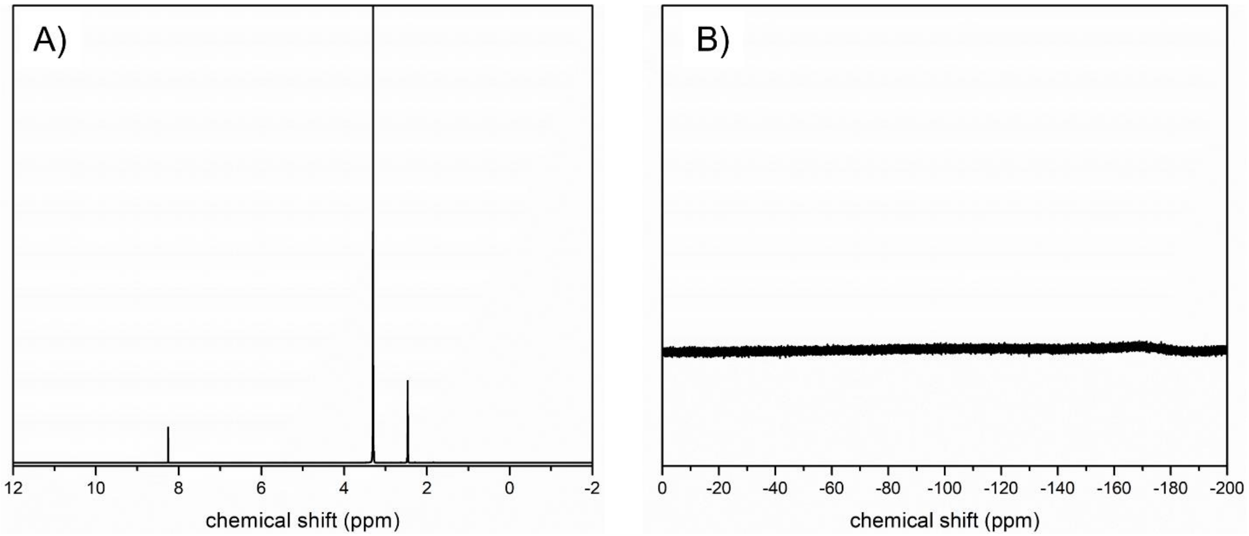

Figure 5.19 A) ^{1}H NMR and B) ^{19}F NMR spectra of $(246FPhO)_2$-F_4SiPc in deuterated chloroform

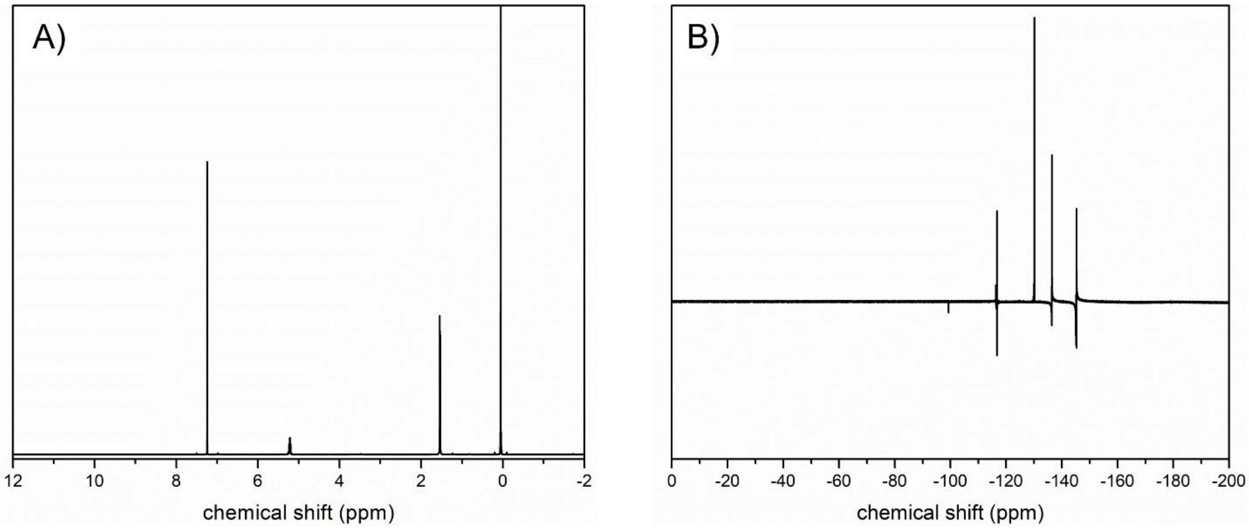

Figure 5.20 A) ^{1}H NMR and B) ^{19}F NMR spectra of $(246FPhO)_2$-F_{16}SiPc in deuterated chloroform

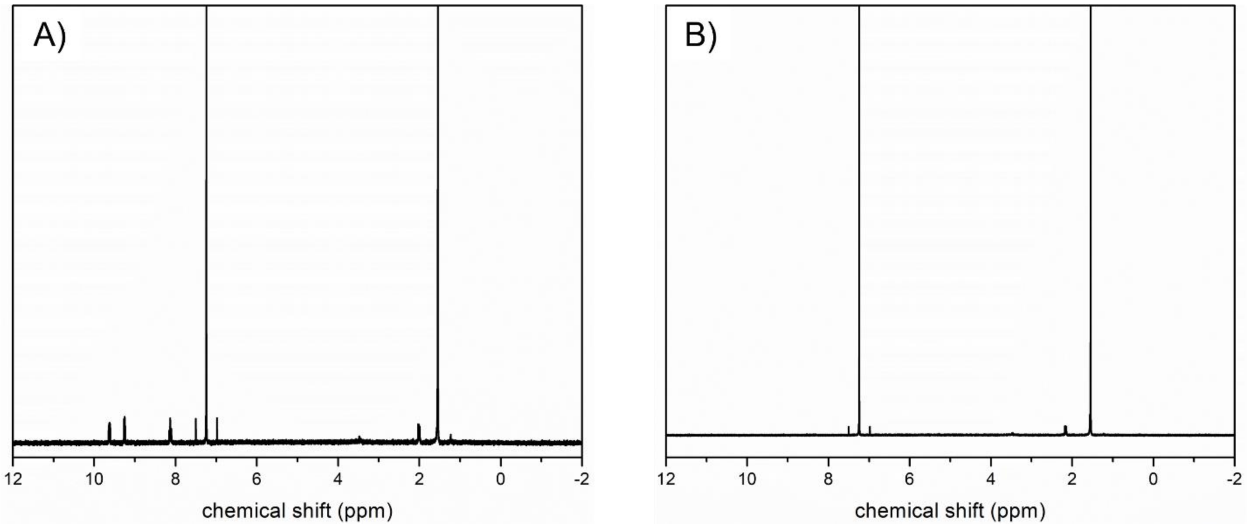

Figure 5.21 A) ^{1}H NMR and B) ^{19}F NMR spectra of $(345FPhO)_2$-F_4SiPc in deuterated chloroform

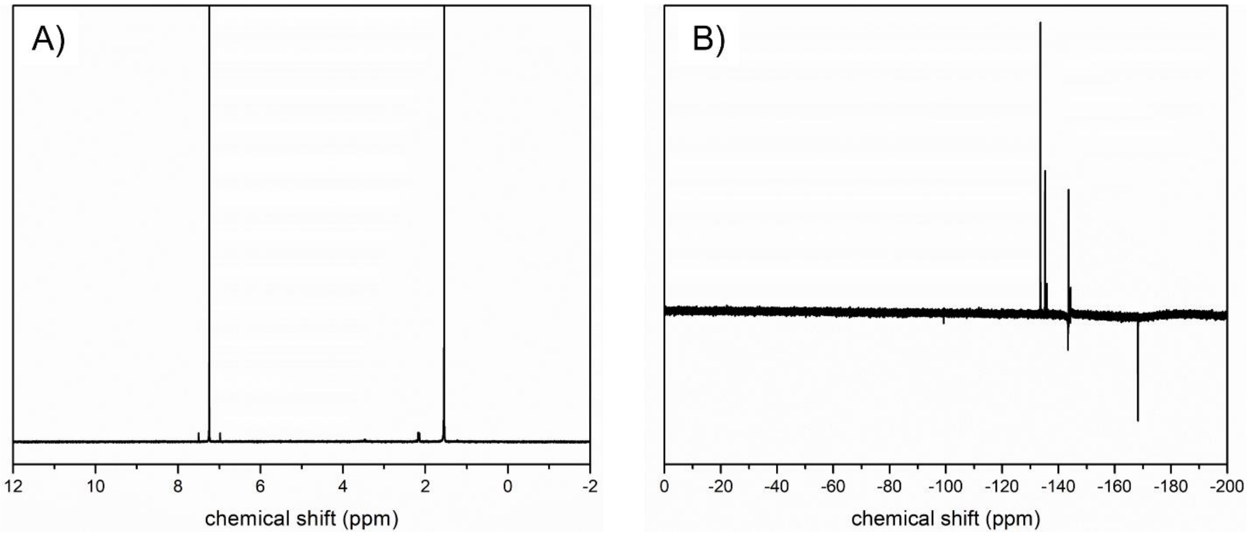

Figure 5.22 A) ^{1}H NMR and B) ^{19}F NMR spectra of (345FPhO)$_2$-F$_{16}$SiPc in deuterated chloroform

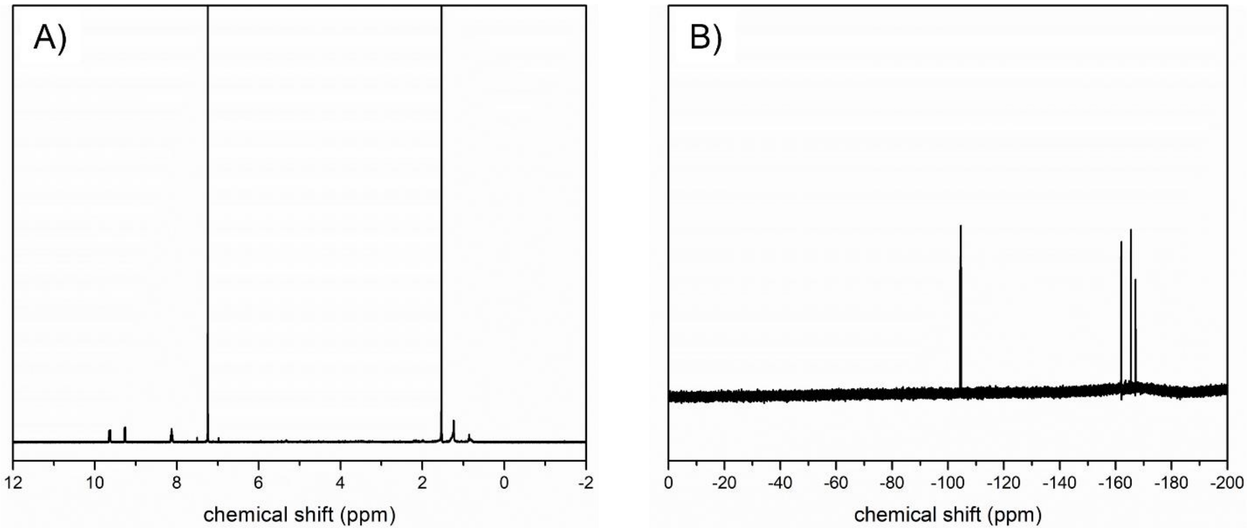

Figure 5.23 A) ^{1}H NMR and B) ^{19}F NMR spectra of (F$_5$PhO)$_2$-F$_4$SiPc in deuterated chloroform

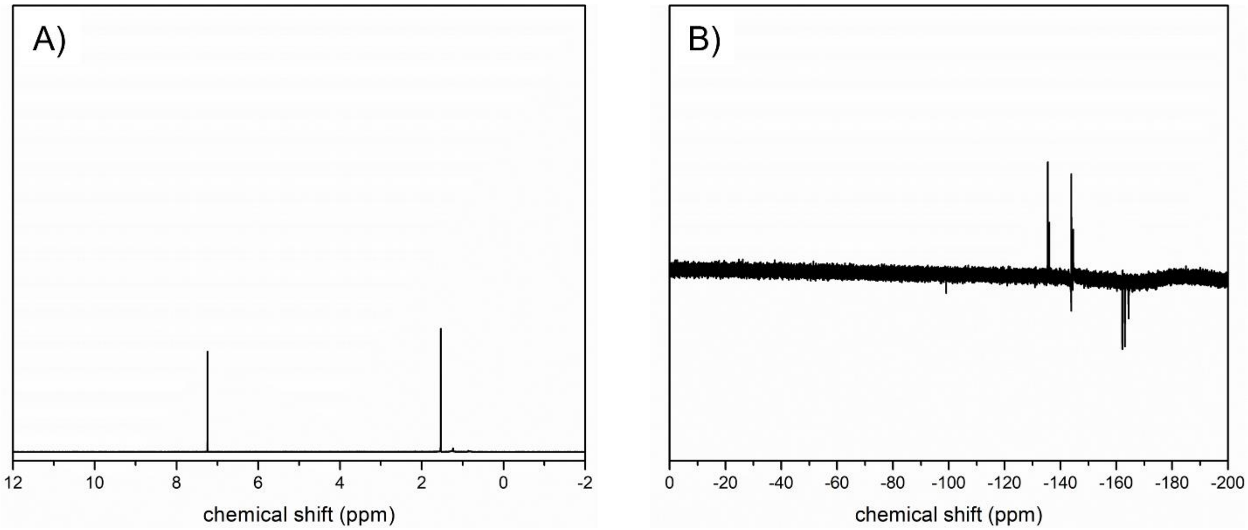

Figure 5.24 A) ^{1}H NMR and B) ^{19}F NMR spectra of $(F_5PhO)_2$-F_{16}SiPc in deuterated chloroform

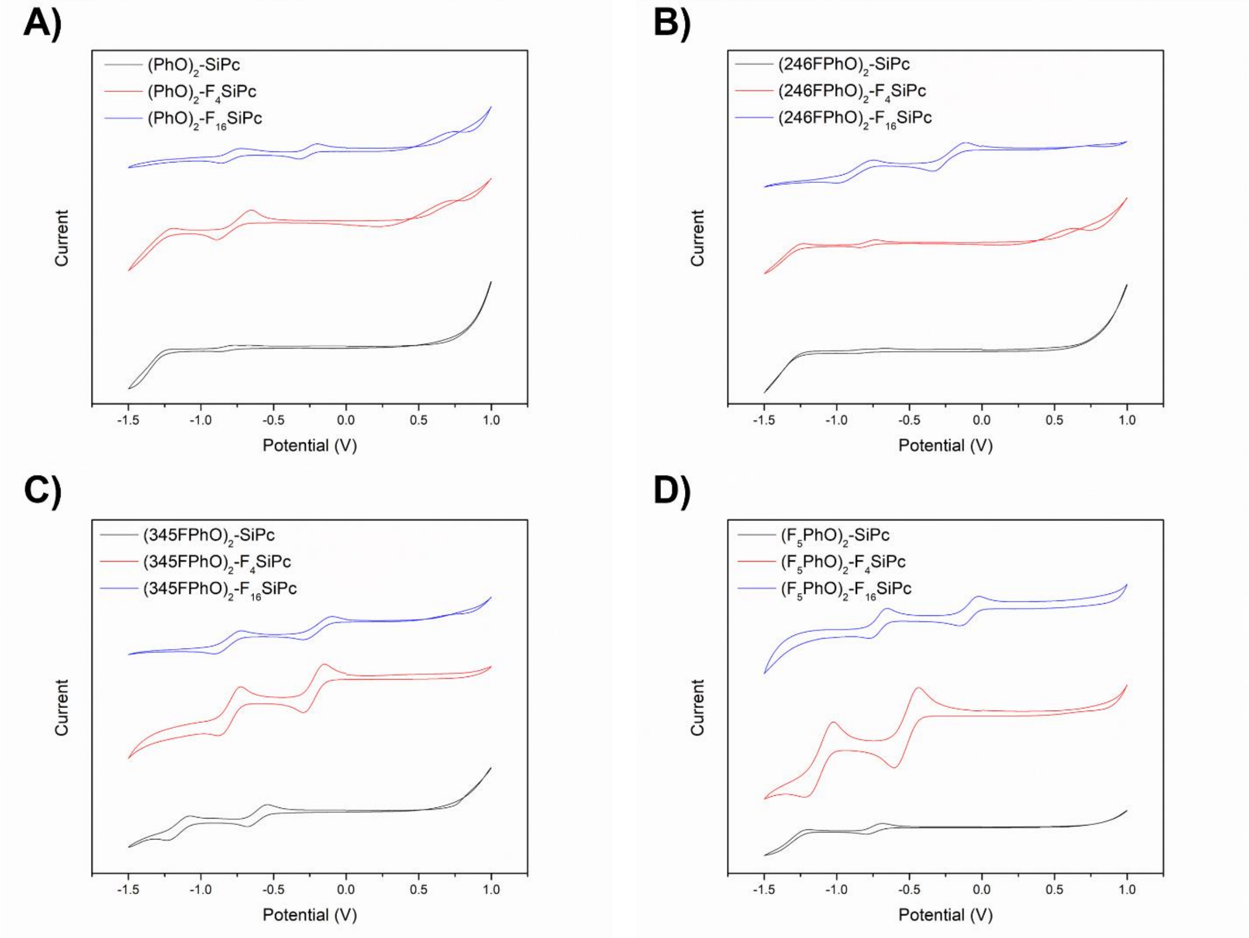

Figure 5.25 Cyclic voltammograms of R_2-F_xSiPcs in this work measured in THF for axial groups A) PhO, B) 246FPhO, C) 345FPhO and D) F_5PhO

Table 5.6 Electrical performance of OTFTs incorporating evaporated R_2-F_xSiPcs with Ag electrodes.

Compound	**μ_e [cm^2·V^{-1}·s^{-1}]^a**	***V_T* [V]^a**	***I_{on}* [A]^b**	***I_{on}/I_{off}***	***n***
$(PhO)_2$-SiPc	2.3± 2.2 x10^{-4}	25.4 ± 4.0	4.53 x10^{-8}	10^3 – 10^4	32
$(PhO)_2$-F_4SiPc	2.6 ± 1.6 x10^{-3}	10.7 ± 2.0	9.01 x10^{-7}	10^4 - 10^5	39
$(PhO)_2$-F_{16}SiPc	1.1 ± 0.6 x10^{-3}	11.2 ± 1.0	8.06 x10^{-7}	10^4	35
$(246FPhO)_2$-SiPc	1.4 ± 1.3 x10^{-3}	24.8 ± 5.3	1.38 x10^{-7}	10^4	32
$(246FPhO)_2$-F_4SiPc	6.6 ± 2.4 x10^{-3}	12.0 ± 1.4	2.82 x10^{-6}	10^4 - 10^5	40
$(246FPhO)_2$-F_{16}SiPc	2.3 ± 0.6 x10^{-3}	13.6 ± 1.4	1.17 x10^{-6}	10^3	39
$(345FPhO)_2$-SiPc	4.6 ± 2.1 x10^{-3}	11.3 ± 4.1	2.94 x10^{-6}	10^4 – 10^5	37
$(345FPhO)_2$-F_4SiPc	3.8 ± 3.4 x10^{-4}	24.1 ± 7.0	1.34 x10^{-6}	10^3	35
$(345FPhO)_2$-F_{16}SiPc	3.4 ± 1.9 x10^{-3}	-10.1 ± 0.9	5.99 x10^{-6}	10^3	10
$(F_5PhO)_2$-SiPc	1.1 ± 0.3 x10^{-2}	10.2 ± 2.2	8.15 x10^{-6}	10^5	38
$(F_5PhO)_2$-F_4SiPc	5.1 ± 4.8 x10^{-3}	6.3 ± 1.5	2.81 x10^{-6}	10^4 - 10^5	37
$(F_5PhO)_2$-F_{16}SiPc	1.3 ± 0.4 x10^{-2}	3.3 ± 2.1	1.33 x10^{-5}	10^3 - 10^4	38

a) μe and *VT* were calculated based on average values

b) *Ion calculated based on median value*

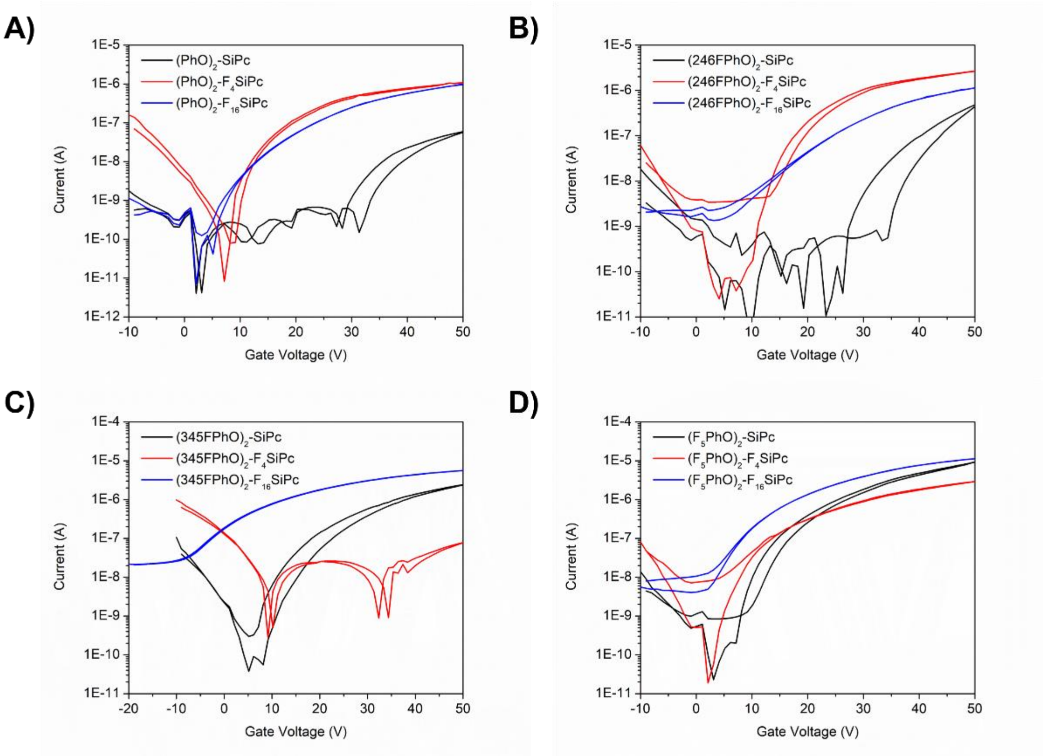

Figure 5.26 Transfer curves (V_{DS} = 50V) R$_2$-F$_x$SiPc derivatives in OTFTs employing Ag electrodes measured in a nitrogen glovebox: A) (PhO)$_2$-F$_x$SiPc, B) (246FPhO)$_2$-F$_x$SiPc, C) (345FPhO)$_2$-F$_x$SiPc and D) (F$_5$PhO)$_2$-F$_x$SiPc.

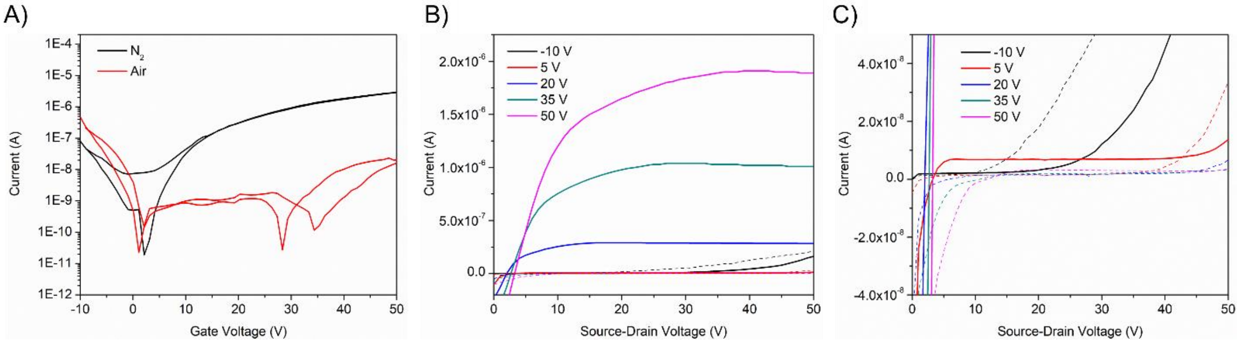

Figure 5.27 A) Transfer curve (V_{DS} = 50V) B) output curve and C) inset of output curve of (F$_5$PhO)$_2$-F$_4$SiPc OTFTs with Ag electrodes characterized in N$_2$ (solid lines in output curve) and air (dashed lines in output curve).

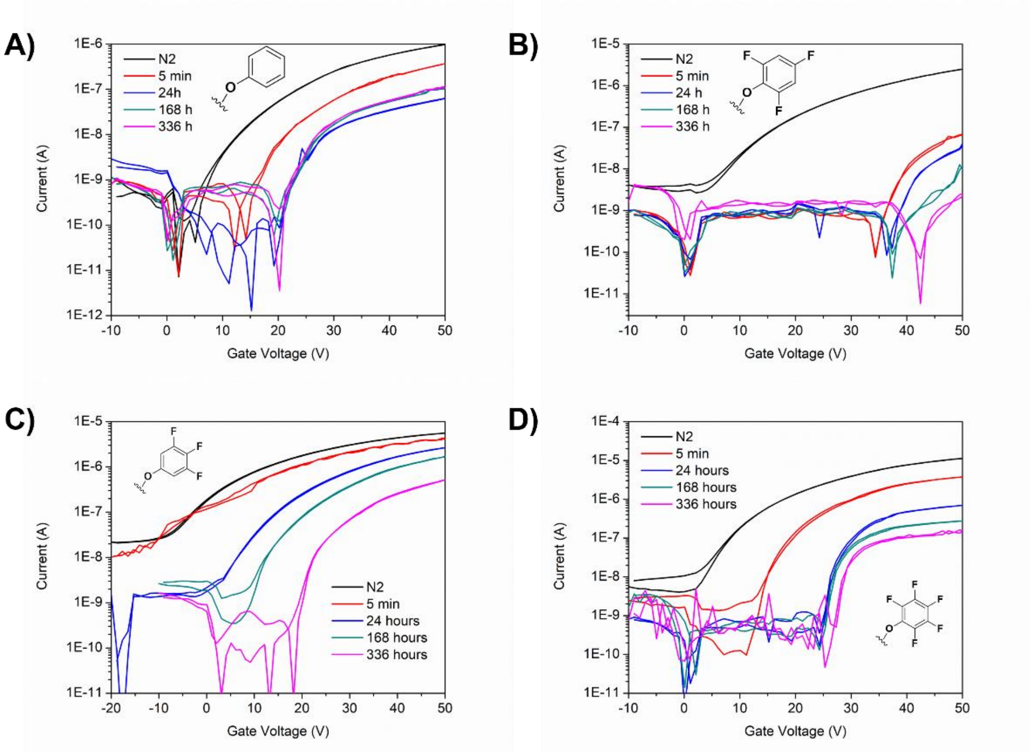

Figure 5.28 Transfer curves (V_{DS} = 50V) R_2-F_{16}SiPc derivatives in OTFTs employing Ag electrodes measured in a nitrogen glovebox and over 336 hours (14 days) in air: A) $(PhO)_2$-F_xSiPc, B) $(246FPhO)_2$-F_xSiPc, C) $(345FPhO)_2$-F_xSiPc and D) $(F_5PhO)_2$-F_xSiPc.

Table 5.7 Electron mobility from first measurement in air up to 14 days (336 hours) for (F_XPhO)-F_{16}SiPcs in BGTC OTFTs using Ag electrodes.

Time (hours)	**μ_e [cm^2·V^{-1}·s^{-1}]**			
	$(PhO)_2$-F_{16}SiPc	$(246FPhO)_2$-F_{16}SiPc	$(345FPhO)_2$-F_{16}SiPc	$(F_5PhO)_2$-F_{16}SiPc
0.08333	5.7 ± 4.4 x10^{-4}	3.4 ± 3.2 x10^{-4}	3.1 ± 0.4 x10^{-3}	8.1 ± 2.8 x10^{-3}
24	2.1 ± 1.3 x10^{-4}	4.6 ± 2.7 x10^{-4}	2.5 ± 0.9 x10^{-3}	3.6 ± 1.5 x10^{-3}
168	3.0 ± 1.9 x10^{-4}	1.6 ± 0.7 x10^{-4}	2.1 ± 1.1 x10^{-3}	2.6 ± 1.3 x10^{-3}
336	3.0 ± 1.4 x10^{-4}	2.6 ± 2.0 x10^{-4}	0.6 ± 0.3 x10^{-3}	0.7 ± 0.5 x10^{-3}

Table 5.8 Transconductance from first measurement in air up to 14 days (336 hours) for (F_XPhO)-F_{16}SiPcs in BGTC OTFTs using Ag electrodes.

Time (hours)	**Transconductance (S)**			
	$(PhO)_2$-F_{16}SiPc	$(246FPhO)_2$-F_{16}SiPc	$(345FPhO)_2$-F_{16}SiPc	$(F_5PhO)_2$-F_{16}SiPc
0.08333	$3.9 \pm 2.0 \times 10^{-9}$	$2.8 \pm 2.7 \times 10^{-9}$	$7.0 \pm 2.6 \times 10^{-8}$	$7.0 \pm 3.4 \times 10^{-8}$
24	$2.8 \pm 2.0 \times 10^{-9}$	$2.4 \pm 1.5 \times 10^{-9}$	$8.0 \pm 3.0 \times 10^{-8}$	$3.1 \pm 1.8 \times 10^{-8}$
168	$3.7 \pm 2.5 \times 10^{-9}$	$1.2 \pm 0.7 \times 10^{-9}$	$4.8 \pm 2.7 \times 10^{-8}$	$2.5 \pm 1.6 \times 10^{-8}$
336	$3.1 \pm 1.5 \times 10^{-9}$	$1.1 \pm 0.8 \times 10^{-9}$	$0.6 \pm 0.3 \times 10^{-8}$	$1.0 \pm 0.7 \times 10^{-8}$

Table 5.9 Threshold voltage shift from first measurement in air up to 14 days (336 hours) relative to values measured in N_2 for (F_XPhO)-F_{16}SiPcs in BGTC OTFTs using Ag electrodes.

Time (hours)	ΔVT			
	$(PhO)_2$-F_{16}SiPc	$(246FPhO)_2$-F_{16}SiPc	$(345FPhO)_2$-F_{16}SiPc	$(F_5PhO)_2$-F_{16}SiPc
0.08333	9.6 ± 6.0	22.4 ± 4.8	7.0 ± 5.5	6.8 ± 4.1
24	11.4 ± 6.8	22.9 ± 4.8	16.5 ± 2.0	12.9 ± 5.4
168	11.5 ± 7.6	22.9 ± 3.5	22.6 ± 2.9	14.6 ± 4.9
336	11.7 ± 8.0	25.3 ± 5.2	27.9 ± 2.0	13.5 ± 6.1

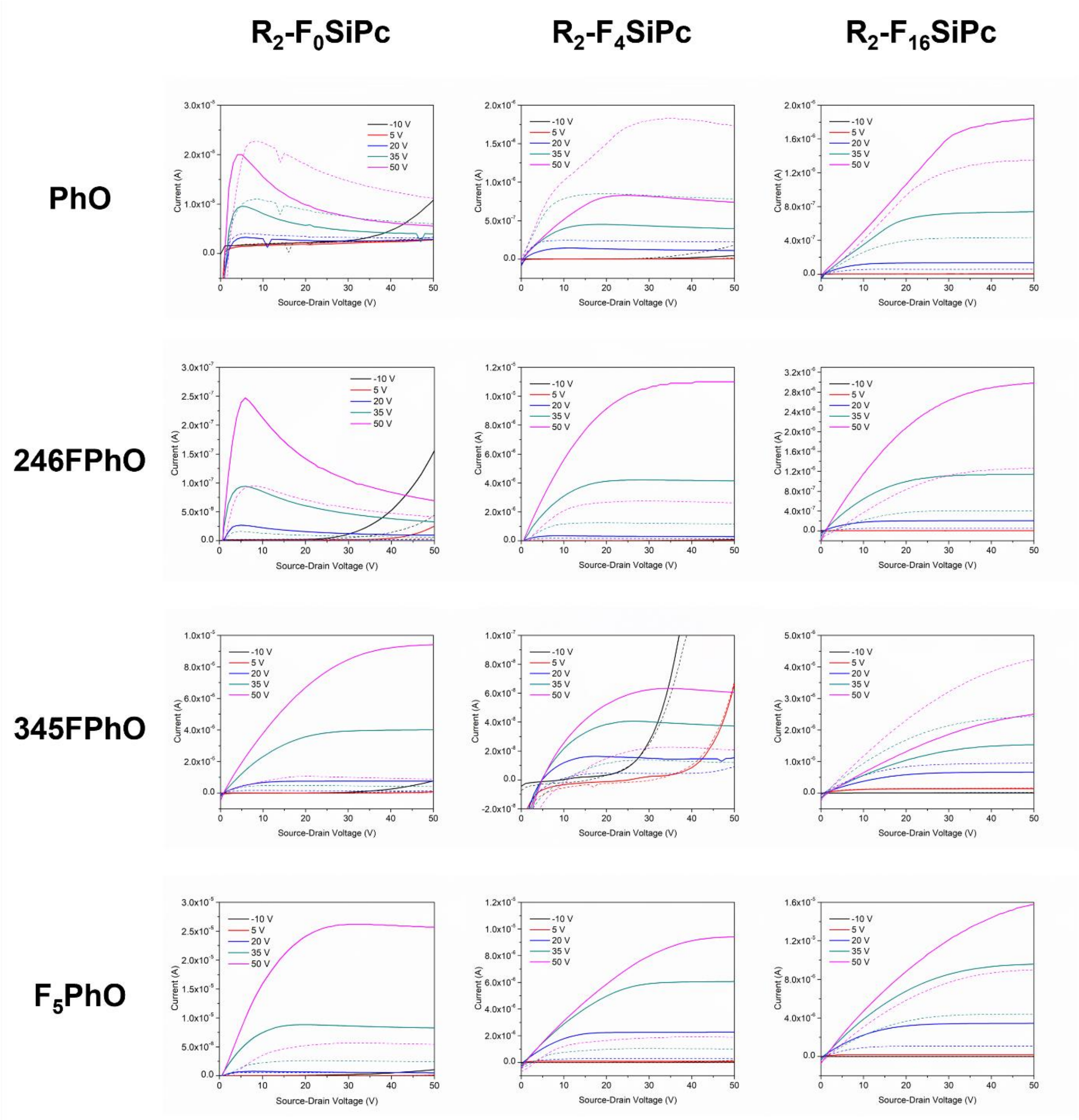

Figure 5.29 Output curves for R_2-F_xSiPc derivatives in BGTC OTFTs with Ag electrodes (dotted lines) and AgMn electrodes (solid lines) measured in a nitrogen glovebox

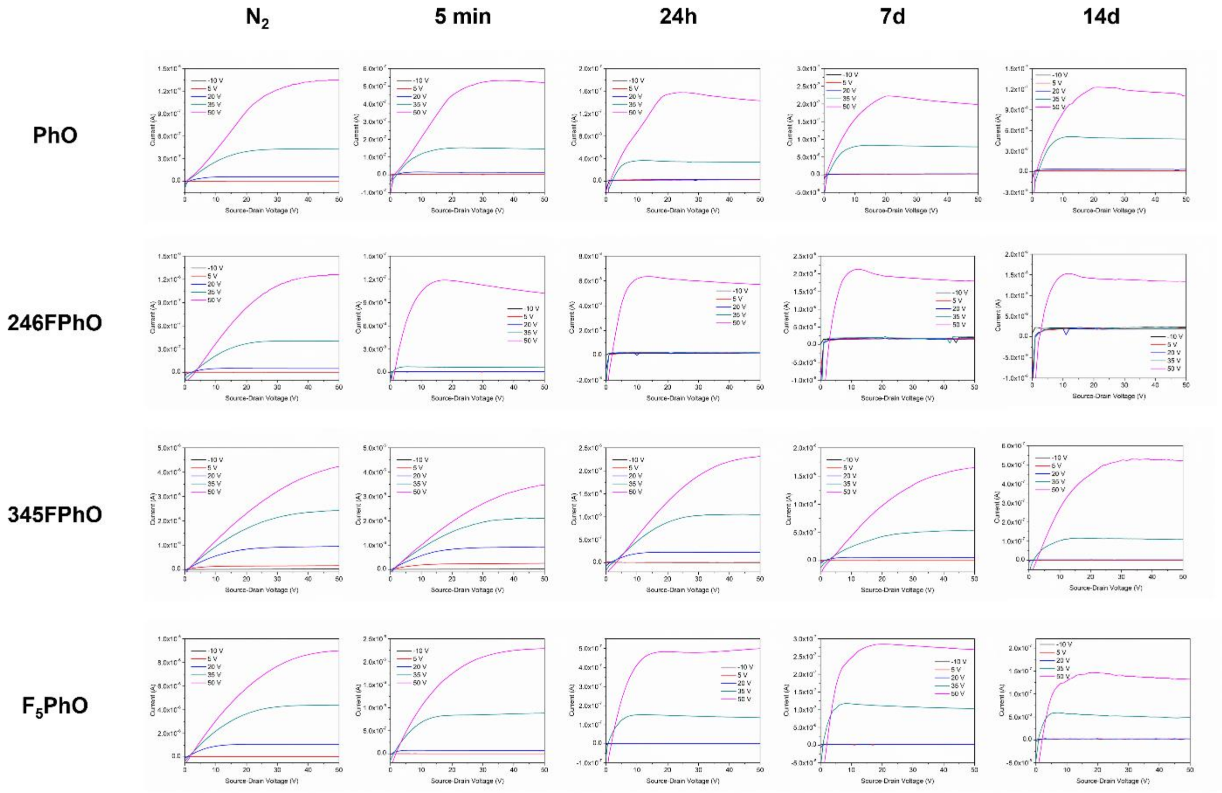

Figure 5.30 Output curves for R$_2$-F$_x$SiPc derivatives in BGTC OTFTs with Ag electrodes measured in a nitrogen glovebox and in air over 14 days (336 hours)

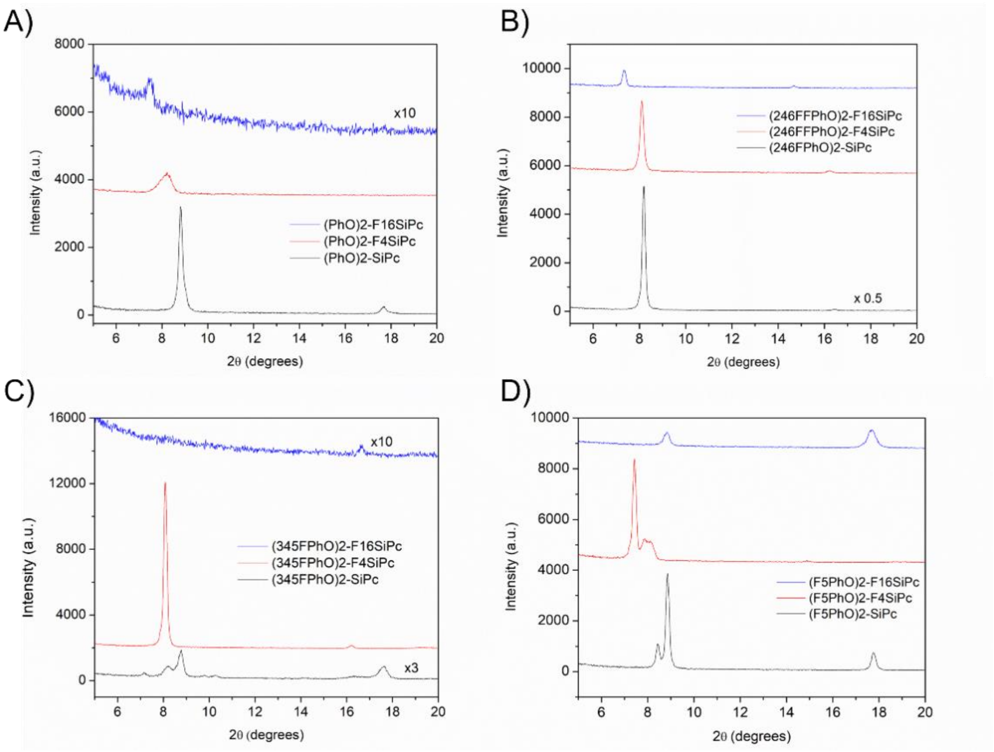

Figure 5.31 X-ray diffraction of R_2-F_xSiPc thin films. A) $(PhO)_2$-F_xSiPc, B) $(246FPhO)_2$-F_xSiPc, C) $(345FPhO)_2$-F_xSiPc and D) $(F_5PhO)_2$-F_xSiPc.

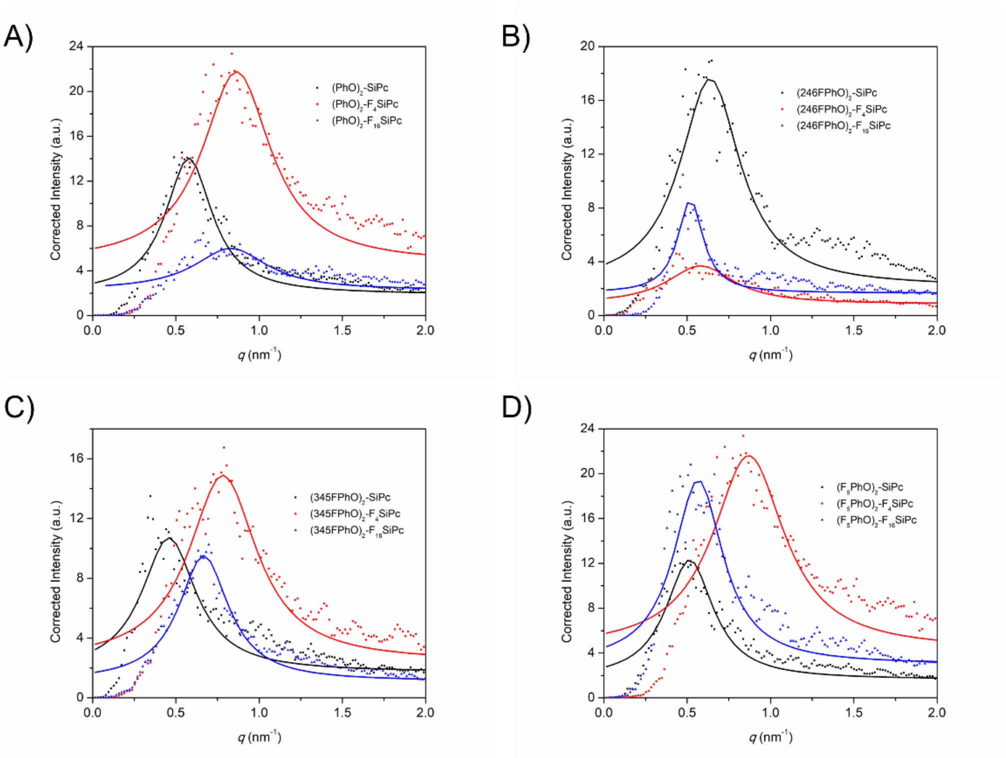

Figure 5.32 Radial power spectral density function of R_2-F_xSiPc films extracted from AFM images. Lorentzian curve fit is used as a tool to better visualize data and serves as a guide for the eye.

References

(1) Uno, M.; Kanaoka, Y.; Cha, B. S.; Isahaya, N.; Sakai, M.; Matsui, H.; Mitsui, C.; Okamoto, T.; Takeya, J.; Kato, T.; Katayama, M.; Usami, Y.; Yamakami, T. Short-Channel Solution-Processed Organic Semiconductor Transistors and Their Application in High-Speed Organic Complementary Circuits and Organic Rectifiers. *Adv. Electron. Mater.* **2015**, *1*, 1500178. https://doi.org/10.1002/aelm.201500178.

(2) Zhang, Y.; Wang, Y.; Gao, C.; Ni, Z.; Zhang, X.; Hu, W.; Dong, H. Recent Advances in N-Type and Ambipolar Organic Semiconductors and Their Multi-Functional Applications. *Chem. Soc. Rev.* **2023**, *52*, 1331–1381. https://doi.org/10.1039/d2cs00720g.

(3) Quinn, J. T. E.; Zhu, J.; Li, X.; Wang, J.; Li, Y. Recent Progress in the Development of N-Type Organic Semiconductors for Organic Field Effect Transistors. *J. Mater. Chem. C* **2017**, *5* (34), 8654–8681. https://doi.org/10.1039/c7tc01680h.

(4) Jones, B. A.; Facchetti, A.; Wasielewski, M. R.; Marks, T. J. Tuning Orbital Energetics in Arylene Diimide Semiconductors. Materials Design for Ambient Stability of n-Type Charge Transport. *J. Am. Chem. Soc.* **2007**, *129* (49), 15259–15278. https://doi.org/10.1021/ja075242e.

(5) Anthopoulos, T. D.; Anyfantis, G. C.; Papavassiliou, G. C.; De Leeuw, D. M. Air-Stable Ambipolar Organic Transistors. *Appl. Phys. Lett.* **2007**, *90* (12). https://doi.org/10.1063/1.2715028.

(6) Tsukamoto, K.; Takagi, K.; Nagano, S.; Hara, M.; Ie, Y.; Osakada, K.; Takeuchi, D. π-Extension of Electron-Accepting Dithiarubicene with a Cyano-Substituted Electron-Withdrawing Group and Application in Air-Stable n-Channel Organic Field Effect Transistors. *J. Mater. Chem. C* **2019**, *7* (40), 12610–12618. https://doi.org/10.1039/c9tc04325j.

(7) Gruntz, G.; Lee, H.; Hirsch, L.; Castet, F.; Toupance, T.; Briseno, A. L.; Nicolas, Y. Nitrile Substitution Effect on Triphenodioxazine-Based Materials for Liquid-Processed Air-Stable n-Type Organic Field Effect Transistors. *Adv. Electron. Mater.* **2015**, *1* (6). https://doi.org/10.1002/aelm.201500072.

(8) Yun, S. W.; Kim, J. H.; Shin, S.; Yang, H.; An, B. K.; Yang, L.; Park, S. Y. High-Performance n-Type Organic Semiconductors: Incorporating Specific Electron-Withdrawing Motifs to Achieve Tight Molecular Stacking and Optimized Energy Levels. *Adv. Mater.* **2012**, *24* (7), 911–915. https://doi.org/10.1002/adma.201103978.

(9) Wang, C.; Dong, H.; Hu, W.; Liu, Y.; Zhu, D. Semiconducting π-Conjugated Systems in Field-Effect Transistors: A Material Odyssey of Organic Electronics. *Chem. Rev.* **2012**, *112* (4), 2208–2267. https://doi.org/10.1021/cr100380z.

(10) Tang, M. L.; Reichardt, A. D.; Wei, P.; Bao, Z. Correlating Carrier Type with Frontier Molecular Orbital Functionalized Acene Derivatives. *J. Am. Chem. Soc.* **2009**, *131* (14), 5264–5273. https://doi.org/https://doi.org/10.1021/ja809659b.

(11) Melville, O. A.; Lessard, B. H.; Bender, T. P. Phthalocyanine-Based Organic Thin-Film Transistors: A Review of Recent Advances. *ACS Applied Materials & Interfaces*. **2015**, 13105–13118. https://doi.org/10.1021/acsami.5b01718.

(12) Denekamp, I. M.; Veenstra, F. L. P.; Jungbacker, P.; Rothenberg, G. A Simple Synthesis of Symmetric Phthalocyanines and Their Respective Perfluoro and Transition-Metal Complexes. *Appl. Organomet. Chem.* **2019**, *33* (5), 4872. https://doi.org/10.1002/aoc.4872.

(13) Cranston, R. R.; Lessard, B. H. Metal Phthalocyanines: Thin-Film Formation, Microstructure, and Physical Properties. *RSC Adv.* **2021**, *11* (35), 21716–21737. https://doi.org/10.1039/d1ra03853b.

(14) Bao, Z.; Lovinger, A. J.; Brown, J. New Air-Stable n-Channel Organic Thin Film Transistors. *J. Am. Chem. Soc.* **1998**, *7863* (24), 207–208. https://doi.org/10.1021/ja9727629.

(15) Jiang, H.; Hu, P.; Ye, J.; Li, Y.; Li, H.; Zhang, X.; Li, R.; Dong, H.; Hu, W.; Kloc, C. Molecular Crystal Engineering: Tuning Organic Semiconductor from p-Type to n-Type by Adjusting Their Substitutional Symmetry. *Adv. Mater.* **2017**, *29* (10). https://doi.org/10.1002/adma.201605053.

(16) Shao, X.; Wang, S.; Li, X.; Su, Z.; Chen, Y.; Xiao, Y. Single Component P-, Ambipolar and n-Type OTFTs Based on Fluorinated Copper Phthalocyanines. *Dye. Pigment.* **2016**, *132*, 378–386. https://doi.org/10.1016/j.dyepig.2016.05.020.

(17) Ouedraogo, S.; Ouedraogo, S.; Meunier-Prest, R.; Kumar, A.; Bayo-Bangoura, M.; Bouvet, M. Modulating the Electrical Properties of Organic Heterojunction Devices Based on Phthalocyanines for Ambipolar Sensors. *ACS Sensors* **2020**, *5* (6), 1849–1857. https://doi.org/10.1021/acssensors.0c00877.

(18) Şahin, Z.; Meunier-Prest, R.; Dumoulin, F.; Kumar, A.; Isci, Ü.; Bouvet, M. Tuning of Organic Heterojunction Conductivity by the Substituents' Electronic Effects in Phthalocyanines for Ambipolar Gas Sensors. *Sensors Actuators, B Chem.* **2021**, *332*, 129505. https://doi.org/10.1016/j.snb.2021.129505.

(19) Comeau, Z. J.; Boileau, N. T.; Lee, T.; Melville, O. A.; Rice, N. A.; Troung, Y.; Harris, C. S.; Lessard, B. H.; Shuhendler, A. J. On-the-Spot Detection and Speciation of Cannabinoids Using Organic Thin-Film Transistors. *ACS Sensors* **2019**, *4* (10), 2706–2715. https://doi.org/10.1021/acssensors.9b01150.

(20) Comeau, Z. J.; Cranston, R. R.; Lamontagne, H. R.; Harris, C. S.; Shuhendler, A. J.; Lessard, B. H. Surface Engineering of Zinc Phthalocyanine Organic Thin-Film Transistors Results in Part-per-Billion Sensitivity towards Cannabinoid Vapor. *Commun. Chem.* **2022**, ***5,*** 178. https://doi.org/10.1038/s42004-022-00797-y.

(21) Raval, H. N.; Sutar, D. S.; Ramgopal Rao, V. Copper(II) Phthalocyanine Based Organic Electronic Devices for Ionizing Radiation Dosimetry Applications. *Org. Electron.* **2013**, *14* (5), 1281–1290. https://doi.org/10.1016/j.orgel.2013.02.026.

(22) Melville, O. A.; Grant, T. M.; Lessard, H. Silicon Phthalocyanines as N-Type Semiconductors in Organic Thin Film Transistors. *J. Mater. Chem. C* **2018**, *6*, 5482–5488. https://doi.org/10.1039/c8tc01116h.

(23) Melville, O. A.; Grant, T. M.; Mirka, B.; Boileau, N. T.; Park, J.; Lessard, B. H. Ambipolarity and Air Stability of Silicon Phthalocyanine Organic Thin-Film Transistors. *Adv. Electron. Mater.* **2019**, *1900087*, 1–7. https://doi.org/10.1002/aelm.201900087.

(24) Lessard, B. H. The Rise of Silicon Phthalocyanine : From Organic Photovoltaics to Organic Thin Film Transistors. *ACS Appl. Mater. Interfaces* **2021**, *13* (27), 31321–31330. https://doi.org/10.1021/acsami.1c06060.

(25) Melville, O. A.; Grant, T. M.; Mirka, B.; Boileau, N. T.; Park, J.; Lessard, B. H. Ambipolarity and Air Stability of Silicon Phthalocyanine Organic Thin-Film Transistors. *Adv. Electron. Mater.* **2019**, *5* (8), 1900087. https://doi.org/10.1002/aelm.201900087.

(26) Cranston, R.; King, B.; Dindault, C.; Grant, T. M.; Rice, N.; Tonnelé, C.; Muccioli, L.; Castet, F.; Swaraj, S.; Lessard, B. H. Highlighting the Processing Versatility of a Silicon Phthalocyanine Derivative for Organic Thin-Film Transistors. *J. Mater. Chem. C* **2022**, *10* (2). https://doi.org/10.1039/d1tc05238a.

(27) Raboui, H.; Lough, A. J.; Plint, T.; Bender, T. P. Position of Methyl and Nitrogen on Axial Aryloxy Substituents Determines the Crystal Structure of Silicon Phthalocyanines. *Cryst. Growth Des.* **2018**, *18* (5), 3193–3201. https://doi.org/10.1021/acs.cgd.8b00298.

(28) Gali, S. M.; Matta, M.; Lessard, B. H.; Castet, F.; Muccioli, L. Ambipolarity and Dimensionality of Charge Transport in Crystalline Group 14 Phthalocyanines: A Computational Study. *J. Phys. Chem. C* **2018**, *122* (5), 2554–2563. https://doi.org/10.1021/acs.jpcc.7b11588.

(29) King, B.; Melville, O. A.; Rice, N. A.; Kashani, S.; Tonnelé, C.; Raboui, H.; Swaraj, S.; Grant, T. M.; McAfee, T.; Bender, T. P.; Ade, H.; Castet, F.; Muccioli, L.; Lessard, B. H. Silicon Phthalocyanines for N-Type Organic Thin-Film Transistors: Development of Structure–Property Relationships. *ACS Appl. Electron. Mater.* **2021**, *3* (1), 325–336. https://doi.org/10.1021/acsaelm.0c00871.

(30) King, B.; Daszcynski, A. J.; Rice, N. A.; Peltekoff, A. J.; Yutronkie, N. J.; Lessard, B. H.; Brusso, J. L. Cyanophenoxy-Substituted Silicon Phthalocyanines for Low Threshold Voltage n-Type Organic Thin-Film Transistors. *ACS Appl. Electron. Mater.* **2021**, *3* (5), 2212–2223. https://doi.org/10.1021/acsaelm.1c00175.

(31) Melville, O. A.; Grant, T. M.; Lochhead, K.; King, B.; Ambrose, R.; Rice, N. A.; Boileau, N. T.; Peltekoff, A. J.; Tousignant, M.; Hill, I. G.; Lessard, B. H. Contact Engineering Using Manganese, Chromium, and Bathocuproine in Group 14 Phthalocyanine Organic Thin-Film Transistors. *ACS Appl. Electron. Mater.* **2020**, *2* (5), 1313–1322. https://doi.org/10.1021/acsaelm.0c00104.

(32) Yutronkie, N. J.; King, B.; Melville, O. A.; Lessard, H. Attaining Air Stability in High Performing N-Type Phthalocyanine Based Organic Semiconductors. *J. Mater. Chem.* **2021**, ***9,*** 10119-10126. https://doi.org/10.1039/d1tc02275j.

(33) Mitra, K.; Hartman, M. C. T. Silicon Phthalocyanines: Synthesis and Resurgent Applications. *Org. Biomol. Chem.* **2021**. https://doi.org/10.1039/d0ob02299c.

(34) Vebber, M. C.; King, B.; French, C.; Toussignant, M.; Ronnasi, B.; Dindault, C.; Wantz, G.; Hirsch, L.; Brusso, J.; Lessard, B. H. From P-type to N-type: Peripheral Fluorination of Axially Substituted Silicon Phthalocyanines Enables Fine Tuning of Charge Transport. *Can. J. Chem. Eng.* **2023**, ASAP. https://doi.org/10.1002/cjce.24843.

(35) Lowbry, M. K.; Starshak, A. J.; John, S. J.; Esposito, N.; Krueger, P. C.; Kenney, M. E. Dichloro(Phthalocyanino)Silicon. *Inorg. Chem.* **1965**, *4* (1), 128.

https://doi.org/10.1021/ic50023a036.

(36) Lessard, B. H.; Grant, T. M.; White, R.; Thibau, E.; Lu, Z. H.; Bender, T. P. The Position and Frequency of Fluorine Atoms Changes the Electron Donor/Acceptor Properties of Fluorophenoxy Silicon Phthalocyanines within Organic Photovoltaic Devices. *J. Mater. Chem. A* **2015**, *3* (48), 24512–24524. https://doi.org/10.1039/c5ta07173a.

(37) Sirringhaus, H. Reliability of Organic Field-Effect Transistors. *Adv. Mater.* **2009**, *21* (38–39), 3859–3873. https://doi.org/10.1002/adma.200901136.

(38) Lessard, B. H.; White, R. T.; Al-Amar, M.; Plint, T.; Castrucci, J. S.; Josey, D. S.; Lu, Z. H.; Bender, T. P. Assessing the Potential Roles of Silicon and Germanium Phthalocyanines in Planar Heterojunction Organic Photovoltaic Devices and How Pentafluoro Phenoxylation Can Enhance π-π Interactions and Device Performance. *ACS Appl. Mater. Interfaces* **2015**, *7* (9), 5076–5088. https://doi.org/10.1021/am508491v.

(39) Lessard, B. H.; Al-Amar, M.; Grant, T. M.; White, R.; Lu, Z. H.; Bender, T. P. From Chloro to Fluoro, Expanding the Role of Aluminum Phthalocyanine in Organic Photovoltaic Devices. *J. Mater. Chem. A* **2015**, *3* (9), 5047–5053. https://doi.org/10.1039/c4ta06759b.

(40) Oleiki, E.; Javaid, S.; Lee, G. Impact of Fluorination on the Energy Level Alignment of an FnZnPc/MAPbI3 Interface. *Nanoscale Adv.* **2022**, *4* (23), 5070–5076. https://doi.org/10.1039/d2na00582d.

(41) Griggs, S.; Marks, A.; Bristow, H.; McCulloch, I. N-Type Organic Semiconducting Polymers: Stability Limitations, Design Considerations and Applications. *J. Mater. Chem. C* **2021**, *9* (26), 8099–8128. https://doi.org/10.1039/D1TC02048J.

(42) King, B.; Melville, O. A.; Rice, N. A.; Kashani, S.; Tonnelé, C.; Raboui, H.; Swaraj, S.; Grant, T. M.; McAfee, T.; Bender, T. P.; Ade, H.; Castet, F.; Muccioli, L.; Lessard, B. H. Silicon Phthalocyanines for N-Type Organic Thin-Film Transistors: Development of Structure Property Relationships. *ACS Appl. Electron. Mater.* **2021**, *3* (1), 325–336. https://doi.org//10.1021/acsaelm.0c00871.

(43) King, B.; Radford, C. L.; Ronnasi, B. Not Just Surface Energy: The Role of Bis(Pentafluorophenoxy) Silicon Phthalocyanine Axial Functionalization and Molecular Orientation on Organic Thin-Film Transistor Performance. *ACS Appl. Mater. Interfaces Interfaces* **2023**, *15* (11), 14937–14947. https://doi.org/10.1021/acsami.2c22789.

(44) Waldrip, M.; Jurchescu, O. D.; Gundlach, D. J.; Bittle, E. G. Contact Resistance in Organic Field-Effect Transistors: Conquering the Barrier. *Adv. Funct. Mater.* **2019**, 1904576. https://doi.org/10.1002/adfm.201904576.

(45) Di Pietro, R.; Fazzi, D.; Kehoe, T. B.; Sirringhaus, H. Spectroscopic Investigation of Oxygen- and Water-Induced Electron Trapping and Charge Transport Instabilities in n-Type Polymer Semiconductors. *J. Am. Chem. Soc.* **2012**, *134* (36), 14877–14889. https://doi.org/10.1021/ja304198e.

(46) Jones, B. A.; Ahrens, M. J.; Yoon, M. H.; Facchetti, A.; Marks, T. J.; Wasielewski, M. R. High-Mobility Air-Stable n-Type Semiconductors with Processing Versatility: Dicyanoperylene-3,4:9,10-Bis(Dicarboximides). *Angew. Chemie - Int. Ed.* **2004**, *43* (46), 6363–6366. https://doi.org/10.1002/anie.200461324.

(47) Schmidt, R.; Oh, J. H.; Sun, Y.; Deppisch, M.; Krause, A.-M.; Radacki, K.; Braunschweig, H.; Könemann, M.; Erk, P.; Bao, Z.; Würthner, F. High-Performance Air-Stable n-Channel Organic Thin Film Transistors Based on Halogenated Perylene Bisimide Semiconductors. *J. Ameri* **2009**, *131* (17), 6215–6228. https://doi.org/10.1021/ja901077a.

(48) Kumagai, S.; Yu, C. P.; Nakano, S.; Annaka, T.; Mitani, M.; Yano, M.; Ishii, H.; Takeya, J.; Okamoto, T. Role of Perfluorophenyl Group in the Side Chain of Small-Molecule n - Type Organic Semiconductors in Stress Stability of Single-Crystal Transistors. *J. Phys. Chem. Lett.* **2021**, *12* (8), 2095–2101. https://doi.org/10.1021/acs.jpclett.0c03012.

(49) Jones, B. A.; Facchetti, A.; Wasielewski, M. R.; Marks, T. J. Tuning Orbital Energetics in Arylene Diimide Semiconductors. Materials Design for Ambient Stability of n-Type Charge Transport. *J. Am. Chem. Soc.* **2007**, *129* (49), 15259–15278. https://doi.org/10.1021/ja075242e.

(50) Okamoto, T.; Kumagai, S.; Fukuzaki, E.; Ishii, H.; Watanabe, G.; Niitsu, N.; Annaka, T.; Yamagishi, M.; Tani, Y.; Sugiura, H.; Watanabe, T.; Watanabe, S.; Takeya, J. Robust, High-Performance n-Type Organic Semiconductors. *Sci. Adv.* **2020**, *6* (18). https://doi.org/10.1126/sciadv.aaz0632.

(51) Oh, J. H.; Sun, Y.-S.; Schmidt, R.; Toney, M. F.; Nordlund, D.; Könemann, M.; Würthner, F.; Bao, Z. Interplay between Energetic and Kinetic Factors on the Ambient Stability of N-Channel Organic Transistors Based on Perylene Diimide Derivatives. *Chem. Mater.* **2009**, *21* (22), 5508–5518. https://doi.org/10.1021/cm902531d.

(52) Tamayo, A.; Salzillo, T.; Mas-Torrent, M. Organic Field-Effect Transistors Based on Ternary Blends Including a Fluorinated Polymer for Achieving Enhanced Device Stability. *Adv. Mater. Interfaces* **2022**, *9* (6), 2101679. https://doi.org/10.1002/admi.202101679.

(53) Reese, C.; Bao, Z. High-Resolution Measurement of the Anisotropy of Charge Transport in Single Crystals. *Adv. Mater.* **2007**, *19* (24), 4535–4538. https://doi.org/10.1002/adma.200701139.

(54) Chen, M.; Yan, L.; Zhao, Y.; Murtaza, I.; Meng, H.; Huang, W. Anthracene-Based Semiconductors for Organic Field-Effect Transistors. *J. Mater. Chem. C* **2018**, *6* (28), 7416–7444. https://doi.org/10.1039/c8tc01865k.

(55) Cranston, R. R.; Vebber, M. C.; Berbigier, J. F.; Brusso, J. L.; Kelly, T. L.; Lessard, B. H. High Performance Solution Processed N-Type OTFTs through Surface Engineered F-F Interactions Using Asymmetric Silicon Phthalocyanines. *Adv. Electron. Mater.* **2022**, 2200696. https://doi.org/10.1002/aelm.202200696.

(56) Ye, L.; Stuard, S. J.; Ade, H. Soft X-Ray Scattering Characterization of Polymer Semiconductors. In *Conjugated Polymers: Properties, Processing and Applications*; **2019**; 427–458. https://doi.org/10.1201/9780429190520-13.

(57) Radford, C. L.; Pettipas, R. D.; Kelly, T. L. Watching Paint Dry: Operando Solvent Vapor Annealing of Organic Solar Cells. *J. Phys. Chem. Lett.* **2020**, *11* (15), 6450–6455. https://doi.org/10.1021/acs.jpclett.0c01934.

(58) Jiao, X.; Ye, L.; Ade, H. Quantitative Morphology–Performance Correlations in Organic Solar Cells: Insights from Soft X-Ray Scattering. *Adv. Energy Mater.* **2017**, *7* (18), 1–22. https://doi.org/10.1002/aenm.201700084.

(59) Yadav, S.; Kumar, P.; Ghosh, S. Optimization of Surface Morphology to Reduce the Effect of Grain Boundaries and Contact Resistance in Small Molecule Based Thin Film Transistors. *Appl. Phys. Lett.* **2012**, *101* (19). https://doi.org/10.1063/1.4766913.

(60) Nguyen, K. V.; Payne, M. M.; Anthony, J. E.; Lee, J. H.; Song, E.; Kang, B.; Cho, K.; Lee, W. H. Grain Boundary Induced Bias Instability in Soluble Acene-Based Thin-Film Transistors. *Sci. Rep.* **2016**, *6*, 33224. https://doi.org/10.1038/srep33224.

Chapter 6. Modulating the majority charge carrier type and performance of organic heterojunction ammonia sensors by increasing peripheral fluorination of the silicon phthalocyanine sublayer

This chapter was submitted to Sensors and Actuators B: Chemical. King B., Ganesh Moorthy, S., Lesniewska, E., Meunier-Prest, R., Bouvet, M., Lessard, B.H., Modulating the majority charge carrier type and performance of organic heterojunction ammonia sensors by increasing peripheral fluorination of the silicon phthalocyanine sublayer, Sensors and Actuators B: Chemical, Submitted Manuscript.*

Context

In this work, I report three R_2-F_XSiPcs as a sublayer in organic heterojunction devices for ammonia (NH_3) sensing with lutetium phthalocyanine ($LuPc_2$) as a top layer. All three R_2-F_XSiPcs had pentafluorophenol (F_5PhO) axial substituents with $X = 0$, 4 or 16 peripheral fluorine atoms. This work was motivated by previously published results incorporating Cl_2-SiPc and $(345FPhO)_2$-SiPc in sensors which both demonstrated a limit of detection (LOD) of a few hundred parts per billion (ppb) and yielded devices with a p-type or “turn-off” response to NH_3. I incorporated R_2-F_XSiPcs into organic heterojunction devices to determine if modifying the axial and peripheral fluorination of the sublayer could switch the polarity from a p-type “turn-off” response to an n-type “turn-on” response. We determined that four peripheral fluorine atoms in the R_2-F_XSiPc structure was sufficient to change the sensor response from “turn-off” to “turn-on”. We also optimized our champion device by post-deposition annealing, which had not previously been explored in organic heterojunction sensors. been previously used to optimize R_2-SiPc OTFTs, to determine whether I could affect the charge transport properties of the device and enhance its sensor performance.

Contributions

Through internship in Prof. Bouvet’s group, I fabricated organic heterojunction devices by physical vapour deposition of R_2-F_XSiPcs and $LuPc_2$. I performed electronic characterization of devices and NH_3 sensing experiments, processed the data, and interpreted the data. I performed annealing experiments on the organic heterojunction devices. I completed impedance spectroscopy measurements and processed the data with Mr. Ganesh Moorthy. I performed Raman spectroscopy measurements and interpreted the data with input from Prof. Bouvet. Impedance spectroscopy data was modelled by Prof. Meunier-Prest and Mr. Ganesh Moorthy. Atomic force microscopy measurements were performed by Prof. Lesniewska and interpreted by me. I wrote the manuscript with input from all five co-authors.

Abstract

Silicon phthalocyanines (R_2-SiPcs) are an emerging class of high-performance organic semiconductors which have recently found application in highly sensitive and selective bilayer organic heterojunction devices for ammonia (NH_3) sensing. We report bilayer heterojunction devices based on axially-substituted bis(pentafluorophenoxy)silicon phthalocyanines of increasing peripheral fluorination (($(F_5PhO)_2$-F_XSiPc) as a bottom layer and lutetium bis-phthalocyanine ($LuPc_2$) and demonstrate how increased peripheral fluorination changes device operation from p-type to n-type in response to NH_3. Sensors fabricated with $(F_5PhO)_2$-F_{16}SiPc exhibits the smallest apparent energy barrier for interfacial charge transport by impedance spectroscopy due to better alignment of the semiconductor molecular orbitals with the semi-occupied molecular orbital of $LuPc_2$. Bilayer heterojunction devices all demonstrated a LOD below 1 ppm with $(F_5PhO)_2$-SiPc/$LuPc_2$ yielding an LOD of 307 ppb and a sensitivity of -0.72 $\%\cdot ppm^{-1}$. Postdeposition thermal annealing of the $(F_5PhO)_2$-SiPc/$LuPc_2$ device is shown to further enhance sensor performance with a two-fold increase in sensitivity to -1.15 $\%\cdot ppm^{-1}$ and a LOD of 198 ppb.

6.1 Introduction

Organic semiconductor-based sensors have seen increased interest because of their relatively low manufacturing cost and synthetic tuneability that can lead to improved sensitivity and selectivity.[1–3] Organic semiconductors can also be incorporated into flexible electronics by printing and thermal evaporation, enabling fabrication of low cost gas sensor arrays.[4] Miniaturization of these sensors has enabled development of portable gas sensors to detect redox gases in occupational settings.[5] The measurement of ammonia (NH_3) is critical since it is produced on the ton scale for use in agriculture, pharmaceuticals and food production,[6] and can be emitted from combustion engines.[7] Additionally, NH_3 concentration in breath is a known biomarker for kidney disease.[8] Short term exposure limits to NH_3 are typically set at 50 ppm over 15 minutes while longer-term exposure limits are set at 20 – 25 ppm over an 8-hour interval.[9] Therefore, prospective NH_3 gas sensors must have a limit of detection (LOD) below 10 ppm with rapid response and recovery times and high selectivity, even in humid environments.[10] Existing NH_3 sensors based on organic chemiresistors[11,12] and organic thin-film transistors (OTFTs)[13–17] offer advantages over metal oxide-based sensors which are typically operated above room temperature and can be less selective. Bilayer heterojunction devices comprised of interdigitated electrodes

(IDE, **Figure 6.1A**) with a high-conductivity material deposited on top of a low-conductivity sublayer have also found success.[18] Unlike chemiresistors, charges accumulate at the organic-organic interface and the relatively large interelectrode distance promotes charge injection vertically through the sublayer to the organic-organic interface.[19] This results in charge transport through the interface rather than directly between the electrodes. Lutetium bis-phthalocyanine ($LuPc_2$, **Figure 6.1B**), a sandwich-structure metal phthalocyanine (MPc), is a common top layer with a high density of charge carriers that can be easily reduced by NH_3,[19] enabling effective sensing. A wide range of organic semiconductors and polymers have been investigated as active sensing materials in organic heterojunction-based NH_3 sensors including MPcs,[20] porphyrins,[21] and perylenes.[19]

MPcs are macrocycles that can chelate various metal/metalloid centers, are thermally stable, and have been widely incorporated into devices including OTFTs.[22] Divalent MPcs such as copper, zinc, cobalt, and nickel MPcs with peripheral functionality (Cl, F, hexylsulfanyl) have also been incorporated into organic heterojunction devices.[20,23,24] Silicon phthalocyanines (R_2-SiPcs) are a class of MPc that have been widely incorporated into OTFTs as n-type or ambipolar organic semiconductors.[25,26] Due to the multiple oxidation states of silicon, R_2-SiPcs can be functionalized with axial ligands including carboxylic acids, phenols, and silanes to tune their π-π interactions, optical and electrochemical properties.[27,28] Recently, our group investigated the effect of axial and peripheral fluorination of silicon phthalocyanine (R_2-F_xSiPc) in OTFTs and found that derivatives with a lowest unoccupied molecular orbital (LUMO) deeper than -4.4 eV exhibited air-stable n-type behaviour.[29,30] We also reported the first organic heterostructure gas sensors incorporating dichloro (Cl_2-SiPc) and bis(3,4,5-fluoro phenoxy) ($(345FPhO)_2$-SiPc) silicon phthalocyanine, which demonstrated good response to NH_3 with LOD below 1 ppm.[31] However, both materials demonstrated p-type responses when exposed to NH_3, likely due to trapping of electrons by moisture and oxygen as the LUMOs were above -4.1 eV.[32,33]

In this work, we incorporated three R_2-F_XSiPcs with increasing peripheral fluorination (**Figure 6.1C**) into organic heterojunction gas sensors to investigate the relationship between the sublayer structure and majority charge carriers. The optical and structural properties of the bilayer films were characterized by UV-vis and Raman spectroscopies, while their surface textures were investigated by atomic force microscopy (AFM). Electrical characterization was carried out by taking current-voltage measurements and charge-transfer studies were performed by impedance spectroscopy. Finally, the NH_3 sensing capabilities were evaluated at room temperature to determine charge carrier type, response kinetics, and sensitivity.

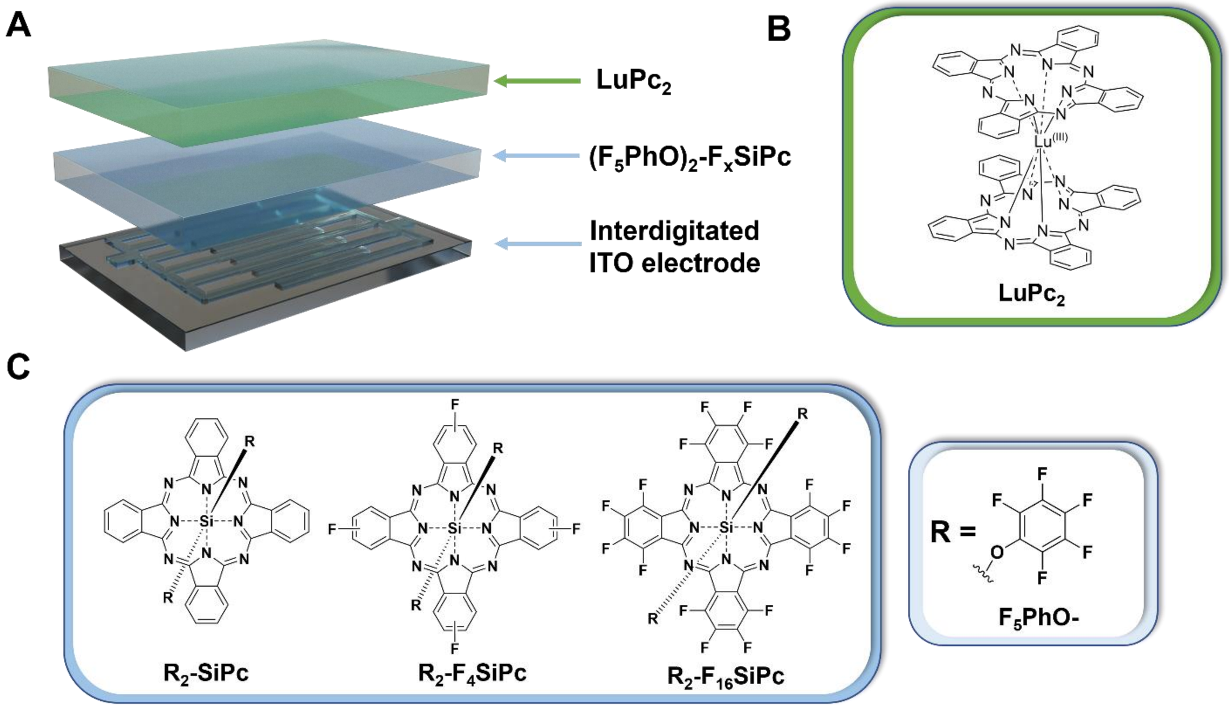

Figure 6.1 A) Schematic drawing of an organic heterostructure device with interdigitated electrodes, B) structure of $LuPc_2$ top layer and C) structures of $(F_5PhO)_2$-F_XSiPc sublayers.

6.2 Experimental Section

Synthesis

Cl_2-SiPc,[34] silicon tetrafluorophthalocyanine (Cl_2-F_4SiPc) and silicon hexadexafluorophthalocyanine (Cl_2-F_{16}SiPc),[29] and their axially functionalized derivatives[30,35] were synthesized based on literature procedures. Synthesis of lutetium bis-phthalocyanine ($LuPc_2$) was adapted from literature, using a home-made thermoregulated vertical oven.[36]

Sensor Fabrication

Sensors were fabricated on IDEs consisting of 125 ITO digits lithographically patterned on a glass substrate with a channel width of 10 µm. IDEs were cleaned through sequential sonication three times each for five minutes in dichloromethane followed by ethanol, followed by drying in an oven at 100 °C for 1 hour. Sensors and samples for thin-film characterization were fabricated by physical vapor deposition onto substrates at room temperature (20–22°C) in a UNIVEX 250 thermal evaporator under secondary vacuum ($P < 2 \times 10^{-6}$ mbar) by evaporating a 50 nm layer of $(F_5PhO)_2$-F_xSiPc at a rate of ≈ 0.25 $Å{\cdot}s^{-1}$ followed by a 50 nm layer of $LuPc_2$ at a rate of ≈ 1 $Å{\cdot}s^{-1}$. The evaporation temperatures were measured in the range of 280 – 290°C for $(F_5PhO)_2$-SiPc, 315 – 330°C for $(F_5PhO)_2$-F_4SiPc, 260 – 280°C for $(F_5PhO)_2$-$F_{16}SiPc$ and 400 – 450°C for $LuPc_2$.

Electrical Measurements

I-V characteristics and sensing measurements were performed at room temperature (20 – 22°C) by sweeping from 0 V to +10 V, followed by a sweep to -10 V, before returning to 0 V all at 0.1 V increments using a Keithley 6517B electrometer.

Gas Sources and Sensing Experiments

Gas cylinders of synthetic air containing NH_3 at concentrations of 985 and 98 ppm (mol/mol) and of dry synthetic air were purchased from Air Liquide. The total flow rate was set to 550 $mL{\cdot}min^{-1}$ by mass flow controllers and exposure/recovery cycles were controlled by switching electronic valves interfaced with homemade software. The volume of the test chamber was 8 cm^3 and details are reported in the literature.[37] Long-exposure NH_3 sensing data was collected at room temperature with three cycles of exposure under 90 ppm of NH_3 in humid air with a relative humidity (RH) of 45% for 10 minutes followed by recovery under synthetic air (RH = 45%) for 30 minutes. Short-exposure NH_3 sensing data was collected at room temperature with four cycles of exposure to a set concentration of NH_3 in the range of 1 ppm to 90 ppm in humid air (RH = 45%) for one minute followed by recovery under synthetic air (RH = 45%) for four minutes. NH_3 concentration was sequentially increased every four exposure/recovery cycles by increments of 20 ppm in the range of 10 – 90 ppm NH_3 and in increments of 2 ppm in the range of 1 to 9 ppm NH_3.

Thin-Film Characterization

Impedance spectroscopy was performed on $(F_5PhO)_2$-$F_XSiPc/LuPc_2$ bilayers with a Solartron SI 1260 impedance analyzer on a replicate of each organic heterojunction device fabricated for sensor studies as described in Section 2.2. Nyquist plots were collected at room temperature (20 – 22°C). The device interfacial properties were studied at a fixed DC voltage of 0 V to 10 V with 1 V increments and a fixed AC voltage of 200 mV over a range of frequencies from

10 Hz to 10 MHz. Data was treated using ZView software. Absorption spectra were collected from 300 - 900 nm using a Cary 50 UV-Vis spectrometer. Raman spectroscopy was performed using a Renishaw inVia microscope with a 473 nm laser. AFM images were collected with a Bruker Icon 2 using nanoDMA PeakForce mapping, as described previously.[31]

6.3 Results and Discussion

Bilayer Characterization

UV-vis spectra of films of $(F_5PhO)_2$-F_XSiPcs, $LuPc_2$, and bilayers are presented in **Figure 6.9**. All three bilayer films possess the main absorption feature of $(F_5PhO)_2$-F_XSiPc films reported in the literature with the onset of absorption beyond 750 nm.[30] The main absorption of $LuPc_2$ at 670 nm overlaps with the Q-band of the $(F_5PhO)_2$-F_xSiPcs, while the absorption at 467 nm corresponds to the transition between a filled orbital toward the semi-occupied molecular orbital of $LuPc_2$.[38,39] Raman measurements on powders of the three $(F_5PhO)_2$-F_XSiPcs, $LuPc_2$ and the bilayer heterojunctions are found in **Figure 6.10-6.11** and **Tables 6.3-6.5**. The Raman spectra of the three $(F_5PhO)_2$-F_XSiPcs are similar between 1310-1600 cm^{-1} which corresponds to stretching vibrations from C=C and C=N bonds.[40] Peripheral fluorination of the R_2-F_XSiPc macrocycle changes both characteristic Raman peaks results in new peaks associated with C-F bonds. For example, the peak at 736 cm^{-1} in $(F_5PhO)_2$-F_{16}SiPc is consistent with vibration of C-F bonds for other peripherally fluorinated F_{16}MPcs.[40] Additionally, peaks from 1600-1620 cm^{-1} are shifted to higher wavenumbers with increasing peripheral fluorination as observed in other F_XMPcs.[41,42] The spectra of the bilayers do not show additional peaks, which suggests degradation of $(F_5PhO)_2$-F_XSiPcs and $LuPc_2$ did not occur during fabrication, which is important due to the primary mode of charge transport being across the organic-organic interface.

Electrical properties of $(F_5PhO)_2$-F_XSiPc/$LuPc_2$ devices were investigated by performing current-voltage (*I-V*) measurements under an applied bias between -10 V and + 10 V (**Figure 6.2 A, D, and G**). *I-V* curves for all three devices are non-linear and symmetric, which is typical of this architecture owing to its operation mechanism where mobile charges accumulate at the interface.[43] Hysteresis is observed in *I-V* curves of $(F_5PhO)_2$-F_4SiPc/$LuPc_2$ and $(F_5PhO)_2$-F_{16}SiPc/$LuPc_2$ heterojunction devices, which is likely due to interfacial charge traps initially present at the organic-organic interface, which has been observed in planar heterojunction solar cells.[44] Other differences in *I-V* characteristics between devices can be attributed to the morphology of the organic-organic interface and the resistance to charge transport in the sublayer. The nonlinearity can be quantified by estimating the apparent energy barrier (U_{TH}) by taking the tangent of the *I-V* curve at high bias and extrapolating it to the *x*-axis. Devices fabricated with $(F_5PhO)_2$-SiPc and $(F_5PhO)_2$-F_4SiPc yielded a similar U_{TH} of 5.3 V and 5.2 V, respectively while devices fabricated with $(F_5PhO)_2$-F_{16}SiPc yielded a U_{TH} of 2.4 V, demonstrating that $(F_5PhO)_2$-F_{16}SiPc likely has a lower resistance to electron injection from the ITO electrodes (work function = 5.2 eV) into the LUMO (4.9 eV) and vertical charge transport to the bilayer interface. This is consistent with our observations of R_2-SiPcs in OTFTs where we attributed a deeper LUMO to a decrease in threshold voltage.[30] Frontier molecular orbital structures of $LuPc_2$ and all three $(F_5PhO)_2$-F_XSiPcs are presented in **Figure 6.12**.

Impedance spectroscopy was carried out in a frequency range of 10 Hz to 10 MHz and varying DC voltage bias from 0 V to 10 V at a constant applied AC bias (AC = 200 mV). The Nyquist plots of all three devices (**Figure 6.2 B, E, and H**) yielded two depressed semicircles in which the first semicircle at high frequency does not change and the second semicircle at low frequency decreases as DC bias increases. This behaviour confirms the presence of an organic heterojunction where the high-frequency semicircle corresponds to bulk charge transport in the sublayer and the low-frequency semicircle corresponds to interfacial transport across the heterojunction formed in the bilayer device.[43,45] Since the high-frequency semicircle does not change with increasing DC bias while the low-frequency semicircle decreases in intensity with increasing DC bias, bulk charge transport remains constant while interfacial charge transport changes. The magnitude of the bulk impedance is lowest for $(F_5PhO)_2$-SiPc/$LuPc_2$ implying that $(F_5PhO)_2$-SiPc has the best bulk charge transport capabilities, which is consistent with OTFTs where it has shown the best electron mobility of all reported R_2-SiPcs in comparison to fluorinated analogues.[27,30] The bulk charge transport properties quantified by the magnitude of the first semicircle correspond to the n-type charge-carrier mobilities we observed in our previous work studying $(F_5PhO)_2$-F_XSiPcs in OTFTs, with $(F_5PhO)_2$-SiPc demonstrating a mobility six times greater than $(F_5PhO)_2$-F_4SiPc OTFTs.[30] $(F_5PhO)_2$-F_{16}SiPc/$LuPc_2$ has the smallest magnitude of interfacial impedance, implying that it has the fastest charge transport across the device, which could be partially attributed to the good frontier orbital alignment between the LUMO of the R_2-F_XSiPc and the SOMO of $LuPc_2$. The relative magnitude of the low and high-frequency semicircles in both $(F_5PhO)_2$-SiPc/$LuPc_2$ and $(F_5PhO)_2$-F_4SiPc/$LuPc_2$ devices is two orders of magnitude larger than the $(F_5PhO)_2$-F_{16}SiPc/$LuPc_2$ device, which suggests significant resistance to interfacial charge transport in the two former devices.

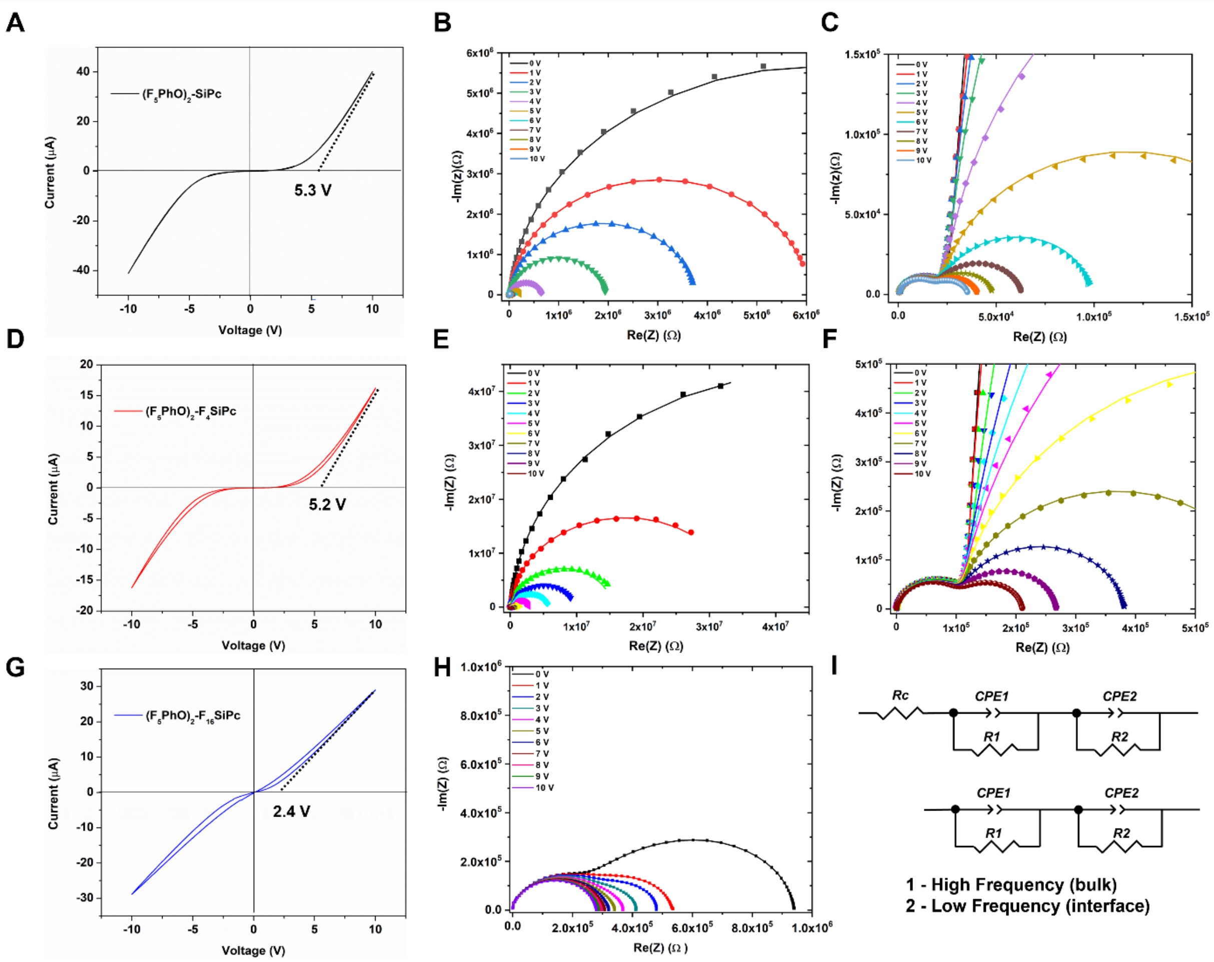

Figure 6.2 A, D and G) *I-V* characteristics and B, C, E, F, H) Nyquist plots of a characteristic heterojunction device of A-C) $(F_5PhO)_2$-SiPc/$LuPc_2$, D-F) $(F_5PhO)_2$-F_4SiPc/$LuPc_2$, G-H) $(F_5PhO)_2$-F_{16}SiPc/$LuPc_2$ and I) Schematic representation of two-component R_i-CPE_i element with (top) and without (bottom) R_C. Nyquist plots were recorded at variable DC voltage in the range of 0 V – 10 V with a constant AC voltage of 200 mV. C and F are insets of B and E to show the magnitude of the first semicircle. Raw data are represented by discrete points and data fit to R_i-CPE_i elements are represented by curves.

To extract values corresponding to bulk and interfacial charge transport, Nyquist plots were fit with two-component R_i-CPE_i elements connected in series as shown in **Figure 6.2I** (top) with a contact resistance term (R_C) added to account for resistance to charge injection between the electrodes and the sublayer common in devices with bottom-contact architectures.[46,47] A CPE is an imperfect capacitor where impedance is defined by **Equation 6.1**:

$$Z_{CPE_i}(\omega) = \frac{1}{Q_i(j\omega)^{\alpha i}} \tag{6.1}$$

Where Q_i is non-ideal capacitance, ω is frequency, and α is a constant from 0 to 1. The CPE is a perfect capacitor when α is equal to 1 or a perfect resistor when α is equal to zero. $(F_5PhO)_2$-$F_{16}SiPc$ was modelled by a two-component R_i-CPE_i elements without R_C (**Figure 6.2I**, bottom) since it was negligible owing to the small injection barrier with the ITO electrodes. The average R_C values of both $(F_5PhO)_2$-$F_XSiPc/LuPc_2$ devices (**Figure 6.13**) are on the order of 10^2 Ω. In the two-component CPE model, R_1-CPE_1 describes the high-frequency semicircle attributed to bulk transport and R_2-CPE_2 describes the low-frequency semicircle attributed to interfacial transport. The fitting resulted in determination of R_i, α_i, and Q_i where "*i*" corresponds to the component number and *R*, α and Q_i correspond to resistance, dispersion, and non-ideal capacitance, respectively. The variation of these parameters for different devices are shown in **Figure 6.3**. Similar to our previous report of R_2-$SiPc/LuPc_2$ organic heterojunction devices, the bulk resistance (R_1, **Figure 6.3A**) is nearly independent of applied bias for $(F_5PhO)_2$-$SiPc/LuPc_2$ and $(F_5PhO)_2$-$F_4SiPc/LuPc_2$ while the interfacial resistance (R_2, **Figure 6.3B**) shows an exponential decay with increasing applied bias.[31] This demonstrates that interfacial charge transport mobility increases with increasing applied bias while bulk charge transport remains approximately constant,[45] with the exception of the $(F_5PhO)_2$-$F_{16}SiPc/LuPc_2$ device where a slight decrease in the magnitude of bulk charge transport is observed at increasing bias, consistent with the Nyquist plot. The α parameters of the devices dictate the capacitive contribution to the total electrical output of each device. In $(F_5PhO)_2$-$F_4SiPc/LuPc_2$ and $(F_5PhO)_2$-$F_{16}SiPc/LuPc_2$ devices, α_1 increases with increasing bias suggesting that the CPE associated with bulk charge transport is highly homogeneous which is consistent with negligible variation in bulk charge transport as bias increases. However, the $(F_5PhO)_2$-$F_{16}SiPc/LuPc_2$ device essentially becomes a resistor beyond a bias of 5 V with only one semicircle present in the Nyquist plot. Q_1 values (**Figure 6.3E)** are an order of magnitude smaller than Q_2 (**Figure 6.3F**) across all three devices indicating that the thickness of the interface is much smaller than that of the bulk which is typical for organic heterojunctions.[48] A slight increase in interfacial non-ideal capacitance is observed for $(F_5PhO)_2$-

SiPc/LuPc$_2$ and (F$_5$PhO)$_2$-F$_4$SiPc/LuPc$_2$ devices which could be attributed to thinning of the interface and overcoming the energy barrier at increased bias.

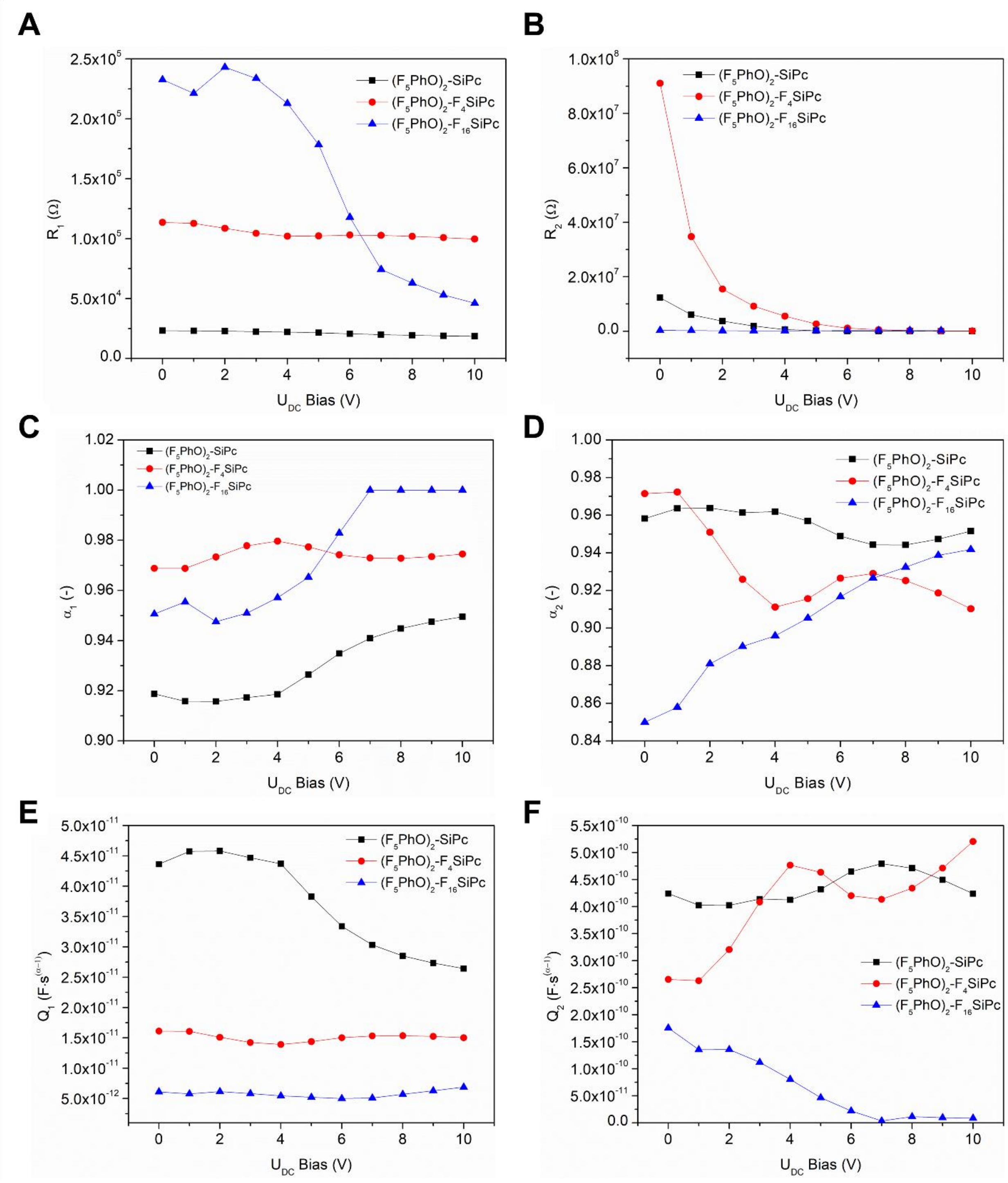

Figure 6.3 Variation of charge transport parameters: A) bulk resistance (R1), B) interfacial resistance (R2), C) alpha associated with bulk (α1), D) alpha associated with the interface (α2), bulk non-ideal capacitance (Q_1) and interfacial non-ideal capacitance (Q_2) with applied DC voltage from 0 V – 10 V and a fixed AC voltage 200 mV for organic heterojunction devices with $(F_5PhO)_2$-SiPc/$LuPc_2$ (black line), $(F_5PhO)_2$-F_4SiPc/$LuPc_2$ (red line) and $(F_5PhO)_2$-F_{16}SiPc/$LuPc_2$ (blue line).

Ammonia Sensing Performance of Heterojunction Sensors

Devices were characterized for their NH_3 vapour sensitivity by exposure-recovery cycles, first with exposure to 90 ppm of NH_3 in humid air (RH = 45%) for 10 minutes followed by recovery under synthetic air (RH = 45%) for 30 minutes (**Figure 6.4**). For $(F_5PhO)_2$-SiPc/$LuPc_2$ (**Figure 6.4A**), current decreases when exposed to 90 ppm NH_3 and increases during the recovery period. This suggests p-type behaviour since the electron donating tendency of NH_3 when holes are the majority charge carrier results in a decrease in current. This is consistent with previously-reported R_2-SiPc/$LuPc_2$ devices, which demonstrated p-type behaviour when exposed to NH_3.[31] Conversely, current increases upon exposure to NH_3 for $(F_5PhO)_2$-F_4SiPc/$LuPc_2$ (**Figure 6.4B**) and $(F_5PhO)_2$-F_{16}SiPc/$LuPc_2$ (**Figure 6.4C**) devices, suggesting n-type behaviour. These results demonstrate the first report of n-type R_2-F_XSiPc/$LuPc_2$ organic heterojunction NH_3 sensors and are consistent with observations in OTFT studies where both $(F_5PhO)_2$-F_4SiPc and $(F_5PhO)_2$-F_{16}SiPc demonstrated n-type charge transport in ambient conditions.[30] Some drift was observed during the collection of I-t data, which suggests incomplete desorption of NH_3 during the recovery step. t_{90}, in which the sensor undergoes 90% of the total change in current (ΔI) during exposure, is reported in **Table 6.1**, with $(F_5PhO)_2$-SiPc/$LuPc_2$ heterojunctions having the most rapid response time of 51 seconds. There is a plateau during exposure and recovery for all three sensors suggesting that NH_3 adsorption/desorption is primarily occurring at the surface of the device and equilibrium is being attained during exposure and recovery steps.

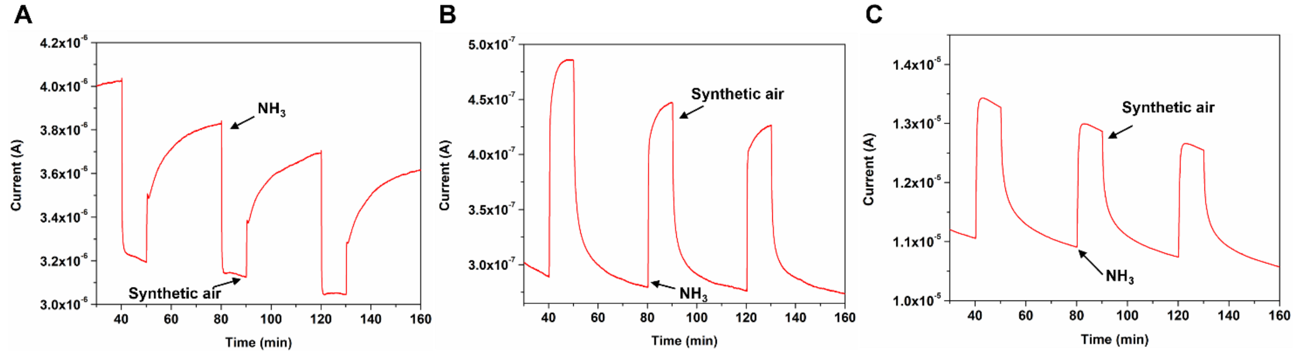

Figure 6.4 Response of A) $(F_5PhO)_2$-SiPc/$LuPc_2$, B) $(F_5PhO)_2$-F_4SiPc/$LuPc_2$ and C) $(F_5PhO)_2$-F_{16}SiPc/$LuPc_2$ heterojunction devices under successive exposure to 90 ppm NH_3 for 10 min and recovery under synthetic air for 30 min at 45% RH and 20–22°C. Data was collected at an applied voltage of 4 V.

To evaluate dynamic response, measurements were taken over a range of concentrations from 1 ppm to 90 ppm with short exposure/recovery cycles of 1 minute/4 minutes. *I-t* curves for sensors with increasing NH_3 concentration from 10 ppm to 90 ppm are shown in **Figure 6.5 A-C.** Quantitative assessment of sensor response with changing concentrations can be achieved by calculating the relative response (RR) with **Equation 6.2**:

$$RR\ (\%) = \frac{I_f - I_0}{I_0} \times 100\% \qquad (2)$$

where I_f and I_0 are the final and initial current values for one exposure.

Calibration curves, which are generated from measuring RR as a function of NH_3 concentration, are shown in **Figure 6.5 D-F** (1 ppm to 90 ppm). Change in current between exposure and recovery is reversible in all three sensor architectures with minimal drift between cycles. Additionally, RR increases as a function of NH_3 concentration demonstrating that all three devices are sensitive to concentration of ammonia in humid air. *I-t* data and calibration curves for NH_3 concentrations from 1 ppm to 9 ppm are shown in **Figure 6.14**.

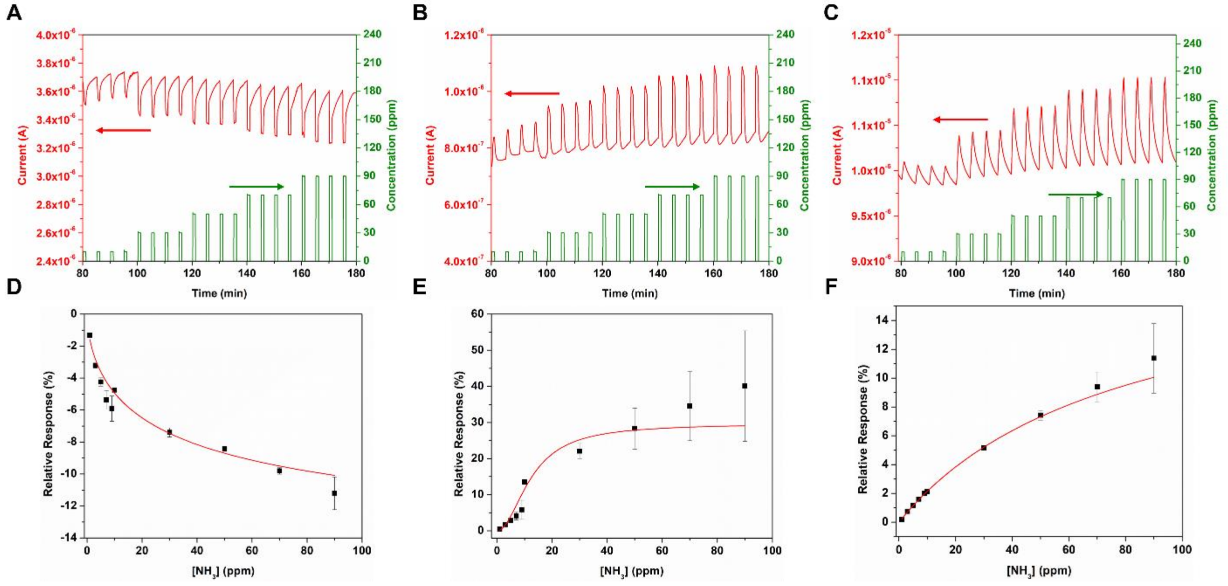

Figure 6.5 A-C) Response of organic heterojunction sensors under successive exposure of NH_3 for 1 min and recovery under synthetic air for 4 min in the range of NH_3 concentration from 10 – 90 ppm at an RH of 45% and room temperature (20 - 22°C) and D-F) variation of RR of organic heterojunction devices for a characteristic A and D) $(F_5PhO)_2$-SiPc/$LuPc_2$ heterojunction device, B and E) $(F_5PhO)_2$-F_4SiPc/$LuPc_2$ heterojunction device and C and F) $(F_5PhO)_2$-F_{16}SiPc/$LuPc_2$ heterojunction device.

All three sensors approach a plateau in RR as concentration approaches 90 ppm, following a Langmuir-type adsorption isotherm with a quasi-linear regime at low concentrations similar to $F_{16}CuPc/LuPc_2$ sensors[10] and $(345FPhO)_2$-$SiPc/LuPc_2$ sensors in our previous work.[31] $(F_5PhO)_2$-$SiPc/LuPc_2$ sensors demonstrated the best sensitivity of -0.72 %·ppm^{-1} with RR increasing from -1.3% at 1 ppm to -11.2% at 90 ppm. $(F_5PhO)_2$-$F_4SiPc/LuPc_2$ sensors had the largest magnitude of average RR of up to 40.1% at 90 ppm, with an RR of 0.49% at 1 ppm. However, there was substantial drift and noise at low concentrations (**Figure 6.14B**) which is not desirable for sensor applications where long-term stability is important. Finally, the $(F_5PhO)_2$-$F_{16}SiPc/LuPc_2$ sensor yielded a change in average RR from 0.19% at 1 ppm to 11.3% at 90 ppm. All three sensors demonstrated an experimentally measured response to 1 ppm NH_3. Operating temperature, and therefore changes in ambient temperature during operation, can influence the performance of gas sensors.[49] Recently reported organic heterojunction gas sensors with $LuPc_2$ as the top layer recently demonstrated an effect of RR on temperature of 0.3 %·°C^{-1}.[50] Therefore, we suspect that the temperature effect on sensors in this work is similarly low given the cycle-after-cycle stability of $(F_5PhO)_2$-$SiPc/LuPc_2$ and $(F_5PhO)_2$-$SiPc/LuPc_2$ heterojunction sensors.

A theoretical LOD, calculated from Equation 6.3, can also be extracted from the calibration curves to estimate the lowest-possible response to NH_3 of the sensors:[51]

$$LOD = \frac{3N}{S \times I_0} \tag{6.3}$$

Where N is the noise of the sensor signal estimated by determining the standard deviation of the current during the recovery period, S is the sensitivity of the sensor in ppm^{-1} and I_0 is the baseline current of the sensor. The LOD of the sensors in this work were estimated to be 307 ppb for $(F_5PhO)_2$-$SiPc/LuPc_2$, 750 ppb for the $(F_5PhO)_2$-$F_4SiPc/LuPc_2$, and 618 ppb for the $(F_5PhO)_2$-$F_{16}SiPc/LuPc_2$, well below the exposure limit guidelines of 20-25 ppm. Performance of sensors in this work is summarized in **Table 6.1** with comparisons to previously reported heterojunction-based sensors presented in **Table 6.6**.

Table 6.1 Comparison of t_{90}, S, and LOD for R_2-F_xSiPc/$LuPc_2$ sensors.

Architecture	Polarity	t_{90} (s)	Sensitivity (%·ppm^{-1})	LOD (ppb)	[NH_3] for LOD (ppm)
$(F_5PhO)_2$-SiPc/$LuPc_2$	P-type	51	- 0.72	307	1 – 9
$(F_5PhO)_2$-F_4SiPc/$LuPc_2$	N-type	134	0.60	750	1 – 9
$(F_5PhO)_2$-F_{16}SiPc/$LuPc_2$	N-type	60	0.23	618	1 – 9

Understanding thin-film texture can provide insight into the device response to NH_3. AFM micrographs of all three devices recorded under controlled atmosphere (RH < 25%) and at a temperature of 22.5°C are presented in **Figure 6.6.** Radial power spectral density functions (PSDFs) of the AFM data was prepared to characterize the domain size, distribution of grain sizes and other differences in thin-film microstructure (**Figure 6.15, Table 6.7**).[52,53] PSDF generated from AFM images provides similar data to resonant soft X-ray scattering,[52,54] and in this case can be used to quantitatively compare films of $LuPc_2$ evaporated on top of each $(F_5PhO)_2$-SiPc. Both $(F_5PhO)_2$-SiPc/$LuPc_2$ (**Figure 6.6A**) and $(F_5PhO)_2$-F_4SiPc/$LuPc_2$ (**Figure 6.6B**) sensors, with mode domain sizes of 9.91 nm and 7.40 nm respectively demonstrated a plateau in current during 1 min/4 min exposure/recovery cycles at high concentrations, which is attributed to the densely packed $LuPc_2$ grains at the surface limiting diffusion of NH_3 through the film to the organic-organic interface where charge transport occurs. Conversely, $(F_5PhO)_2$-F_{16}SiPc/$LuPc_2$ organic heterojunctions (**Figure 6.6C**) yield a surface topography which had a significantly larger mode domain size of 21.2 nm with large grain boundaries and a surface with a relatively large RMS roughness of 10.38 nm. The rough and porous film of $(F_5PhO)_2$-F_{16}SiPc/$LuPc_2$ organic heterojunctions could enable better diffusion through the film to the interface and access to additional adsorption/desorption sites similar to what was proposed for Cl_2-SiPc/$LuPc_2$ sensors.[31]

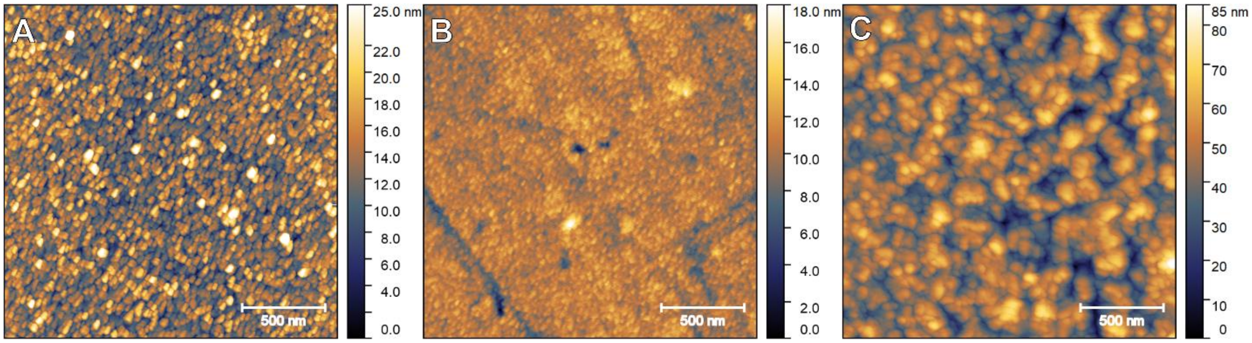

Figure 6.6 AFM images of A) $(F_5PhO)_2$-SiPc/$LuPc_2$, B) $(F_5PhO)_2$-F_4SiPc/$LuPc_2$ and C) $(F_5PhO)_2$-F_{16}SiPc/$LuPc_2$ bilayer films coated on a glass substrate.

Humidity is a common environmental variable that can interfere with the performance of NH_3 sensors. The response of all three sensors to humidity was measured by taking *I-t* measurements over a stepwise increase in RH from 30 - 60% followed by a stepwise decrease in RH back to 30% in 10% increments and is presented in **Figure 6.7**. $(F_5PhO)_2$-SiPc/$LuPc_2$ and $(F_5PhO)_2$-F_4SiPc/$LuPc_2$ devices demonstrate both a forward and reverse response to humidity. However, neither sensor fully recovers to the initial current at 30% RH. While the $(F_5PhO)_2$-SiPc/$LuPc_2$ device demonstrates a step-wise increase with increasing RH, it appears to have a unique *I-t* feature at 60% RH with similar properties to Cl_2-SiPc/$LuPc_2$.[31] This suggests that at high RH, there is an irreversible effect on the performance of $(F_5PhO)_2$-SiPc/$LuPc_2$ devices. A similar irreversible effect of humidity is observed for of $(F_5PhO)_2$-F_{16}SiPc/$LuPc_2$ devices. However, we must point out the small current increase from 30% to 60% RH, namely +15%, against +100% for $(F_5PhO)_2$-SiPc/$LuPc_2$. The effect of humidity is still higher for $(F_5PhO)_2$-F_4SiPc/$LuPc_2$, with a current multiplied by 2.7 from 30% to 60% RH, but with a better reversibility compared to the two other devices.

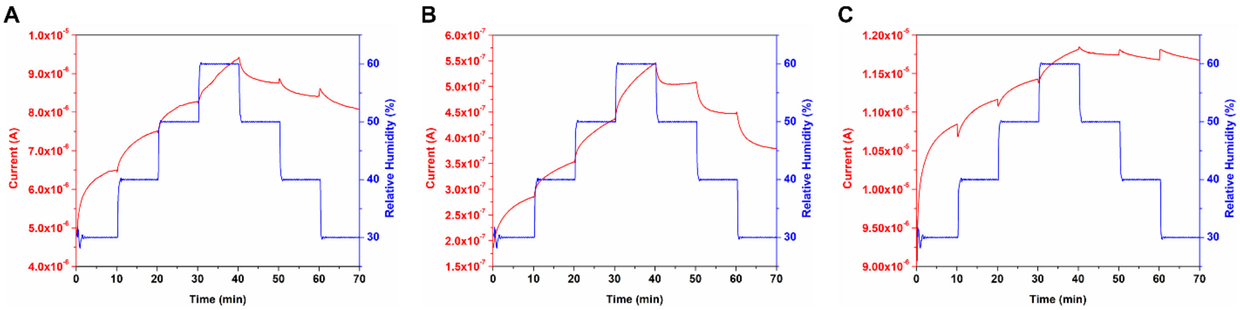

Figure 6.7 Response of A) $(F_5PhO)_2$-SiPc/$LuPc_2$, B) $(F_5PhO)_2$-F_4SiPc/$LuPc_2$ and C) $(F_5PhO)_2$-F_{16}SiPc/$LuPc_2$ heterojunction devices towards changes in RH from 30% to 60% and then to 30% at 20 - 22°C. Data was collected at an applied voltage of 4 V.

Thermal Annealing of $(F_5PhO)_2$-SiPc/$LuPc_2$ Organic Heterojunction Device

Thermal annealing is a common post-processing technique used to tune device performance by rearranging crystalline packing structures in organic semiconductor thin-films.[55] Thermal annealing has been demonstrated to improve the conductivity of ZnPc-based OTFTs where annealing at 70°C produced an order of magnitude increase in on/off current ratio.[56] Additionally, thermal annealing of VOPc films for NO_2 and humidity sensing was found to improve the connectivity of grains in the polycrystalline semiconductor film and improve device performance.[57] Our previous work demonstrated that thermal annealing of bis(tri-n-propylsilyl oxide) silicon phthalocyanine OTFTs decreased the threshold voltage as annealing temperature was increased from room temperature to 150°C under vacuum.[58] Motivated by these results, we prepared $(F_5PhO)_2$-SiPc/$LuPc_2$ devices, which had the highest sensitivity and LOD, and annealed them under vacuum for 1 hour at 100°C to measure the impact on sensor performance. After annealing, *I-V* curves (**Figure 6.8A**) continue to demonstrate nonlinear behaviour with a slight positive shift in U_{TH} from 5.3 V to 5.7 V and a larger current above 6 V for the forward and reverse sweeps. This suggests a physical change in the device occurred at one or both interfaces to change electronic properties of the device, similar to P3HT:PCBM bulk heterojunction solar cells which showed an increase in dark *I-V* characteristics due to annealing [59]. Hysteresis was observed in the negative voltage range of the annealed device, which could be attributed a small amount of polarization of the sample [60]. Sensing experiments were performed on the annealed devices for long exposure/recovery cycles (**Figure 6.8B**) and short exposure/recovery cycles (**Figure 6.8C**) where the annealed device demonstrated a 77% increase in the magnitude of ΔI from -6.43x10^{-7} A to -1.14x10^{-6} A and an increase in RR from -17.4% to -41.8% under exposure to NH_3 vapour (RH of 45%) during long exposure. The calibration curve from short exposure data (**Figure 6.8D**) also differs from the pristine device, demonstrating a saturation in the RR of approximately -32.0% at 90 ppm NH_3, which is a near three-fold increase compared to pristine devices. The increase in RR also holds at lower concentrations, with the annealed device outperforming the baseline in the range of 9 ppm to 1 ppm (**Figure 6.18**). While the response time corresponding to exposure (t_{90}) of the annealed device increased, the sensitivity due to annealing increases from -0.72 %·ppm^{-1} to -1.15 %·ppm^{-1} and the LOD is enhanced from 307 ppb to 192 ppb. A summary of the performance for room temperature and annealed heterojunction devices is presented in **Table 6.2.**

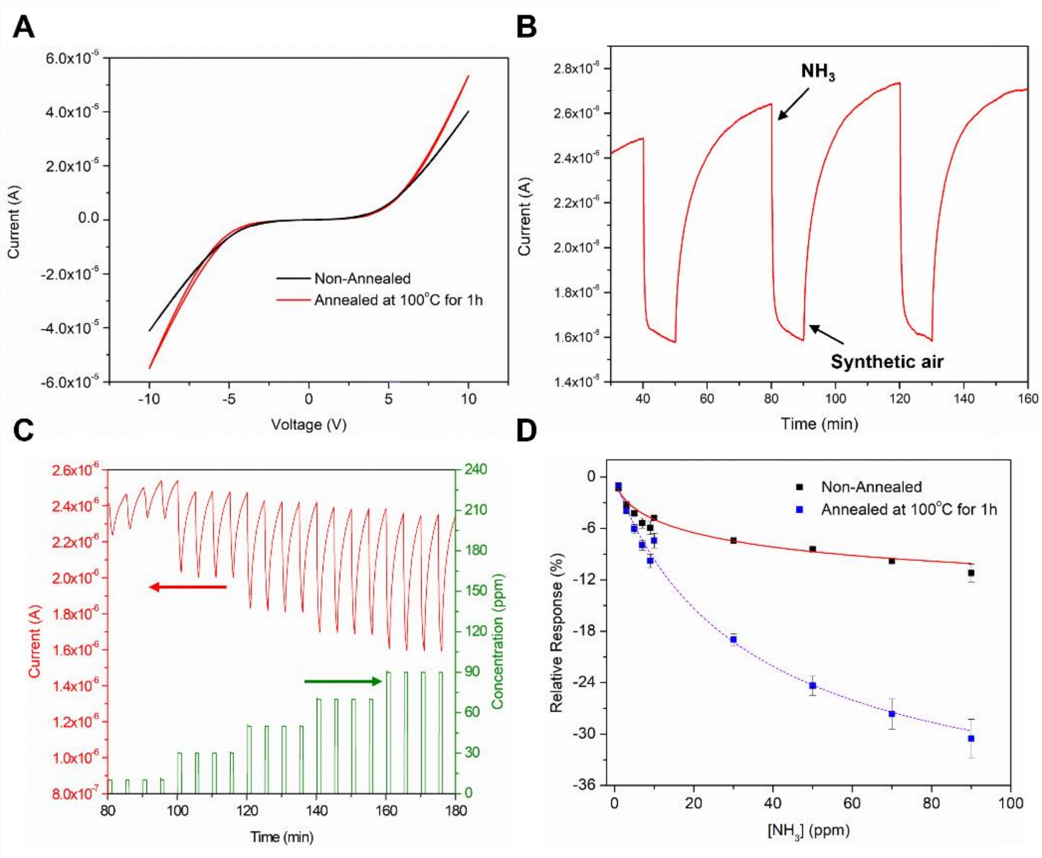

Figure 6.8 A) *I-V* characteristics of $(F_5PhO)_2$-SiPc/$LuPc_2$ heterojunctions before and after annealing at 100 °C for 1 h, response of annealed $(F_5PhO)_2$-SiPc/$LuPc_2$ heterojunctions under B) successive exposure to 90 ppm NH_3 for 10 min and recovery under synthetic air for 30 min, C) successive exposure of NH_3 for 1 min and recovery under synthetic air for 4 min in the range of NH_3 concentration from 10 – 90 ppm, and D) RR of heterojunction device before and after thermal annealing at 100 °C for one hour. Heterojunctions were measured at 45% RH and 20 - 22°C. Data in panels B–D was collected at an applied voltage of 4 V.

Table 6.2 Comparison of t_{90}, S, and LOD for $(F_5PhO)_2$-F_0SiPc heterojunctions before and after thermal annealing at 100 °C under vacuum. Sensor data was collected at an applied voltage of 4 V.

Condition	Polarity	t_{90} (s)	Sensitivity (%·ppm^{-1})	LOD (ppb)	[NH_3] for LOD (ppm)
Room Temperature	P-type	51	- 0.72	307	1–9
Annealed at 100 °C	P-type	96	- 1.15	198	1–9

AFM of the annealed device (**Figure 6.19**) showed a near-identical film texture to the non annealed device with small, densely packed grains. PSDFs of the films shown in **Figure 6.20** and corresponding data in **Table 6.7** demonstrate near-identical distributions of feature sizes, with mode domain sizes of 9.91 nm for the non-annealed film and 9.36 nm for the post-annealed film and similar RMS roughness of 3.48 nm and 3.11 nm, respectively. This demonstrates that thermal annealing has a negligible impact on the texture of the $LuPc_2$ film and the performance enhancement due to annealing is likely a result of changes in the sublayer-electrode or organic-organic interface. Impedance spectroscopy measurements were completed to quantify changes to bulk and interfacial charge transport due to annealing. Nyquist plots (**Figure 6.16A** and **Figure 6.16C**) show an increase in the relative magnitude of the high-frequency semicircles after annealing, suggesting change in bulk charge transport. The increase in magnitude of the high-frequency semicircle (**Figure 6.16B** and **Figure 6.16D**) indicates a decrease in bulk charge transport after annealing. However, the low-frequency semicircle decreases in magnitude at a faster rate for the annealed device, indicating a reduced resistance to interfacial charge transport as bias increases. These observations are confirmed by fitting the data to R_i-CPE models which show that R_1 (**Figure 6.17A**) of the annealed device is three times higher while the magnitude of R_2 of the annealed device (**Figure 6.17B**) is similar above 2 V. α_1 of the annealed device (**Figure 6.17C**) remains close to 1 and increases with increasing bias, indicating that R-CPE element is close to an ideal capacitor and is relatively homogeneous. This behaviour is expected since the microstructure of the film should remain relatively homogeneous in the bulk. However, α_2 of the annealed device (**Figure 6.17D**) remains relatively constant and then decreases above U_{TH} to a more significant degree than the non-annealed device, which demonstrates an enhancement in heterogeneity of the device which can be correlated with the higher concentration of mobile charges arriving at the interface and extending the conductive network by filling charge traps.[45]

6.4 Conclusion

We have demonstrated the influence of peripheral fluorination of $(F_5PhO)_2$-F_xSiPcs on the behaviour of organic bilayer heterojunction-based NH_3 sensors. Increasing the number of peripheral fluorine atoms from zero to four in the $(F_5PhO)_2$-F_xSiPcs was sufficient to switch the polarity of the device from p-type to n-type behaviour upon exposure to NH_3, with $(F_5PhO)_2$-F_{16}SiPc/$LuPc_2$ having the smallest magnitude U_{TH} of 2.0 V likely owing to the relatively good LUMO alignment of $(F_5PhO)_2$-F_{16}SiPc with the SOMO of $LuPc_2$ and negligible contact resistance. $(F_5PhO)_2$-SiPc/$LuPc_2$ demonstrated the best sensitivity at -0.72 %·ppm^{-1}, t_{90} of 51 s and best LOD of 307 ppb with a quasi-linear calibration curve in the measurement range of 1 ppm to 9 ppm.

Thermal annealing of $(F_5PhO)_2$-SiPc devices at 100 °C under vacuum reduced the resistance to interfacial transport at high DC voltage. The annealed device also outperformed the pristine device with a 1.6-fold increase in sensitivity to -1.15 %·ppm^{-1} and enhanced LOD of 198 ppb. To the best of our knowledge, this is the first time that postdeposition thermal annealing has been reported to enhance the sensing performance of organic heterojunction gas sensors and merits further investigation.

Acknowledgements

This work was supported by NSERC Discovery grant RGPIN 2020-04079 (B.H.L.), the Canada Research Chairs Program 950-230724 (B.H.L.) and NSERC CGS-D (B.K.). The authors also acknowledge the Conseil Régional de Bourgogne Franche-Comté through the Envergure Program MatElectroCap (2020-2024) and a PhD grant (S. G. M.). The *Agence Nationale de la Recherche is thanked* for funding through the ANR project Porph4Sens ANR-22-CE06-0039-01. The authors thank the Plateforme d'Analyses Chimiques et de Synthèse Moléculaire de l'Université de Bourgogne (PACSMUB) and the SATT Sayens for technical support in the Raman analyses. The authors also thank Dr. Joseph G. Manion for producing Figure 1A.

Supporting Information

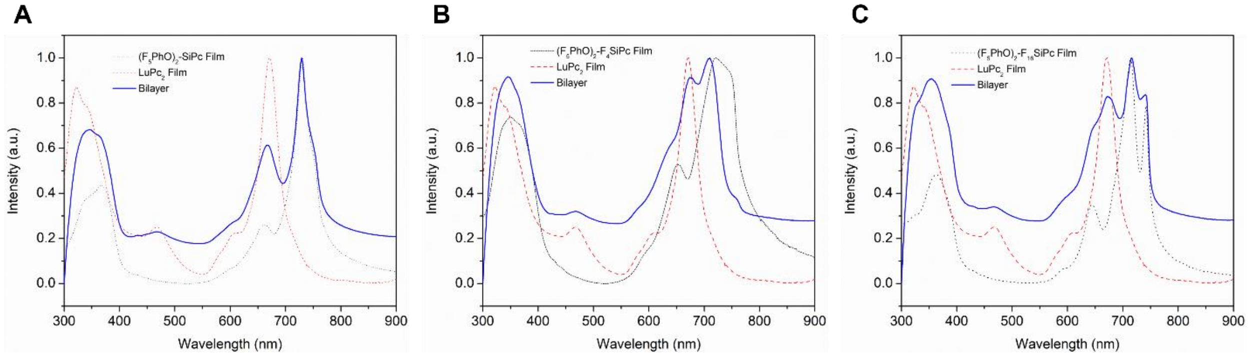

Figure 6.9 Combined UV-Visible spectra of $(F_5PhO)_2$-$F_XSiPc/LuPc_2$ bilayer (blue line) superimposed with the spectra of an $LuPc_2$ film (red, dashed line) and $(F_5PhO)_2$-F_XSiPc film (black, dotted line) for A) X = 0, B) X = 4 and C) X = 16 peripheral fluorine atoms.

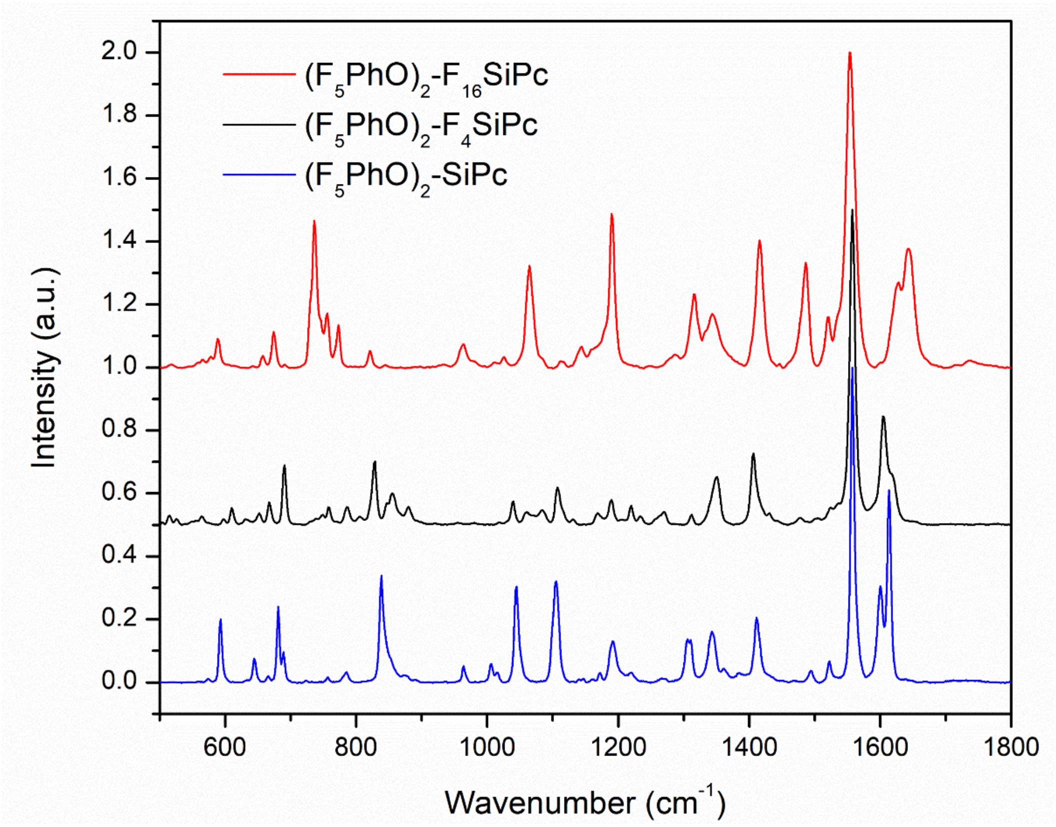

Figure 6.10 Stacked Raman spectra of $(F_5PhO)_2$-F_XSiPc crystals.

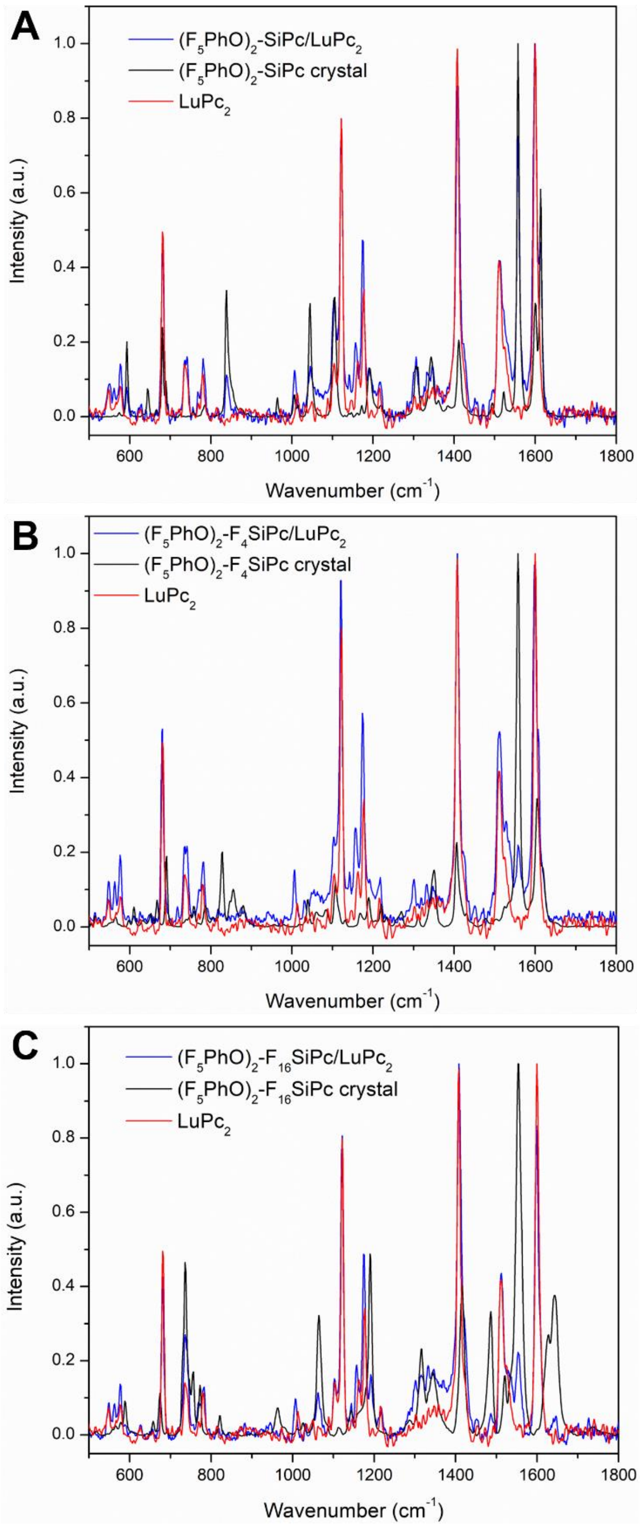

Figure 6.11 Superimposed Raman spectra of (F$_5$PhO)$_2$-F$_X$SiPc/LuPc$_2$ bilayer (blue line), LuPc$_2$ powder (red line) and (F$_5$PhO)$_2$-F$_X$SiPc crystals (black line) for A) X = 0, B) X = 4 and C) X = 16 peripheral fluorine atoms.

Table 6.3 Raman data (in cm^{-1}) of $(F_5PhO)_2$-SiPc/$LuPc_2$ bilayer heterojunction devices compared to each product as evaporated crystals or powder, and their bond attribution.

$(F_5PhO)_2$-SiPc evaporated crystals	$(F_5PhO)_2$-SiPc / $LuPc_2$ heterojunctions	$LuPc_2$ powder	Assignment
	550 w	548 w	Pc breathing
		564 w	Pc breathing
	577 w	578 w	Pc breathing
593 w	592 w		
644 w			Pc breathing
680 w	681 m	682 s	Pc breathing
690 w			
	742 w	735 m	C-H wag
756 w			
785 w	781 w	781 m	C=N aza stretching
838 m	838 w		Aromatic C-H
964 w			
1005 w	1006 w		
1015 w		1012 w	C-H bending
		1033 w	C-H bending
1044 m	1045 w		
1105 m	1104 m	1104 w	C-H bending
	1122 s	1122 s	C-H bending
		1147 w	Pyrrole breathing
	1157 w	1163 w	
	1175 m	1177 m	C-H bending
1191 w			
		1217 w	C-H bending
	1306 w	1303 w	C-H bending
1310 w			
	1333 w	1333 w	C=C pyrrole and benzene stretching
1343 w	1347 w	1347 w	
		1360 w	
1411 w	1408 s	1408 s	Isoindole stretching
1494 w			
	1512 m	1512 s	Coupling of pyrrole and aza stretching
1522 w			
1557 s	1557 s		
1600 m	1599 s	1601 s	Benzene stretching
1613 m	1614 m		

Table 6.4 Raman data (in cm^{-1}) of $(F_5PhO)_2$-F_4SiPc/$LuPc_2$ bilayer heterojunction devices compared to each product as evaporated crystals or powder, and their bond attribution.

$(F_5PhO)_2$-F_4SiPc evaporated crystals	$(F_5PhO)_2$-F_4SiPc / $LuPc_2$ heterojunctions	$LuPc_2$ powder	Assignment
	545 w	548 w	Pc breathing
564 w	563 w	564 w	Pc breathing
	577 w	578 w	Pc breathing
610 w			
667 w			Pc breathing
	680 m	682 s	Pc breathing
690 m			
	742 m	735 m	C-H wag
758 w			Aromatic C-F
786 w	781 m	781 m	C=N aza stretching
828 m			Aromatic C-H
855 w			
880 w			
	1006 w	1012 w	C-H bending
1039 w		1033 w	C-H bending
1107 w	1108 w	1104 w	C-H bending
	1121 s	1122 s	C-H bending
	1157 w	1147 w	Pyrrole breathing
1168 w		1163 w	
	1174 m	1177 m	C-H bending
1190 w			
1220 w		1217 w	C-H bending
1234 w			
1270 w			
	1301 s	1303 w	C-H bending
1312 w			
	1332 w	1333 w	C=C pyrrole and benzene stretching
1351 w		1347 w	
		1360 w	
1406 m	1408 s	1408 s	Isoindole stretching
	1512 m	1512 s	Coupling of pyrrole and aza stretching
1557 s	1558 w		
1604 m	1598 s	1601 s	Benzene stretching

Table 6.5 Raman data (in cm^{-1}) of $(F_5PhO)_2$-F_{16}SiPc/LuPc$_2$ bilayer heterojunction devices compared to each product as evaporated crystals or powder, and their bond attribution.

$(F_5PhO)_2$-F_{16}SiPc evaporated crystals	$(F_5PhO)_2$-F_{16}SiPc / LuPc$_2$ heterojunctions	LuPc$_2$ powder	Assignment
	547 w	548 w	Pc breathing
	562 w	564 w	Pc breathing
	577 w	578 w	Pc breathing
589 w			
657 w			Pc breathing
674 w			
	680 m	682 s	Pc breathing
736 m	735 m	735 m	Aromatic C-F
756 w			
773 w	769 w		
	782 w	781 m	C=N aza stretching
821 w			
963 w			
	1007 w	1012 w	C-H bending
		1033 w	C-H bending
1064 m	1062 w		
		1104 w	C-H bending
	1121 s	1122 s	C-H bending
1144 w		1147 w	Pyrrole breathing
	1156 w	1163 w	
	1175 m	1177 m	C-H bending
1190 m	1192 w		
		1217 w	C-H bending
		1303 w	C-H bending
1316 m			
		1333 w	C=C pyrrole and benzene stretching
1343 w		1347 w	
		1360 w	
	1408 s	1408 s	Isoindole stretching
1416 m			
1486 m	1486 w		
	1512 m	1512 s	Coupling of pyrrole and aza stretching
1521 w			
1554 s	1555 w		C=C stretch
	1598 s	1601 s	Benzene stretching
1623 m			

1643 m	1647 w		

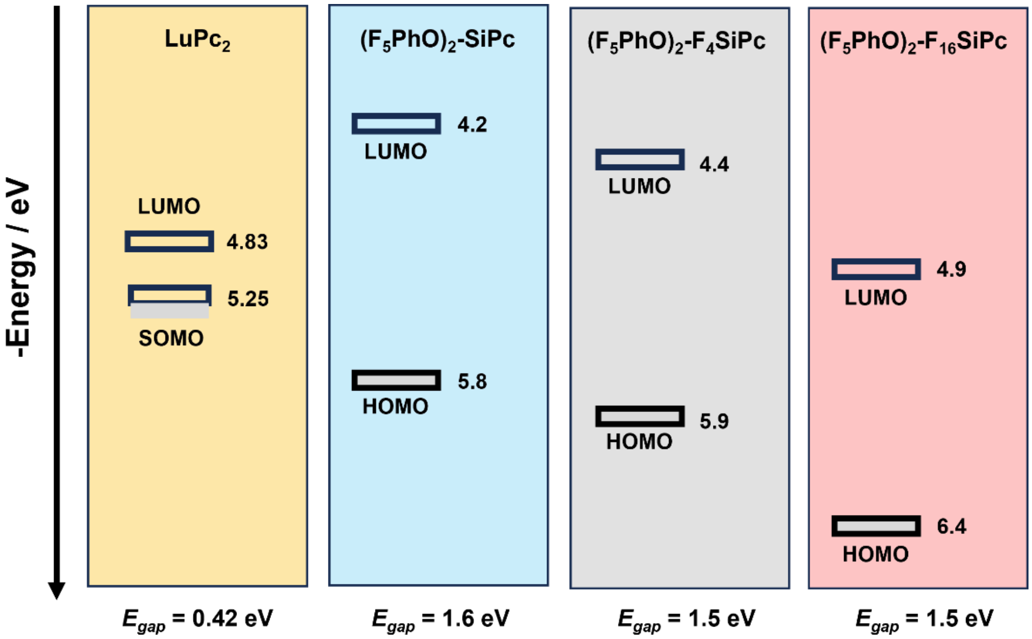

Figure 6.12 Energy levels of frontier orbitals of LuPc$_2$, (F$_5$PhO)$_2$-SiPc, (F$_5$PhO)$_2$-F$_4$SiPc and (F$_5$PhO)$_2$-F$_{16}$SiPc.

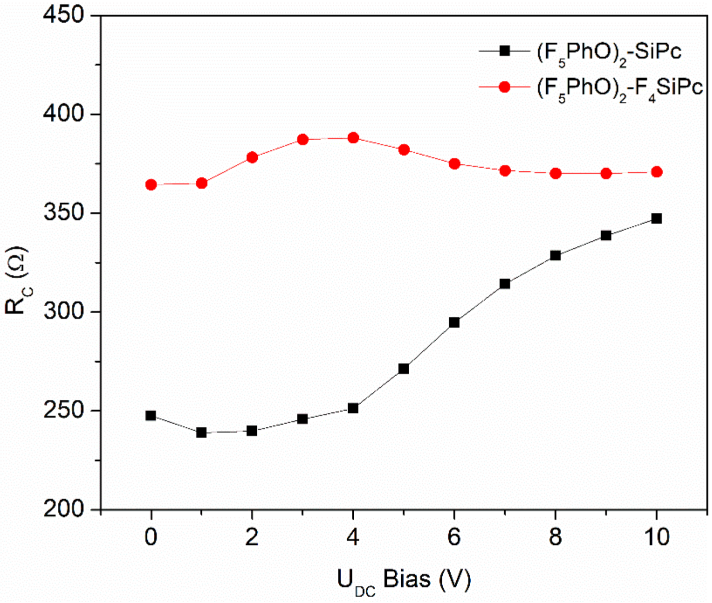

Figure 6.13 Contact resistance (R_C) of organic heterojunction sensors extracted from R_i-CPE models.

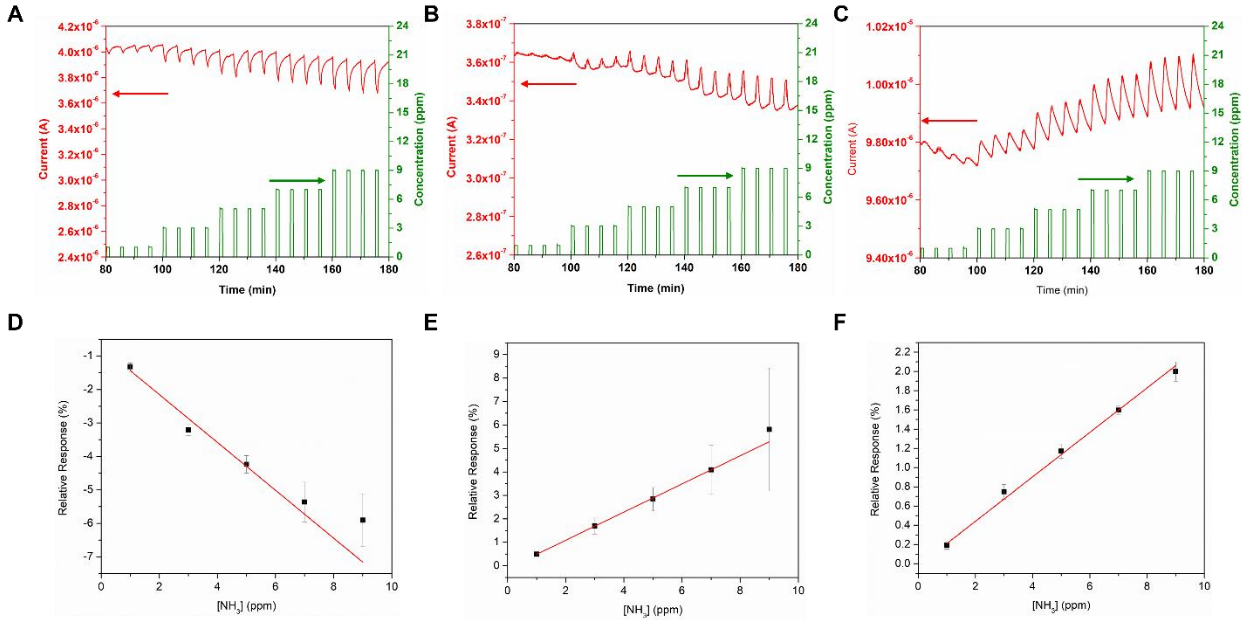

Figure 6.14 A-C) Response of organic heterojunction sensors under successive exposure of NH_3 for 1 min and recovery under synthetic air for 4 min in the range of NH_3 concentration from 1 – 9 ppm at an RH of 45% and room temperature (20 - 22°C) and D-F) variation of RR of organic heterojunction devices for a characteristic A and D) $(F_5PhO)_2$-SiPc/$LuPc_2$ heterojunction device, B and E) $(F_5PhO)_2$-F_4SiPc/$LuPc_2$ heterojunction device and C and F) $(F_5PhO)_2$-F_{16}SiPc/$LuPc_2$ heterojunction device. Sensing data for all three configurations was collected at an applied voltage of 4 V.

Table 6.6 Comparison of S and LOD for R_2-F_xSiPc sensors in this work compared to previously reported resistors and organic heterojunction sensors.

Device (Type of charge carriers)	**S (% ppm^{-1})**	**LOD (ppb)**	**[NH_3] (ppm)**	**Reference**
$LuPc_2$ resistor (p)*	-0.02	/	25	[1]
CoPc[β-O(4-CF_3-Ph)$_4$] resistor (n)	0.17	420	14-16	[2]
PEDOT/PSS-SWCNT resistor (p)	-0.21	200	2-100	[3]
(345F)$_2$-SiPc/$LuPc_2$ (p)*	-0.6	310	5	[4]
Cl_2-SiPc/$LuPc_2$ (p)*	-0.13	100	10	[4]
Cu(F_{16}Pc)/pNiDPP (n)*	0.403	228	1-50	[5]
Ace-PQ-Ni/$LuPc_2$ (p)	-0.059	156	5-10	[6]
AM6/$LuPc_2$ (p)	-0.21	115	5-10	[6]
(F_5PhO)$_2$-SiPc/$LuPc_2$ (p)	-0.47	307	1-9	This work
(F_5PhO)$_2$-F_4SiPc (n)	0.45	750	1-9	This work
(F_5PhO)$_2$-F_{16}SiPc (n)	0.22	618	1-9	This work

*Sensors fabricated with IDE channel widths of 75 µm.

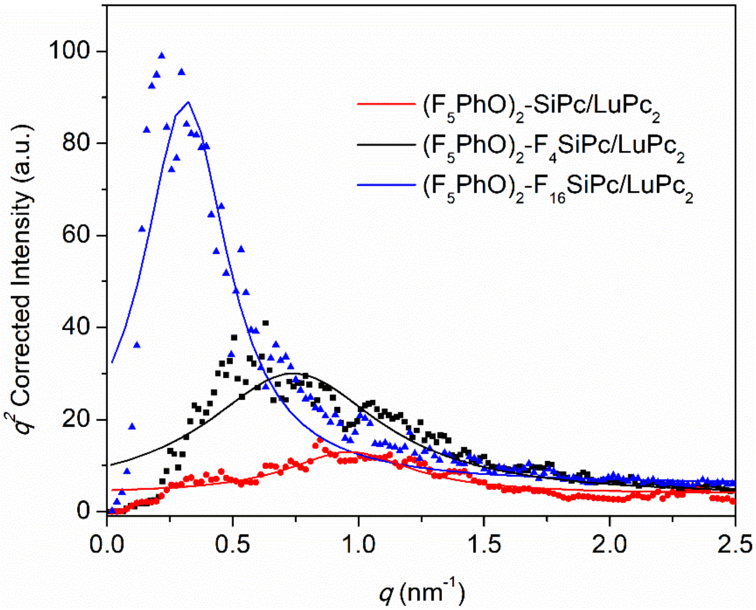

Figure 6.15 Radial power spectral density function of $(F_5PhO)_2$-F_xSiPc/LuPc$_2$ heterojunction devices extracted from AFM images. Lorentzian curve fit is used as a tool to better visualize data and serves as a guide for the eye.

Table 6.7 Summary of radial power spectral density values for $(F_5PhO)_2$-F_XSiPc/LuPc$_2$ heterojunction devices calculated from AFM height images in **Figure 6** and corrected by q^2; mode domain sizes by PSDF analysis and RMS roughness calculated from AFM images.

Sublayer	**Iq^2_{max}** [-]	**Mode Domain Size (nm)**	**FWHM** [-]	**RMS Roughness (nm)**
$(F_5PhO)_2$-SiPc	0.634	9.91	0.85	3.48
$(F_5PhO)_2$-F_4SiPc	0.849	7.40	0.64	1.23
$(F_5PhO)_2$-F_{16}SiPc	0.296	21.2	0.41	10.38

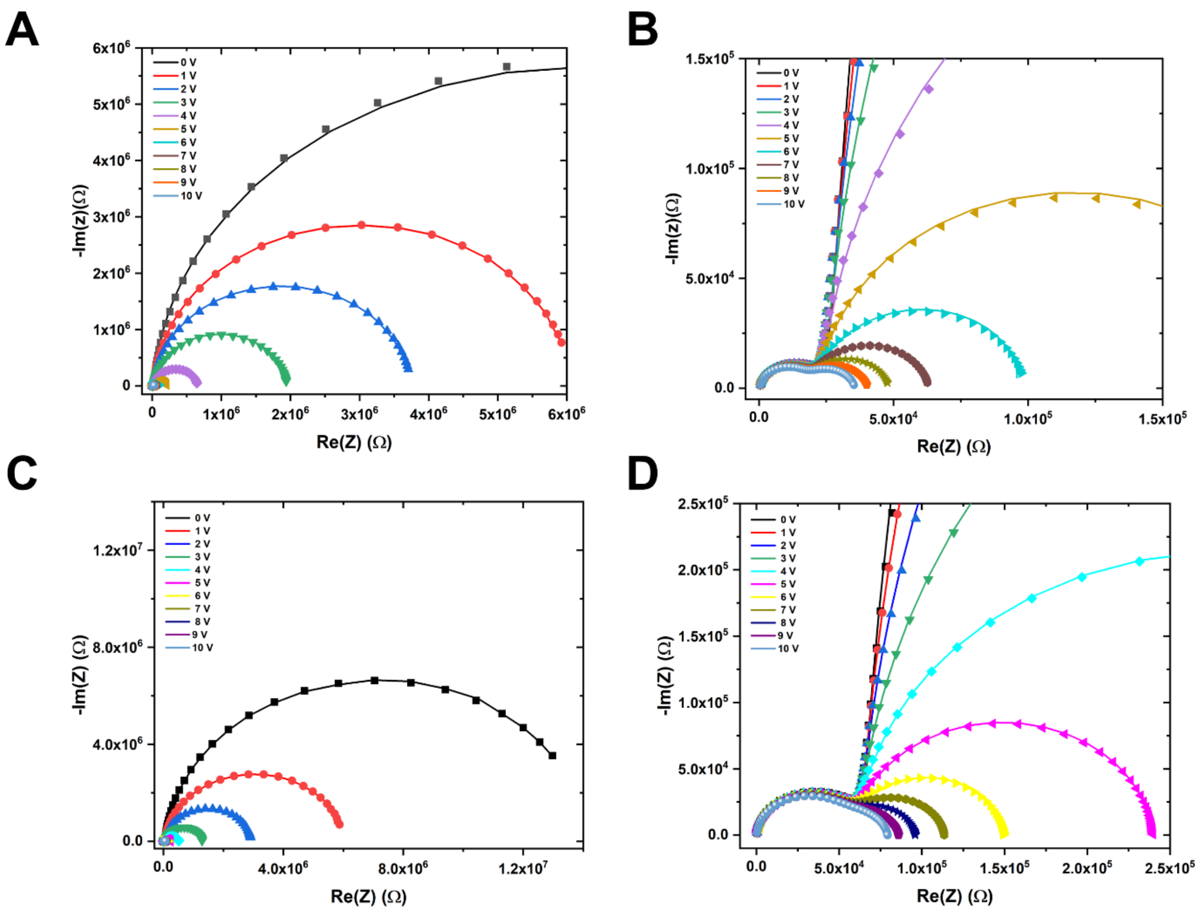

Figure 6.16 Nyquist plots of characteristic $(F_5PhO)_2$-SiPc/$LuPc_2$ heterojunction device A and B) before annealing and C and D) after annealing at 100 °C for 1h under vacuum. Figures B and D are insets of A and C, respectively.

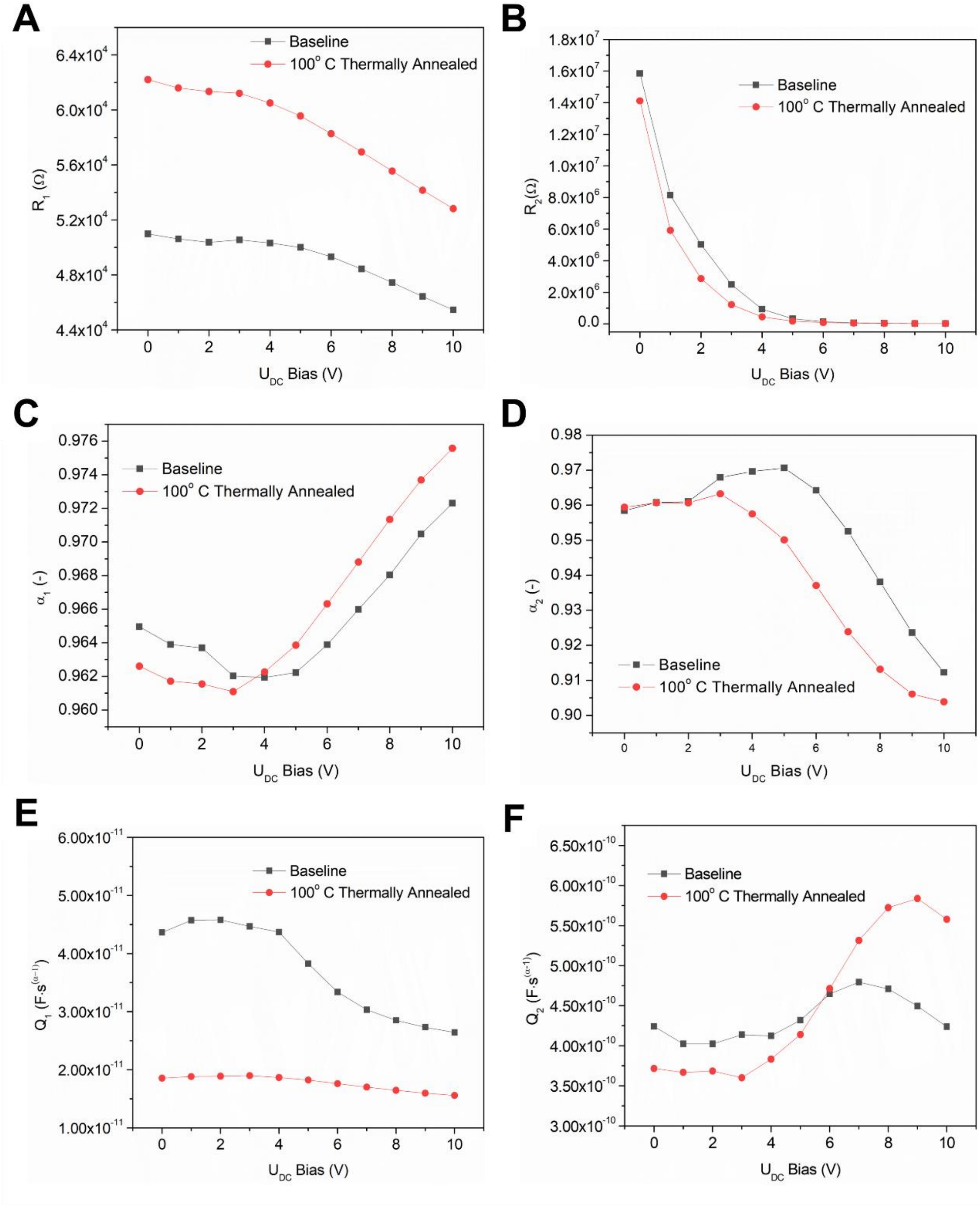

Figure 6.17 Variation of charge transport parameters: A) bulk resistance (R1), B) interfacial resistance (R2), C) alpha associated with bulk (α1), D) alpha associated with the interface (α1), bulk capacitance ($C1_{eff}$) and interfacial capacitance ($C2_{eff}$) with applied DC voltage from 0 V – 10 V and a fixed AC voltage 200 mV for organic heterojunction devices with $(F_5PhO)_2$-SiPc before thermal annealing (black line), and after thermal annealing under vacuum at 100 °C for 1 hour (red line).

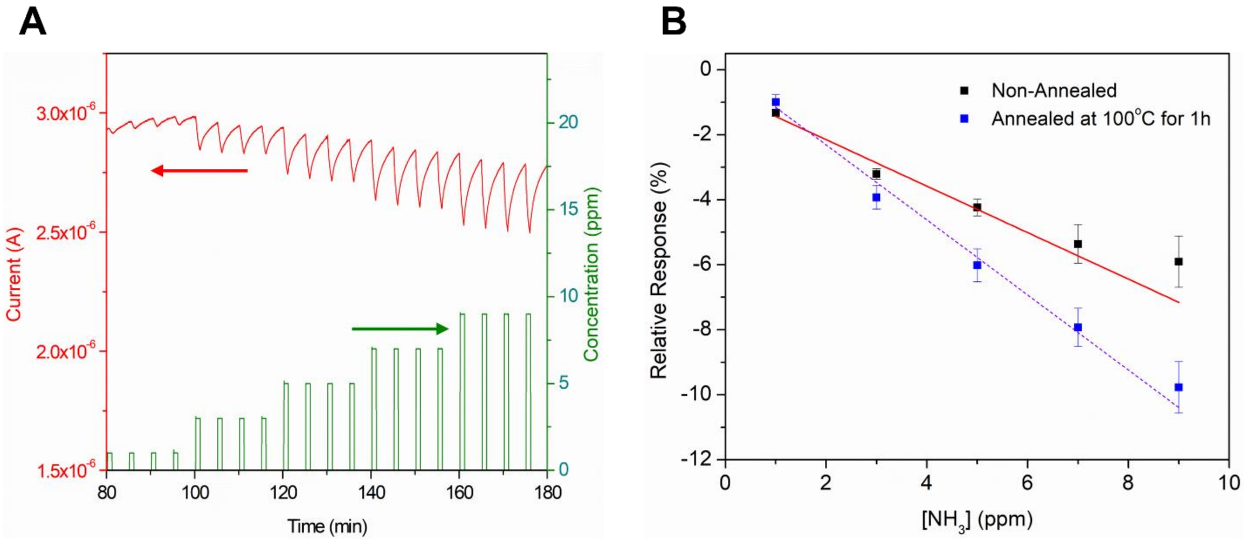

Figure 6.18 A) Response of $(F_5PhO)_2$-SiPc/LuPc$_2$ heterojunctions under successive exposure of NH_3 for 1 min and recovery under synthetic air for 4 min in the range of NH_3 concentration from 1 – 9 ppm and B) relative response of heterojunction device before and after thermal annealing at 100 °C for one hour. Heterojunctions were measured at 45% relative humidity (RH) and room temperature (20 - 22°C). Sensing data was collected at an applied voltage of 4 V.

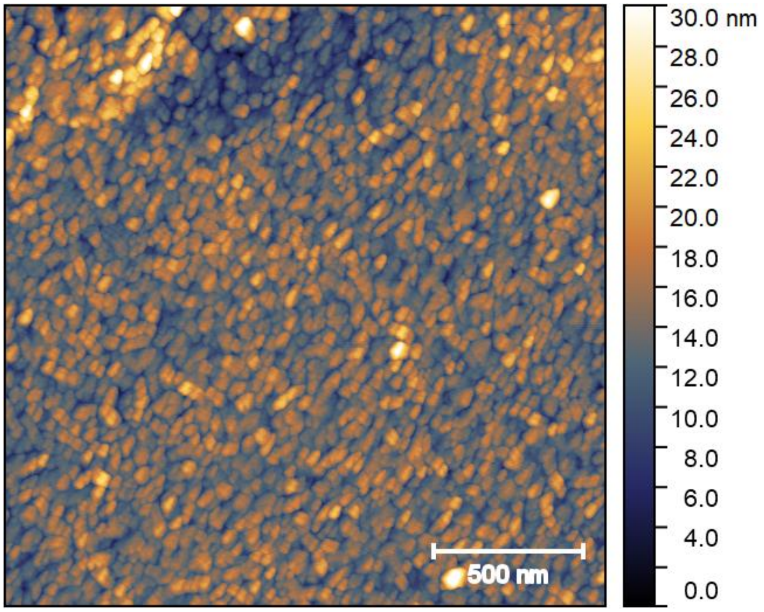

Figure 6.19 Atomic force microscopy image of $(F_5PhO)_2$-SiPc/LuPc$_2$ heterojunction device after thermal annealing at at 100°C for one hour under vacuum.

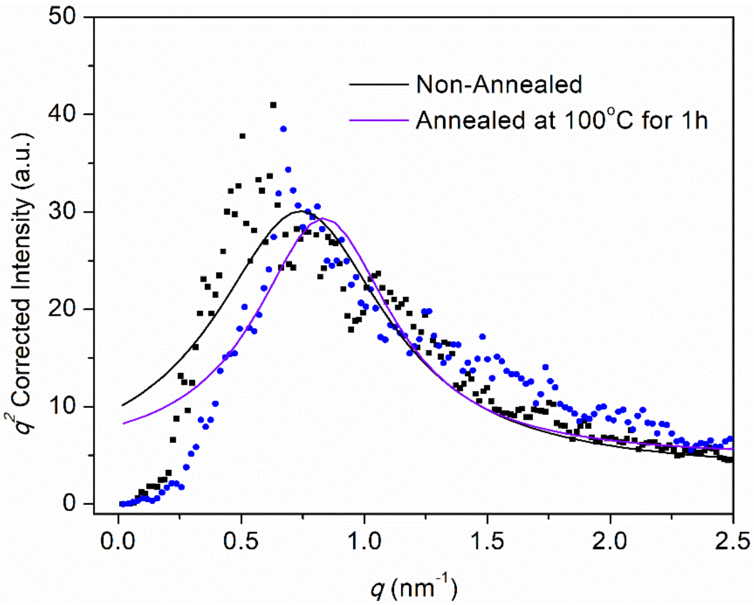

Figure 6.20 Radial power spectral density function of $(F_5PhO)_2$-$F_xSiPc/LuPc_2$ heterojunction devices processed at room temperature or thermally annealed at 100°C for 1 hour under vacuum, extracted from AFM images. Lorentzian curve fit is used as a tool to better visualize data and serves as a guide for the eye.

Table 6.8 Summary of radial power spectral density values for $(F_5PhO)_2$-$F_xSiPc/LuPc_2$ heterojunction devices processed at room temperature or thermally annealed at 100°C for 1 hour under vacuum. Values calculated from AFM height images and corrected by q^2; mode domain sizes by PSDF analysis and RMS roughness calculated from AFM images.

Condition	**$Iq^2{}_{max}$ [-]**	**Mode Domain Size (nm)**	**FWHM [-]**	**RMS Roughness (nm)**
Pre-Anneal	0.634	9.91	0.85	3.48
Post-Anneal	0.671	9.36	0.68	3.11

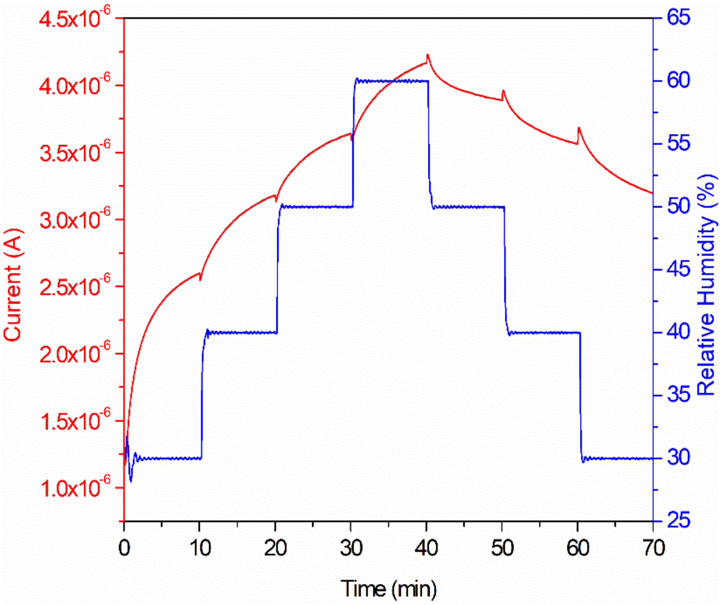

Figure 6.21 Response of $(F_5PhO)_2$-SiPc/LuPc heterojunction devices annealed at 100 °C under vacuum for 1h towards changes in RH from 30% to 60% and then to 30% at room temperature (20 - 22°C). Humidity response data was collected at an applied voltage of 4 V.

Supporting Information References

[1] Bouvet, M.; Gaudillat, P.; Suisse, J.-M. Lanthanide Macrocyclic Complexes: From Molecules to Materials and From Materials to Devices. *J. Porphyrins Phthalocyanines* **2013**, *17*, 628–635.

[2] Duan, X.; Zhang, Y.; Wang, H.; Dai, F.; Yang, G.; Chen, Y. A Phthalocyanine Sensor Array Based on Sensitivity and Current Changes for Highly Sensitive Identification of Three Toxic Gases at Ppb Levels. *New J. Chem.* **2020**, *44* (31), 13240–13248.

[3] Jian, J.; Guo, X.; Lin, L.; Cai, Q.; Cheng, J.; Li, J. Gas-Sensing Characteristics of Dielectrophoretically Assembled Composite Film of Oxygen Plasma-Treated SWCNTs and PEDOT/PSS Polymer. *Sens. Actuators: B. Chem.* **2013**, *178*, 279–288.

[4] Ganesh Moorthy, S.; King, B.; Kumar, A.; Lesniewska, E.; Lessard, B. H.; Bouvet, M. Molecular Engineering of Silicon Phthalocyanine to Improve the Charge Transport and Ammonia Sensing Properties of Organic Heterojunction Gas Sensors. *Adv. Sens. Res.* **2022**, 2200030.

[5] Bengasi, G.; Meunier-Prest, R.; Baba, K.; Kumar, A.; Pellegrino, A. L.; Boscher, N. D.; Bouvet, M. Molecular Engineering of Porphyrin-Tapes/Phthalocyanine Heterojunctions for a Highly Sensitive Ammonia Sensor. *Adv. Electron. Mater.* **2020**, *6* (12), 2000812.

[6] Ganesh Moorthy, S.; Arvidson, J; Meunier-Prest, R; Wang, H; Bouvet, M. π-Extended porphyrin-phthalocyanine heterojunction devices exhibiting high ammonia sensitivity with a remarkable light effect. *ACS. Sensors.* ***2024**, Accepted.*

References

(1) Zhao, S.; Hou, S.; Fan, H.; Wang, Z.; Yu, J. High Performance Nitrogen Dioxide Sensor Based on Organic Thin-Film Transistor Utilizing P3HT/OH-MWCNTs Blend Film. *Synth. Met.* **2020**, *269* (September), 116569. https://doi.org/10.1016/j.synthmet.2020.116569.

(2) Wu, M.; Hou, S.; Yu, X.; Yu, J. Recent Progress in Chemical Gas Sensors Based on Organic Thin Film Transistors. *J. Mater. Chem. C* **2020**, *8* (39), 13482–13500. https://doi.org/10.1039/d0tc03132a.

(3) Duan, G.; Huang, S.; Feng, Z.; Xie, P.; Zhang, F.; Zhou, Y.; Han, S. T. Three-Terminal Artificial Olfactory Sensors Based on Emerging Materials: Mechanism and Application. *Adv. Funct. Mater.* **2023**, *33* (10), 202209969. https://doi.org/10.1002/adfm.202209969.

(4) Zhang, X.; Pu, Z.; Su, X.; Li, C.; Zheng, H.; Li, D. Flexible Organic Field-Effect Transistors-Based Biosensors: Progress and Perspectives. *Anal. Bioanal. Chem.* **2023**, *415* (9), 1607–1625. https://doi.org/10.1007/s00216-023-04553-6.

(5) Surya, S. G.; Raval, H. N.; Sonar, P.; Salama, K. N.; Rao, V. R. Trends in Analytical Chemistry Organic Fi Eld Effect Transistors (OFETs) in Environmental Sensing and Health Monitoring : A Review. *Trends Anal. Chem.* **2019**, *111* (2), 27–36. https://doi.org/10.1016/j.trac.2018.11.027.

(6) Chehade, G.; Dincer, I. Progress in Green Ammonia Production as Potential Carbon-Free Fuel. *Fuel* **2021**, *299* (February), 120845. https://doi.org/10.1016/j.fuel.2021.120845.

(7) Timmer, B.; Olthuis, W.; Van Den Berg, A. Ammonia Sensors and Their Applications - A Review. *Sensors Actuators, B Chem.* **2005**, *107* (2), 666–677. https://doi.org/10.1016/j.snb.2004.11.054.

(8) Yu, S.-Y.; Tung, T.-W.; Yang, H.-Y.; Chen, G.-Y.; Shih, C.-C.; Lee, Y.-C.; Chen, C.-C.; Zan, H.-W.; Meng, H.-F.; Lu, C.-J.; Wang, C.-L.; Jian, W.-B.; Soppera, O. A Versatile Method to Enhance the Operational Current of Air- Stable Organic Gas Sensor for Monitoring of Breath Ammonia in Hemodialysis Patients. *ACS Sensors* **2019**, *4* (4), 1023–1031. https://doi.org/10.1021/acssensors.9b00223.

(9) Wyer, K. E.; Kelleghan, D. B.; Blanes-vidal, V.; Schauberger, G.; Curran, T. P. Ammonia Emissions from Agriculture and Their Contribution to Fine Particulate Matter : A Review of Implications for Human Health. *J. Environ. Manage.* **2022**, *323* (12), 116285. https://doi.org/10.1016/j.jenvman.2022.116285.

(10) Mateos, M.; Meunier-Prest, R.; Suisse, J. M.; Bouvet, M. Modulation of the Organic Heterojunction Behavior, from Electrografting to Enhanced Sensing Properties. *Sensors Actuators, B Chem.* **2019**, *299*, 126968. https://doi.org/10.1016/j.snb.2019.126968.

(11) He, J.; Liang, B.; Yan, X.; Liu, F.; Wang, J.; Yang, Z.; You, R.; Wang, C.; Sun, P.; Yan, X.; Lin, H.; Kang, B.; Wang, Y.; Lu, G. A TPA-DCPP Organic Semiconductor Film-Based Room Temperature NH3 Sensor for Insight into the Sensing Properties. *Sensors Actuators B. Chem.* **2021**, *327*, 128940. https://doi.org/10.1016/j.snb.2020.128940.

(12) Sharma, A. K.; Mahajan, A.; Kumar, S.; Debnath, A. K.; Aswal, D. K. Tailoring of the Chlorine Sensing Properties of Substituted Metal Phthalocyanines Non-Covalently Anchored on Single-Walled Carbon Nanotubes. *RSC Adv.* **2018**, *8* (57), 32719–32730. https://doi.org/10.1039/c8ra05529g.

(13) Zhou, X.; Niu, K.; Wang, Z.; Huang, L.; Chi, L. An Ammonia Detecting Mechanism for Organic Transistors as Revealed by Their Recovery Processes. *Nanoscale* **2018**, *10* (18), 8832–8839.

https://doi.org/10.1039/c8nr01275j.

(14) Xie, T.; Xie, G.; Su, Y.; Hongfei, D.; Ye, Z.; Jiang, Y. Ammonia Gas Sensors Based on Poly (3-Hexylthiophene)-Molybdenum Disulfide Film Transistors. *Nanotechnology* **2016**, *27* (6). https://doi.org/10.1088/0957-4484/27/6/065502.

(15) Yu, J.; Yu, X.; Zhang, L.; Zeng, H. Ammonia Gas Sensor Based on Pentacene Organic Field-Effect Transistor. *Sensors Actuators, B Chem.* **2012**, *173*, 133–138. https://doi.org/10.1016/j.snb.2012.06.060.

(16) Anisimov, D. S.; Abramov, A. A.; Gaidarzhi, V. P.; Kaplun, D. S.; Agina, E. V; Ponomarenko, S. A. Food Freshness Measurements and Product Distinguishing by a Portable Electronic Nose Based on Organic Field-Effect Transistors. *ACS Omega* **2023**, *8* (5), 4649−4654. https://doi.org/10.1021/acsomega.2c06386.

(17) Kumar, A.; Castro, M.; Feller, J.-F. Review on Sensor Array-Based Analytical Technologies for Quality Control of Food and Beverages. *Sensors* **2023**, *23* (8), 32719–32730. https://doi.org/10.1039/C8RA05529G.

(18) Parra, V.; Brunet, J.; Pauly, A.; Bouvet, M. Molecular Semiconductor-Doped Insulator (MSDI) Heterojunctions: An Alternative Transducer for Gas Chemosensing. *Analyst* **2009**, *134* (9), 1776–1778. https://doi.org/10.1039/b906786h.

(19) Bouvet, M.; Xiong, H.; Parra, V. Molecular Semiconductor-Doped Insulator (MSDI) Heterojunctions: Oligothiophene/Bisphtalocyanine (LuPc2) and Perylene/Bisphthalocyanine as New Structures for Gas Sensing. *Sensors Actuators, B Chem.* **2010**, *145* (1), 501–506. https://doi.org/10.1016/j.snb.2009.12.064.

(20) Ouedraogo, S.; Meunier-Prest, R.; Kumar, A.; Bayo-Bangoura, M.; Bouvet, M. Modulating the Electrical Properties of Organic Heterojunction Devices Based on Phthalocyanines for Ambipolar Sensors. *ACS Sensors* **2020**, *5* (6), 1849–1857. https://doi.org/10.1021/acssensors.0c00877.

(21) Kumar, A.; Alami Mejjati, N.; Meunier-Prest, R.; Krystianiak, A.; Heintz, O.; Lesniewska, E.; Devillers, C. H.; Bouvet, M. Tuning of Interfacial Charge Transport in Polyporphine/Phthalocyanine Heterojunctions by Molecular Geometry Control for an Efficient Gas Sensor. *Chem. Eng. J.* **2022**, *429* (August 2021), 132453. https://doi.org/10.1016/j.cej.2021.132453.

(22) Melville, O. A.; Lessard, B. H.; Bender, T. P. Phthalocyanine-Based Organic Thin-Film Transistors: A Review of Recent Advances. *ACS Applied Materials & Interfaces*. 2015, pp 13105–13118. https://doi.org/10.1021/acsami.5b01718.

(23) Şahin, Z.; Meunier-Prest, R.; Dumoulin, F.; Kumar, A.; Isci, Ü.; Bouvet, M. Tuning of Organic Heterojunction Conductivity by the Substituents' Electronic Effects in Phthalocyanines for Ambipolar Gas Sensors. *Sensors Actuators, B Chem.* **2021**, *332*, 129505. https://doi.org/10.1016/j.snb.2021.129505.

(24) Bengasi, G.; Meunier-Prest, R.; Baba, K.; Kumar, A.; Pellegrino, A. L.; Boscher, N. D.; Bouvet, M. Molecular Engineering of Porphyrin-Tapes/Phthalocyanine Heterojunctions for a Highly Sensitive Ammonia Sensor. *Adv. Electron. Mater.* **2020**, *6* (12), 1–12. https://doi.org/10.1002/aelm.202000812.

(25) Melville, O. A.; Grant, T. M.; Mirka, B.; Boileau, N. T.; Park, J.; Lessard, B. H. Ambipolarity and Air Stability of Silicon Phthalocyanine Organic Thin-Film Transistors. *Adv. Electron. Mater.* **2019**, *5* (8), 1900087. https://doi.org/10.1002/aelm.201900087.

(26) Lessard, B. H. The Rise of Silicon Phthalocyanine : From Organic Photovoltaics to Organic Thin

Film Transistors. *ACS Appl. Mater. Interfaces* **2021**, *13* (27), 31321–31330. https://doi.org/10.1021/acsami.1c06060.

(27) King, B.; Melville, O. A.; Rice, N. A.; Kashani, S.; Tonnelé, C.; Raboui, H.; Swaraj, S.; Grant, T. M.; McAfee, T.; Bender, T. P.; Ade, H.; Castet, F.; Muccioli, L.; Lessard, B. H. Silicon Phthalocyanines for N-Type Organic Thin-Film Transistors: Development of Structure–Property Relationships. *ACS Appl. Electron. Mater.* **2021**, *3* (1), 325–336. https://doi.org/10.1021/acsaelm.0c00871.

(28) Cranston, R. R.; Vebber, M. C.; Berbigier, J. F.; Rice, N. A.; Tonnelé, C.; Comeau, Z. J.; Boileau, N. T.; Brusso, J. L.; Shuhendler, A. J.; Castet, F.; Muccioli, L.; Kelly, T. L.; Lessard, B. H. Thin-Film Engineering of Solution-Processable n-Type Silicon Phthalocyanines for Organic Thin-Film Transistors. *ACS Appl. Mater. Interfaces* **2021**, *13* (1), 1008–1020. https://doi.org/10.1021/acsami.0c17657.

(29) Vebber, M. C.; King, B.; French, C.; Toussignant, M.; Ronnasi, B.; Dindault, C.; Wantz, G.; Hirsch, L.; Brusso, J.; Lessard, B. H. From P-type to N-type: Peripheral Fluorination of Axially Substituted Silicon Phthalocyanines Enables Fine Tuning of Charge Transport. *Can. J. Chem. Eng.* **2023**, No. January, 1–13. https://doi.org/10.1002/cjce.24843.

(30) King, B.; Vebber, M. C.; Ewenike, R.; Dupuy, M.; French, C.; Brusso, J. L.; Lessard, B. H. Peripherally Fluorinated Silicon Phthalocyanines: How Many Fluorine Groups Are Necessary for Air-Stable Electron Transport in Organic Thin-Film Transistors? *Chem. Mater.* **2023**, *35* (20), 8517–8528. https://doi.org/10.1021/acs.chemmater.3c01342.

(31) Ganesh Moorthy, S.; King, B.; Kumar, A.; Lesniewska, E.; Lessard, B. H.; Bouvet, M. Molecular Engineering of Silicon Phthalocyanine to Improve the Charge Transport and Ammonia Sensing Properties of Organic Heterojunction Gas Sensors. *Advaned Sens. Res.* **2023**, *2200030*, 1–13. https://doi.org/10.1002/adsr.202200030.

(32) Jones, B. A.; Facchetti, A.; Wasielewski, M. R.; Marks, T. J. Tuning Orbital Energetics in Arylene Diimide Semiconductors. Materials Design for Ambient Stability of n-Type Charge Transport. *J. Am. Chem. Soc.* **2007**, *129* (49), 15259–15278. https://doi.org/10.1021/ja075242e.

(33) Anthopoulos, T. D.; Anyfantis, G. C.; Papavassiliou, G. C.; De Leeuw, D. M. Air-Stable Ambipolar Organic Transistors. *Appl. Phys. Lett.* **2007**, *90* (12). https://doi.org/10.1063/1.2715028.

(34) Lowbry, M. K.; Starshak, A. J.; John, S. J.; Esposito, N.; Krueger, P. C.; Kenney, M. E. Dichloro(Phthalocyanino)Silicon. *Inorg. Chem.* **1965**, *4* (1), 128. https://doi.org/10.1021/ic50023a036.

(35) Melville, O. A.; Grant, T. M.; Lochhead, K.; King, B.; Ambrose, R.; Rice, N. A.; Boileau, N. T.; Peltekoff, A. J.; Tousignant, M.; Hill, I. G.; Lessard, B. H. Contact Engineering Using Manganese, Chromium, and Bathocuproine in Group 14 Phthalocyanine Organic Thin-Film Transistors. *ACS Appl. Electron. Mater.* **2020**, *2* (5), 1313–1322. https://doi.org/10.1021/acsaelm.0c00104.

(36) Clarisse, C.; Riou, M. T. Synthesis and Characterization of Some Lanthanide Phthalocyanines. *Inorganica Chim. Acta* **1987**, *130* (1), 139–144. https://doi.org/10.1016/S0020-1693(00)85943-5.

(37) Gaudillat, P.; Wannebroucq, A.; Suisse, J.-M.; Bouvet, M. Bias and Humidity Effects on the Ammonia Sensing of Perylene Derivative / Lutetium Bisphthalocyanine MSDI Heterojunctions. *Sensors Actuators B Chem.* **2016**, *222*, 910–917. https://doi.org/10.1016/j.snb.2015.09.015.

(38) Even, R.; Simon, J. Optical Properties of Thin Films of Molecular Semiconductors. *Chem. Phys. Lett.* **1989**, *156* (6), 609–614. https://doi.org/10.1016/S0009-2614(89)87241-0.

(39) Ortí, E.; Brédas, J. L.; Clarisse, C. Electronic Structure of Phthalocyanines : Theoretical Investigation of the Optical Properties of Phthalocyanine Monomers , Dimers , and Crystals Electronic Structure of Phthalocyanlnes : Theoretical Investigation of the Optical Properties of Phthalocyanln. *J. Chem. Phys.* **1990**, *92* (2), 1228–1235. https://doi.org/10.1063/1.458131.

(40) Basova, T. V; Mikhaleva, N. S.; Hassan, A. K.; Kiselev, V. G. Thin Films of Fluorinated 3d -Metal Phthalocyanines as Chemical Sensors of Ammonia : An Optical Spectroscopy Study. *Sensors Actuators B. Chem.* **2016**, *227*, 634–642. https://doi.org/10.1016/j.snb.2015.12.079.

(41) Shao, X.; Wang, S.; Li, X.; Su, Z.; Chen, Y.; Xiao, Y. Single Component P-, Ambipolar and n-Type OTFTs Based on Fluorinated Copper Phthalocyanines. *Dye. Pigment.* **2016**, *132*, 378–386. https://doi.org/10.1016/j.dyepig.2016.05.020.

(42) Bonegardt, D.; Klyamer, D.; Krasnov, P.; Sukhikh, A.; Basova, T. Effect of the Position of Fluorine Substituents in Tetrasubstituted Metal Phthalocyanines on Their Vibrational Spectra. *J. Fluor. Chem.* **2021**, *246*, 109780. https://doi.org/10.1016/j.jfluchem.2021.109780.

(43) Kumar, A.; Meunier-Prest, R.; Lesniewska, E.; Bouvet, M. Chemical Interplay of Electrode Geometry and Bias on Charge Transport in Organic Heterojunction Gas Sensors. *Sensors Actuators B. Chem.* **2022**, *369*, 132313. https://doi.org/10.1016/j.snb.2022.132313.

(44) Gangishetty, M. K.; Scott, R. W. J.; Kelly, T. L. Effect of Relative Humidity on Crystal Growth, Device Performance and Hysteresis in Planar Heterojunction Perovskite Solar Cells. *Nanoscale* **2016**, *8* (12), 6300–6307. https://doi.org/10.1039/c5nr04179a.

(45) Miller, K. A.; Yang, R. D.; Hale, M. J.; Park, J.; Fruhberger, B.; Colesniuc, C. N.; Schuller, I. K.; Kummel, A. C.; Trogler, W. C. Electrode Independent Chemoresistive Response for Cobalt Phthalocyanine in the Space Charge Limited Conductivity Regime. *J. Phys. Chem. B* **2006**, *110* (1), 361–366. https://doi.org/10.1021/jp053104a.

(46) Waldrip, M.; Jurchescu, O. D.; Gundlach, D. J.; Bittle, E. G. Contact Resistance in Organic Field-Effect Transistors: Conquering the Barrier. *Adv. Funct. Mater.* **2020**, *30* (20), 1904576. https://doi.org/10.1002/adfm.201904576.

(47) Hirschorn, B.; Orazem, M. E.; Tribollet, B.; Vivier, V.; Frateur, I.; Musiani, M. Electrochimica Acta Determination of Effective Capacitance and Film Thickness from Constant-Phase-Element Parameters. *Electrochem. Acta* **2010**, *55* (21), 6218–6227. https://doi.org/10.1016/j.electacta.2009.10.065.

(48) Lau, K. M.; Tang, J. X.; Sun, H. Y.; Lee, C. S.; Lee, S. T.; Yan, D. Interfacial Electronic Structure of Copper Phthalocyanine and Copper Hexadecafluorophthalocyanine Studied by Photoemission. *Appl. Phys. Lett.* **2006**, *88* (17), 67–70. https://doi.org/10.1063/1.2198484.

(49) Boileau, N. T.; Melville, O. A.; Mirka, B.; Cranston, R.; Lessard, B. H. P and N Type Copper Phthalocyanines as Effective Semiconductors in Organic Thin-Film Transistor Based DNA Biosensors at Elevated Temperatures. *RSC Adv.* **2019**, *9* (4), 2133–2142. https://doi.org/10.1039/c8ra08829b.

(50) Ganesh Moorthy, S.; Arvidson, J.; Meunier-prest, R.; Wang, H.; Bouvet, M. π-Extended Porphyrin–Phthalocyanine Heterojunction Devices Exhibiting High Ammonia Sensitivity with a Remarkable Light Effect. *ACS Sensors* **2024**, *ASAP*. https://doi.org/10.1021/acssensors.3c02247.

(51) Indrayanto, G. Validation of Chromatographic Methods of Analysis: Application for Drugs That Derived From Herbs. In *Profiles of Drug Substances, Excipients and Related Methodology*; Elsevier Inc., 2018; Vol. 43, pp 359–392. https://doi.org/10.1016/bs.podrm.2018.01.003.

(52) Ye, L.; Stuard, S. J.; Ade, H. Soft X-Ray Scattering Characterization of Polymer Semiconductors. In *Conjugated Polymers: Properties, Processing and Applications*; 2019; pp 427–458. https://doi.org/10.1201/9780429190520-13.

(53) Radford, C. L.; Pettipas, R. D.; Kelly, T. L. Watching Paint Dry: Operando Solvent Vapor Annealing of Organic Solar Cells. *J. Phys. Chem. Lett.* **2020**, *11* (15), 6450–6455. https://doi.org/10.1021/acs.jpclett.0c01934.

(54) Jiao, X.; Ye, L.; Ade, H. Quantitative Morphology–Performance Correlations in Organic Solar Cells: Insights from Soft X-Ray Scattering. *Adv. Energy Mater.* **2017**, *7* (18), 1700084. https://doi.org/10.1002/aenm.201700084.

(55) McAfee, T.; Hoffman, B. C.; You, X.; Atkin, J. M.; Ade, H.; Dougherty, D. B. Morphological, Optical, and Electronic Consequences of Coexisting Crystal Orientations in β-Copper Phthalocyanine Thin Films. *J. Phys. Chem. C* **2016**, *120* (33), 18616–18621. https://doi.org/10.1021/acs.jpcc.6b05043.

(56) Faris, T.; Basova, T.; Chaure, N. B.; Sharma, A. K.; Durmus, M. Effects of Annealing on Device Parameters of Organic Field Effect Transistors Using Liquid- Crystalline Tetrasubstituted. *Europhys. Lett.* **2014**, *106* (5), 58002. https://doi.org/10.1209/0295-5075/106/58002.

(57) Zhu, Y.; Zhang, Y.; Yu, J.; Zhou, C.; Yang, C.; Wang, L.; Wang, L.; Ma, L.; Wang, L. J. Highly-Sensitive Organic Field Effect Transistor Sensors for Dual Detection of Humidity and NO2. *Sensors Actuators B Chem.* **2023**, *374* (October 2022), 132815. https://doi.org/10.1016/j.snb.2022.132815.

(58) Cranston, R.; King, B.; Dindault, C.; Grant, T. M.; Rice, N.; Tonnelé, C.; Muccioli, L.; Castet, F.; Swaraj, S.; Lessard, B. H. Highlighting the Processing Versatility of a Silicon Phthalocyanine Derivative for Organic Thin-Film Transistors. *J. Mater. Chem. C* **2022**, *10* (2). https://doi.org/10.1039/d1tc05238a.

(59) Treat, N. D.; Shuttle, C. G.; Toney, M. F.; Hawker, C. J.; Chabinyc, M. L. In Situ Measurement of Power Conversion Efficiency and Molecular Ordering during Thermal Annealing in P3HT:PCBM Bulk Heterojunction Solar Cells. *J. Mater. Chem.* **2011**, *21* (39), 15224–15231. https://doi.org/10.1039/c1jm12677f.

(60) Lee, J. W.; Kim, S. G.; Bae, S. H.; Lee, D. K.; Lin, O.; Yang, Y.; Park, N. G. The Interplay between Trap Density and Hysteresis in Planar Heterojunction Perovskite Solar Cells. *Nano Lett.* **2017**, *17* (7), 4270–4276. https://doi.org/10.1021/acs.nanolett.7b01211.

Chapter 7. Conclusions and Future Work

7.1 Overall Conclusion

R_2-F_XSiPcs are promising electron transporting or n-type candidate materials for next-generation organic electronic devices and chemical sensors, with well understood chemistry that can enable the synthesis of large quantities of materials for industrially produced electronics. The chemical structure of silicon phthalocyanines can be modified at the axial and peripheral positions to tune intermolecular interactions, solubility, optical properties, charge transport and air stability in organic thin-film transistors. Continuing to develop our understanding of how the structure of R_2-F_XSiPcs influences their electronic properties and how deposition and processing of films from these materials affects their performance in devices is paramount to making them competitive as a supplement to silicon or metal oxide-based electronics and sensors.

In **Chapter 2** of this thesis, I developed structure-property relationships for a catalogue of 11 R_2-SiPc derivatives with a range of axial substituents integrated as the semiconductor in OTFTs. Films of R_2-SiPcs were fabricated on substrates held at room temperature and at an identical deposition rate of 0.2 $Å\cdot s^{-1}$ for a total thickness of 300 Å to directly compare their film forming properties and resulting device performance. I determined that increasing the electron-withdrawing character of the axial groups, quantified by their Hammett Parameter, resulted in a decrease in V_T across the range of derivatives. Additionally, we demonstrated from GIWAXS experiments that our best-performing material, F_{10}-SiPc, had both pseudo edge-on and pseudo face-on of crystalline domains relative to the substrate, while our poorest-performing material NpCOO-SiPc, had a primarily edge-on orientation. While NpCOO-SiPc demonstrated primarily edge-on orientation and should have yielded better μ_e, we demonstrated by DFT measurements that this derivative had the worst predicted conductivity and electronic coupling, which could explain its relatively poor performance in OTFTs. This work served as a fundamental study of thin films of R_2-SiPcs and identified key material design considerations for this class of materials.

In **Chapter 3** of this thesis, I applied the structure-property relationship for V_T that I developed in **Chapter 2** and integrated three novel R_2-SiPcs containing cyanophenoxy and fluoro-cyanophenoxy axial moieties into OTFTs for the first time. I demonstrated that the relationship between electron withdrawing axial groups and V_T continued to hold and achieved a record low V_T for thermally evaporated R_2-SiPc of 4.8V for bis(3-fluoro,4-cyano) silicon phthalocyanine

($(3F,4CN)_2$-SiPc). While this performance was promising, I observed dewetting of the $(3F,4CN)_2$-SiPc film from the substrate surface. To stabilize the film, I incorporated polymer brushes based on polystyrene and poly(methyl methacrylate) into the OTFT architecture as a SAM. Films fabricated on polystyrene brushes remained stable after seven days, while those fabricated on bare silicon dioxide and poly(methyl methacrylate) surfaces showed evidence of dewetting after the same amount of time. This work demonstrated that additional novel R_2-SiPc derivatives with electron withdrawing axial groups can be developed to further reduce device V_T and that surface chemistry is a useful tool for stabilizing films from dewetting.

In **Chapter 4** of this thesis, I investigated how surface chemistry influences the film texture and resulting device performance of OTFTs with F_{10}-SiPc as the semiconductor both by using self-assembled monolayers and weak epitaxial growth (WEG) to understand their effect how the film formation of tetravalent R_2-SiPcs differ from divalent MPcs. I selected SAMs with a range of terminal groups and surface energies including CH_3, CF_3 and phenyl groups to provide a broad range of functional surfaces and *p*-6P as the WEG template owing to its broad use in fabricating OTFTs with highly crystalline metal phthalocyanine semiconductor films. I determined that matching the surface energy of the SAM and the semiconductor does not necessarily yield devices with the highest mobility similar to other polycrystalline semiconductors and that F_{10}-SiPc demonstrated unique WEG behaviour among reported MPcs. F_{10}-SiPc demonstrated a mix of pseudo face-on orientations extracted from GIWAXS measurements, rather than adopting some degree of edge-on orientation for divalent CuPc and ZnPc or Cl_2-SnPc. While the WEG method still yielded relatively well-ordered films with a relatively large amount of crystalline mass, pentafluorophenoxy axial groups evidently interacted with the monolayer and complicated interactions that occur at the semiconductor-dielectric interface.

In **Chapter 5** of this thesis, I reported eight novel peripherally-fluorinated and axially substituted silicon phthalocyanine derivatives (R_2-F_XSiPcs) to study their optical and electronic properties including their performance in OTFTs, the influence of axial and peripheral fluorination on air stability and determining if these materials could effectively transport electrons in air. Peripheral fluorination resulted in a shift in the frontier molecular orbitals of R_2-F_XSiPcs of up to 0.9 eV by increasing peripheral fluorination from zero to sixteen atoms similar to other reported peripherally fluorinated R_2-F_XSiPcs and F_XMPcs. I also demonstrated a clear relationship between OTFT V_T and semiconductor LUMO levels for both Ag and Ag/Mn electrodes. Additionally, all four R_2-F_{16}SiPc and $(F_5PhO)_2$-F_4SiPc demonstrated air-stable electron transport at room temperature and a humidity of 40%. I showed that all four R_2-F_{16}SiPc derivatives demonstrated only a small change in V_T over 14 days stored in ambient conditions after their first measurement, and that $(F_5PhO)_2$-F_4SiPc was the first R_2-F_4SiPc derivative to ever yield air-stable electron transport. I therefore showed for the first time that fluorination of axial ligands can affect the air-stability of R_2-F_XSiPcs in OTFTs and sixteen peripheral fluorine atoms is not a prerequisite for air-stable devices.

Finally, in **Chapter 6** of this thesis, I reported three R_2-F_XSiPcs with pentafluorophenoxy axial substituents, $(F_5PhO)_2$-F_XSiPcs where X = 0, 4 or 16 fluorine atoms, as a low-conductivity sublayer in organic heterojunction devices for NH_3 gas sensors with $LuPc_2$ as a top layer to understand how peripheral fluorination affects the majority charge carrier type in this architecture. I confirmed the preservation of the integrity of the $(F_5PhO)_2$-F_xSiPc layers by Raman spectroscopy. I also demonstrated that increasing the number of peripheral fluorine atoms from zero to four in the $(F_5PhO)_2$-F_xSiPc macrocycle was sufficient to switch the polarity of the device from p-type to n-type behaviour upon exposure to NH_3. Finally, I demonstrated that all three devices had a reversible and dynamic response in the range of 1 ppm – 90 ppm of NH_3 in humid air with a limit of detection less or equal to 1 ppm which is below the short- and long-term exposure limits in occupational settings. The highest-performing device based on $(F_5PhO)_2$-SiPc (F_{10}-SiPc) had the best sensitivity of -0,47 %·ppm^{-1}, response time (t_{90}) of 54 s and best LOD of 471 ppb with a linear calibration curve in the full measurement range of 1 ppm to 90 ppm. I further optimized the $(F_5PhO)_2$-SiPc/$LuPc_2$ device by thermal annealing and achieved a two-fold increase in sensitivity to -0.94 %·ppm^{-1} and enhanced LOD of 242 ppb, demonstrates that this sensor architecture can be optimized by post-deposition processing.

7.2 Recommendations for Future Work

Given the broad range of available R_2-F_XSiPc derivatives, their processing versatility, and their excellent performance in OTFT and gas sensor applications, there is a significant amount of work worth pursuing that could make the use of these materials more widespread in electronics. Based on the work presented in this thesis, I propose two areas of future work that are unexplored or underexplored which could yield improved R_2-F_XSiPc-based OTFTs and heterojunction gas sensors.

7.2.1 Functional polymer brush SAMs by nitroxide mediated polymerization

In **Chapter 1** of this thesis, I presented a brief discussion on the benefits of polymer brushes as self-assembled monolayers for OTFT applications including enhanced operational stability and in **Chapter 3**, I demonstrated how we incorporated polymer brushes into the OTFT architecture to stabilize R_2-SiPc films to dewetting from the dielectric surface. Additionally, in **Chapter 4** of this thesis, I discuss the influence of surface energy and functional SAMs on the morphology and performance of R_2-SiPc-based OTFTs. To build on this work, I propose that functional silane-terminated polymer brushes be explored as SAMs in R_2-F_XSiPc-based OTFTs to tune their morphology, electronic properties, and performance. Many polymerization techniques are available where polymers can be processed by coupling a polymer chain to a silane, which provides a pathway for grafting that is similar to SAMs such as octodecyltrichlorosilane (OTS).[1,2] Grafting-from by surface-initiated polymerization has been reported by employing three techniques: Nitroxide-Mediated Polymerization (NMP),[3,4] Atom-Transfer Radical Polymerization (ATRP)[5–7] and Reversible addition-fragmentation chain transfer polymerization (RAFT).[8] The technique I propose to synthesize these polymers is NMP, which is a controlled radical polymerization (CRP) technique that is a simple, robust and scalable technique which can be used to synthesize well-defined polymers and which is compatible with both grafting-to and grafting-from approaches.[4] NMP is generally desirable over ATRP where transition metal catalysts can still be present in the final polymers[9] and RAFT where sulfer-based chain transfer agents have to be removed.[10] NMP has also been used to synthesize a broad range of vinylic homopolymers, including styrenics,[11] methacrylates,[12] acrylamides[10] and carbazole-based pendant polymers. Our group also has a significant amount of experience with NMP and I have published work as a lead author or co-author on studies reporting the synthesis and characterization of polymers[13] and grafting of functional polymers onto oxide surfaces.[3,14] I expect that the incorporation of grafted polymer SAMs synthesized by NMP will provide benefits to OTFTs with R_2-F_XSiPcs as the semiconductor, including improving their long-term operating stability under applied bias stress like other reports for polymer-based SAMs in the literature.[15] This performance enhancement would be useful for sensors since it would minimize drift in V_T that occurs due to the application of a constant bias[16] and make OTFT-based sensors more viable for long-term monitoring. Additionally, there are a significant number of available monomers which can be polymerized by NMP,[17] and the monomer functionality could be easily tuned to modify the surface energy of the dielectric or induce favourable molecular orientation of the semiconductor to enhance device performance similar to what we have observed in **Chapter 4** of this thesis and from solution-processed R_2-SiPcs.[18]

7.2.2 Morphology control and processing of organic heterojunction sensors

In **Chapter 6** of this thesis, I presented work on the development of R_2-F_XSiPc-based organic heterojunction sensors for the detection of NH_3 and demonstrated that post-deposition thermal annealing is a promising technique for enhancing the performance of these sensors. I demonstrated that thermal annealing of $(F_5PhO)_2$-SiPc/$LuPc_2$ heterojunctions under vacuum at 100 °C affects both the bulk and interfacial resistance to charge transport, as well as yielded an enhancement in the sensitivity and limit of detection of the sensor. However, the effect of annealing temperature is not well understood since only one condition was studied. To further explore the effect of thermal annealing on these devices, I propose that a broader range of temperatures be explored to better understand the influence of annealing on the interface and films. The influence of thermal annealing in the temperature range of room temperature to 185 °C has been explored by our group for both solution processable and evaporated R_2-SiPcs where we demonstrated that annealing results in changes to the crystallinity of the film and changes in molecular orientation of crystalline domains.[19,20] In addition to thermal annealing experiments, I also recommend that a broader range of both fabrication and post-processing experiments be completed to further enhance the performance of R_2-F_XSiPc-based organic heterojunction gas sensors. Many processes which have successfully optimized the performance of OTFT sensors could likely be applied to organic heterojunction gas sensors. For example, the morphology of both the sublayer and the $LuPc_2$ layer could be modified by controlling the deposition rate if both layers are evaporated. Comeau et al. demonstrated that the sensor performance towards cannabinoid vapours of ZnPc OTFTs evaporated to achieve a range of semiconductor film crystallinities.[21] Films evaporated on room temperature substrates at a rate of 1 $Å \cdot s^{-1}$ demonstrated the most significant change in -%$\Delta\mu$ of 7×10^{-3} $cm^2 \cdot V^{-1} \cdot s^{-1}$, -$\Delta V_T$ of 17.5V and decrease in $I_{on/off}$ of 2×10^3, compared to the next lowest-crystallinity films which demonstrate changes in -%$\Delta\mu$ of 4×10^{-3} $cm^2 \cdot V^{-1} \cdot s^{-1}$, -$\Delta V_T$ of 4.4V and no decrease in $I_{on/off}$, respectively. I also recommend that solution-processed R_2-SiPcs be explored as the sublayer in organic heterojunction gas sensors with $LuPc_2$ owing to their potential for incorporation into large-area printed electronics and processability in different solvents. The morphology of solution-processed organic semiconductors, including the degree of crystallization and the size of crystallites, depend critically on solvent selection.[22,23] Cranston et al. demonstrated that processing one R_2-SiPc in toluene as opposed to chloroform resulted in an order of magnitude enhancement in μ_e and shift in VT of 14.7 V.[18] The impact of solvent selection on OTFT gas sensor performance has been explored in the literature. For example, Yu and coworkers reported ultra-sensitive NO_2 gas sensors based on tri-isopropylsilyly-ethynyl (TIPS)-pentacene OTFTs which were fabricated by using chlorobenzene, 1,2-dichlorobenzene, toluene and *o*-xylene.[24] While OTFTs processed in chlorobenzene and *o*-xylene demonstrated the best μ and I_{on}, the sensing performance of devices processed with *o*-xylene demonstrated enhanced sensing response with a relative response of 274.8% compared to 28.8% for chlorobenzene processed devices and 49.9% for 1,2-dichlorobenzene-processed devices owing to the higher density of grain boundaries in the film. Based on our group's experience with solution processed semiconductors and gas sensors, the solution processing of R_2-SiPcs could enable an additional pathway towards high-performance organic heterojunction gas sensors for NH_3 by enabling textural control through different spin-coating parameters.

References

(1) Ha, J.; Chung, S.; Pei, M.; Cho, K.; Yang, H.; Hong, Y. One-Step Interface Engineering for All-Inkjet-Printed, All-Organic Components in Transparent, Flexible Transistors and Inverters: Polymer Binding. *ACS Appl. Mater. Interfaces* **2017**, *9* (10), 8819–8829. https://doi.org/10.1021/acsami.6b14702.

(2) Melville, O. A.; Grant, T. M.; Lessard, H. Silicon Phthalocyanines as N-Type Semiconductors in Organic Thin Film Transistors. *J. Mater. Chem. C* **2018**, *6*, 5482–5488. https://doi.org/10.1039/c8tc01116h.

(3) Melville, O. A.; King, B.; Imperiale, C.; Lessard, B. H. Orthogonally Processable Carbazole-Based Polymer Thin Films by Nitroxide-Mediated Polymerization. *Langmuir* **2016**, *32*, 13640–13648.

(4) Cunningham, M.; Billon, L.; Save, M. *Surface-Initiated Nitroxide- Mediated Polymerization*; 2015.

(5) Page, Z. A.; Narupai, B.; Pester, C. W.; Bou Zerdan, R.; Sokolov, A.; Laitar, D. S.; Mukhopadhyay, S.; Sprague, S.; McGrath, A. J.; Kramer, J. W.; Trefonas, P.; Hawker, C. J. Novel Strategy for Photopatterning Emissive Polymer Brushes for Organic Light Emitting Diode Applications. *ACS Cent. Sci.* **2017**, *3* (6), 654–661. https://doi.org/10.1021/acscentsci.7b00165.

(6) Li, L.; Hu, W.; Chi, L.; Fuchs, H. Polymer Brush and Inorganic Oxide Hybrid Nanodielectrics for High Performance Organic Transistors. *J. Phys. Chem. B* **2010**, *114* (16), 5315–5319. https://doi.org/10.1021/jp100928d.

(7) Ge, F.; Wang, X.; Zhang, Y.; Song, E.; Zhang, G.; Lu, H.; Cho, K.; Qiu, L. Modulating the Surface via Polymer Brush for High-Performance Inkjet-Printed Organic Thin-Film

Transistors. *Adv. Electron. Mater.* **2017**, *3* (1). https://doi.org/10.1002/aelm.201600402.

(8) Tria, M. C.; Liao, K. S.; Alley, N.; Curran, S.; Advincula, R. Electrochemically Crosslinked Surface-Grafted PVK Polymer Brushes as a Hole Transport Layer for Organic Photovoltaics. *J. Mater. Chem.* **2011**, *21* (28), 10261–10264. https://doi.org/10.1039/c1jm11068c.

(9) Lessard, B. H. *Novel Materials : From Nanoporous Materials to Micro-Electronics*; 2016.

(10) Savelyeva, X.; Li, L.; Maric, M. Using Controlled Radical Polymerization to Confirm the Lower Critical Solution Temperature of an N-(Alkoxyalkyl) Acrylamide Polymer in Aqueous Solution. *J. Polym. Sci. Part A Polym. Chem.* **2015**, *53* (1), 59–67. https://doi.org/10.1002/pola.27437.

(11) Vinas, J.; Chagneux, N.; Gigmes, D.; Trimaille, T.; Favier, A.; Bertin, D. SG1-Based Alkoxyamine Bearing a N-Succinimidyl Ester: A Versatile Tool for Advanced Polymer Synthesis. *Polymer (Guildf).* **2008**, *49* (17), 3639–3647. https://doi.org/10.1016/j.polymer.2008.06.017.

(12) Lessard, B. H.; Marić, M. Incorporating Glycidyl Methacrylate into Block Copolymers Using Poly(Methacrylate-Ran-Styrene) Macroinitiators Synthesised by Nitroxide Mediated Polymerization. *J. Polym. Sci. Part A Polym. Chem.* **2009**, *47* (10), 2574–2588. https://doi.org/10.1002/pola.

(13) King, B.; Lessard, B. H. Controlled Synthesis and Degradation of Poly (N-(Isobutoxymethyl) Acrylamide) Homopolymers and Block Copolymers. *Macromol. React. Eng.* **2017**, *10* (2), 1–10. https://doi.org/10.1002/mren.201600073.

(14) King, B.; Daszcynski, A. J.; Rice, N. A.; Peltekoff, A. J.; Yutronkie, N. J.; Lessard, B. H.; Brusso, J. L. Cyanophenoxy-Substituted Silicon Phthalocyanines for Low Threshold Voltage n-Type Organic Thin-Film Transistors. *ACS Appl. Electron. Mater.* **2021**, *3* (5), 2212–2223. https://doi.org/10.1021/acsaelm.1c00175.

(15) Kim, K.; An, T. K.; Kim, J.; Jeong, Y. J.; Jang, J.; Kim, H.; Baek, J. Y.; Kim, Y. H.; Kim, S. H.; Park, C. E. Grafting Fluorinated Polymer Nanolayer for Advancing the Electrical Stability of Organic Field-Effect Transistors. *Chem. Mater.* **2014**, *26* (22), 6467–6476. https://doi.org/10.1021/cm5030266.

(16) Yousefi, N.; Caba, C.; Hu, A.; Mooney, M.; Zhang, S.; Agostinis, A. D.; Mirhassani, M.; Ahamed, M. J.; Tong, Y.; Rondeau-Gagné, S. Building a Versatile Platform for the Detection of Protein-Protein Interactions Based on Organic Field-Effect Transistors. *ACS Appl. Electron. Mater.* **2022**, *4* (10), 4972–4981. https://doi.org/10.1021/acsaelm.2c00983.

(17) Nicolas, J.; Guillaneuf, Y.; Lefay, C.; Bertin, D.; Gigmes, D.; Charleux, B. Nitroxide-Mediated Polymerization. *Prog. Polym. Sci.* **2013**, *38* (1), 63–235. https://doi.org/10.1016/j.progpolymsci.2012.06.002.

(18) Cranston, R. R.; Vebber, M. C.; Berbigier, J. F.; Brusso, J. L.; Kelly, T. L.; Lessard, B. H. High Performance Solution Processed N-Type OTFTs through Surface Engineered F-F Interactions Using Asymmetric Silicon Phthalocyanines. *Adv. Electron. Mater.* **2022**, *8* (12), 2200696. https://doi.org/10.1002/aelm.202200696.

(19) Cranston, R.; Vebber, M. C.; Berbigier, J. F.; Rice, N. A.; Tonnelé, C.; Comeau, Z.; Boileau,

N. T.; Shuhendler, A. J.; Castet, F.; Muccioli, L.; Kelly, T. L.; Lessard, B. H. Thin-Film Engineering of Solution Processable n-Type Silicon Phthalocyanines for Organic Thin-Film Transistors. *Adv. Electron. Mater.* **2020**.

(20) Cranston, R.; King, B.; Dindault, C.; Grant, T. M.; Rice, N.; Tonnelé, C.; Muccioli, L.; Castet, F.; Swaraj, S.; Lessard, B. H. Highlighting the Processing Versatility of a Silicon Phthalocyanine Derivative for Organic Thin-Film Transistors. *J. Mater. Chem. C* **2022**, *10* (2). https://doi.org/10.1039/d1tc05238a.

(21) Comeau, Z. J.; Cranston, R. R.; Lamontagne, H. R.; Harris, C. S.; Shuhendler, A. J.; Lessard, B. H. Surface Engineering of Zinc Phthalocyanine Organic Thin-Film Transistors Results in Part-per-Billion Sensitivity towards Cannabinoid Vapor. *Commun. Chem.* **2022**, *5* (1), 1–8. https://doi.org/10.1038/s42004-022-00797-y.

(22) Lee, H.; Park, C.; Sin, D. H.; Park, J. H.; Cho, K. Recent Advances in Morphology Optimization for Organic Photovoltaics. *Adv. Mater.* **2018**, *30* (34), 1–39. https://doi.org/10.1002/adma.201800453.

(23) Ho, D.; Lee, J.; Park, S.; Park, Y.; Cho, K.; Campana, F.; Lanari, D.; Facchetti, A.; Seo, S. Y.; Kim, C.; Marrocchi, A.; Vaccaro, L. Green Solvents for Organic Thin-Film Transistor Processing. *J. Mater. Chem. C* **2020**, *8* (17), 5786–5794. https://doi.org/10.1039/d0tc00512f.

(24) Shao, B.; Liu, Y.; Zhuang, X.; Hou, S.; Han, S.; Yu, X.; Yu, J. Crystallinity and Grain Boundary Control of TIPS-Pentacene in Organic Thin-Film Transistors for the Ultra-High Sensitive Detection of NO2. *J. Mater. Chem. C* **2019**, *7* (33), 10196–10202. https://doi.org/10.1039/c9tc01219b.

Chapter 8. Additional Contributions

8.1 Exposure to Solvent Vapours for Enhanced N-type OTFT Stability.

Samantha Brixi, Halynne R. Lamontagne, Benjamin King, Adam J. Shuhendler and Benoît H. Lessard*

Publication date: 26th July 2023

Citation: *Mater. Adv.*, **2023**, **4** (20), 4707-4711.

DOI: https://doi.org/10.1039/D3MA00402C

Abstract

To achieve commercialization of organic electronics, the field must see an improvement in both performance and material stability while maintaining a low cost of fabrication. To achieve this, low-cost additives provide a viable solution. A variety of additives containing amine and silane functional groups were tested to determine their impact on the performance and air-stability of n-type semiconductor poly{[N,N′-bis(2-octyldodecyl)-naphthalene-1,4,5,8-bis(dicarboximide)-2,6-diyl]-alt-5,5′-(2,2′-bithiophene)} (P(NDI2OD-T2)) in organic thin film transistors. Aniline and pyridine were found to both have a minimal impact on P(NDI2OD-T2) performance in an inert environment, but to improve stability of electron mobility and threshold voltage in air. Therefore, these compounds, or other compounds based on their structure, would be ideal candidates as additives for the improvement of n-type transistors.

Contribution

I performed grazing-incidence wide-angle X-ray scattering measurements for this study. I also reviewed the prepared manuscript.

8.2 From P-type to N-type: Peripheral Fluorination of Axially Substituted Silicon Phthalocyanines Enables Fine Tuning of Charge Transport.

Mário C. Vebber, Benjamin King, Callum French, Mathieu Tousignant, Bahar Ronnasi, Chloé Dindault, Guillaume Wantz, Lionel Hirsch, Jaclyn Brusso, Benoît H. Lessard*

Publication date: 15th January 2023

Citation: *Can. J. Chem. Eng.,* **2023**, 101 (6), 3019-3031.

DOI: https://doi.org/10.1002/cjce.24843

Abstract

Silicon phthalocyanines (R_2-SiPcs) are a family of promising tunable materials for organic electronic applications. We report the chemistry of the synthesis of axially substituted fluorinated SiPcs (tb-Ph)$_2$-F_xSiPc (where $X = 0, 4, 8$, or 16) and explore how the degree of fluorination effects optical and electronic properties. A new treatment with boron trichloride was included to obtain Cl_2-F_XSiPcs from F_2-F_XSiPcs, activating the axial position for further functionalization. We observed that as the degree of fluorination increased, so did the electron affinity of the compounds, leading to a drop in frontier orbital levels, as measured by electrochemistry and ultraviolet photoelectron spectroscopy (UPS). The deeper energy levels enabled successful (tb-Ph)$_2$-F_4SiPc and poly [[6,7-difluoro[(2-hexyldecyl)oxy]-[5,8-quinoxalinediyl]-2,5-thiophenediyl]] (PTQ10) blends for organic photovoltaics and photodetectors. All four compounds were incorporated in organic thin-film transistors (OTFTs), where the degree of fluorination influenced device operation, changing it from p-type conduction for (tb-Ph)$_2$-F_0SiPc, to ambipolar for (tb-Ph)$_2$-F_4SiPc, and n-type for (tb-Ph)$_2$-F_8SiPc and (tb-Ph)$_2$-F_{16}SiPc. The OTFT devices made with (tb-Ph)$_2$-F_{16}SiPc achieved a low average threshold voltage of 7.0 V in N_2 and retained its n-type mobility when exposed to air.

Contribution

I fabricated and characterized OTFTs for this study and prepared samples for solid-state UV-Vis spectroscopy. I also performed and interpreted device data, atomic force microscopy and X-ray diffraction measurements for this study. I edited the experimental section of the manuscript and wrote the section on OTFTs, as well as reviewed and edited the final version of the manuscript.

8.3 Molecular Engineering of Silicon Phthalocyanine to Improve the Charge Transport and Ammonia Sensing Properties of Organic Heterojunction Gas Sensors

Sujithkumar Ganesh Moorthy, Benjamin King, Abhishek Kumar, Eric Lesniewska, Benoît H Lessard, Marcel Bouvet

Publication date: 18th December 2022

Citation: *Adv. Sensor Res.*, **2023**, 2 (3), 2200030.

DOI: https://doi.org/10.1002/adsr.202200030

Abstract

Novel organic heterostructures fabricated with a bilayer consisting of an axially substituted silicon phthalocyanine (R_2-SiPc) derivative and lutetium bis-phthalocyanine ($LuPc_2$) are investigated for their ammonia sensing properties. Surface and microstructure characterization of the heterostructure films reveal either compact or highly porous surface topography in $(345F)_2$-SiPc and Cl_2-SiPc-based heterostructures, while electrical characterization reveals a strong influence of the axial substituent in R_2-SiPc on NH_3 sensing capabilities. Electrical characterization further demonstrates an apparent energy barrier for interfacial charge transport, which is higher in the $(345F)_2$-SiPc/$LuPc_2$ heterojunction device. In-depth charge transport studies by impedance spectroscopy further reveal a resistive interface in $(345F)_2$-SiPc/$LuPc_2$ and faster bulk and interfacial charge transport in Cl_2-SiPc/$LuPc_2$ heterojunction devices. Different interfacial charge transport capabilities and surface topographies affect NH_3 sensing properties of the two heterojunction devices, in which $(345F)_2$-SiPc/$LuPc_2$ reveals a fast and non-linear response with a limit of detection (LOD) of 310 ppb, while Cl_2-SiPc/$LuPc_2$ exhibits a slow, and linear response to NH_3 with LOD of 100 ppb. Finally, different metrological parameters of the two sensors are correlated to the respective gas-material interactions, in which adsorption and diffusion regimes are modulated by the surface topography and hydrophobicity of the sensing layer.

Contribution

I prepared part of the introduction for this manuscript and reviewed and edited the final version of the manuscript.

8.4 Contact Engineering in Single-Walled Carbon Nanotube Thin-Film Transistors: Implications for Silane-Treated SiO_2 Substrates.

Brendan Mirka, Nicole A. Rice, Chloé M. Richard, Dominique Lefebvre, Benjamin King, William J. Bodnaryk, Darryl Fong, Alex Adronov, and Benoît H. Lessard*

Publication Date: 15th September 2022

Citation: *ACS Appl. Nano Mater.*, **2022**, 5 (9), 12487–12495.

DOI: https://doi.org/10.1021/acsanm.2c02052

Abstract

Semiconducting single-walled carbon nanotubes (sc-SWCNTs) are promising candidates for thin-film transistors (TFTs). The interface between this semiconducting material and the metal electrodes is critical for both device performance and mechanical robustness, such as adhesion. Sc-SWCNTs were incorporated into top-contact TFTs with different source-drain contact interlayers as a means of improving gold adhesion to silane-treated SiO_2 substrates and to study the effect of the contact interlayers on TFT performance. Molybdenum trioxide (MoO_3), manganese (Mn), chromium (Cr), and 2,9-dimethyl-4,7-diphenyl-1,10-phenanthroline (BCP) were all investigated as potential contact interlayers. The incorporation of contact interlayers significantly improved TFT device yield; additionally, the presence of a MoO_3 or Mn interlayer resulted in a much higher yield of working TFTs compared to devices made using bare Au. Sc-SWCNT TFTs characterized in air showed a smaller dependence on the contact interlayer compared to TFTs characterized in nitrogen, despite differences in the work function of the contact electrodes. In air, there was little to no difference in contact resistance and other metrics when comparing MoO_3–Au and Au contacts, while a drop in performance was observed for Mn–Au-, Cr–Au-, and BCP–Au-based devices. When testing in nitrogen, Mn–Au was comparable to Au and MoO_3–Au contacts. These differences suggest oxygen adsorption at the contact surface and that the contact interface is contributing to changes in electrical performance depending on the choice of contact material.

Contribution

I fabricated electrodes by physical vapour deposition for adhesion testing.

8.5 Correlating morphology, molecular orientation and transistor performance of bis(penta fluorophenoxy) silicon phthalocyanine using Scanning Transmission X-ray Microscopy.

Chloé Dindault, Benjamin King, Phillip Williams, Joseph Habib Absi, Marie D. M. Faure, Sufal Swaraj, and Benoît H. Lessard.

Publication Date: 9th May, 2022

Citation: *Chem. Mater.*, **2022**, 34 (10), 4496–4504.

DOI: https://doi.org/10.1021/acs.chemmater.2c00277

Abstract

Understanding the effect of processing conditions on thin-film morphology is required to develop high-performance organic thin-film electronics such as organic thin-film transistors. Thin films of bis(pentafluorophenoxy) silicon phthalocyanine (F_{10}-SiPc) were evaporated onto surfaces treated with or without octyltrichlorosilane while being held at different substrate temperatures from room temperature to 150 °C. Scanning transmission X-ray microscopy (STXM), performed at various orientations of the linearly polarized monochromatic X-rays, was used to investigate the resulting film morphology. By monitoring the intensity of the $\pi_{C=C^*}$ transition from the fluorinated substituent as a function of the polarization angle, we were able to determine the local molecular orientation. Processing the compositional maps enabled the development of structure–property relationships between processing conditions through plane domain sizes and grain boundaries. Atomic force microscopy, which only characterizes the thin-film surface, corroborated the STXM morphology results. This study highlights the potential of STXM to enable a comprehensive characterization across the entire thickness of silicon phthalocyanine thin films and simultaneously prove molecular orientational maps in addition to the morphological features of the domains of the film, not just the surface.

Contribution

I synthesized and purified the silicon phthalocyanine derivative, and prepared surface treated STXM membranes and substrates for device fabrication in this study. I fabricated, tested, and characterized OTFTs and interpreted the device data. I also completed and interpreted atomic force microscopy measurements. I reviewed and edited the final version of the manuscript.

8.6 Employing aldol condensation to prepare benzodifurandione-based small molecules for application in thin-film transistors.

Anindya Ganguly, Benjamin King, and Benoît H. Lessard and Jaclyn L. Brusso*

Publication Date: 4th May, 2022
Citation: Synth. Met., **2022**, 287, 117090.
DOI: https://doi.org/10.1016/j.synthmet.2022.117090

Abstract

A family of benzodifurandione-based small molecules is reported by employing aldol condensation reactions with aldehydes of selected heterocycles, ring-fused functional groups, and fluorinated phenyl substituents. The influence of the peripheral moieties on the resulting optical and electrochemical properties were analyzed, revealing that the absolute energy levels within this series of benzodifurandione-based small molecules are significantly impacted, whereas the difference in HOMO/LUMO energy gap is moderate. Upon incorporation of these materials into organic thin-film transistors through physical vapor deposition, the thiophene-capped benzodifurandione derivative exhibited average hole mobilities of 10^{-4} $cm^2 \cdot V^{-1} \cdot s^{-1}$ both in air and vacuum. Although device performance was less than ideal for this series of compounds, this may be attributed to poor thin film morphology as determined by atomic force microscopy.

Contribution

I fabricated and characterized OTFTs for this study and interpreted the data. I completed solid-state UV-Vis spectroscopy, X-ray diffraction, and atomic force microscopy measurements and interpreted the data. I wrote the experimental and results sections related to thin-film and device fabrication, characterization, UV-Vis, X-ray diffraction and atomic force microscopy. I reviewed and edited the final version of the manuscript.

8.7 Highlighting the processing versatility of a silicon phthalocyanine derivative for organic thin-film transistors.

Rosemary R. Cranston, Benjamin King, Chloé Dindault, Trevor M. Grant, Nicole A. Rice, Claire Tonnelé, Luca Muccioli, Frédéric Castet, Sufal Swaraj and Benoît H. Lessard

Citation: *J. Mater. Chem. C*, **2022**, 10, 485-495.

Publication Date: 16th December 2021

DOI: https://doi.org/10.1039/D1TC05238A

Abstract

Silicon phthalocyanine (SiPc) derivatives have recently emerged as promising materials for n-type organic thin-film transistors (OTFTs) with the ability to be fabricated either by solid state or solution processes through axial functionalization. Among those, bis(tri-*n*-propylsilyl oxide) SiPc ($(3PS)_2$-SiPc) is unique as it can be processed by sublimation, while being soluble enough for solution processing. In this work, the charge transport properties of $(3PS)_2$-SiPc and its polymorphic forms were studied through Kinetic Monte Carlo (KMC) simulations and density functional theory (DFT) calculations along with the characterization of $(3PS)_2$-SiPc in n-type OTFTs fabricated by physical vapour deposition (PVD) and spin coating. Post-deposition thin-film characterization by X-ray diffraction (XRD), atomic force microscopy (AFM), and scanning transmission X-ray microscopy (STXM) was used to assess film morphology and microstructure in relation to the electrical performance of OTFTs. The differences in film formation by PVD and solution fabrication had little effect on OTFT performance with comparable field-effect mobility and threshold voltage ranging between 0.01–0.04 $cm^2 V^{-1} s^{-1}$ and 18–36 V respectively. Consistent charge transport properties of $(3PS)_2$-SiPc OTFTs achieved at different fabrication conditions highlights the processing versatility of this material.

Contribution

I fabricated $(3PS)_2$-SiPc OTFTs and processed them by thermal annealing. I also characterized the electrical performance of these devices and characterized their thin-film crystallinity and morphology by X-ray diffraction and atomic force microscopy. Finally, I contributed to the experimental and results sections of the written manuscript and edited the final version of the manuscript prior to submission.

8.8 Exploring ellagic acid as a building block in the design of organic semiconductors.

Mélanie Cyr, Benjamin King, Benoît H. Lessard and Jaclyn L. Brusso*

Citation: *Dye. Pigm.*, **2022**, 199, 109998.

Publication Date: 11th December 2021

DOI: https://doi.org/10.1016/j.dyepig.2021.109998

Abstract

Ellagic acid (H_4EA), a natural polyphenol, is an ideal candidate in the search for sustainable materials for use in organic electronics due to its strong resemblance to other well-known polyaromatic hydrocarbons being employed in the field such as pyrene. The work presented herein focuses on the functionalization of H_4EA with aryl moieties via S_NAr reactions, thereby affording a facile two-step approach to tailor the optoelectronic properties of the resulting organic semiconductors. In particular, pyrazine and quinoxaline moieties were selected to due to the presence of additional nitrogen atoms along with the π-system afforded through their molecular frameworks. The results presented demonstrate that such functionalization of H_4EA does in fact impact the finetuning of the photophysical and structural properties of the resulting materials. Although performance was less than ideal when implemented into thin-film transistors, this may be attributed to poor film morphology. Nonetheless, this work introduces new green materials to the field, through which facile functionalization can be realized.

Contribution

I fabricated and characterized OTFTs for this study and interpreted the data. I completed solid-state UV-Vis spectroscopy, X-ray diffraction, and atomic force microscopy measurements and interpreted the data. I wrote the experimental and results sections related to thin-film and device fabrication, characterization, UV-Vis, X-ray diffraction and atomic force microscopy. I reviewed and edited the final version of the manuscript.

8.9 Attaining air stability in high performing n-type phthalocyanine based organic semiconductors.

Nathan J. Yutronkie, Benjamin King, Owen A. Melville, Benoît H. Lessard and Jaclyn L. Brusso*

Citation: *J. Mater. Chem. C.*, **2021**, *9,* 10119-10126.

Publication Date: 19th July 2021

DOI: https://doi.org/10.1039/D1TC02275J

Abstract

The perfluorinated analogue of silicon phthalocyanine (**F_2-F_{16}SiPc**) has been synthesized as a novel air-stable n-type organic semiconductor. The design of **F_2-F_{16}SiPc** facilitates strong electron conduction through peripheral fluorination that deepens molecular orbital energies, while contributing to an extensive network of $\pi\cdots\pi'$ and $F\cdots F'$ interactions that promote a highly symmetric three-dimensional assembly as determined *via* single-crystal X-ray diffraction. When incorporated into organic thin-film transistors (OTFTs), electron mobilities for **F_2-F_{16}SiPc**-based devices reached performances on par with current benchmark phthalocyanine-based devices under inert environments (up to 0.30 $cm^2\ V^{-1}\ s^{-1}$), while surpassing performances under atmospheric conditions (up to 0.17 $cm^2\ V^{-1}\ s^{-1}$). These observations highlight the impact molecular and crystallographic engineering has in the development of organic-based electronics, as the **F_2-F_{16}SiPc** building block lays new grounds for the development of air-stable n-type OTFTs.

Contribution

I fabricated all OTFTs in this work and characterized their electronic properties in nitrogen and in air. I also took UV-Vis spectroscopy, X-ray diffraction and atomic force microscopy measurements of semiconductor films. Finally, I prepared the experimental and results sections of the manuscript related to OTFTs and thin-film characterization and reviewed the final manuscript prior to submission.

8.10 Contact Engineering using Manganese, Chromium and Bathocuproine in Group 14 Phthalocyanine Organic Thin-Film Transistors

Owen A. Melville, Trevor M. Grant, Kate Lochhead, Benjamin King, Ryan Ambrose, Nicole A. Rice, Nicholas T. Boileau, Alexander J. Peltekoff, Mathieu N. Tousignant, Ian G. Hill, and Benoît H. Lessard*

Citation: *ACS Appl. Electron. Mater.* **2020**, 2 (5), 1313-1322.

Publication Date: 24th March 2020

DOI: https://doi.org/10.1021/acsaelm.0c00104

Abstract

Silicon and tin(IV) phthalocyanines, which have been demonstrated as simple-to-synthesize materials for n-type organic thin-film transistors (OTFTs), have relatively shallow lowest unoccupied molecular orbital (LUMO) levels that create a Schottky barrier with the gold source–drain contacts typically used in device fabrication. To reduce the contact resistance (R_C) associated with this barrier and improve the OTFT performance, we fabricated bottom-gate top-contact (BGTC) devices using low-work-function metals (Mn/Cr) and an electron dopant material (bathocuproine, BCP) as contact interlayers. We characterized two tin phthalocyanines (SnPcs), tin bis(pentafluorophenoxy)phthalocyanine (F_{10}-SnPc) and tin bis(2,4,6-trifluorophenoxy)phthalocyanine (246F-SnPc), as organic semiconductors (OSCs) and compared them to their silicon phthalocyanine (SiPc) analogues. We found that using Mn and Cr interlayers with SiPc OTFTs reduces R_C to as low as 11.8 kΩ cm and reduces the threshold voltage (V_T) to as low as 7.8 V while improving linear region characteristics compared to devices using silver or gold electrodes only. BCP interlayers appear to reduce V_T in all SiPc and SnPc devices and increase the off-state conductivity of SnPc devices if covering the entire OSC. Overall, this work demonstrates the potential for metal interlayers and solid-state organic interlayers for improving electron transport in low-cost, n-type OTFTs using group 14 phthalocyanines.

Contribution

I fabricated devices of F_{10}-SiPc and 246F-SiPc with gold and silver electrodes and manganese and BCP interlayers and characterized their electronic properties. I also reviewed the manuscript prior to submission.